

# **Experimental and Computational Approaches to Investigate the High Oxidation State Oxo- and Hydroxido- Redox Chemistry of Osmium**

by

Daniel Malan Emmanuel van Niekerk

*Dissertation presented for the degree of  
Doctor of Philosophy in Chemistry at  
Stellenbosch University*



Supervisor: Dr W. J. Gerber  
Co-supervisor: Prof. K. R. Koch  
Faculty of Science  
Department of Chemistry and Polymer Science

March 2016

## **Declaration**

By submitting this dissertation electronically, I declare that the entirety of the work contained therein is my own, original work, that I am the sole author thereof (save to the extent explicitly otherwise stated), that reproduction and publication thereof by Stellenbosch University will not infringe any third party rights and that I have not previously in its entirety or in part submitted it for obtaining any qualification.

March 2016

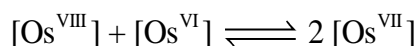
Copyright © 2016 University of Stellenbosch

All rights reserved

## Abstract

The Os<sup>VIII</sup> oxo/hydroxido complexes that are abundant in mild to relatively concentrated basic aqueous solutions are Os<sup>VIII</sup>O<sub>4</sub>, [Os<sup>VIII</sup>O<sub>4</sub>(OH)]<sup>-</sup> and two *cis*-[Os<sup>VIII</sup>O<sub>4</sub>(OH)<sub>2</sub>]<sup>2-</sup> species. Os<sup>VIII</sup> complexes that contain water ligands are thermodynamically unfavoured *w.r.t.* the abovementioned complexes. Os<sup>VIII</sup>O<sub>4</sub> reacts with hydroxide in two, consecutive, elementary coordination sphere expansion steps to form the [Os<sup>VIII</sup>O<sub>4</sub>(OH)]<sup>-</sup> complex and then the *cis*-[Os<sup>VIII</sup>O<sub>4</sub>(OH)<sub>2</sub>]<sup>2-</sup> species. The thermodynamic driving force of the first reaction is the bonding energy of the Os<sup>VIII</sup>-OH metal-hydroxido ligand, while of the second reaction it is the larger hydration energy of the doubly-charged *cis*-[Os<sup>VIII</sup>O<sub>4</sub>(OH)<sub>2</sub>]<sup>2-</sup> in comparison with that of the two, singly-charged reactants. The DFT-calculated  $\Delta G^{\circ}_{rxn}$  in the simulated aqueous phase (COSMO) is -2.42 kcal.mol<sup>-1</sup> for the first reaction and -0.61 kcal.mol<sup>-1</sup> for the second reaction (PBE-D3 functional) and agree to within 1 kcal.mol<sup>-1</sup> with reported values, at -2.69 and 0.33 kcal.mol<sup>-1</sup>, respectively. The thermodynamically most stable paramagnetic Os<sup>VII</sup> product species in a 2.0 M NaOH aqueous matrix are the five-coordinate *trans*-[Os<sup>VII</sup>O<sub>3</sub>(OH)<sub>2</sub>]<sup>-</sup> and octahedral *mer*-[Os<sup>VII</sup>O<sub>3</sub>(OH)<sub>3</sub>]<sup>2-</sup> stereoisomers. The thermodynamic driving force of the coordination sphere expansion reaction of *trans*-[Os<sup>VII</sup>O<sub>3</sub>(OH)<sub>2</sub>]<sup>-</sup> with a hydroxide ion to form *mer*-[Os<sup>VII</sup>O<sub>3</sub>(OH)<sub>3</sub>]<sup>2-</sup> is the larger hydration energy of the doubly-charged *mer*-[Os<sup>VII</sup>O<sub>3</sub>(OH)<sub>3</sub>]<sup>2-</sup> complex in comparison with that of the two, singly-charged reactants. The thermodynamically most stable Os<sup>VI</sup> species obtained *via* DFT is the diamagnetic *trans*-[Os<sup>VI</sup>O<sub>2</sub>(OH)<sub>4</sub>]<sup>2-</sup> species and the spin state of this species was confirmed with Evans method, <sup>1</sup>H NMR spectroscopy experiments. DFT-calculated metal-ligand bond lengths of the global energy minimum geometry of *trans*-[Os<sup>VI</sup>O<sub>2</sub>(OH)<sub>4</sub>]<sup>2-</sup> correlates well with reported X-ray crystal structure data. QTAIM and EDA analyses indicate that the Os<sup>VIII</sup>=O, Os<sup>VI</sup>=O and Os<sup>VII</sup>=O bonding interactions are ionic (closed-shell) and that Os<sup>VIII</sup>-OH, Os<sup>VI</sup>-OH and Os<sup>VII</sup>-OH bonding interactions are polar covalent (dative) while NCI analysis indicates that relatively weak intramolecular hydrogen bonding interactions occur between neighbouring oxo and hydroxido ligands in the [Os<sup>VIII</sup>O<sub>4</sub>(OH)]<sup>-</sup> and *cis*-[Os<sup>VIII</sup>O<sub>4</sub>(OH)<sub>2</sub>]<sup>2-</sup> species.

Diamagnetic Os<sup>VIII</sup> oxo/hydroxido, [Os<sup>VIII</sup>O<sub>4</sub>(OH)<sub>*n*</sub>]<sup>*n-*</sup> (*n* = 1, 2), (of *d*<sup>0</sup> electron configuration) and *trans*-[Os<sup>VI</sup>O<sub>2</sub>(OH)<sub>4</sub>]<sup>2-</sup> species (*d*<sup>2</sup>) react in a 1:1 mole ratio, in a 2.0 M NaOH aqueous matrix, to form paramagnetic Os<sup>VII</sup> product species (*d*<sup>1</sup>), equation 1.



1

The forward (comproportionation) reaction, equation 1, is first order w.r.t. the  $\text{Os}^{\text{VIII}}$  and  $\text{Os}^{\text{VI}}$  concentrations while the reverse (disproportionation) reaction is second order w.r.t. the  $\text{Os}^{\text{VII}}$  concentration. From non-linear least squares fits of stopped-flow UV-Vis spectroscopy kinetic traces, rate constants, thermodynamic activation energies and standard reaction energies were determined. The forward reaction is endothermic whilst the activation enthalpy of the reverse reaction is negative. A kinetic isotope effect (KIE) for the forward and reverse reactions, equation 1, are both approximately 1.1 providing evidence that the rate-determining step of the reactions coincide with the transfer of a proton. DFT-calculated standard reaction energies for the  $\text{Os}^{\text{VI}}$  &  $\text{Os}^{\text{VIII}}$  comproportionation reaction at 298.15 K (*e.g.* PBE,  $\Delta H^\circ_{rxn}$ ,  $\Delta S^\circ_{rxn}$  and  $\Delta G^\circ_{rxn}$  are 21.13 kcal.mol<sup>-1</sup>, 71.06 cal.mol<sup>-1</sup>.K<sup>-1</sup> and -0.06 kcal.mol<sup>-1</sup>, respectively) compare well with experimentally determined observed values ( $\Delta H^\circ_{rxn(\text{obs})}$ ,  $\Delta S^\circ_{rxn(\text{obs})}$  and  $\Delta G^\circ_{rxn(\text{obs})}$  are  $17.1 \pm 1.2$  kcal.mol<sup>-1</sup>,  $61.0 \pm 4.3$  cal.mol<sup>-1</sup>.K<sup>-1</sup> and  $-1.1 \pm 2.5$  kcal.mol<sup>-1</sup>, respectively). The DFT-calculated, most energetically favoured comproportionation reaction mechanism consists of (i) the formation of a (singlet state) adduct,  $[\text{Os}^{\text{VIII}}=\text{O}\cdots\text{HO}-\text{Os}^{\text{VI}}]^{3-}$ , (ii) ‘spin-forbidden’, concerted electron-proton transfer (EPT) from the  $\text{Os}^{\text{VIII}}$  monomer to the *trans*- $[\text{Os}^{\text{VI}}\text{O}_2(\text{OH})_4]^{2-}$  monomer to form a (triplet state) dimer,  $[\text{Os}^{\text{VII}}-\text{OH}\cdots\text{O}=\text{Os}^{\text{VII}}]^{3-}$ , (iii) separation of the  $\text{Os}^{\text{VII}}$  monomers and ultimately (iv) interconversion of the separated species to form a combination of the *trans*- $[\text{Os}^{\text{VII}}\text{O}_3(\text{OH})_2]^-$  and *mer*- $[\text{Os}^{\text{VII}}\text{O}_3(\text{OH})_3]^{2-}$  stereoisomers. EPT from the  $\text{Os}^{\text{VIII}}$  monomer to the  $\text{Os}^{\text{VI}}$  monomer is the rate-determining step of the reversible comproportionation reaction, corroborating the experimental evidence (KIE). Good agreement between experimental and DFT-calculated activation energies were obtained for the stepwise EPT reaction pathway. Sequential electron proton transfer (ET-PT or PT-ET) mechanisms for equation 1 are shown, *via* DFT calculations, not to occur in a 2.0 M NaOH matrix at 298.15 K.

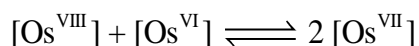
From non-linear least squares fits of UV-Vis spectroscopy kinetic traces, rate constants, thermodynamic activation energies and standard reaction energies for the reduction of  $\text{Os}^{\text{VIII}}$  with methanol ( $\text{CH}_3\text{OH}$  or  $\text{CD}_3\text{OH}$ ) in a 2.0 M NaOH aqueous matrix were determined. Cleavage of an  $\alpha$ -C-H bond in  $\text{CH}_3\text{OH}$  and the cleavage of an  $\alpha$ -C-D bond in  $\text{CD}_3\text{OH}$  are the rate-determining step for the two reactions. The relatively large KIE value,  $k_{\text{H}}/k_{\text{D}}$ , of approximately 11.82 (298.15 K) obtained is indicative of a normal, primary isotope effect. The complete, five-step DFT-calculated reaction pathway consists of (i) non-covalent dimer

formation of the reactants, (ii) hydrogen atom transfer (HAT) of an  $\alpha$ -C-H bond of CH<sub>3</sub>OH to *cis*-[Os<sup>VIII</sup>O<sub>4</sub>(OH)<sub>2</sub>]<sup>2-</sup>, (iii) PT of the O-H hydrogen of  $\cdot$ CH<sub>2</sub>OH to *mer*-[Os<sup>VII</sup>O<sub>3</sub>(OH)<sub>3</sub>]<sup>2-</sup>, (iv) ET from  $\cdot$ CH<sub>2</sub>O $\cdot$  to *trans*-[Os<sup>VII</sup>O<sub>4</sub>(OH)<sub>2</sub>]<sup>-</sup>, and (v) separation of the products. The organic and inorganic monomers involved in the elucidated reaction mechanism do not separate from one another between steps (ii) to (iv), but stay bound to one another *via* intermolecular hydrogen bonding interactions in order to firstly, decrease the PT/ET transfer distance between them, and secondly, to avoid the formation of highly energetically unfavourable cationic, anionic or radical monomer species. The mechanistic study agreed with our experimentally determined result that the rate-determining step of the reaction involves the cleavage of an  $\alpha$ -C-H bond in CH<sub>3</sub>OH. Fair agreement between activation energies of DFT-calculated (PBE-D3 functional), 19.1 kcal.mol<sup>-1</sup> ( $\Delta^\ddagger H^\circ$ ), -38.1 cal.mol<sup>-1</sup>.K<sup>-1</sup> ( $\Delta^\ddagger S^\circ$ ) and 30.5 kcal.mol<sup>-1</sup> ( $\Delta^\ddagger G^\circ$ ), and experimentally determined, 14.4  $\pm$  1.2 kcal.mol<sup>-1</sup> ( $\Delta^\ddagger H^\circ$ ), -12.5  $\pm$  4.1 cal.mol<sup>-1</sup>.K<sup>-1</sup> ( $\Delta^\ddagger S^\circ$ ) and 18.1  $\pm$  2.4 kcal.mol<sup>-1</sup> ( $\Delta^\ddagger G^\circ$ ), parameters were obtained.

## Uittreksel

Die Os<sup>VIII</sup> oxo/hydroxido komplekse wat volop is in matig tot relatief gekonsentreerde basiese waterige oplossings is Os<sup>VIII</sup>O<sub>4</sub>, [Os<sup>VIII</sup>O<sub>4</sub>(OH)]<sup>-</sup> en twee *cis*-[Os<sup>VIII</sup>O<sub>4</sub>(OH)<sub>2</sub>]<sup>2-</sup> spesies. Os<sup>VIII</sup> komplekse wat water ligande bevat is termodinamies ongunstig t.o.v. die bogenoemde komplekse. Os<sup>VIII</sup>O<sub>4</sub> reageer met hidrosied in twee agtereenvolgende, elementêre stappe naamlik; koördinasie sfeer uitbreiding na die [Os<sup>VIII</sup>O<sub>4</sub>(OH)]<sup>-</sup> kompleks gevolg deur die *cis*-[Os<sup>VIII</sup>O<sub>4</sub>(OH)<sub>2</sub>]<sup>2-</sup> spesie. Die termodinamiese dryfkrag van die eerste reaksie is die bindingsenergie van die Os<sup>VIII</sup>-OH metaal-hydroxido ligand, terwyl van die tweede reaksie is dit die groter hidrasie energie van die dubbel-gelaaide *cis*-[Os<sup>VIII</sup>O<sub>4</sub>(OH)<sub>2</sub>]<sup>2-</sup> in vergelyking met dié van die twee, een-een-gelaaide reaktante. Die DFT-benaderde  $\Delta G^{\circ}_{\text{rxn}}$  in die gesimuleerde waterige fase (COSMO) is -2.42 kcal.mol<sup>-1</sup> vir die eerste reaksie en -0.61 kcal.mol<sup>-1</sup> vir die tweede reaksie (PBE-D3 funksies) en stem ooreen binne 1 kcal.mol<sup>-1</sup> met rapporteerde waardes, teen -2.69 en 0.33 kcal.mol<sup>-1</sup> onderskeidelik. Die termodinamies mees stabiele paramagnetiese Os<sup>VII</sup> produk spesies in 'n 2.0 M NaOH waterige matriks is die vyf-koördineerde *trans*-[Os<sup>VII</sup>O<sub>3</sub>(OH)<sub>2</sub>]<sup>-</sup> en oktaëdriese *mer*-[Os<sup>VII</sup>O<sub>3</sub>(OH)<sub>3</sub>]<sup>2-</sup> stereoisomere. Die termodinamiese dryfkrag van die koördinasie sfeer uitbreiding reaksie van *trans*-[Os<sup>VII</sup>O<sub>3</sub>(OH)<sub>2</sub>]<sup>-</sup> met 'n hidrosiedioon om *mer*-[Os<sup>VII</sup>O<sub>3</sub>(OH)<sub>3</sub>]<sup>2-</sup> te vorm is die groter hidrasie energie van die dubbel-gelaaide *mer*-[Os<sup>VII</sup>O<sub>3</sub>(OH)<sub>3</sub>]<sup>2-</sup> kompleks in vergelyking met dié van die twee, een-een-gelaaide reaktante. Die termodinamies mees stabiele Os<sup>VI</sup> spesies verkry *via* DFT is die diamagnetiese *trans*-[Os<sup>VI</sup>O<sub>2</sub>(OH)<sub>4</sub>]<sup>2-</sup> spesies. Die spin toestand van hierdie spesie is bevestig deur middel van die Evans metode, <sup>1</sup>H-KMR spektroskopie eksperimente. DFT-berekene metaal-ligand bindings lengtes van die globale energie minimum geometrie van *trans*-[Os<sup>VI</sup>O<sub>2</sub>(OH)<sub>4</sub>]<sup>2-</sup> korreleer goed met gerapporteerde X-straal kristalstruktuur data. QTAIM en EDA ontledings dui daarop dat die Os<sup>VIII</sup>=O, Os<sup>VI</sup>=O en Os<sup>VII</sup>=O binding interaksies ioniese is ('closed-shell') en dat Os<sup>VIII</sup>-OH, Os<sup>VI</sup>-OH en Os<sup>VII</sup>-OH binding interaksies polêr kovalente (datief) is, terwyl NCI analise dui aan dat relatief swak intramolekulêre waterstofbinding interaksie plaas vind tussen naburige oxo en hydroxido ligande in die [Os<sup>VIII</sup>O<sub>4</sub>(OH)]<sup>-</sup> en *cis*-[Os<sup>VIII</sup>O<sub>4</sub>(OH)<sub>2</sub>]<sup>2-</sup> spesies.

Diamagnetiese Os<sup>VIII</sup> oxo/hydroxido, [Os<sup>VIII</sup>O<sub>4</sub>(OH)<sub>*n*</sub>]<sup>*n-*</sup> (*n* = 1, 2), (van *d*<sup>0</sup> elektronkonfigurasie) en *trans*-[Os<sup>VI</sup>O<sub>2</sub>(OH)<sub>4</sub>]<sup>2-</sup> spesies (*d*<sup>2</sup>) reageer in 'n 1:1 mol verhouding, in 'n 2.0 M NaOH waterige matriks, om paramagnetiese Os<sup>VII</sup> produk spesies (*d*<sup>1</sup>) te vorm, vergelyking 1.



1

Die vorentoe (komproportionasie) reaksie, vergelyking 1, is eerste orde met betrekking tot die  $\text{Os}^{\text{VIII}}$  en  $\text{Os}^{\text{VI}}$  konsentrasies terwyl die omgekeerde (disproporsionerings) reaksie tweede orde is met betrekking tot die  $\text{Os}^{\text{VII}}$  konsentrasie. Van nie-lineêre kleinste kwadratiese passings op stop-vloei, UV-Vis spektroskopiese kinetiese spore is; reaksie tempos, termodinamiese aktiveringsenergieë en standaard reaksie energieë bepaal. Die voorwaartse reaksie is endotermies terwyl die aktivering entalpie van die terugwaartse reaksie negatief is. Die kinetiese isotoop effek (KIE) vir die voorwaartse en terugwaartse reaksies, vergelyking 1, is albei ongeveer 1.1, ter bewyse dat die tempo-beperkende stap van die reaksies ooreenstem met die oordrag van 'n proton. DFT-berekende standaard reaksie energieë vir die  $\text{Os}^{\text{VI}}$  &  $\text{Os}^{\text{VIII}}$  komproportionasie reaksie by 298.15 K (bv PBE,  $\Delta H^{\circ}_{\text{rxn}}$ ,  $\Delta S^{\circ}_{\text{rxn}}$  en  $\Delta G^{\circ}_{\text{rxn}}$  is 21.13 kcal.mol<sup>-1</sup>, 71.06 cal.mol<sup>-1</sup>.K<sup>-1</sup> en -0.06 kcal.mol<sup>-1</sup> onderskeidelik) en vergelyk goed met eksperimenteel waargeneemde waardes ( $\Delta H^{\circ}_{\text{rxn(ops)}}$ ,  $\Delta S^{\circ}_{\text{rxn(ops)}}$  en  $\Delta G^{\circ}_{\text{rxn(ops)}}$  is  $17.1 \pm 1.2$  kcal.mol<sup>-1</sup>,  $61.0 \pm 4.3$  cal.mol<sup>-1</sup>.K<sup>-1</sup> en  $-1.1 \pm 2.5$  kcal.mol<sup>-1</sup> onderskeidelik). Die DFT-berekende, mees energie voordelige meganisme vir komproportionasie bestaan uit (i) die vorming van 'n ('singlet-state') nie-kovalente dimeer,  $[\text{Os}^{\text{VIII}}=\text{O}\cdots\text{HO}-\text{Os}^{\text{VI}}]^{3-}$ , (ii) 'n spin-verbode elektron-proton oordrag (EPT) uit die  $\text{Os}^{\text{VIII}}$  monomeer met die *trans*- $[\text{Os}^{\text{VI}}\text{O}_2(\text{OH})_4]^{2-}$  monomeer om 'n tweede ('triplet-state') nie-kovalente dimeer te vorm,  $[\text{Os}^{\text{VII}}-\text{OH}\cdots\text{O}=\text{Os}^{\text{VIII}}]^{3-}$ , (iii) die skeiding van die  $\text{Os}^{\text{VII}}$  monomere en uiteindelik (iv) van die onderling geskeide spesies om 'n kombinasie van die *trans*- $[\text{Os}^{\text{VII}}\text{O}_3(\text{OH})_2]^{-}$  en *mer*- $[\text{Os}^{\text{VII}}\text{O}_3(\text{OH})_3]^{2-}$  stereoisomere te vorm. EPT van die  $\text{Os}^{\text{VIII}}$  monomeer na die  $\text{Os}^{\text{VI}}$  monomeer is die tempo-beperkende stap van die omkeerbare komproportionasie reaksie, ter ondersteuning van eksperiment (KIE). Goeie ooreenkoms tussen eksperimentele en DFT-berekende aktiveringsenergieë is verkry vir die stapsgewyse EPT reaksie pad. Die sekwensiële elektron proton oordrag (ET-PT of PT-ET) meganismes vir vergelyking 1 vind nie, *via* DFT berekeninge, plaas in 'n 2.0 M NaOH matriks teen 298.15 K nie.

Vanuit nie-lineêre kleinste kwadratiese passings op UV-Vis spektroskopiese kinetiese spore, is reaksie tempos, termodinamiese aktiveringsenergieë en standaard reaksie energie vir die reduksie van  $\text{Os}^{\text{VIII}}$  met metanol ( $\text{CH}_3\text{OH}$  of  $\text{CD}_3\text{OH}$ ) in 'n 2.0 M NaOH waterige matriks bepaal. Klowing (Cleaving) van 'n  $\alpha$ -C-H binding in  $\text{CH}_3\text{OH}$  en die klowing van 'n  $\alpha$ -C-D binding in  $\text{CD}_3\text{OH}$  is die tempo-beperkende stap vir die twee reaksies. Die relatiewe groot KIE waarde  $k_{\text{H}}/k_{\text{D}}$ , van ongeveer 11.82 (298.15 K) verkry is 'n aanduiding van 'n normale,

primêre isotoop effek. Die volledige vyf-stap-DFT-berekende reaksie pad bestaan uit (i) nie-kovalente dimeer vorming van die reagense, (ii) waterstofatoom oordrag (HAT) van 'n  $\alpha$ -C-H binding van CH<sub>3</sub>OH na *cis*-[Os<sup>VIII</sup>O<sub>4</sub>(OH)<sub>2</sub>]<sup>2-</sup>, (iii) PT van die O-H waterstof van  $\cdot$ CH<sub>2</sub>OH na *mer*-[Os<sup>VII</sup>O<sub>3</sub>(OH)<sub>3</sub>]<sup>2-</sup>, (iv) ET van  $\cdot$ CH<sub>2</sub>O<sup>-</sup> na *trans*-[Os<sup>VII</sup>O<sub>4</sub>(OH)<sub>2</sub>]<sup>-</sup> en (v) die skeiding van die produkte. Die organiese en anorganiese monomere betrokke in die meganisme bly gebind aan mekaar tussen stappe (ii) tot (iv), *via* intermolekulêre waterstofbinding interaksies om eerstens, PT/ET oordrag afstand te verminder, en tweedens, om die vorming van hoogs energie ongunstige kationiese, anioniese of radikale monomeer spesies te voorkom. Die meganistiese studie stem ooreen met ons eksperimentele bepaling, dat die tempo-beperkende stap van die reaksie behels die klowing van 'n  $\alpha$ -C-H binding in CH<sub>3</sub>OH. Billike ooreenkoms tussen aktivering energie van DFT-bereken (PBE-D3 funksionele), 19.1 kcal.mol<sup>-1</sup> ( $\Delta^\ddagger H^\circ$ ), -38.1 cal.mol<sup>-1</sup>.K<sup>-1</sup> ( $\Delta^\ddagger S^\circ$ ) en 30.5 kcal.mol<sup>-1</sup> ( $\Delta^\ddagger G^\circ$ ), en eksperimenteel bepaal, 14.4 ± 1.2 kcal.mol<sup>-1</sup> ( $\Delta^\ddagger H^\circ$ ), -12.5 ± 4.1 cal.mol<sup>-1</sup>.K<sup>-1</sup> ( $\Delta^\ddagger H^\circ$ ) en 18.1 ± 2.4 kcal.mol<sup>-1</sup> ( $\Delta^\ddagger H^\circ$ ), parameters is verkry.



## **Acknowledgements**

I would like to acknowledge and thank the following people for contributions to my studies:

First and foremost, my project supervisor, Dr Gerber, for the supervision, mentoring and motivation throughout the research and writing up of the project.

Secondly, my co-supervisor, Prof. Koch, for all the suggestions and contributions offered during progress presentation meetings.

Finally, the three students who have been a part of our relatively young research group over the past three years including Dr Geswindt, Sean O’Kennedy and Barend Greyling, for everyday chemistry-related discussions.

## Publications and Posters

### This study

We intend to, in the near future, publish the work presented in this thesis.

### Other work

W. J. Gerber, P. -H. van Wyk, D. M. E. van Niekerk and K. R. Koch, *Phys. Chem. Chem. Phys.*, *The fundamental flaw of the HSAB principle is revealed by a complete speciation analysis of the  $[PtCl_{6-n}Br_n]^{2-}$  ( $n = 0 - 6$ ) system*, DOI: 10.1039/c4cp05294c

### Conferences

A section of the work presented by this thesis was presented as a poster at the 16<sup>th</sup> South African Chemical Institute (SACI) inorganic chemistry conference in 2013 (INORG2013) entitled: *Experimental and Computational Approaches to Investigate the High Oxidation State Oxo- and Hydroxido- Redox Chemistry of Osmium*

## Glossary

AIL	Atomic interaction line
BCP	Bond critical point
BSSE	Basis set superposition error
COSMO	Conductor-like screening model
DFT	Density functional theory
ECP	Effective core potential
EDA	Energy decomposition analysis
EPR	Electron paramagnetic resonance
EPT	concerted electron-proton transfer
ET	electron transfer
ETS-NOCV	Extended transition state, natural orbitals for chemical valence
GGA	Generalised gradient approximation
HAT	Hydrogen atom transfer
Hz	Hertz
KIE	Kinetic isotope effect
MECP	Minimum energy crossing point
NCI	Non-covalent interactions
NMR	Nuclear Magnetic Resonance
PCET	Proton-coupled electron transfer
PES	Potential energy surface
PGMs	Platinum group metals
PT	Proton transfer

QTAIM	Quantum Theory of Atoms in Molecules
RDG	Reduced density gradient
SCF	Self-consistent field
UV-Vis	Ultra-Violet Visible
vdW	van der Waals

# Table of Contents

<b>1. Introduction and Background</b>	<b>1</b>
1.1 A short history of osmium	1
1.2 General coordination chemistry of osmium	2
1.3 Industrial applications of osmium	3
1.4 Osmium refining and project problem identification	4
1.5 Specific aims of this study	9
1.6 Chemical reactions that involve the transfer of electrons and/or protons	9
1.6.1 Proton-coupled electron transfer (PCET)	10
1.6.2 Minimum energy crossing points (MECP)	16
1.7 Density functional theory (DFT)	17
1.7.1 Dispersion corrections with DFT	19
<b>2. Experimental and Computational Methods</b>	<b>26</b>
2.1 Experimental methods	26
2.1.1 Apparatus	26
2.1.2 Software used to process experimentally obtained data	27
2.1.3 Reagents utilised	27
2.1.4 Preparation and standardisation procedure of sodium hydroxide solutions	28
2.1.5 Preparation and storage of high purity potassium osmate	28
2.1.6 Preparation and storage of osmium tetroxide	28
2.1.7 Determination of osmium concentration – the thiourea	

colourimetric method	30
2.1.7.1    Experimental procedure	30
2.2    Computational methodology	31
<b>3. A DFT Study to Unravel the Kinetics and Thermodynamics of Os<sup>VIII</sup> oxo/hydroxido/aqua Complexes in Aqueous Matrices</b>	<b>38</b>
3.1    Introduction	38
3.2    Results and discussion	40
3.2.1    Thermodynamics and energy decomposition analysis (EDA) of Os <sup>VIII</sup> oxo/hydroxido/aqua complexes	40
3.2.2    Kinetics of coordination sphere expansion reactions 3.3 & 3.4	56
3.2.3    QTAIM analysis of the electron density topology of the Os <sup>VIII</sup> species	60
3.2.4    Non-covalent interactions (NCI) analysis of the Os <sup>VIII</sup> species	63
3.3    Conclusions	67
<b>4. A Spectroscopic Study of the Comproportionation Reaction of [Os<sup>VIII</sup>O<sub>4</sub>(OH)<sub>n</sub>]<sup>n-</sup> (n = 1, 2) and <i>trans</i>-[Os<sup>VI</sup>O<sub>2</sub>(OH)<sub>4</sub>]<sup>2-</sup> Species in a 2.0 M NaOH Aqueous Matrix</b>	<b>70</b>
4.1    Introduction	70
4.2    Results and discussion	71
4.2.1    Spectroscopic evidence of paramagnetic Os <sup>VII</sup> species	71
4.2.2    Os <sup>VI</sup> & Os <sup>VIII</sup> comproportionation reaction kinetics	79
4.2.2.1    Variable concentration, constant temperature	80
4.2.2.2    Variable temperature, constant concentration	84

4.2.2.3	Kinetic isotope effect (KIE) experiment – partially deuterated osmium sample	90
4.3	Conclusions	92
<b>5. Density Functional Theory (DFT) Speciation Study of Os<sup>VI</sup> and Os<sup>VII</sup> oxo/hydroxido Species; a Closer Look at the Thermodynamics of the Os<sup>VI</sup> &amp; Os<sup>VIII</sup> Comproportionation Reaction</b>		<b>97</b>
5.1	Introduction	97
5.2.	Results and discussion	98
5.2.1	DFT speciation study of the anionic Os <sup>VI</sup> complexes	98
5.2.2	DFT speciation study of the anionic Os <sup>VII</sup> complexes	100
5.2.3	Thermodynamic driving force of <i>trans</i> -[Os <sup>VII</sup> O <sub>3</sub> (OH) <sub>2</sub> ] <sup>-</sup> and <i>mer</i> -[Os <sup>VII</sup> O <sub>3</sub> (OH) <sub>3</sub> ] <sup>2-</sup> interconversion	105
5.2.4	Mechanism of reaction 5.7 - coordination sphere expansion?	107
5.2.5	QTAIM analysis of the electron density topology of the Os <sup>VI</sup> and Os <sup>VII</sup> species	108
5.2.6	Re-evaluation of the Evans method experiment for a five-coordinate Os <sup>VII</sup> oxo/hydroxido product species	111
5.2.7	Comparison of DFT-calculated and experimental thermodynamic standard reaction energies. Putting it all together – well, almost	112
5.3	Conclusions	131
<b>6. A DFT Mechanistic Study of the Os<sup>VI</sup> &amp; Os<sup>VIII</sup> Comproportionation Reaction in a Basic Aqueous Matrix</b>		<b>135</b>
6.1	Introduction	135
6.2	Results and discussion	139

6.2.1	Mechanism of the Os <sup>VI</sup> & Os <sup>VIII</sup> comproportionation reaction	139
6.2.2	Combining all the data for the EPT pathways	166
6.3	Conclusions	176
<b>7. A Kinetic UV-Vis Spectroscopic and DFT Mechanistic Study of the Redox Reaction of [Os<sup>VIII</sup>O<sub>4</sub>(OH)<sub>n</sub>]<sup>n-</sup> (n = 1, 2) and Methanol in a Basic Aqueous Matrix</b>		<b>180</b>
7.1	Introduction	180
7.2	Results and discussion	182
7.2.1	UV-Vis kinetic investigation of Os <sup>VIII</sup> reduction with methanol	182
7.2.1.1	Variable temperature, constant [Os <sup>VIII</sup> ] and [CH <sub>3</sub> OH]	183
7.2.1.2	Variable [CD <sub>3</sub> OD], constant [Os <sup>VIII</sup> ] and temperature	191
7.2.1.3	Variable temperature, constant [Os <sup>VIII</sup> ] and [CD <sub>3</sub> OD]	195
7.2.2	DFT investigation of Os <sup>VIII</sup> reduction with methanol (CH <sub>3</sub> OH)	205
7.2.2.1	Thermodynamics of Os <sup>VIII</sup> reduction with methanol	205
7.2.2.2	Preliminary mechanistic considerations of Os <sup>VIII</sup> reduction with methanol	206
7.2.2.3	DFT mechanistic study of <i>cis</i> -[Os <sup>VIII</sup> O <sub>4</sub> (OH) <sub>2</sub> ] <sup>2-</sup> reduction with methanol	208
7.2.2.4	DFT mechanistic study of [Os <sup>VIII</sup> O <sub>4</sub> (OH)] <sup>-</sup> reduction with methanol	222
7.3	Conclusions	224
<b>8. Conclusions</b>		<b>230</b>
<b>Appendix – supplementary information</b>		



# CHAPTER 1

---

## Introduction and Background

### 1.1 A short history of osmium

Osmium was named by Smithson Tennant in 1804 due to the characteristic odour of osmium tetroxide (derived from the Greek word *osme* – meaning smell, odour) after discovering the element in 1803. It is interesting to note that Tennant had earlier proposed to call the element *ptène* (from *ptenos* – meaning volatile), but was persuaded to abandon this idea.<sup>1</sup> Tennant had heated (to red heat, with caustic soda) the insoluble black residues which were left after the digestion of native platinum by *aqua regia*, cooled the melt and dissolved the resulting mass in water. The resulting yellow filtrate was acidified, which led to the generation of a white, volatile oxide, of which Tennant wrote:<sup>1</sup>

*“It stains the skin of a dark colour which cannot be effaced... (it has) a pungent and penetrating smell... from the extraction of a very volatile metal oxide... this smell is of its most distinguishing characters, I should on that account incline to call the metal Osmium”*

He obtained the osmium metal by reducing an aqueous solution of the oxide with copper, silver or zinc. The “volatile metal oxide” that Tennant referred to was osmium tetroxide, which is now known to have highly toxic effects, as documented by Brunot.<sup>2</sup> Brunot exposed himself to the toxic vapours in order to ascertain its toxicity. Upon exposure to the vapour, he noticed a metallic taste in his mouth and found that smoking was unpleasant; after 30 minutes, his eyes were smarting and tearing; after three hours, his chest was constricted and he had difficulty breathing. When he went outside, he noticed large haloes around street lights.

Subsequent research into the toxicity of osmium tetroxide revealed that the unpleasant side effects experienced by Brunot were a result of the reduction of the osmium tetroxide onto his eyes, skin and the mucosa of his airways. Concentrations in the air as low as  $10^{-7}$  g.m<sup>-3</sup> can cause lung congestion, skin and severe eye damage.<sup>3</sup>

Due to its toxicity, meticulous care must be taken when working with osmium in all its forms, particularly since it can be oxidised by atmospheric oxygen to form the volatile osmium tetroxide species.

## 1.2 General coordination chemistry of osmium

Osmium can be stable, depending on the ligand coordinated, in a wide variety of oxidation states.<sup>4</sup> It is the most versatile of all the platinum group metals (PGMs), even more so than Rhenium or Ruthenium. Examples of the main classes of complexes found for each oxidation state of osmium are listed in Table 1.1.

**Table 1.1. Oxidation states in coordination complexes of osmium.**<sup>4</sup>

Oxidation state	$d^n$	Abundance	Typical stabilising ligands	Examples <sup>a</sup>
VIII	$d^0$	Fairly rare	F <sup>-</sup> , O <sup>2-</sup> , N <sup>3-</sup>	OsO <sub>4</sub> , [OsO <sub>3</sub> F <sub>3</sub> ] <sup>-</sup> , [OsO <sub>3</sub> N] <sup>-</sup>
VII	$d^1$	Rare	F <sup>-</sup> , O <sup>2-</sup>	OsF <sub>7</sub> , [OsO <sub>4</sub> ] <sup>-</sup> , OsOF <sub>5</sub>
VI	$d^2$	Relatively common	F <sup>-</sup> , O <sup>2-</sup> , N <sup>3-</sup>	OsF <sub>6</sub> , <i>trans</i> -[OsO <sub>2</sub> X <sub>4</sub> ] <sup>n-</sup> , [OsNX <sub>4</sub> ] <sup>-</sup>
V	$d^3$	Rare	F <sup>-</sup>	[OsF <sub>6</sub> ] <sup>-</sup> , [OsF <sub>5</sub> ] <sub>4</sub>
IV	$d^4$	Common	F <sup>-</sup> , Cl <sup>-</sup> , Br <sup>-</sup> , I <sup>-</sup> , OH <sup>-</sup> , PR <sub>3</sub> , OH <sup>-</sup> , LR <sub>3</sub>	[OsX <sub>6</sub> ] <sup>2-</sup> , [Os(NH <sub>3</sub> ) <sub>4</sub> X <sub>2</sub> ] <sup>2+</sup> , <i>trans</i> -Os(LR <sub>3</sub> ) <sub>2</sub> X <sub>4</sub>
III	$d^5$	Common	Cl <sup>-</sup> , Br <sup>-</sup> , I <sup>-</sup> , NH <sub>3</sub> , acac, en, LR <sub>3</sub>	[OsX <sub>6</sub> ] <sup>3-</sup> , [Os(NH <sub>3</sub> ) <sub>6</sub> ] <sup>3+</sup> , [Os en <sub>3</sub> ] <sup>3+</sup> , Os(LR <sub>3</sub> ) <sub>3</sub> X <sub>3</sub>
II	$d^6$	Common	CN <sup>-</sup> , bipy, phen, NO <sup>+</sup> , terpy, LR <sub>3</sub>	[Os(CN) <sub>6</sub> ] <sup>4-</sup> , [Os(bipy) <sub>3</sub> ] <sup>2+</sup> , [Os(phen) <sub>3</sub> ] <sup>2+</sup> , [Os(NO)X <sub>5</sub> ] <sup>2-</sup> , <i>trans</i> -Os(LR <sub>3</sub> ) <sub>4</sub> X <sub>2</sub>
I	$d^7$	Doubtful	? NO <sup>+</sup>	Os(NO)(PPh <sub>3</sub> ) <sub>2</sub> Cl <sub>2</sub>
0	$d^8$	Fairly rare	CO, P(OR) <sub>3</sub> , PF <sub>3</sub>	Os(CO) <sub>5</sub> , Os <sub>3</sub> (CO) <sub>12</sub> , Os{P(OR) <sub>3</sub> } <sub>5</sub> , Os(PF <sub>3</sub> ) <sub>5</sub>
-I	$d^9$	Very rare	NO	Os(NO)depe <sub>2</sub>
-II	$d^{10}$	Fairly rare	NO <sup>+</sup> , CO, PF <sub>3</sub>	Os(NO) <sub>2</sub> (PPh <sub>3</sub> ) <sub>2</sub> , [Os(CO) <sub>4</sub> ] <sup>2-</sup> , [Os(PF <sub>3</sub> ) <sub>4</sub> ] <sup>2-</sup>

<sup>a</sup> L = P, As or Sb; R = alkyl or aryl; X = Cl, Br, I.

The major reason for osmium's versatility is due to the position that this element assumes within the group of transition metals in the periodic table.<sup>4</sup> As a member of the third row of transition metals, the outer 5*d* orbitals are fairly exposed, which increases the electrophilic

character of its  $5d$  orbitals towards coordinating ligands. In addition, its central position within the third row transition metals allows for the attainment of (i) the  $d^0$  electronic configuration typical of elements to the left of osmium in the periodic table and (ii) the  $d^{10}$  electronic configuration typical of elements to the right of osmium in the periodic table.<sup>4</sup> Consequently, osmium is classified as a metal which adopts various oxidation states through the nature of the coordinating ligands, making the chemistry of osmium quite unique and dynamic.

High oxidation state osmium species (VIII & VI oxidation states) are associated with strong  $\sigma$ - and  $\pi$ -donor ligands such as  $F^-$ ,  $O^{2-}$  and  $N^{3-}$ , since these ligands tend to form stable complexes with ions possessing few or no  $d$ -electrons.<sup>4</sup> Osmium(IV) and (III) oxidation state species are associated with ‘conventional’ ligands, *i.e.* those that have  $\sigma$ -donating capabilities such as ammonia, halides ( $F^-$ ,  $Cl^-$ ,  $Br^-$  and  $I^-$ ) and ethylenediamine. Low oxidation state osmium species (II to -II oxidation states) are associated with ligands having strong  $\pi$ -acceptor capabilities such as  $CO$  and  $NO^+$ , while ligands with moderate  $\pi$ -acceptor capabilities (*e.g.*  $CN^-$ , bipy, phen) will tend to favour the Osmium(II) ( $d^6$ ) oxidation state.

### 1.3 Industrial applications of osmium

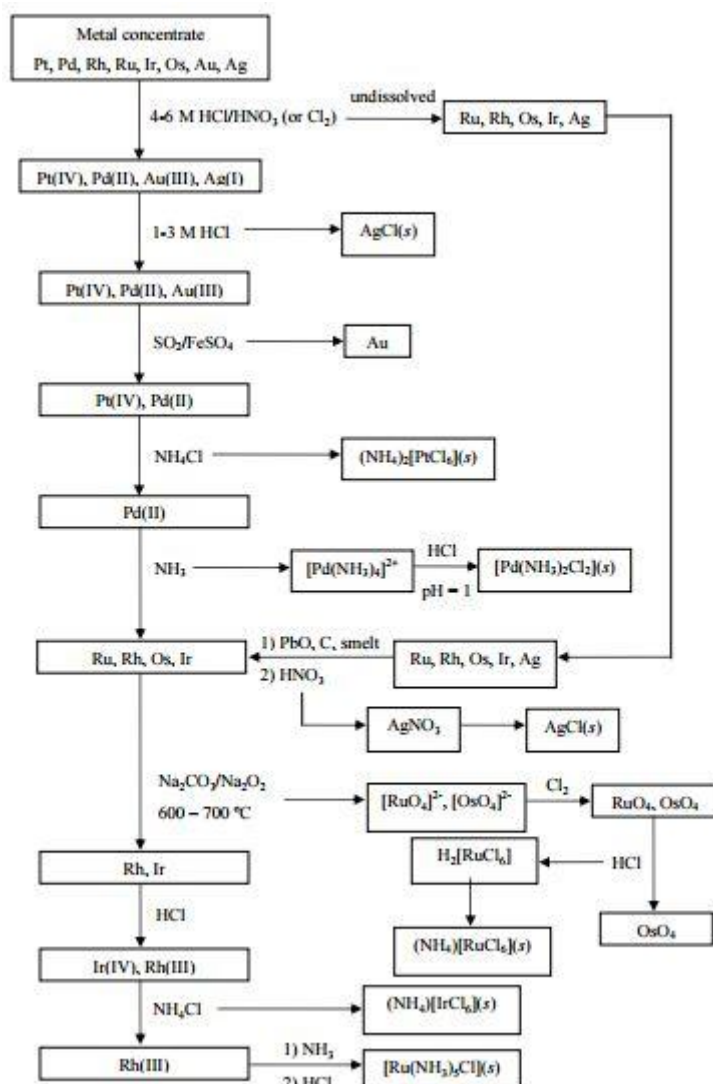
Due to its high density ( $22.587 \pm 0.009 \text{ g.cm}^{-3}$ ), osmium is frequently used in small quantities in alloys where frictional wear must be minimised. These alloys are typically used in ballpoint pen tips, fountain pen tips, record player needles, electrical contacts and high pressure bearings. It is therefore not surprising that osmium is no longer considered industrially important, considering this limited list of applications. A less dated application of osmium is the platinum/osmium (90:10 ratio) alloy used in implants such as pacemakers and replacement valves.<sup>5</sup> This alloy is used predominantly due to its resistance to corrosion, but is difficult and expensive to manufacture. Osmium tetroxide, although highly toxic, is still used as a biological fixative, for the preservation of biological tissue and its delineation for optical and electronic microscopy.<sup>6</sup>

The most useful application of osmium tetroxide is that it can act as a catalyst in organic oxidation reactions.<sup>7-11</sup> The most famous of these reactions is the industrially important dihydroxylation of alkenes in which osmium selectively *cis*-hydroxylate unsaturated organic compounds.<sup>12-20</sup> The usefulness of this reaction was highlighted when K. Barry Sharpless shared the 2001 Nobel Prize in Chemistry for his “development of catalytic asymmetric synthesis... on chirally catalysed oxidation reactions.”<sup>21</sup>

Due to the limited number of applications of osmium, in comparison with other PGMs, it is important to obtain a better understanding of its chemistry through further investigation of its properties under well-defined conditions. At present, osmium is extracted from platinum metal concentrates, Section 1.4, and ultimately stored in the form of the high oxidation state, potassium osmate salt,  $K_2[Os^{VI}O_2(OH)_4]$ . Due to the excess of stored osmium, it would be highly beneficial to the mining industry if useful applications of the osmate salt could be found.

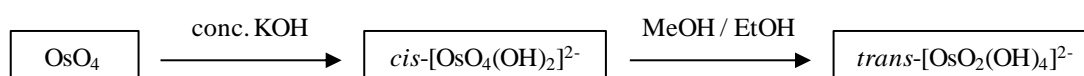
#### 1.4 Osmium refining and project problem identification

The modern method of extracting osmium does not differ greatly from Tennant's original procedure.<sup>1</sup> Scheme 1.1 depicts a simplified overview of the industrial separation process of precious metals from platinum metal concentrates.



**Scheme 1.1.** Conventional refining method for the separation of precious metals.<sup>22,23</sup>

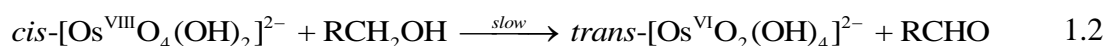
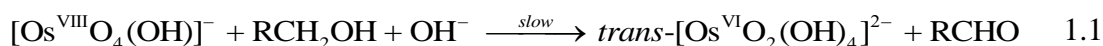
In the industrial separation process, osmium is separated from other PGMs by oxidative distillation.<sup>24-26</sup> The evolved Os<sup>VIII</sup>O<sub>4</sub> vapour is subsequently absorbed into a concentrated aqueous hydroxide solution, Scheme 1.2, to form the non-volatile perosmate, presumably the *cis*-[Os<sup>VIII</sup>O<sub>4</sub>(OH)<sub>2</sub>]<sup>2-</sup> complex dianion. The latter Os<sup>VIII</sup> oxo/hydroxido species is then reduced, by the addition of methanol or ethanol, to form a violet-coloured osmate salt, most likely the *trans*-[Os<sup>VI</sup>O<sub>2</sub>(OH)<sub>4</sub>]<sup>2-</sup> species. Several years ago, Anglo American Platinum contacted our research group to investigate the deceptively simple sequence of chemical reactions depicted by Scheme 1.2, since the available literature at that time differed from what was actually occurring in their refining plants.



**Scheme 1.2.** Simplified overview of osmium separation to produce *trans*-[OsO<sub>2</sub>(OH)<sub>4</sub>]<sup>2-</sup>.<sup>24-26</sup>

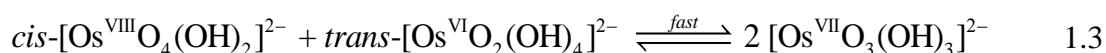
The study presented here focuses on three main related themes that deal with the chemistry of the reactions shown in Scheme 1.2. In particular, it is aimed to address the uncertainty in the reviewed literature regarding the oxidation of alcohols by Os<sup>VIII</sup> in basic aqueous media:

A relatively recent UV-Vis spectroscopy kinetic study<sup>27</sup> reported that the reduction of Os<sup>VIII</sup> oxo/hydroxido species with aliphatic alcohols in a 2.0 M NaOH aqueous matrix, at 298.15 K, occurs *via* a one-step, two-electron transfer to form *trans*-[Os<sup>VI</sup>O<sub>2</sub>(OH)<sub>4</sub>]<sup>2-</sup> species and an aldehyde, equations 1.1 & 1.2.



where R = H, CH<sub>3</sub>.

However, the authors discovered that an additional, relatively rapid, reaction was occurring simultaneously.<sup>27</sup> Since *trans*-[Os<sup>VI</sup>O<sub>2</sub>(OH)<sub>4</sub>]<sup>2-</sup> (of *d*<sup>2</sup> electron configuration) and *cis*-[Os<sup>VIII</sup>O<sub>4</sub>(OH)<sub>2</sub>]<sup>2-</sup> (*d*<sup>0</sup>) species are present in the reaction solution, the authors proposed that the ‘additional’ reaction is a comproportionation of the two high oxidation state Os<sup>VIII</sup> and Os<sup>VI</sup> dianions to form two paramagnetic [Os<sup>VII</sup>O<sub>3</sub>(OH)<sub>3</sub>]<sup>2-</sup> (*d*<sup>1</sup>) species, equation 1.3.



Though several reported kinetic studies pertaining to the reduction of  $\text{Os}^{\text{VIII}}\text{O}_4$  with molecular hydrogen, alcohols, diols and  $\alpha$ -hydroxy acids in basic aqueous matrices agree that the  $\text{Os}^{\text{VIII}}$  species are reduced to the  $\text{trans-}[\text{Os}^{\text{VI}}\text{O}_2(\text{OH})_4]^{2-}$  complex anion in a single, two-electron step, they do not report the formation of an  $\text{Os}^{\text{VII}}$  species during the reduction of  $\text{Os}^{\text{VIII}}$  to  $\text{Os}^{\text{VI}}$ .<sup>28-39</sup>

When Gerber *et al.*<sup>27</sup> recorded the kinetic traces of  $\text{Os}^{\text{VIII}}$  reduction as a function of the organic substrate (MeOH or EtOH), they observed that the absorbance first increases to a maximum, Figures 1.1 and 1.2. Since the only species in the solution that absorbs light at 370 nm are osmium species,<sup>27</sup> it was deduced that at least one more osmium species, other than an  $\text{Os}^{\text{VIII}}$  oxo/hydroxido or  $\text{trans-}[\text{Os}^{\text{VI}}\text{O}_2(\text{OH})_4]^{2-}$  species, is also present in solution.

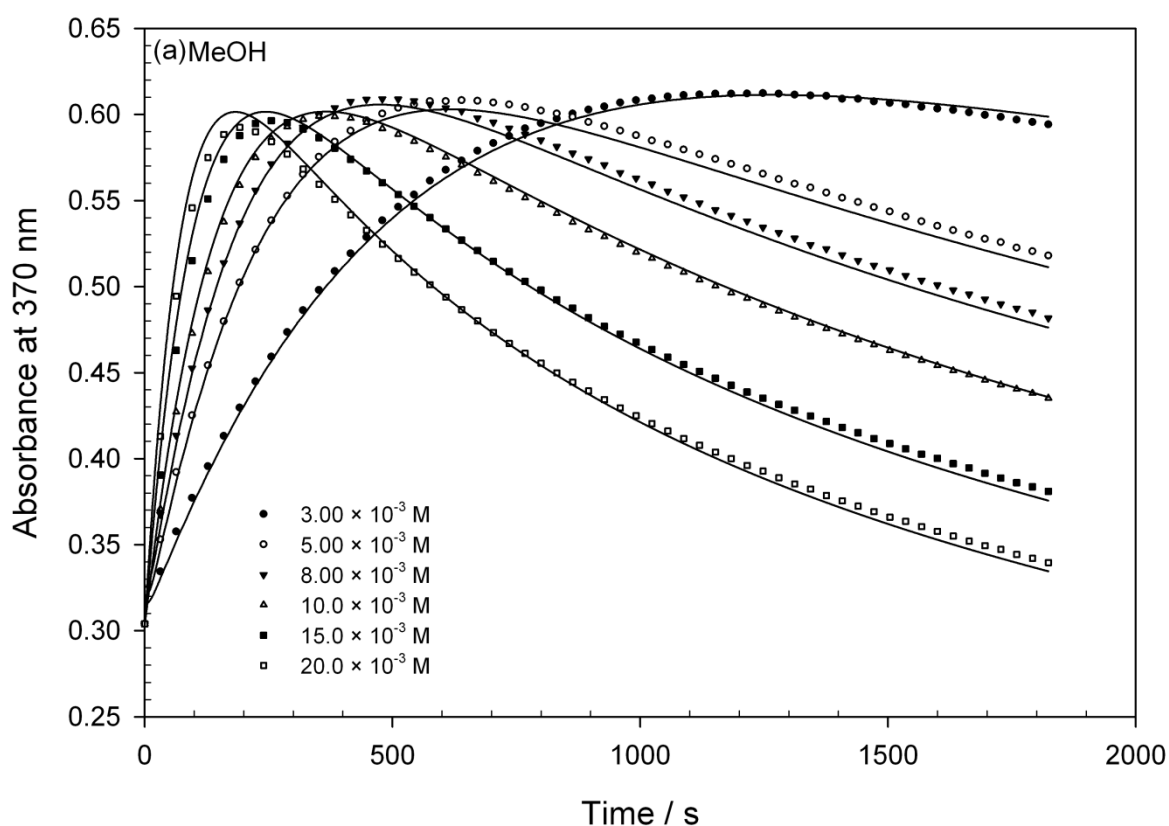


**Figure 1.1.** Kinetic traces depicting the change in absorbance as a function of time for the reactions of  $\text{Os}^{\text{VIII}}$  and methanol in a 2.0 M NaOH aqueous matrix at 298.15 K.<sup>27</sup> Reprinted with permission.

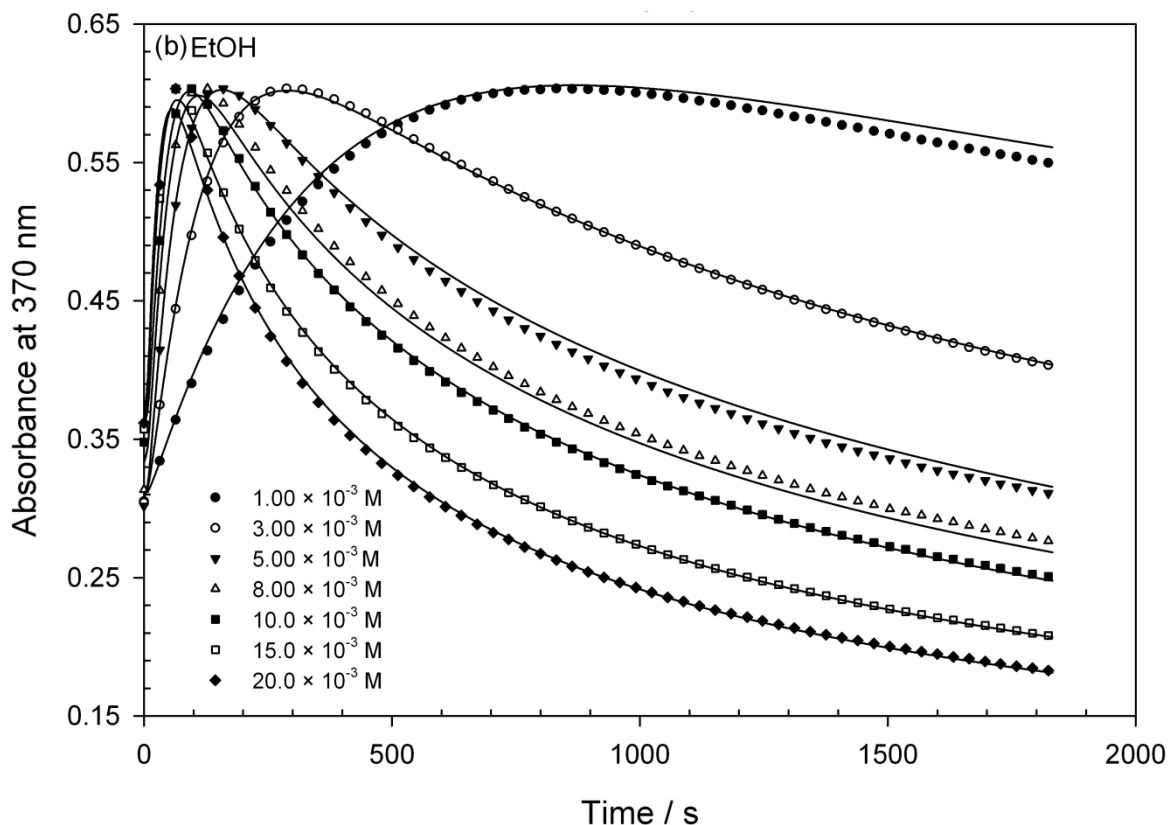


**Figure 1.2.** Kinetic traces depicting the change in absorbance as a function of time for the reactions of Os<sup>VIII</sup> and ethanol in a 2.0 M NaOH aqueous matrix at 298.15 K.<sup>27</sup> Reprinted with permission.

This unexpected and previously unreported result was verified by the addition of *trans*-[Os<sup>VI</sup>O<sub>2</sub>(OH)<sub>4</sub>]<sup>2-</sup> to *cis*-[Os<sup>VIII</sup>O<sub>4</sub>(OH)<sub>2</sub>]<sup>2-</sup> in the absence of aliphatic alcohols.<sup>27</sup> The unknown reaction was systematically studied using Job's method, Figure 1.3, as well as mole ratio titrations, Figure 1.4, to elucidate the reaction stoichiometry and thermodynamics. In addition to establishing the stoichiometry of the additional reaction, the study negates the possibility that an Os-alcohol complex forms.

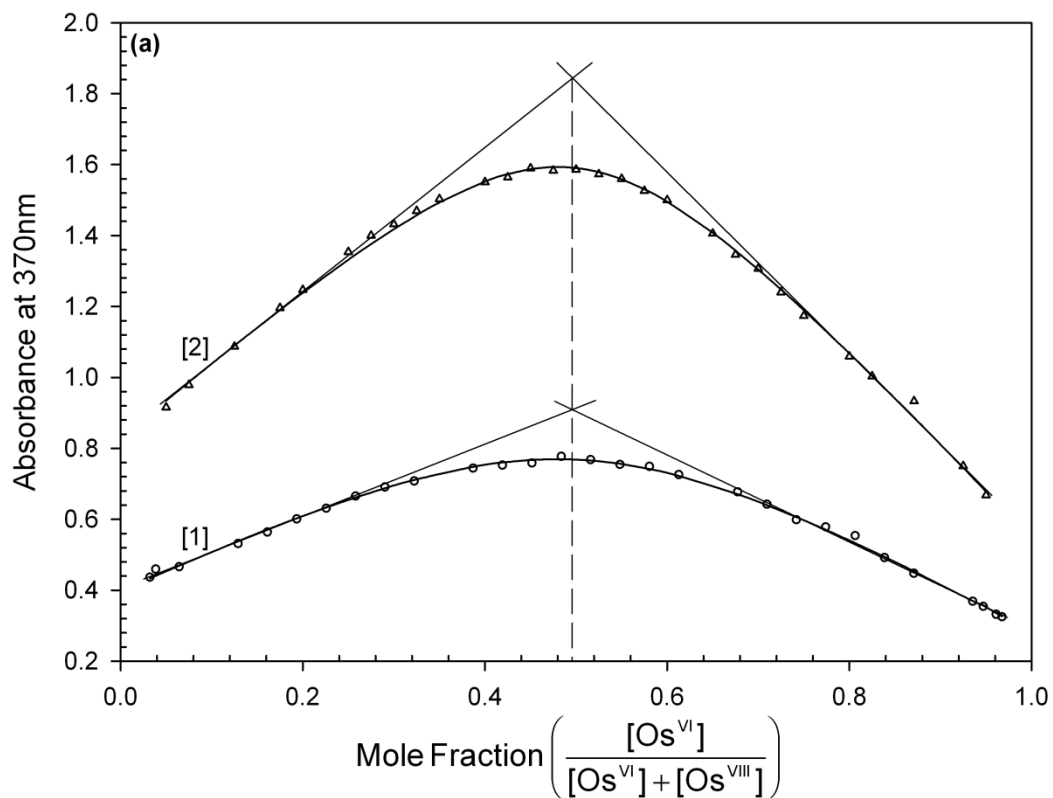


Figure 1.3. Job plots depicting 1:1 stoichiometry between  $\text{Os}^{\text{VI}}$  and  $\text{Os}^{\text{VIII}}$  reactants.<sup>27</sup> Reprinted with permission.

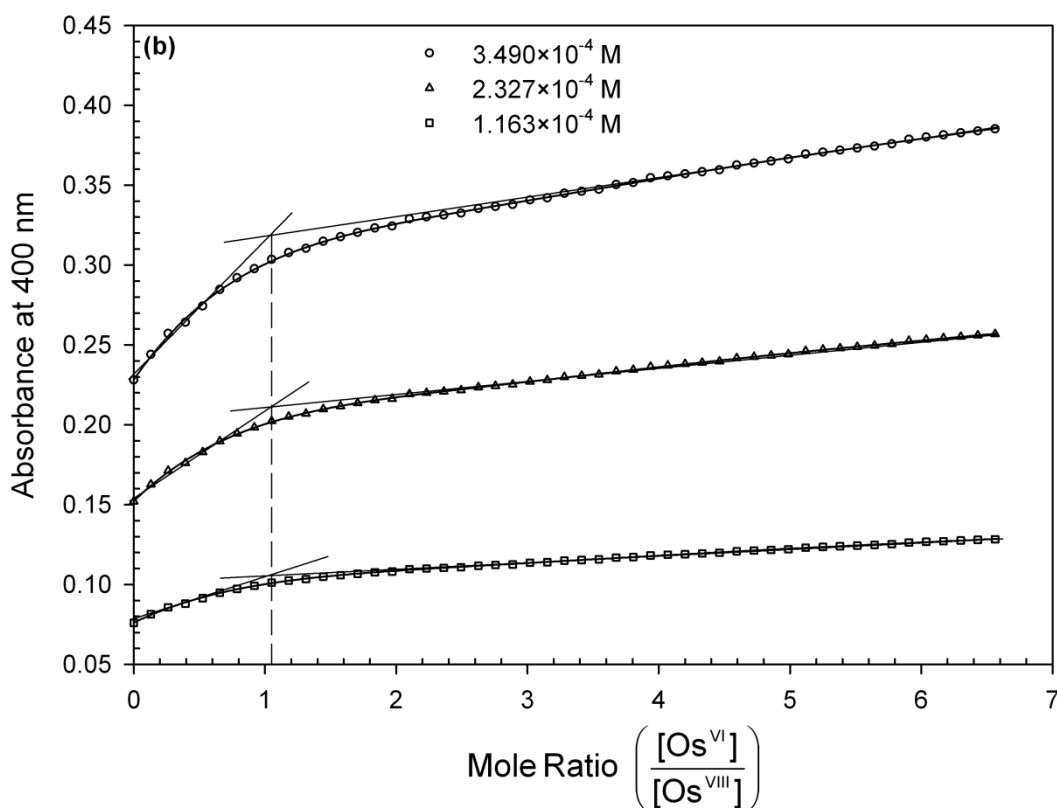


Figure 1.4.  $\text{Os}^{\text{VI}}$  vs.  $\text{Os}^{\text{VIII}}$  mole ratio titrations supporting the proposed 1:1 stoichiometry.<sup>27</sup> Reprinted with permission.



Subsequent to the publication of the Os<sup>VI</sup> & Os<sup>VIII</sup> comproportionation reaction in 2011,<sup>27</sup> we realised that the deceptively simple chemical reactions described are much more complex than originally thought. This brings us to the specific aims that were outlined for the project.

### 1.5 Specific aims of this study

The basis of this thesis is to corroborate and continue the research on the initial findings regarding the Os<sup>VI</sup> & Os<sup>VIII</sup> comproportionation reaction.<sup>1</sup> In summary, there are three overarching themes:

- (i) Detailed thermodynamic speciation studies of Os<sup>VIII</sup> (Chapter 3), Os<sup>VI</sup> and Os<sup>VII</sup> (Chapter 5) oxo/hydroxido species in basic aqueous media with density functional theory (DFT),
- (ii) Investigation of the proposed Os<sup>VI</sup> & Os<sup>VIII</sup> comproportionation reaction in basic aqueous media, using <sup>1</sup>H NMR spectroscopy and stopped-flow UV-Vis spectroscopy kinetic methods to prove that the reaction does indeed occur (Chapters 4 and 5), and DFT studies to subsequently elucidate the reaction mechanism (Chapter 6), and
- (iii) Spectroscopic and DFT speciation study of the kinetics, thermodynamics and reaction mechanism pertaining to the reduction of Os<sup>VIII</sup> oxo/hydroxido species with methanol in basic aqueous media (Chapter 7).

In order to investigate the reduction of Os<sup>VIII</sup> oxo/hydroxido species with methanol in basic aqueous media, theme (iii), it is necessary to first investigate the Os<sup>VI</sup> & Os<sup>VIII</sup> comproportionation reaction, theme (ii), since both these species are then present in solution.<sup>27</sup> However, in order to investigate both of these mentioned reactions properly, *i.e.* schemes (iii) and (ii), it is essential to first fully understand the details regarding the thermodynamics of all the reactant and product species involved, which include Os<sup>VIII</sup>, Os<sup>VI</sup> and Os<sup>VII</sup> oxo/hydroxido species.<sup>27</sup>

### 1.6 Chemical reactions that involve the transfer of electrons and/or protons

The oxidation of methanol with Os<sup>VIII</sup> oxo/hydroxido species involves the transfer of electrons and probably protons.<sup>27</sup> The proposed Os<sup>VI</sup> & Os<sup>VIII</sup> comproportionation reaction also involves the transfer of an electron, from the *trans*-[Os<sup>VI</sup>O<sub>2</sub>(OH)<sub>4</sub>]<sup>2-</sup> species, and possibly

---

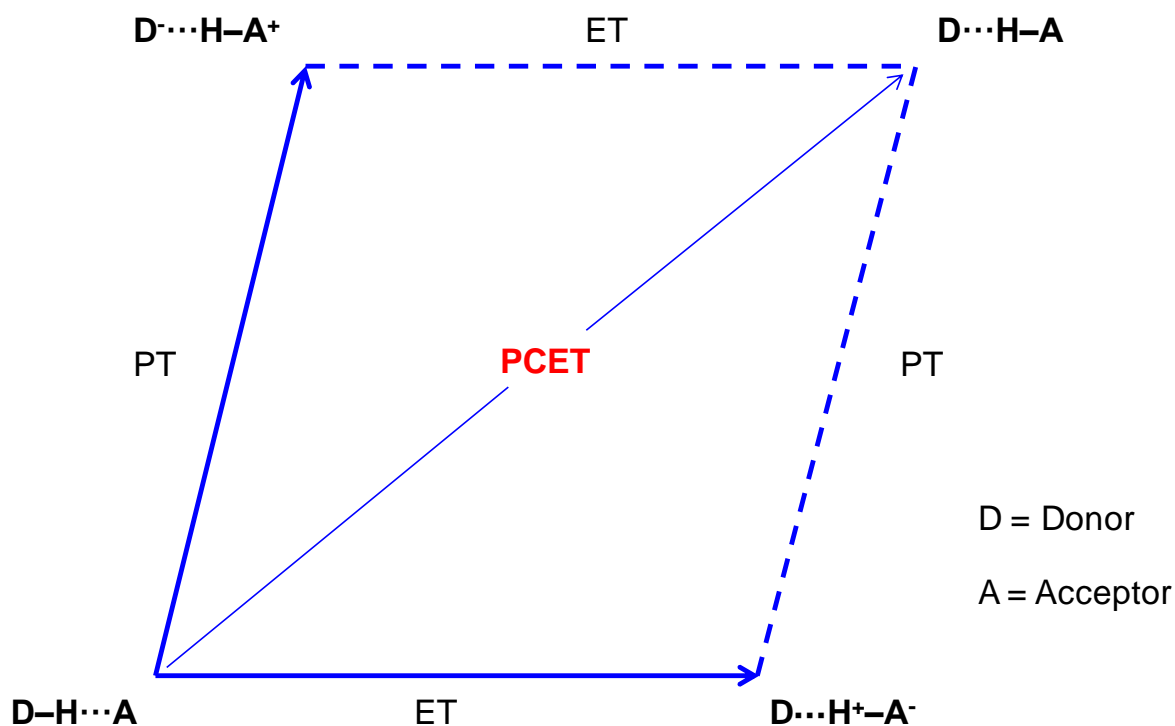
<sup>1</sup> To prevent duplication, the reader is referred to the introductions of Chapters 3 – 7 for specific, in-depth discussions which serve as the main motivations and problem identifications for this study.

also the transfer of a proton (*vide infra*).<sup>27</sup> Reactions that involve such transfer(s) are classified under a specific ‘class’ of chemical reactions, known as proton-coupled electron transfer (PCET), Section 1.6.1.

The postulated Os<sup>VII</sup> oxo/hydroxido product species<sup>27</sup> of the proposed Os<sup>VI</sup> & Os<sup>VIII</sup> comproportionation reaction has the rare  $d^1$  electronic configuration (Table 1.1). Since the total electronic spin changes during this reaction, *i.e.* the ‘transition state/s’ is/are neither a singlet (as are the reactants) nor a triplet (as are the postulated products); a minimum energy crossing point (MECP) is used to describe the processes, Section 1.6.2.

### 1.6.1 Proton-coupled electron transfer (PCET)

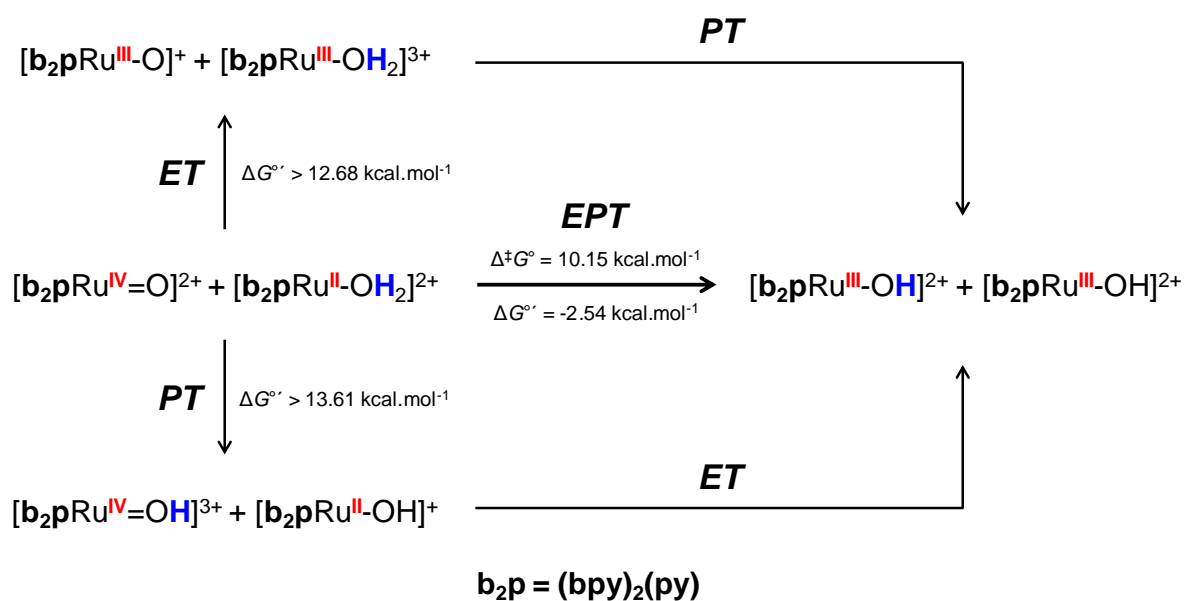
Chemical reactions that involve the transfer of an electron and a proton can occur by sequential or concerted mechanisms.<sup>40</sup> Sequential mechanisms proceed by initial electron transfer (ET) or initial proton transfer (PT) and the concerted mechanism, termed proton-coupled electron transfer (PCET), takes place without formation of any intermediates. These three energy pathways, the sequential ET-PT and PT-ET steps and concerted electron-proton transfer are illustrated in Scheme 1.3.



**Scheme 1.3.** Sequential and concerted electron-proton transfer pathways.

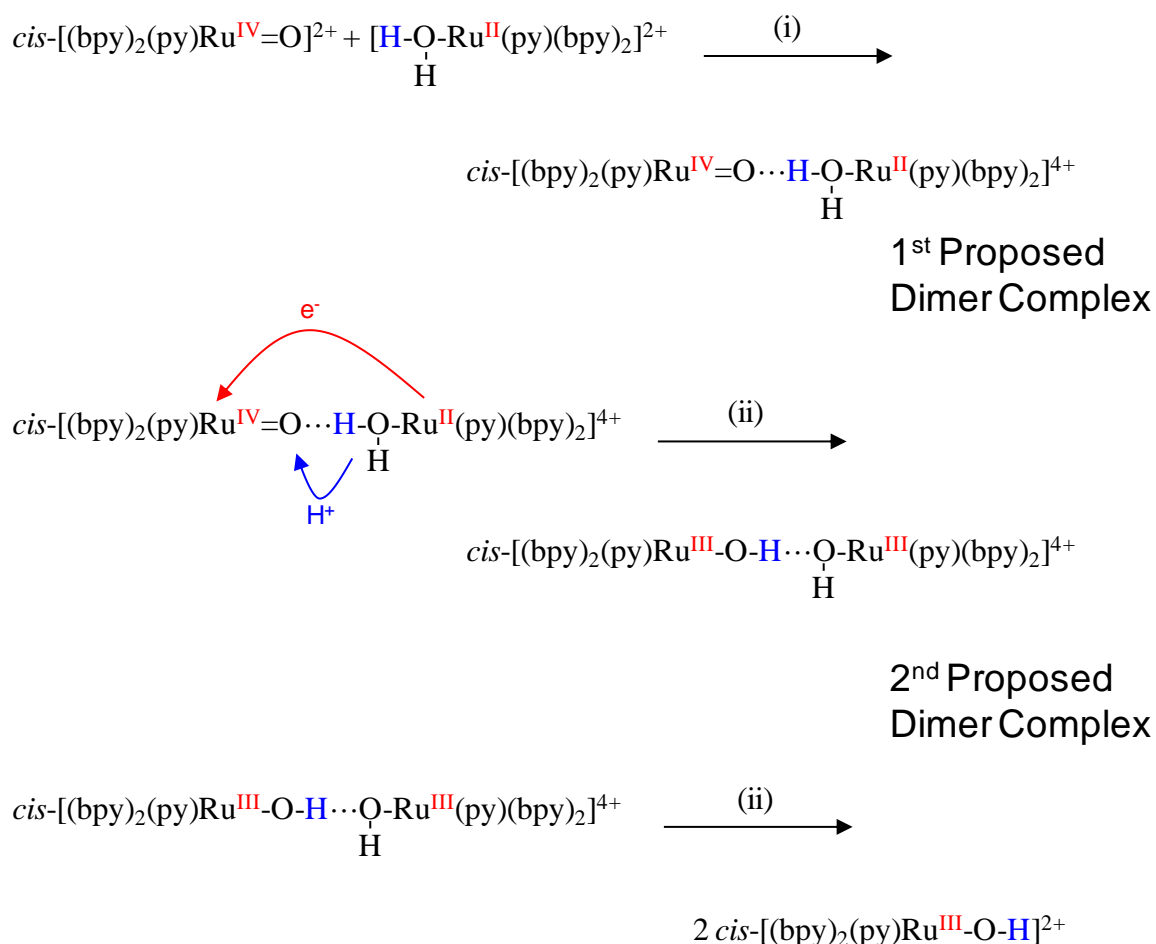
The term PCET was introduced in 1981 to describe an elementary step, like electron transfer or proton transfer, but in which electrons and protons transfer together.<sup>40</sup> It has since come to be used more broadly to describe reactions and half reactions in which both electrons and protons are transferred without regard to mechanism. However, the nomenclature used to describe the various pathways in concerted electron-proton transfer has not been standardised and conflicting nomenclature has been used. Alternate terms from the literature include acronyms such as CEP (concerted electron-proton transfer),<sup>41</sup> CPET (concerted proton-electron transfer)<sup>42</sup> and ET-PT (electron transfer proton transfer)<sup>43</sup>. The use of EPT,<sup>40</sup> as used in this study, is descriptive, consistent with existing terminology and provides a systematic nomenclature for a family of reactions that differ in microscopic detail, but in all of which concerted electron-proton transfer is the defining redox event.

The term PCET was originally used to describe the concerted  $e^-/H^+$  transfer process (EPT) that occurs in the comproportionation reaction between  $[Ru^{IV}(bpy)_2(py)(O)]^{2+}$  ( $[Ru^{IV}=O]^{2+}$ ) (of  $d^4$  configuration) and  $[Ru^{II}(bpy)_2(py)(OH_2)]^{2+}$  ( $[Ru^{II}-OH_2]^{2+}$ ) ( $d^6$ ).<sup>44-49</sup> In this reaction an electron and proton are transferred simultaneously from  $[Ru^{II}-OH_2]^{2+}$  to  $[Ru^{IV}=O]^{2+}$  to give two  $[Ru^{III}-OH]^{2+}$  ( $d^5$ ) species. Furthermore, it is reported that, at pH = 7, EPT dominates the comproportionation reaction because it avoids the high energy intermediates that form for stepwise PT and ET pathways, Scheme 1.4. The minimum values of  $\Delta G^\circ$  cited for PT and ET, regarded as minimum free energies of activation, were found to be comparatively larger than the experimental free energy of activation, ruling them out as major contributors to the comproportionation reaction.



**Scheme 1.4.** (Adapted)  $\text{Ru}^{\text{II}}$  &  $\text{Ru}^{\text{IV}}$  comproportionation reaction PCET pathways (at pH = 7) by means of initial electron transfer (via stepwise ET-PT), initial proton transfer (via stepwise PT-ET) and concerted electron-proton transfer (EPT).<sup>40</sup>

A three-step mechanism was described for the EPT pathway in the comproportionation reaction which consists of (i) hydrogen-bond preassociation of the reactants, (ii) concerted electron-proton transfer (EPT) and (iii) separation of the products, Scheme 1.5.<sup>44-49</sup>



**Scheme 1.5.** (*Adapted*) Three-step reaction mechanism described for comproportionation via EPT.<sup>40</sup>

Preassociation with hydrogen bonding is required because of the short-range nature of proton transfer.<sup>40</sup> Given the high frequency of the O-H vibrational modes for a proton transfer, at or near room temperature, the proton transfer step is inherently quantum mechanical with rapid rates relying on preassociation to minimise the proton transfer distance and maximise the vibrational wave function overlap. Because of the proton's heavier mass,  $\nu(\text{E-H})$  wave functions fall off with distance much more rapidly than electronic wave functions, by  $\lambda_e/\lambda_H \approx 40$ . The decrease in radial extension necessitates hydrogen bonding to minimise the proton transfer distance (proton tunnelling distance) in EPT. Consequently, PT is fundamentally limited to short distances, whereas the electron, as the lighter particle, may transfer over very long distances.<sup>40</sup>

In the key EPT step, Scheme 1.5, concerted  $e^-/\text{H}^+$  transfer occurs with electron transfer from a metal-based  $d\pi$  orbital ( $t_{2g}$  in  $O_h$  symmetry) at the donor,  $[\text{Ru}^{\text{II}}-\text{OH}]^{2+}$ , to a  $d\pi$  acceptor orbital at the acceptor,  $[\text{Ru}^{\text{IV}}=\text{O}]^{2+}$ .<sup>44-49</sup> Proton transfer occurs from a  $\sigma(\text{O-H})$  orbital at the donor,  $[\text{Ru}^{\text{II}}-\text{OH}]^{2+}$ , to an O-based lone pair orbital at the acceptor,  $[\text{Ru}^{\text{IV}}=\text{O}]^{2+}$ . Importantly, in an

EPT elementary step *electrons and protons transfer from different orbitals on the donor to different orbitals on the acceptor*.

Moreover, the  $e^-/H^+$  donor orbitals and the  $e^-/H^+$  acceptor orbitals in EPT interact electronically, which enables ‘simultaneous’ transfer (*vide infra*).<sup>40</sup> ‘Simultaneous’ in this sense means rapid relative to the periods for coupled vibrations (tens of femtoseconds) and solvent modes (~1 ps). Furthermore, in EPT there is no discrete ET or PT intermediate equilibrated with its surroundings. If there were, the underlying thermodynamics would be those of the intermediate and not those of the final EPT products.

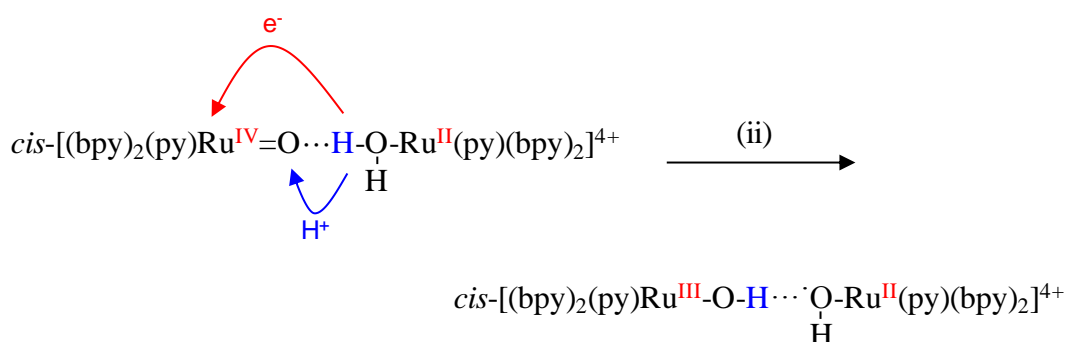
Both the hydrogen bonding and EPT steps, Scheme 1.5, require energetically accessible orbital binding sites at both the proton donor and proton acceptor monomer reactants.<sup>40</sup> Both the strength and symmetry of the donor-H and acceptor-H bonds play an important role. The proton tunnelling distance increases as asymmetry increases, decreasing rate and increasing kinetic isotope effects. Nearly symmetric hydrogen bonds between highly electronegative atoms (found in biological structures, for example) minimise the proton transfer distance which causes enhanced EPT rates.

Proton motion along the proton transfer coordinate is described by a linear combination of the high frequency (2000-4000  $\text{cm}^{-1}$ )  $\nu(\text{E-H})$  vibrational modes before and after proton transfer occurs.<sup>50-52</sup> Because of the high quantum spacings between these vibrational levels, proton transfer occurs by way of quantum mechanical tunnelling and not classical barrier crossing.

The electron transfer part of EPT is induced by an electrostatic perturbation between electron donor and acceptor.<sup>40</sup> The perturbation causes the donor and acceptor electronic wave functions to mix. Furthermore, hydrogen bonding can also promote  $d\pi-d\pi$  electronic coupling along the hydrogen bond as in  $[\text{Ru}^{\text{IV}}=\text{O}\cdots\text{H}-\text{O}(\text{H})\text{Ru}^{\text{II}}]$  EPT, Scheme 1.5.

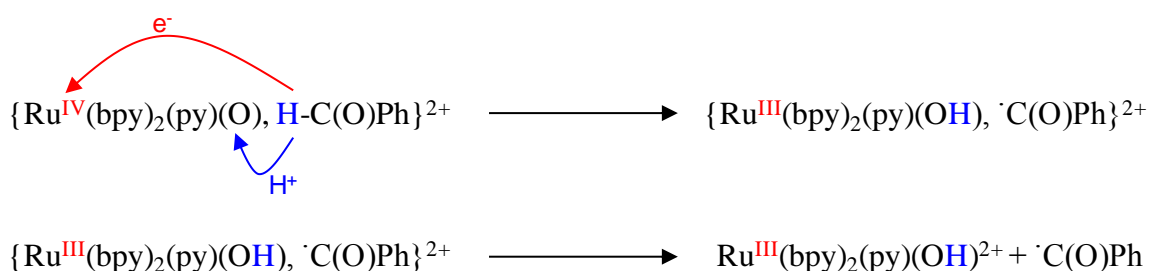
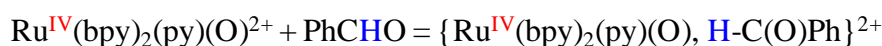
The EPT mechanism, Scheme 1.5, leads to the final, energetically stable  $[\text{Ru}^{\text{III}}-\text{OH}]^{2+}$  products and is thermodynamically favoured to the products of the H-atom transfer (HAT) mechanism.<sup>49</sup> Both the HAT and EPT pathways are elementary steps by which PCET can occur.<sup>40</sup> However, in contrast to EPT, in HAT *both the transferring electron and proton come from the same bond in one of the reactants*.  $e^-/H^+$  transfer occurs from a  $\sigma(\text{O-H})$  orbital at  $[\text{Ru}^{\text{II}}-\text{OH}_2]^{2+}$  to electron ( $d\pi_{\text{Ru}}$ )/proton ( $p_{\text{O}}$ ) acceptor orbitals at  $[\text{Ru}^{\text{VI}}=\text{O}]^{2+}$ , giving  $[\text{Ru}^{\text{III}}-\text{OH}]^{2+}$  and a high energy charge transfer intermediate,  $[\text{Ru}^{\text{II}}-\text{O}^\bullet-\text{H}]^{2+}$ , Scheme 1.6. The latter

is accessible by UV excitation of  $[\text{Ru}^{\text{III}}\text{-OH}]^{2+}$ ,  $[\text{Ru}^{\text{III}}\text{-OH}]^{2+} \xrightarrow{h\nu} [\text{Ru}^{\text{II}}\text{-O}\cdot\text{H}]^{2+}$ , with  $\lambda_{\text{max}}$  at  $\sim 320$  nm.



**Scheme 1.6.** (Adapted) HAT reaction mechanism for the same reactants.<sup>40</sup>

Another example of HAT is in the oxidation of benzaldehyde by  $[\text{Ru}^{\text{IV}}(\text{bpy})_2(\text{py})(\text{O})]^{2+}$ , Scheme 1.7.<sup>40</sup> Concerted  $e^-/\text{H}^+$  transfer occurs from benzaldehyde, but both the transferring electron and proton come from the  $\sigma(\text{O}-\text{H})$  bond of the aldehyde. In this reaction, the orbital pathway at  $[\text{Ru}^{\text{IV}}=\text{O}]^{2+}$  remains the same with electron transfer occurring to the  $d\pi$  electron acceptor orbital while  $\text{H}^+$  transfer occurs to a lone pair in a proton-acceptor orbital at  $[\text{Ru}^{\text{IV}}=\text{O}]^{2+}$ . This is an example of a mixed-orbital pathway.



**Scheme 1.7.** (Adapted) An example of HAT reaction mechanism of the oxidation of benzaldehyde.<sup>40</sup>

The extent to which each of the possible pathways contributes for any PCET reaction depends on the energy changes that occur at each one of the steps. It is crucial that when investigating chemical reactions of this category, the thermochemistry and the intrinsic barriers of all the various individual reaction steps are considered in order to identify which pathway(s) are dominant.

### 1.6.2 Minimum energy crossing points (MECP)

Chemical reactions that involve a change in electronic spin are often referred to as ‘spin-forbidden’, however it is more appropriate to say that it is associated with a certain degree of spin-‘forbiddenness’, which is determined by the magnitude of the spin-orbit coupling term (SOC) of the system’s Hamiltonian.<sup>53-55</sup> Spin changes tend to be more strictly forbidden when the affected electrons are localised on light atoms and less so when they are on transition metals, Figure 1.5.

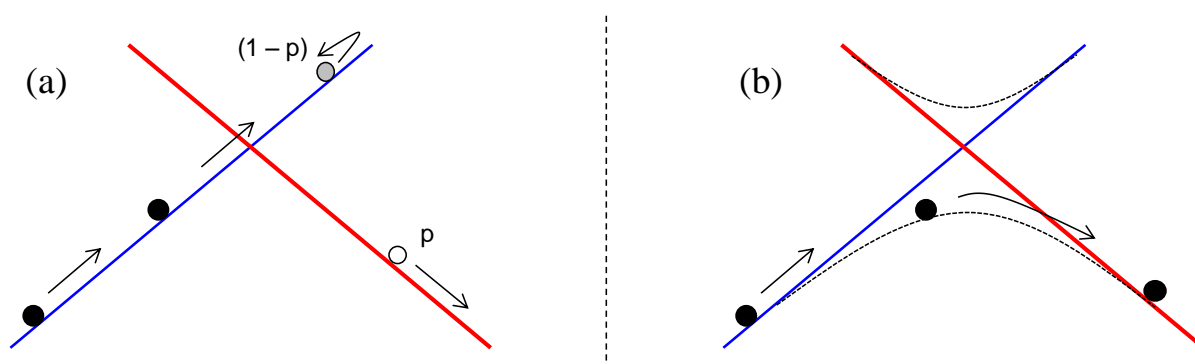


**Figure 1.5.** (Adapted) Schematic description of spin changes, in the low (a) and high (b) spin-orbit coupling limits.

A spin change can be thought of as occurring when the motion of the atoms of the chemical species brings the system into the region where the two potential energy surfaces (PESs) cross, and spin-orbit coupling then enables a ‘hop’ from one surface to the other. This is shown in part (a) of Figure 1.5, which also shows that this hopping is associated with a probability, shown as  $p$ . This first description is appropriate when spin-orbit coupling is small, so that the electronic structure is best described in terms of the two pure (or diabatic) spin states. However, spin-orbit coupling can be very strong in transition metal compounds, so that a better, or at least equally good, description of the electronic structure in the ‘crossing’ region involves electronic states and PESs of a mixed spin character, arising from an avoided crossing of the pure spin states. This mixed spin character is shown as dashed lines in Figure 1.5(b). The system then simply moves towards the crossing region, traverses it smoothly on the lowest mixed-spin (or ‘adiabatic’) surface, with the overall spin undergoing similarly smooth transition from one limiting value to the other. In this description, a spin-forbidden reaction is not very different from normal, spin-allowed, reactions. This is because the barriers forming the transition states in such reactions can be thought of as arising following the (strongly) avoided crossing of two diabatic surfaces. Except in extreme cases, spin-orbit



coupling in spin-forbidden reactions is rarely so strong that the adiabatic states differ significantly in energy from the diabatic ones, except within a fairly small region around the crossing point of the latter. For this reason, finding the crossing point gives valuable information as to the relative energy of the regions a spin-forbidden reaction must necessarily pass through.

The MECP is not a stationary point on either of the individual spin surfaces. The point at which the two spin surfaces cross provides an estimate of the *lower energy limit* to the MECP because all other degrees of freedom are optimised separately on the two surfaces. Therefore, the “crossing point” located using this technique is in fact two *different* points, which, depending on which unique parameter is chosen and on the features of the two PESs, may or may not be very similar to each other and to the real MECP. It is important that the Franck-Condon principle, which requires that both energies and geometries be the same in order for the spin-hopping to take place, is complied with. A measure of how different the two points are can be obtained by computing single-point energies on each PES at the partially optimised geometry of the other one. These energies can also be used as very rough *upper energy limits* for the MECP. From these, estimated upper limits to the enthalpy, entropy and Gibbs free energy can also be determined from subsequent vibrational frequencies analyses of these data points. For this reason, there are two estimated lower limits and two estimated upper limits to the MECP for  $\Delta^\ddagger H^\circ$ ,  $\Delta^\ddagger S^\circ$  and  $\Delta^\ddagger G^\circ$  which can be obtained. Spin-forbidden transition state theory requires that two factors are taken into account:

- (i) The critical energy required for the reaction to occur, which in a spin-forbidden reaction is defined by the MECP between two PESs corresponding to the two different pure spin states.
- (ii) The probability of hopping from one surface to the other in the vicinity of the crossing region, which is largely defined by the spin-orbit coupling matrix element between the two electronic wave functions.

## 1.7 Density functional theory (DFT)<sup>56</sup>

Computational chemistry has evolved in the last two decades from a curiosity of theoreticians to a mainstream tool used by many chemists, physicists and engineers who are interested in research and development. In this time, density functional theory (DFT) has become the dominant method for modelling chemistry at the molecular level.

DFT implements the Born-Oppenheimer approximation, which assumes that nuclei move so slowly compared to electrons that they can be regarded as stationary, and is derived from the Kohn-Sham approach, which is an important first-principles computational method used to predict chemical properties accurately and to analyse and interpret these properties in relatively convenient and simple chemical terms. DFT methods partition the electronic energy of a system into kinetic energy ( $E_T$ ), potential energy of nuclear-electron attraction and nuclear-nuclear repulsion ( $E_V$ ), electron-electron repulsion ( $E_J$ ), and exchange-correlation ( $E_{XC}$ ), which accounts for the remaining electron-electron interactions, equation 1.4.

$$E = E_T + E_V + E_J + E_{XC} \quad 1.4$$

Furthermore, the  $E_{XC}$  term comprises two components. The exchange term takes into account interactions between electrons of same spin, while the correlation term takes into account interactions between electrons of different spin.

There are several reasons for DFT's popularity and success:

- (i) The Kohn-Sham method implies a one-electron picture of many-electron systems but yields, in principle, an accurate electron density volume, along with its related properties, and the total energy. The exact exchange-correlation (XC) functional is unknown, however, several currently available XC functionals can provide, in many cases, “chemical” accuracy of just a few kcal.mol<sup>-1</sup> for binding energies. Furthermore, the quest for more accurate XC functionals, based on a more detailed understanding of the underlying physics, is continuing.
- (ii) DFT preserves the one-electron molecular orbital (MO) view on chemical reactions and properties, at all levels of approximation. DFT-calculated orbitals are therefore suitable for typical MO-theoretical analyses and interpretations. Moreover, the Kohn-Sham approach effectively incorporates all correlation effects.
- (iii) DFT is a relatively efficient computational method and its fundamental scaling properties do not deteriorate when methodological precision is increased, *i.e.* when a more accurate XC functional is applied. Furthermore, recent research paves the way to implementations that scale only linearly with the size of the computed system, which in turn brings fundamental quantum chemical methods of systems with hundreds of atoms within the computationally reasonable range.

Finally, DFT provides superior accuracy compared to Hartree-Fock theory or semi-empirical approaches while also being well suited for molecules that contain metal atoms. In contrast to conventional *ab initio* methods, such as MP2 (Møller-Plesset perturbation theory to second order), CI (configuration interaction) or CC (coupled cluster) calculations, DFT enables the accurate treatment of relatively large systems, making it the ideal computational methodology for this project. Details of the various software packages, along with the specific DFT methodologies used, are outlined in detail in Chapter 2 (Section 2.2).

### 1.7.1 Dispersion corrections with DFT

To better understand the inability of DFT to describe long range dispersion forces, some deliberation on the nature and origin of these forces are warranted. The discovery and subsequent description of these forces find their roots in electromagnetism, through the work of James C. Maxwell, who distilled the behaviour of oscillating electrical and magnetic fields into four characteristic equations. Heinrich Hertz then showed that the oscillations of electric charge could induce and effectively absorb electromagnetic waves, with P.N. Lebedev who conjectured in 1894 that atoms and molecules could act as senders and receivers of these electrical fields, which in turn based on the action and reaction, resulted in a physical force. It is this response, and more so the extent of these charge fluctuating responses, which lead to the net stabilisation of molecules *via* van der Waals (vdW) forces.<sup>57</sup>

In the presence of an external field, atoms and molecules alter the shape and form of their electron density distribution. In the case of a monochromatic source of uniform field strength, this response would be linear. This, however, is not the case for interacting atoms and molecules, which respond to alternating field strengths and directional vectors. The intensity of interaction is therefore proportional to the ability of a particular atom or molecule to form polar electrical moments. Three main classes of vdW interactions are segregated on this basis, as illustrated in Figure 1.6.<sup>57</sup>

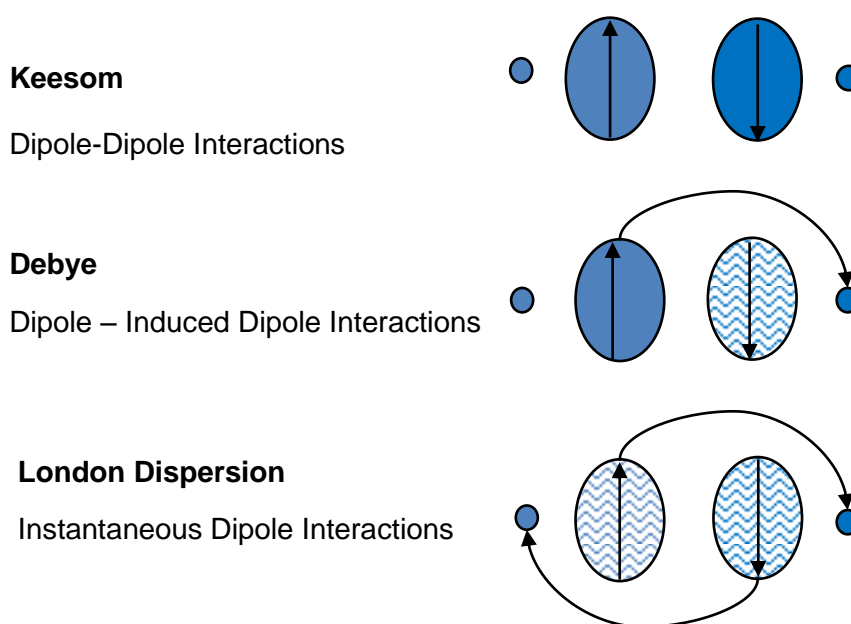


**Figure 1.6.** Schematic illustration of the three classes of vdW interactions.

The global trend in all three cases is the inverse sixth-order proportionality of force to distance,  $C/r^6$ , which serves as a time-averaged characterisation of the net attractive force. Therefore, considering the time independence of DFT methods, no fundamental approximation of this class of forces can be made.

The development of dispersion corrected functionals can be traced back by the introduction of the DFT-D method first proposed by Grimme in 2006. In subsequent modifications, up until DFT-D3, the basis and means of implementation remained relatively constant throughout the series. The general form of the dispersion corrected functionals include the conventional energy approximation theme and an atom pair wise summation approximation as presented in equations 1.5 and 1.6.<sup>58,59</sup>

$$E_{\text{DFT-D}} = E_{\text{DFT}} + E_{\text{disp}} \quad 1.5$$

$$E_{\text{disp}} = \sum_{AB} \sum_{n=6,8,10} S_n \frac{C_n^{AB}}{r_{AB}^n} f_{d,n}(r_{AB}) \quad 1.6$$

where  $C_n^{AB}$  denotes the dispersion coefficient approximated for interacting species  $A$  and  $B$ , over the separation range  $r_{AB}$ . To mitigate singularities as the separation distance  $r_{AB}$  approaches zero, the additional damping term  $f_{d,n}(r_{AB})$  is introduced.

In the development of DFT-D methods, the initial functional, now denoted as DFT-D1, was limited to empirically estimated dispersion coefficients for only H, C, N, O, F and Ne, to the highest order of  $n = 2$ . Albeit the limited range, this addition greatly improved the accuracy of intermolecular interaction energies in comparison to standard functional methods.<sup>60</sup>

The DFT-D2 method included updated  $C_6$  dispersion coefficients, now calculated by means of the London formula for dispersion. This was achieved by DFT/PBE0 calculations of the atomic ionization potentials and static dipole polarisabilities. This updated method included support for all elements up to Xenon. For elements of the Group I, II and transition metals, the difference of free atoms and the atoms characteristics in typical bonding situations are sufficiently large so that the calculated dispersion coefficients would be meaningless. Instead, the author assigned the average dispersion coefficient of the previous group VIII, and following group III elements, to these atoms. Through this means, the DFT-D2 method could achieve the wide range of supported elements.<sup>58</sup>

The significant modification of the DFT-D3 method was the *ab-initio* calculation of the interaction dispersion coefficients of known pairs, *i.e.*  $C_n^{AB}$ , as opposed to discrete averaging of interaction pairs of previous methods. This meant that, whereas previous methods relied on empirically averaged static values, the D3 method utilised calculated averages for exact pairs. This explicit estimation of exact bond pairs resulted in increased accuracies for all periodical elements. DFT-D3 also introduced higher order distance dependence terms ( $n = 6, 8$  and  $10$ ), which could better describe short range and therefore intramolecular interaction.<sup>59</sup>

Up until DFT-D3, there was no fundamental grounding for the use of the damping correction term. It was merely dependant on the bond pair summation of the vdW radii. Becke and Johnson proposed an alternative, based on the instantaneous in-space dipole moment of the Fermi exchange hole. The format differed in the sense that damping was now introduced as a sum in the denominator. The modification thus had a more fundamental basis for the application, in addition to increased accuracies for short range, intramolecular dispersion.<sup>61,62,63</sup>

---

**References**

1. W. P. Griffith, *The Chemistry of the Rarer Platinum Metals (Os, Ru, Ir & Rh)*, Chapter 3, Interscience, 1967.
2. F. R. Brunot, *J. Ind. Hyg. Toxicol.*, 1933, 136.
3. A. I. G. McLaughlin, R. Milton and K. M. A. Perry, *Brit. J. Ind. Med.*, 1946, 183.
4. W. P. Griffith, *Comprehensive Coordination Chemistry. The synthesis, reactions, properties and applications of coordination compounds. Vol. 4.* Ed. G. Wilkinson. Pergamon Press, Oxford, 1987.
5. <<http://www.webelements.com/osmium/uses/>>.
6. W. P. Griffith, *Platinum Metals Review*, 2004, 48(4), 182.
7. A. H. Éll, A. Closson, H. Adolfsson and J.-E. Bäckvall, *Adv. Synth. Catal.*, 2003, **345**, 1012.
8. S. M. Desai, N. N. Halligudi and S. T. Nandibewoor, *Int. J. Chem. Kinet.*, 1999, **31**, 583.
9. N. P. Shetti, R. R. Hosamani and S. T. Nandibewoor, *Research Letters in Inorganic Chemistry*, 2008, **216058**.
10. K. Byadagi, M. Meti, S. Nandibewoor and S. Chimatadar, *Ind. Eng. Chem. Res.*, 2013, **52**, 9011.
11. M. P. Singh, H. S. Singh, M. C. Gangwar, P. Thakur and A. K. Singh, *P. Indian Acad. Sci. A.*, 1975, **41**.
12. K. B. Sharpless, W. Amberg, Y. L. Bennani, G. A. Crispino, J. Hartung, K. -S. Jeong, H.-L. Kwong, K. Morikawa, Z. -M. Wang, D. Xu and X. -L. Zhang, *J. Org. Chem.*, 1992, **57**, 2768 and references cited therein.
13. G. A. Crispino, K. -S. Jeong, H. C. Kolb, Z. -M. Wang, D. Xu and K. B. Sharpless, *J. Org. Chem.*, 1993, **58**, 3785.
14. H. B. Henbest, W. R. Jackson and B. C. G. Robb, *J. Chem. Soc. B*, 1966, 803.
15. K. A. Jørgensen and R. Hoffmann, *J. Am. Chem. Soc.*, 1986, **108**, 1867.

16. E. N. Jacobsen, I. Marko, M. B. France, J. S. Svendsen and K. B. Sharpless, *J. Am. Chem. Soc.*, 1989, **111**, 737.
17. J. S. M. Wai, I. Marko, J. S. Svendsen, M. G. Finn, E. N. Jacobsen and K. B. Sharpless, *J. Am. Chem. Soc.*, 1989, **111**, 1123.
18. E. J. Corey, M. C. Noe and S. Sarshar, *J. Am. Chem. Soc.*, 1993, **115**, 3828.
19. T. Göbel and K. B. Sharpless, *Angew. Chem., Int. Ed. Engl.*, 1993, **32**, 1329.
20. P. Norrby, H. C. Kolb and K. B. Sharpless, *Organometallics*, 1994, **13**, 344.
21. “The Nobel Prize in Chemistry 2001”. *Nobelprize.org*. Nobel Media AB 2014. <[http://www.nobelprize.org/nobel\\_prizes/chemistry/laureates/2001/](http://www.nobelprize.org/nobel_prizes/chemistry/laureates/2001/)>.
22. H. Renner, *Ullmann’s Encyclopedia of Industrial Chemistry, Vol. A21*, fifth ed., VCH Publishers, 1992.
23. R. I. Edwards, W. A. M. t. Riele and G. J. Bernfield, *Recovery of the platinum-group metals (technology of the Platinum-group metals), Vol. A1*, Springer, Berlin, 1986.
24. R. I. Edwards, W. A. M. t. Riele and G. J. Bernfield, *Gmelin Handbook of Inorganic Chemistry, Suppl. Vol. A1*, ed. J. K. Acres and K. Swars, Springer Verlag, Berlin, 1986.
25. G. Schmuckler and B. Limoni-Relis, *Sep. Sci. Technol.*, 1995, **30(3)**, 337.
26. F. L. Bernardis, R. A. Grant and D. C. Sherrington, *React. Funct. Polym.*, 2005, **65**, 205.
27. T. E. Geswindt, W. J. Gerber, H. E. Rohwer and K. R. Koch, *Dalton Trans.*, 2011, **40**, 8581.
28. A. Dehestani, W. H. Lam, D. A. Hrovat, E. R. Davidson, W. T. Borden and J. M. Mayer, *J. Am. Chem. Soc.*, 2005, **127**, 3423.
29. P. VeeraSomaiah, K. B. Reddy, B. Sethuram and T. Navaneeth Rao, *J. Indian Chem. Soc.*, 1988, **27A**, 876.
30. P. VeeraSomaiah, K. B. Reddy, B. Sethuram and T. Navaneeth Rao, *J. Indian Chem. Soc.*, 1989, **66**, 755.

31. H. S. Singh, S. P. Singh, S. M. Singh, R. K. Singh and A. K. Sisodia, *J. Phys. Chem.*, 1975, **79(18)**, 1920.
32. N. P. Singh, V. N. Singh, H. S. Singh and M. P. Singh, *Aust. J. Chem.*, 1970, **23**, 921.
33. V. N. Singh, H. S. Singh and B. B. L. Saxena, *J. Am. Chem. Soc.*, 1969, **91(10)**, 2643.
34. H. S. Singh, *Oxidation of Organic Compounds with Osmium Tetroxide, in Organic synthesis by oxidation with metal compounds*, ed. W. J. Mijs and C. R. H. de Jonge, Plenum Press, New York, 1986.
35. N. P. Singh, V.N. Singh and M. P. Singh, *Aust. J. Chem.*, 1968, **21**, 2913.
36. B. Singh, A. K. Singh, M. B. Singh and A. P. Singh, *Tetrahedron*, 1986, **42**, 715.
37. K. K. S. Gupta and B. A. Begum, *Transition Met. Chem.*, 1998, **23**, 295.
38. K. K. S. Gupta and B. A. Begum, *Int. J. Chem. Kinet.*, 1999, **31(7)**, 477.
39. W. P. Griffith and M. Suriaatmaja, *Can. J. Chem.*, 2001, **79**, 598–606.
40. D. R. Weinberg, C. J. Gagliardi, J. F. Hull, C. F. Murphy, C. A. Kent, B. C. Westlake, A. Paul, D. H. Ess, D. G. McCafferty and T. J. Meyer, *Chem. Rev.*, 2012, **112**, 4016.
41. M. Sjodin, S. Styring, H. Wolpher, Y. H. Xu, L. C. Sun and L. Hammarström, *J. Am. Chem. Soc.*, 2005, **127**, 3855.
42. C. Costentin, *Chem. Rev.*, 2008, **108**, 2145.
43. R. I. Cukier and D. G. Nocera, *Annu. Rev. Phys. Chem.*, 1998, **49**, 337.
44. N. Iordanova and S. Hammes-Schiffer, *J. Am. Chem. Soc.*, 2002, **124**, 4848.
45. R. A. Binstead and T. J. Meyer, *J. Am. Chem. Soc.*, 1987, **109**, 3287.
46. B. T. Farrer and H. H. Thorp, *Inorg. Chem.*, 1999, **38**, 2497.
47. B. A. Moyer and T. J. Meyer, *J. Am. Chem. Soc.*, 1978, **100**, 3601.
48. R. A. Binstead, B. A. Moyer, G. J. Samuels and T. J. Meyer, *J. Am. Chem. Soc.*, 1981, **103**, 2897.
49. T. J. Meyer and M. H. V. Huynh, *Inorg. Chem.*, 2003, **42**, 8140.



50. S. Hammes-Schiffer, A. A. Stuchebrukhov, *Chem. Rev.*, 2010, **110**, 6939.
51. S. Hammes-Schiffer, E. Hatcher, H. Ishikita, J. H. Skone and A. V. Soudachov, *Coord. Chem. Rev.*, 2008, **252**, 384.
52. A. Chakraborty, V. Pak Michael and S. Hammes-Schiffer, *Phys. Rev. Lett.*, 2008, **101**, 153001.
53. R. Poli and J. N. Harvey, *Chem. Soc. Rev.*, 2003, **32**, 1.
54. K. M. Smith, R. Poli and J. N. Harvey, *New J. Chem.*, 2000, **24**, 77.
55. J. N. Harvey, *Phys. Chem. Chem. Phys.*, 2007, **9**, 331.
56. G. te Velde, F. M. Bickelhaupt, E. J. Baerends, C. Fonseca Guerra, S. J. A. Snijders and T. Ziegler, *J. Comp. Chem.* 2001, **22**, 931.
57. V. A. Parsegian, *Van der Waals forces: a handbook for biologists, chemists, engineers, and physicists*, Cambridge Univ. Press, 2006.
58. S. Grimme, *J. Comput. Chem.*, 2006, **27**, 1787.
59. S. Grimme, J. Anthony, S. Ehrlich, and H. Krieg, *J. Chem. Phys.*, 2010, **132**, 154104.
60. S. Grimme, *J. Comput. Chem.*, 2004, **25**, 1463.
61. A. D. Becke and E. R. Johnson, *J. Chem. Phys.*, 2006, **124**, 014104.
62. A. D. Becke and E. R. Johnson, *J. Chem. Phys.*, 2005, **123**, 154101.
63. S. Grimme, S. Ehrlich and L. Goerigk, *J. Comput. Chem.*, 2011, **32**, 1456.

# CHAPTER 2

## Experimental and Computational Methods

### 2.1 Experimental methods

#### 2.1.1 Apparatus

- UV-Vis absorbance spectra were recorded using Applied Photophysics' Chirascan<sup>TM</sup>-plus, combined Circular Dichroism/Fluorescence spectropolarimeter. Applied Photophysics' SF.3 accessory unit, mounted on the spectropolarimeter, was utilised for real-time, stopped-flow UV-Vis absorbance spectral recordings, Figure 2.1.

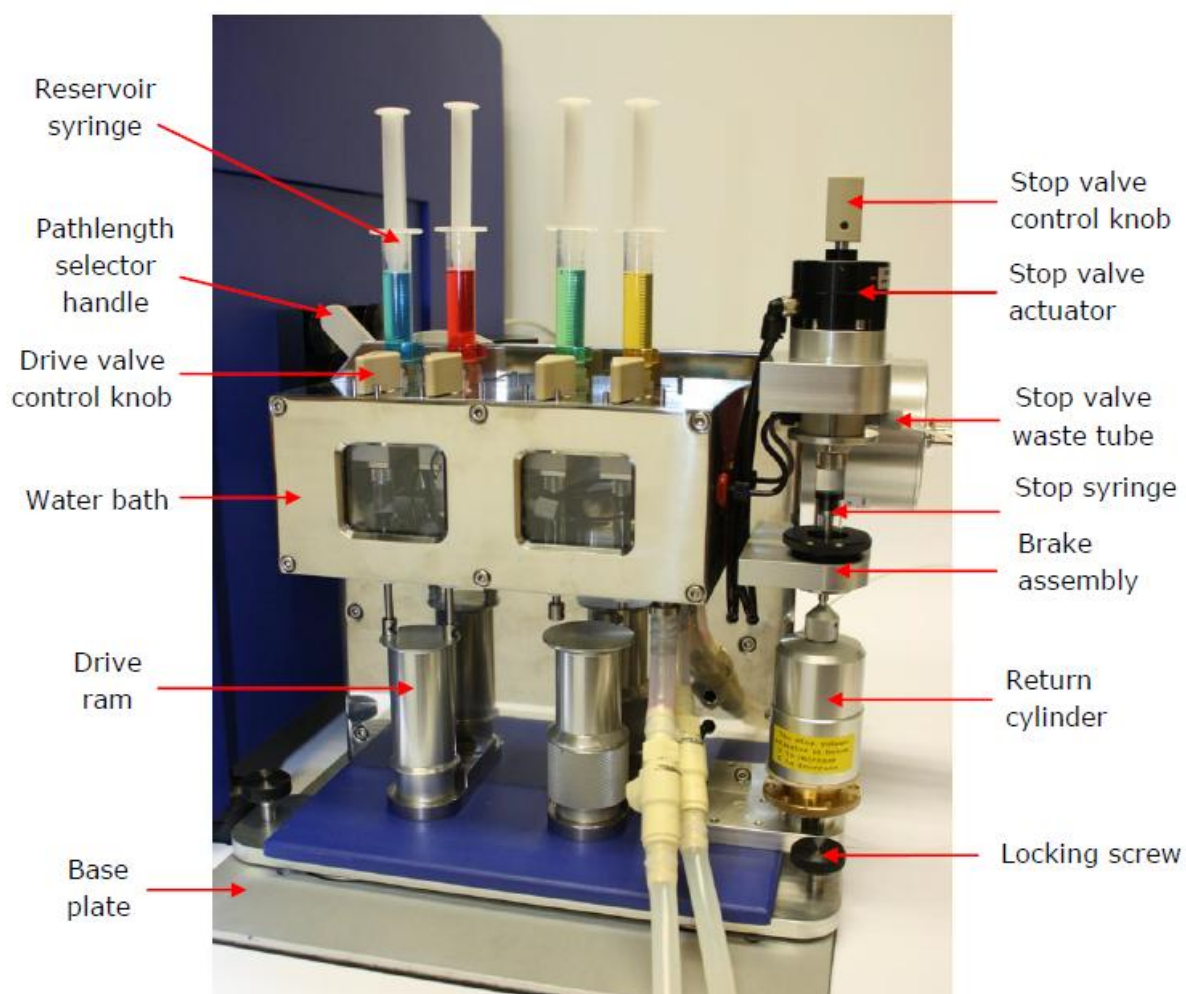


**Figure 2.1.** The fully assembled SF.3 accessory unit mounted on the Chirascan<sup>TM</sup>-plus Spectropolarimeter.<sup>1</sup>

A PolyScience circulating thermostat controller was used to ensure that the desired temperature ( $\pm 0.5^\circ\text{C}$ ) of the spectrophotometer's cuvette holder was maintained during spectral recordings. Quartz cuvettes, of a 1 cm path length, were used for all spectral recordings.

- $^1\text{H}$  NMR spectra were recorded at 298.15 K on a Varian <sup>Unity</sup> Inova, 600 MHz, Liquid State NMR spectrometer.

### 2.1.2 Software used to process experimentally obtained data

The Windows 7 Professional compatible software used during this study includes:

- Applied Photophysics' Pro-Data Viewer (version 4.2.6) software program, for the processing of UV-Vis spectral data;
- The commercially available software program distributed by Biokin Ltd, Program Dynafit (version 3.28.070), for the analysis and simulation of kinetic and equilibrium UV-Vis data;
- Mestrelab Research's MestReNova (version 7.1.2-10008) software program, for the processing of  $^1\text{H}$  NMR spectral data;
- Systat Software's SigmaPlot (for Windows version 11.0.0.77) software program, for the creation of several graphs;
- CambridgeSoft's ChemDraw Ultra (version 8.0) software program, for the creation of several figures;
- Matlab (version 8.1) software program, for the simulations of chemical reactions via numerical analyses; and
- Various Microsoft Office 2007 software programs.

### 2.1.3 Reagents utilised

A crude potassium osmate salt,  $\text{K}_2[\text{Os}^{\text{VI}}\text{O}_2(\text{OH})_4]$ , obtained from Anglo Platinum Ltd (South Africa) was the source of all osmium solutions that were prepared and utilised in this project. These preparatory procedures are outlined in **2.1.5** & **2.1.6**.

Furthermore, all aqueous solutions were prepared and diluted to the desired concentrations using type 1+ quality, MilliQ, water with a resistivity of 18.2 M $\Omega$  cm. MilliQ water was obtained by employing a Synergy Millipore water purification system to polish distilled water and remove any residual contaminants.

All the remaining reagents that were utilised, along with their respective, specified purities and suppliers are listed in Table 2.1.

**Table 2.1. Reagents utilised during this study.**

	Reagent	Chemical formula (linear)	Purity (%)	Supplier
salts	sodium hydroxide	NaOH	≥ 98	Sigma-Aldrich Co. Ltd.
	potassium hydroxide	KOH	88.7	SMM Instruments (Pty) Ltd.
	thiourea	CH <sub>4</sub> NS <sub>2</sub>	99	Sigma-Aldrich Co. Ltd.
liquids	hydrochloric acid	HCl	min. 32	Riedel-de Haën
	carbon tetrachloride	CCl <sub>4</sub>	min. 99.5	Merck Chemicals (Pty) Ltd.
	hydrogen peroxide	H <sub>2</sub> O <sub>2</sub>	min. 30	Merck Chemicals (Pty) Ltd.
	orthophosphoric acid	H <sub>3</sub> PO <sub>4</sub>	min. 85	Merck Chemicals (Pty) Ltd.
	<i>tert</i> -butanol	(CH <sub>3</sub> ) <sub>3</sub> COH	99+	Sigma-Aldrich Co. Ltd.
	methanol	CH <sub>3</sub> OH	min. 99.9	Sigma-Aldrich Co. Ltd.

#### 2.1.4 Preparation and standardisation procedure of sodium hydroxide solutions

Carefully weighed quantities of sodium hydroxide pellets were dissolved in MilliQ water to the desired concentration, and the freshly prepared solutions were subsequently titrated against standardised hydrochloric acid solutions. The total volume of the titrant at the endpoint was at least 25 mL for each titration. Titrations were repeated until consistent results were obtained.

#### 2.1.5 Preparation and storage of high purity potassium osmate

In order to obtain high purity K<sub>2</sub>[Os<sup>VI</sup>O<sub>2</sub>(OH)<sub>4</sub>] crystals, the crude salt obtained from Anglo Platinum Ltd (South Africa) was firstly dissolved into a warm 2.0 M KOH aqueous solution. The warm solution was subsequently filtered under vacuum in order to remove insoluble impurities. The obtained filtrate was allowed to cool in an ice bath in order to facilitate recrystallisation of K<sub>2</sub>[Os<sup>VI</sup>O<sub>2</sub>(OH)<sub>4</sub>]. Ethanol was often added to the filtrate in order to remove excess KOH and facilitate crystal growth, although this was not always necessary. Finally, the evolved, high purity K<sub>2</sub>[Os<sup>VI</sup>O<sub>2</sub>(OH)<sub>4</sub>] crystals were filtered and dried under vacuum for storage in an inert, sealed container.

#### 2.1.6 Preparation and storage of osmium tetroxide

Pure Os<sup>VIII</sup>O<sub>4</sub> solutions were prepared by the oxidative distillation of the high purity osmate salt, K<sub>2</sub>[Os<sup>VI</sup>O<sub>2</sub>(OH)<sub>4</sub>]. The volatile tetroxide is significantly more soluble in CCl<sub>4</sub> than in water and was therefore selected as the storage solvent.<sup>2</sup> Furthermore, the UV-Vis spectrum

of  $\text{Os}^{\text{VIII}}\text{O}_4$  in  $\text{CCl}_4$  does not change as a function of time,<sup>3</sup> indicating the stability of the tetroxide in this solvent.  $\text{H}_2\text{O}_2$  was selected as the oxidising agent for the preparation of pure  $\text{Os}^{\text{VIII}}\text{O}_4$  solutions, which was further acidified with  $\text{H}_3\text{PO}_4$  in order to enhance its oxidising capacity.<sup>4</sup>

A simplified diagram of the experimental setup employed for the preparation of pure  $\text{Os}^{\text{VIII}}\text{O}_4$  solutions is shown in Figure 2.2.

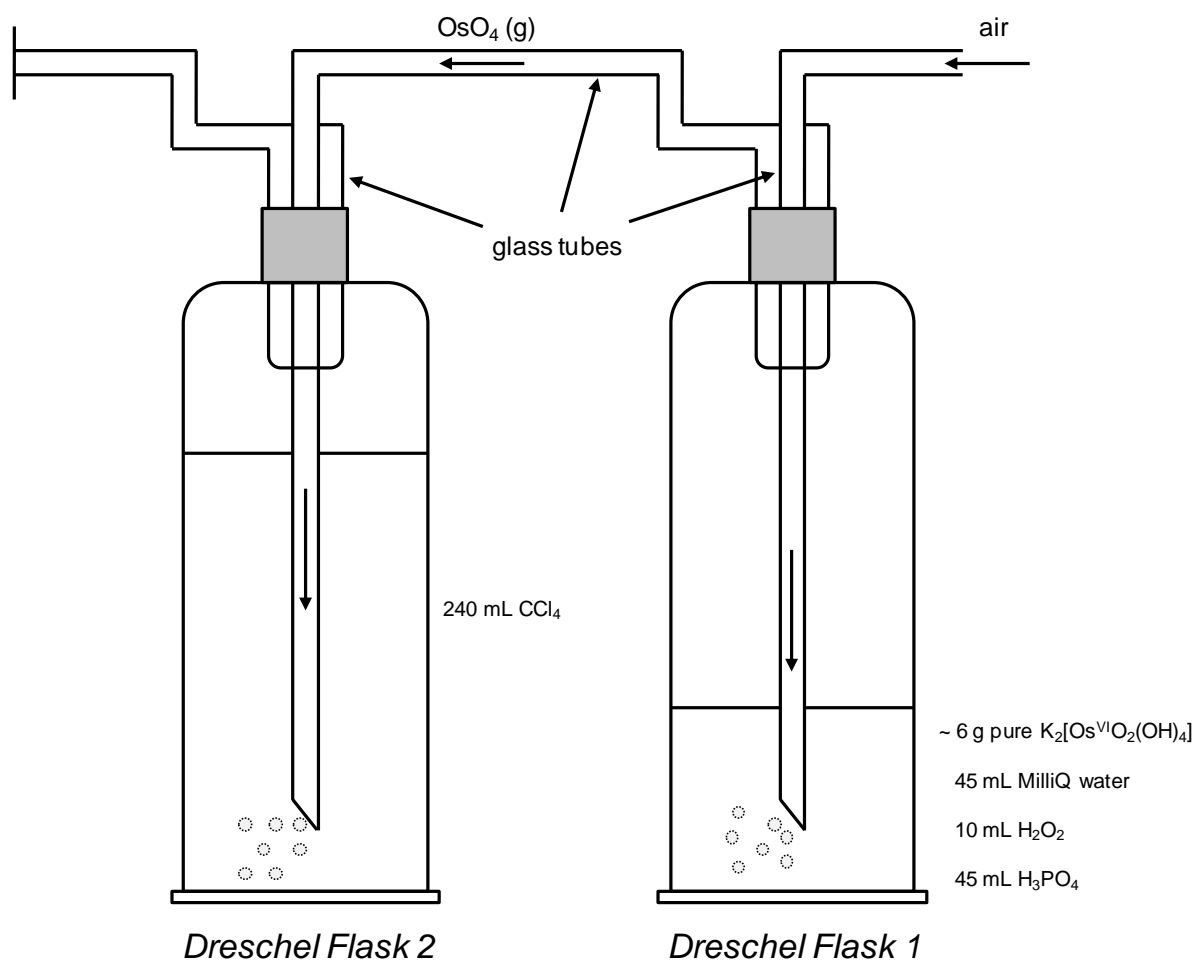


**Figure 2.2.** Simplified diagram illustrating the experimental setup and procedure for the preparation of pure  $\text{Os}^{\text{VIII}}\text{O}_4$  solutions in  $\text{CCl}_4$ .

Approximately 240 mL of  $\text{CCl}_4$  was transferred into Dreschel flask 2, Figure 2.2, while approximately six grams of  $\text{K}_2[\text{Os}^{\text{VI}}\text{O}_2(\text{OH})_4]$  was added to Dreschel flask 1. A hydrogen peroxide solution consisting of 45 mL MilliQ water, 10 mL  $\text{H}_2\text{O}_2$  (30%) and 45 mL  $\text{H}_3\text{PO}_4$  (85%) was then carefully transferred to flask 1. The glass tubes, as shown by Figure 2.2, were connected to the Dreschel flasks immediately after the addition of the hydrogen peroxide solution.

The dissolved osmate in Dreschel flask 1 is oxidised by the added hydrogen peroxide to form osmium tetroxide. In order to trap the evolved tetroxide vapour into the CCl<sub>4</sub> solvent contained in flask 2, a stream of air, purging the contents in flask 1, was forced through the glass attachments. After approximately ten hours, the Os<sup>VIII</sup>O<sub>4</sub>/CCl<sub>4</sub> contents in flask 2 were transferred to a stoppered dark glass container for storage.

Aqueous solutions of osmium tetroxide were prepared by extracting osmium tetroxide from the prepared CCl<sub>4</sub> stock solution into MilliQ water. The extraction process was allowed to progress for at least one hour, with a constant agitation applied to the mixture, before the aqueous phase was separated from the organic phase. The aqueous phase was subsequently filtered through Whatman 41 filter paper (wetted prior to filtration with MilliQ water) to remove any residual CCl<sub>4</sub> present in the aqueous phase.

### 2.1.7 Determination of osmium concentration – the thiourea colourimetric method

In all instances, the total osmium concentration was determined according to the thiourea colourimetric method<sup>3</sup> as described by Sauerbrunn and Sandell.<sup>5</sup> This method is based on reaction 2.1, where osmium tetroxide reacts with excess thiourea in an acidic medium.



The high oxidation state osmium species is reduced by thiourea, which also coordinates to the metal centre, to form the cationic, [Os<sup>III</sup>(NH<sub>2</sub>CSNH<sub>2</sub>)<sub>6</sub>]<sup>3+</sup> species. Moreover, each equivalent of osmium reacts with eleven equivalents of thiourea and three equivalents of acid. Sauerbrunn and Sandell reported that reaction 2.1 reaches equilibrium after approximately three days at 298.15 K.<sup>5</sup> By contrast, the reaction of osmium hexachlorooxmium(IV), [OsCl<sub>6</sub>]<sup>2-</sup>, with thiourea under the same conditions as in the latter reaction, was found to be significantly slower, *i.e.* approximately eight days were required to reach equilibrium.

#### 2.1.7.1 Experimental procedure

A 0.657 M thiourea stock solution was prepared in a 5.091 M HCl aqueous matrix. These concentrations were previously shown to be optimal for samples such as those used in this study.<sup>3</sup> In order to obtain accurate osmium concentration measurements, 0.5 mL of the particular high oxidation state osmium solution (of unknown concentration) was transferred with 15 mL of the thiourea stock solution and 14.5 mL MilliQ water into a 25 mL volumetric

flask. The flask was allowed to stand for eight days at 298.15 K prior to UV-Vis spectroscopy analysis of the sample. The use of excess quantities of thiourea was to ensure that all osmium is reduced to  $[\text{Os}^{\text{III}}(\text{NH}_2\text{CSNH}_2)_6]^{3+}$ , a species that has a characteristic UV-Vis absorbance spectrum profile. Furthermore, the ratios used to prepare the reduced osmium species were done specifically to ensure that the obtained UV-Vis absorbance value at 490 nm would be between approximately 0.2 and 0.9 au. The molar extinction coefficient of the reduced osmium species at this wavelength is  $3750.6 \text{ L}\cdot\text{mol}^{-1}\cdot\text{cm}^{-1}$ .<sup>3</sup>

## 2.2 Computational methodology

Most calculations employed the Amsterdam Density Functional program (ADF 2012.02) developed by Baerends, Ziegler, and co-workers.<sup>6-8</sup> Geometries were fully optimised at the scalar-relativistic zero-order regular approximation (ZORA)<sup>9-13</sup> level using (i) the local density approximation (LDA)<sup>14</sup> functional (ii) the generalised gradient approximation (GGA) functionals PBE,<sup>15</sup> modified PBE (mPBE)<sup>16</sup>, PBE that include dispersion correction terms {PBE-D,<sup>17</sup> PBE-D3,<sup>18</sup> PBE-D3(BJ)<sup>19</sup> and PBE-dDsC<sup>20</sup>}, BLYP<sup>21-24</sup> and BLYP that include dispersion correction terms (BLYP-D<sup>17</sup> and BLYP-D3<sup>18</sup>), PW91,<sup>25</sup> and (iii) the meta-GGA functional, M06L<sup>26,27</sup>. These calculations were done with an all-electron, quadruple- $\zeta$  plus polarisation (QZ4P) function basis set for Os and the even-tempered pVQZ basis set for O and H.<sup>28</sup> Optimisation in the gas phase as well as those using an implicit solvent model, namely the conductor-like screening model (COSMO),<sup>29-32</sup> with the parameters of water,<sup>\*</sup> were done with the abovementioned combinations of functionals and basis sets. All of the obtained structures were characterised as potential energy surface (PES) minima or transition states by analysing the Hessian matrix.<sup>33-37</sup>

In order to identify the stable conformer geometries, conformational analyses were performed by monitoring the electronic energy, in a sequence of linear transit calculations (relaxed scans), as a function of the relevant  $\sigma$  O-Os-O-H torsion angle reaction coordinate constraint (partial convergence optimisation at each step) by systematic rotation of the constrained angle. The resulting local minimum/minima obtained from the linear transit calculations were subsequently submitted for complete (full convergence optimisation) geometry optimisation calculations by the implementation of the abovementioned parameters/procedures.

---

\*  $\epsilon$  = dielectric constant = 78.39 and Rad = radius of the rigid sphere H<sub>2</sub>O molecules = 1.93 Å.

Transition state geometries were obtained by doing a sequence of calculations. Firstly, a rough approximation of the reaction path was obtained by monitoring the electronic energy as a function of the relevant  $\sigma$  Os-OH bond length reaction coordinate constraint (partial optimisation at each step). Secondly, the geometry at the highest energy of the linear transit calculation, which is the initial geometry of the transition state search, was submitted for a frequencies calculation.<sup>33-37</sup> This is done in order to obtain a good starting Hessian with one imaginary frequency that corresponds to the motion along that reaction coordinate. Thirdly, the initial geometry, for which the Hessian matrix has been calculated in the frequencies calculation, was submitted for a transition state search calculation. Lastly, the geometry calculated from the transition state search calculation was submitted for another frequencies calculation<sup>33-37</sup> in order to verify that only one imaginary frequency, which correctly corresponds to the relevant reaction coordinate, is present.

Bonding analysis<sup>38,39</sup> presented in this study is based on the ETS-NOCV approach which is a combination of the extended transition state (ETS) method with the natural orbitals for chemical valence (NOCV) scheme.<sup>40</sup> In our analysis, each system is divided up into two individual fragments followed by ETS-NOCV analysis to study the interaction between these subsystems. The contours and colour-coded plots of the NOCV deformation-density contributions and molecular electrostatic potential were plotted based on the ADF graphical user interface (GUI).<sup>41</sup>

Both the quantum theory of atoms in molecules (QTAIM)<sup>42,43</sup> and the non-covalent interactions (NCI)<sup>44</sup> analyses were done using the AIMAll software package<sup>45</sup> on geometry optimised structures that were obtained with ADF.<sup>6-8</sup> Wavefunctional files (.wfx) used for QTAIM analysis were created using Gaussian 09,<sup>46</sup> with an effective core potential (ECP), Lanl2DZ,<sup>47-49</sup> on Os and the correlation-consistent, cc-pVQZ,<sup>50</sup> basis set for O and H. The polarisable conductor calculation model (CPCM)<sup>51,52</sup> was used to account for aqueous solvation effects.

The xyz coordinates of the equilibrium geometries obtained in this study are included in Microsoft Word documents on the accompanying CD attached at the back page of the thesis in the folders:

(i) Optimised\_Coordinates/gas\_phase (for geometries obtained in the gas phase) and



(ii) Optimised\_Coordinates/simulated\_aqueous\_phase (for geometries obtained in the simulated aqueous phase).

Also included on the attached CD are Microsoft Word documents containing the raw absorbance (a.u.) vs. time (seconds), xy data from our UV-Vis spectroscopy kinetics experiments, in the folders:

(i) UV\_Vis\_Kinetic\_Traces/Chapter\_4 (related to theme (ii) in Chapter 1) and

(ii) UV\_Vis\_Kinetic\_Traces/Chapter\_7 (related to theme (iii) in Chapter 1).

---

**References**

1. Applied Photophysics, Chirascan<sup>TM</sup>-plus, SF.3 User Manual, 2010.
2. W. P. Griffith, *The Chemistry of the Rarer Platinum Metals (Os, Ru, Ir & Rh)*, Chapter 3, Interscience, 1967.
3. T. E. Geswindt, MSc Thesis, 2009, NMMU, South Africa.
4. B. J. McFadzean, MSc Thesis, 2004, University of Port Elizabeth, South Africa.
5. R. D. Sauerbrunn and E. B. Sandell, *J. Am. Chem. Soc.*, 1953, **75**, 3554.
6. G. te Velde, F. M. Bickelhaupt, S. J. A. van Gisbergen, C. Fonseca Guerra, E. J. Baerends, J. G. Snijders and T. Ziegler, *J. Comput. Chem.*, 2001, **22**, 931.
7. C. Fonseca Guerra, J. G. Snijders, G. te Velde and E. J. Baerends, *Theor. Chem. Acc.*, 1998, **99**, 391.
8. E. J. Baerends, J. Autschbach, D. Bashford, A. Bérces, F. M. Bickelhaupt, C. Bo, P. M. Boerrigter, L. Cavallo, D. P. Chong, L. Deng, R. M. Dickson, D. E. Ellis, M. van Faassen, L. Fan, T. H. Fischer, C. Fonseca Guerra, A. Ghysels, A. Giammona, S. J. A. van Gisbergen, A. W. Götz, J. A. Groeneveld, O. V. Gritsenko, M. Grüning, F. E. Harris, P. van den Hoek, C. R. Jacob, H. Jacobsen, L. Jensen, G. van Kessel, F. Kootstra, M. V. Krykunov, E. van Lenthe, D. A. McCormack, A. Michalak, M. Mitoraj, J. Neugebauer, V. P. Nicu, L. Noodleman, V. P. Osinga, S. Patchkovskii, P. H. T. Philipsen, D. Post, C. C. Pye, W. Ravenek, J. I. Rodríguez, P. Ros, P. R. T. Schipper, G. Schreckenbach, M. Seth, J. G. Snijders, M. Solà, M. Swart, D. Swerhone, G. te Velde, P. Vernooijs, L. Versluis, L. Visscher, O. Visser, F. Wang, T. A. Wesolowski, E. M. van Wezenbeek, G. Wiesenecker, S. K. Wolff, T. K. Woo, A. L. Yakovlev, and T. Ziegler, ADF2012.02, SCM, Theoretical Chemistry, Vrije Universiteit, Amsterdam, The Netherlands, <http://www.scm.com>.
9. E. van Lenthe, E. J. Baerends and J. G. Snijders, *J. Chem. Phys.*, 1993, **99**, 4597.
10. E. van Lenthe, E. J. Baerends and J. G. Snijders, *J. Chem. Phys.*, 1994, **101**, 9783.
11. E. van Lenthe, A. E. Ehlers and E. J. Baerends, *J. Chem. Phys.*, 1999, **110**, 8943.
12. E. van Lenthe, J. G. Snijders and E. J. Baerends, *J. Chem. Phys.*, 1996, **105**, 6505.

13. E. van Lenthe, R. van Leeuwen, E. J. Baerends and J. G. Snijders, *Int. J. Quantum Chem.*, 1996, **57**, 281.
14. S. H. Vosko, L. Wilk and M. Nusair, *Can. J. Phys.*, 1980, **58(8)**, 1200.
15. J. P. Perdew, K. Burke and M. Ernzerhof, *Phys. Rev. Lett.*, 1996, **77**, 3865.
16. C. Adamo and V. Barone, *J. Chem. Phys.*, 1996, **116**, 5933.
17. S. Grimme, *J. Comput. Chem.*, 2006, **27**, 1787.
18. S. Grimme, J. Anthony, S. Ehrlich and H. Krieg, *J. Chem. Phys.*, 2010, **132**, 154104.
19. S. Grimme, S. Ehrlich and L. Goerigk, *J. Comput. Chem.*, 2011, **32**, 1457.
20. S. N. Steinmann and C. Corminboeuf, *J. Chem. Theory Comput.*, 2011, **7**, 3567.
21. A. D. Becke, *Phys. Rev. A.*, 1988, **38**, 3098.
22. C. Lee, W. Yang and R. G. Parr, *Phys. Rev. B.*, 1988, **37**, 785.
23. B. G. Johnson, P. M. W. Gill and J. A. Pople, *J. Chem. Phys.*, 1993, **98**, 5612.
24. T. V. Russo, R. L. Martin and P. J. Hay, *J. Chem. Phys.*, 1994, **101**, 7729.
25. J. P. Perdew, J. A. Chevary, S. H. Vosko, K. A. Jackson, M. R. Pederson, D. J. Sing and C. Fiolhais, *Phys. Rev. B.*, 1992, **46**, 6671.
26. Y. Zhao and D. G. Truhlar, *J. Chem. Phys.*, 2006, **125**, 194101.
27. Y. Zhao and D. G. Truhlar, *Theor. Chem. Acc.*, 2008, **120**, 215.
28. E. van Lenthe and E. J. Baerends, *J. Comput. Chem.*, 2003, **24**, 1142.
29. C. C. Pye and T. Ziegler, *Theor. Chem. Acc.*, 1999, **101**, 396.
30. A. Klamt and G. Schüürmann, *J. Chem. Soc. Perk. T. 2.*, 1993, 799.
31. A. Klamt, *J. Phys. Chem.*, 1995, **99**, 2224.
32. A. Klamt and V. Jones, *J. Chem. Phys.*, 1996, **105**, 9972.
33. A. Bérces, R. M. Dickson, L. Fan, H. Jacobsen, D. Swerhone and T. Ziegler, *Comput. Phys. Commun.*, 1997, **100**, 247.

34. H. Jacobsen, A. Bérces, D. Swerhone and T. Ziegler, *Comput. Phys. Commun.*, 1997, **100**, 263.
35. S. K. Wolff, *Int. J. Quantum Chem.*, 2005, **104**, 645.
36. L. Fan and T. Ziegler, *J. Chem. Phys.*, 1992, **96**, 9005.
37. L. Fan and T. Ziegler, *J. Phys. Chem.*, 1992, **96**, 6937.
38. T. Ziegler and A. Rauk, *Inorg. Chem.*, 1979, **18**, 1558.
39. T. Ziegler and A. Rauk, *Inorg. Chem.*, 1979, **18**, 1755.
40. M. Mitoraj, A. Michalak and T. Ziegler, *J. Chem. Theory Comput.*, 2009, **5**, 962.
41. GUI 2014, SCM, Amsterdam, The Netherlands, <http://www.scm.com>
42. J. I. Rodríguez, R. F. W. Bader, P. W. Ayers, C. Michel, A. W. Götz and C. Bo, *Chem. Phys. Lett.*, 2009, **472**, 149.
43. J. I. Rodríguez, *J. Comput. Chem.*, 2013, **34**, 681.
44. E. R. Johnson, S. Keinan, P. Mori-Sanchez, J. Contreras-Garcia, A. J. Cohen and W. Yang, *J. Am. Chem. Soc.*, 2010, **132**, 6498.
45. AIMAll (Version 15.05.18), Todd A. Keith, TK Gristmill Software, Overland Park KS, USA, 2015 ([aim.tkgristmill.com](http://aim.tkgristmill.com))
46. Gaussian 09, Revision D.01, M. J. Frisch, G. W. Trucks, H. B. Schlegel, G. E. Scuseria, M. A. Robb, J. R. Cheeseman, G. Scalmani, V. Barone, B. Mennucci, G. A. Petersson, H. Nakatsuji, M. Caricato, X. Li, H. P. Hratchian, A. F. Izmaylov, J. Bloino, G. Zheng, J. L. Sonnenberg, M. Hada, M. Ehara, K. Toyota, R. Fukuda, J. Hasegawa, M. Ishida, T. Nakajima, Y. Honda, O. Kitao, H. Nakai, T. Vreven, J. A. Montgomery, Jr., J. E. Peralta, F. Ogliaro, M. Bearpark, J. J. Heyd, E. Brothers, K. N. Kudin, V. N. Staroverov, T. Keith, R. Kobayashi, J. Normand, K. Raghavachari, A. Rendell, J. C. Burant, S. S. Iyengar, J. Tomasi, M. Cossi, N. Rega, J. M. Millam, M. Klene, J. E. Knox, J. B. Cross, V. Bakken, C. Adamo, J. Jaramillo, R. Gomperts, R. E. Stratmann, O. Yazyev, A. J. Austin, R. Cammi, C. Pomelli, J. W. Ochterski, R. L. Martin, K. Morokuma, V. G. Zakrzewski, G. A. Voth, P. Salvador, J. J. Dannenberg,

- 
- S. Dapprich, A. D. Daniels, O. Farkas, J. B. Foresman, J. V. Ortiz, J. Cioslowski, and D. J. Fox, Gaussian, Inc., Wallingford CT, 2013.
47. P. J. Hay and W. R. Wadt, *J. Chem. Phys.*, 1985, **82**, 270.
  48. W. R. Wadt and P. J. Hay, *J. Chem. Phys.*, 1985, **82**, 284.
  49. P. J. Hay and W. R. Wadt, *J. Chem. Phys.*, 1985, **82**, 299.
  50. T. H. Dunning Jr., *J. Chem. Phys.*, 1989, **90**, 1007.
  51. V. Barone and M. Cossi, *J. Phys. Chem. A.*, 1998, **102**, 1995.
  52. M. Cossi, N. Rega, G. Scalmani and V. Barone, *J. Comp. Chem.*, 2003, **24**, 669.

## CHAPTER 3

---

### A DFT Study to Unravel the Kinetics and Thermodynamics of Os<sup>VIII</sup> oxo/hydroxido/aqua Complexes in Aqueous Matrices

#### 3.1 Introduction

There is extensive literature dealing with the use of Os<sup>VIII</sup>O<sub>4</sub> as a homogeneous catalyst for the oxidation of several organic compounds in a variety of acidic and basic aqueous solutions.<sup>1-5</sup> However, when Os<sup>VIII</sup>O<sub>4</sub> is extracted from CCl<sub>4</sub> into an aqueous hydroxide solution several possible Os<sup>VIII</sup> oxo/hydroxido/aqua complexes can form.<sup>6-12</sup> To date, only the Os<sup>VIII</sup>O<sub>4</sub><sup>13</sup> and the *cis*-[Os<sup>VIII</sup>O<sub>4</sub>(OH)<sub>2</sub>]<sup>2-</sup> species<sup>14-16</sup> have been characterised experimentally, by means of X-ray diffraction spectrometry. This leaves a window for conjecture as to what other Os<sup>VIII</sup> species might exist in aqueous hydroxide solutions and which of these actually participate in reported catalytic reactions. From observed Os<sup>VIII</sup>O<sub>4</sub> UV-Vis spectral changes during ‘weak acid/strong base’ titrations, Galbács *et al.*<sup>7</sup> proposed a reaction model given by equations 3.1 & 3.2 with calculated  $K_{a1}$  and  $K_{a2}$  acid dissociation equilibrium constants, listed in Table 3.1.

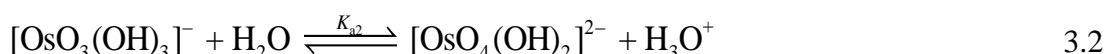
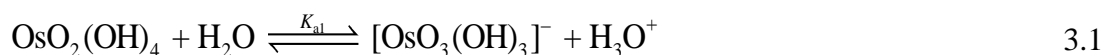


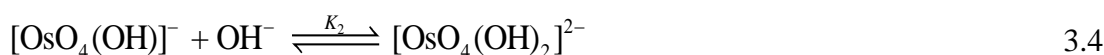
**Table 3.1. Acid dissociation and the corresponding coordination sphere expansion equilibrium constants of reactions 3.1 – 3.4.**

Lit.	$K_{a1}$	$K_1$	$K_{a2}$	$K_2$
6	$1.3 \times 10^{-12}$	130	-	-
7	$6.3 \times 10^{-13}$	63	$4.0 \times 10^{-15}$	0.40
8	$8.8 \times 10^{-13}$	88	$7.5 \times 10^{-15}$	0.75

The Os<sup>VIII</sup> oxo/hydroxido complexes proposed to be in solution by Galbács *et al.*<sup>7</sup> are all six-coordinate complexes, Os<sup>VIII</sup>O<sub>2</sub>(OH)<sub>4</sub>, [Os<sup>VIII</sup>O<sub>3</sub>(OH)<sub>3</sub>]<sup>-</sup> and [Os<sup>VIII</sup>O<sub>4</sub>(OH)<sub>2</sub>]<sup>2-</sup>, with the latter presumably the *cis* stereoisomer species. Griffith<sup>12</sup> additionally proposes a six-coordinate

species containing a water ligand,  $[\text{Os}^{\text{VIII}}\text{O}_4(\text{OH})(\text{H}_2\text{O})]^-$ . Apart from the abovementioned  $\text{Os}^{\text{VIII}}$  species, there is experimental support for a five-coordinate  $[\text{Os}^{\text{VIII}}\text{O}_4(\text{OH})]^-$  complex anion from several X-ray crystal structures of five-coordinate  $[\text{Os}^{\text{VIII}}\text{O}_4\text{L}]$  derivatives (where L is a nitrogen donor ligand).<sup>17</sup> Moreover, a density functional theory (DFT) {B3LYP functional, LanL2DZ and 6-31+G(d,p) bases sets for Os and all other atoms, respectively} computational study by Mayer *et al.*<sup>6</sup> also supports that a five-coordinate  $[\text{Os}^{\text{VIII}}\text{O}_4(\text{OH})]^-$  complex anion may exist in the gas phase.

If a five-coordinated  $[\text{Os}^{\text{VIII}}\text{O}_4(\text{OH})]^-$  species is present, then the reactions expected to take place are not that of a relatively weak acid reacting with water, as depicted by equations 3.1 & 3.2, but rather coordination sphere expansion reactions (*vide infra*),<sup>6-12</sup> equations 3.3 & 3.4.



The equilibrium constants of the two differing reaction schemes, 3.1 & 3.2 and 3.3 & 3.4, are mathematically related to each other as shown, for example, in equations 3.5 and 3.6.

$$K_1 = \frac{[\text{OsO}_4(\text{OH})^-]}{[\text{OsO}_4][\text{OH}^-]} \quad 3.5$$

$$K_1 K_w = \frac{[\text{OsO}_4(\text{OH})^-][\text{H}_3\text{O}^+]}{[\text{OsO}_4]} = \frac{[\text{OsO}_3(\text{OH})_3^-][\text{H}_3\text{O}^+]}{[\text{OsO}_2(\text{OH})_4]} = K_{a1} \quad 3.6$$

Although the equilibrium constants are mathematically related (equation 3.6), the actual chemical reactions are fundamentally different, giving rise to chemical species which differ significantly from a structural point of view and of course their physicochemical properties. Detailed knowledge of the chemical speciation of  $\text{Os}^{\text{VIII}}$  complexes in basic aqueous solutions is currently unclear and is of significant importance if comproportionation<sup>11</sup> and catalytic reactions<sup>1-5</sup> involving these species are to be mechanistically understood. This lack of clarity is highlighted by the variety of suggestions of what the catalytically active  $\text{Os}^{\text{VIII}}$  species could be, *e.g.* it has been reported that the catalytically active  $\text{Os}^{\text{VIII}}$  species for the oxidation of olefins<sup>1</sup> and of allyl alcohols<sup>2</sup> in mildly acidic aqueous solutions are the  $\text{Os}^{\text{VIII}}\text{O}_4$  and  $[\text{H}_2\text{Os}^{\text{VIII}}\text{O}_5]$  complexes, respectively. Moreover, in aqueous alkaline solutions the catalytically active  $\text{Os}^{\text{VIII}}$  species for the oxidation of L-tryptophan,<sup>3</sup> chloramphenicol,<sup>4</sup>

sorbitol and mannitol<sup>5</sup> are reported to be the  $[\text{Os}^{\text{VIII}}\text{O}_4(\text{OH})_2]^{2-}$  and/or  $\text{Os}^{\text{VIII}}\text{O}_4$  complexes. To add even more complexity, Gerber *et al.*<sup>11</sup> reported that the oxidation of methanol and ethanol with  $\text{Os}^{\text{VIII}}$  in a 2.0 M NaOH aqueous solution results in an additional comproportionation reaction between an  $\text{Os}^{\text{VIII}}$  species and a *trans*- $[\text{Os}^{\text{VI}}\text{O}_2(\text{OH})_4]^{2-}$  complex to form two postulated  $[\text{Os}^{\text{VII}}\text{O}_3(\text{OH})_3]^{2-}$  complexes. The formation of the  $\text{Os}^{\text{VII}}$  complex, in addition to several  $\text{Os}^{\text{VIII}}$  species, underlines the uncertainty pertaining to what the actual catalytically active osmium species in solution are likely to be.<sup>1-5</sup>

Electronic structure methods, and in particular density functional theory (DFT), are valuable tools used to probe chemical reactions involving transition metals.<sup>18</sup> If progress is to be made in understanding the mechanistic aspects of reactions in which  $\text{Os}^{\text{VIII}}$  acts as a catalyst or in terms of the synthesis of novel  $\text{Os}^{\text{VIII}}$  complexes, it is pertinent that the most abundant  $\text{Os}^{\text{VIII}}$  species should be identified under well-defined conditions. In this study we report a systematic DFT theoretical study to (i) confirm whether the postulated chemical reactions 3.1 & 3.2 or 3.3 & 3.4 are responsible for the observed UV-Vis spectral changes reported in the literature;<sup>7</sup> (ii) investigate if any  $\text{Os}^{\text{VIII}}$  complexes that contain water ligands exist in appreciable quantities in solution; (iii) elucidate the nature of the metal-ligand bonding interactions as well as possible intramolecular hydrogen bonding interactions between neighbouring ligands; and (iv) investigate the anticipated importance of hydration energies pertaining to the thermodynamic stability of  $\text{Os}^{\text{VIII}}$  oxo/hydroxido/aqua complexes.

## 3.2 Results and discussion

### 3.2.1 Thermodynamics and energy decomposition analysis (EDA) of $\text{Os}^{\text{VIII}}$ oxo/hydroxido/aqua complexes

The wavelengths at which the UV-Vis absorption maxima of  $\text{Os}^{\text{VIII}}\text{O}_4$  in water, carbon tetrachloride ( $\text{CCl}_4$ ) and the gas phase occur are essentially identical, Figure A.1,<sup>11</sup> apart from the broader absorption lines in the solvent phases. The agreement of absorption maxima observed in these phases as a function of wavelength provides compelling evidence that  $\text{Os}^{\text{VIII}}\text{O}_4$  does not react with water to form  $\text{Os}^{\text{VIII}}$  complexes with coordinated water ligands. Nonetheless, several hypothetical five- and six-coordinate  $\text{Os}^{\text{VIII}}$  aqua complexes,  $[\text{Os}^{\text{VIII}}\text{O}_4(\text{H}_2\text{O})]$ , *cis*- $[\text{Os}^{\text{VIII}}\text{O}_4(\text{H}_2\text{O})_2]$  and *trans*- $[\text{Os}^{\text{VIII}}\text{O}_4(\text{H}_2\text{O})_2]$ , were submitted for geometry optimisation and subsequent vibrational frequencies analysis calculations. In the gas phase, the Os-water “ligand” distance increases with each self-consistent field (SCF) iteration until unphysical bond lengths are observed ( $> 7.0\text{\AA}$ ). This “trend” was observed



using a variety of DFT functionals (LDA, several GGA's and one MetaGGA); with the inclusion or exclusion of relativistic effects (ZORA) and irrespective of basis set quality. Conversely, in the simulated aqueous phase the geometries converge, Figure 3.1, where the  $\text{O}_4\text{Os}^{\text{VIII}}\text{---OH}_2$  distances are 3.18 Å and 3.25 Å in the  $[\text{Os}^{\text{VIII}}\text{O}_4]\cdot\text{H}_2\text{O}$  and  $[\text{Os}^{\text{VIII}}\text{O}_4]\cdot 2\text{H}_2\text{O}$  structures, respectively. However, one negative frequency, corresponding to a bending (rocking) motion of  $\text{H}_2\text{O}$ , was obtained for both the  $[\text{Os}^{\text{VIII}}\text{O}_4]\cdot\text{H}_2\text{O}$  and  $[\text{Os}^{\text{VIII}}\text{O}_4]\cdot 2\text{H}_2\text{O}$  structures, despite performing both the geometry optimisation and frequencies analysis calculations at the highest available integration accuracy. From these results it is reasonable to conclude that there are no minima on the multidimensional potential energy surface (PES) w.r.t.  $\text{Os}^{\text{VIII}}$  complexes that have coordinated water ligands. This corroborates the conclusion from the essentially identical UV-Vis spectra of  $\text{Os}^{\text{VIII}}\text{O}_4$  obtained in various solvents and in the gas phase.

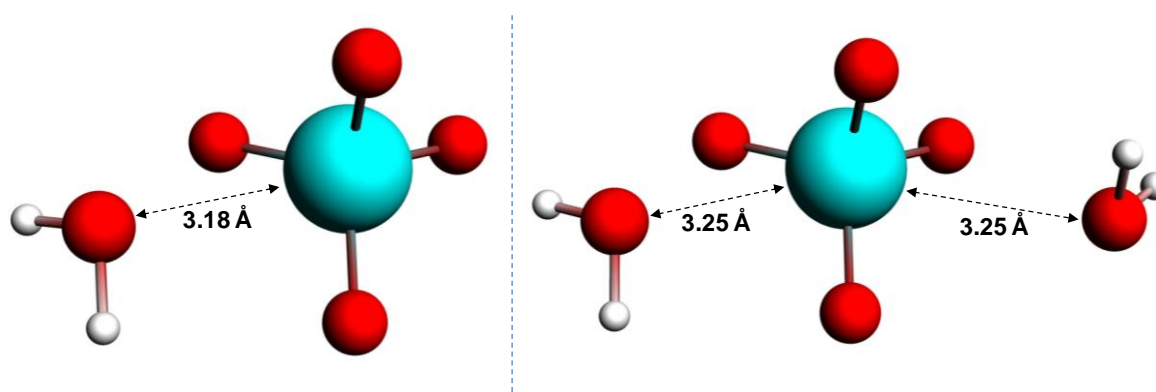


**Figure 3.1.** Converged geometries of  $[\text{Os}^{\text{VIII}}\text{O}_4]\cdot\text{H}_2\text{O}$  (left) and  $[\text{Os}^{\text{VIII}}\text{O}_4]\cdot 2\text{H}_2\text{O}$  (right) in the simulated aqueous phase (PBE functional).

Galbács *et al.*<sup>7</sup> suggest that  $\text{Os}^{\text{VIII}}\text{O}_4$  transforms into an Osmium(VIII) acid,  $\text{Os}^{\text{VIII}}\text{O}_2(\text{OH})_4$ , by means of nucleophilic attack of either hydroxide ions or of water, indicated by reaction 3.1, followed by subsequent deprotonation. To probe this we identified the global minimum energy conformation of the  $\text{Os}^{\text{VIII}}\text{O}_2(\text{OH})_4$  complex, Figure A.2, so that the equilibrium constant of reaction 3.7 could be calculated (in the simulated aqueous phase).



<sup>2</sup> Equation 3.7 has been given earlier, as equation 1.4, and is therefore shown again in parenthesis. For the ease of reading, repeated equations are shown in this way throughout the thesis.

The DFT-calculated (PBE functional) standard reaction Gibbs free energy ( $\Delta G^\circ_{rxn}$ ) for reaction 3.7 is  $73.22 \text{ kcal.mol}^{-1}$ , which equates to a  $K_{eq}$  value of  $2.14 \times 10^{-54}$ . Formation of  $\text{Os}^{\text{VIII}}\text{O}_2(\text{OH})_4$  is highly thermodynamically unfavourable and therefore the suggestion by Galbács *et al.*<sup>7</sup> is not supported by these calculations. This result calls into question the validity of the subsequent sequence of reactions, shown in equations 3.1 & 3.2.

In contrast to the abovementioned  $\text{Os}^{\text{VIII}}$  aqua complexes, equilibrium geometries of the  $\text{Os}^{\text{VIII}}$  species depicted by equations 3.3 & 3.4 were found relatively easily in both the gas and simulated aqueous phase. The molecular graphs of  $\text{Os}^{\text{VIII}}\text{O}_4$ ,  $[\text{Os}^{\text{VIII}}\text{O}_4(\text{OH})]^-$ ,  $cis_1$ - $[\text{Os}^{\text{VIII}}\text{O}_4(\text{OH})_2]^{2-}$ ,  $cis_2$ - $[\text{Os}^{\text{VIII}}\text{O}_4(\text{OH})_2]^{2-}$  and  $trans$ - $[\text{Os}^{\text{VIII}}\text{O}_4(\text{OH})_2]^{2-}$  are shown in Figure 3.2.

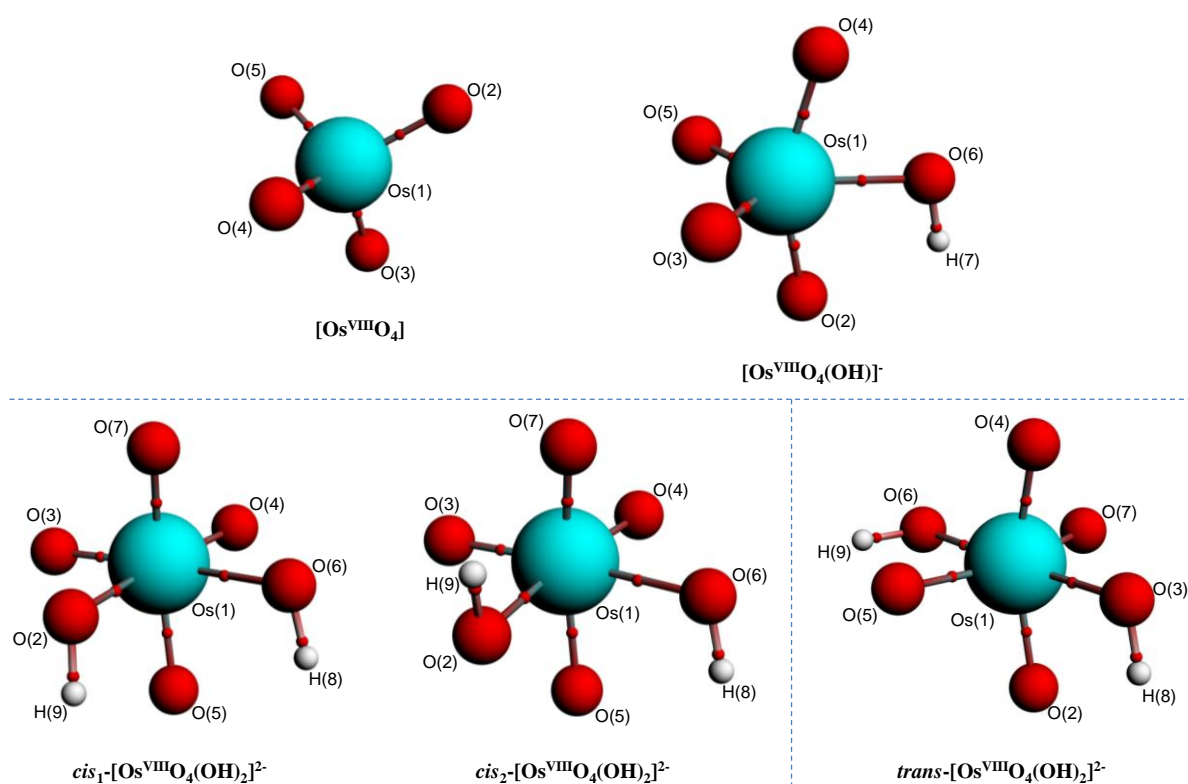


**Figure 3.2.** Molecular graphs of stable  $\text{Os}^{\text{VIII}}$  oxo/hydroxido structures in the simulated aqueous phase (PBE functional) pertaining to equations 3.3 & 3.4 with small red spheres representing (3,-1) critical points.

Comparison of experimentally obtained IR vibrational frequencies and Os-O bond lengths of  $\text{Os}^{\text{VIII}}\text{O}_4$ <sup>13,19,20</sup> agrees well with that obtained from the DFT calculations, Table 3.2 and Table 3.3, supporting the computational methodology.

**Table 3.2. Computed and experimental harmonic frequencies of Os<sup>VIII</sup>O<sub>4</sub> (cm<sup>-1</sup>).**

mode <i>i</i>	Computed (PBE)		Experimental <sup>19</sup>	
	gas phase	COSMO (aqueous)	gas phase (observed)	gas phase (estimated)
1 (A <sub>1</sub> )	985.1	984.2	965.2	974.3
2 (E)	333.3	326.2	333.1	345.2
3 (T <sub>2</sub> )	968.2	941.7	960.5	976.9
4 (T <sub>2</sub> )	329.9	313.9	329.0	345.0

**Table 3.3. Computed and experimental Os=O bond length of Os<sup>VIII</sup>O<sub>4</sub> (Å).**

Computed (PBE)		Experimental		
gas phase	COSMO (aqueous)	gas phase <sup>20</sup>	Crystallographic <sup>13</sup>	
1.7125	1.7115	1.712 (3)	1.684 (7)	1.710 (7)

A detailed conformational analysis of the five-coordinate [Os<sup>VIII</sup>O<sub>4</sub>(OH)]<sup>-</sup> species reveals only one stable equilibrium geometry, shown in Figure 3.2, with a coordinated hydroxido ligand positioned pseudo-equatorially. There is no experimental X-ray diffraction data of the [Os<sup>VIII</sup>O<sub>4</sub>(OH)]<sup>-</sup> species available for direct comparison. However, the equilibrium constants listed in Table 3.1 can be compared to our DFT-calculated values of the coordination sphere expansion reaction, equation 3.3, in order to establish its validity. This explains why Mayer *et al.*<sup>6</sup> do not report their gas phase, DFT-calculated equilibrium constants to compare with the available experimental data. Our calculated  $\Delta G^\circ_{rxn}$  of reaction 3.3, Table 3.4, in the gas phase compare poorly with experiment for all the functionals used, where the equilibrium constant,  $K_1$ , is overestimated by thirty to forty orders of magnitude. By contrast, apart from the LDA functional, the agreement between experiment and DFT-calculated  $\Delta G^\circ_{rxn}$  in the simulated aqueous phase is, in our opinion, excellent considering the relatively small average experimental  $\Delta G^\circ_{rxn}$  of approximately -2.69 kcal.mol<sup>-1</sup>.<sup>6-8</sup>

**Table 3.4.** Calculated standard reaction Gibbs free energies in kcal.mol<sup>-1</sup> and equilibrium constants of reaction 3.3 at 298.15 K.

Functional	gas phase		COSMO (aqueous)	
	$\Delta G^\circ_{rxn}$	$K_1$	$\Delta G^\circ_{rxn}$	$K_1$
LDA	-58.95	$1.61 \times 10^{43}$	-15.63	$2.85 \times 10^{11}$
PBE	-45.76	$3.50 \times 10^{33}$	-1.60	14.97
PBE-D	-46.36	$9.61 \times 10^{33}$	-1.19	7.50
PBE-D3	-46.30	$8.69 \times 10^{33}$	-2.42	59.20
PBE-D3(BJ)	-47.01	$2.87 \times 10^{34}$	-3.01	160.86
PBE-dDsC	-46.87	$2.27 \times 10^{34}$	-2.84	121.13
mPBE	-43.96	$1.68 \times 10^{32}$	0.18	0.74
BLYP	-41.47	$2.49 \times 10^{30}$	4.50	$5.05 \times 10^{-4}$
BLYP-D	-41.08	$1.28 \times 10^{30}$	3.43	$3.07 \times 10^{-3}$
BLYP-D3	-41.18	$1.52 \times 10^{30}$	3.37	$3.39 \times 10^{-3}$
PW91	-46.93	$2.51 \times 10^{34}$	-2.70	95.33
M06L	-45.13	$1.19 \times 10^{33}$	-0.98	5.20
<b>Experimental<sup>a</sup></b>			<b>-2.69</b>	<b>93.67</b>

<sup>a</sup> Calculated average experimental value taken from references 6, 7 and 8.

It may, however, be argued that the calculated values obtained by BLYP, BLYP-D and BLYP-D3 compare poorly with the experimental value since they do not have the correct sign of  $\Delta G^\circ_{rxn}$  w.r.t. reaction 3.3. This is not problematic if the following is taken into account and to simplify the discussion we consider a relatively easy to conceptualise reaction 3.8.



If  $K_{ex}$  is equal to one there is a 1:1 concentration ratio of A and B, and  $\Delta G^\circ_{rxn}$  of reaction 3.8 is equal to zero. If the concentration ratio of A and B is 0.4:0.6, then  $K_{ex}$  is equal to 1.5 and  $\Delta G^\circ_{rxn}$  has a slight negative value equalling  $-1.005 \text{ kJ.mol}^{-1}$ . By contrast, if the concentration ratio of A and B is 0.6:0.4 the  $K_{ex}$  is equal to 0.66 and  $\Delta G^\circ_{rxn}$  has a slight positive number of  $1.005 \text{ kJ.mol}^{-1}$ . Even though  $\Delta G^\circ_{rxn}$  is now positive a significant amount of B is still present at equilibrium. The same argument holds for reaction 3.3 w.r.t. the positive BLYP, BLYP-D and BLYP-D3  $\Delta G^\circ_{rxn}$ 's obtained and therefore the agreement with experiment is actually quite good.

The DFT calculations, Table 3.4, provide strong support for the formation of a five-coordinate  $[\text{Os}^{\text{VIII}}\text{O}_4(\text{OH})]^-$  species. Moreover, in the gas phase the DFT computational results largely favour the formation of a five-coordinate  $[\text{Os}^{\text{VIII}}\text{O}_4(\text{OH})]^-$  species

( $\Delta G^\circ_{rxn} \approx -46 \text{ kcal.mol}^{-1}$ ) whereas in the simulated solvent, COSMO aqueous phase model, the  $\Delta G^\circ_{rxn}$  is only slightly negative or positive, Table 3.4. This suggests that hydration energy plays a large role in decreasing the relative thermodynamic stability of the  $[\text{Os}^{\text{VIII}}\text{O}_4(\text{OH})]^-$  species w.r.t. the reactants. The COSMO calculated hydration energies of  $\text{Os}^{\text{VIII}}\text{O}_4$ ,  $\text{OH}^-$  and  $[\text{Os}^{\text{VIII}}\text{O}_4(\text{OH})]^-$  are -10.26, -96.09 and -58.94  $\text{kcal.mol}^{-1}$  (PBE functional), respectively. The relatively large hydration energy of the high charge density hydroxide anion compared to the other species decreases the gas phase  $\Delta G^\circ_{rxn}$  of reaction 3.3 by approximately 40 – 47  $\text{kcal.mol}^{-1}$ , depending on the functional used. Considering the above, the thermodynamic driving force of reaction 3.3 is the bonding energy of a hydroxido ligand. To investigate this further, insight into the bonding interaction occurring between the  $\text{Os}^{\text{VIII}}\text{O}_4$  and  $\text{OH}^-$  moieties is necessary. Consequently, we performed an energy decomposition analysis (EDA) as proposed by Rauk and Ziegler.<sup>21</sup> Although Bader criticises energy partition schemes,<sup>22</sup> due to fact that unique partitioning cannot be performed, there are many examples, notably by Frenking,<sup>23</sup> where chemical insight and estimation of bond dissociation energies can be obtained to describe the physical properties of the chemical system at hand. The bond dissociation energy,  $D_e$ , between two fragments Q and P (Q =  $\text{Os}^{\text{VIII}}\text{O}_4$ , P =  $\text{OH}^-$ ) consist of two main energetic contributions, namely the interaction ( $\Delta E_{int}$ ) and preparation energy ( $\Delta E_{prep}$ ), equation 3.9.  $\Delta E_{prep}$  is also known as the ‘deformation energy’ and is the electronic energy difference between compound QP and the fragments Q and P present in their equilibrium geometry.

$$-D_e = \Delta E_{int} + \Delta E_{prep} \quad 3.9$$

The  $\Delta E_{int}$  term between two fragments is defined as the sum of several main energetic contributions, equation 3.10.

$$\Delta E_{int} = \Delta E_{Pauli} + \Delta E_{elstat} + \Delta E_{orb} + \Delta E_{disp} + \Delta E_{solv} \quad 3.10$$

The first two terms of  $\Delta E_{int}$ , equation 3.10, are computed by using the unperturbed fragments and account for the Pauli (steric) repulsion ( $\Delta E_{Pauli}$ ) and electrostatic interaction ( $\Delta E_{elstat}$ ), whilst the third term ( $\Delta E_{orb}$ ) represents the energy released when the fragment electron densities are allowed to relax to their equilibrium electron densities. For covalent bonds the absolute value of  $\Delta E_{orb}$  is larger than  $\Delta E_{elstat}$ , while the opposite holds true for ionic bonds. Dispersion and solvation energies ( $\Delta E_{disp}$  and  $\Delta E_{solv}$ , respectively) make up the remaining contributions to the total  $\Delta E_{int}$ . It should be noted that the energy decomposition analysis is

dependent on the nature and structure of the chosen fragments, especially for charged species.<sup>24</sup> The interaction energies are biased by the nature of the fragments and the charge transfer between them which makes the determination of the relative ionicity/covalency of the Os<sup>VIII</sup>-OH bond challenging. This is discussed further when the topological analysis of the electron density using the QTAIM method is presented below (Section 3.2.3). The calculated EDA results obtained using the above approach for the [Os<sup>VIII</sup>O<sub>4</sub>(OH)]<sup>-</sup> anion were done in both gas and simulated aqueous phases (Table 3.5).

**Table 3.5.** EDA of the Os<sup>VIII</sup>-OH ligand bond of [Os<sup>VIII</sup>O<sub>4</sub>(OH)]<sup>-</sup> in the gas and simulated aqueous phase.

Functional	phase	$\Delta E_{int}$	$\Delta E_{Pauli}$	$\Delta E_{elstat}$	$\Delta E_{orb}$	$\Delta E_{disp}$	$\Delta E_{solv}$	$\Delta E_{prep}$	$-D_e$
PBE	gas	-104.97	270.48	-241.60	-133.85	-	-	48.68	-56.29
	aqueous	-162.66	270.66	-242.33	-132.08	-	-58.91	49.25	-113.41
PBE-D	gas	-105.60	267.58	-239.56	-132.96	-0.66	-	48.88	-56.72
	aqueous	-163.43	268.21	-240.61	-131.35	-0.71	-58.97	49.56	-113.87
PBE-D3	gas	-105.60	269.75	-241.13	-133.64	-0.58	-	48.81	-56.79
	aqueous	-163.37	270.11	-241.98	-131.97	-0.60	-58.93	49.46	-113.91
PBE-D3(BJ)	gas	-106.19	272.11	-242.63	-134.43	-1.24	-	48.79	-57.40
	aqueous	-163.88	271.89	-243.08	-132.55	-1.24	-58.90	49.28	-114.60
PBE-dDsC	gas	-105.89	273.21	-243.39	-134.67	-1.04	-	48.60	-57.29
	aqueous	-163.37	272.58	-243.44	-132.61	-0.99	-58.91	48.94	-114.43

From this data it is seen that the calculated values of  $\Delta E_{Pauli}$ ,  $\Delta E_{elstat}$ ,  $\Delta E_{orb}$  and  $\Delta E_{prep}$  differ by less than approximately 1.20 kcal.mol<sup>-1</sup> in both the gas and simulated aqueous phase while  $\Delta E_{disp}$ , as obtained by four different dispersion correction methods, contributes only minimally to  $\Delta E_{int}$ . In the gas phase approximately two-thirds of the stabilisation of the Os<sup>VIII</sup>-OH metal-hydroxido bond is due to electrostatic contributions which reflect its ionic character. The ratio of  $\Delta E_{elstat}:\Delta E_{orb}$  remains approximately 1.80 regardless of whether the analysis is done in the gas or simulated aqueous phase. It is the  $\Delta E_{solv}$  contribution, of approximately -58.90 kcal.mol<sup>-1</sup>, which dramatically changes  $\Delta E_{int}$  (and therefore also  $D_e$ ) in the simulated aqueous phase. Since the calculated  $\Delta E_{int}$  value is negative in both phases, solvation (hydration) energy is not an essential component to promote the formation of the metal-hydroxido bond in [Os<sup>VIII</sup>O<sub>4</sub>(OH)]<sup>-</sup>. Taking these factors into account leads to the same conclusion mentioned previously, that reaction 3.3 is thermodynamically driven by the bonding energy of the Os<sup>VIII</sup>-OH metal-hydroxido ligand.

The nature of the Os<sup>VIII</sup>-OH metal-hydroxido bond can be further analysed by using ETS-NOCV which is a combined charge and energy decomposition scheme for bond analysis.<sup>25</sup> The  $\Delta E_{orb}$  stabilising contribution (Table 3.5), representing the interactions between the

occupied molecular orbitals of one fragment with the unoccupied molecular orbitals of the other fragment, as well as the mixing of occupied and virtual orbitals within the same fragment (inner-fragment polarisation), is linked to the electronic bonding effect from the formation of a chemical bond. ETS-NOCV yields the contributions from the different natural orbitals (constructed from the fragment orbitals) to the total orbital contribution.

The sum of the calculated energies of the two major deformation-density channels,  $\Delta\rho_1$  and  $\Delta\rho_2$ , to the covalent contribution of the Os<sup>VIII</sup>-OH bond energy make up approximately 85% of the total orbital energy stabilisation (Table 3.6).

**Table 3.6.** ETS-NOCV calculated energies (kcal.mol<sup>-1</sup>), in the simulated aqueous phase, of the two highest deformation-density contributions,  $\Delta\rho_1$  and  $\Delta\rho_2$ , of the Os<sup>VIII</sup>-OH bond in [Os<sup>VIII</sup>O<sub>4</sub>(OH)]<sup>-</sup>.

Functional	$\Delta\rho_1$	$\Delta\rho_2$	$\Delta E_{orb.}$
PBE	-91.49 (69.3%)	-21.19 (16.0%)	-132.08
PBE-D	-90.97 (69.3%)	-21.08 (16.1%)	-131.35
PBE-D3	-91.43 (69.3%)	-21.17 (16.0%)	-131.97
PBE-D3(BJ)	-91.81 (69.3%)	-21.27 (16.0%)	-132.55
PBE-dDsC	-91.83 (69.2%)	-21.26 (16.0%)	-132.61

The two highest deformation-density channels,  $\Delta\rho_1$  and  $\Delta\rho_2$ , are shown in Figure 3.3. They are approximately -91.51 (69%) and -21.20 (16%) kcal.mol<sup>-1</sup> and correspond to  $\sigma$ - and  $\pi$ -donations, respectively, from the occupied  $2p$  orbitals of the hydroxido oxygen to the empty  $6d$  orbitals of the osmium metal-centre.

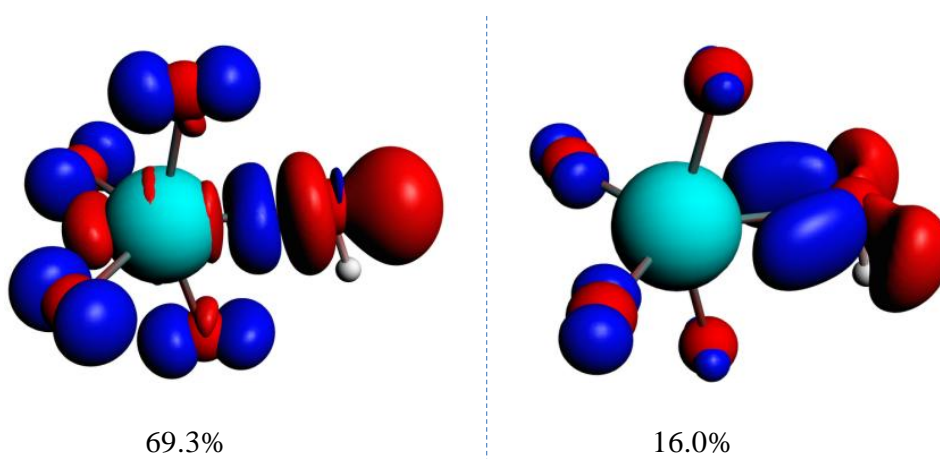


**Figure 3.3.** Natural orbitals for the Chemical Valence (NOCV) showing the two largest contributions to the orbital energy of each of the Os<sup>VIII</sup>-OH interactions of [Os<sup>VIII</sup>O<sub>4</sub>(OH)]<sup>-</sup> in the simulated aqueous phase with the PBE functional (contribution presented as percentage of the total orbital interaction energy).

Following the study pertaining to reaction 3.3, we first proceeded to investigate whether the octahedral  $\text{Os}^{\text{VIII}}$  complex that contains a water ligand,  $[\text{Os}^{\text{VIII}}\text{O}_4(\text{OH})(\text{H}_2\text{O})]^-$ , that Griffith proposed is thermodynamically favoured w.r.t. the identified species shown in Figure 3.2.<sup>12</sup> Only one stable geometry of the *cis* stereoisomer was found, Figure 3.4, while numerous attempts to optimise the *trans* stereoisomer were not successful. In all those calculations the Os-water “ligand” distance increases with each self-consistent field (SCF) iteration.

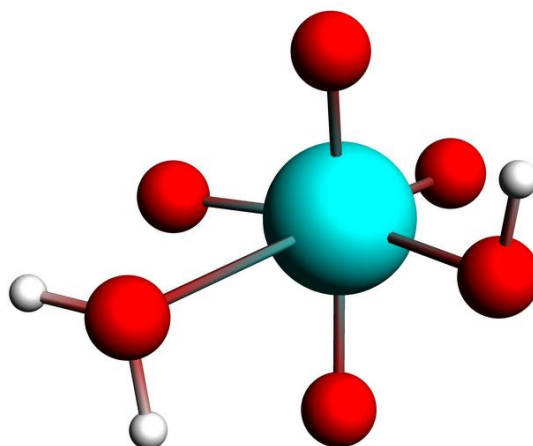
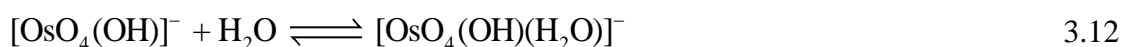
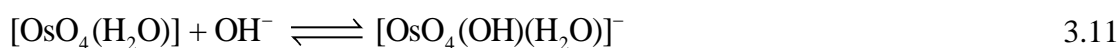


**Figure 3.4.** Equilibrium geometry of *cis*- $[\text{Os}^{\text{VIII}}\text{O}_4(\text{OH})(\text{H}_2\text{O})]^-$  in the simulated aqueous phase (PBE functional).

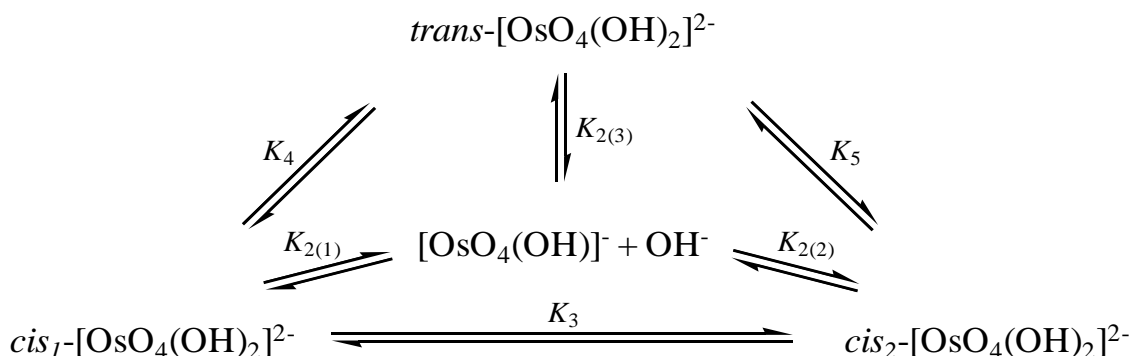
The mechanism of formation of the *cis*- $[\text{Os}^{\text{VIII}}\text{O}_4(\text{OH})(\text{H}_2\text{O})]^-$  complex cannot occur according to, the hypothetical, reaction 3.11 since  $[\text{Os}^{\text{VIII}}\text{O}_4(\text{H}_2\text{O})]$  does not exist. However, *cis*- $[\text{Os}^{\text{VIII}}\text{O}_4(\text{OH})(\text{H}_2\text{O})]^-$  can form according to reaction 3.12, where the already-identified five-coordinate  $[\text{Os}^{\text{VIII}}\text{O}_4(\text{OH})]^-$  complex reacts with a water molecule.



The DFT-calculated (PBE functional)  $\Delta G^\circ_{\text{rxn}}$  for reaction 3.12 in the simulated aqueous phase is  $9.10 \text{ kcal.mol}^{-1}$ , which equates to a  $K_{\text{eq}}$  value of  $2.14 \times 10^{-7}$ . Formation of this complex is not thermodynamically favoured and it cannot account for the second equivalence point of the acid/base titration data reported by Galbács *et al.*<sup>7</sup> We conclude that the dominant  $\text{Os}^{\text{VIII}}$  species above “pH” 14.4 [spectrum of Galbács *et al.*<sup>7</sup>] is not  $[\text{Os}^{\text{VIII}}\text{O}_4(\text{OH})(\text{H}_2\text{O})]^-$ . The second equivalence point [spectrum of Galbács *et al.*<sup>7</sup>] must be due to the formation of a different  $\text{Os}^{\text{VIII}}$  species, possibly an octahedral  $[\text{Os}^{\text{VIII}}\text{O}_4(\text{OH})_2]^{2-}$  complex, as depicted by equation 3.4.



To investigate reaction 3.4 in more detail, conformational analyses using relaxed potential energy scans were performed in order to identify equilibrium structures of the six-coordinate  $\text{Os}^{\text{VIII}}$  species. Three stable equilibrium geometries were found, two *cis* and one *trans* structure, as shown in Figure 3.2. A diagram that briefly summarises the three coordination sphere expansion reactions and the stereoisomer interchange of the three six-coordinate  $\text{Os}^{\text{VIII}}$  oxo/hydroxido species is shown in Scheme 3.1.

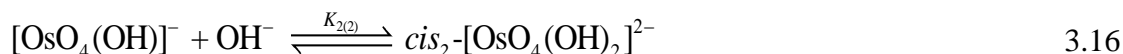
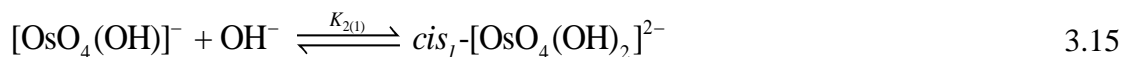


**Scheme 3.1.** Coordination sphere expansion reactions of  $[\text{Os}^{\text{VIII}}\text{O}_4(\text{OH})]^-$  ( $K_{2(1)}$ ,  $K_{2(2)}$  and  $K_{2(3)}$ ) and stereoisomer interchange reactions of  $[\text{Os}^{\text{VIII}}\text{O}_4(\text{OH})_2]^{2-}$  species ( $K_3$ ,  $K_4$  and  $K_5$ ).

The DFT-calculated equilibrium constants of the isomerisation reactions 3.13 and 3.14 are  $K_3 = 1.03$  and  $K_4 = 1.0 \times 10^6$ , respectively, *i.e.* the two *cis* conformations are approximately  $10 \text{ kcal.mol}^{-1}$  more thermodynamically stable than the *trans*-species. The ratio of *cis*- to *trans*- $[\text{Os}^{\text{VIII}}\text{O}_4(\text{OH})_2]^{2-}$  species is approximately a million to one and therefore the *trans* species is not taken into account when the second coordination sphere expansion of the five-coordinate  $[\text{Os}^{\text{VIII}}\text{O}_4(\text{OH})]^-$  to the six-coordinate  $[\text{Os}^{\text{VIII}}\text{O}_4(\text{OH})_2]^{2-}$  species is discussed below.



Experimentally, the two *cis*- $[\text{Os}^{\text{VIII}}\text{O}_4(\text{OH})_2]^{2-}$  species in solution cannot be distinguished from one another. Therefore, in order to calculate  $K_2$  by means of DFT, equation 3.4 has to be re-written as shown in equations 3.15 and 3.16. Addition of the equilibrium expressions associated with equations 3.15 and 3.16 results in equation 3.17 which relates the equilibrium constant of equation 3.4 with those in equations 3.15 and 3.16. The associated standard reaction Gibbs free energy of the second coordination sphere expansion of the five-coordinate  $[\text{Os}^{\text{VIII}}\text{O}_4(\text{OH})]^-$  to the six-coordinate  $[\text{Os}^{\text{VIII}}\text{O}_4(\text{OH})_2]^{2-}$  species is given by equation 3.18.



$$\begin{aligned} K_{2(1)} + K_{2(2)} &= \frac{\text{cis}_1\text{-}[\text{OsO}_4(\text{OH})_2]^{2-}}{[\text{OsO}_4(\text{OH})^-][\text{OH}^-]} + \frac{\text{cis}_2\text{-}[\text{OsO}_4(\text{OH})_2]^{2-}}{[\text{OsO}_4(\text{OH})^-][\text{OH}^-]} \\ &= \frac{[\text{OsO}_4(\text{OH})_2]^{2-}}{[\text{OsO}_4(\text{OH})^-][\text{OH}^-]} = K_2 \end{aligned} \quad 3.17$$

$$\text{where} \quad \text{cis}_1\text{-}[\text{OsO}_4(\text{OH})_2]^{2-} + \text{cis}_2\text{-}[\text{OsO}_4(\text{OH})_2]^{2-} = [\text{OsO}_4(\text{OH})_2]^{2-}$$

$$\Delta G_{rxn}^\circ = -RT \ln \{K_{2(1)} + K_{2(2)}\} = -RT \ln(K_2) \quad 3.18$$

In the gas phase the calculated  $\Delta G_{rxn}^\circ$  values of reaction 3.4 (3.15, 3.16) are large and positive, Table 3.7, in contrast to the large and negative values of reaction 3.3. Conversely, the agreement between experimental and DFT-calculated standard reaction Gibbs free energies in the simulated aqueous phase are excellent, excluding the LDA functional. This result once again highlights the importance of hydration energy since the accuracy of the DFT-calculated  $\Delta G_{rxn}^\circ$  values of both reactions 3.3 & 3.4 in the presence of the simulated aqueous phase are vastly superior to those calculated in the gas phase. The hydration energies (PBE functional) of the doubly-charged  $\text{cis}_1\text{-}$  and  $\text{cis}_2\text{-}[\text{Os}^{\text{VIII}}\text{O}_4(\text{OH})_2]^{2-}$  species are  $-219.40$  and  $-217.98$  kcal.mol<sup>-1</sup>, respectively, and are relatively large compared to the hydration energies of  $[\text{OH}]^-$  and  $[\text{Os}^{\text{VIII}}\text{O}_4(\text{OH})]^-$ ,  $-96.09$  and  $-58.94$  kcal.mol<sup>-1</sup>, respectively. This implies that the hydration energy of the  $\text{cis-}[\text{Os}^{\text{VIII}}\text{O}_4(\text{OH})_2]^{2-}$  species is the thermodynamic driving force of reaction 3.4. The good agreement between experimental<sup>7,8</sup> and calculated thermodynamic parameters provides good evidence that the  $\text{Os}^{\text{VIII}}$  species present in basic aqueous solutions are  $\text{Os}^{\text{VIII}}\text{O}_4$ ,  $[\text{Os}^{\text{VIII}}\text{O}_4(\text{OH})]^-$  and two  $\text{cis-}[\text{Os}^{\text{VIII}}\text{O}_4(\text{OH})_2]^{2-}$  complexes, *i.e.* equations 3.3 & 3.4 and not equations 3.1 & 3.2.

**Table 3.7. Calculated standard reaction Gibbs free energies in kcal.mol<sup>-1</sup> and equilibrium constants of reaction 3.4 at 298.15 K.**

Functional	gas phase		COSMO (aqueous)	
	$\Delta G^\circ_{rxn}$	$K_{eq}$	$\Delta G^\circ_{rxn}$	$K_{eq}$
LDA	52.39	$3.95 \times 10^{-39}$	-10.79	$8.06 \times 10^7$
PBE	62.03	$3.43 \times 10^{-46}$	-0.03	1.06
PBE-D	60.03	$9.89 \times 10^{-45}$	-2.61	82.23
PBE-D3	60.91	$2.27 \times 10^{-45}$	-0.61	2.82
PBE-D3(BJ)	60.93	$2.18 \times 10^{-45}$	-0.95	4.96
PBE-dDsC	60.58	$3.93 \times 10^{-45}$	-1.15	6.95
mPBE	63.07	$5.86 \times 10^{-47}$	1.48	0.08
BLYP	65.25	$1.48 \times 10^{-48}$	3.12	0.01
BLYP-D	60.40	$5.34 \times 10^{-45}$	-0.32	1.70
BLYP-D3	61.03	$1.85 \times 10^{-45}$	0.42	0.49
PW91	60.82	$2.61 \times 10^{-45}$	-0.98	5.23
M06L	59.74	$1.62 \times 10^{-44}$	-3.92	$7.48 \times 10^2$
<b><u>Experimental<sup>a</sup></u></b>			<b><u>0.33</u></b>	<b><u>0.58</u></b>

<sup>a</sup> Calculated average experimental value taken from references 7 and 8.

The results of EDA calculations performed on the Os<sup>VIII</sup>-OH bonds of the three six-coordinate [Os<sup>VIII</sup>O<sub>4</sub>(OH)<sub>2</sub>]<sup>2-</sup> species are encapsulated in Table 3.8. The two hydroxido ligands in each of the three complex species are indistinguishable from one another due to their spatial symmetry and therefore the calculated  $D_e$  values of the bonds of both ligands were the same regardless of which one was chosen.

**Table 3.8. EDA of the Os<sup>VIII</sup>-OH ligand bond of [Os<sup>VIII</sup>O<sub>4</sub>(OH)<sub>2</sub>]<sup>2-</sup> complexes in the gas and simulated aqueous phase.**

Species	Functional	phase	$\Delta E_{int}$	$\Delta E_{Pauli}$	$\Delta E_{elstat}$	$\Delta E_{orb.}$	$\Delta E_{disp.}$	$\Delta E_{solv.}$	$\Delta E_{prep}$	$-D_e$	
<i>cis</i> <sub>1</sub> - [OsO <sub>4</sub> (OH) <sub>2</sub> ] <sup>2-</sup>	PBE	gas	32.79	176.92	-65.66	-78.47	-	-	18.29	51.08	
		aqueous	-178.05	187.28	-70.78	-75.13	-	-219.42	16.52	-161.53	
	PBE-D	gas	31.40	173.01	-62.77	-77.47	-0.66	-	17.97	49.37	
		aqueous	-179.65	182.98	-67.45	-74.05	-1.44	-219.69	16.22	-163.43	
	PBE-D3	gas	31.84	176.29	-65.16	-78.31	-0.98	-	18.13	49.97	
		aqueous	-179.12	186.43	-70.20	-74.93	-0.99	-219.43	16.45	-162.67	
	PBE-D3(BJ)	gas	32.19	176.90	-65.48	-78.16	-1.07	-	17.94	50.13	
		aqueous	-178.47	186.45	-70.05	-74.41	-1.07	-219.39	15.91	-162.56	
	PBE-dDsC	gas	32.02	178.62	-66.65	-78.54	-1.41	-	17.70	49.72	
		aqueous	-178.48	187.02	-70.41	-74.52	-1.17	-219.40	15.74	-162.74	
	<i>cis</i> <sub>2</sub> - [OsO <sub>4</sub> (OH) <sub>2</sub> ] <sup>2-</sup>	PBE	gas	32.47	174.69	-64.63	-77.59	-	-	18.04	50.51
			aqueous	-177.42	185.02	-69.50	-75.44	-	-217.50	16.19	-161.23
PBE-D		gas	30.88	170.36	-61.65	-76.39	-1.44	-	18.87	49.75	
		aqueous	-179.06	179.67	-65.47	-74.04	-1.46	-217.76	15.92	-163.14	
PBE-D3		gas	31.35	173.75	-64.07	-77.34	-0.99	-	18.04	49.39	
		aqueous	-178.72	182.98	-68.19	-74.97	-0.99	-217.55	16.31	-162.41	
PBE-D3(BJ)		gas	31.59	174.90	-64.77	-77.47	-1.07	-	17.96	49.55	
		aqueous	-178.24	184.39	-69.02	-75.06	-1.06	-217.49	15.91	-162.33	
PBE-dDsC		gas	31.50	176.80	-66.03	-77.89	-1.38	-	17.68	49.18	
		aqueous	-178.23	240.99	-69.32	-75.14	-1.16	-217.52	15.72	-162.51	
<i>trans</i> - [OsO <sub>4</sub> (OH) <sub>2</sub> ] <sup>2-</sup>		PBE	gas	17.51	227.41	-102.11	-107.79	-	-	42.64	60.15
			aqueous	-195.87	237.32	-108.96	-104.06	-	-220.17	42.74	-153.13
	PBE-D	gas	16.42	226.46	-101.58	-107.56	-0.90	-	42.80	59.22	
		aqueous	-197.54	234.65	-107.27	-103.36	-1.02	-220.54	43.25	-154.29	
	PBE-D3	gas	16.71	227.32	-102.11	-107.77	-0.73	-	42.66	59.37	
		aqueous	-196.77	236.93	-108.75	-103.96	-0.76	-220.23	42.80	-153.97	
	PBE-D3(BJ)	gas	16.63	229.12	-103.31	-108.21	-0.97	-	42.63	59.26	
		aqueous	-196.92	240.36	-111.15	-104.91	-0.97	-220.25	42.82	-154.10	
	PBE-dDsC	gas	16.57	230.83	-104.46	-108.60	-1.20	-	42.38	58.95	
		aqueous	-196.80	240.99	-111.52	-105.00	-0.98	-220.29	42.60	-154.20	

In contrast to the Os<sup>VIII</sup>-OH bond in the [Os<sup>VIII</sup>O<sub>4</sub>(OH)]<sup>-</sup> complex, the stabilisation contributions from the orbital and electrostatic interactions of all three [Os<sup>VIII</sup>O<sub>4</sub>(OH)<sub>2</sub>]<sup>2-</sup> complexes, as calculated for in the gas phase, are not large enough to yield negative  $D_e$  values. This result reflects why the large positive calculated  $\Delta G_{rxn}^{\circ}$  values in the gas phase, Table 3.7, were obtained. The ratio of  $\Delta E_{elstat}:\Delta E_{orb}$  in each of the two *cis*-[Os<sup>VIII</sup>O<sub>4</sub>(OH)<sub>2</sub>]<sup>2-</sup> complex species is approximately 0.83 and 0.92 in the gas and simulated aqueous phase, respectively, and approximately 0.95 and 1.05 for the *trans*-[Os<sup>VIII</sup>O<sub>4</sub>(OH)<sub>2</sub>]<sup>2-</sup> complex in the gas and simulated aqueous phase. The Os<sup>VIII</sup>-OH interaction has slightly less covalent character in the *trans*-[Os<sup>VIII</sup>O<sub>4</sub>(OH)<sub>2</sub>]<sup>2-</sup> species. The electrostatic stabilisation of the Os<sup>VIII</sup>-OH interaction of all three species is less compared to that of [Os<sup>VIII</sup>O<sub>4</sub>(OH)]<sup>-</sup> since the two

fragments involved are now both anionic, resulting in lower attraction as compared to when only one fragment is negatively charged. Similarly to that of the  $[\text{Os}^{\text{VIII}}\text{O}_4(\text{OH})]^-$  complex, contributions of  $\Delta E_{\text{disp}}$  are minimal for all three complexes. Despite the fact that the *trans*- $[\text{Os}^{\text{VIII}}\text{O}_4(\text{OH})_2]^{2-}$  complex has a more favourable  $\Delta E_{\text{int}}$  compared to that of the two *cis*- $[\text{Os}^{\text{VIII}}\text{O}_4(\text{OH})_2]^{2-}$  species, it is the significantly larger deformation energy contribution which makes  $D_e$ , and also the relative stability of the *trans*- $[\text{Os}^{\text{VIII}}\text{O}_4(\text{OH})_2]^{2-}$  complex, less than that of the two *cis*- $[\text{Os}^{\text{VIII}}\text{O}_4(\text{OH})_2]^{2-}$  species. EDA analysis therefore provides a reason why the *trans*- $[\text{Os}^{\text{VIII}}\text{O}_4(\text{OH})_2]^{2-}$  complex is thermodynamically less stable compared to the two *cis*- $[\text{Os}^{\text{VIII}}\text{O}_4(\text{OH})_2]^{2-}$  species. The bond dissociation energy of the *trans*- $[\text{Os}^{\text{VIII}}\text{O}_4(\text{OH})_2]^{2-}$  species is approximately 9.53 (gas phase) and 8.52 kcal.mol<sup>-1</sup> (simulated aqueous phase) less favourable compared to the two *cis*- $[\text{Os}^{\text{VIII}}\text{O}_4(\text{OH})_2]^{2-}$  species. The calculated  $\Delta E_{\text{int}}$  and  $D_e$  values in the gas phase are relatively large positive values meaning that formation of the second Os<sup>VIII</sup>-OH metal-hydroxido bond is thermodynamically unfavourable in the absence of an adequate solvation (hydration) energy contribution. It is only when the hydration energy,  $\Delta E_{\text{solv}}$  contribution, is present that negative  $\Delta E_{\text{int}}$  and  $D_e$  values are obtained. Therefore, in contrast to reaction 3.3, reaction 3.4 is thermodynamically driven by the larger hydration energy of the doubly-charged  $[\text{Os}^{\text{VIII}}\text{O}_4(\text{OH})_2]^{2-}$  species in comparison with that of the two singly-charged reactants, *i.e.*  $[\text{Os}^{\text{VIII}}\text{O}_4(\text{OH})]^-$  and a hydroxide anion.

Calculated results of ETS-NOCV analysis of the Os<sup>VIII</sup>-OH bond in the three six-coordinate  $[\text{Os}^{\text{VIII}}\text{O}_4(\text{OH})_2]^{2-}$  species are similar to that obtained in the five-coordinate  $[\text{Os}^{\text{VIII}}\text{O}_4(\text{OH})]^-$  species. The sum of the calculated energies of the two major deformation-density channels,  $\Delta\rho_1$  and  $\Delta\rho_2$ , to the covalent contribution of the Os<sup>VIII</sup>-OH bond energy make up approximately 85% of the total orbital stabilisation (Table 3.9).

**Table 3.9.** ETS-NOCV calculated energies ( $\text{kcal.mol}^{-1}$ ), in the simulated aqueous phase, of the two highest deformation-density contributions,  $\Delta\rho_1$  and  $\Delta\rho_2$ , of the  $\text{Os}^{\text{VIII}}\text{-OH}$  bond in  $[\text{Os}^{\text{VIII}}\text{O}_4(\text{OH})]^-$ .

Species	Functional	$\Delta\rho_1$	$\Delta\rho_2$	$\Delta E_{orb.}$
<i>cis</i> <sub>1</sub> - $[\text{OsO}_4(\text{OH})_2]^{2-}$	PBE	-53.26 (70.9%)	-11.01 (14.7%)	-75.13
	PBE-D	-52.66 (71.1%)	-10.76 (14.5%)	-74.05
	PBE-D3	-53.14 (70.9%)	-10.97 (14.6%)	-74.93
	PBE-D3(BJ)	-53.28 (71.6%)	-10.31 (13.9%)	-74.41
	PBE-dDsC	-53.32 (71.6%)	-10.34 (13.9%)	-74.52
<i>cis</i> <sub>2</sub> - $[\text{OsO}_4(\text{OH})_2]^{2-}$	PBE	-53.07 (70.4%)	-10.44 (13.8%)	-75.44
	PBE-D	-52.19 (70.5%)	-10.20 (13.8%)	-74.04
	PBE-D3	-52.68 (70.3%)	-10.46 (14.0%)	-74.97
	PBE-D3(BJ)	-53.04 (70.7%)	-10.17 (13.5%)	-75.06
	PBE-dDsC	-53.07 (70.6%)	-10.19 (13.6%)	-75.14
<i>trans</i> - $[\text{OsO}_4(\text{OH})_2]^{2-}$	PBE	-75.03 (72.1%)	-13.94 (13.4%)	-104.06
	PBE-D	-74.61 (72.2%)	-13.80 (13.4%)	-103.36
	PBE-D3	-74.97 (72.1%)	-13.92 (13.4%)	-103.96
	PBE-D3(BJ)	-75.44 (71.9%)	-14.19 (13.5%)	-104.91
	PBE-dDsC	-75.48 (71.9%)	-14.21 (13.5%)	-105.00

The two highest deformation-density channels,  $\Delta\rho_1$  and  $\Delta\rho_2$ , contribute approximately 71% and 16% and correspond to  $\sigma$ - and  $\pi$ - donations, respectively, from the occupied  $2p$  orbitals of the hydroxido oxygen to the empty  $6d$  orbitals of the osmium metal-centre, Figure 3.5.

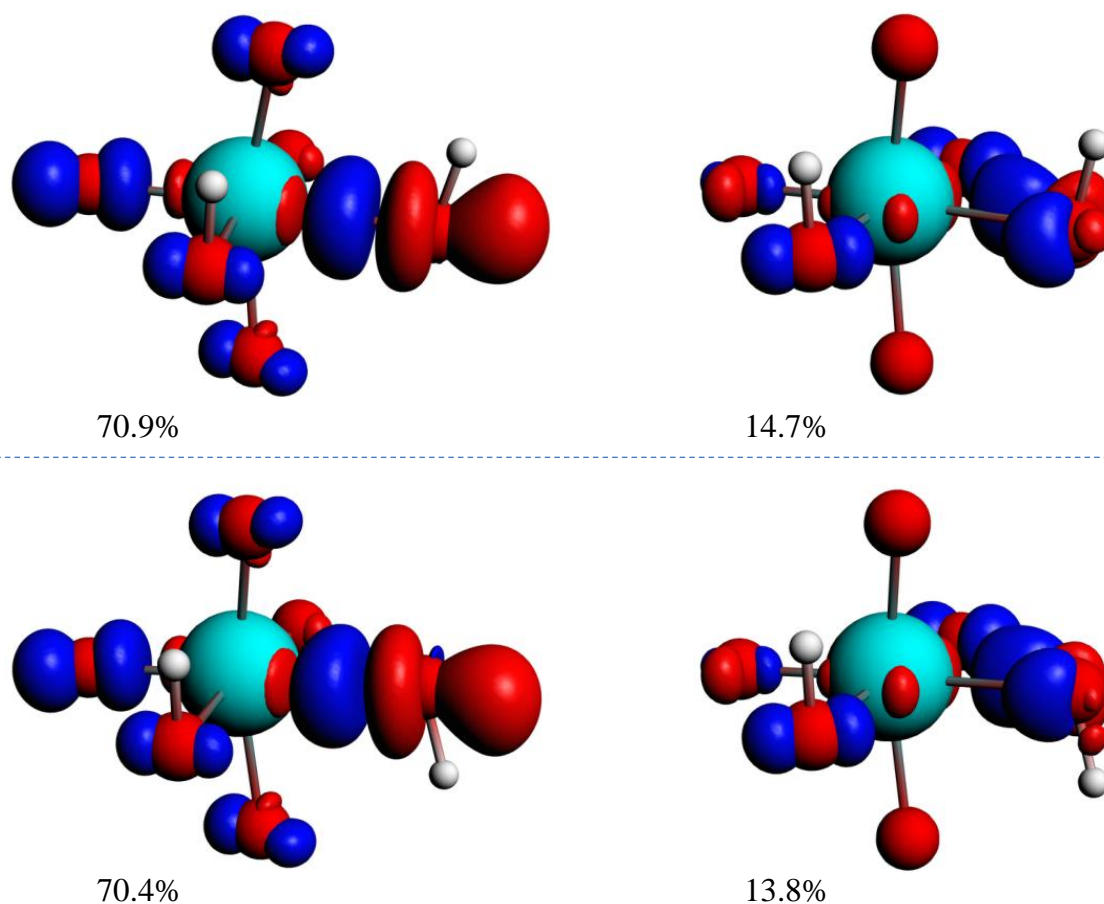


**Figure 3.5.** Natural orbitals for the Chemical Valence (NOCV) showing the two largest contributions to the orbital energy of each of the Os<sup>VIII</sup>-OH interactions of *cis*<sub>1</sub>-[Os<sup>VIII</sup>O<sub>4</sub>(OH)<sub>2</sub>]<sup>2-</sup> (top) and *cis*<sub>2</sub>-[Os<sup>VIII</sup>O<sub>4</sub>(OH)<sub>2</sub>]<sup>2-</sup> (bottom) in the simulated aqueous phase with the PBE functional (contribution presented as percentage of the total orbital interaction energy).

A graphical assessment of how well the DFT-calculated (PBE and PBE-D3 functionals) equilibrium constants of reactions 3.3 and 3.4 compare to the experimentally obtained values is shown in Figure 3.6 where the Os<sup>VIII</sup> species distribution as a function of hydroxide concentration is plotted.

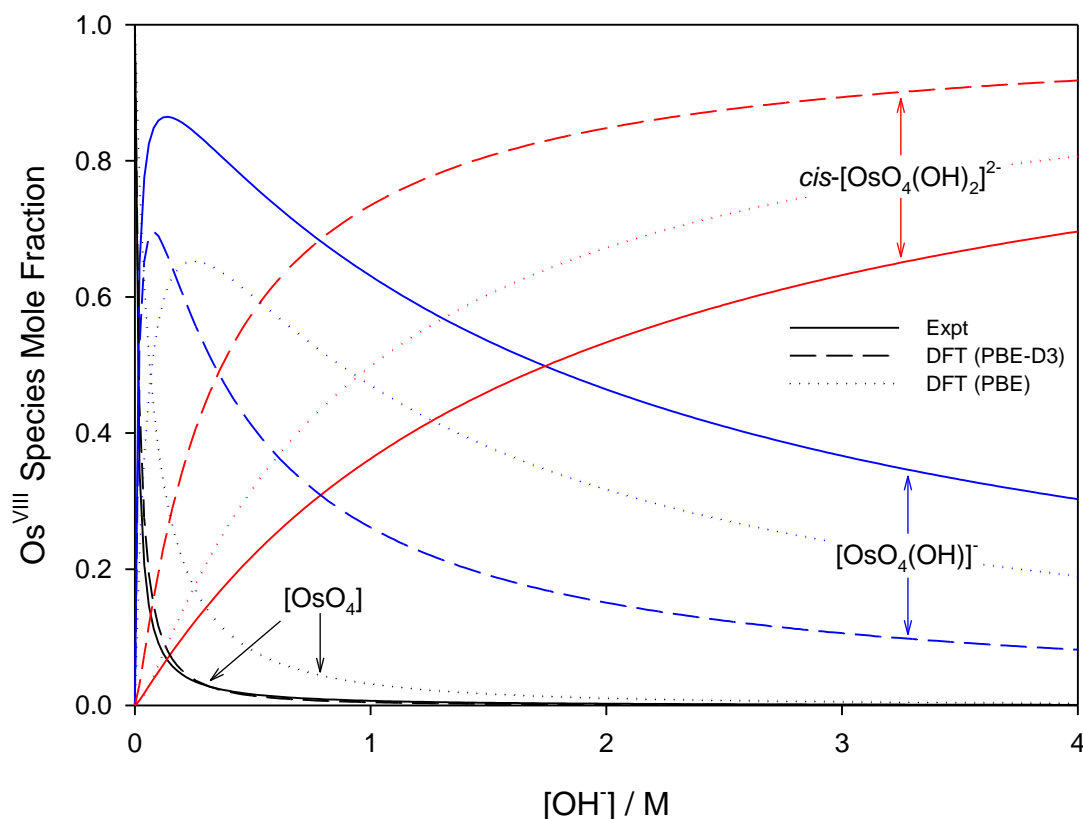


**Figure 3.6.** Speciation curve of  $[\text{OsO}_4(\text{OH})_n]^{n-}$  ( $n = 0, 1, 2$ ) as a function of hydroxide concentration as calculated from DFT (PBE and PBE-D3 functionals) in contrast to experiment.<sup>26</sup>

### 3.2.2 Kinetics of coordination sphere expansion reactions 3.3 & 3.4

It is found experimentally that when a neutral aqueous  $\text{Os}^{\text{VIII}}$  solution is mixed with a relatively concentrated hydroxide solution that a rapid colour change occurs due to coordination sphere expansion reactions 3.3 & 3.4. Stopped-flow kinetics experiments were performed at 298.15 K in an attempt to quantify the rate at which these reactions occur. However, the spectral change occurs in such a small time scale that for all practical purposes a ‘constant’ absorbance versus time signal is obtained, *i.e.* the expected absorbance when  $\text{Os}^{\text{VIII}}$  is present at equilibrium in 2.0 M hydroxide is already observed at the first data point, at 0.001 seconds, which corresponds to the earliest possible reading that the instrument is capable of making. This indicates that the activation Gibbs energy barriers for coordination sphere expansion reactions are relatively low. A computational study was subsequently performed to ascertain the mechanism of coordination sphere expansion and to obtain reaction energy barriers, *i.e.* does hydroxide coordinate directly to  $\text{Os}^{\text{VIII}}\text{O}_4$  and then to  $[\text{Os}^{\text{VIII}}\text{O}_4(\text{OH})]^-$  in two, consecutive, elementary reaction steps as depicted in equations 3.3 &



3.4? In Figure 3.7 (a) the Os<sup>VIII</sup>O<sub>4</sub> species' electrostatic surface potential defined at the 0.03 au electron density indicate that the Os<sup>VIII</sup> atom has four  $\sigma$ -holes<sup>27</sup> of equal magnitude, *i.e.* regions where the Os atom has less electron density compared to neighbouring regions. For this reason a linear transit, relaxed scan, calculation in which a hydroxide ligand was incrementally moved closer to one of the four Os<sup>VIII</sup>  $\sigma$ -holes was performed. The relaxed scan calculations were only done in the simulated aqueous phase. The structure found at the maximum of the potential energy surface was subsequently submitted for a transition state search. The converged geometry structure where the Os<sup>VIII</sup>-OH distance is 3.43 Å, Figure 3.7 (b), has one negative vibrational frequency, corresponding to a saddle point on the PES and one degree of freedom, where the hydroxide oxygen atom vibrates towards and back w.r.t. the Os<sup>VIII</sup> atom. The Gibbs energies of activation of the forward and reverse reactions, reaction 3.3, and their associated rate constants were calculated using equation 3.19, and are listed in Table 3.10.

$$k(T) = \frac{k_B T}{hc^\circ} e^{-\Delta^\ddagger G^\circ/RT} \quad 3.19$$

The rate constants obtained of reaction 3.3 are relatively large and falls in the range of a diffusion-controlled rate-limiting step.<sup>28</sup>

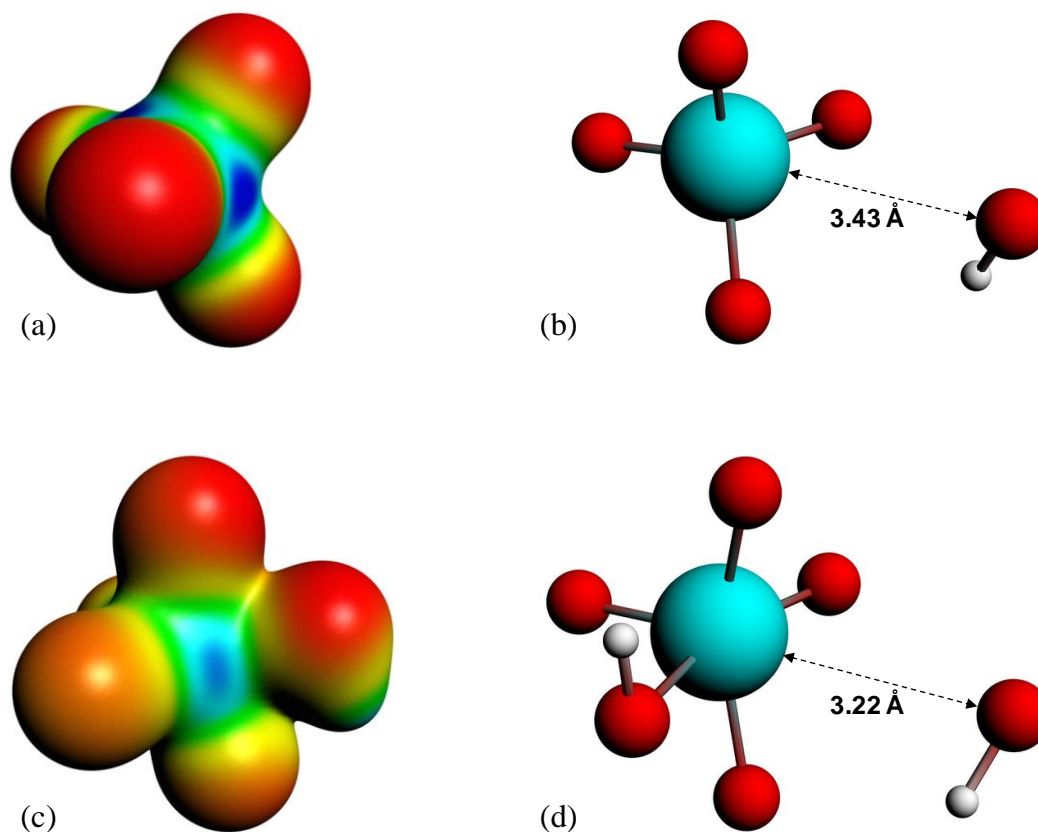


**Figure 3.7.** (a) and (c): Electrostatic surface potential maps of the optimised geometries of  $\text{Os}^{\text{VIII}}\text{O}_4$  and  $[\text{Os}^{\text{VIII}}\text{O}_4(\text{OH})]^-$  in the simulated aqueous phase (PBE functional) corresponding to a density isosurface value of 0.03 au. Negatively and positively charged regions are indicated by red and blue colouring, respectively. (b) and (d): Molecular graphs of the calculated transition state structures (PBE functional) of reactions 3.3 & 3.4, respectively.

**Table 3.10.** Calculated Gibbs Free Energies of activation in  $\text{kcal.mol}^{-1}$  and rate constants of reaction 3.3 at 298.15 K where  $k_1$  and  $k_{-1}$  are the forward and reverse rate constants, respectively.

Functional	$\Delta^\ddagger G^\circ_{\text{forward}}$	$k_1$ ( $\text{L.mol}^{-1}.\text{s}^{-1}$ )	$\Delta^\ddagger G^\circ_{\text{reverse}}$	$k_{-1}$ ( $\text{s}^{-1}$ )
PBE	6.59	$9.23 \times 10^7$	8.19	$6.16 \times 10^6$
PBE-D	6.10	$2.08 \times 10^8$	7.30	$2.78 \times 10^7$
PBE-D3	5.92	$2.85 \times 10^8$	8.34	$4.82 \times 10^6$
PBE-D3(BJ)	7.05	$4.21 \times 10^7$	10.06	$2.61 \times 10^5$
PBE-dDsC	7.31	$2.70 \times 10^7$	10.16	$2.23 \times 10^5$

From Figure 3.7 (c) it is observed that the  $[\text{Os}^{\text{VIII}}\text{O}_4(\text{OH})]^-$  species has two equivalent  $\sigma$ -holes. In a similar fashion to the method used to describe the mechanism of reaction 3.3, the “incoming” hydroxido ligand was placed in line with the  $\text{Os}^{\text{VIII}}$  atom  $\sigma$ -hole and a linear transit relaxed scan calculation was performed. The transition state geometry structure where the  $\text{Os}^{\text{VIII}}\text{-OH}$  distance is 3.22 Å, Figure 3.7 (d), has one negative vibrational frequency

where the hydroxide oxygen atom vibrates towards and back w.r.t. the Os<sup>VIII</sup> atom. Reactions 3.3 & 3.4 occur as two elementary steps. The Gibbs energies of activation of the forward and reverse reactions, reaction 3.4 (or more specifically reaction 3.16;  $cis_2$ -[Os<sup>VIII</sup>O<sub>4</sub>(OH)<sub>2</sub>]<sup>2-</sup> is slightly more thermodynamically favourable compared to  $cis_1$ -[Os<sup>VIII</sup>O<sub>4</sub>(OH)<sub>2</sub>]<sup>2-</sup>), and their associated rate constants were calculated using equation 3.19 and are listed in Table 3.11.

**Table 3.11. Calculated Gibbs Free Energies of activation in kcal.mol<sup>-1</sup> and rate constants of reaction 3.16 at 298.15 K where  $k_2$  and  $k_{-2}$  are the forward and reverse rate constants, respectively.**

Functional	$\Delta^\ddagger G^\circ_{forward}$	$k_2$ (L.mol <sup>-1</sup> .s <sup>-1</sup> )	$\Delta^\ddagger G^\circ_{reverse}$	$k_{-2}$ (s <sup>-1</sup> )
PBE	11.74	$1.54 \times 10^4$	11.77	$1.45 \times 10^4$
PBE-D	7.79	$1.22 \times 10^7$	10.40	$1.48 \times 10^5$
PBE-D3	10.81	$7.40 \times 10^4$	11.42	$2.62 \times 10^4$
PBE-D3(BJ)	10.50	$1.26 \times 10^5$	11.44	$2.54 \times 10^4$
PBE-dDsC	10.45	$1.36 \times 10^5$	11.60	$1.95 \times 10^4$

The calculated rate constants obtained for reaction 3.16 (Table 3.11) are relatively large, yet on estimation an order of magnitude less when compared to reaction 3.3. We attribute this result in part to the repulsion between the two negatively charged species which increases the  $\Delta^\ddagger G^\circ$  activation energy barrier. From reactions 3.3 and 3.16, the rate law equations 3.20 – 3.22 are derived. Using the rate constants obtained with the PBE-dDsC functional, the species concentration evolution curves as a function of time were calculated, Figure 3.8. The initial conditions in this hypothetical “stopped-flow” kinetics calculation are two aqueous solutions of equal volume where one syringe contains Os<sup>VIII</sup>O<sub>4</sub> at 10.0 mM and the other contains 4.0 M [OH]<sup>-</sup>. It is seen in Figure 3.8 that reactions 3.3 and 3.16 reach equilibrium in less than 0.00003 seconds which explains our experimental stopped-flow kinetics results.

$$\frac{d[\text{OsO}_4]}{dt} = -k_1[\text{OsO}_4][\text{OH}^-] + k_{-1}[\text{OsO}_4(\text{OH})^-] \quad 3.20$$

$$\begin{aligned} \frac{d[\text{OsO}_4(\text{OH})^-]}{dt} &= k_1[\text{OsO}_4][\text{OH}^-] - k_{-1}[\text{OsO}_4(\text{OH})^-] - k_2[\text{OsO}_4(\text{OH})^-][\text{OH}^-] \\ &+ k_{-2}cis\text{-}[\text{OsO}_4(\text{OH})_2^{2-}] \end{aligned} \quad 3.21$$

$$\frac{dcis\text{-}[\text{OsO}_4(\text{OH})_2^{2-}]}{dt} = k_2[\text{OsO}_4(\text{OH})^-][\text{OH}^-] - k_{-2}cis\text{-}[\text{OsO}_4(\text{OH})_2^{2-}] \quad 3.22$$

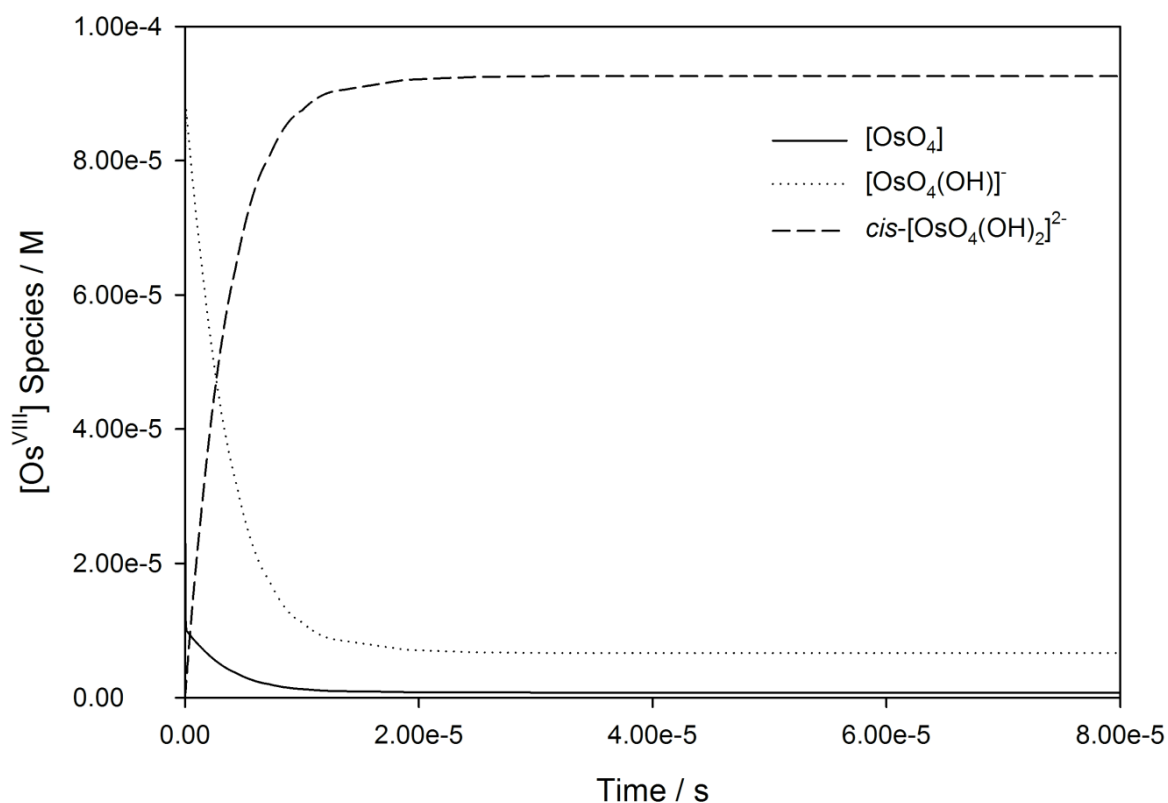


**Figure 3.8.** Simulated kinetic traces of  $\text{Os}^{\text{VIII}}\text{O}_4$  reacting with  $\text{OH}^-$  in 2M NaOH as a function of time (PBE-dDsC functional).

### 3.2.3 QTAIM analysis of the electron density topology of the $\text{Os}^{\text{VIII}}$ species

In order to further characterise the nature of the  $\text{Os}^{\text{VIII}}$ -oxo and  $\text{Os}^{\text{VIII}}$ -hydroxido bonding interactions and to investigate whether possible intramolecular interactions occur, we performed a topological analysis of the electron density according to the quantum theory of atoms in molecules (QTAIM).<sup>29,30</sup> The definition for atoms to be chemically bonded, according to this theory, is based on the existence of a (3,-1) bond critical point (BCP) or a saddle point along a line of maximum electron density,  $\rho$ , also called an atomic interaction line (AIL) linking the nuclei of neighbouring atoms. At the BCP the gradient of the electron density vanishes,  $\nabla\rho(\mathbf{r}) = 0$ , and the sum of the three eigenvalues ( $\lambda_1$  and  $\lambda_2$  are negative,  $\lambda_3$  is positive), obtained from the electron density Hessian matrix, known as the Laplacian,  $\nabla^2\rho(\mathbf{r})_b$ , may have either a net positive or negative value. A positive Laplacian value at the BCP indicates a local depletion of charge. This is indicative of an ionic (closed-shell) type of bonding. A negative Laplacian value is a sign of a local concentration of charge and is indicative of a shared/covalent interaction. However, a positive Laplacian value could in some cases be misleading, as the classification of the bond between two “closed-shell”

interacting atoms is also determined by a second index, the total electronic energy density,  $E_b^e$ , at the BCP. This term is defined as the sum of the kinetic energy density,  $G_b$ , which usually dominates in a non-covalent bond, and the potential energy density,  $V_b$ , which is usually negative and is associated with accumulation of charge between the nuclei. In clearly covalent bonds both the  $\nabla^2\rho(\mathbf{r})_b$  and  $E_b^e = G_b + V_b$  are negative whilst the electron density at the BCP is larger than 0.1. In less clear cases, where the  $\nabla^2\rho(\mathbf{r})_b$  has a relatively small positive value, the magnitude of  $E_b^e$  can be used to further classify the bond, from being slightly covalent to purely ionic, *e.g.* if  $\nabla^2\rho > 0$  and  $E_b^e$  is negative the bond is called dative on the other hand if  $E_b^e$  is positive the bond is ionic. Moreover, the  $G_b/\rho_b$  ratio index is generally accepted to be less than unity for shared interactions and greater than unity for closed-shell interactions. The calculated BCP's electron density topology indices of all Os<sup>VIII</sup> species (PBE functional) are listed in Table 3.12 (see Table A.1 for values obtained using PBE-D3(BJ) functional) and the molecular graphs obtained illustrated in Figure 3.2.

**Table 3.12. QTAIM indices computed at the BCPs (PBE functional). All values are expressed in atomic units. Os<sup>VIII</sup>=O and Os<sup>VIII</sup>-OH BCPs are highlighted in red and blue, respectively.**

Species	BCP #	Atoms	$\lambda_1$	$\lambda_2$	$\lambda_3$	$\rho_b$	$\nabla^2\rho_b$	$G_b$	$G_b/\rho_b$	$V_b$	$E_b^e$
OsO <sub>4</sub>	1	Os(1)-O(2)	-0.4443	-0.4443	1.7880	0.2712	0.8993	0.4052	1.4944	-0.5903	-0.1850
	2	Os(1)-O(3)	-0.4443	-0.4443	1.7880	0.2712	0.8993	0.4052	1.4944	-0.5903	-0.1850
	3	Os(1)-O(4)	-0.4443	-0.4443	1.7880	0.2712	0.8993	0.4052	1.4944	-0.5903	-0.1850
	4	Os(1)-O(5)	-0.4443	-0.4443	1.7880	0.2712	0.8993	0.4052	1.4944	-0.5903	-0.1850
[OsO <sub>4</sub> (OH)] <sup>-</sup>	1	Os(1)-O(2)	-0.3538	-0.3329	1.5003	0.2239	0.8136	0.3250	1.4514	-0.4492	-0.1242
	2	Os(1)-O(3)	-0.4147	-0.4123	1.6415	0.2542	0.8145	0.3614	1.4216	-0.5228	-0.1614
	3	Os(1)-O(4)	-0.3623	-0.3455	1.5474	0.2298	0.8395	0.3375	1.4690	-0.4680	-0.1305
	4	Os(1)-O(6)	-0.2092	-0.1916	0.7818	0.1380	0.3810	0.1445	1.0476	-0.1954	-0.0509
	5	Os(1)-O(5)	-0.4155	-0.4133	1.6439	0.2546	0.8150	0.3621	1.4219	-0.5240	-0.1619
	6	O(6)-H(7)	-1.8296	-1.8016	1.2740	0.3631	-2.3572	0.0843	0.2323	-0.7580	-0.6737
<i>cis</i> - [OsO <sub>4</sub> (OH) <sub>2</sub> ] <sup>2-</sup>	1	Os(1)-O(2)	-0.1369	-0.1256	0.5727	0.1025	0.3102	0.1057	1.0309	-0.1354	-0.0297
	2	Os(1)-O(3)	-0.3648	-0.3614	1.5863	0.2344	0.8600	0.3468	1.4800	-0.4818	-0.1350
	3	Os(1)-O(4)	-0.3642	-0.3613	1.5843	0.2341	0.8589	0.3463	1.4790	-0.4810	-0.1347
	4	Os(1)-O(5)	-0.3469	-0.3321	1.4740	0.2204	0.7950	0.3158	1.4331	-0.4354	-0.1196
	5	Os(1)-O(6)	-0.1331	-0.1225	0.5577	0.1005	0.3022	0.1028	1.0221	-0.1315	-0.0288
	6	Os(1)-O(7)	-0.3596	-0.3434	1.5360	0.2271	0.8330	0.3321	1.4620	-0.4587	-0.1267
	7	O(6)-H(8)	-1.7883	-1.7632	1.3006	0.3682	-2.2508	0.0948	0.2574	-0.7523	-0.6575
	8	O(2)-H(9)	-1.7907	-1.7657	1.2998	0.3680	-2.2566	0.0943	0.2563	-0.7529	-0.6585
<i>cis</i> <sub>2</sub> - [OsO <sub>4</sub> (OH) <sub>2</sub> ] <sup>2-</sup>	1	Os(1)-O(2)	-0.1356	-0.1245	0.5678	0.1018	0.3078	0.1047	1.0287	-0.1340	-0.0293
	2	Os(1)-O(3)	-0.3647	-0.3616	1.5859	0.2343	0.8597	0.3467	1.4796	-0.4817	-0.1349
	3	Os(1)-O(4)	-0.3650	-0.3619	1.5878	0.2345	0.8609	0.3472	1.4806	-0.4823	-0.1351
	4	Os(1)-O(5)	-0.3534	-0.3377	1.5042	0.2237	0.8132	0.3237	1.4468	-0.4468	-0.1231
	5	Os(1)-O(6)	-0.1351	-0.1241	0.5654	0.1015	0.3062	0.1042	1.0265	-0.1335	-0.0292
	6	Os(1)-O(7)	-0.3530	-0.3373	1.5026	0.2236	0.8123	0.3233	1.4462	-0.4462	-0.1229
	7	O(6)-H(8)	-1.7904	-1.7655	1.3000	0.3682	-2.2559	0.0945	0.2566	-0.7529	-0.6585
	8	O(2)-H(9)	-1.7908	-1.7658	1.3000	0.3683	-2.2567	0.0945	0.2565	-0.7531	-0.6586

The Laplacian at all the Os<sup>VIII</sup>=O BCPs of all complexes are positive, ranging from 0.76 to 0.86, and the  $G_b/\rho_b$  ratio is always more than unity, from 1.41 to 1.48, indicating ionic bonding interactions. Since the  $E_b^e$  is negative in all cases, from -0.16 to -0.11, the interaction has a slight covalent character. The ionicity of the bonding interactions is less in the case of the Os<sup>VIII</sup>-OH BCPs in all the complexes. The Laplacian has a smaller positive value, from 0.30 to 0.38, while the  $G_b/\rho_b$  ratio is only slightly greater than unity, from 1.02 to 1.06. These results, along with the negative  $E_b^e$  values, from -0.05 to -0.03, qualify these interactions as polar covalent (dative) and corroborate the results obtained by the EDA analysis. The O-H bonding interactions are clearly covalent as indicated by the large negative Laplacian values, from -2.36 to -2.25, and the large negative  $E_b^e$  values, from -0.67 to -0.66. The  $G_b/\rho_b$  ratio is also much smaller than unity, from 0.23 to 0.26. No qualitative changes are observed when topological analysis of the electron density is performed in the gas phase (Tables A.2 and A.3). The Laplacian of the electron density, plotted along the Os<sup>VIII</sup>-O-H plane of all four Os<sup>VIII</sup> species, shown in Figure 3.9, allows for the visualisation of the charge density

distribution at an  $\text{Os}^{\text{VIII}}=\text{O}$ ,  $\text{Os}^{\text{VIII}}-\text{OH}$  and O-H BCP which displays the relative ionic (blue), polar covalent (green) and covalent (red) character of their bonding interactions, respectively. Moreover, it is evident from the molecular graphs obtained using QTAIM, Figure 3.2, that no intramolecular bonding interactions between neighbouring hydroxido and oxo ligands in any of the  $\text{Os}^{\text{VIII}}$  species are present due to the absence of BCPs other than those of the  $\text{Os}^{\text{VIII}}=\text{O}$  and  $\text{Os}^{\text{VIII}}-\text{OH}$  bonds.

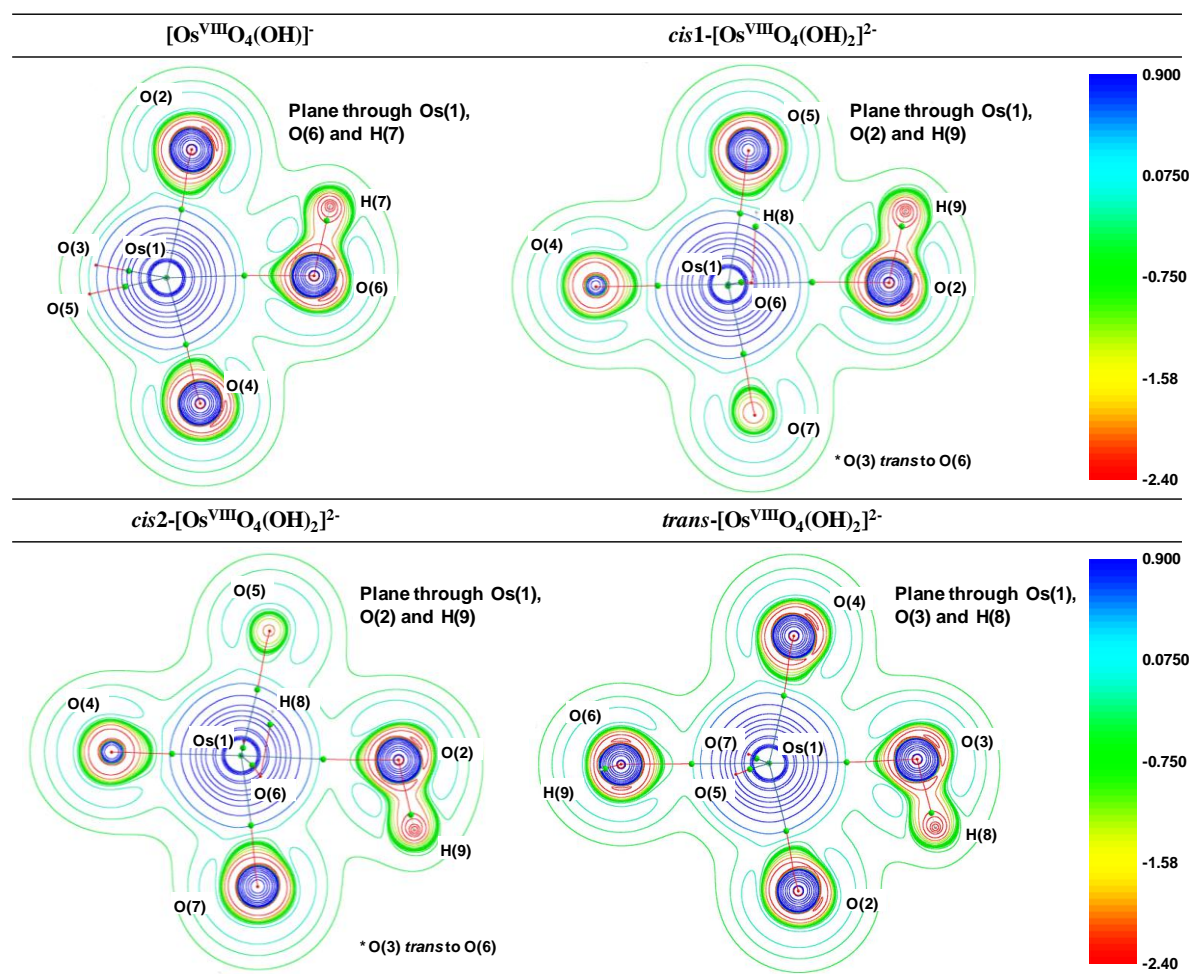


**Figure 3.9.** The Laplacian of the electron density ( $\nabla^2\rho$ ) of each of the  $\text{Os}^{\text{VIII}}$  oxo/hydroxido complexes in the simulated aqueous phase (PBE functional) with numbering scheme used in **Table 3.12**. BCPs are indicated as small green spheres. Red and blue colouring corresponds to regions of local charge accumulation and depletion, respectively.

### 3.2.4 Non-covalent interactions (NCI) analysis of the $\text{Os}^{\text{VIII}}$ species

The more recent Non-Covalent Interactions (NCI) method is frequently used to recognise and categorise intra- and intermolecular bonding interactions in a wide variety of chemical systems.<sup>31</sup> This is based on a 2D plot of the reduced density gradient (RDG),  $s$ , as a function

of the sign of  $\lambda_2$  multiplied with the electron density,  $\rho$ , equation 3.23. A bonding interaction, *e.g.* hydrogen bonding or  $\pi$ - $\pi$  stacking is characterised by an accumulation of electron density in a particular region in 3D space and in these cases  $\lambda_2 < 0$ . By contrast, repulsive interactions have a  $\lambda_2 > 0$ .

$$s = \frac{1}{2(3\pi^2)^{\frac{1}{3}}} \frac{|\nabla\rho|}{\rho^{\frac{4}{3}}} \quad 3.23$$

Points where  $s = 0$  correspond to BCPs due to annihilation of the density gradient. A non-covalent interactions (NCI) analysis of the five-coordinate  $[\text{Os}^{\text{VIII}}\text{O}_4(\text{OH})]^-$  species, Figure 3.10, indicates that a relatively weak stabilisation is present between neighbouring oxo and hydroxido ligands. Although the trough at approximately  $\text{sign}(\lambda_2)\rho \approx -0.03$  au does not terminate at RDG of zero, a weak attractive intramolecular hydrogen bonding interaction between H(7) & O(2) is present. The trough corresponding to this interaction is visualised in 3D space in Figure 3.10 (b) as a red region. The four troughs between -0.25 and -0.22 au are due to ionic (closed-shell)  $\text{Os}^{\text{VIII}}=\text{O}$  bonds while the trough at -0.14 au is due to the polar covalent (dative)  $\text{Os}^{\text{VIII}}-\text{OH}$  bond and these correspond with the BCPs found in the abovementioned QTAIM analysis (Section 3.2.3). It is also evident that there are troughs with positive  $\lambda_2$  values that do not extend to a RDG of zero. These troughs are also visualised in 3D space Figure 3.10 (b) as blue regions and are indicative of repulsive interactions between oxygen moieties, O(4) & O(6) and O(6) & O(2), of neighbouring ligands.

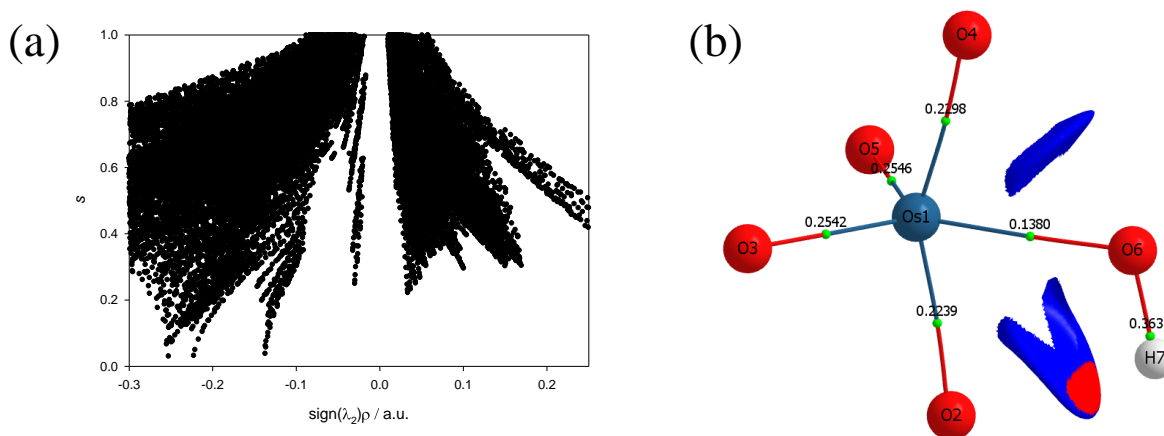


**Figure 3.10.** (a): Plot of the reduced density gradient  $s$  and  $\text{sign}(\lambda_2)\rho$  of  $[\text{Os}^{\text{VIII}}\text{O}_4(\text{OH})]^-$  in the simulated aqueous phase (PBE functional). (b): Taking the positions of the troughs at approximately -0.025 into account, the plotted NCI isosurface corresponding to cut-off values of  $s = 0.6$  au and  $0.03 < \rho < 0.01$  au captures the intramolecular stabilisation interaction. Red and blue colouring corresponds to regions of negative and positive  $\lambda_2$  values, respectively. Electron density values,  $\rho_b$ , at the BCPs are included.



The NCI analyses of the *cis*<sub>1</sub>-[Os<sup>VIII</sup>O<sub>4</sub>(OH)<sub>2</sub>]<sup>2-</sup>, *cis*<sub>2</sub>-[Os<sup>VIII</sup>O<sub>4</sub>(OH)<sub>2</sub>]<sup>2-</sup> and *trans*-[Os<sup>VIII</sup>O<sub>4</sub>(OH)<sub>2</sub>]<sup>2-</sup> species indicate relatively weak intramolecular hydrogen bonding interactions between neighbouring oxo and hydroxido ligands, Figure 3.11. Both the hydroxido hydrogens in each of the three complexes have weak intramolecular hydrogen bonding interactions with a neighbouring oxo ligand. The troughs at  $\text{sign}(\lambda_2)\rho$  range from -0.02 to -0.04 au are due to these attractive interactions and are visualised in 3D space in Figure 3.11 as red regions. The four troughs between -0.23 and -0.21 au are due to ionic (closed-shell) Os<sup>VIII</sup>=O bonds while the two troughs at approximately -0.10 au are due to the polar covalent (dative) Os<sup>VIII</sup>-OH bonds. Several repulsive interactions between oxygen moieties of neighbouring ligands are also present, similarly to those present in the five-coordinate [Os<sup>VIII</sup>O<sub>4</sub>(OH)]<sup>-</sup> complex anion.

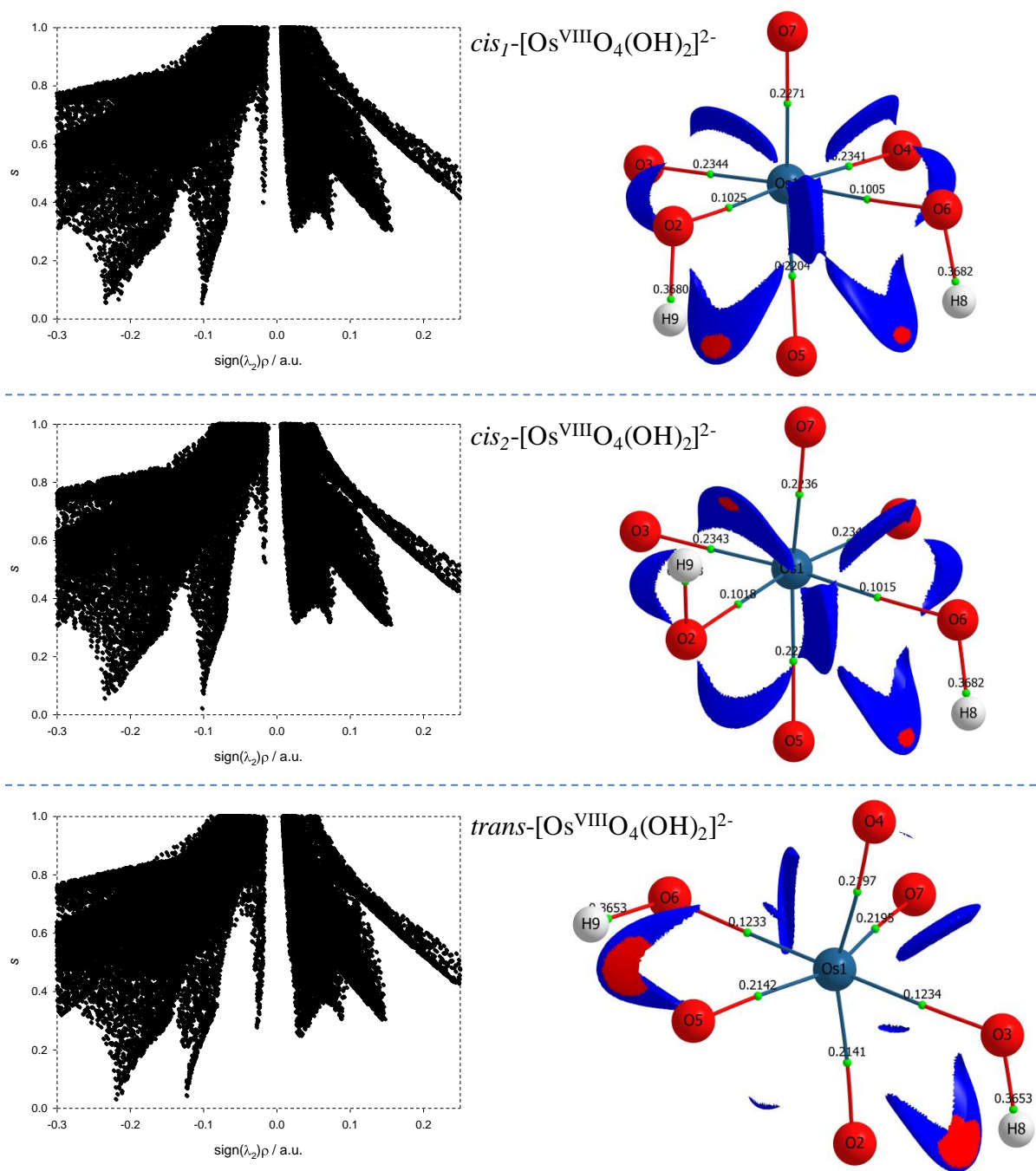


**Figure 3.11.** Left: Plots of the reduced density gradient  $s$  and  $\text{sign}(\lambda_2)\rho$  of the  $\text{cis}_1$ - (top),  $\text{cis}_2$ - (middle) and  $\text{trans}$ - (bottom)  $[\text{Os}^{\text{VIII}}\text{O}_4(\text{OH})_2]^{2-}$  complexes in the simulated aqueous phase (PBE functional). Right: Taking the positions of the troughs at approximately  $-0.025$  into account, plotted NCI isosurfaces corresponding to cut-off values of  $s = 0.6$  au and  $0.03 < \rho < 0.01$  au captures the respective intramolecular stabilisation interactions. Red and blue colouring corresponds to regions of negative and positive  $\lambda_2$  values, respectively. Electron density values,  $\rho_b$ , at the BCPs are included.

### 3.3 Conclusions

We have demonstrated that DFT computational methodologies, mainly with GGA functionals, are successful in elucidating the equilibrium structures and energies of Os<sup>VIII</sup> oxo/hydroxido species that are present in aqueous basic solutions. Our calculations provide evidence that the Os<sup>VIII</sup> species present in basic aqueous solutions are Os<sup>VIII</sup>O<sub>4</sub>, [Os<sup>VIII</sup>O<sub>4</sub>(OH)]<sup>-</sup> and two *cis*-[Os<sup>VIII</sup>O<sub>4</sub>(OH)<sub>2</sub>]<sup>2-</sup> complexes and that water-bonded Os<sup>VIII</sup> species most likely do not exist. Good agreement with reported, experimentally obtained  $\Delta G^{\circ}_{rxn}$  values pertaining to the two coordination sphere expansion reactions validates the DFT methodology used. The thermodynamic driving force of the first reaction is the bonding energy of the Os<sup>VIII</sup>-OH metal-hydroxido ligand present in [Os<sup>VIII</sup>O<sub>4</sub>(OH)]<sup>-</sup> and of the second reaction it is the larger hydration energy of the doubly-charged *cis*-[Os<sup>VIII</sup>O<sub>4</sub>(OH)<sub>2</sub>]<sup>2-</sup> species in comparison with that of the two, singly-charged reactants. Both reactions have relatively low transition state energy,  $\Delta^{\ddagger}G^{\circ}$ , barriers.

QTAIM and EDA analyses indicate that Os<sup>VIII</sup>=O bonding interactions are ionic (closed-shell) whereas the Os<sup>VIII</sup>-OH bonding interactions are polar covalent (dative). NCI analysis of both the [Os<sup>VIII</sup>O<sub>4</sub>(OH)]<sup>-</sup> and *cis*-[Os<sup>VIII</sup>O<sub>4</sub>(OH)<sub>2</sub>]<sup>2-</sup> species indicate the presence of weak intramolecular hydrogen bonding interactions between neighbouring oxo and hydroxido ligands.

The results obtained in this study allow for subsequent investigations which aim to describe the mechanism of the proposed comproportionation reaction by Gerber *et al.*<sup>11</sup> Furthermore, the clarity w.r.t. the Os<sup>VIII</sup> speciation can now be used to make informed suggestions regarding which Os<sup>VIII</sup> complexes are the active catalysts in future studies where they may be used as a potential catalyst in similarly basic aqueous solutions.

---

**References**

1. A. H. Éll, A. Closson, H. Adolfsson and J.-E. Bäckvall, *Adv. Synth. Catal.*, 2003, **345**, 1012.
2. S. M. Desai, N. N. Halligudi and S. T. Nandibewoor, *Int. J. Chem. Kinet.*, 1999, **31**, 583.
3. N. P. Shetti, R. R. Hosamani and S. T. Nandibewoor, *Research Letters in Inorganic Chemistry*, 2008, **216058**.
4. K. Byadagi, M. Meti, S. Nandibewoor and S. Chimatadar, *Ind. Eng. Chem. Res.*, 2013, **52**, 9011.
5. M. P. Singh, H. S. Singh, M. C. Gangwar, P. Thakur and A. K. Singh, *P. Indian Acad. Sci. A.*, 1975, **41**.
6. A. Dehestani, W. H. Lam, D. A. Hrovat, E. R. Davidson, W. T. Borden and J. M. Mayer, *J. Am. Chem. Soc.*, 2005, **127**, 3423.
7. Z. M. Galbács, A. Zsednai and L. J. Csányi, *Transition Met. Chem.*, 1983, **8**, 328.
8. B. J. McFadzean, PhD Dissertation, 2008, NMMU, South Africa.
9. N. N. Ivan-Emin, N. A. Nevskaya, N. N. Nevskii and A. S. Izmailovich, *Russ. J. Inorg. Chem. (Engl. Transl.)*, 1984, **29**, 710.
10. H. C. Jewiss, W. Levason, M. Tajik, M. Webster and N. P. C. Walker, *J. Chem. Soc., Dalton Trans.*, 1985, 199.
11. T. E. Geswindt, W. J. Gerber, H. E. Rohwer and K. R. Koch, *Dalton Trans.*, 2011, **40**, 8581.
12. W. P. Griffith, *The Chemistry of the Rarer Platinum Metals (Os, Ru, Ir & Rh)*, Chapter 3, Interscience, 1967.
13. B. Krebs and K. D. Hasse, *Acta Crystallogr., Sect. B*, 1976, **32**, 1334.
14. N. N. Nevskii, B. Ivan-Emin, O. N. A. Nevskaya and N. V. Belov, *Dokl. Akad. Nauk SSSR*, 1983, 226, 245.

15. Z. Y. Lin and M. B. Hall, *Coord. Chem. Rev.*, 1993, **123**, 149.
16. D. T. Richens, *The Chemistry of Aqua Ions*; John Wiley and Sons, New York, 1997.
17. D. W. Nelson, A. Gypser, P. T. Ho, H. C. Kolb, T. Kondo, H.-L. Kwong, A. McGrath, E. A. Rubin, P.-O. Norbby, K. P. Gable and K. B. Sharpless, *J. Am. Chem. Soc.*, 1997, **119**, 1840.
18. C. J. Cramer and D. G. Truhlar, *Phys. Chem. Chem. Phys.*, 2009, **11**, 10757.
19. R. S. McDowell and M. Goldblatt, *Inorg. Chem.*, 1971, **10(3)**, 625.
20. H. M. Seip and R. Stølevik, *Acta Chem. Scand.*, 1966, **20**, 385.
21. T. Ziegler and A. Rauk, *Inorg. Chem.*, 1979, **18**, 1558.
22. R. F. W. Bader, *Atoms in Molecules. A Quantum Theory*, Oxford University Press, Oxford, 1990.
23. M. von Hopffgarten and G. Frenking, *WIREs Comput. Mol. Sci.*, 2012, **2**, 43.
24. Y. Jeanvoine, P. Miró, F. Martelli, C. J. Cramer and R. Spezia, *Phys. Chem. Chem. Phys.*, 2012, **14**, 14822.
25. M. Mitoraj, A. Michalak and T. Ziegler, *J. Chem. Theory Comput.*, 2009, **5**, 962.
26. E. C. Hosten, *Complex Species Distribution* (version 3.1), NMMU.
27. T. Clark, M. Hennemann, J. S. Murray and P. Politzer, *J. Mol. Model.*, 2007, **13**, 291.
28. O. von Berg and P. H. von Hippel, *Ann. Rev. Biophys. Chem.*, 1985, **14**, 131.
29. J. I. Rodríguez, R. F. W. Bader, P. W. Ayers, C. Michel, A. W. Götz and C. Bo, *Chem. Phys. Lett.*, 2009, **472**, 149.
30. J. I. Rodríguez, *J. Comput. Chem.*, 2013, **34**, 681.
31. E. R. Johnson, S. Keinan, P. Mori-Sanchez, J. Contreras-Garcia, A. J. Cohen and W. Yang, *J. Am. Chem. Soc.*, 2010, **132**, 6498.

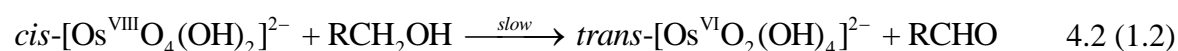
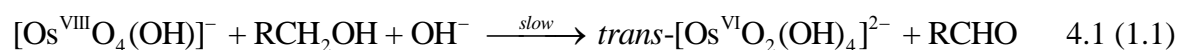
# CHAPTER 4

---

## A Spectroscopic Study of the Comproportionation Reaction of $[\text{Os}^{\text{VIII}}\text{O}_4(\text{OH})_n]^{n-}$ ( $n = 1, 2$ ) and $\text{trans}-[\text{Os}^{\text{VI}}\text{O}_2(\text{OH})_4]^{2-}$ Species in a 2.0 M NaOH Aqueous Matrix

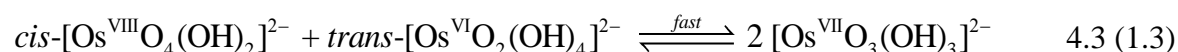
### 4.1 Introduction

Several reported kinetic studies pertaining to the reduction of  $\text{Os}^{\text{VIII}}\text{O}_4$  with molecular hydrogen, alcohols, diols and  $\alpha$ -hydroxy acids in basic aqueous matrices agree that the  $\text{Os}^{\text{VIII}}$  species are reduced to the  $\text{trans}-[\text{Os}^{\text{VI}}\text{O}_2(\text{OH})_4]^{2-}$  complex anion in a single, two-electron step,<sup>1-13</sup> equations 4.1 & 4.2. Moreover, these reactions are reported to be first order w.r.t. the reducing agent and the total  $\text{Os}^{\text{VIII}}$  concentration.<sup>1-13</sup>



where  $\text{R} = \text{H}, \text{CH}_3$ .

However, in a relatively recent UV-Vis spectroscopy kinetic study of the reduction of  $\text{Os}^{\text{VIII}}$  oxo/hydroxido species,  $[\text{Os}^{\text{VIII}}\text{O}_4(\text{OH})_n]^{n-}$  ( $n = 1, 2$ ), with aliphatic alcohols in a 2.0 M NaOH aqueous matrix at 298.15 K, Gerber *et al.*<sup>1</sup> discovered that an additional, relatively rapid, reaction was occurring whilst reactions 4.1 & 4.2 progresses. The authors proposed that the ‘additional’ reaction is a comproportionation of the two high oxidation state  $\text{Os}^{\text{VIII}}$  and  $\text{Os}^{\text{VI}}$  dianions to form two paramagnetic  $[\text{Os}^{\text{VII}}\text{O}_3(\text{OH})_3]^{2-}$  ( $d^1$ ) species, equation 4.3.



In support of a paramagnetic oxo/hydroxido osmium species are reported EPR (electron paramagnetic resonance)<sup>14,15</sup> spectroscopic and polarographic<sup>16</sup> data, obtained in the late 1960’s, in a relatively high hydroxide concentration aqueous matrix. However, recently attempted EPR (at 298.0 K) and  $^{189}\text{Os}$  nuclear magnetic resonance (NMR) spectroscopy (at 292.0 K and 14.1 T) measurements have been unable to provide evidence that the reaction

products are paramagnetic as, in both cases, it is thought that the fast relaxation (electronic and nuclear, respectively) are responsible for the lack of any observable resonance signals.<sup>1</sup> Numerous attempts to obtain suitable crystals for single crystal X-ray diffraction have been unsuccessful, thus direct structural support for the postulated Os<sup>VII</sup> complex dianions, including possible stereoisomers thereof, is lacking.<sup>1</sup>

Apart from the four studies mentioned above,<sup>1,14-16</sup> all other literature found<sup>2-13</sup> do not report the formation of an Os<sup>VII</sup> species during the reduction of Os<sup>VIII</sup> to Os<sup>VI</sup>. In particular, Mayer *et al.*<sup>2</sup>, who reported the reduction of Os<sup>VIII</sup>O<sub>4</sub> with molecular hydrogen in basic aqueous matrices, argue that an [Os<sup>VII</sup>O<sub>3</sub>(OH)<sub>3</sub>]<sup>2-</sup> species is thermodynamically unstable w.r.t. Os<sup>VI</sup> and Os<sup>VIII</sup> species<sup>3</sup> based on their DFT-calculated, bond dissociation free energies (BDFEs). They concluded from these results that:

““[Os<sup>VII</sup>O<sub>3</sub>(OH)<sub>3</sub>]<sup>2-</sup>” is not observed in alkaline mixtures of Os<sup>VIII</sup>O<sub>4</sub>(OH)<sub>*n*</sub><sup>*n-*</sup> and Os<sup>VI</sup>O<sub>2</sub>(OH)<sub>4</sub><sup>2-</sup>.”

Either the proposed Os<sup>VI</sup> & Os<sup>VIII</sup> comproportionation reaction depicted by equation 4.3 does not occur in basic aqueous matrices or several studies<sup>2-13</sup> have failed to detect this reaction and therefore their results must, at the least, be reinterpreted.

In this study we aim to (i) prove that the proposed comproportionation reaction does occur and that the reaction products are indeed paramagnetic, (ii) study the kinetics of the comproportionation reaction and obtain the associated thermodynamic parameters, by means of stopped-flow UV-Vis spectroscopy experiments and (iii) obtain experimental evidence that might hint towards the comproportionation reaction mechanism.

## 4.2 Results and discussion

### 4.2.1 Spectroscopic evidence of paramagnetic Os<sup>VII</sup> species

An Evans method experiment<sup>17-20</sup> was performed as an alternative spectroscopic technique in an attempt to determine whether the reaction of Os<sup>VIII</sup> with Os<sup>VI</sup> produces paramagnetic products. The Evans method is a <sup>1</sup>H NMR spectroscopy experiment used to measure the magnetic susceptibility of a solution. This is visualised by a <sup>1</sup>H NMR resonance signal

<sup>3</sup> Os<sup>VI</sup> refers specifically to the *trans*-[Os<sup>VI</sup>O<sub>2</sub>(OH)<sub>4</sub>]<sup>2-</sup> complex dianion while Os<sup>VIII</sup> refers to a combination of the [Os<sup>VIII</sup>O<sub>4</sub>(OH)]<sup>-</sup> and *cis*-[Os<sup>VIII</sup>O<sub>4</sub>(OH)<sub>2</sub>]<sup>2-</sup> complex anions that are simultaneously present in a 2.0 M NaOH aqueous matrix (see Chapter 3).

frequency shift of a suitable co-dissolved compound, such as *tert*-butanol, due to the additional magnetic field caused by the presence of an accompanying paramagnetic species. A reference coaxial NMR tube, Figure 4.1, contains a *tert*-butanol/D<sub>2</sub>O mixture (1:9), ([NaOH] = 2.0 M) while the outer, sample tube contains the same composition mixture plus the possible paramagnetic species being probed.

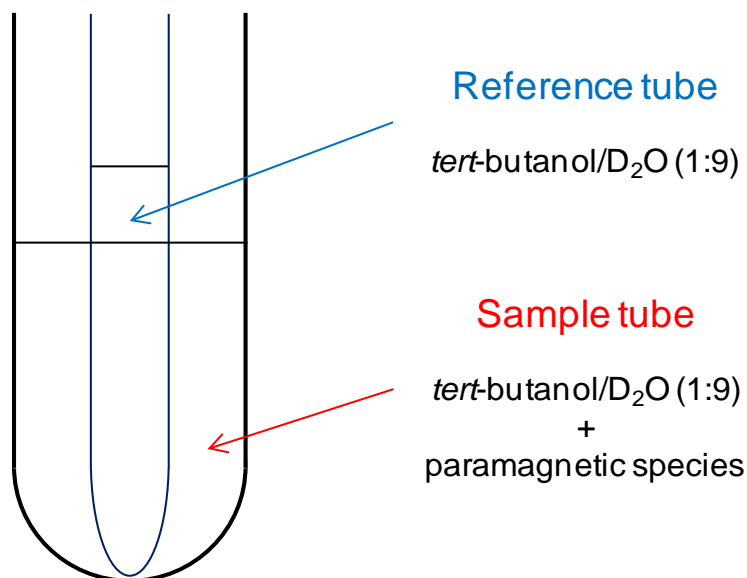


**Figure 4.1.** Illustration of a coaxial NMR tube used in Evans method experiments to obtain direct measurements of magnetic susceptibilities.

Unlike primary and secondary aliphatic alcohols, *tert*-butanol is not oxidised by Os<sup>VIII</sup> oxo/hydroxido species,<sup>4</sup> making it the ideal co-dissolved reference compound for our experiments. The details that explain this unique feature are related to the mechanism of aliphatic alcohol oxidation which is discussed in Chapter 7.

If the reaction of Os<sup>VIII</sup> and Os<sup>VI</sup> does produce paramagnetic product species, we expect to observe a frequency shift in the <sup>1</sup>H NMR spectrum of the CH<sub>3</sub> protons of *tert*-butanol in the sample tube solution. The relative frequency shift that is expected to occur then enables the calculation of the number of unpaired electrons of the accompanying paramagnetic compound.

In order to determine whether the Os<sup>VIII</sup> or Os<sup>VI</sup> reactant species would individually induce a <sup>1</sup>H NMR resonance frequency shift of the sample tube's *tert*-butanol CH<sub>3</sub> protons, separate

<sup>4</sup> Since Os<sup>VIII</sup> does not oxidise *tert*-butanol, we postulate that  $\alpha$ -C-H, and not O-H, hydrogen atom transfer (HAT) of the alcohol species being oxidised by Os<sup>VIII</sup> is crucial to these redox reactions (see Chapter 7).



solutions of Os<sup>VIII</sup> and of Os<sup>VI</sup>, in 2.0 M NaOH aqueous matrices, were analysed at 298.15 K. The resonance signals of the samples' *tert*-butanol CH<sub>3</sub> protons frequency did not shift in either of these two solutions w.r.t. the reference *tert*-butanol CH<sub>3</sub> protons. Moreover, increasing the Os<sup>VIII</sup> and Os<sup>VI</sup> species concentration, in their individual sample tubes, also does not induce a <sup>1</sup>H NMR, *tert*-butanol CH<sub>3</sub>, resonance frequency shift. Therefore, the osmium species in both the reactant-containing solutions have no unpaired electrons, *i.e.* they are diamagnetic, and corroborates the literature that propose the two 5*d*-electrons of [Os<sup>VI</sup>O<sub>2</sub>(OH)<sub>4</sub>]<sup>2-</sup> are paired in the *d*<sub>xy</sub> orbital.<sup>21</sup>

An equilibrium mole ratio experiment was subsequently performed, at 298.15 K, where increasing amounts of the high purity osmate crystals, K<sub>2</sub>[Os<sup>VI</sup>O<sub>2</sub>(OH)<sub>4</sub>], were dissolved in the sample tube which contained, initially, the *tert*-butanol/D<sub>2</sub>O mixture plus Os<sup>VIII</sup> (at a concentration of 0.1241 M) in a 2.0 M NaOH aqueous matrix. When solutions containing these mixtures of the Os<sup>VIII</sup> and Os<sup>VI</sup> reactants were analysed, the resonance signal of the *tert*-butanol CH<sub>3</sub> protons of the sample tube shifted downfield, Figure 4.2. The magnitude of the downfield chemical shift of the signal of the *tert*-butanol CH<sub>3</sub> protons frequency increased as the ([Os<sup>VI</sup>]/[Os<sup>VIII</sup>]) mole ratio increased. Moreover, the <sup>1</sup>H NMR signals broaden as the ([Os<sup>VI</sup>]/[Os<sup>VIII</sup>]) mole ratio increases. Paramagnetic species are known to accelerate transverse relaxation, hence decreasing *T*<sub>2</sub>, resulting in broader resonance signals. Both results provide strong evidence that the osmium reaction products have unpaired electrons, *i.e.* they are paramagnetic species.

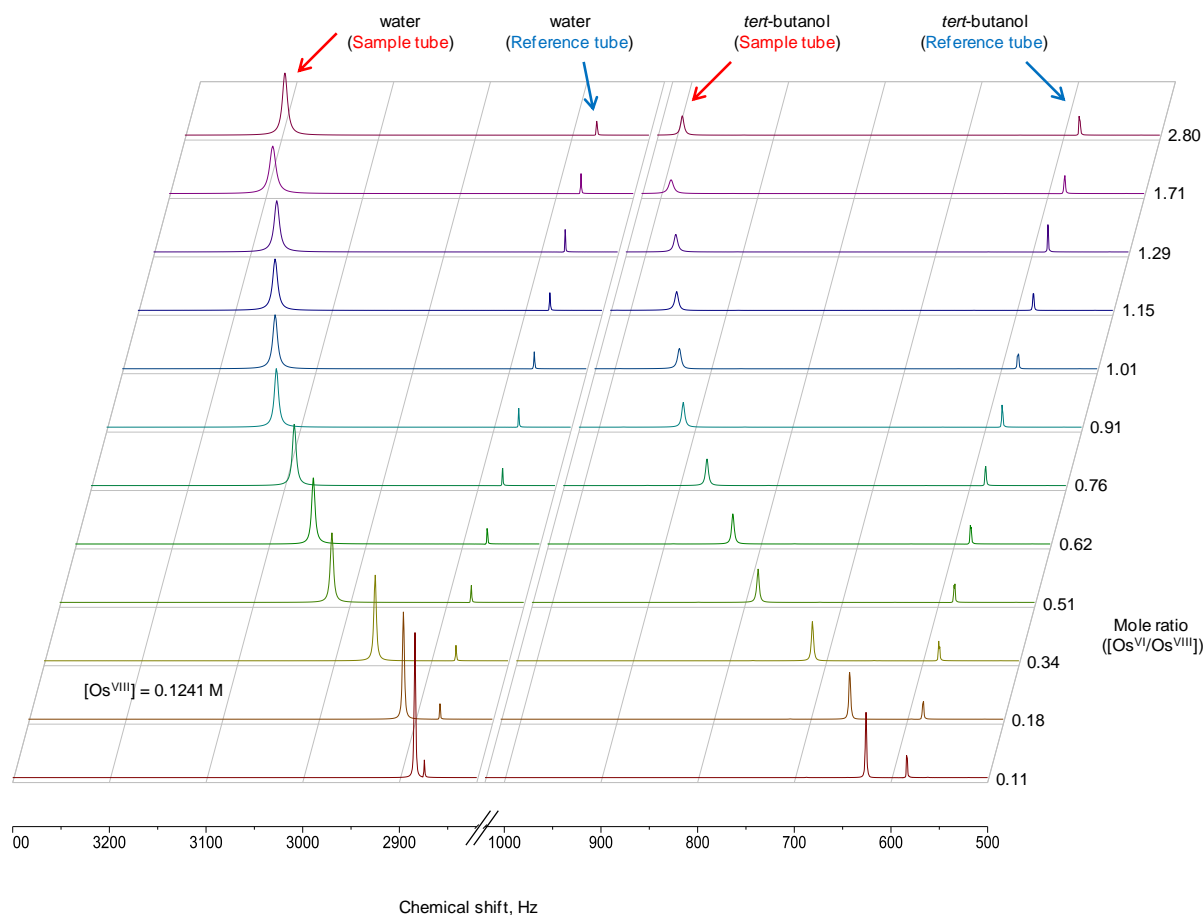
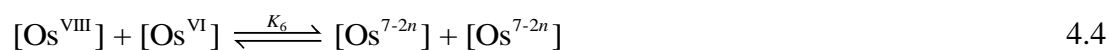


**Figure 4.2.** Resonance signals of water (left) and *tert*-butanol (right) of the sample solution (downfield shifting) and reference solution (no shifting) tubes in an overlay of the <sup>1</sup>H NMR spectra at different mole ratios of ([Os<sup>VI</sup>]/[Os<sup>VIII</sup>]).

The magnitude of the observed chemical shift of the *tert*-butanol CH<sub>3</sub> protons in the sample tube as a function of the ([Os<sup>VI</sup>]/[Os<sup>VIII</sup>]) mole ratio is plotted in Figure 4.3. Two linear trends were fitted that intersect at approximately one. It follows that the stoichiometric ratio of the reactants in the proposed comproportionation reaction is 1:1, equation 4.4.



where  $n$  may vary between 0 and 3.

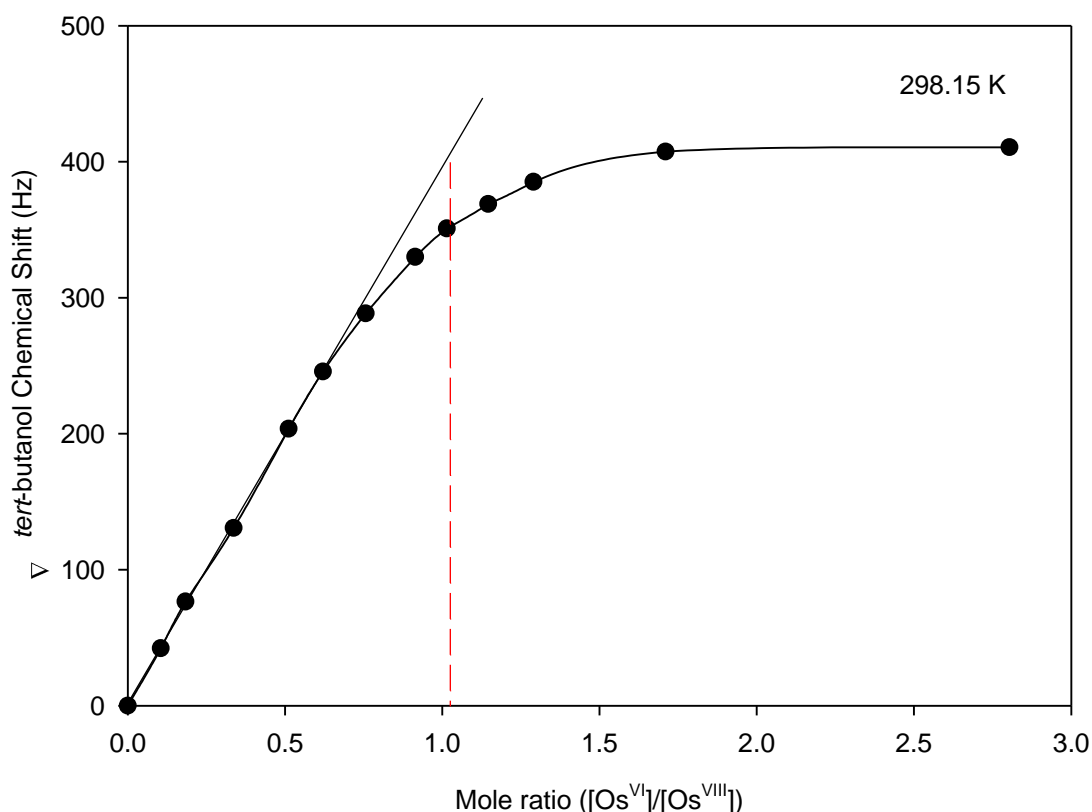


**Figure 4.3.** Change in chemical shift as a function of the  $([\text{Os}^{\text{VI}}]/[\text{Os}^{\text{VIII}}])$  mole ratio.

The data obtained from the Evans method experiment allows for the determination of magnetic susceptibilities, and therefore also an estimate of the number of unpaired electrons.<sup>17-20</sup> The chemical shift of a given proton resonance signal in the spectrum of a molecule is dependent on the bulk susceptibility of the medium in which the molecule is found. The shift of a proton resonance frequency,  $\delta\nu$  {with  $\delta\nu = \nu_{\text{alcohol}} - (\nu_{\text{alcohol}} + \text{complex})$ }, of an inert substance (*tert*-butanol) due to the presence of paramagnetic solute species is given by the expression shown in equation 4.5.

$$\delta\nu = \frac{\nu_0 2\pi(\chi_v - \chi_v')}{3} \quad 4.5$$

where:

$\delta\nu$  = frequency separation between the two resonances peaks (Hz),

$\nu_0$  = applied field/ spectrometer frequency = 600 000 000 (Hz), while

$\chi_v$  is the volume susceptibility of the sample tube/solution containing the paramagnetic ions and

$\chi_v'$  is the volume susceptibility of the reference tube/solution without ions.

The mass susceptibility of the *dissolved* substance,  $\chi$ , is thus given by equation 4.6.

$$\chi = \frac{3\delta v}{2\pi v_0 m} + \chi_0 + \frac{\chi_0(d_0 - d_s)}{m} \quad 4.6$$

where:

$\chi$  = mass susceptibility of the solute ( $\text{cm}^3 \cdot \text{g}^{-1}$ ),

$\chi_0$  = mass susceptibility of the pure solvent ( $\text{cm}^3 \cdot \text{g}^{-1}$ ),

$m$  = mass of the paramagnetic substance contained in 1 mL of solution ( $\text{g} \cdot \text{cm}^{-3}$ ),

$d_0$  = density of the pure solvent ( $\text{g} \cdot \text{cm}^{-3}$ ) and

$d_s$  = density of the solution ( $\text{g} \cdot \text{cm}^{-3}$ ).

The mass susceptibility must subsequently be corrected for the diamagnetism of the constituent atoms, equation 4.7.

$$\chi^{corr} = \chi + \sum \chi^{dia} \quad 4.7$$

However, for relatively small molecules, such as mononuclear complex ions, the diamagnetic corrections,  $\chi^{dia}$ , are often negligible.<sup>22</sup> Conversely, relatively large, paramagnetic supramolecular assemblies<sup>23</sup> or biomolecules<sup>24</sup> require a dependable determination of the diamagnetic contribution, since temperature-dependant paramagnetism is then often only a small part of the whole signal.<sup>24</sup> Due to the relatively small size of the postulated  $[\text{Os}^{\text{VII}}\text{O}_3(\text{OH})_3]^{2-}$  species,  $\chi^{dia}$  was assumed to be negligible, such that  $\chi^{corr} = \chi$ .

In order to determine the required values of  $m$  for each data point of the mole ratio experiment (Figure 4.2), the concentration of the reaction products were first calculated. These were obtained by using the equilibrium constant value of 9.33 ( $\pm 0.4$ ), at 298.15 K, reported by Gerber *et al.*<sup>1</sup> Furthermore, the obtained concentration values were multiplied by the molecular weight of the postulated  $[\text{Os}^{\text{VII}}\text{O}_3(\text{OH})_3]^{2-}$  species, at 289.2502  $\text{g} \cdot \text{mol}^{-1}$ , to convert the units appropriately, *i.e.* from  $\text{mol} \cdot \text{cm}^{-3}$  to  $\text{g} \cdot \text{cm}^{-3}$ .

As the difference between  $d_o$  and  $d_s$  is negligible (total concentration of osmium species is relatively small) the last term of equation 4.6 is set to zero, yielding equation 4.8. This term is often omitted when relatively dilute solutions are studied.<sup>18-20,25,26</sup>

$$\chi = \frac{3\delta\nu}{2\pi\nu_0 m} + \chi_0 \quad 4.8$$

Rearrangement of equation 4.8, such that  $\delta\nu$  is the subject of the formula, yields equation 4.9.

$$\delta\nu = \frac{2\pi\nu_0 m(\chi - \chi_0)}{3} \quad 4.9$$

Therefore, the plot of  $\delta\nu$  vs.  $m$  gives a slope, equation 4.10.

$$\frac{\delta\nu}{m} = \frac{2\pi\nu_0}{3} (\chi - \chi_0) \quad 4.10$$

A linear trend for  $\delta\nu$  vs.  $m$  was obtained, Figure 4.4, which indicates that the data is suitable for subsequent calculations to estimate the number of unpaired electrons of the reaction products. Moreover, the linearity obtained demonstrates that the calculated equilibrium constant used to determine  $m$ , obtained from the study by Gerber *et al.*<sup>1</sup>, are reliable and consistent with the obtained <sup>1</sup>H NMR spectral data. The 95% confidence interval and 95% confidence errors of the slope and the intercept are shown on the graph in Figure 4.4.

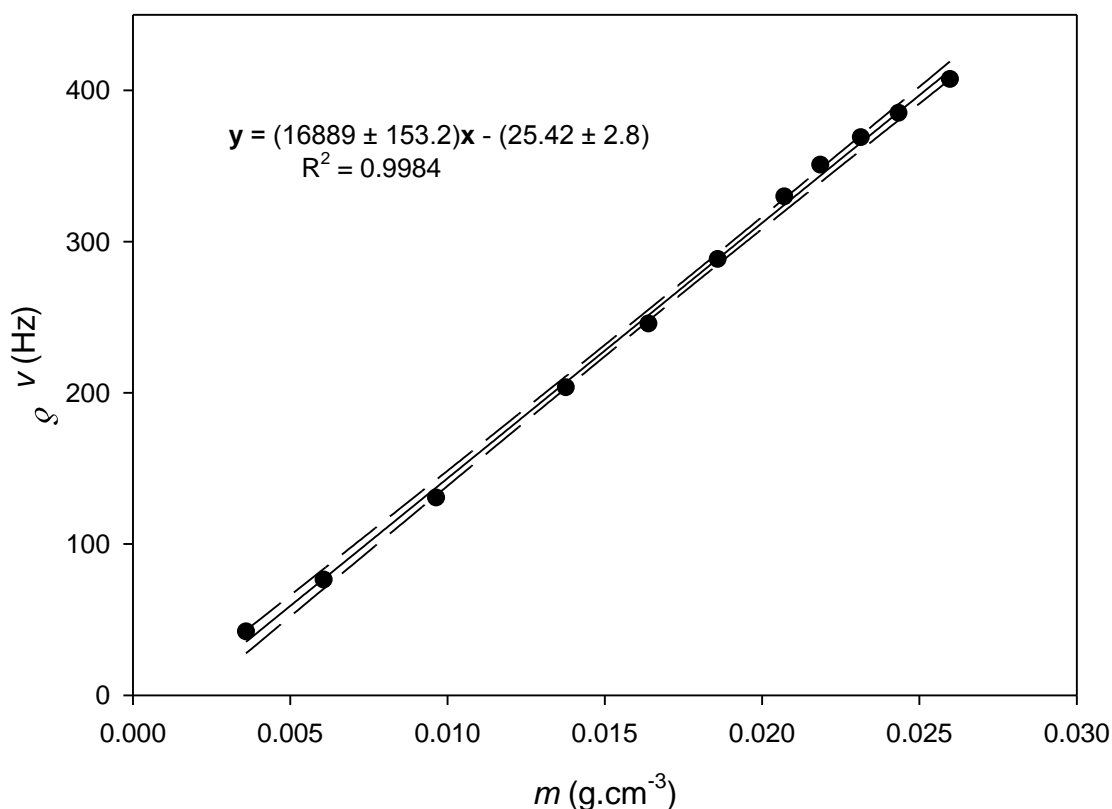


**Figure 4.4.** Change in chemical shift as a function of the mass of the postulated  $[\text{Os}^{\text{VII}}\text{O}_3(\text{OH})_3]^{2-}$  paramagnetic species contained in 1 mL.

In order to obtain the magnetic properties of the paramagnetic product species, the mass susceptibility is converted to molar susceptibility,  $\chi_M$ , by multiplying  $\chi$  by the molecular weight of the paramagnetic species. The calculated molar magnetic susceptibility,  $\chi_M$ , which then equates to  $0.00389 \pm 0.00004$ , is used to determine the effective magnetic moment,  $\mu_{\text{eff}}$ , at 298.15 K, using equation 4.11.<sup>5</sup>

$$\mu_{\text{eff}} = \sqrt{8\chi_M T} \quad 4.11$$

$$= 3.05 \pm 0.01$$

$$= 2\sqrt{S(S+1)} \quad 4.12$$

$$= \sqrt{n(n+2)} \quad 4.13$$

$S$ , equation 4.12, is the spin quantum number and  $n$ , equation 4.13, is the number of unpaired electrons. Substitution of the experimentally obtained data gives an estimated value for  $S$  of

<sup>5</sup> Relativistic effects were not taken into account when calculating  $\mu_{\text{eff}}$ .

$1.103 \pm 0.007$  and  $n$  of  $2.21 \pm 0.01$ , Table 4.1. Therefore, each paramagnetic species has approximately 1.1 electrons. This result is consistent with the postulate that both final products are  $\text{Os}^{\text{VII}}$  species,<sup>1</sup> since an  $\text{Os}^{\text{VII}}$  species has one unpaired  $5d$  electron, Table 1.1.

**Table 4.1. Experimentally determined magnetic properties of two reaction products, a postulated  $[\text{Os}^{\text{VII}}\text{O}_3(\text{OH})_3]^{2-}$  complex, obtained from the Evans method experiment.**

Procedure	$\mu_{\text{eff}}$	$S$	$n$
experimental	$3.05 \pm 0.01$	$1.103 \pm 0.007$	$2.21 \pm 0.01$
theoretical	2.83	1	2

The obtained Evans method data provides compelling evidence that the reaction does occur by way of comproportionation, with  $\text{Os}^{\text{VI}}$  donating one electron to  $\text{Os}^{\text{VIII}}$ . Furthermore, if  $\text{Os}^{\text{VI}}$  donates both its valence electrons to  $\text{Os}^{\text{VIII}}$  the products would be in the same oxidation states as the reactants, *i.e.* diamagnetic  $\text{Os}^{\text{VIII}}$  and  $\text{Os}^{\text{VI}}$  species, respectively. Formation of other possible paramagnetic osmium species, such as  $\text{Os}^{5-2n}$  ( $n = 0 - 2$ ), can be excluded when taking into account that for such species to form, more electrons than are present in the valence shell of an  $\text{Os}^{\text{VI}}$  species ( $d^2$ ) are required. Moreover, an  $\text{Os}^{\text{VIII}}$  species has zero  $5d$  valence electrons.

The Evans method experiment, therefore, succeeded in proving that  $\text{Os}^{\text{VI}}$  and  $\text{Os}^{\text{VIII}}$  species react in a 1:1 ratio by way of comproportionation and that the  $\text{Os}^{\text{VII}}$  product species have one unpaired electron each.

#### 4.2.2 $\text{Os}^{\text{VI}}$ & $\text{Os}^{\text{VIII}}$ comproportionation reaction kinetics

When  $\text{Os}^{\text{VI}}$  (violet) is added to an aqueous solution containing  $\text{Os}^{\text{VIII}}$  in 2.0 M NaOH at room temperature, a rapid colour change occurs from light yellow to orange. The reaction rate of  $\text{Os}^{\text{VIII}}$  and  $\text{Os}^{\text{VI}}$  species is too fast to monitor using conventional UV-Vis spectroscopy techniques which are applicable for reactions that take relatively long ( $> 10$  minutes) to reach equilibrium.

We therefore opted to use stopped-flow UV-Vis spectroscopy to further study the reaction of  $\text{Os}^{\text{VIII}}$  and  $\text{Os}^{\text{VI}}$  species. The aim of this kinetic study is to determine the reaction stoichiometry and to calculate thermodynamic activation energy parameters ( $\Delta^\ddagger H^\circ$ ,  $\Delta^\ddagger S^\circ$  and  $\Delta^\ddagger G^\circ$ ) from reaction rate constants as well as standard reaction energy parameters ( $\Delta H^\circ_{\text{rxn}}$ ,  $\Delta S^\circ_{\text{rxn}}$  and  $\Delta G^\circ_{\text{rxn}}$ ). Three sets of experiments were done that included variable concentration (Section 4.2.2.1) and variable temperature (Section 4.2.2.2) stopped-flow UV-Vis

spectroscopy. Lastly, to probe the comproportionation reaction mechanism, a kinetic isotope effect (KIE) experiment was performed (Section 4.2.2.3). In all three sets of experiments, the UV-Vis absorbance signal of the comproportionation reaction was monitored at 370 nm. At this wavelength the extinction coefficients of the reactants and products have been reported.<sup>1,2,13</sup>

#### 4.2.2.1 Variable concentration, constant temperature

The concentration of  $\text{Os}^{\text{VIII}}$  was kept constant at  $0.1404 \pm 0.0009$  mM, while the ( $[\text{Os}^{\text{VI}}]/[\text{Os}^{\text{VIII}}]$ ) mole ratio was varied from approximately 0.22 to 2.09. Furthermore, the experiments were performed in a 2.0 M NaOH aqueous matrix at 295.1 K. Ten kinetic measurement acquisition runs were performed at four different ( $[\text{Os}^{\text{VI}}]/[\text{Os}^{\text{VIII}}]$ ) mole ratios. The trends depicting absorbance vs. time, shown as symbols in Figure 4.5, are the average of the ten runs.

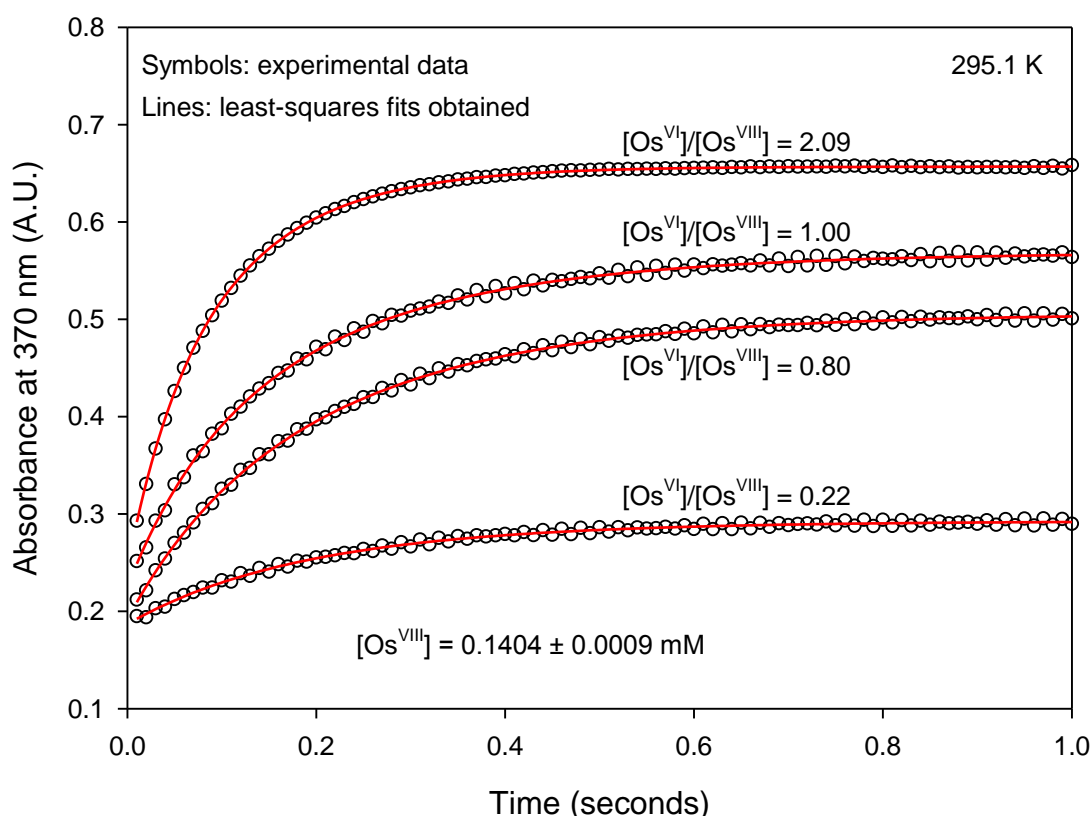


**Figure 4.5.** Kinetic traces depicting the change in absorbance at various ( $[\text{Os}^{\text{VI}}]/[\text{Os}^{\text{VIII}}]$ ) mole ratios, at 295.1 K for the  $\text{Os}^{\text{VI}}$  &  $\text{Os}^{\text{VIII}}$  comproportionation reaction. The mole ratio at which each of the acquisitions was recorded is shown.

It can be seen from Figure 4.5 that the ‘final’ absorbance value (when equilibrium has been reached) is higher with an increase in the ( $[\text{Os}^{\text{VI}}]/[\text{Os}^{\text{VIII}}]$ ) mole ratio, *i.e.* an increase in



reaction product formation. These trends are consistent with the literature which reports the molar extinction coefficient of the product species to be greater than the sum of the reactant species at 370 nm.<sup>1,2,13</sup>

In Chapter 2 we reported that the coordination sphere expansion/contraction reactions of the Os<sup>VIII</sup> oxo/hydroxido species (equations 3.3 and 3.4) in a 2.0 M NaOH aqueous matrix are close to diffusion-controlled at 298.15 K.<sup>6</sup> It is therefore assumed that all coordination sphere expansion/contraction reactions, even those that may involve Os<sup>VII</sup> species (*vide infra*), are at equilibrium throughout the kinetic runs at 295.1 K. The rate-determining step is therefore the forward (comproportionation) and reverse (disproportionation) reactions.

The simplest reaction model is given by equation 4.14.



The corresponding rate laws of the proposed comproportionation reaction in a 2.0 M NaOH aqueous matrix is given by equations 4.15 & 4.16.

$$\frac{d[\text{Os}^{\text{VIII}}]}{dt} = \frac{d[\text{Os}^{\text{VI}}]}{dt} = -k_{6(\text{obs})}[\text{Os}^{\text{VIII}}][\text{Os}^{\text{VI}}] + k_{-6(\text{obs})}[\text{Os}^{\text{VII}}][\text{Os}^{\text{VII}}] \quad 4.15$$

$$\frac{d[\text{Os}^{\text{VII}}]}{dt} = 2k_{6(\text{obs})}[\text{Os}^{\text{VIII}}][\text{Os}^{\text{VI}}] - 2k_{-6(\text{obs})}[\text{Os}^{\text{VII}}][\text{Os}^{\text{VII}}] \quad 4.16$$

At this stage we do not specify which Os<sup>VIII</sup> species, *i.e.* [Os<sup>VIII</sup>O<sub>4</sub>(OH)]<sup>-</sup> or *cis*-[Os<sup>VIII</sup>O<sub>4</sub>(OH)<sub>2</sub>]<sup>2-</sup> or both, reacts with Os<sup>VI</sup>. As the coordination sphere expansion/contraction reactions are at equilibrium during the kinetic runs, the concentrations of the two species are related to each other *via* equation 3.4 which can then be substituted into the rate laws, equations 4.15 & 4.16. This would bring about the introduction of constant ‘parameters’, such as the equilibrium constant of equation 3.4 ( $K_2$ ) and hydroxide concentration. These parameters can then be factored out of the rate constants,  $k_{6(\text{obs})}$  and  $k_{-6(\text{obs})}$ , at an appropriate time when more is known w.r.t. the mechanism of the Os<sup>VI</sup> & Os<sup>VIII</sup> comproportionation reaction and which Os<sup>VII</sup> species are present. In Chapter 5, Section 5.2.7, the complete rate

<sup>6</sup> Stopped-flow kinetics experiments were performed at 298.15 K in an attempt to quantify the rate at which these reactions occur. However, the spectral change occurs in such a small time scale that for all practical purposes a ‘constant’ absorbance versus time signal is obtained, *i.e.* the expected absorbance when Os<sup>VIII</sup> is present at equilibrium in 2.0 M hydroxide is already observed at the first data point, at 0.001 seconds.

laws are presented, where we also provide more evidence that the coordination sphere expansion/contraction reactions of Os<sup>VIII</sup> and Os<sup>VII</sup> species are essentially at equilibrium during the comproportionation reaction.

Using the software Program Dynafit,<sup>27</sup> the rate laws, equations 4.15 & 4.16, were simulated and the obtained non-linear least squares fits, shown as lines in Figure 4.5, are excellent. The calculated rate constants, Table 4.2, remain the same irrespective of the Os<sup>VI</sup> concentration which confirms that the proposed comproportionation reaction is first order w.r.t. Os<sup>VI</sup> concentration. Moreover, the results confirm that the disproportionation reaction is second order w.r.t. Os<sup>VII</sup> concentration since two Os<sup>VII</sup> species are the final products of the comproportionation reaction. A complete kinetic mole ratio experiment to determine the reaction order w.r.t. the Os<sup>VIII</sup> species was not performed as the total Os<sup>VIII</sup> concentrations used for the experiments in Sections 4.2.2.1, 4.2.2.2 and 4.2.2.3 (depicted by Figures 4.5, 4.6 and 4.10) were different and the obtained rate constants do not vary as a function of the Os<sup>VIII</sup> concentration (*vide infra*). Therefore, the proposed comproportionation reaction is first order w.r.t. Os<sup>VIII</sup> concentration by inference. The rate constants and equilibrium constants obtained at the four differing [Os<sup>VI</sup>]/[Os<sup>VIII</sup>] ratios agree to within experimental error, Table 4.2.

**Table 4.2. Calculated rate and equilibrium constants of the comproportionation reaction at 295.1 K (exp. 4.2.2.1).**

[Os <sup>VI</sup> ]/[Os <sup>VIII</sup> ]	$k_{6(\text{obs})} (\text{M}^{-1} \cdot \text{s}^{-1})$	$k_{-6(\text{obs})} (\text{M}^{-1} \cdot \text{s}^{-1})$	$K_{6(\text{obs})} = (k_{6(\text{obs})}/k_{-6(\text{obs})})$
0.22	$(3.861 \pm 0.006) \times 10^4$	$(6.43 \pm 0.04) \times 10^3$	$6.00 \pm 0.03$
0.80	$(3.821 \pm 0.005) \times 10^4$	$(6.23 \pm 0.11) \times 10^3$	$6.14 \pm 0.11$
1.00	$(3.880 \pm 0.014) \times 10^4$	$(6.34 \pm 0.10) \times 10^3$	$6.12 \pm 0.09$
2.09	$(3.897 \pm 0.015) \times 10^4$	$(6.38 \pm 0.23) \times 10^3$	$6.12 \pm 0.25$

Extinction coefficients calculated from the non-linear least squares fits for the Os<sup>VIII</sup> and Os<sup>VI</sup> species agree well with previously reported experimental values,<sup>1,2,13</sup> Table 4.3.<sup>7</sup> However, the Os<sup>VII</sup> species' extinction coefficient, listed in the literature at approximately 5800 L.mol<sup>-1</sup>.cm<sup>-1</sup> (at 298.15 K),<sup>1</sup> does not compare well with that obtained in this study. We interpret the reported value to be the sum total for two Os<sup>VII</sup> species, an error in the paper by

<sup>7</sup> If the reaction product is assumed to be a dimer complex, Os<sub>2</sub><sup>VII</sup>, instead of two monomer Os<sup>VII</sup> species then the calculated molar extinction coefficient of Os<sup>VI</sup> is approximately 900 L.mol<sup>-1</sup>.cm<sup>-1</sup>, which differs significantly from the reported literature value of  $210.6 \pm 6.4$  L.mol<sup>-1</sup>.cm<sup>-1</sup>, and effectively rules out the possibility that the product is a dimer.

Gerber *et al.*<sup>1</sup>, *i.e.* the extinction coefficient of the Os<sup>VII</sup> species should have been divided by a factor of two since two monomer Os<sup>VII</sup> species are formed. Therefore, at approximately 2900 L.mol<sup>-1</sup>.cm<sup>-1</sup> per Os<sup>VII</sup> species, the correlation is comparatively good.

The good non-linear least squares fits obtained, Figure 4.5, and the good agreement of calculated molar extinction coefficients, Table 4.3, with that obtained in the literature validates the proposed reaction model, equation 4.14.

**Table 4.3. Comparison of the calculated and literature high oxidation state osmium species' molar extinction coefficients at 370 nm obtained from the variable concentration kinetics experiment (exp. 4.2.2.1).**

osmium species	Calculated (L.mol <sup>-1</sup> .cm <sup>-1</sup> )	Literature <sup>1,2,13</sup> (L.mol <sup>-1</sup> .cm <sup>-1</sup> )	
([Os <sup>VIII</sup> O <sub>4</sub> (OH)] <sup>-</sup> + <i>cis</i> -[Os <sup>VIII</sup> O <sub>4</sub> (OH) <sub>2</sub> ] <sup>2-</sup> )	1259.0 ± 8.8	1159.7 ± 7.1	1165.6 <sup>a</sup>
[Os <sup>VI</sup> O <sub>2</sub> (OH) <sub>4</sub> ] <sup>2-</sup>	232.8 ± 5.5	210.6 ± 6.4	231.2 <sup>a</sup>
[Os <sup>VII</sup> O <sub>3</sub> (OH) <sub>3</sub> ] <sup>2-</sup> <sup>b</sup>	2475.7 ± 13.8	~ 2900	-

<sup>a</sup> Values extrapolated from reported UV-Vis absorbance spectra.<sup>2,13</sup>

<sup>b</sup> Postulated molecular formula of Os<sup>VII</sup>.<sup>1</sup>

The reported rate constants for the forward and reverse reactions for equation 4.3 at 298.15 K by Gerber *et al.*<sup>1</sup>, 620.9 ± 14.6 M<sup>-1</sup>.s<sup>-1</sup> and 65.7 ± 1.2 M<sup>-1</sup>.s<sup>-1</sup>, respectively, differ significantly from the data obtained in this study, Table 4.2. However, the ratio of the reported rate constants for reaction 4.3 agrees quantitatively with the data obtained here, Table 4.2. The reasons for this apparent discrepancy between the absolute values of rate constants are as follows:

In this study the change in absorbance vs. time data for the comproportionation reaction is obtained *directly* with stopped-flow UV-Vis spectroscopy, whereas in the study by Gerber *et al.*<sup>1</sup> the model that was fitted to the data is given by equations 4.1 – 4.3, *i.e.* the aliphatic alcohol oxidation reaction, is much slower (by a factor of approximately 1500x) than the comproportionation reaction. The program used to simulate those kinetic traces, Kinetic<sub>5</sub> Ver,<sup>28</sup> optimised the rate constants for reaction 4.3 to their 'lowest' absolute values, such that reaction 4.3 is essentially at equilibrium the whole time as reactions 4.1 & 4.2 progress. Increasing both the forward and reverse rate constants, by the same factor, does not improve the non-linear least squares fits and hence the program converged on the smallest absolute rate constant values. Their ratio, which is correct, is equal to the equilibrium constant obtained here.

#### 4.2.2.2 Variable temperature, constant concentration

The concentrations of  $\text{Os}^{\text{VIII}}$  and  $\text{Os}^{\text{VI}}$  were equal to each other at  $0.1498 \pm 0.0044$  mM in 2.0 M NaOH aqueous matrices. Ten kinetic measurement acquisition runs were performed at four different temperatures between 279.9 and 292.5 K. The trends depicting absorbance vs. time, shown as symbols in Figure 4.6, are the average of the ten runs at each temperature.

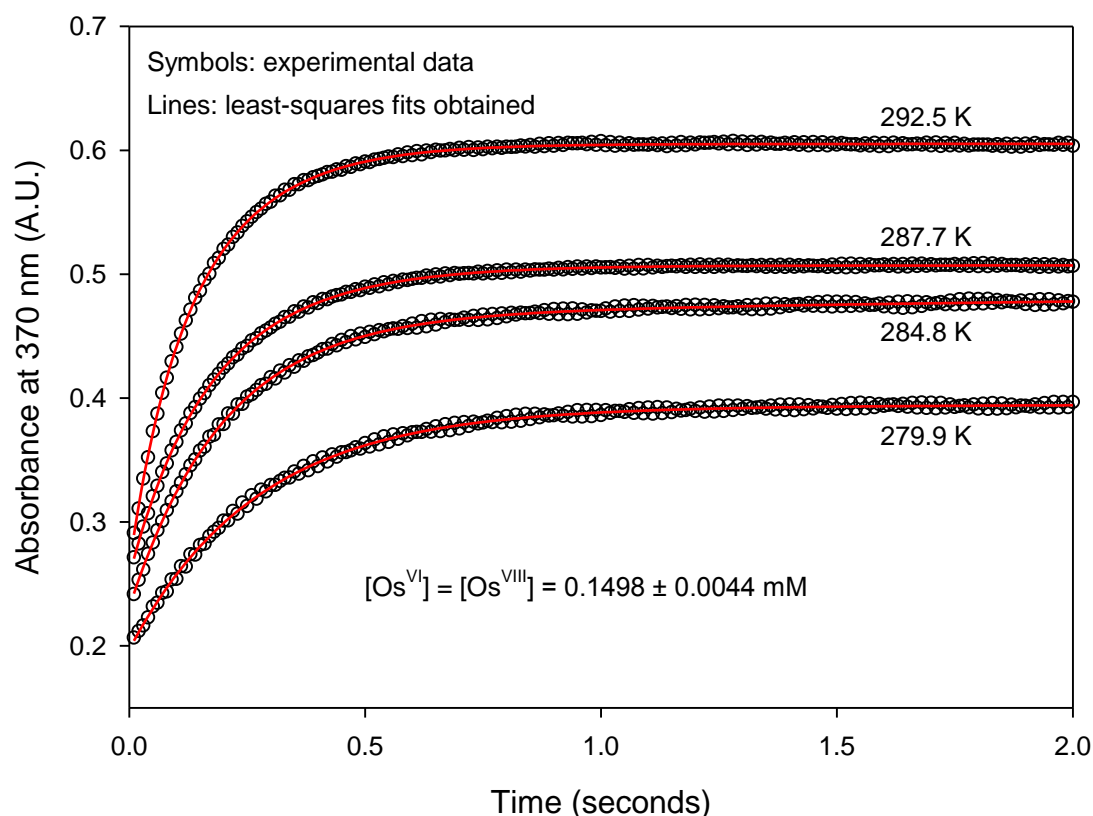


**Figure 4.6.** Kinetic traces depicting the change in absorbance at various temperatures for the  $\text{Os}^{\text{VI}}$  &  $\text{Os}^{\text{VIII}}$  comproportionation reaction. The temperatures at which each of the acquisitions was recorded are shown.

From Figure 4.6 it can be seen that the reaction reaches equilibrium, *i.e.* regions where the absorbance remains unchanged with time, in a shorter period of time at higher temperatures. It is also observed that the ‘final’ absorbance value (when equilibrium has been reached) is higher as the temperature increases. The obtained trends imply that more products are formed at higher temperatures. The calculated standard reaction enthalpy,  $\Delta H^{\circ}_{\text{rxn}(\text{obs})}$ , for the  $\text{Os}^{\text{VI}}$  &  $\text{Os}^{\text{VIII}}$  comproportionation reaction is therefore expected to be positive, *i.e.* endothermic.

In order to determine the extent to which the  $\text{Os}^{\text{VIII}}$  species distribution is influenced by the change in temperature, we monitored the absorbance of a sample of  $\text{Os}^{\text{VIII}}$  in a 2.0 M NaOH aqueous matrix at temperatures ranging between 278.4 and 298.7 K, Figure 4.7. Only

relatively small changes of the spectra were observed, which provides evidence that the  $\text{Os}^{\text{VIII}}$  species distribution is largely independent of temperature or that the molar extinction coefficients of the  $[\text{Os}^{\text{VIII}}\text{O}_4(\text{OH})]^-$  and  $\text{cis}-[\text{Os}^{\text{VIII}}\text{O}_4(\text{OH})_2]^{2-}$  species at 370 nm are close in absolute magnitude. If a change in temperature does significantly alter the  $\text{Os}^{\text{VIII}}$  and  $\text{Os}^{\text{VII}}$  (*vide infra*) species distributions, we expect that when performing the non-linear least squares fits to the experimental data, Figure 4.6, that the change in  $\text{Os}^{\text{VIII}}$  and  $\text{Os}^{\text{VII}}$  (*vide infra*) species distributions will possibly be reflected in the optimised molar extinction coefficients for  $\text{Os}^{\text{VIII}}$  and  $\text{Os}^{\text{VII}}$  or that non-linear Eyring and van't Hoff plots will be obtained. It is assumed, for now, that the  $\text{Os}^{\text{VIII}}$  and  $\text{Os}^{\text{VII}}$  (*vide infra*) species distributions are independent of temperature.

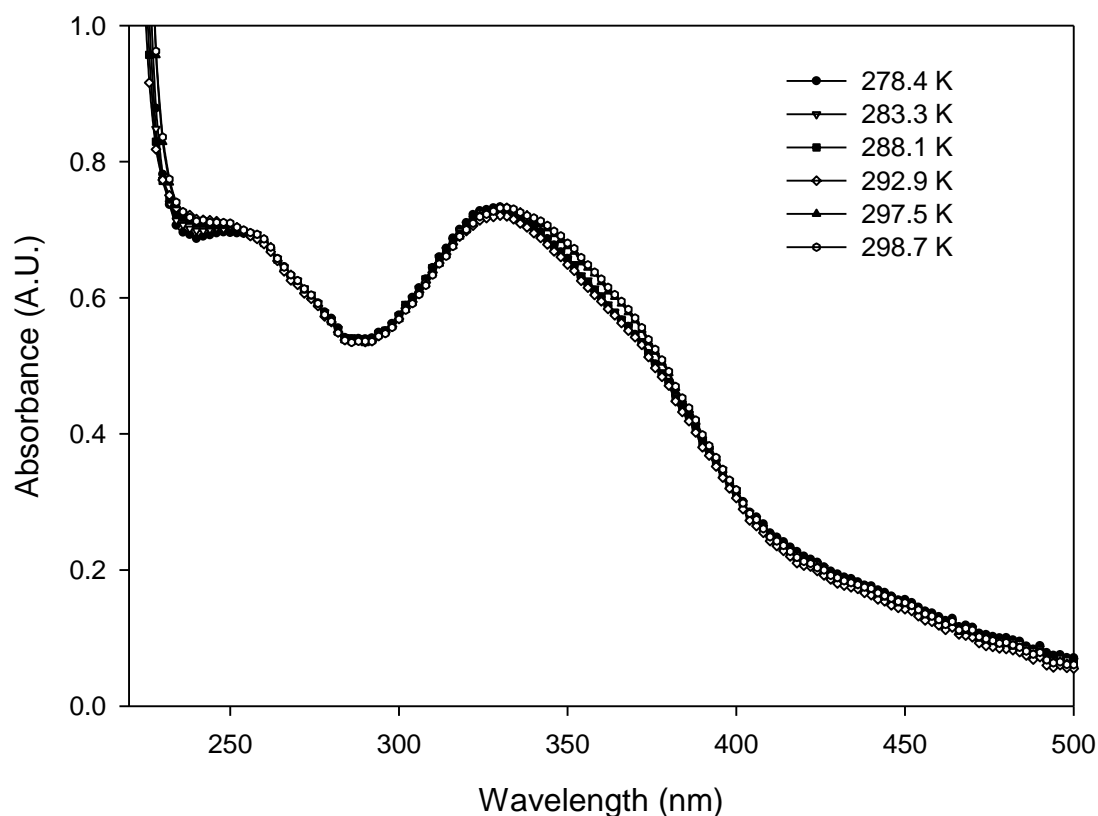


**Figure 4.7.** UV-Vis spectra of  $\text{Os}^{\text{VIII}}$  in a 2.0 M NaOH aqueous matrix at various temperatures. Spectra are virtually unchanged between 278.4 and 298.7 K. The change in species distribution of  $[\text{Os}^{\text{VIII}}\text{O}_4(\text{OH})]^-$  and  $\text{cis}-[\text{Os}^{\text{VIII}}\text{O}_4(\text{OH})_2]^{2-}$  in this temperature range is negligible.

The rate laws given by equations 4.15 & 4.16 were simulated using the software Program Dynafit,<sup>27</sup> and the obtained non-linear least squares fits, Figure 4.6, are excellent. Interestingly, while the forward, *i.e.* comproportionation, reaction rate constant,  $k_{6(\text{obs})}$ , increases as the temperature is raised, the reverse, *i.e.* disproportionation, reaction rate

constant,  $k_{-6(\text{obs})}$ , decreases (Table 4.4). The significance of this feature is discussed in Chapter 6, where a detailed mechanistic investigation of the comproportionation reaction is presented.

**Table 4.4. Calculated rate and equilibrium constants of the comproportionation at various temperatures (exp. 4.2.2.2).**

Temperature (K)	$k_{6(\text{obs})} (\text{M}^{-1} \cdot \text{s}^{-1})$	$k_{-6(\text{obs})} (\text{M}^{-1} \cdot \text{s}^{-1})$	$K_{6(\text{obs})} = (k_{6(\text{obs})}/k_{-6(\text{obs})})$
279.9	$(1.44 \pm 0.05) \times 10^4$	$(1.32 \pm 0.04) \times 10^4$	$1.093 \pm 0.002$
284.8	$(1.92 \pm 0.09) \times 10^4$	$(1.18 \pm 0.05) \times 10^4$	$1.630 \pm 0.001$
287.7	$(2.36 \pm 0.11) \times 10^4$	$(9.61 \pm 0.43) \times 10^3$	$2.456 \pm 0.001$
292.5	$(3.31 \pm 0.17) \times 10^4$	$(8.69 \pm 0.46) \times 10^3$	$3.805 \pm 0.002$
294.5 <sup>8</sup>	$(3.76 \pm 0.01) \times 10^4$	$(7.57 \pm 0.07) \times 10^3$	$4.967 \pm 0.033$

Linear trends were obtained for the Eyring plots for both the comproportionation and disproportionation reactions, Figure 4.8. Furthermore, all five data points are within the 95% confidence interval while the calculated errors<sup>29</sup> of  $\Delta^\ddagger H^\circ_{(\text{obs})}$  and  $\Delta^\ddagger S^\circ_{(\text{obs})}$  values are relatively small, Table 4.5. The fifth data point (highlighted red in Figures 4.8 and 4.9) is obtained from the data in Section 4.2.2.3 at 294.5 K and at a Os<sup>VI</sup>:Os<sup>VIII</sup> mole ratio of 1:1.

<sup>8</sup> Calculated from the KIE experiment, Section 4.2.2.3.

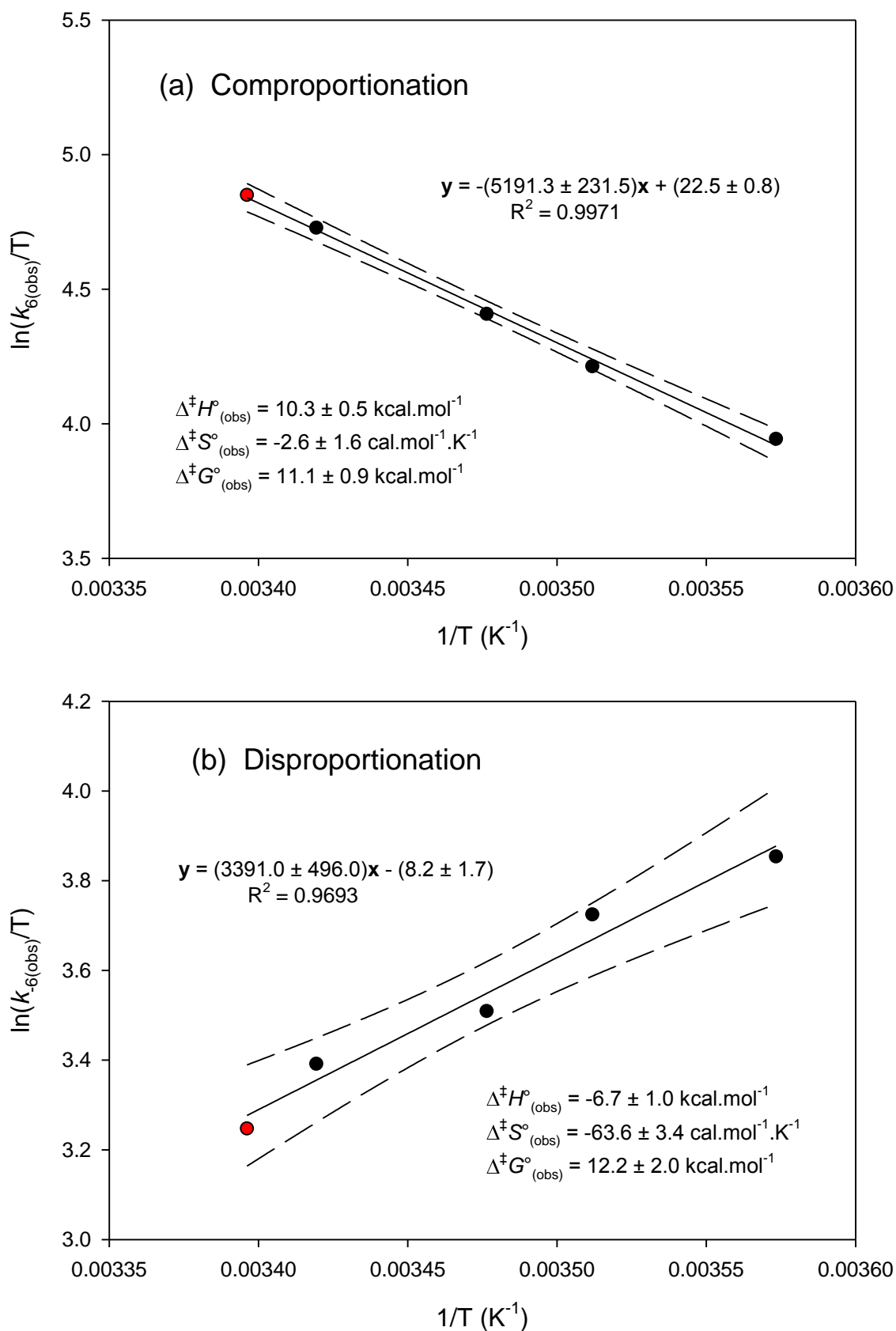


**Figure 4.8.** Eyring plots with 95% confidence intervals for the (a)  $\text{Os}^{\text{VI}}$  &  $\text{Os}^{\text{VIII}}$  comproportionation and (b)  $\text{Os}^{\text{VII}}$  &  $\text{Os}^{\text{VII}}$  disproportionation reactions (exp. 4.2.2.2).

**Table 4.5. Activation energies of Os<sup>VI</sup> & Os<sup>VIII</sup> comproportionation and Os<sup>VII</sup> & Os<sup>VII</sup> disproportionation reactions (exp. 4.2.2.2).**

Reaction	$\Delta^\ddagger H^\circ_{(obs)}$ (kcal.mol <sup>-1</sup> )	$\Delta^\ddagger S^\circ_{(obs)}$ (cal.mol <sup>-1</sup> .K <sup>-1</sup> )	$\Delta^\ddagger G^\circ_{(obs)}$ (kcal.mol <sup>-1</sup> )
comproportionation	10.3 ± 0.5	-2.6 ± 1.6	11.1 ± 0.9
disproportionation	-6.7 ± 1.0	-63.6 ± 3.4	12.2 ± 2.0

Extinction coefficients calculated from the non-linear least squares fits for the Os<sup>VIII</sup>, Os<sup>VI</sup> and Os<sup>VII</sup> species agree well with previously reported experimental values, Table 4.6.<sup>1,2,13</sup> The good agreement of extinction coefficients with that reported in the literature as well as the linearity of the Eyring plots validates the assumptions made for the derivation of the reaction model, equation 4.14.

**Table 4.6. Comparison of the calculated and literature high oxidation state osmium species' molar extinction coefficients at 370 nm obtained from the variable temperature kinetics experiment (exp. 4.2.2.2).**

osmium species	Calculated (L.mol <sup>-1</sup> .cm <sup>-1</sup> )	Literature <sup>1,2,13</sup> (L.mol <sup>-1</sup> .cm <sup>-1</sup> )	
([Os <sup>VIII</sup> O <sub>4</sub> (OH)] <sup>-</sup> + <i>cis</i> -[Os <sup>VIII</sup> O <sub>4</sub> (OH) <sub>2</sub> ] <sup>2-</sup> )	1281.0 ± 15.8	1159.7 ± 7.1	1165.6
<i>trans</i> -[Os <sup>VI</sup> O <sub>2</sub> (OH) <sub>4</sub> ] <sup>2-</sup>	261.1 ± 12.2	210.6 ± 6.4	231.2
[Os <sup>VII</sup> O <sub>3</sub> (OH) <sub>3</sub> ] <sup>2-</sup>	2311.6 ± 51.8	~ 2900	-

Combining the Eyring plots yielded a linear van't Hoff plot, Figure 4.9, and all five data points are also within the 95% confidence interval. The standard reaction enthalpy,  $\Delta H^\circ_{rxn(obs)}$ , and entropy,  $\Delta S^\circ_{rxn(obs)}$  are both positive, at  $17.1 \pm 1.2$  kcal.mol<sup>-1</sup> and  $61.0 \pm 4.3$  cal.mol<sup>-1</sup>.K<sup>-1</sup>, respectively, while the standard reaction Gibbs free energy,  $\Delta G^\circ_{rxn(obs)}$ , at 298.15 K is slightly negative, at  $-1.1 \pm 2.5$  kcal.mol<sup>-1</sup>, Table 4.7. Gerber *et al.*<sup>1</sup> reported a calculated equilibrium constant for the comproportionation reaction,  $K_{com}$  (expressed as  $K_{6(obs)}$  in this study), at 298.15 of  $9.3 \pm 0.4$ , which equates to a  $\Delta G^\circ_{rxn}$  of approximately  $-1.3$  kcal.mol<sup>-1</sup>. The excellent agreement obtained from different experimental techniques<sup>9</sup> provides even further validation regarding the accuracy of the calculated rate constants as well as the reaction model, equation 4.14, used as the basis to simulate the kinetic traces. Moreover, this also provides strong

<sup>9</sup> In contrast to our directly calculated values from stopped-flow experiments, the reported equilibrium constant by Gerber *et al.*<sup>1</sup> was determined (i) indirectly, from mole ratio kinetic titration experiments of Os<sup>VIII</sup> with aliphatic alcohols and (ii) directly, from equilibrium mole ratio and mole fraction, *i.e.* ([Os<sup>VI</sup>]/[Os<sup>VIII</sup>]) and ([Os<sup>VI</sup>]/[Os<sup>VI</sup>] + [Os<sup>VIII</sup>]), respectively, experiments at different total reagent concentrations.



evidence that coordination sphere expansion/contraction reactions' equilibrium constants (*vide infra*) do not vary significantly as a function of temperature.

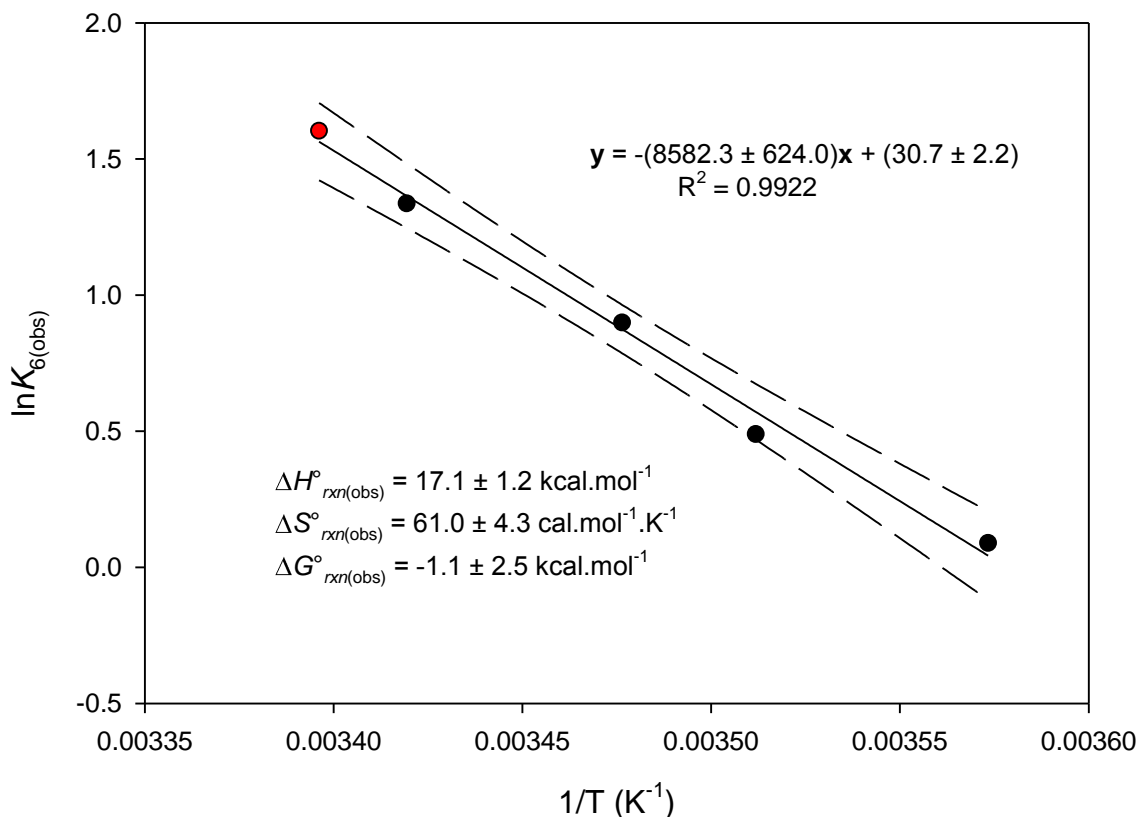


**Figure 4.9.** van't Hoff plot with 95% confidence interval for the comproportionation reaction (exp. 4.2.2.2).

**Table 4.7. Standard reaction energies of the  $\text{Os}^{\text{VI}}$  &  $\text{Os}^{\text{VIII}}$  comproportionation reaction (exp. 4.2.2.2).**

$\Delta H^\circ_{\text{rxn}(\text{obs})}$ ( $\text{kcal.mol}^{-1}$ )	$\Delta S^\circ_{\text{rxn}(\text{obs})}$ ( $\text{cal.mol}^{-1}.\text{K}^{-1}$ )	$\Delta G^\circ_{\text{rxn}(\text{obs})}$ ( $\text{kcal.mol}^{-1}$ )
$17.1 \pm 1.2$	$61.0 \pm 4.3$	$-1.1 \pm 2.5$

The stopped-flow UV-Vis kinetics experiments corroborate the Evans method experiment, Figure 4.3, that the  $\text{Os}^{\text{VI}}$  and  $\text{Os}^{\text{VIII}}$  species react in a 1:1 ratio. Furthermore, the results provide further confirmation that the final products of the comproportionation reaction are two monomer species. In addition the van't Hoff plot analysis yields that the  $\text{Os}^{\text{VI}}$  and  $\text{Os}^{\text{VIII}}$  comproportionation reaction is endothermic, Table 4.7, while Eyring plot analysis, Figure 4.8, yields that the activation enthalpy of the disproportionation reaction,  $\Delta^\ddagger H^\circ_{\text{dis}(\text{obs})}$ , is negative, Table 4.5.

#### 4.2.2.3 Kinetic isotope effect (KIE) experiment – partially deuterated osmium sample

From several literature reports that are summarised in Chapter 1, Section 1.7.1, we suspect that the proposed comproportionation reaction, equation 4.3, may be part of a class of chemical reactions called proton-coupled electron transfer (PCET). If proton transfer (from either the  $\text{Os}^{\text{VI}}$  to  $\text{Os}^{\text{VIII}}$  or from the solvent to  $\text{Os}^{\text{VIII}}$ ) is the rate-determining step of the reaction, then the replacement of hydrogen by deuterium should alter the reaction rates and hence the calculated rate constants of both the forward and reverse reactions of an equal magnitude, *i.e.* the equilibrium constant,  $K_{6(\text{obs})}$ , should not change. KIE experiments are standard methodology of analysis for numerous enzymatic, organic and inorganic reactions that involve the transfer of a proton and electron ever since 1949, when Westheimer<sup>30</sup> identified the coupling of the proton to a redox event *via* a KIE for the oxidation of alcohols by chromic acid.

The experiment was performed in a 2.0 M NaOH aqueous solution with a solvent composition, by volume, of  $\text{D}_2\text{O}:\text{H}_2\text{O}$  in a 1:1 ratio, at 294.5 K, and was subsequently repeated in non-deuterated (control) solutions under the same conditions. Furthermore, the concentration of the  $\text{Os}^{\text{VI}}$  species in the one syringe was equal to the concentration of the  $\text{Os}^{\text{VIII}}$  species in the other syringe at  $0.1268 \pm 0.0018$  mM. The trends depicting absorbance vs. time, shown as symbols in Figure 4.10, are the average of the ten runs of the partially deuterated and control samples.

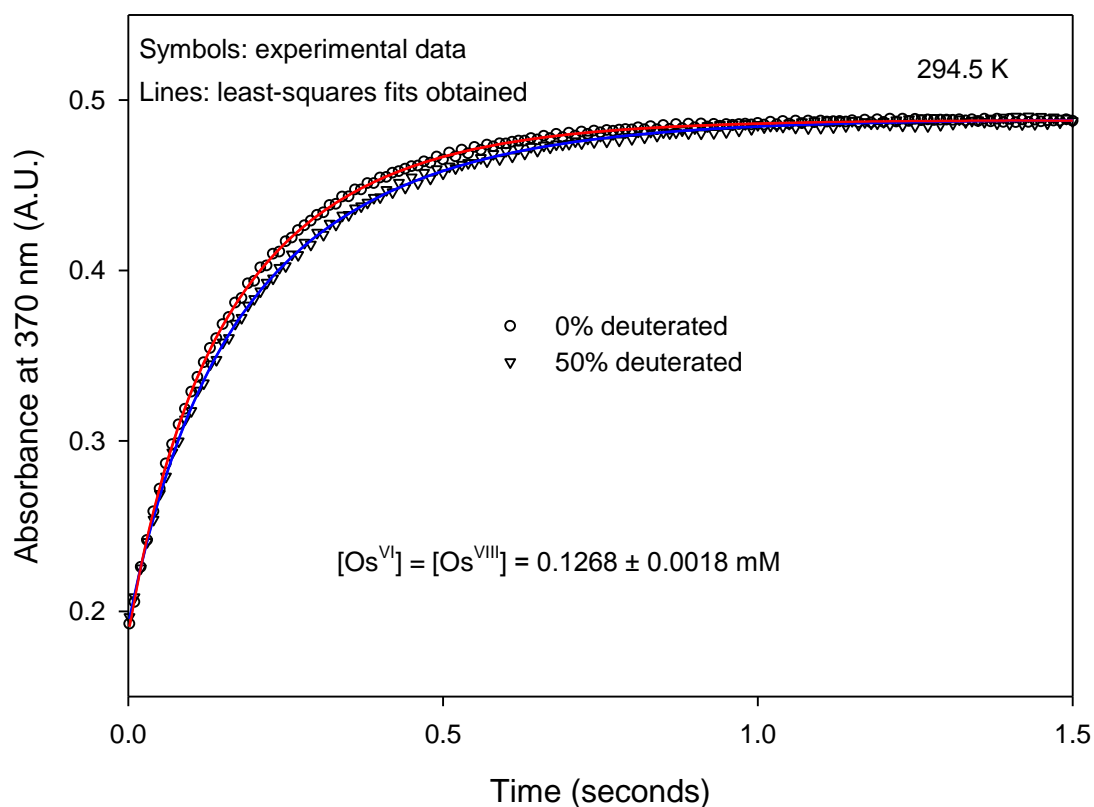


**Figure 4.10.** Kinetic traces depicting the change in absorbance in partially deuterated and non-deuterated (control) solutions for the  $\text{Os}^{\text{VI}}$  &  $\text{Os}^{\text{VIII}}$  comproportionation reaction.

The reaction that contained the partially deuterated solutions reached equilibrium in a longer period of time compared to the non-deuterated (control), *i.e.* essentially ‘protonated’, solutions. Furthermore, the final absorbance values of the two obtained kinetic traces are equivalent, confirming that the observed differences between the kinetic traces, Figure 4.10, are not due to experimental error, *i.e.* erroneous temperature control regulation or reagent concentrations etc.

Using the software Program Dynafit,<sup>27</sup> the rate laws given by equations 4.15 & 4.16 were simulated and the obtained non-linear least squares fits, shown as lines in Figure 4.10, are excellent. The reaction rates of comproportionation and disproportionation both decreased by the same factor when the reactant-containing solutions were partially deuterated while the calculated equilibrium constants for both samples did not change, Table 4.8.

**Table 4.8.** Calculated rate and equilibrium constants of the comproportionation reaction (exp. 4.2.2.3).

Solvent composition	$k_{6(\text{obs})} (\text{M}^{-1} \cdot \text{s}^{-1})$	$k_{-6(\text{obs})} (\text{M}^{-1} \cdot \text{s}^{-1})$	$K_{6(\text{obs})} = (k_{6(\text{obs})}/k_{-6(\text{obs})})$
$\text{H}_2\text{O}$	$(3.762 \pm 0.014) \times 10^4$	$(7.57 \pm 0.07) \times 10^3$	$4.97 \pm 0.03$
0.5 $\text{D}_2\text{O}$ / 0.5 $\text{H}_2\text{O}$	$(3.317 \pm 0.004) \times 10^4$	$(6.66 \pm 0.02) \times 10^3$	$4.98 \pm 0.01$

A  $k(\text{H}_2\text{O})/k(0.5 \times \text{D}_2\text{O})$  kinetic isotope effect (KIE) for the comproportionation and disproportionation reactions are the same, within experimental error, at approximately 1.134 and 1.137, respectively, which provides evidence that the rate-determining step of the  $\text{Os}^{\text{VI}}$  &  $\text{Os}^{\text{VIII}}$  comproportionation reaction coincides with a proton transfer event and that proton transfer from  $\text{Os}^{\text{VI}}$  to  $\text{Os}^{\text{VIII}}$  and from  $\text{Os}^{\text{VII}}$  to  $\text{Os}^{\text{VII}}$  most probably does occur. Moreover, the observed KIE is consistent with the postulated molecular formula of the products,  $[\text{Os}^{\text{VII}}\text{O}_3(\text{OH})_3]^{2-}$ ,<sup>1</sup> which can form if proton transfer from  $\text{Os}^{\text{VI}}$  to  $\text{Os}^{\text{VIII}}$  takes place. If no KIE were observed, then the possibility exists that the comproportionation and disproportionation reactions do not consist of proton transfer. If that were the case, the comproportionation reaction could consist of electron transfer only or the proton source (in forming the products) could be from the solvent.

The obtained least squares fits from the KIE experiment yielded extinction coefficient values of the reactants and products, Table 4.9, in good agreement with those obtained in Section 4.2.2.1 (Table 4.3) and Section 4.2.2.2 (Table 4.6).

**Table 4.9. Comparison of the calculated and literature high oxidation state osmium species' molar extinction coefficients at 370 nm obtained from the KIE experiment at 294.5 K.**

osmium species	Calculated ( $\text{L}\cdot\text{mol}^{-1}\cdot\text{cm}^{-1}$ )	Literature <sup>1,2,13</sup> ( $\text{L}\cdot\text{mol}^{-1}\cdot\text{cm}^{-1}$ )	
$([\text{Os}^{\text{VIII}}\text{O}_4(\text{OH})]^- + \text{cis}-[\text{Os}^{\text{VIII}}\text{O}_4(\text{OH})_2]^{2-})$	$1275.7 \pm 5.0$	$1159.7 \pm 7.1$	1165.6
$\text{trans}-[\text{Os}^{\text{VI}}\text{O}_2(\text{OH})_4]^{2-}$	$247.2 \pm 3.1$	$210.6 \pm 6.4$	231.2
$[\text{Os}^{\text{VII}}\text{O}_3(\text{OH})_3]^{2-}$	$2466.3 \pm 3.5$	$\sim 2900$	-

### 4.3 Conclusions

The Evans method  $^1\text{H}$  NMR spectroscopy experimental results confirmed that the reaction of diamagnetic  $\text{Os}^{\text{VIII}}$  oxo/hydroxido and  $\text{trans}-[\text{Os}^{\text{VI}}\text{O}_2(\text{OH})_4]^{2-}$  species, in an 2.0 M NaOH aqueous matrix at 298.15 K, does in fact occur and that the product species formed are paramagnetic. Moreover, the stoichiometric ratio of the  $\text{Os}^{\text{VIII}}$  and  $\text{Os}^{\text{VI}}$  reactants in the comproportionation reaction is 1:1.

For the first time, the rate constants of the proposed comproportionation reaction have been determined directly using stopped-flow UV-Vis spectroscopy analysis. The proposed reaction model used to simulate the obtained kinetic data was validated by the linearity of the Eyring and van't Hoff plots, the good agreement of calculated molar extinction coefficients with those reported in the literature<sup>1,2,13</sup> and the good agreement of the standard reaction Gibbs

free energy ( $\Delta G^\circ_{rxn(obs)} = -1.1 \pm 2.5 \text{ kcal.mol}^{-1}$ ) with that reported by Gerber *et al.*<sup>1</sup> The forward (comproportionation) reaction is first order w.r.t. Os<sup>VI</sup> and Os<sup>VIII</sup> concentrations while the reverse (disproportionation) reaction is second order w.r.t. Os<sup>VII</sup> concentration. According to our Eyring and van't Hoff plot analyses, the activation enthalpy of disproportionation,  $\Delta^\ddagger H^\circ_{dis(obs)}$ , is negative ( $-6.7 \pm 1.0 \text{ kcal.mol}^{-1}$ ) and the comproportionation reaction is endothermic ( $\Delta H^\circ_{rxn(obs)} = 17.1 \pm 1.2 \text{ kcal.mol}^{-1}$ ).

Chemical reactions that display apparent negative activation enthalpies have been reported to consist of more than one elementary reaction step due to the formation of intermediate<sup>10</sup> species in the reaction mechanism.<sup>31</sup> This suggests that a similar mechanism may be responsible for the observed negative activation enthalpy for disproportionation and that the reaction most probably consists of at least two consecutive elementary reactions.

In a partially deuterated aqueous solvent composition, the rate-constants of the comproportionation and disproportionation reactions decrease by the same magnitude, as revealed by the  $\frac{k(\text{H}_2\text{O})}{k(0.5 \times \text{D}_2\text{O})}$  kinetic isotope effect (KIE) of approximately 1.134 and 1.137, respectively. Furthermore, this result provides evidence that the rate-determining step of the Os<sup>VI</sup> & Os<sup>VIII</sup> and Os<sup>VII</sup> & Os<sup>VII</sup> comproportionation/disproportionation reaction coincides with a PT event and that PT from Os<sup>VI</sup> to Os<sup>VIII</sup> is most likely coupled to the electron transfer, redox event.

The formation of the Os<sup>VII</sup> complex, in addition to several Os<sup>VIII</sup> species, in 2.0 M NaOH aqueous solutions, emphasises the uncertainty pertaining to what the actual catalytically active osmium species are in reported studies.<sup>2-13</sup> The reported studies that have failed to detect this comproportionation reaction when they utilised Os<sup>VIII</sup> oxo/hydroxido species as catalyst precursors in basic aqueous solutions must therefore reinterpret their incomplete results.

The experimental results are, however, unable to confirm the physical nature of the final products or the reaction mechanism. Quantum mechanical calculations are necessary to corroborate the experimental results so that the nature of all the high oxidation state osmium

---

<sup>10</sup> Intermediate species are molecular entities with a lifetime appreciably longer than a molecular vibration (corresponding to a local potential energy minimum depth greater than  $RT$ ) that are formed (directly or indirectly) from the reactants and reacts further to give (either directly or indirectly) the products of a chemical reaction; also the corresponding chemical species.

species (Chapter 5), as well as the associated reaction mechanisms involved in the comproportionation reaction (Chapter 6), can be identified.

---

**References**

1. T. E. Geswindt, W. J. Gerber, H. E. Rohwer and K. R. Koch, *Dalton Trans.*, 2011, **40**, 8581.
2. A. Dehestani, W. H. Lam, D. A. Hrovat, E. R. Davidson, W. T. Borden and J. M. Mayer, *J. Am. Chem. Soc.*, 2005, **127**, 3423.
3. P. VeeraSomaiah, K. B. Reddy, B. Sethuram and T. Navaneeth Rao, *J. Indian Chem. Soc.*, 1988, **27A**, 876.
4. P. VeeraSomaiah, K. B. Reddy, B. Sethuram and T. Navaneeth Rao, *J. Indian Chem. Soc.*, 1989, **66**, 755.
5. H. S. Singh, S. P. Singh, S. M. Singh, R. K. Singh and A. K. Sisodia, *J. Phys. Chem.*, 1975, **79(18)**, 1920.
6. N. P. Singh, V. N. Singh, H. S. Singh and M. P. Singh, *Aust. J. Chem.*, 1970, **23**, 921.
7. V. N. Singh, H. S. Singh and B. B. L. Saxena, *J. Am. Chem. Soc.*, 1969, **91(10)**, 2643.
8. H. S. Singh, *Oxidation of Organic Compounds with Osmium Tetroxide, in Organic synthesis by oxidation with metal compounds*, ed. W. J. Mijs and C. R. H. de Jonge, Plenum Press, New York, 1986.
9. N. P. Singh, V.N. Singh and M. P. Singh, *Aust. J. Chem.*, 1968, **21**, 2913.
10. B. Singh, A. K. Singh, M. B. Singh and A. P. Singh, *Tetrahedron*, 1986, **42**, 715.
11. K. K. S. Gupta and B. A. Begum, *Transition Met. Chem.*, 1998, **23**, 295.
12. K. K. S. Gupta and B. A. Begum, *Int. J. Chem. Kinet.*, 1999, **31(7)**, 477.
13. W. P. Griffith and M. Suriaatmaja, *Can. J. Chem.*, 2001, **79**, 598–606.
14. I. N. Marov, G. M. Khomushka, V. K. Belyaeva and E. K. Ivanova, *Russ. J. Inorg. Chem.*, 1984, **29**, 146.
15. J. S. Mayell, *I & EC Product Res. Dev.*, 1968, **7(2)**, 129.
16. J. E. Bevay, G. Nowogrocki and G. Tridot, *Bull. Soc. Chim. Fr.*, 1967, 2030.

17. D. F. Evans, *J. Chem. Soc.*, 1959, 2003.
18. J. Löliger and R. Scheffold, *J. Chem. Educ.*, 1972, **49**, 646.
19. T. H. Crawford and J. Swanson, *J. Chem. Educ.*, 1971, **48**, 382.
20. D. F. Evans and T. A. James, *J. Chem. Soc. Dalton Trans.*, 1979, 723.
21. K. A. K. Lott and M. C. R. Symons, *J. Chem. Soc.*, 1960, 973.
22. D. H. Grant, *J. Chem. Educ.*, 1995, **72**, 39.
23. C. Piguet, E. Rivara-Minten, G. Hopfgartner and J. -C. G. Bünzli, *Helv. Chim. Acta*, 1995, **78**, 1651.
24. O. Kahn, *Molecular Magnetism*, VCH: New York-Weinheim-Cambridge, 1994, Chapters 1 and 3.
25. K. A. Reeder, E. V. Dose and L. J. Wilson, *Inorg. Chem.*, 1978, **17**, 1071.
26. H. Toftlund, *Coord. Chem. Rev.*, 1989, **94**, 67.
27. P. Kuzmic, *Anal. Biochem.*, 1996, **237**, 260.
28. W. J. Gerber, PhD Dissertation, University of Port Elizabeth, South Africa, 2005.
29. J. N. Miller, *Analyst*, 1991, **116**, 3.
30. F. H. Westheimer, *Chem. Rev.*, 1949, **45**, 419.
31. X. Han, R. Lee, T. Chen, J. Luo. Y. Lu and K. -W. Huang, *Sci. Rep.*, 2013, **3**, 2557.



# CHAPTER 5

---

## Density Functional Theory (DFT) Speciation Study of Os<sup>VI</sup> and Os<sup>VII</sup> oxo/hydroxido Species; a Closer Look at the Thermodynamics of the Os<sup>VI</sup> & Os<sup>VIII</sup> Comproportionation Reaction

### 5.1 Introduction

From the Evans method and stopped-flow UV-Vis spectroscopy kinetics experiments (Chapter 4), the stoichiometry and spin state of the Os<sup>VI</sup> & Os<sup>VIII</sup> comproportionation reaction products were deduced. However, a more detailed discussion of the comproportionation reaction is hampered due to a lack of knowledge of the chemical composition and equilibrium geometries of the Os<sup>VII</sup> products and possibly the Os<sup>VI</sup> reactant species. In an attempt to interpret the thermodynamics (Chapter 4) and ultimately the kinetics and mechanism (Chapter 6) of the Os<sup>VI</sup> & Os<sup>VIII</sup> comproportionation reaction in more detail, a speciation study of the reactant and product species must first be conducted. Moreover, this line of inquiry is not only crucial for the comproportionation reaction, but also to shed light on several studies where Os<sup>VIII</sup> species are used as catalysts<sup>1-5</sup> and in the reduction Os<sup>VIII</sup> oxo/hydroxido species with aliphatic alcohols in basic aqueous media.<sup>6-17</sup>

There are several studies in the literature that have utilised DFT for aqueous phase speciation studies to complement data obtained from spectroscopic techniques.<sup>18-20</sup> In particular, electronic structure methods have been useful in providing detailed structural information, relative energies of different possible spin states and stereoisomers, estimation of equilibrium constants and the contribution/influence of aqueous hydration energies. DFT speciation calculations of the Os<sup>VIII</sup> oxo/hydroxido/aqua species in aqueous matrices are discussed extensively in Chapter 3 and only the results thereof that are particularly relevant to the present discussion are briefly summarised here. A solution of Os<sup>VIII</sup> in a 2.0 M NaOH aqueous matrix at 298.15 K contains two abundant Os<sup>VIII</sup> oxo/hydroxido species. They are the [Os<sup>VIII</sup>O<sub>4</sub>(OH)]<sup>-</sup> ([Os<sup>VIII</sup>=O]) and *cis*-[Os<sup>VIII</sup>O<sub>4</sub>(OH)<sub>2</sub>]<sup>2-</sup> ([Os<sup>VIII</sup>=O]<sup>2-</sup>) species and are present in a ratio of approximately 0.46:0.54 ( $K_2 = 0.58$ )<sup>21,22</sup> while the amount of Os<sup>VIII</sup>O<sub>4</sub> is negligible.<sup>23</sup> Both the five-coordinate and six-coordinate Os<sup>VIII</sup> species have a  $d^0$  electron configuration and are capable of accepting an electron from [Os<sup>VI</sup>O<sub>2</sub>(OH)<sub>4</sub>]<sup>2-</sup> ([Os<sup>VI</sup>-OH]<sup>2-</sup>),

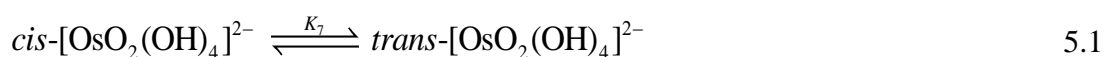
of  $d^2$  electron configuration, in a comproportionation reaction to form two  $d^1$  product species. From the onset we already know that in a 2.0 M NaOH aqueous matrix, at 298.15 K, at least two comproportionation reactions can occur in parallel, where  $[\text{Os}^{\text{VIII}}=\text{O}]^-$  and  $[\text{Os}^{\text{VIII}}=\text{O}]^{2-}$  compete with one another to react with  $[\text{Os}^{\text{VI}}-\text{OH}]^{2-}$ .<sup>24</sup>

In this chapter we report a systematic DFT speciation study to (i) determine whether the *trans* or *cis* stereoisomer of the octahedral  $[\text{Os}^{\text{VI}}\text{O}_2(\text{OH})_4]^{2-}$  complex anion is thermodynamically more stable in an aqueous solution; (ii) investigate whether the singlet state  $[\text{Os}^{\text{VI}}\text{O}_2(\text{OH})_4]^{2-}$  species is thermodynamically more stable than the triplet state species, and thereby corroborate the Evans method experiment result (Chapter 4); (iii) probe the chemical structure of the paramagnetic  $\text{Os}^{\text{VII}}$  product species, *i.e.* determine whether the thermodynamically most stable species are five-coordinate ( $[\text{Os}^{\text{VII}}-\text{OH}]^-$ ), six-coordinate ( $[\text{Os}^{\text{VII}}-\text{OH}]^{2-}$ ) or a mixture of both; (iv) elucidate the nature of the metal-ligand bonding interactions of the  $\text{Os}^{\text{VI}}$  and  $\text{Os}^{\text{VII}}$  complex species and; (v) ultimately to compare DFT-calculated thermodynamic parameters with the experimentally obtained van't Hoff plot analysis values, Table 4.5.

## 5.2. Results and discussion

### 5.2.1 DFT speciation study of the anionic $\text{Os}^{\text{VI}}$ complexes

Extensive conformational analysis of the octahedral  $\text{Os}^{\text{VI}}$  species, *via* relaxed potential energy surface scans, yielded several (*e.g.* eight for the PBE functional) distinct minimum energy conformations of the *trans* stereoisomer in the simulated aqueous phase. The global minimum energy conformation of *trans*- $[\text{Os}^{\text{VI}}-\text{OH}]^{2-}$ , Figure 5.1 (a), is approximately thirty times more abundant than any other *trans* conformer, and approximately 10 kcal.mol<sup>-1</sup> (PBE functional) thermodynamically more stable than that of the *cis* stereoisomer, Figure 5.1 (b). The equilibrium constant,  $K_7$ , for reaction 5.1, which depicts the interconversion between *cis* and *trans* stereoisomers, equates to a value of approximately  $2.1 \times 10^7$  and provides a possible explanation why there are no reported crystal structures of the *cis* stereoisomer.



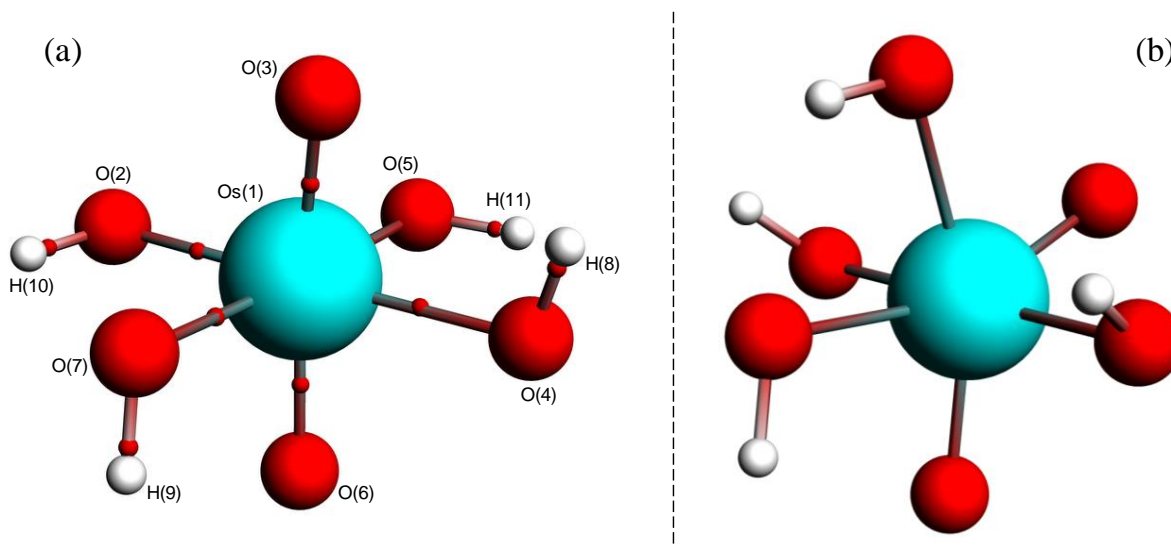
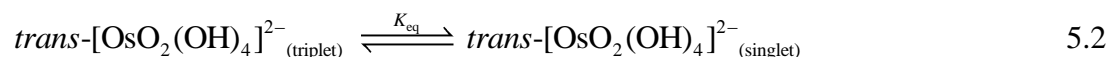


**Figure 5.1.** Molecular graphs of the global minimum energy geometries of (a)  $trans\text{-}[\text{Os}^{\text{VI}}\text{O}_2(\text{OH})_4]^{2-}$  and (b)  $cis\text{-}[\text{Os}^{\text{VI}}\text{O}_2(\text{OH})_4]^{2-}$  in the simulated aqueous phase (PBE functional) with small red spheres representing (3,-1) critical points (Numbering included for  $trans\text{-}[\text{Os}^{\text{VI}}\text{O}_2(\text{OH})_4]^{2-}$  for AIMs analysis, Section 5.2.5).

Moreover, the singlet state of the  $trans\text{-}[\text{Os}^{\text{VI}}\text{-OH}]^{2-}$  species is approximately  $18 \text{ kcal.mol}^{-1}$  (PBE functional) thermodynamically more stable than the triplet state complex, which equates to a  $K_{\text{eq}}$  value for reaction 5.2 of approximately  $1.6 \times 10^{13}$ . This corroborates the Evans method experiment result (Chapter 4) that the abundant  $[\text{Os}^{\text{VI}}\text{-OH}]^{2-}$  species are diamagnetic.



DFT-calculated metal-ligand bond lengths of the global minimum  $trans\text{-}[\text{Os}^{\text{VI}}\text{-OH}]^{2-}$  species' equilibrium geometry, Table 5.1, correlates well with reported values obtained from X-ray crystal structure data.<sup>25,26</sup> The accuracy of the computational methodology w.r.t. the obtained geometry, which was also attained in the study of the  $\text{Os}^{\text{VIII}}$  species in Chapter 3, offers assurance that further DFT-calculated geometries of all high oxidation state osmium species involved in the comproportionation reaction, using the same methodology, are reliable. This is particularly important w.r.t. the  $\text{Os}^{\text{VII}}$  product species (Section 5.2.2) for which there is no experimental crystal structure data with which to compare.

**Table 5.1. Computed and experimental Os=O and Os-OH bond lengths of *trans*-[Os<sup>VI</sup>-OH]<sup>2-</sup> (Å).**

Ligand	DFT (PBE functional)		Experimental	
	gas phase	COSMO (aqueous)	Lit. <sup>25</sup>	Lit. <sup>26</sup>
Os=O	1.7643	1.7618	1.75(2)	1.77
	1.7647	1.7625		
Os-OH	2.1672	2.1278	1.99(2)	2.03
	2.0001	1.9895		
	2.0009	1.9894		
	2.1687	2.1287		

### 5.2.2 DFT speciation study of the anionic Os<sup>VII</sup> complexes

With the ground state geometries and energies of the reactants determined, we turned our attention to the comproportionation reaction's paramagnetic products. In Chapter 3 we reported that the interchange between five-coordinate ([Os<sup>VIII</sup>=O]<sup>-</sup>) and six-coordinate ([Os<sup>VIII</sup>=O]<sup>2-</sup>) Os<sup>VIII</sup> oxo/hydroxido species, equation 3.4, are related *via* a coordination sphere expansion/contraction reaction mechanism with a hydroxide anion. We took this as evidence that the final products of the comproportionation reaction could also possibly be five-coordinate and/or six-coordinate Os<sup>VII</sup> oxo/hydroxido species, depending on their relative thermodynamic stabilities, and that a similar mechanism is most likely responsible for interchange between them (*vide infra*). Extensive conformational analyses of *cis*- and *trans*- [Os<sup>VII</sup>O<sub>3</sub>(OH)<sub>2</sub>]<sup>-</sup> ([Os<sup>VII</sup>-OH]<sup>-</sup>) and of *fac*- and *mer*- [Os<sup>VII</sup>O<sub>3</sub>(OH)<sub>3</sub>]<sup>2-</sup> ([Os<sup>VII</sup>-OH]<sup>2-</sup>) complexes were performed and several distinct minimum energy conformations were obtained for each of these four possible stereoisomers. The global minimum energy geometries of the Os<sup>VII</sup> stereoisomers in the simulated aqueous phase are shown in Figure 5.2.<sup>11</sup>

<sup>11</sup> High oxidation state metal complexes with H<sub>2</sub>O ligands are mostly unknown or have not been reported, indicating that such species are not thermodynamically stable, *e.g.* Figures 3.1 and 3.4.

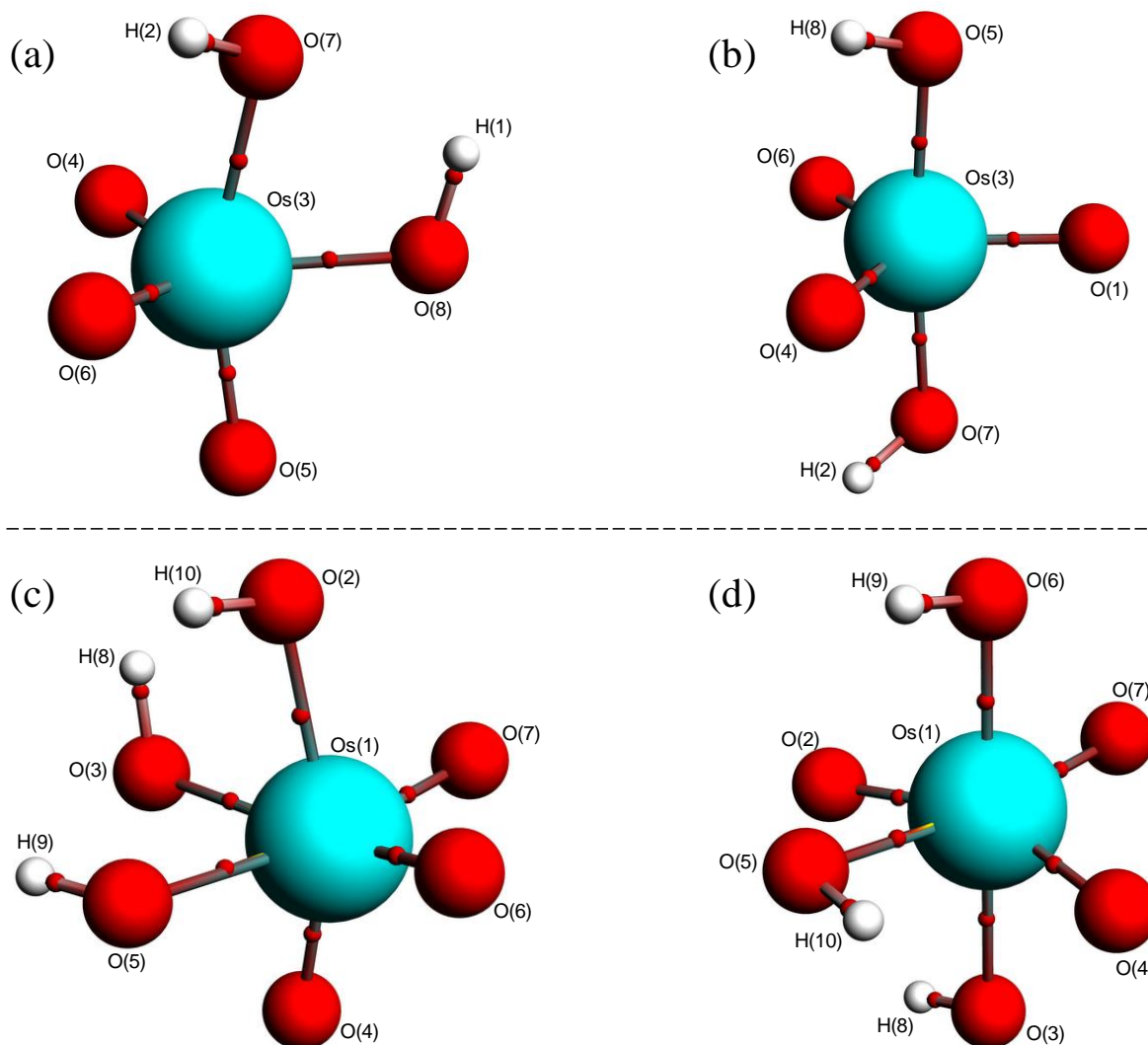
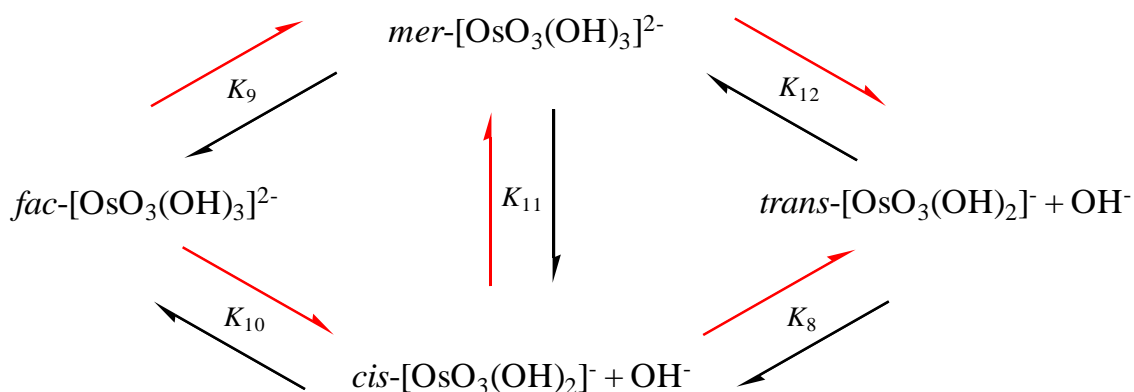


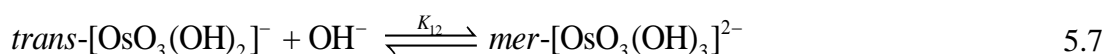
**Figure 5.2.** Molecular graphs of the global minimum energy geometries of the *cis*- (a) and *trans*- (b)  $[\text{Os}^{\text{VII}}\text{-OH}]$  and *fac*- (c) and *mer*- (d)  $[\text{Os}^{\text{VII}}\text{-OH}]^{2-}$  complexes in the simulated aqueous phase (PBE functional) with small red spheres representing (3,-1) critical points.

The four distinct  $\text{Os}^{\text{VII}}$  stereoisomer species are related to each other *via* a reaction network, Scheme 5.1, of rapid, stereoisomer interchange reactions, equations 5.3 & 5.4, and most probably coordination sphere expansion/contraction reactions, equations 5.5 – 5.7. In support of the statement that these reactions are rapid, are the stopped-flow UV-Vis spectroscopy kinetic traces obtained for the comproportionation reaction, Figures 4.5, 4.6 and 4.10 in Chapter 4. When reactant-containing solutions of  $\text{Os}^{\text{VI}}$  and  $\text{Os}^{\text{VIII}}$  are mixed, the absorbance values steadily increase with time until they reach a plateau after approximately 1.5 seconds, *i.e.* a maximum value corresponding to a state of equilibrium. If there was a noticeable time lag between the interconverting  $\text{Os}^{\text{VII}}$  species, Scheme 5.1, the increase in absorbance before equilibrium and steady signal after equilibrium would have exhibited further increases or

decreases in absorbance, since the molar extinction coefficients of the four Os<sup>VII</sup> species are most probably not equal to each another at 370 nm. There are no observable increases or decreases in absorbance, indicating either that the Os<sup>VII</sup> product species do not interchange at all or that the interchange between them is rapid, even on this timescale.



**Scheme 5.1.** Stereoisomer interchange of five- and six-coordinate Os<sup>VII</sup> oxo/hydroxido species. Red arrows indicate the direction in which the interchange is spontaneous (for various PBE functionals that include or exclude dispersion corrections) in the simulated aqueous phase at 298.15 K.



There are four possible Os<sup>VII</sup> products of the comproportionation reaction and the energies reported in Table 5.2 all refer to the following reaction, equation 5.8.



where  $X = cis-[OsO_3(OH)_2]^- + OH^-$ ,  $fac-[OsO_3(OH)_3]^{2-}$  or  $mer-[OsO_3(OH)_3]^{2-}$ .

The *trans* five-coordinate Os<sup>VII</sup> oxo/hydroxido species (distorted trigonal bipyramidal, Figure 5.2B) is consistently lower in Gibbs energy than the *cis* stereoisomer (Figure 5.2A) at 298.15 K, Table 5.2, by approximately 5 kcal.mol<sup>-1</sup>. The equilibrium constant for reaction 5.3 ranges between  $5.6 \times 10^2$  (LDA) and  $2.7 \times 10^4$  (BLYP-D). Likewise, the *mer* (distorted octahedral, Figure 5.2D) stereoisomer of the six-coordinate Os<sup>VII</sup> oxo/hydroxido species is thermodynamically more stable, by approximately 3 kcal.mol<sup>-1</sup>, than the corresponding *fac* (Figure 5.2C) species at 298.15 K, yielding an equilibrium constant between 43 (BLYP-D) and 200 (BLYP) for reaction 5.4.

**Table 5.2. Thermodynamic reaction energies of reaction 5.8 in the simulated aqueous phase (298.15 K).**

XC category	Functional	X	$\Delta H_{rxn}^{\circ}$ (kcal.mol <sup>-1</sup> )	$\Delta S_{rxn}^{\circ}$ (cal.mol <sup>-1</sup> .K <sup>-1</sup> )	$\Delta G_{rxn}^{\circ}$ (kcal.mol <sup>-1</sup> )
LDA	LDA	<i>cis</i> -[Os <sup>VII</sup> O <sub>3</sub> (OH) <sub>2</sub> ] <sup>-</sup> + OH <sup>-</sup>	3.42	-1.09	3.75
		<i>fac</i> -[Os <sup>VII</sup> O <sub>3</sub> (OH) <sub>3</sub> ] <sup>2-</sup>	-18.08	-35.29	-7.56
		<i>mer</i> -[Os <sup>VII</sup> O <sub>3</sub> (OH) <sub>3</sub> ] <sup>2-</sup>	-21.01	-36.15	-10.23
	PBE	<i>cis</i> -[Os <sup>VII</sup> O <sub>3</sub> (OH) <sub>2</sub> ] <sup>-</sup> + OH <sup>-</sup>	4.47	-1.52	4.93
		<i>fac</i> -[Os <sup>VII</sup> O <sub>3</sub> (OH) <sub>3</sub> ] <sup>2-</sup>	-5.68	-34.73	4.67
		<i>mer</i> -[Os <sup>VII</sup> O <sub>3</sub> (OH) <sub>3</sub> ] <sup>2-</sup>	-8.91	-35.87	1.79
	PBE-D	<i>cis</i> -[Os <sup>VII</sup> O <sub>3</sub> (OH) <sub>2</sub> ] <sup>-</sup> + OH <sup>-</sup>	4.71	-1.21	5.07
		<i>fac</i> -[Os <sup>VII</sup> O <sub>3</sub> (OH) <sub>3</sub> ] <sup>2-</sup>	-7.77	-34.32	2.46
		<i>mer</i> -[Os <sup>VII</sup> O <sub>3</sub> (OH) <sub>3</sub> ] <sup>2-</sup>	-10.57	-35.52	0.02
PBE-D3	<i>cis</i> -[Os <sup>VII</sup> O <sub>3</sub> (OH) <sub>2</sub> ] <sup>-</sup> + OH <sup>-</sup>	4.58	-1.41	5.00	
	<i>fac</i> -[Os <sup>VII</sup> O <sub>3</sub> (OH) <sub>3</sub> ] <sup>2-</sup>	-6.85	-34.76	3.51	
	<i>mer</i> -[Os <sup>VII</sup> O <sub>3</sub> (OH) <sub>3</sub> ] <sup>2-</sup>	-9.86	-35.79	0.81	
PBE-D3(BJ)	<i>cis</i> -[Os <sup>VII</sup> O <sub>3</sub> (OH) <sub>2</sub> ] <sup>-</sup> + OH <sup>-</sup>	4.32	-2.46	5.06	
	<i>fac</i> -[Os <sup>VII</sup> O <sub>3</sub> (OH) <sub>3</sub> ] <sup>2-</sup>	-6.70	-36.33	4.13	
	<i>mer</i> -[Os <sup>VII</sup> O <sub>3</sub> (OH) <sub>3</sub> ] <sup>2-</sup>	-9.76	-37.44	1.40	
PBE-dDsC	<i>cis</i> -[Os <sup>VII</sup> O <sub>3</sub> (OH) <sub>2</sub> ] <sup>-</sup> + OH <sup>-</sup>	4.35	-2.41	5.06	
	<i>fac</i> -[Os <sup>VII</sup> O <sub>3</sub> (OH) <sub>3</sub> ] <sup>2-</sup>	-6.79	-36.29	4.03	
	<i>mer</i> -[Os <sup>VII</sup> O <sub>3</sub> (OH) <sub>3</sub> ] <sup>2-</sup>	-9.94	-37.37	1.20	
GGA	mPBE	<i>cis</i> -[Os <sup>VII</sup> O <sub>3</sub> (OH) <sub>2</sub> ] <sup>-</sup> + OH <sup>-</sup>	4.58	-2.76	5.40
		<i>fac</i> -[Os <sup>VII</sup> O <sub>3</sub> (OH) <sub>3</sub> ] <sup>2-</sup>	-4.05	-36.53	6.84
		<i>mer</i> -[Os <sup>VII</sup> O <sub>3</sub> (OH) <sub>3</sub> ] <sup>2-</sup>	-7.25	-37.78	4.01
	BLYP	<i>cis</i> -[Os <sup>VII</sup> O <sub>3</sub> (OH) <sub>2</sub> ] <sup>-</sup> + OH <sup>-</sup>	4.99	-2.03	5.60
		<i>fac</i> -[Os <sup>VII</sup> O <sub>3</sub> (OH) <sub>3</sub> ] <sup>2-</sup>	-0.90	-35.68	9.74
		<i>mer</i> -[Os <sup>VII</sup> O <sub>3</sub> (OH) <sub>3</sub> ] <sup>2-</sup>	-4.42	-36.97	6.60
	BLYP-D	<i>cis</i> -[Os <sup>VII</sup> O <sub>3</sub> (OH) <sub>2</sub> ] <sup>-</sup> + OH <sup>-</sup>	5.35	-2.35	6.05
		<i>fac</i> -[Os <sup>VII</sup> O <sub>3</sub> (OH) <sub>3</sub> ] <sup>2-</sup>	-4.24	-35.31	6.29
		<i>mer</i> -[Os <sup>VII</sup> O <sub>3</sub> (OH) <sub>3</sub> ] <sup>2-</sup>	-6.96	-36.95	4.06
	BLYP-D3	<i>cis</i> -[Os <sup>VII</sup> O <sub>3</sub> (OH) <sub>2</sub> ] <sup>-</sup> + OH <sup>-</sup>	5.36	-2.08	5.98
		<i>fac</i> -[Os <sup>VII</sup> O <sub>3</sub> (OH) <sub>3</sub> ] <sup>2-</sup>	-3.44	-36.14	7.33
		<i>mer</i> -[Os <sup>VII</sup> O <sub>3</sub> (OH) <sub>3</sub> ] <sup>2-</sup>	-6.47	-37.23	4.62
	PW91	<i>cis</i> -[Os <sup>VII</sup> O <sub>3</sub> (OH) <sub>2</sub> ] <sup>-</sup> + OH <sup>-</sup>	4.47	-2.23	5.13
		<i>fac</i> -[Os <sup>VII</sup> O <sub>3</sub> (OH) <sub>3</sub> ] <sup>2-</sup>	-6.46	-36.63	4.46
		<i>mer</i> -[Os <sup>VII</sup> O <sub>3</sub> (OH) <sub>3</sub> ] <sup>2-</sup>	-9.69	-37.71	1.55
MetaGGA	M06L	<i>cis</i> -[Os <sup>VII</sup> O <sub>3</sub> (OH) <sub>2</sub> ] <sup>-</sup> + OH <sup>-</sup>	4.97	-2.37	5.67
		<i>fac</i> -[Os <sup>VII</sup> O <sub>3</sub> (OH) <sub>3</sub> ] <sup>2-</sup>	-10.78	-31.66	-1.34
		<i>mer</i> -[Os <sup>VII</sup> O <sub>3</sub> (OH) <sub>3</sub> ] <sup>2-</sup>	-13.78	-33.02	-3.93



All calculations that were done using GGA functionals yield the *trans*-[Os<sup>VII</sup>-OH]<sup>-</sup> stereoisomer species as the lowest in Gibbs energy at 298.15 K, *i.e.* the *trans* species is the thermodynamically most stable of *all* Os<sup>VII</sup> oxo/hydroxido product species. However, two functionals, namely LDA and M06L, yield the *mer*-[Os<sup>VII</sup>-OH]<sup>2-</sup> species as the stereoisomer with the lowest Gibbs energy at the same temperature. Given the good agreement between DFT speciation data with that of experiment for Os<sup>VIII</sup> oxo/hydroxido species (Chapter 3), we expect the results obtained here with PW91, PBE (and PBE with dispersion corrections) to be more reliable compared to the results when other functionals are used. Furthermore, the magnitudes of the equilibrium constants for reactions 5.3 and 5.4,  $K_8$  and  $K_9$ , respectively, imply that five-coordinate *cis*, and six-coordinate *fac*, species' concentrations are considerably lower (by approximately 4600 and 100 times, respectively) than the *trans* and *mer* species, respectively. At 298.15 K, the *cis* and *fac* species would therefore not yield any observable UV-Vis signal in the context of the kinetic experiments discussed in Chapter 4.

The equilibrium constant for reaction 5.7,  $K_{12}$ , at 298.15 K varies from approximately 0.05 (PBE) to 0.96 (PBE-D), indicating that significant quantities of both these species are present at equilibrium. However, PBE and PBE-D are most probably the two least accurate of the five PBE functionals, due to the lack of and overestimation, respectively, of dispersion corrections. Therefore,  $K_{12}$ , as calculated with PBE-D3 (0.26), PBE-D3(BJ) (0.09) and PBE-dDsC (0.13) are likely more reliable, such that a more accurate equilibrium constant for the reaction is closer to approximately 0.1. For practical purposes, the *trans* and *mer* stereoisomers are considered the most abundant species and hence be considered w.r.t. the Os<sup>VII</sup> oxo/hydroxido speciation. Moreover, reaction 5.7 is exothermic according to calculated energies from *all* functionals.  $\Delta H^\circ_{rxn}$  of reaction 5.7 ranges between -8.91 kcal.mol<sup>-1</sup> (PBE) and -10.57 kcal.mol<sup>-1</sup> (PBE-D). Therefore, the equilibrium constant for reaction 5.7,  $K_{12}$ , is expected to decrease with an increase in temperature, *i.e.* more *trans* species will be present at equilibrium.

### 5.2.3 Thermodynamic driving force of *trans*-[Os<sup>VII</sup>O<sub>3</sub>(OH)<sub>2</sub>]<sup>-</sup> and *mer*-[Os<sup>VII</sup>O<sub>3</sub>(OH)<sub>3</sub>]<sup>2-</sup> interconversion

In Chapter 3 we reported that the thermodynamic driving force for the second coordination sphere expansion reaction of Os<sup>VIII</sup> (equation 3.4) is due to the larger hydration energy of the doubly-charged product species, *cis*-[Os<sup>VIII</sup>O<sub>4</sub>(OH)<sub>2</sub>]<sup>2-</sup> {-217.98 kcal.mol<sup>-1</sup> (PBE functional)}, compared to the reactants, [Os<sup>VIII</sup>O<sub>4</sub>(OH)]<sup>-</sup> (-58.94 kcal.mol<sup>-1</sup>) and OH<sup>-</sup> (-96.09 kcal.mol<sup>-1</sup>).

We therefore proceeded to perform a similar set of EDA<sup>27</sup> calculations to determine the thermodynamic driving force for reaction 5.7. The six-coordinate Os<sup>VII</sup> oxo/hydroxido complex, *mer*-[Os<sup>VII</sup>-OH]<sup>2-</sup>, Figure 5.2C, which is also a doubly-charged product of the reaction between [Os<sup>VII</sup>-OH]<sup>-</sup> and a hydroxide anion contains three dissimilar, w.r.t. spatial position, metal-hydroxido ligands, Os<sup>VII</sup>(1)-O(6)-H(9), Os<sup>VII</sup>(1)-O(5)-H(10) and Os<sup>VII</sup>(1)-O(3)-H(8). EDA calculations where fragments of the ‘complex’ without one of these hydroxido’s, [Os<sup>VII</sup>O<sub>3</sub>(OH)<sub>2</sub>]<sup>-</sup>, and the other fragment is the corresponding hydroxido, OH<sup>-</sup>, were done. These results are encapsulated in Table 5.3.

**Table 5.3. Energy decomposition analysis (EDA) in kcal.mol<sup>-1</sup> of the three Os<sup>VII</sup>-OH ligands of the *mer*-[Os<sup>VII</sup>-OH]<sup>2-</sup> complex in the simulated aqueous phase.**

Ligand	Functional	$\Delta E_{int}$	$\Delta E_{Pauli}$	$\Delta E_{elstat}$	$\Delta E_{orb.}$	$\Delta E_{disp.}$	$\Delta E_{solv.}$	$\Delta E_{prep}$	$-D_e$
Os <sup>VII</sup> (1)-O(5)-H(10)	PBE	-180.59	174.91	-71.55	-62.00	0.00	-221.95	26.76	-153.83
	PBE-D	-182.32	169.90	-67.62	-60.60	-1.64	-222.36	26.22	-156.10
	PBE-D3	-181.71	174.08	-70.97	-61.79	-1.04	-221.99	26.14	-155.57
	PBE-D3(BJ)	-181.42	175.04	-71.53	-61.92	-1.06	-221.95	25.77	-155.65
	PBE-dDsC	-181.32	175.35	-71.65	-61.94	-1.09	-221.99	25.60	-155.72
Os <sup>VII</sup> (1)-O(6)-H(9)	PBE	-190.48	192.20	-81.20	-79.53	0.00	-221.95	32.97	-157.51
	PBE-D	-192.37	188.80	-78.55	-78.95	-1.31	-222.36	33.04	-159.33
	PBE-D3	-191.45	191.58	-80.74	-79.42	-0.88	-221.99	32.87	-158.58
	PBE-D3(BJ)	-191.40	193.93	-82.39	-80.04	-0.95	-221.95	32.91	-158.49
	PBE-dDsC	-191.44	194.28	-82.63	-80.06	-1.04	-221.99	32.83	-158.61
Os <sup>VII</sup> (1)-O(3)-H(8)	PBE	-207.97	262.74	-133.62	-115.21	0.00	-221.88	49.79	-158.18
	PBE-D	-209.75	261.59	-132.24	-115.37	-1.45	-222.28	49.78	-159.97
	PBE-D3	-209.02	262.60	-133.45	-115.27	-0.98	-221.92	49.76	-159.26
	PBE-D3(BJ)	-208.71	263.48	-133.96	-115.34	-1.02	-221.87	49.56	-159.15
	PBE-dDsC	-208.63	264.33	-134.42	-115.56	-1.06	-221.92	49.34	-159.29

The absolute values of the various energetic contributions of the three hydroxido bonds of the *mer*-[Os<sup>VII</sup>-OH]<sup>2-</sup> complex differ significantly from each other. However, for all three bonds the ratio of  $\Delta E_{elstat}:\Delta E_{orb}$  is approximately 1.10 throughout, which indicates slightly more ionic than covalent character. Furthermore, contributions of  $\Delta E_{disp}$  are minimal in all three cases. However, the largest energetic contribution to the interaction energies is that of solvation (hydration) energy,  $\Delta E_{solv.}$ . In the absence of this contribution,  $\Delta E_{int}$  is a positive value. Moreover, the hydration energy difference between the reactants and products (PBE functional) is 62.78 kcal.mol<sup>-1</sup>. Therefore, similarly to the coordination sphere expansion reaction between five- and six-coordinate Os<sup>VIII</sup> species in an aqueous matrix, the thermodynamic driving force for reaction 5.7 is the larger solvation (hydration) energy of the

doubly-charged  $mer$ -[Os<sup>VII</sup>-OH]<sup>2-</sup> species (-221.73 kcal.mol<sup>-1</sup>) compared to the reactants,  $trans$ -[Os<sup>VII</sup>-OH]<sup>-</sup> (-62.86 kcal.mol<sup>-1</sup>) and OH<sup>-</sup> (-96.09 kcal.mol<sup>-1</sup>).

Furthermore,  $\Delta E_{int}$  for the Os<sup>VII</sup>(1)-O(5)-H(10) ligand is the least negative and is therefore the weakest metal-hydroxido bonding interaction of the three, Figure 5.2. The bond lengths of the three dissimilar hydroxido ligands, Table 5.4, also reflect this. The Os<sup>VII</sup>(1)-O(5)-H(10) distance is considerably longer than the two hydroxido ligands positioned  $trans$  to one another, irrespective of DFT functional used to optimise the geometries. Interestingly, bond dissociation of this hydroxido ligand will result in the formation of the thermodynamically more stable of the five-coordinate Os<sup>VII</sup> oxo/hydroxido stereoisomer species, namely  $trans$ -[Os<sup>VI</sup>-OH]<sup>-</sup>, equation 5.7. These results collectively indicate how the thermodynamically favoured five-coordinate ( $trans$ ) and six-coordinate ( $mer$ ) Os<sup>VII</sup> species are related to one another.

**Table 5.4. Computed Os-OH bond lengths of  $mer$ -[Os<sup>VII</sup>O<sub>3</sub>(OH)<sub>3</sub>]<sup>2-</sup> (Å).**

Functional	Os <sup>VII</sup> (1)-O(6)-H(9)	Os <sup>VII</sup> (1)-O(5)-H(10)	Os <sup>VII</sup> (1)-O(3)-H(8)
PBE	1.988	2.144	2.079
PBE-D	1.990	2.150	2.083
PBE-D3	1.989	2.145	2.080
PBE-D3(BJ)	1.988	2.145	2.076
PBE-dDsC	1.987	2.144	2.075

#### 5.2.4 Mechanism of reaction 5.7 - coordination sphere expansion?

In Chapter 3, Section 3.4.2, the mechanism of the coordination sphere expansion/contraction reaction of [Os<sup>VIII</sup>O<sub>4</sub>(OH)]<sup>-</sup> to  $cis$ -[Os<sup>VIII</sup>O<sub>4</sub>(OH)<sub>2</sub>]<sup>2-</sup>, equation 3.4, was found by performing a set of linear transit, relaxed scan, calculations. A similar procedure to that described in Section 3.4.2 was done in an attempt to obtain the reaction mechanism of reaction 5.7. However, there were several computational complications during these calculations. As the metal-hydroxido bond distance of  $mer$ -[Os<sup>VII</sup>O<sub>3</sub>(OH)<sub>3</sub>]<sup>2-</sup>, *i.e.* Os(1)-O(5)-H(10), ‘increases’ during the linear transit calculation, O(5) of the dissociating hydroxido gradually ‘moves’ towards the neighbouring hydrogen, H(9), most probably due to an attractive electrostatic interaction between these two moieties. The obtained change in electronic energy along this reaction coordinate exhibited an erratic PES, *i.e.* the energy does not steadily increase towards an expected maximum value, which would correspond to an initial estimate of the transition state. Instead, the electrostatic interaction between H(9) and O(5) causes the

electronic energy to abruptly decrease after several SCF iterations, making the data unreliable to identify a transition state. Decreasing the linear transit calculation's step size, increasing the integration accuracy or changing the dispersion correction method (or without any, *i.e.* PBE) for the calculations do not prevent the mentioned problem from occurring.

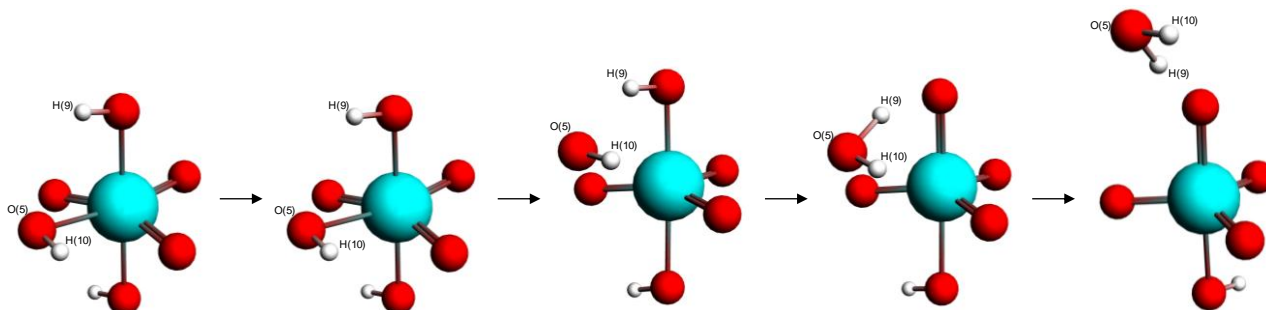


**Figure 5.3.** Brief illustration of how the molecular graph of *trans*-[Os<sup>VII</sup>O<sub>3</sub>(OH)<sub>2</sub>]<sup>-</sup> and OH<sup>-</sup> fragments, from *mer*-[Os<sup>VII</sup>O<sub>3</sub>(OH)<sub>3</sub>]<sup>2-</sup>, progress during the linear transit relaxed scan (PBE functional).

Several efforts to ‘remedy’ the computational procedure were made in an attempt to obtain reliable results. However, imposing a second, or more, geometric constraint(s) on the calculation, *e.g.* by ‘freezing’ the O(5)-H(10) distance, either does not prevent O(5) from ‘moving’ towards H(9) or convergence criteria are not satisfied. Other geometric constraints imposed on the calculation proved equally unsuccessful.

The fact that the mechanism for reaction 5.7 was not obtained using the mentioned procedure does not imply that coordination sphere expansion/contraction does not occur or that it is not rapid or close to diffusion-controlled kinetics. However, based on the calculated results obtained for reaction 3.4, Table 3.11, we expect that similarly low activation Gibbs energy barriers apply for reaction 5.7, as can be inferred from the stopped-flow UV-Vis spectroscopy kinetic traces obtained for the comproportionation reaction, Figures 4.5, 4.6 and 4.10 in Chapter 4.

### 5.2.5 QTAIM analysis of the electron density topology of the Os<sup>VI</sup> and Os<sup>VII</sup> species

In order to further characterise the nature of the metal-oxo (Os<sup>VI</sup>=O & Os<sup>VII</sup>=O) and metal-hydroxido (Os<sup>VI</sup>-OH & Os<sup>VII</sup>-OH) bonding interactions in the *trans*-[Os<sup>VI</sup>-OH]<sup>2-</sup> complex {Figure 5.1(a)} and the four stereoisomers of the Os<sup>VII</sup> oxo/hydroxido complexes (Figure 5.2), we performed a topological analysis of the electron density according to the quantum theory of atoms in molecules (QTAIM).<sup>28,29</sup> Similarly to Os<sup>VIII</sup> oxo/hydroxido species (Figure 3.2), there are no intramolecular BCPs between neighbouring ligands in any of these five

species. The calculated BCPs' electron density topology indices (PBE functional) are listed in Table 5.5 (see Table A.4 for values obtained using PBE-D3(BJ) functional).

**Table 5.5. QTAIM indices computed at the BCPs (PBE functional). All values are expressed in atomic units. Os<sup>VI</sup>=O & Os<sup>VII</sup>=O and Os<sup>VI</sup>-OH & Os<sup>VII</sup>-OH BCPs are highlighted in red and blue, respectively.**

Species	BCP #	Atoms	$\lambda_1$	$\lambda_2$	$\lambda_3$	$\rho_b$	$\nabla^2\rho_b$	$G_b$	$G_b/\rho_b$	$V_b$	$E_b^s$
<i>trans</i> -[Os <sup>VI</sup> -OH] <sup>2-</sup>	1	Os(1)-O(2)	-0.1813	-0.1176	0.8282	0.1311	0.5293	0.1674	1.2771	-0.2109	-0.0436
	2	Os(1)-O(3)	-0.3766	-0.3655	1.7654	0.2303	1.0233	0.3601	1.5638	-0.4892	-0.1291
	3	Os(1)-O(4)	-0.1311	-0.0786	0.5412	0.0963	0.3315	0.1052	1.0915	-0.1317	-0.0266
	4	Os(1)-O(5)	-0.1813	-0.1174	0.8280	0.1311	0.5293	0.1673	1.2769	-0.2109	-0.0435
	5	Os(1)-O(6)	-0.3756	-0.3646	1.7617	0.2299	1.0215	0.3593	1.5629	-0.4879	-0.1287
	6	Os(1)-O(7)	-0.1308	-0.0787	0.5400	0.0962	0.3306	0.1049	1.0906	-0.1314	-0.0265
	7	O(4)-H(8)	-1.7915	-1.7624	1.2996	0.3686	-2.2543	0.0954	0.2588	-0.7543	-0.6590
	8	O(7)-H(9)	-1.7888	-1.7598	1.2985	0.3683	-2.2501	0.0953	0.2587	-0.7531	-0.6578
	9	O(2)-H(10)	-1.7546	-1.7300	1.2739	0.3598	-2.2106	0.0897	0.2493	-0.7320	-0.6424
	10	O(5)-H(11)	-1.7540	-1.7294	1.2739	0.3598	-2.2095	0.0897	0.2494	-0.7318	-0.6421
<i>trans</i> -[Os <sup>VII</sup> -OH] <sup>-</sup>	1	Os(3)-O(7)	-0.1838	-0.1660	0.8557	0.1352	0.5059	0.1656	1.2250	-0.2130	-0.0474
	2	O(1)-Os(3)	-0.3977	-0.3598	1.6378	0.2383	0.8803	0.3391	1.4229	-0.4811	-0.1420
	3	Os(3)-O(4)	-0.3678	-0.3214	1.5062	0.2264	0.8170	0.3121	1.3785	-0.4402	-0.1281
	4	Os(3)-O(5)	-0.1845	-0.1666	0.8589	0.1355	0.5078	0.1662	1.2265	-0.2138	-0.0476
	5	Os(3)-O(6)	-0.4411	-0.4179	1.8259	0.2562	0.9669	0.3792	1.4799	-0.5439	-0.1647
	6	H(2)-O(7)	-1.8165	-1.7945	1.2683	0.3649	-2.3427	0.0867	0.2377	-0.7591	-0.6724
	7	O(5)-H(8)	-1.8156	-1.7937	1.2679	0.3648	-2.3413	0.0867	0.2376	-0.7587	-0.6720
<i>cis</i> -[Os <sup>VII</sup> -OH] <sup>-</sup>	1	Os(3)-O(7)	-0.1528	-0.1424	0.7015	0.1170	0.4063	0.1341	1.1461	-0.1723	-0.0382
	2	Os(3)-O(8)	-0.2161	-0.1995	0.9103	0.1478	0.4947	0.1721	1.1647	-0.2296	-0.0575
	3	Os(3)-O(4)	-0.4414	-0.4342	1.8133	0.2595	0.9377	0.3764	1.4503	-0.5458	-0.1694
	4	Os(3)-O(6)	-0.3762	-0.3478	1.5255	0.2315	0.8016	0.3140	1.3567	-0.4486	-0.1345
	5	Os(3)-O(5)	-0.3510	-0.3183	1.5549	0.2252	0.8856	0.3261	1.4483	-0.4520	-0.1259
	6	H(2)-O(7)	-1.8277	-1.8060	1.2725	0.3650	-2.3612	0.0877	0.2402	-0.7657	-0.6780
	7	H(1)-O(8)	-1.8334	-1.8099	1.2559	0.3602	-2.3874	0.0829	0.2302	-0.7627	-0.6798
<i>mer</i> -[Os <sup>VII</sup> -OH] <sup>2-</sup>	1	Os(1)-O(2)	-0.3709	-0.3555	1.6712	0.2277	0.9447	0.3415	1.4999	-0.4694	-0.1280
	2	Os(1)-O(3)	-0.1553	-0.1142	0.6351	0.1097	0.3656	0.1194	1.0892	-0.1528	-0.0334
	3	Os(1)-O(4)	-0.3712	-0.3537	1.6695	0.2273	0.9447	0.3411	1.5005	-0.4686	-0.1275
	4	Os(1)-O(5)	-0.1243	-0.0946	0.5384	0.0940	0.3195	0.1022	1.0876	-0.1283	-0.0261
	5	Os(1)-O(6)	-0.1829	-0.1651	0.8449	0.1342	0.4969	0.1629	1.2135	-0.2098	-0.0469
	6	Os(1)-O(7)	-0.3216	-0.2787	1.4362	0.2094	0.8359	0.2983	1.4247	-0.4064	-0.1081
	7	O(3)-H(8)	-1.7957	-1.7663	1.2942	0.3678	-2.2678	0.0932	0.2533	-0.7533	-0.6601
	8	O(6)-H(9)	-1.7951	-1.7718	1.2727	0.3626	-2.2942	0.0883	0.2436	-0.7502	-0.6619
	9	O(5)-H(10)	-1.7814	-1.7607	1.2989	0.3679	-2.2432	0.0950	0.2584	-0.7509	-0.6559
<i>fac</i> -[Os <sup>VII</sup> -OH] <sup>2-</sup>	1	Os(1)-O(2)	-0.1482	-0.1342	0.6593	0.1114	0.3770	0.1234	1.1078	-0.1579	-0.0345
	2	Os(1)-O(3)	-0.1569	-0.1309	0.6449	0.1100	0.3570	0.1185	1.0773	-0.1527	-0.0342
	3	Os(1)-O(4)	-0.3759	-0.3590	1.6387	0.2325	0.9039	0.3370	1.4497	-0.4711	-0.1340
	4	Os(1)-O(5)	-0.1319	-0.1056	0.5810	0.0998	0.3435	0.1106	1.1074	-0.1394	-0.0289
	5	Os(1)-O(6)	-0.3856	-0.3742	1.6939	0.2372	0.9341	0.3490	1.4715	-0.4885	-0.1395
	6	Os(1)-O(7)	-0.3157	-0.2835	1.4413	0.2093	0.8421	0.3000	1.4332	-0.4081	-0.1082
	7	O(3)-H(8)	-1.8146	-1.7884	1.2885	0.3651	-2.3145	0.0915	0.2507	-0.7617	-0.6702
	8	O(5)-H(9)	-1.7847	-1.7632	1.2928	0.3664	-2.2551	0.0941	0.2569	-0.7520	-0.6579
	9	O(2)-H(10)	-1.7919	-1.7663	1.2834	0.3647	-2.2747	0.0914	0.2507	-0.7516	-0.6601

The Laplacian at all metal-oxo (Os<sup>VI</sup>=O & Os<sup>VII</sup>=O) BCPs are positive, ranging between 0.80 to 1.02, and the  $G_b/\rho_b$  ratio is considerably more than unity, 1.36 to 1.56, indicating ionic

bonding interactions. The (*trans*) oxo ligands of Os<sup>VI</sup> are slightly more ionic than the oxo ligands of the Os<sup>VII</sup> species, where they are not always positioned *trans* from one another, *e.g.* *fac* stereoisomer. Since the  $E_b^e$  is negative in all cases, at approximately -0.13, these bonding interactions have a slight covalent character.

The relative ionicity of the bonding interactions at the metal-hydroxido (Os<sup>VI</sup>-OH & Os<sup>VII</sup>-OH) BCPs is less compared to Os=O bonds. The Laplacian has a smaller positive value, ranging from 0.33 to 0.53, while the  $G_b/\rho_b$  ratio is only slightly more than unity, from 1.08 to 1.28. These results, along with the negative  $E_b^e$  values, from -0.06 to -0.03, qualify all these metal-hydroxido bonding interactions as dative or polar covalent. Furthermore, calculated values of the electron density,  $\rho_b$ , at the BCPs of the three dissimilar Os<sup>VII</sup>-OH metal-hydroxido ligands of *mer*-[Os<sup>VII</sup>O<sub>3</sub>(OH)<sub>3</sub>]<sup>2-</sup> are in agreement that the Os<sup>VII</sup>(1)-O(5)-H(10) ligand, where  $\rho_b$  equals 0.0940, has the weakest bonding interaction and corroborates the computed Os<sup>VII</sup>-OH bond lengths, Table 5.4, and reported EDA results, Table 5.3, in Section 5.2.3.

The O-H bonding interactions are clearly covalent as the large negative Laplacian values, from -2.39 to -2.21, and the large negative  $E_b^e$  values, from -0.68 to -0.64, indicate. The  $G_b/\rho_b$  ratio is also much smaller than unity, from 0.23 to 0.26.

The differences between the calculated BCP indices of the Os<sup>VIII</sup> (Table 3.12), Os<sup>VI</sup> and Os<sup>VII</sup> oxo/hydroxido species are noticeably small. Minor variations in these values are mainly due to the relative position of a given ligand within the complex, *i.e.* metal-oxo bonds that are *trans* to an oxo ligand are generally (but not consistently) different in character, in terms of relative ionicity/covalency, compared to those that are *trans* to a hydroxido ligand, while a similar general trend is seen w.r.t. the metal-hydroxido bonds. Furthermore, the oxidation state of the osmium complex does not either greatly affect the nature of the metal-oxo and metal-hydroxido bonding interactions.

The relative orientation of a hydroxido ligand also has an effect on the ligands' bonding interactions. In cases where an O-H bond of a hydroxido ligand is 'aligned' towards an oxo ligand, the metal-hydroxido bond length is relatively longer and has a relatively smaller  $\rho_b$  value at the BCP compared to when it is 'aligned' towards a hydroxido ligand. This effect is most probably caused by the presence of weak, attractive intramolecular hydrogen bonding interactions (which QTAIMS is unable to identify) between neighbouring ligands, causing minor changes.

Lastly, there are no qualitative changes observed for when topological analysis of the electron density is performed with the inclusion of dispersion corrections, *i.e.* PBE-D3(BJ) functional (Table A.4).

### 5.2.6 Re-evaluation of the Evans method experiment for a five-coordinate Os<sup>VII</sup> oxo/hydroxido product species

Repeating the set of Evans method calculations,<sup>30-33</sup> equations 4.5 – 4.13, using the molecular weight of a five-coordinate [Os<sup>VII</sup>O<sub>3</sub>(OH)<sub>2</sub>]<sup>-</sup> species, at 272.2429 g.mol<sup>-1</sup>, also results in a linear trend for  $\delta\nu$  vs.  $m$ , Figure 5.3. The 95% confidence interval and 95% confidence errors of the slope and the intercept are shown on the graph in Figure 5.4.

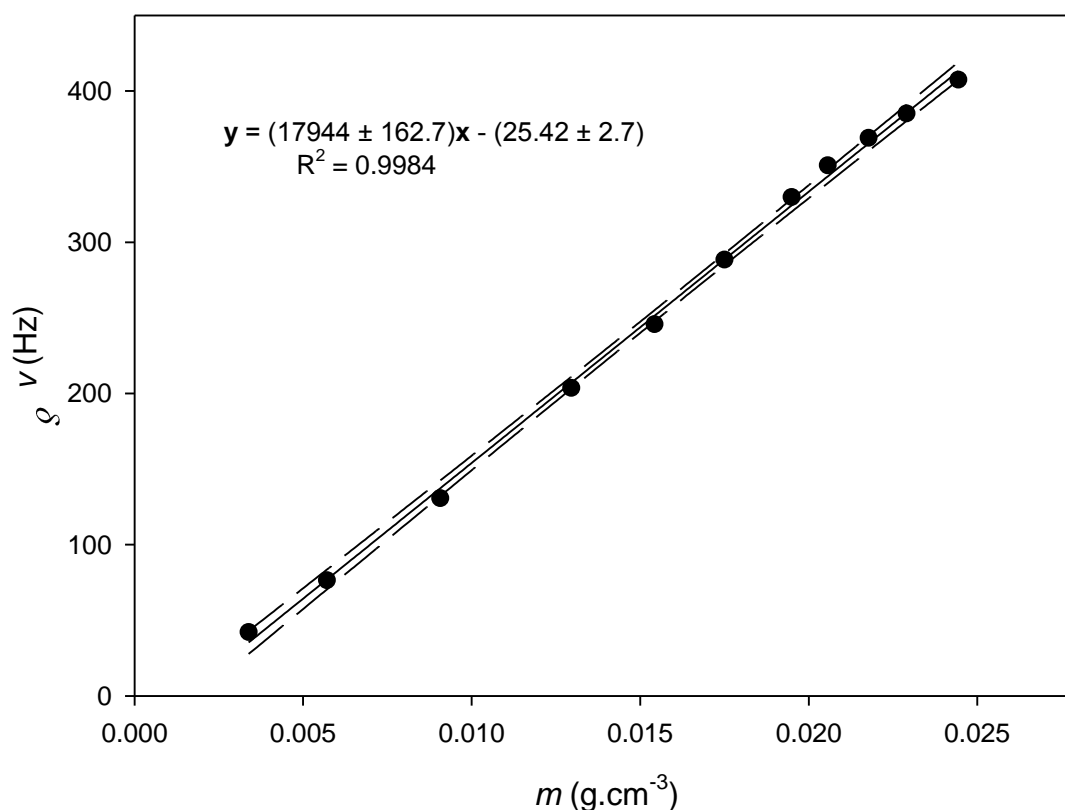


**Figure 5.4.** Change in chemical shift as a function of the mass of the postulated [Os<sup>VII</sup>O<sub>3</sub>(OH)<sub>2</sub>]<sup>-</sup> paramagnetic species contained in 1 mL.

Using the molecular weight of a [Os<sup>VII</sup>O<sub>3</sub>(OH)<sub>2</sub>]<sup>-</sup> species yields an estimated value for  $S$  (spin quantum number) of  $1.147 \pm 0.007$  and  $n$  (number of unpaired electrons) of  $2.29 \pm 0.01$ , Table 5.6. The results are similar to those that used the molecular weight of a [Os<sup>VII</sup>O<sub>3</sub>(OH)<sub>3</sub>]<sup>2-</sup> species in the calculations.

**Table 5.6. Experimentally determined magnetic properties of a postulated  $[\text{Os}^{\text{VII}}\text{O}_3(\text{OH})_2]^-$  complex and of a postulated  $[\text{Os}^{\text{VIII}}\text{O}_3(\text{OH})_3]^{2-}$  complex obtained from the Evans method experiment.**

Procedure	Molecular formula	$\mu_{\text{eff}}$	$S$	$n$
experimental	$[\text{Os}^{\text{VIII}}\text{O}_3(\text{OH})_3]^{2-}$	$3.05 \pm 0.01$	$1.103 \pm 0.007$	$2.21 \pm 0.01$
	$[\text{Os}^{\text{VII}}\text{O}_3(\text{OH})_2]^-$	$3.14 \pm 0.01$	$1.147 \pm 0.007$	$2.29 \pm 0.01$
theoretical		2.83	1	2

Interpretation of the data does not change for this scenario and that the reaction takes place by way of a comproportionation mechanism remains intact. However, since the final products are a combination of five-coordinate (*trans*) and six-coordinate (*mer*) species at 298.15 K, Section 5.2.2, the experimental value of  $n$  is between 2.21 and 2.29, which equates to a value of between approximately 1.10 and 1.15 per monomer product species.

### 5.2.7 Comparison of DFT-calculated and experimental thermodynamic standard reaction energies. Putting it all together – well, almost

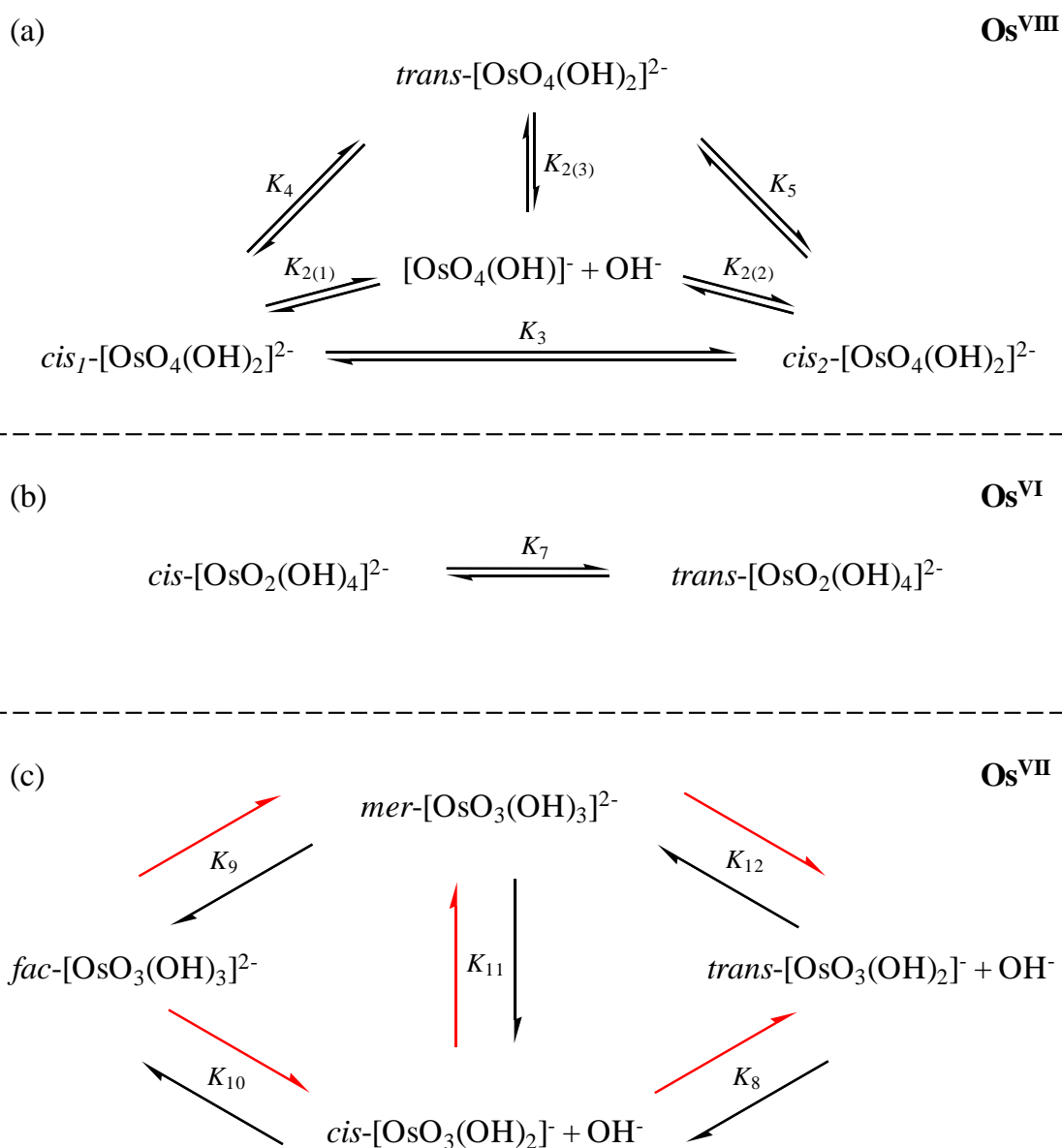
The DFT speciation analyses of the reactants and products of the  $\text{Os}^{\text{VI}}$  &  $\text{Os}^{\text{VIII}}$  comproportionation reaction can now be used in principle to compare the computational and experimental  $\Delta G^\circ_{\text{rxn}}$ 's (at 298.15 K). However, several inquiries must first be addressed to make a meaningful comparison. Until now, the comproportionation reaction was generically identified as equation 5.9.



When considering that several  $\text{Os}^{\text{VIII}}$  oxo/hydroxido reactant species (Chapter 3) as well as  $\text{Os}^{\text{VII}}$  oxo/hydroxido product species (Section 5.2.2) were identified *via* DFT, shown in Scheme 5.2, the question arises: which  $\text{Os}^{\text{VIII}}$  and  $\text{Os}^{\text{VII}}$  species must be used in equation 5.9 to define the comproportionation reaction in order to calculate the  $\Delta G^\circ_{\text{rxn}}$ ? Moreover, kinetic and equilibrium analysis of the  $\text{Os}^{\text{VI}}$  &  $\text{Os}^{\text{VIII}}$  comproportionation reaction presented in Chapter 4, equation 4.14, did not take into account which particular  $\text{Os}^{\text{VIII}}$  species reacts with *trans*- $[\text{Os}^{\text{VI}}\text{O}_2(\text{OH})_4]^{2-}$  and neither was the “identity” or stereochemistry of the  $\text{Os}^{\text{VII}}$  product species, *i.e.* five-coordinate or six-coordinate, taken into account. This leads to the second major inquiry that must be addressed, which is the fact that the experimentally determined (Chapter 4) comproportionation reaction  $\Delta G^\circ_{\text{rxn}(\text{obs})}$ ,  $-1.1 \pm 2.5 \text{ kcal.mol}^{-1}$ , cannot be used directly for comparison since the calculated rate constants,  $k_{6(\text{obs})}$  and  $k_{-6(\text{obs})}$ , were only



observed rate constants, *i.e.* composite constants, and not the thermodynamically correct or ‘true’ rate constants. In order to correlate DFT-calculated  $\Delta H^\circ_{rxn}$ ,  $\Delta S^\circ_{rxn}$  and  $\Delta G^\circ_{rxn}$  with the stopped-flow kinetics’  $\Delta H^\circ_{rxn}$ ,  $\Delta S^\circ_{rxn}$  and  $\Delta G^\circ_{rxn}$ , it is now necessary to rewrite the reaction model, equation 5.9, and the corresponding rate laws, in terms of specific Os<sup>VIII</sup>, Os<sup>VI</sup> and Os<sup>VII</sup> species instead of total Os<sup>VIII</sup>, Os<sup>VI</sup> and Os<sup>VII</sup> concentrations. This is done to prove that the original rate laws, derived in Chapter 4, are recovered, with the added bonus that  $k_{6(\text{obs})}$  and  $k_{-6(\text{obs})}$  can now be transformed into  $k_6$  and  $k_{-6}$ , *i.e.* the ‘true’ rate constants, when it is assumed that all activity coefficients are equal to unity. Once the ‘true’ rate constants are known, the equilibrium constant obtained from the ratio of the rate constants,  $K_{6(\text{true})}$ , and hence the  $\Delta G^\circ_{rxn}$  (true), can be calculated and compared with the DFT-calculated values.



**Scheme 5.2.** Os<sup>VIII</sup> (a) and Os<sup>VI</sup> (b) reactants and Os<sup>VII</sup> (c) product oxo/hydroxido species.

In a simulated aqueous phase (COSMO), at equilibrium, the most abundant osmium reactants were identified as *trans*-[Os<sup>VI</sup>O<sub>2</sub>(OH)<sub>4</sub>]<sup>2-</sup>, [Os<sup>VIII</sup>O<sub>4</sub>(OH)]<sup>-</sup> and *cis*-[Os<sup>VIII</sup>O<sub>4</sub>(OH)<sub>2</sub>]<sup>2-</sup> while the abundant products were identified as *trans*-[Os<sup>VII</sup>O<sub>3</sub>(OH)<sub>2</sub>]<sup>-</sup> and *mer*-[Os<sup>VII</sup>O<sub>3</sub>(OH)<sub>3</sub>]<sup>2-</sup>. These species are used here as the representative metric in order to estimate DFT obtained  $\Delta H^\circ_{rxn}$ ,  $\Delta S^\circ_{rxn}$  and  $\Delta G^\circ_{rxn}$  values of the Os<sup>VI</sup> & Os<sup>VIII</sup> comproportionation reaction. The other, less abundant species may be important from a mechanistic and kinetic point of view. However, in terms of thermodynamics, only the abovementioned species are considered. The relative standard Gibbs energy of formation diagram of the reactants and possible products is illustrated in Figure 5.6.

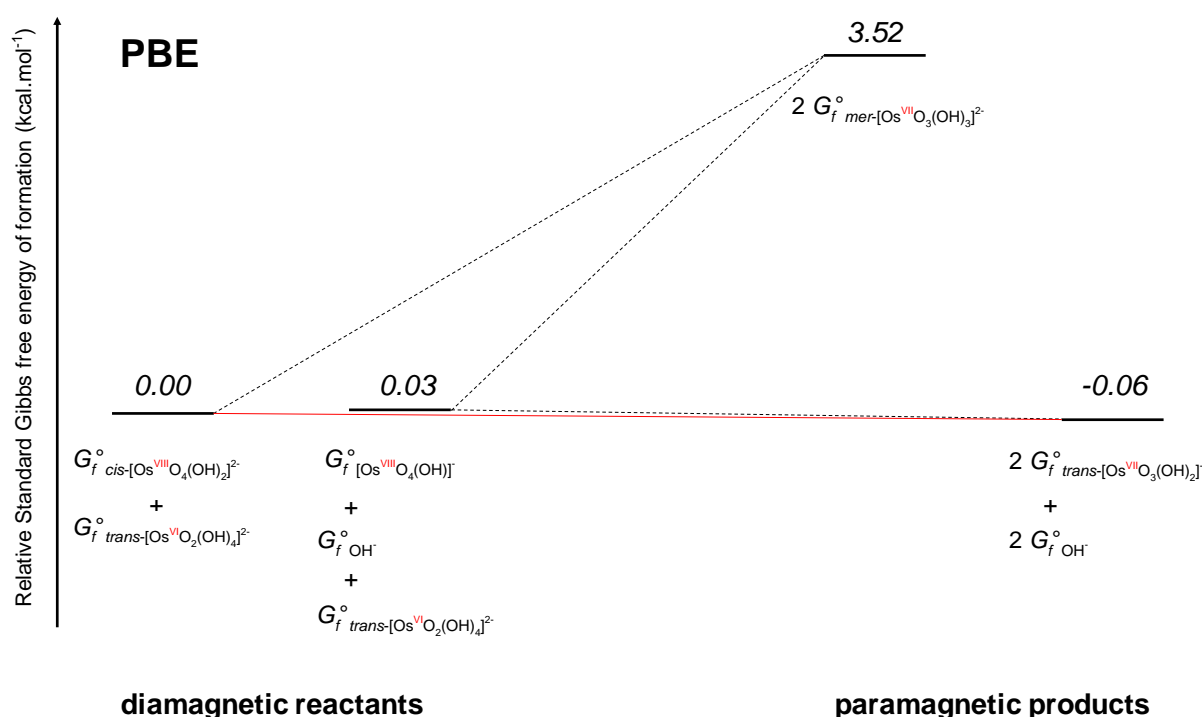
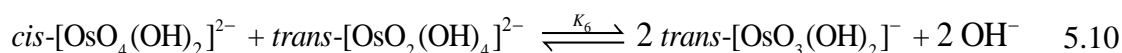


**Figure 5.6.** Relative standard Gibbs free energies of formation (kcal.mol<sup>-1</sup>) of the reactants and products of the Os<sup>VI</sup> & Os<sup>VIII</sup> comproportionation reaction in the simulated aqueous phase (PBE functional). Solid red line depicts the energy change between the reactant and product states of lowest Gibbs energy, equation 5.10.

The lines in Figure 5.6 (dotted and solid) represent four possible comproportionation reactions. It is evident that combinations of reactants and products other than that depicted by the red line in Figure 5.6 would result in less thermodynamically favourable comproportionation reaction energies. The states of lowest Gibbs energy of the system are therefore represented by the reaction between *cis*-[Os<sup>VIII</sup>O<sub>4</sub>(OH)<sub>2</sub>]<sup>2-</sup> and *trans*-[Os<sup>VI</sup>O<sub>2</sub>(OH)<sub>4</sub>]<sup>2-</sup> to yield two *trans*-[Os<sup>VII</sup>O<sub>3</sub>(OH)<sub>2</sub>]<sup>-</sup> and two hydroxide species. Our generic

comproportionation reaction representation, equation 5.9, is replaced by equation 5.10, which now refers to specific osmium species.



The DFT-calculated thermodynamic parameters in the gas and simulated aqueous phase for reaction 5.10, obtained with several functionals, are listed in Table 5.7. The DFT-calculated thermodynamic parameters for reaction 5.11 are listed in the appendix, Table A.5. Apart from LDA, all other functionals consistently yield that reaction 5.10 is the thermodynamically favoured comproportionation reaction in the simulated aqueous phase. With the PBE, dispersion-corrected PBE and PW91 functionals, the  $\Delta G^\circ_{rxn}$  for reaction 5.10 varies between -0.06 and 3.14 kcal.mol<sup>-1</sup>, whilst for the BLYP and dispersion-corrected BLYP functionals, substantially more negative values are obtained, varying between -4.29 (BLYP-D) and -9.80 kcal.mol<sup>-1</sup> (BLYP).

**Table 5.7. Calculated standard reaction thermodynamic energies for reaction 5.10.**

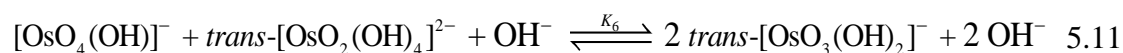
XC category	Functional	gas phase			COSMO (aqueous)		
		$\Delta H^\circ_{rxn}$ (kcal.mol <sup>-1</sup> )	$\Delta S^\circ_{rxn}$ (cal.mol <sup>-1</sup> .K <sup>-1</sup> )	$\Delta G^\circ_{rxn}$ (kcal.mol <sup>-1</sup> )	$\Delta H^\circ_{rxn}$ (kcal.mol <sup>-1</sup> )	$\Delta S^\circ_{rxn}$ (cal.mol <sup>-1</sup> .K <sup>-1</sup> )	$\Delta G^\circ_{rxn}$ (kcal.mol <sup>-1</sup> )
GGA	LDA	-73.41	73.00	-95.18	47.52	73.31	25.66
	PBE	-97.75	70.86	-118.88	21.13	71.06	-0.06
	PBE-D	-94.67	69.89	-115.51	24.31	71.01	3.14
	PBE-D3	-95.81	70.86	-116.94	23.09	70.88	1.96
	PBE-D3(BJ)	-95.71	71.03	-116.88	23.00	72.89	1.27
	PBE-dDsC	-94.99	71.18	-116.21	23.57	73.09	1.78
	mPBE	-100.48	69.98	-121.35	17.71	73.31	-4.14
	BLYP	-104.67	70.23	-125.61	11.88	72.70	-9.80
	BLYP-D	-99.47	69.02	-120.04	17.62	73.49	-4.29
	BLYP-D3	-100.31	69.83	-121.13	16.29	72.77	-5.40
	PW91	-95.61	71.23	-116.84	22.92	73.60	0.98
MetaGGA	M06L	-90.44	71.82	-111.85	30.55	61.66	12.16
<b>Experimental<sup>a</sup></b>				<b>17.1 ± 1.2</b>	<b>61.0 ± 4.3</b>	<b>-1.1 ± 2.5</b>	

<sup>a</sup> Observed standard reaction energies obtained from stopped-flow UV-Vis kinetics experiments, Chapter 4.

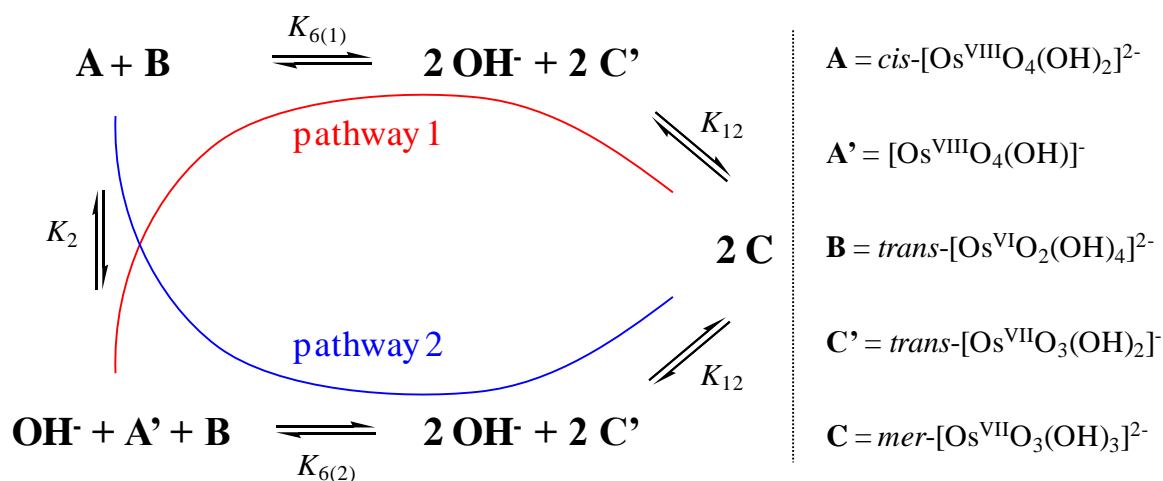
From Figure 5.6 it is seen that the  $\Delta G^\circ_{rxn}$  for reaction 5.11 is only 0.03 kcal.mol<sup>-1</sup> (PBE functional) thermodynamically less favoured than reaction 5.10.<sup>12</sup> However, with all the

<sup>12</sup> Due to the  $\Delta G^\circ_{rxn}$  of reaction 3.4, *i.e.*  $cis-[Os^{VIII}O_4(OH)_2]^{2-}$  is slightly lower in Gibbs energy than  $[Os^{VIII}O_4(OH)]^-$  plus  $OH^-$  at 298.15 K. See Table 3.7 for all functionals' values.

functionals used, reaction 5.10 is thermodynamically more favoured than 5.11 and the  $\Delta G^\circ_{rxn}$  difference increases by approximately  $0.9 \text{ kcal.mol}^{-1}$  {PBE-D3(BJ) for example} when dispersion is included. From a quantum chemical computational perspective, and as will be seen later, when comparison is made with experimental thermodynamic parameters  $\Delta G^\circ_{rxn}$ ,  $\Delta H^\circ_{rxn}$  and  $\Delta S^\circ_{rxn}$ , that reaction 5.10 is the most probable comproportionation reaction.



In contrast to how  $\Delta G^\circ_{rxn}$  was calculated using DFT, reaction 5.10, in kinetics the specific reaction pathway is also of importance. Depending on which Os<sup>VIII</sup> and Os<sup>VII</sup> species actually participate ‘directly’ in the comproportionation/disproportionation reaction, several reaction pathways are possible in addition to Os<sup>VIII</sup> or Os<sup>VII</sup> coordination sphere expansion/contraction reactions. The number of possible reaction pathways is far too excessive for all of them to be discussed here. Instead, to reach the goal here, which is to correlate the DFT-calculated  $\Delta G^\circ_{rxn}$ ,  $\Delta H^\circ_{rxn}$  and  $\Delta S^\circ_{rxn}$  with the experimental stopped-flow kinetic data, only two of the possible reaction pathways are discussed below. The discussion below has three objectives: (i) to mathematically recover the comproportionation rate laws used in Chapter 4, equations 4.15 & 4.16, when taking into account that specific osmium species react, *e.g.* when the *cis*-[Os<sup>VIII</sup>O<sub>4</sub>(OH)<sub>2</sub>]<sup>2-</sup> species reacts with *trans*-[Os<sup>VI</sup>O<sub>2</sub>(OH)<sub>4</sub>]<sup>2-</sup> as opposed to when the [Os<sup>VIII</sup>O<sub>4</sub>(OH)]<sup>-</sup> species reacts with *trans*-[Os<sup>VI</sup>O<sub>2</sub>(OH)<sub>4</sub>]<sup>2-</sup>; (ii) to analyse whether the experimentally obtained  $\Delta G^\circ_{rxn}$ ,  $\Delta H^\circ_{rxn}$  and  $\Delta S^\circ_{rxn}$  will vary by significant or insignificant amounts when taking into account that specific Os<sup>VIII</sup> and Os<sup>VII</sup> species react, *i.e.* to show that it is reasonable to use the observed experimental thermodynamic parameters  $\Delta G^\circ_{rxn(\text{obs})}$ ,  $\Delta H^\circ_{rxn(\text{obs})}$  and  $\Delta S^\circ_{rxn(\text{obs})}$ , as determined in Chapter 4, Table 4.7, for direct comparison with the DFT data and; (iii) to show a numerical experiment that illustrates how the magnitude of the Os<sup>VIII</sup> coordination sphere expansion/contraction reaction rate constants influence the rate of the comproportionation reaction. We would like to emphasise that the reaction pathways proposed below are not now under scrutiny and will be expanded and extensively discussed when the mechanism of the comproportionation reaction is investigated in Chapter 6.



**Scheme 5.3.** Two reaction pathways of Os<sup>VI</sup> & Os<sup>VIII</sup> and Os<sup>VII</sup> & Os<sup>VII</sup> comproportionation/disproportionation.

### Pathway 1

Pathway 1 consists of three simultaneous equilibria, equations 5.12 – 5.14, where it is assumed that only the *cis*-[Os<sup>VIII</sup>O<sub>4</sub>(OH)<sub>2</sub>]<sup>2-</sup> species reacts with *trans*-[Os<sup>VI</sup>O<sub>2</sub>(OH)<sub>4</sub>]<sup>2-</sup>.



The complete set of rate laws for pathway 1, equations 5.15 – 5.19, are therefore:

$$\frac{d[A]}{dt} = -k_2[A'][OH^-] + k_{-2}[A] \quad 5.15$$

$$\frac{d[A]}{dt} = +k_2[A'][OH^-] - k_{-2}[A] - k_{6(1)}[A][B] + k_{-6(1)}[OH^-]^2[C']^2 \quad 5.16$$

$$\frac{d[B]}{dt} = -k_{6(1)}[A][B] + k_{-6(1)}[OH^-]^2[C']^2 \quad 5.17$$

$$\frac{d[C']}{dt} = +2k_{6(1)}[A][B] - 2k_{-6(1)}[OH^-]^2[C']^2 - k_{12}[OH^-][C'] + k_{-12}[C] \quad 5.18$$

$$\frac{d[C]}{dt} = +k_{12}[OH^-][C'] - k_{-12}[C] \quad 5.19$$

Since  $[\text{OH}^-]$  is present in large excess compared to the osmium species, the concentration of hydroxide changes by negligible amounts, *i.e.* it is not necessary to include the rate law  $d[\text{OH}^-]/dt$  in this discussion.

To simplify matters initially, we again assume that coordination sphere expansion/contraction reactions of  $\text{Os}^{\text{VIII}}$  and  $\text{Os}^{\text{VII}}$  are at equilibrium w.r.t. the time frame in which the comproportionation reaction occurs. This assumption decreases the number of rate laws and reduces the complexity of the complete set of rate laws, equations 5.15 – 5.19, to the set of ordinary differential equations given by 5.20 – 5.22.

$$\frac{d[\text{A}]}{dt} = -k_{6(1)}[\text{A}][\text{B}] + k_{-6(1)}[\text{OH}^-]^2[\text{C}]^2 \quad 5.20$$

$$\frac{d[\text{B}]}{dt} = -k_{6(1)}[\text{A}][\text{B}] + k_{-6(1)}[\text{OH}^-]^2[\text{C}]^2 \quad 5.21$$

$$\frac{d[\text{C}]}{dt} = +2k_{6(1)}[\text{A}][\text{B}] - 2k_{-6(1)}[\text{OH}^-]^2[\text{C}]^2 \quad 5.22$$

Moreover, another consequence of the assumption that  $\text{Os}^{\text{VIII}}$  and  $\text{Os}^{\text{VII}}$  coordination sphere expansion/contraction reactions are at equilibrium, is that we can now express the concentrations of the individual species, A and A', in terms of the total  $\text{Os}^{\text{VIII}}$  concentration,  $[\text{Os}^{\text{VIII}}]_{\text{T}}$ , using equations 5.23 & 5.24, yielding equations 5.25 & 5.26. Similarly, the individual C and C' species can be expressed in terms of the total  $\text{Os}^{\text{VII}}$  concentration,  $[\text{Os}^{\text{VII}}]_{\text{T}}$ , using equations 5.27 & 5.28, yielding equations 5.29 & 5.30. Moreover,  $[\text{Os}^{\text{VI}}]_{\text{T}}$  consists of only B, equation 5.31.

$$K_2 = \left( \frac{[\text{A}]}{[\text{A}'][\text{OH}^-]} \right) \quad 5.23$$

where

$$[\text{Os}^{\text{VIII}}]_{\text{T}} = [\text{A}] + [\text{A}'] \quad 5.24$$

Substitution of  $[\text{A}']$  and  $[\text{A}]$ , respectively:

$$[\text{A}] = \left( \frac{K_2[\text{OH}^-]}{K_2[\text{OH}^-] + 1} \right) [\text{Os}^{\text{VIII}}]_{\text{T}} \quad 5.25$$

$$[A] = \left( \frac{1}{K_2[\text{OH}^-] + 1} \right) [\text{Os}^{\text{VIII}}]_{\text{T}} \quad 5.26$$

Similarly:

$$K_{12} = \left( \frac{[C]}{[C'][\text{OH}^-]} \right) \quad 5.27$$

where

$$[\text{Os}^{\text{VII}}]_{\text{T}} = [C] + [C'] \quad 5.28$$

Substitution of [C'] and [C], respectively:

$$[C] = \left( \frac{K_{12}[\text{OH}^-]}{K_{12}[\text{OH}^-] + 1} \right) [\text{Os}^{\text{VII}}]_{\text{T}} \quad 5.29$$

$$[C'] = \left( \frac{1}{K_{12}[\text{OH}^-] + 1} \right) [\text{Os}^{\text{VII}}]_{\text{T}} \quad 5.30$$

Furthermore,

$$[\text{Os}^{\text{VI}}]_{\text{T}} = [B] \quad 5.31$$

Substituting for [A], [B] and [C'] into the ordinary differential equations 5.20 – 5.22 gives the rate laws in terms of  $[\text{Os}^{\text{VIII}}]_{\text{T}}$ ,  $[\text{Os}^{\text{VI}}]_{\text{T}}$  and  $[\text{Os}^{\text{VII}}]_{\text{T}}$ , equations 5.32 – 5.34:

$$\frac{d[A]}{dt} = -k_{6(1)} \left( \frac{K_2[\text{OH}^-]}{K_2[\text{OH}^-] + 1} \right) [\text{Os}^{\text{VIII}}]_{\text{T}} [\text{Os}^{\text{VI}}]_{\text{T}} + k_{-6(1)} [\text{OH}^-]^2 \left( \frac{1}{K_{12}[\text{OH}^-] + 1} \right)^2 [\text{Os}^{\text{VII}}]_{\text{T}}^2 \quad 5.32$$

$$\frac{d[B]}{dt} = -k_{6(1)} \left( \frac{K_2[\text{OH}^-]}{K_2[\text{OH}^-] + 1} \right) [\text{Os}^{\text{VIII}}]_{\text{T}} [\text{Os}^{\text{VI}}]_{\text{T}} + k_{-6(1)} [\text{OH}^-]^2 \left( \frac{1}{K_{12}[\text{OH}^-] + 1} \right)^2 [\text{Os}^{\text{VII}}]_{\text{T}}^2 \quad 5.33$$

$$\frac{d[C']}{dt} = +2 k_{6(1)} \left( \frac{K_2[\text{OH}^-]}{K_2[\text{OH}^-] + 1} \right) [\text{Os}^{\text{VIII}}]_{\text{T}} [\text{Os}^{\text{VI}}]_{\text{T}} - 2 k_{-6(1)} [\text{OH}^-]^2 \left( \frac{1}{K_{12}[\text{OH}^-] + 1} \right)^2 [\text{Os}^{\text{VII}}]_{\text{T}}^2 \quad 5.34$$

Equations 5.32 – 5.34 above represent the rate laws of the comproportionation reaction when specific  $\text{Os}^{\text{VIII}}$  and  $\text{Os}^{\text{VII}}$  species react (according to pathway 1) and recovers the rate laws used in Chapter 4 for the non-linear least squares fitting of the stopped-flow UV-Vis

spectroscopy kinetic data. Moreover, we can now investigate how  $K_{6(\text{obs})}$  (approximately 6.40 at 298.15 K) will change when taking into account that (i) specific  $\text{Os}^{\text{VIII}}$  and  $\text{Os}^{\text{VII}}$  species react and that (ii) coordination sphere expansion/contraction reactions of  $\text{Os}^{\text{VIII}}$  and  $\text{Os}^{\text{VII}}$  are at equilibrium. At equilibrium  $d[\text{A}]/dt$ , equation 5.32, is equal to zero. Rearrangement of equation 5.32 (at equilibrium) yields equation 5.35.

$$\frac{k_{6(1)} \left( \frac{K_2[\text{OH}^-]}{K_2[\text{OH}^-] + 1} \right)}{k_{-6(1)} \left( \frac{1}{K_{12}[\text{OH}^-] + 1} \right)^2} = \frac{[\text{OH}^-]^2 [\text{Os}^{\text{VII}}]_{\text{T}}^2}{[\text{Os}^{\text{VIII}}]_{\text{T}} [\text{Os}^{\text{VI}}]_{\text{T}}} \quad 5.35$$

As mentioned earlier, the hydroxide concentration is constant at 2.0 M at all times. To make equation 5.35 consistent with the work in Chapter 4, equation 5.35 is rearranged to equations 5.36 – 5.38 below. Equation 5.38 represents the ‘true’ thermodynamic equilibrium constant when taking into consideration all assumptions regarding reaction pathway 1 and that all activity coefficients are equal to unity.

$$\frac{k_{6(1)} \left( \frac{K_2[\text{OH}^-]}{K_2[\text{OH}^-] + 1} \right)}{k_{-6(1)} \left( \frac{1}{K_{12}[\text{OH}^-] + 1} \right)^2 [\text{OH}^-]^2} = \frac{[\text{Os}^{\text{VII}}]_{\text{T}}^2}{[\text{Os}^{\text{VIII}}]_{\text{T}} [\text{Os}^{\text{VI}}]_{\text{T}}} = K_{6(\text{obs})} \quad 5.36$$

$$K_{6(\text{obs})} = \frac{k_{6(\text{obs})}}{k_{-6(\text{obs})}} = \frac{k_{6(1)} \left( \frac{K_2[\text{OH}^-]}{K_2[\text{OH}^-] + 1} \right)}{k_{-6(1)} \left( \frac{1}{K_{12}[\text{OH}^-] + 1} \right)^2 [\text{OH}^-]^2} \quad 5.37$$

$$\frac{k_{6(1)}}{k_{-6(1)}} = K_{6(\text{true})} = \left[ \frac{\left( \frac{1}{K_{12}[\text{OH}^-] + 1} \right)^2 [\text{OH}^-]^2}{\left( \frac{K_2[\text{OH}^-]}{K_2[\text{OH}^-] + 1} \right)} \right] \frac{k_{6(\text{obs})}}{k_{-6(\text{obs})}} \quad 5.38$$

It is now necessary to evaluate the term in the square brackets in equation 5.38 to determine by what magnitude  $K_{6(\text{true})}$  will differ from  $K_{6(\text{obs})}$  at 298.15 K. The experimental equilibrium constant  $K_2$  is equal to approximately 0.58,<sup>21,22</sup> Table 3.7, whilst the DFT-calculated  $K_{12}$



equilibrium constant with the PBE functionals (with and without dispersion corrections) varies from approximately 0.05 (PBE) to 0.96 (PBE-D), Table 5.8.

**Table 5.8. DFT-calculated standard reaction Gibbs free energy and corresponding equilibrium constant,  $K_{12}$ , of reaction 5.7 at 298.15 K in the simulated aqueous phase.**

Functional	$\Delta G_{rxn}^{\circ}$ (kcal.mol <sup>-1</sup> )	$K_{12}$
PBE	1.79	0.05
PBE-D	0.02	0.96
PBE-D3	0.81	0.26
PBE-D3(BJ)	1.40	0.09
PBE-dDsC	1.20	0.13

For example, when substituting  $K_2$  with 0.58,  $K_{12}$  with the DFT-calculated PBE functional value of 0.05 and [OH<sup>-</sup>] with 2.0 into the square brackets term of equation 5.38 gives a correction factor of approximately 6.18, equation 5.39.

$$\left[ \frac{\left( \frac{1}{(0.05 \times 2) + 1} \right)^2 [2]^2}{\left( \frac{0.58 \times 2}{(0.58 \times 2) + 1} \right)} \right] = 6.18 \quad 5.39$$

The values for the term in square brackets, *i.e.* the correction factors, for the other four functionals, together with the corresponding  $K_{6(\text{true})}$  and  $\Delta G_{rxn}^{\circ}$  (true) values for pathway 1 are listed in Table 5.9.

**Table 5.9. Correction factors for  $K_{6(\text{obs})}$  and approximate  $K_{6(\text{true})}$  and  $\Delta G_{rxn}^{\circ}$  (true) values for the comproportionation reaction at 298.15 K (pathway 1).**

Functional	correction factor	$K_{6(\text{true})}$	$\Delta G_{rxn}^{\circ}$ (true) (kcal.mol <sup>-1</sup> )
PBE	6.18	39.56	-2.18
PBE-D	0.87	5.59	-1.02
PBE-D3	3.27	20.91	-1.80
PBE-D3(BJ)	5.27	33.75	-2.08
PBE-dDsC	4.67	29.90	-2.01

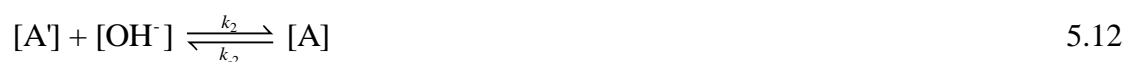
Making these corrections to  $K_{6(\text{obs})}$  in order to calculate  $\Delta G_{rxn}^{\circ}$  (true) yields a range of values for the comproportionation reaction of approximately -2.18 (PBE) to -1.02 kcal.mol<sup>-1</sup> (PBE-

D). However, PBE and PBE-D are most probably the two least accurate of the five functionals, due to the lack of and overestimation, respectively, of dispersion corrections. The experimental  $\Delta G^\circ_{rxn}$  without these corrections, *i.e.*  $\Delta G^\circ_{rxn(obs)}$ , is  $-1.1 \pm 2.5$  kcal.mol<sup>-1</sup>, Table 4.7. When the correction factors are included, Table 5.9,  $\Delta G^\circ_{rxn(obs)}$  only changes by a relatively small amount. Furthermore, since  $\Delta G^\circ_{rxn}$  (true) is within the experimental error range of  $\Delta G^\circ_{rxn(obs)}$ , we thus justify comparing  $\Delta G^\circ_{rxn(obs)}$  directly with our DFT-calculated values, Table 5.7. Moreover, since the observed equilibrium constant,  $K_{6(obs)}$ , is multiplied by a constant correction factor value, the slope of the van't Hoff plot in Figure 4.9 will not change. Therefore, the observed standard reaction enthalpy,  $\Delta H^\circ_{rxn(obs)}$  does not change and we can then also compare the experimental  $\Delta H^\circ_{rxn(obs)}$  of  $17 \pm 1.2$  kcal.mol<sup>-1</sup> directly with our DFT-calculated values. Since  $\Delta G^\circ_{rxn}$  (true)  $\approx \Delta G^\circ_{rxn(obs)} = \Delta H^\circ_{rxn(obs)} - T\Delta S^\circ_{rxn(obs)}$ , the observed standard reaction entropy can now also be compared directly, *i.e.*  $\Delta S^\circ_{rxn}$  (true)  $\approx \Delta S^\circ_{rxn(obs)} = 61.0 \pm 4.3$  cal.mol<sup>-1</sup>.K<sup>-1</sup>.

We have now shown that when taking into consideration specific osmium species, according to pathway 1 (Scheme 5.3), that  $\Delta G^\circ_{rxn}$  (true) does not change significantly from  $\Delta G^\circ_{rxn(obs)}$ ,  $\Delta H^\circ_{rxn(obs)}$  remains the same and  $\Delta S^\circ_{rxn(obs)} \approx \Delta S^\circ_{rxn}$  (true).

### Pathway 2:

Pathway 2 consists of three simultaneous equilibria, equations 5.12, 5.40 and 5.14, where it is assumed that only the  $[\text{Os}^{\text{VIII}}\text{O}_4(\text{OH})^-]$  species reacts with *trans*- $[\text{Os}^{\text{VI}}\text{O}_2(\text{OH})_4]^{2-}$ .



The complete set of rate laws for pathway 2, equations 5.41 – 5.44 and 5.19, are therefore:

$$\frac{d[\text{A}']}{dt} = -k_2[\text{A}'][\text{OH}^-] + k_{-2}[\text{A}] - k_{6(2)}[\text{A}'][\text{B}] + k_{-6(2)}[\text{OH}^-][\text{C}]^2 \quad 5.41$$

$$\frac{d[\text{A}']}{dt} = +k_2[\text{A}'][\text{OH}^-] - k_{-2}[\text{A}] \quad 5.42$$

$$\frac{d[B]}{dt} = -k_{6(2)}[A'][B] + k_{-6(2)}[OH^-][C]^2 \quad 5.43$$

$$\frac{d[C']}{dt} = +2k_{6(2)}[A'][B] - 2k_{-6(2)}[OH^-][C]^2 - k_{12}[OH^-][C] + k_{-12}[C] \quad 5.44$$

$$\frac{d[C]}{dt} = +k_{12}[OH^-][C] - k_{-12}[C] \quad 5.19$$

When making the same assumptions as made for pathway 1, Section 5.2.6.2, the number of rate laws decreases and the complexity of the complete set of rate laws is reduced, and equations 5.41 – 5.44 and 5.19 are now given by the set of ordinary differential equations 5.45 – 5.47.

$$\frac{d[A]}{dt} = -k_{6(2)}[A][B] + k_{-6(2)}[OH^-][C]^2 \quad 5.45$$

$$\frac{d[B]}{dt} = -k_{6(2)}[A][B] + k_{-6(2)}[OH^-][C]^2 \quad 5.46$$

$$\frac{d[C]}{dt} = +2k_{6(2)}[A][B] - 2k_{-6(2)}[OH^-][C]^2 \quad 5.47$$

Substituting for  $[A']$ ,  $[B]$  and  $[C']$  into the ordinary differential equations 5.45 – 5.47 gives the rate laws in terms of  $[Os^{VIII}]_T$ ,  $[Os^{VI}]_T$  and  $[Os^{VII}]_T$ , equations 5.48 – 5.50:

$$\frac{d[A']}{dt} = -k_{6(2)} \left( \frac{1}{K_2[OH^-] + 1} \right) [Os^{VIII}]_T [Os^{VI}]_T + k_{-6(2)} [OH^-] \left( \frac{1}{K_{12}[OH^-] + 1} \right)^2 [Os^{VII}]_T^2 \quad 5.48$$

$$\frac{d[B]}{dt} = -k_{6(2)} \left( \frac{1}{K_2[OH^-] + 1} \right) [Os^{VIII}]_T [Os^{VI}]_T + k_{-6(2)} [OH^-] \left( \frac{1}{K_{12}[OH^-] + 1} \right)^2 [Os^{VII}]_T^2 \quad 5.49$$

$$\frac{d[C']}{dt} = +2k_{6(2)} \left( \frac{1}{K_2[OH^-] + 1} \right) [Os^{VIII}]_T [Os^{VI}]_T - 2k_{-6(2)} [OH^-] \left( \frac{1}{K_{12}[OH^-] + 1} \right)^2 [Os^{VII}]_T^2 \quad 5.50$$

At equilibrium  $d[A']/dt$ , equation 5.48, is equal to zero. Rearrangement of equation 5.48 yields equation 5.51. In a similar manner as shown above, *i.e.* equations 5.36 – 5.38, equation 5.52 is derived from equation 5.51.

$$\frac{k_{6(2)} \left( \frac{1}{K_2[\text{OH}^-] + 1} \right)}{k_{-6(2)} \left( \frac{1}{K_{12}[\text{OH}^-] + 1} \right)^2} = \frac{[\text{OH}^-][\text{Os}^{\text{VII}}]_{\text{T}}^2}{[\text{Os}^{\text{VIII}}]_{\text{T}}[\text{Os}^{\text{VI}}]_{\text{T}}} \quad 5.51$$

$$\frac{k_{6(2)}}{k_{-6(2)}} = K_{6(\text{true})} = \left[ \frac{\left( \frac{1}{K_{12}[\text{OH}^-] + 1} \right)^2 [\text{OH}^-]}{\left( \frac{1}{K_2[\text{OH}^-] + 1} \right)} \right] \frac{k_{6(\text{obs})}}{k_{-6(\text{obs})}} \quad 5.52$$

The term in the square brackets in equation 5.52 is evaluated to determine by what magnitude  $K_{6(\text{true})}$  will differ from  $K_{6(\text{obs})}$  at 298.15 K. For example, when substituting  $K_2$  with 0.58,  $K_{12}$  with the DFT-calculated PBE functional value of 0.05 and  $[\text{OH}^-]$  with 2.0 into the square brackets term of equation 5.52 gives a correction factor of approximately 3.58, equation 5.53.

$$\left[ \frac{\left( \frac{1}{(0.05 \times 2) + 1} \right)^2 [2]}{\left( \frac{1}{(0.58 \times 2) + 1} \right)} \right] = 3.58 \quad 5.53$$

The values for the term in square brackets, *i.e.* the correction factors, for the other four functionals, together with the corresponding  $K_{6(\text{true})}$  and  $\Delta G^\circ_{\text{rxn}}$  (true) values for pathway 2 are listed in Table 5.10.

**Table 5.10.** Correction factors for  $K_{6(\text{obs})}$  and approximate  $K_{6(\text{true})}$  and  $\Delta G^\circ_{\text{rxn}}$  (true) values for the comproportionation reaction at 298.15 K (pathway 2).

Functional	correction factor	$K_{6(\text{true})}$	$\Delta G^\circ_{\text{rxn}}$ (true) (kcal.mol <sup>-1</sup> )
PBE	3.58	22.95	-1.86
PBE-D	0.51	3.24	-0.70
PBE-D3	1.89	12.13	-1.48
PBE-D3(BJ)	3.06	19.58	-1.76
PBE-dDsC	2.71	17.34	-1.69

Making these corrections to  $K_{6(\text{obs})}$  results in a range of  $\Delta G^\circ_{\text{rxn}}$  (true) values for the comproportionation reaction of approximately -1.86 (PBE) to -0.70 kcal.mol<sup>-1</sup> (PBE-D). The correction factors for pathway 2, Table 5.10, are smaller than for pathway 1, Table 5.9, and

are reflected by the relatively smaller difference between  $\Delta G^{\circ}_{rxn(obs)}$  and  $\Delta G^{\circ}_{rxn}$  (true) values. Furthermore, all the  $\Delta G^{\circ}_{rxn}$  (true) values for pathway 2 fall within the experimental error range of  $\Delta G^{\circ}_{rxn(obs)}$ . Using the same arguments as before, we can now directly compare  $\Delta G^{\circ}_{rxn(obs)}$ ,  $\Delta H^{\circ}_{rxn(obs)}$  and  $\Delta S^{\circ}_{rxn(obs)}$  with DFT-calculated standard reaction energies as listed in Table 5.7.

We are now in a position to make a meaningful comparison between the experimental and DFT-calculated thermodynamic parameters. Apart from the LDA functional, and to a lesser extent the M06L functional, the standard thermodynamic reaction energies for equation 5.10, in the simulated aqueous phase, agree very well in our opinion, Table 5.7, especially when  $\Delta H^{\circ}_{rxn}$  and  $\Delta S^{\circ}_{rxn}$  terms are also considered. It is evident from the relative standard enthalpy and entropy of formation diagrams in Figures 5.7 and 5.8 and Tables A5 – A7 that the most probable comproportionation reaction is the one described by equation 5.10, not the reaction described by equation 5.11. Furthermore, the DFT-calculated  $\Delta G^{\circ}_{rxn}$  for reaction 5.10 in the gas phase is approximately  $120 \text{ kcal.mol}^{-1}$  more negative than that in the simulated aqueous phase. This large discrepancy is due to the neglect of hydration energies for the osmium equilibrium geometries in the gas phase. The total hydration energy (PBE functional) of the two doubly-charged reactants, *cis*-[Os<sup>VIII</sup>O<sub>4</sub>(OH)<sub>2</sub>]<sup>2-</sup> ( $-217.98 \text{ kcal.mol}^{-1}$ ) and *trans*-[Os<sup>VI</sup>O<sub>2</sub>(OH)<sub>4</sub>]<sup>2-</sup> ( $-220.53 \text{ kcal.mol}^{-1}$ ), is approximately  $120 \text{ kcal.mol}^{-1}$  more than that of the four singly-charged products, *trans*-[Os<sup>VII</sup>O<sub>3</sub>(OH)<sub>2</sub>]<sup>-</sup> ( $2 \times -62.86 \text{ kcal.mol}^{-1}$ ) and OH<sup>-</sup> ( $2 \times -96.09 \text{ kcal.mol}^{-1}$ ). This result is consistent with previous results where the inclusion of hydration energies resulted in excellent agreement of  $\Delta G^{\circ}_{rxn}$  for the coordination sphere expansion reactions of Os<sup>VIII</sup> oxo/hydroxido species, equations 3.3 & 3.4, which lends more credibility to our interpretation of the comproportionation reaction, equation 5.10.

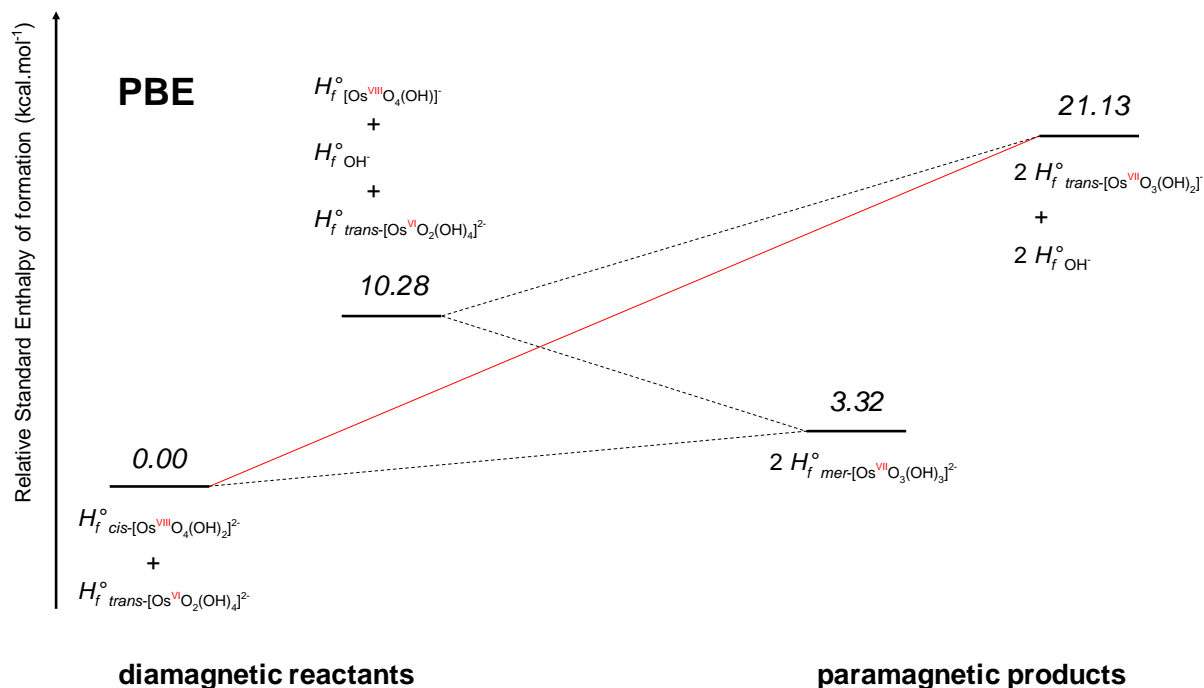


**Figure 5.7.** Relative standard enthalpies of formation (kcal.mol<sup>-1</sup>) of the reactants and products of the Os<sup>VI</sup> & Os<sup>VIII</sup> comproportionation reaction in the simulated aqueous phase (PBE functional). Solid red line depicts the energy change between the reactant and product states of lowest Gibbs energy, equation 5.10.

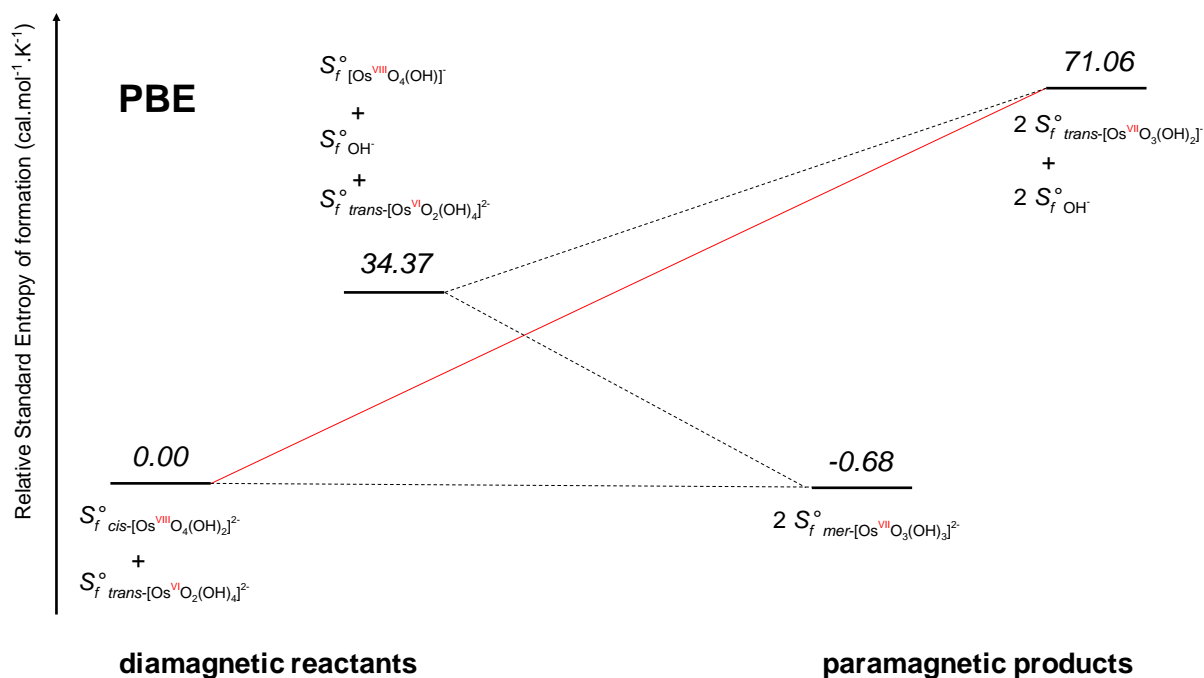


**Figure 5.8.** Relative standard entropies of formation (cal.mol<sup>-1</sup>.K<sup>-1</sup>) of the reactants and products of the Os<sup>VI</sup> & Os<sup>VIII</sup> comproportionation reaction in the simulated aqueous phase (PBE functional). Solid red line depicts the energy change between the reactant and product states of lowest Gibbs energy, equation 5.10.

### Evidence to support the assumptions that Os<sup>VIII</sup> and Os<sup>VII</sup> coordination sphere expansion/contraction reactions are at equilibrium

Our DFT-calculated Gibbs energies of activation for coordination sphere expansion reactions of Os<sup>VIII</sup> oxo/hydroxido species, equations 3.3 & 3.4, coupled with the stopped-flow kinetics experiment, discussed in Chapters 4 and 5, agree that Os<sup>VIII</sup> and Os<sup>VII</sup> coordination sphere expansion reactions are rapid in comparison with the Os<sup>VI</sup> & Os<sup>VIII</sup> comproportionation reaction, equation 5.10. The question we want to answer here is: to what extent do the rate constants,  $k_2$  &  $k_{-2}$ , of the Os<sup>VIII</sup> coordination sphere expansion reaction, equation 3.4, have to be decreased before a visible difference would be noticed for the species' concentration (conc.) vs. time profiles of the comproportionation reaction? These numerical experiments are also done as further justification for the assumptions that Os<sup>VIII</sup> and Os<sup>VII</sup> coordination sphere expansion/contraction reactions, equations 3.4 and 5.7, are, for all practical purposes, at equilibrium while the Os<sup>VI</sup> & Os<sup>VIII</sup> comproportionation reaction progresses.

The reaction model used for these simulations is given by pathway 1, Scheme 5.3, where the full set of rate laws, equations 5.15 – 5.19, were solved with the following initial conditions:

$[\text{OH}^-] = 2.0 \text{ M}$ ,  $[\text{A}] = 0.9096 \text{ mM}$ ,  $[\text{A}'] = 0.4944 \text{ mM}$ ,  $[\text{B}] = 1.404 \text{ mM}$  and  $[\text{C}] = [\text{C}'] = 0$ ;

$k_{6(1)}$  &  $k_{-6(1)} = 4.8 \times 10^4$  &  $6.5 \times 10^3 \text{ M}^{-1}.\text{s}^{-1}$ , respectively,  $k_2$  &  $k_{-2} = 4.8 \times 10^5$  &  $5.2 \times 10^5 \text{ M}^{-1}.\text{s}^{-1}$ , respectively, and  $k_{12}$  &  $k_{-12} = 1.0 \times 10^6$  &  $1.5 \times 10^7 \text{ M}^{-1}.\text{s}^{-1}$ , respectively.

The obtained reactant and product species' conc. vs. time profiles are shown in Figure 5.9.

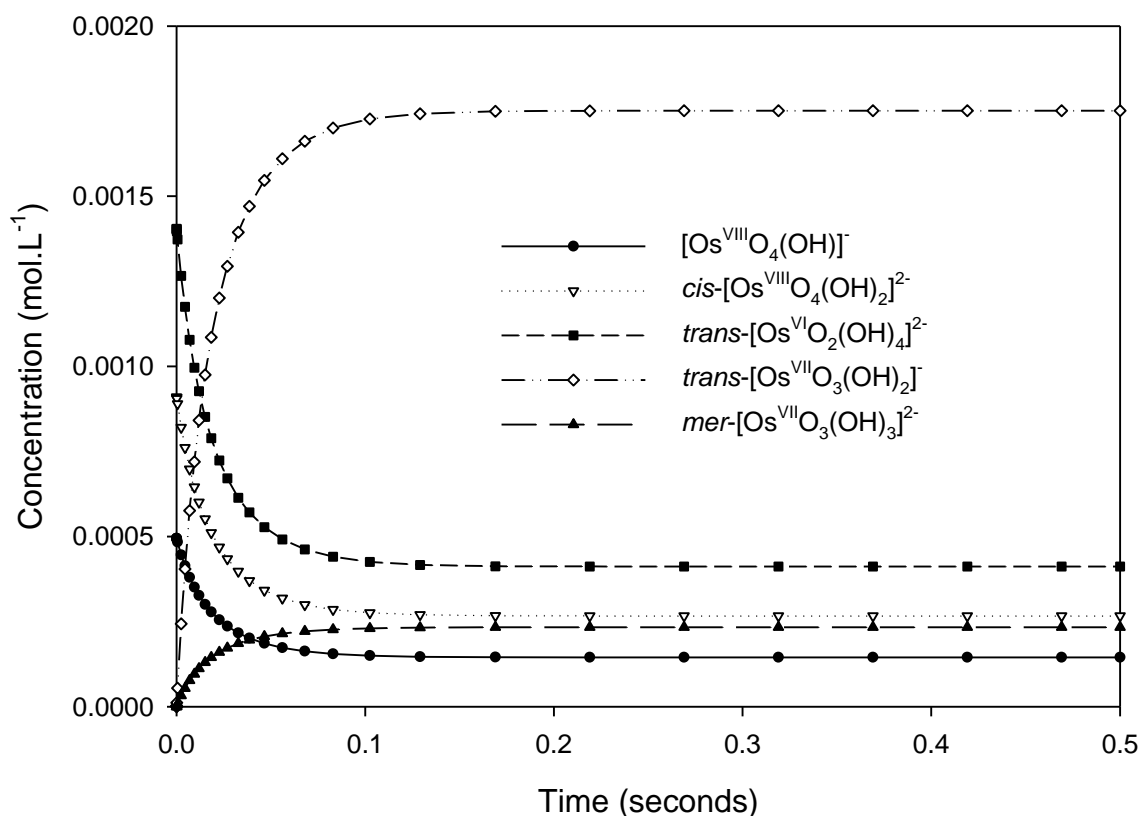


**Figure 5.9.** Concentrations of the individual, abundant osmium species as a function of time as the  $\text{Os}^{\text{VI}}$  &  $\text{Os}^{\text{VIII}}$  comproportionation reaction progresses. Reactions 3.4 and 5.7 are at equilibrium, *i.e.*  $k_2$  &  $k_{-2}$  equals  $4.8 \times 10^5$  &  $5.2 \times 10^5 \text{ M}^{-1} \cdot \text{s}^{-1}$ , respectively, while  $k_{12}$  &  $k_{-12}$  equals  $1.0 \times 10^6$  &  $1.5 \times 10^7 \text{ M}^{-1} \cdot \text{s}^{-1}$ , respectively.

We then set out to solve the set of rate laws, equations 5.20 – 5.22, that were obtained when the equilibrium assumption was made w.r.t. coordination sphere expansion/contraction of  $\text{Os}^{\text{VIII}}$  and  $\text{Os}^{\text{VII}}$  species, using the following initial conditions:

$$[\text{OH}^-] = 2.0 \text{ M}, [\text{Os}^{\text{VIII}}]_{\text{T}} = [\text{Os}^{\text{VI}}]_{\text{T}} = 1.404 \text{ mM} \text{ and } [\text{Os}^{\text{VII}}]_{\text{T}} = 0;$$

$$k_{6(1)} \text{ \& } k_{-6(1)} = 4.8 \times 10^4 \text{ \& } 6.5 \times 10^3 \text{ M}^{-1} \cdot \text{s}^{-1}, \text{ respectively.}$$

The obtained reactant and product species' conc. vs. time profiles are shown as lines in Figure 5.10.



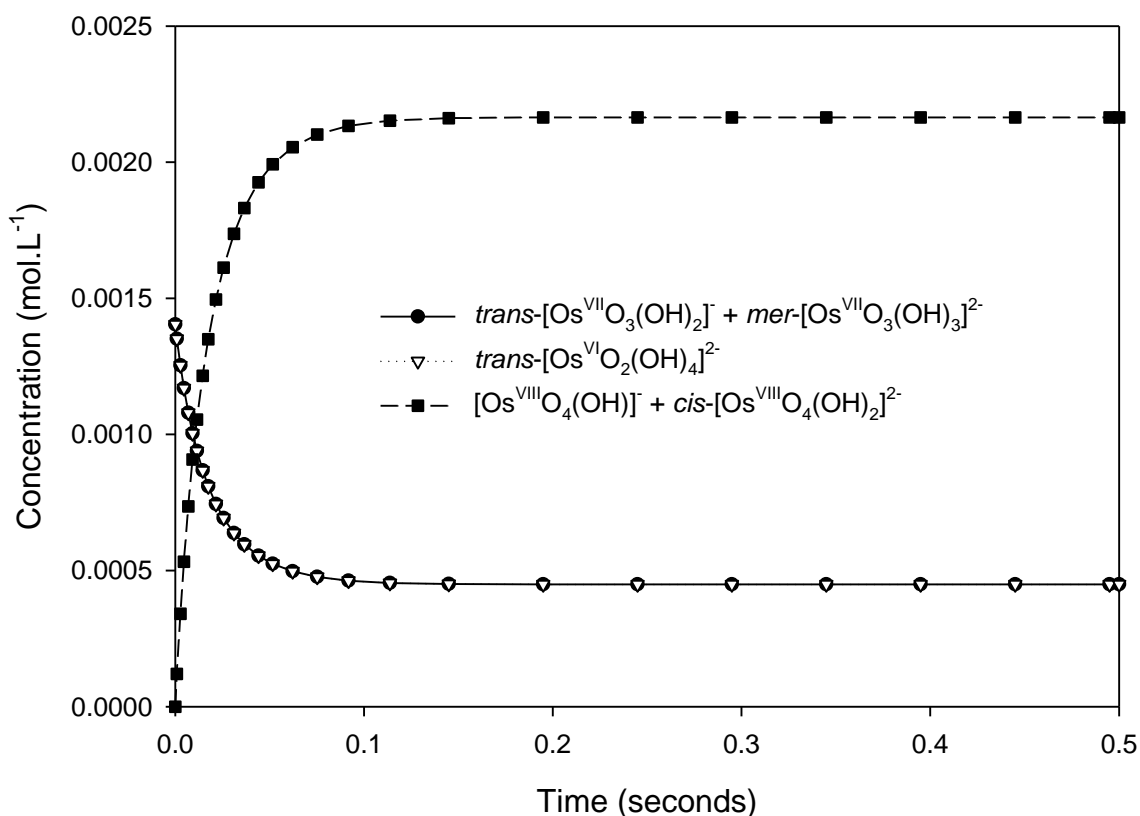


**Figure 5.10.**  $[\text{Os}^{\text{VIII}}]_{\text{T}}$ ,  $[\text{Os}^{\text{VI}}]_{\text{T}}$  and  $[\text{Os}^{\text{VII}}]_{\text{T}}$  as a function of time as the  $\text{Os}^{\text{VI}}$  &  $\text{Os}^{\text{VIII}}$  comproportionation reaction progresses. Reactions 3.4 and 5.7 are at equilibrium, *i.e.*  $k_2$  &  $k_{-2}$  equals  $4.8 \times 10^5$  &  $5.2 \times 10^5 \text{ M}^{-1} \cdot \text{s}^{-1}$ , respectively, while  $k_{12}$  &  $k_{-12}$  equals  $1.0 \times 10^6$  &  $1.5 \times 10^7 \text{ M}^{-1} \cdot \text{s}^{-1}$ , respectively.

To illustrate that the two sets of rate laws, equations 5.15 – 5.19 (Figure 5.9) and 5.20 – 5.22 (Figure 5.10), are equivalent with the mentioned initial conditions, rate constants and equilibrium constants, we took the sum of the osmium species' concentrations data in Figure 5.9 and all the rate constants used to plot the lines in Figure 5.10:

$$[\text{OH}^-] = 2.0 \text{ M}, [\text{Os}^{\text{VIII}}]_{\text{T}} = [\text{A}] + [\text{A}'] = 1.404 \text{ mM}, [\text{Os}^{\text{VI}}]_{\text{T}} = [\text{B}] = 1.404 \text{ mM} \text{ and } [\text{Os}^{\text{VII}}]_{\text{T}} = [\text{C}] + [\text{C}'] = 0;$$

$$k_{6(1)} \text{ \& } k_{-6(1)} = 4.8 \times 10^4 \text{ \& } 6.5 \times 10^3 \text{ M}^{-1} \cdot \text{s}^{-1}, \text{ respectively, } k_2 \text{ \& } k_{-2} = 4.8 \times 10^5 \text{ \& } 5.2 \times 10^5 \text{ M}^{-1} \cdot \text{s}^{-1}, \text{ respectively, and } k_{12} \text{ \& } k_{-12} = 1.0 \times 10^6 \text{ \& } 1.5 \times 10^7 \text{ M}^{-1} \cdot \text{s}^{-1}, \text{ respectively.}$$

As expected, after plotting the reactant and product species' conc. vs. time profiles, a perfect match between the two sets of rate laws is obtained, as shown by the symbols in Figure 5.10.

We then set out to solve the full set of rate laws, equations 5.15 – 5.19, using the same input parameters used to obtain Figure 5.9, but now the values of  $k_2$  &  $k_{-2}$  were systematically decreased as shown in Table 5.11. Similar to the previous experiment, the concentrations of

the individual osmium species were added, *e.g.*  $[\text{Os}^{\text{VIII}}]_{\text{T}} = [\text{A}] + [\text{A}']$  and  $[\text{Os}^{\text{VII}}]_{\text{T}} = [\text{C}] + [\text{C}']$ , Figure 5.11.<sup>13</sup>

**Table 5.11.** Rate constants for  $\text{Os}^{\text{VIII}}$  coordination sphere expansion/contraction used to simulate to what extent  $[\text{Os}^{\text{VIII}}]_{\text{T}}$  and  $[\text{Os}^{\text{VII}}]_{\text{T}}$  with time may deviate from our reaction model.

Simulation (see Figure 5.11)	$k_2$ ( $\text{M}^{-1} \cdot \text{s}^{-1}$ )	$k_{-2}$ ( $\text{M}^{-1} \cdot \text{s}^{-1}$ )	$K_2 = k_2/k_{-2}$
(a)	$4.80 \times 10^5$	$5.22 \times 10^5$	0.92
(b)	$4.80 \times 10^4$	$5.22 \times 10^4$	0.92
(c)	$4.80 \times 10^3$	$5.22 \times 10^3$	0.92
(d)	$4.80 \times 10^2$	$5.22 \times 10^2$	0.92
(e)	$4.80 \times 10$	$5.22 \times 10$	0.92
(f)	4.80	5.22	0.92
(g)	$4.80 \times 10^{-1}$	$5.22 \times 10^{-1}$	0.92

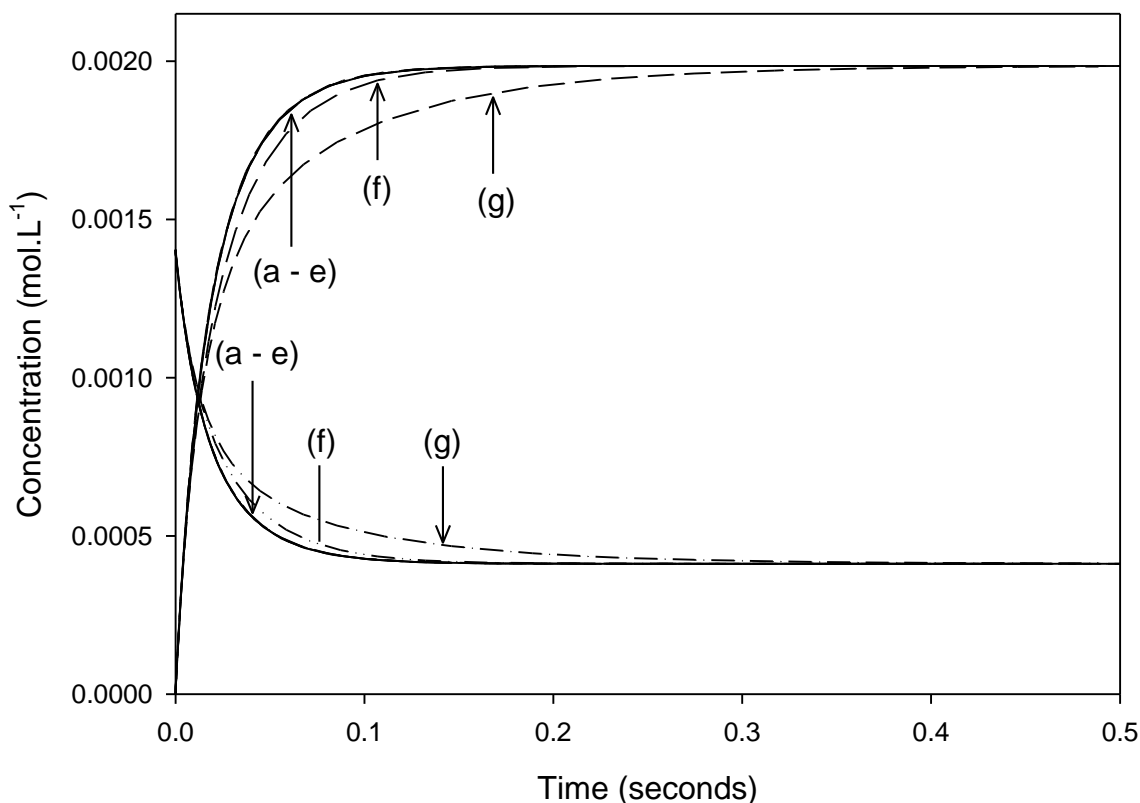


**Figure 5.11.**  $[\text{Os}^{\text{VIII}}]_{\text{T}}$  and  $[\text{Os}^{\text{VII}}]_{\text{T}}$  as a function of time as the  $\text{Os}^{\text{VI}}$  &  $\text{Os}^{\text{VIII}}$  comproportionation reaction progresses. The trends are virtually unchanged between  $k_2$  &  $k_{-2}$  values of  $4.80 \times 10^5$  &  $5.22 \times 10^5 \text{ M}^{-1} \cdot \text{s}^{-1}$  (a) to  $4.80 \times 10$  &  $5.22 \times 10 \text{ M}^{-1} \cdot \text{s}^{-1}$  (e).

<sup>13</sup> Equilibrium constants  $K_2$  and  $K_{12}$  (298.15 K) used for the numerical analyses are 0.92 and 0.07, respectively, instead of the calculated average experimental value of 0.58<sup>21,22</sup> and the PBE-D3(BJ) value of 0.09, respectively. The exact values of  $K_2$  and  $K_{12}$  will not influence qualitatively the simulated conc. vs. time profiles.

It is evident that deviations in the conc. vs. time profiles occur when  $k_2$  &  $k_{-2}$  are significantly lower, *i.e.* by five orders of magnitude, than what is considered close to diffusion-controlled. The numerical experiment provides further evidence that our assumptions that  $\text{Os}^{\text{VIII}}$  and  $\text{Os}^{\text{VII}}$  coordination sphere expansion/contraction reactions are at equilibrium while the  $\text{Os}^{\text{VI}}$  &  $\text{Os}^{\text{VIII}}$  comproportionation reaction progresses are valid. Therefore, our earlier conclusion that the observed and ‘true’ thermodynamic parameters can be used interchangeably is further justified.

### 5.3 Conclusions

According to our DFT-calculated energies, using a variety of functionals, the reducing agent in the comproportionation reaction is the diamagnetic *trans*- $[\text{Os}^{\text{VI}}\text{O}_2(\text{OH})_4]^{2-}$  species. We have further demonstrated that DFT computational methodologies are successful in elucidating the equilibrium structures and energies of paramagnetic  $\text{Os}^{\text{VII}}$  oxo/hydroxido product species that are present in aqueous basic solutions, which experimental studies have been unable to do. DFT calculations provide evidence that the abundant  $\text{Os}^{\text{VII}}$  species present in basic aqueous solutions at 298.15 K are a combination of the *trans*- $[\text{Os}^{\text{VII}}\text{O}_3(\text{OH})_2]^-$  and *mer*- $[\text{Os}^{\text{VII}}\text{O}_3(\text{OH})_3]^{2-}$  stereoisomers. Furthermore, the thermodynamic driving force of the diffusion-controlled, coordination sphere expansion reaction of the *trans*- $[\text{Os}^{\text{VII}}\text{O}_3(\text{OH})_2]^-$  complex to form the *mer*- $[\text{Os}^{\text{VII}}\text{O}_3(\text{OH})_3]^{2-}$  complex, is the larger hydration energy of the doubly-charged *mer*- $[\text{Os}^{\text{VII}}\text{O}_3(\text{OH})_3]^{2-}$  species in comparison with that of the reactants.

Based on the good agreement between reported, X-ray crystal structure data and our DFT-calculated equilibrium geometries of the  $\text{Os}^{\text{VIII}}$  ( $\text{OsO}_4$ ) complex and  $\text{Os}^{\text{VI}}$  (*trans*- $[\text{OsO}_2(\text{OH})_4]^{2-}$ ) complex, it is reasonable to assume that a similar level of accuracy regarding the  $\text{Os}^{\text{VII}}$  product species’ geometries are obtained. QTAIM and EDA analyses indicate that  $\text{Os}^{\text{VI}}=\text{O}$  and  $\text{Os}^{\text{VII}}=\text{O}$  bonding interactions are ionic (closed-shell) whereas the  $\text{Os}^{\text{VI}}-\text{OH}$  and  $\text{Os}^{\text{VII}}-\text{OH}$  bonding interactions are polar covalent (dative).

Re-evaluation of the Evans method data, Chapter 4, when taking into consideration that the products of the  $\text{Os}^{\text{VI}}$  &  $\text{Os}^{\text{VIII}}$  comproportionation reaction are a combination of five-coordinate and six-coordinate monomer species at 298.15 K, yields that the product species have approximately one (between 1.10 and 1.15) unpaired electron each. The re-evaluated result corroborates the postulate that the final products are  $\text{Os}^{\text{VII}}$  species,<sup>23</sup> and justifies the DFT geometry optimisation calculations of the product species as  $\text{Os}^{\text{VII}}$  complexes.

Observed standard reaction energies of the Os<sup>VI</sup> & Os<sup>VIII</sup> comproportionation reaction, Chapter 4, compare well with DFT-calculated energies in the simulated aqueous phase when comparing the energy differences between the reactant and product states that are lowest in Gibbs energy to describe the reaction, *i.e.* equation 5.10. By contrast, DFT-calculated energies in the gas phase compare poorly, due to the neglect of hydration energies. After correcting for the observed rate constants and observed thermodynamic parameters from stopped-flow UV-Vis spectroscopy kinetics experiments, Chapter 4, it is observed that irrespective of whether [Os<sup>VIII</sup>O<sub>4</sub>(OH)]<sup>-</sup> or *cis*-[Os<sup>VIII</sup>O<sub>4</sub>(OH)<sub>2</sub>]<sup>2-</sup> are considered the species that react with *trans*-[Os<sup>VI</sup>O<sub>2</sub>(OH)<sub>4</sub>]<sup>2-</sup> (corresponding to two dissimilar reaction pathways) that the ‘true’ thermodynamic parameters are within the experimental error range of the observed values. The simplified reaction model used in Chapter 4 is thus validated since the rate laws used to simulate the stopped-flow UV-Vis spectroscopy kinetics data are recovered. The assumptions that Os<sup>VIII</sup> and Os<sup>VII</sup> coordination sphere expansion/contraction reactions, equations 3.4 and 5.7, are at equilibrium while the Os<sup>VI</sup> & Os<sup>VIII</sup> comproportionation reaction progresses were validated by a set of numerical experiments.

The results obtained in this study have provided a platform from where the mechanism of the Os<sup>VI</sup> & Os<sup>VIII</sup> comproportionation reaction can be investigated.

---

**References**

1. A. H. Éll, A. Closson, H. Adolfsson and J.-E. Bäckvall, *Adv. Synth. Catal.*, 2003, **345**, 1012.
2. S. M. Desai, N. N. Halligudi and S. T. Nandibewoor, *Int. J. Chem. Kinet.*, 1999, **31**, 583.
3. N. P. Shetti, R. R. Hosamani and S. T. Nandibewoor, *Research Letters in Inorganic Chemistry*, 2008, **216058**.
4. K. Byadagi, M. Meti, S. Nandibewoor and S. Chimatadar, *Ind. Eng. Chem. Res.*, 2013, **52**, 9011.
5. M. P. Singh, H. S. Singh, M. C. Gangwar, P. Thakur and A. K. Singh, *P. Indian Acad. Sci. A.*, 1975, **41**.
6. A. Dehestani, W. H. Lam, D. A. Hrovat, E. R. Davidson, W. T. Borden and J. M. Mayer, *J. Am. Chem. Soc.*, 2005, **127**, 3423.
7. P. VeeraSomaiah, K. B. Reddy, B. Sethuram and T. Navaneeth Rao, *J. Indian Chem. Soc.*, 1988, **27A**, 876.
8. P. VeeraSomaiah, K. B. Reddy, B. Sethuram and T. Navaneeth Rao, *J. Indian Chem. Soc.*, 1989, **66**, 755.
9. H. S. Singh, S. P. Singh, S. M. Singh, R. K. Singh and A. K. Sisodia, *J. Phys. Chem.*, 1975, **79(18)**, 1920.
10. N. P. Singh, V. N. Singh, H. S. Singh and M. P. Singh, *Aust. J. Chem.*, 1970, **23**, 921.
11. V. N. Singh, H. S. Singh and B. B. L. Saxena, *J. Am. Chem. Soc.*, 1969, **91(10)**, 2643.
12. H. S. Singh, *Oxidation of Organic Compounds with Osmium Tetroxide, in Organic synthesis by oxidation with metal compounds*, ed. W. J. Mijs and C. R. H. de Jonge, Plenum Press, New York, 1986.
13. N. P. Singh, V.N. Singh and M. P. Singh, *Aust. J. Chem.*, 1968, **21**, 2913.
14. B. Singh, A. K. Singh, M. B. Singh and A. P. Singh, *Tetrahedron*, 1986, **42**, 715.

15. K. K. S. Gupta and B. A. Begum, *Transition Met. Chem.*, 1998, **23**, 295.
16. K. K. S. Gupta and B. A. Begum, *Int. J. Chem. Kinet.*, 1999, **31(7)**, 477.
17. W. P. Griffith and M. Suriaatmaja, *Can. J. Chem.*, 2001, **79**, 598–606.
18. J. Vázquez, C. Bo, J. M. Poblet, J. de Pablo and J. Bruno, *Inorg. Chem.*, 2003, **42**, 6136.
19. L. Guimarães, H. A. de Abreu, H. A. Duarte, *Chem. Phys.*, 2007, **333**, 10.
20. W. W. Rudolph, D. Fischer and G. Irmer, *Appl. Spectrosc.*, 2006, **60**, 130.
21. Z. M. Galbács, A. Zsednai and L. J. Csányi, *Transition Met. Chem.*, 1983, **8**, 328.
22. B. J. McFadzean, PhD Dissertation, 2008, NMMU, South Africa.
23. T. E. Geswindt, W. J. Gerber, H. E. Rohwer and K. R. Koch, *Dalton Trans.*, 2011, **40**, 8581.
24. A. D. McNaught and A. Wilkinson, *IUPAC. Compendium of Chemical Terminology, 2<sup>nd</sup> ed. (the "Gold Book").* Blackwell Scientific Publications, Oxford, 1997. (Last update: 2014-02-24)
25. R. K. Murmann and C. L. Barnes, *Z. Krist. - New Cryst. St.*, 2002, **217**, 303.
26. L. O. Avtomyan, V. G. Andrianov and M. A. Porai-Kohits, *Zh. Strukt. Khim.*, 1962, **3**, 685.
27. T. Ziegler and A. Rauk, *Inorg. Chem.*, 1979, **18**, 1558.
28. J. I. Rodríguez, R. F. W. Bader, P. W. Ayers, C. Michel, A. W. Götz and C. Bo, *Chem. Phys. Lett.*, 2009, **472**, 149.
29. J. I. Rodríguez, *J. Comput. Chem.*, 2013, **34**, 681.
30. D. F. Evans, *J. Chem. Soc.*, 1959, 2003.
31. J. Lölliger and R. Scheffold, *J. Chem. Educ.*, 1972, **49**, 646.
32. T. H. Crawford and J. Swanson, *J. Chem. Educ.*, 1971, **48**, 382.
33. D. F. Evans and T. A. James, *J. Chem. Soc. Dalton Trans.*, 1979, 723.

# CHAPTER 6

---

## A DFT Mechanistic Study of the Os<sup>VI</sup> & Os<sup>VIII</sup> Comproportionation Reaction in a Basic Aqueous Matrix

### 6.1 Introduction

There are several key experimental and computational results (Chapters 3 – 5) and reports from the literature<sup>1-8</sup> that were taken into consideration before we set out to systematically elucidate the mechanism of the *trans*-[Os<sup>VI</sup>O<sub>2</sub>(OH)<sub>4</sub>]<sup>2-</sup> (Os<sup>VI</sup>) & [Os<sup>VIII</sup>O<sub>4</sub>(OH)<sub>*n*</sub>]<sup>*n-*</sup> (*n* = 1, 2) (Os<sup>VIII</sup>) comproportionation reaction in a basic aqueous matrix, equation 6.1.



The comproportionation reaction mechanism of Ru<sup>II</sup>(bpy)<sub>2</sub>(py)(OH<sub>2</sub>)<sup>2+</sup> ([Ru<sup>II</sup>-OH<sub>2</sub>]<sup>2+</sup>) and Ru<sup>IV</sup>(bpy)<sub>2</sub>(py)(O)<sup>2+</sup> ([Ru<sup>IV</sup>=O]<sup>2+</sup>) complex cations, reported by Meyer *et al.*<sup>2</sup>, consists of monomer reactants forming a proposed ‘preassociation’ complex, *i.e.* an intermediate species,<sup>14</sup> *via* proposed intermolecular hydrogen bonding, Scheme 1.5. The subsequent redox event involves the simultaneous transfer of an electron (ET) and a proton (PT) to form a ‘post-association’ complex. In the third and final step, the ‘post-association’ complex dissociates to form two identical Ru<sup>III</sup>(bpy)<sub>2</sub>(py)(OH)<sup>2+</sup> ([Ru<sup>III</sup>-OH]<sup>2+</sup>) species. This reaction pathway, known as concerted electron-proton transfer (EPT), was found to be energetically favoured to initial electron transfer (*via* stepwise ET-PT) or initial proton transfer (*via* stepwise PT-ET) pathways, Scheme 1.4.

In Chapter 4 we reported that the Os<sup>VII</sup> & Os<sup>VII</sup> disproportionation reaction has a negative observed activation enthalpy,  $\Delta^\ddagger H^\circ_{dis}$ . There are only a few reports in the literature of experimentally observed negative activation enthalpies for chemical reactions.<sup>3-8</sup> One

---

<sup>14</sup> Intermediate species are molecular entities with a lifetime appreciably longer than a molecular vibration (corresponding to a local potential energy minimum depth greater than *RT*) that are formed (directly or indirectly) from the reactants and reacts further to give (either directly or indirectly) the products of a chemical reaction; also the corresponding chemical species.

recently published article by Han *et al.*<sup>3</sup> reported an investigation of this phenomenon in a catalysed Mannich reaction of an imine and a fluorinated ketoester, Figure 6.1.

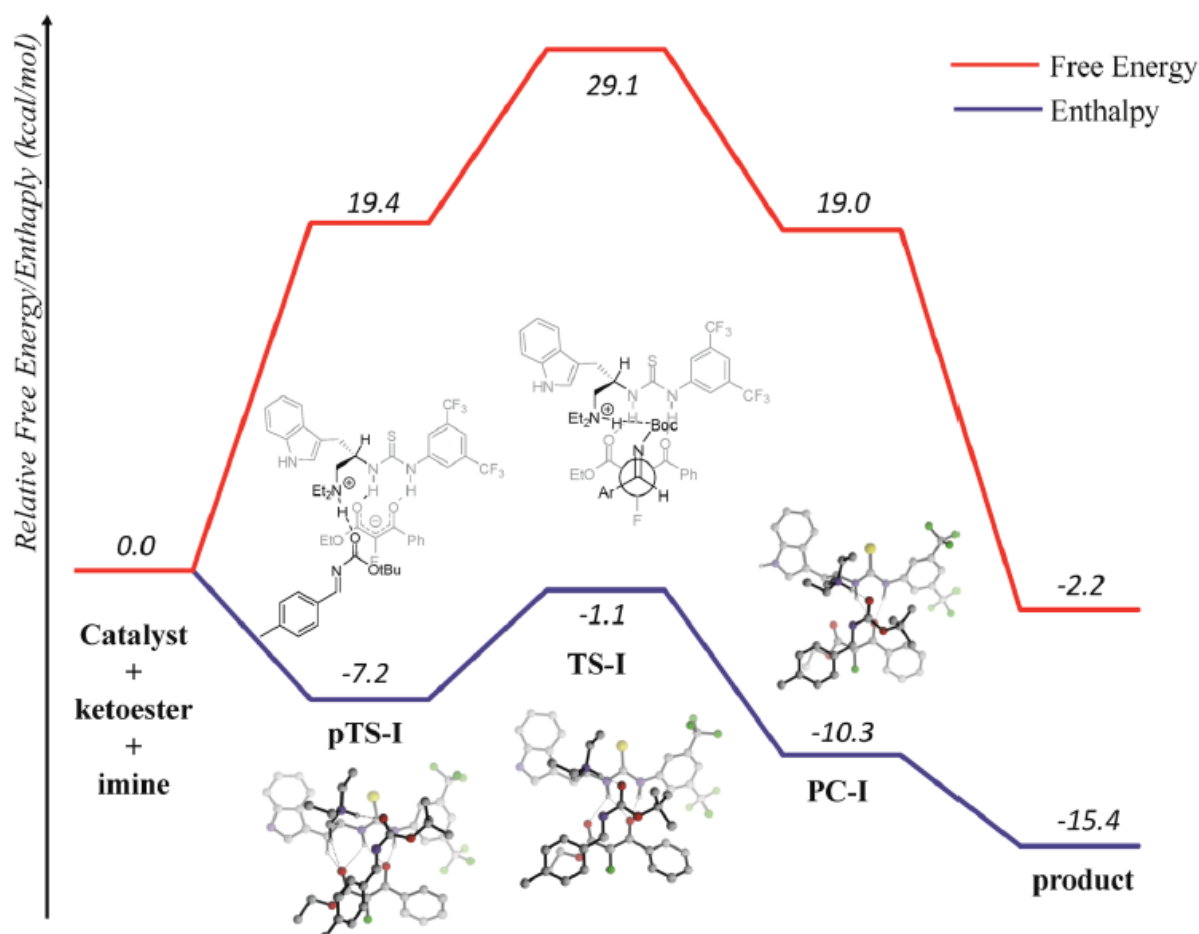


**Figure 6.1.** Reaction profile diagram for an asymmetric Mannich reaction.<sup>3</sup>

Han *et al.*<sup>3</sup> elucidated the stepwise mechanism of the reaction with DFT and found a pathway which consists of three consecutive elementary steps. The first step is highly exothermic and involves the formation of a ‘pre-transition state complex’ (pTS-I in Figure 6.1), *i.e.* an intermediate species which consists of a ‘multiple hydrogen bonding network’, between the monomer reactant species (substrates and catalyst). The extensive intermolecular hydrogen bonding of the initial adduct lowers the electronic energy, w.r.t. the monomer reactants, on the potential energy surface. In the subsequent reaction step the electronic energy increases when reaching the transition state (TS-I in Figure 6.1), such that the enthalpy of the system at the transition state is lower than the sum of the (infinitely separated) monomer reactant species. The overall enthalpy change of transition state TS-I relative to the starting substrates is negative,  $-1.1 \text{ kcal.mol}^{-1}$ , which is the cause of the observed inverse dependence of reaction rate constant with temperature. The reported studies by Meyer *et al.*<sup>2</sup> and by Han *et al.*<sup>3</sup> offer



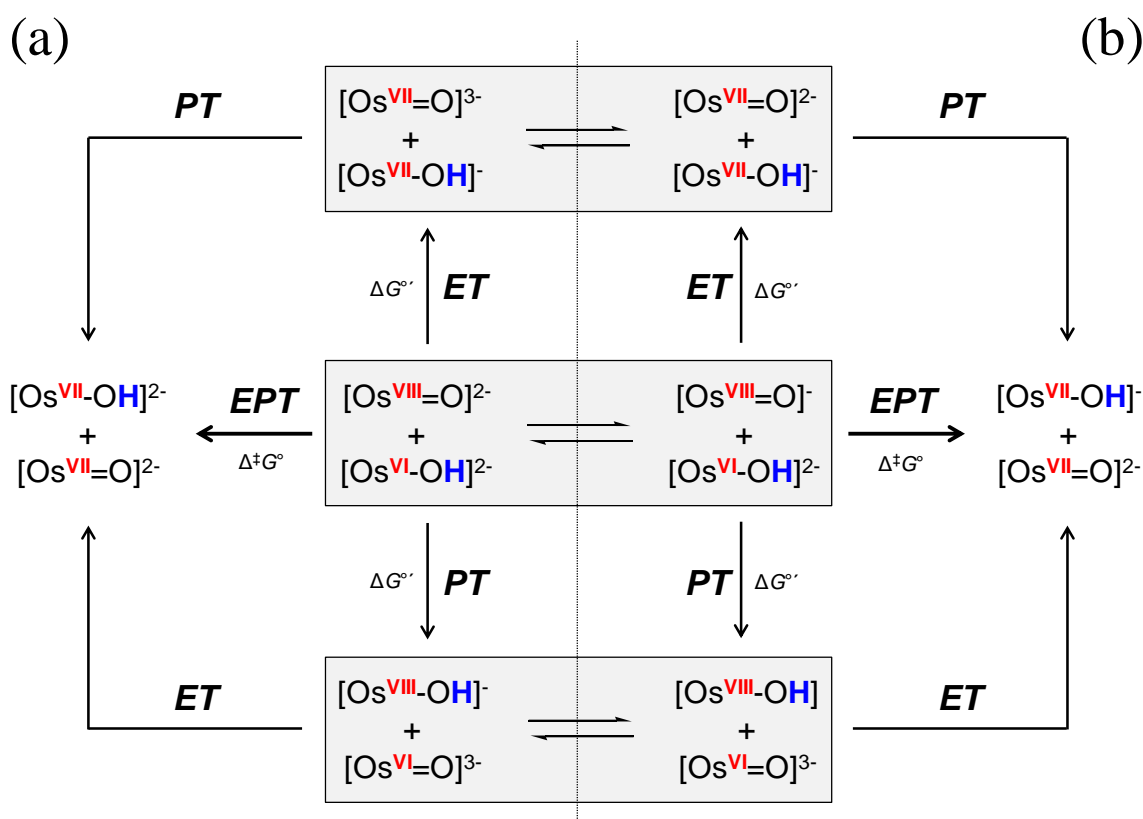
useful insight w.r.t. the Os<sup>VII</sup> & Os<sup>VII</sup> disproportionation reaction: the observed negative activation enthalpy,  $\Delta^\ddagger H^\circ_{dis}$ , determined from the stopped-flow kinetics experiments (Table 4.5) indicates that the Os<sup>VII</sup> & Os<sup>VII</sup> disproportionation reaction mechanism could involve the formation of a ‘preassociation’ complex (*vide infra*) as suggested by Meyer *et al.*<sup>2</sup> for the Ru<sup>II</sup> & Ru<sup>IV</sup> system and by Han *et al.*<sup>3</sup> for the Mannich reaction.

Furthermore, in the Ru<sup>II</sup> & Ru<sup>IV</sup> comproportionation reaction the most energetically favoured proton-coupled electron transfer (PCET) pathway is reported to occur *via* EPT, Scheme 1.4.<sup>2</sup> Therefore, according to the definition of EPT,<sup>2</sup> ET occurs from a metal-based  $d\pi$  orbital ( $t_{2g}$  in  $O_h$  symmetry) of [Ru<sup>II</sup>-OH]<sup>2+</sup>, to a  $d\pi$  acceptor orbital at the acceptor, [Ru<sup>IV</sup>=O]<sup>2+</sup>, while simultaneous PT occurs from a  $\sigma$ (O-H) orbital at [Ru<sup>II</sup>-OH<sub>2</sub>]<sup>2+</sup> to an O-based lone pair orbital at [Ru<sup>IV</sup>=O]<sup>2+</sup>, *i.e.* the proton source (in forming the products) is *not* from the solvent. This proposed mechanism ties in with the observed kinetic isotope effect (KIE), Section 4.2.2.3, which provided evidence that the rate-determining step of the Os<sup>VI</sup> & Os<sup>VIII</sup> comproportionation reaction coincides with a PT event and that PT from Os<sup>VI</sup> to Os<sup>VIII</sup> most probably does occur. The striking similarities of the Ru<sup>II</sup> & Ru<sup>IV</sup> and Os<sup>VI</sup> & Os<sup>VIII</sup> comproportionation reactions, in combination with the observed negative activation enthalpy,  $\Delta^\ddagger H^\circ_{dis}$ , as determined from the stopped-flow UV-Vis spectroscopy kinetics experiments (Chapter 4), prompted us to determine whether thermodynamically stable, non-covalent dimers (adducts),<sup>15</sup> or ‘preassociation’ complexes in Meyer *et al.*’s terminology<sup>2</sup>, of Os<sup>VI</sup> and Os<sup>VIII</sup> monomer reactant species exist, *i.e.* minima on the PES with zero negative vibrational frequencies, as the first step of our mechanistic investigation. However, the investigation of reactions that may involve the transfer of electrons and protons, *i.e.* PCET reactions, requires that the individual elementary steps for both concerted and sequential pathways must be considered.

In contrast to the Ru<sup>II</sup> & Ru<sup>IV</sup> comproportionation reaction, the Os<sup>VI</sup> & Os<sup>VIII</sup> comproportionation reaction has additional complexity that must be taken into account. There are two Os<sup>VIII</sup> oxo/hydroxido species present in appreciable amounts in a 2.0 M NaOH aqueous matrix at 298.15 K, namely the six-coordinate [Os<sup>VIII</sup>=O]<sup>2-</sup> species and the five-coordinate [Os<sup>VIII</sup>=O]<sup>-</sup> species, and both can potentially react with [Os<sup>VI</sup>-OH]<sup>2-</sup>.<sup>1</sup> Therefore,

<sup>15</sup> A new chemical species AB, each molecular entity of which is formed by direct combination of two separate molecular entities A and B in such a way that there is change in connectivity, but no loss, of atoms within the moieties A and B.

the mechanistic study must include the investigation of six possible PCET pathways, namely the ET-PT, PT-ET and EPT pathways where  $[\text{Os}^{\text{VIII}}=\text{O}]^{2-}$  is the electron-proton acceptor, Scheme 6.1 (a), and those where  $[\text{Os}^{\text{VIII}}=\text{O}]^-$  is the electron-proton acceptor, Scheme 6.1 (b). In order to distinguish these two possible competing reaction pathways from one another, the reactions of  $[\text{Os}^{\text{VIII}}=\text{O}]^{2-}$  with  $[\text{Os}^{\text{VI}}-\text{OH}]^{2-}$  and those of  $[\text{Os}^{\text{VIII}}=\text{O}]^-$  with  $[\text{Os}^{\text{VI}}-\text{OH}]^{2-}$  are referred to, in further discussions, as the ‘six-coordinate’ and the ‘five-coordinate’ PCET pathways, respectively, for convenience.



**Scheme 6.1.** A simplified overview of the  $\text{Os}^{\text{VI}}$  &  $\text{Os}^{\text{VIII}}$  comproportionation, ‘six-coordinate’ (a) and ‘five-coordinate’ (b), reaction PCET pathways by means of initial electron transfer (*via* stepwise ET-PT) initial proton transfer (*via* stepwise PT-ET) and concerted electron-proton transfer (EPT).

In this study we aim to (i) systematically elucidate the mechanism of the  $\text{Os}^{\text{VI}}$  &  $\text{Os}^{\text{VIII}}$  comproportionation reaction in an aqueous matrix taking into consideration the results obtained from our experimental and DFT studies (Chapters 3 – 5) as well as reported results from the literature.<sup>1-8</sup> Our mechanistic study also aims to (ii) investigate the anticipated importance that dispersion may have on the geometries and energies of the calculated osmium species in the various possible PCET reaction pathways, particularly since dispersion is expected to contribute significantly towards the stabilisation of anticipated non-covalent

dimers (*vide infra*). To probe this factor comprehensively, several similar functionals that differ only w.r.t. dispersion correction were selected for further calculations, including PBE, PBE-D, PBE-D3, PBE-D3(BJ) and PBE-dDsC. Furthermore, these five functionals yielded excellent agreement to experimentally determined  $\Delta G^{\circ}_{rxn}$  values of the coordination sphere expansion reactions of Os<sup>VIII</sup> oxo/hydroxido monomer reactant species, depicted by equations 3.3 & 3.4 and listed in Tables 3.4 & 3.7, and the thermodynamics of the comproportionation reaction, Table 5.7, which justifies our choice regarding which functionals were selected with which to continue working. Finally, we aim to (iii) revisit the experimentally determined kinetics results and compare the activation energies from Chapter 4 to those obtained here with DFT.

## 6.2 Results and discussion

### 6.2.1 Mechanism of the Os<sup>VI</sup> & Os<sup>VIII</sup> comproportionation reaction

In order to obtain insight w.r.t. the manner in which the [Os<sup>VIII</sup>=O]<sup>2-</sup> or [Os<sup>VIII</sup>=O]<sup>-</sup> reactants could possibly aggregate with [Os<sup>VI</sup>-OH]<sup>2-</sup> to form non-covalent dimers, we analysed the calculated electrostatic surface potentials of the monomer species' equilibrium structures, Figure 6.2. The [Os<sup>VIII</sup>=O]<sup>2-</sup> (a), [Os<sup>VIII</sup>=O]<sup>-</sup> (b) and [Os<sup>VI</sup>-OH]<sup>2-</sup> (c) species' electrostatic surface potentials defined at the 0.03 au electron density isosurface reveals that the negatively charged regions are located at oxo- and hydroxido-ligand oxygens and that the positively charged regions are located at hydroxido-ligand hydrogens. It is therefore conceivable that intermolecular hydrogen bonding interactions between the reactants occur *via* these moieties. Moreover, the electrostatic surface potentials of the osmium reactants in the simulated aqueous phase are not shown here, as they are visibly indistinguishable from those in the gas phase.

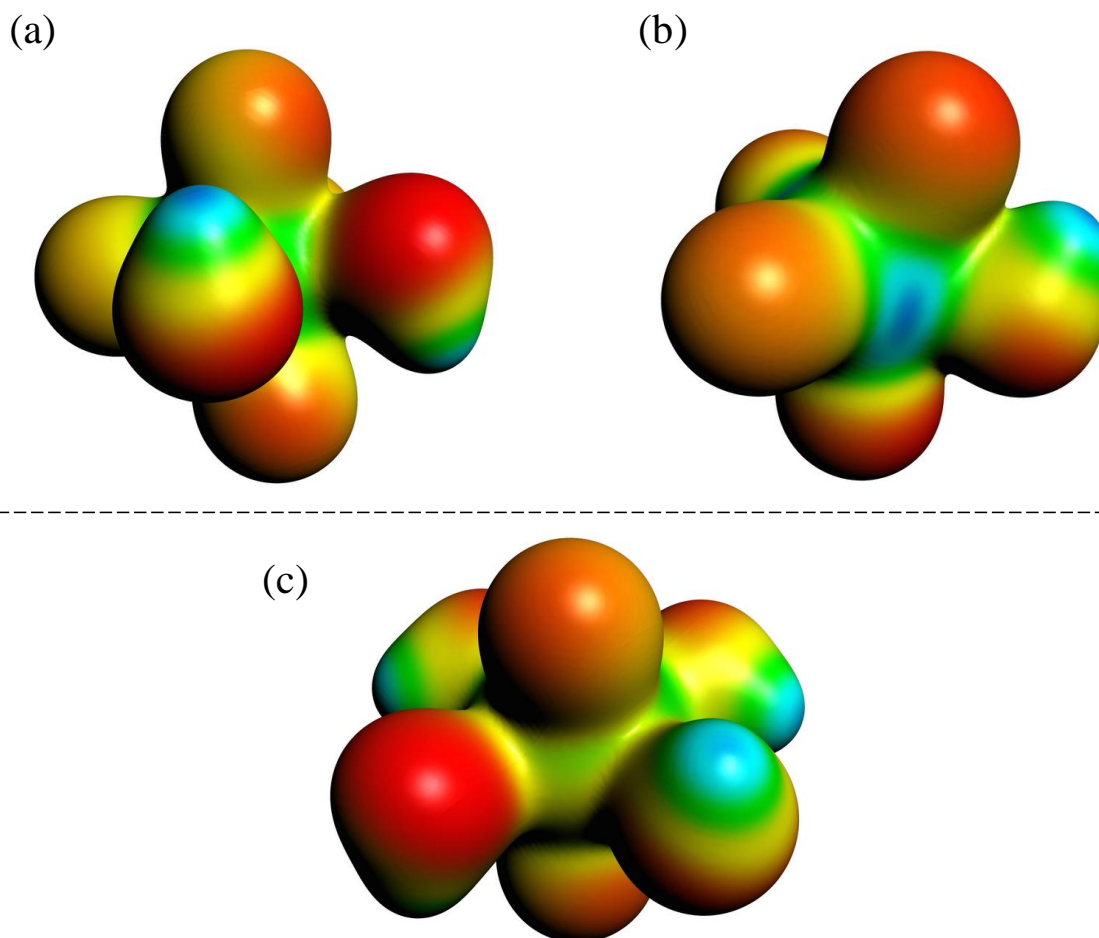


**Figure 6.2.** Electrostatic surface potential maps of the optimised geometries of the  $[\text{Os}^{\text{VIII}}=\text{O}]^{2-}$  (a),  $[\text{Os}^{\text{VIII}}=\text{O}]^{-}$  (b) and  $[\text{Os}^{\text{VI}}-\text{OH}]^{2-}$  (c) species in the gas phase (PBE-D3 functional) corresponding to a density isosurface value of 0.03 au. Negatively and positively charged regions are indicated by red and blue colouring, respectively.

Since a proton of  $[\text{Os}^{\text{VI}}-\text{OH}]^{2-}$  most likely transfers to an O-based lone pair orbital at  $[\text{Os}^{\text{VIII}}=\text{O}]^{2-}$  or  $[\text{Os}^{\text{VIII}}=\text{O}]^{-}$  in the comproportionation reaction (*vide infra*), the initial starting geometries chosen for geometry optimisation calculations were positioned such that a hydroxido-ligand hydrogen of the  $[\text{Os}^{\text{VI}}-\text{OH}]^{2-}$  monomer is aligned towards an oxo ligand of the  $[\text{Os}^{\text{VIII}}=\text{O}]^{2-}$  or  $[\text{Os}^{\text{VIII}}=\text{O}]^{-}$  monomer. Taking the above into consideration, we subsequently performed geometry optimisation calculations of potential quadruply-charged and triply-charged non-covalent dimers in the gas phase. For all functionals used in the study, the distance between the  $\text{Os}^{\text{VIII}}$  and  $\text{Os}^{\text{VI}}$  monomers increased with each successive SCF iteration, most probably due to Coulombic repulsion between the negatively charged monomers, such that they did not converge as ‘stable’ non-covalent dimers. We subsequently repeated the geometry optimisation calculations in a simulated aqueous phase. The information used to initially position the monomers for the calculations proved to be

particularly useful as the geometries of quadruply-charged ( $[\text{Os}^{\text{VIII}}=\text{O}\cdots\text{HO}-\text{Os}^{\text{VI}}]^{4-}$ ) and triply-charged ( $[\text{Os}^{\text{VIII}}=\text{O}\cdots\text{HO}-\text{Os}^{\text{VI}}]^{3-}$ ) non-covalent dimers converged relatively easily, Figure 6.3 (a) and (b), respectively, for all functionals used in the study, *i.e.* with or without dispersion corrections. Subsequent vibrational frequencies analyses confirm that the species are local minima on the PES as no negative frequencies were obtained.

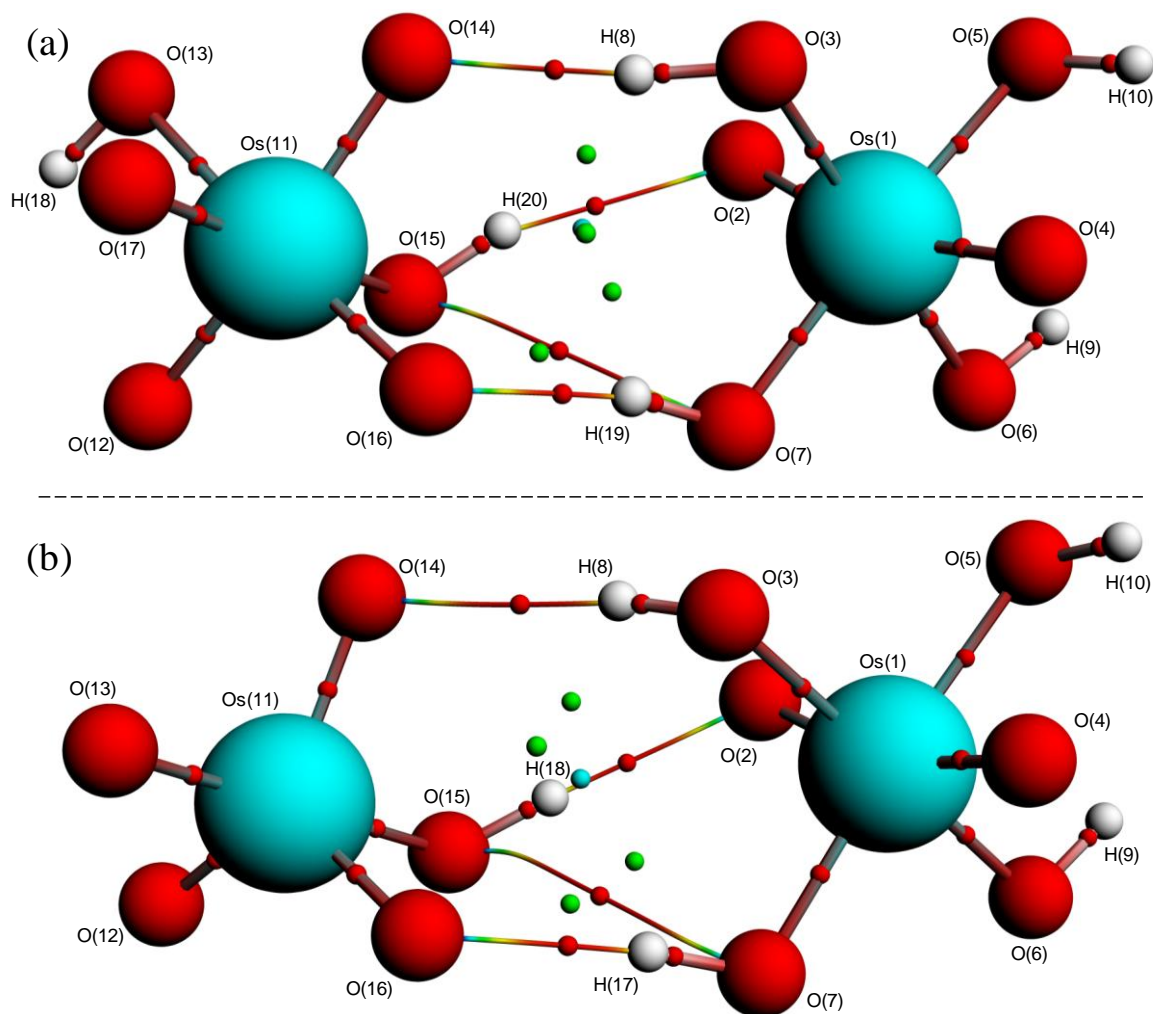


**Figure 6.3.** Molecular graphs of  $[\text{Os}^{\text{VIII}}=\text{O}\cdots\text{HO}-\text{Os}^{\text{VI}}]^{4-}$  (a) and  $[\text{Os}^{\text{VIII}}=\text{O}\cdots\text{HO}-\text{Os}^{\text{VI}}]^{3-}$  (b) in the simulated aqueous phase {PBE-D3(BJ) functional} showing three atomic interaction lines corresponding to intermolecular hydrogen bonds between the monomers. The small red, green and blue spheres represent (3,-1), (3,+1) and (3,+3) critical points, respectively.

The electrostatic surface potential defined at the 0.03 au electron density isosurface of the non-covalent dimers, Figure 6.4, illustrates how the relative charge distribution of the monomers changes when aggregated to one another in the simulated aqueous phase. Due to intermolecular hydrogen bonding interactions (*vide infra*), the charge visibly decreases on the interacting oxygens and correspondingly increases on the interacting hydrogens.

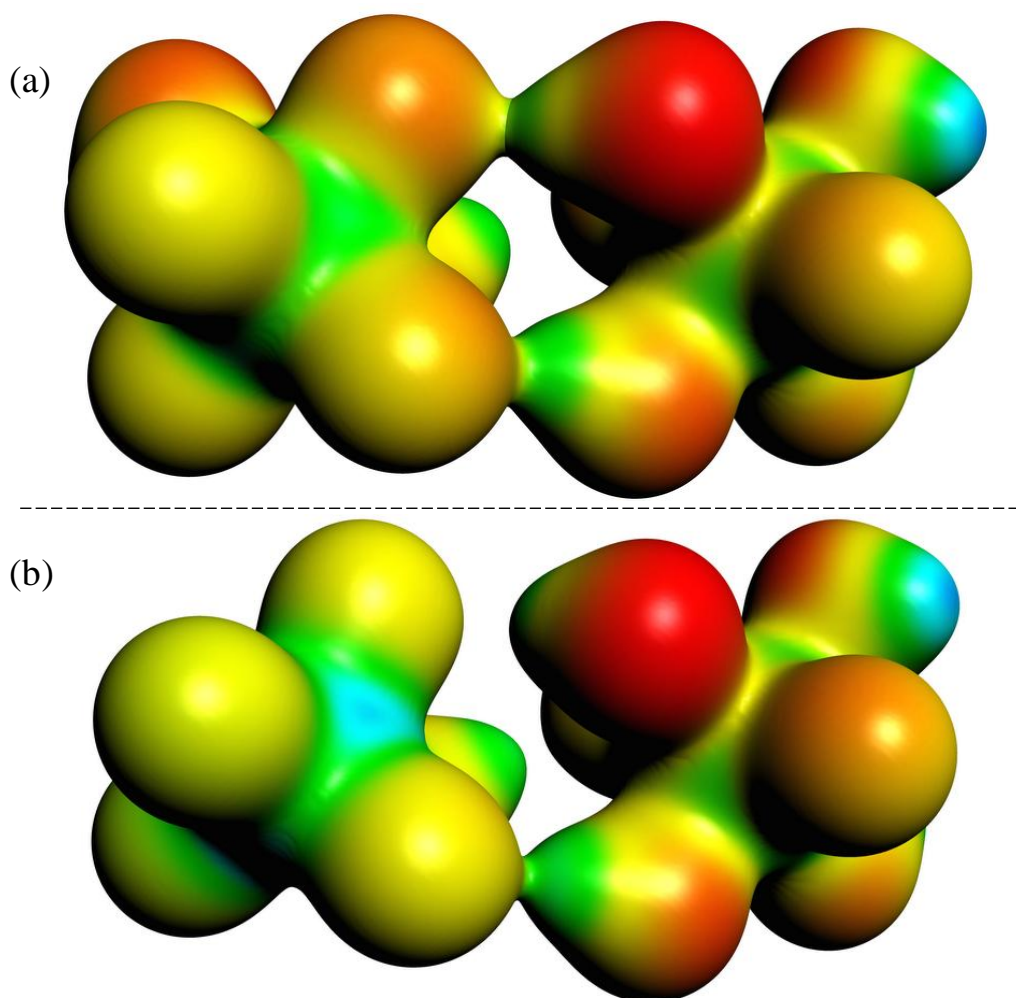


**Figure 6.4.** Electrostatic surface potential maps of the quadruply-charged  $[\text{Os}^{\text{VIII}}=\text{O}\cdots\text{HO}-\text{Os}^{\text{VI}}]^{4-}$  (a) and triply-charged  $[\text{Os}^{\text{VIII}}=\text{O}\cdots\text{HO}-\text{Os}^{\text{VI}}]^{3-}$  (b) non-covalent dimers in the simulated aqueous (PBE-D3 functional) phase corresponding to a density isosurface value of 0.03 au. Negatively and positively charged regions are indicated by red and blue colouring, respectively.

To investigate why the monomers do not aggregate to form non-covalent dimers in the gas phase, we performed a sequence of single-point energy calculations using the equilibrium geometries of the monomers (in the simulated aqueous phase) present in the quadruply-charged  $[\text{Os}^{\text{VIII}}=\text{O}\cdots\text{HO}-\text{Os}^{\text{VI}}]^{4-}$  non-covalent dimer, as a function of the distance between the monomers. This was done in the gas phase as well as in the simulated aqueous phase, Figure 6.5. The distance between the two Os metal centres (abbreviated as ‘ $\text{Os}^{\text{VIII}} - - - \text{Os}^{\text{VI}}$ ’) was selected as the x-axis variable, while the electronic bonding energy, y-axis variable, at a distance of ten angstrom was arbitrarily set to zero.

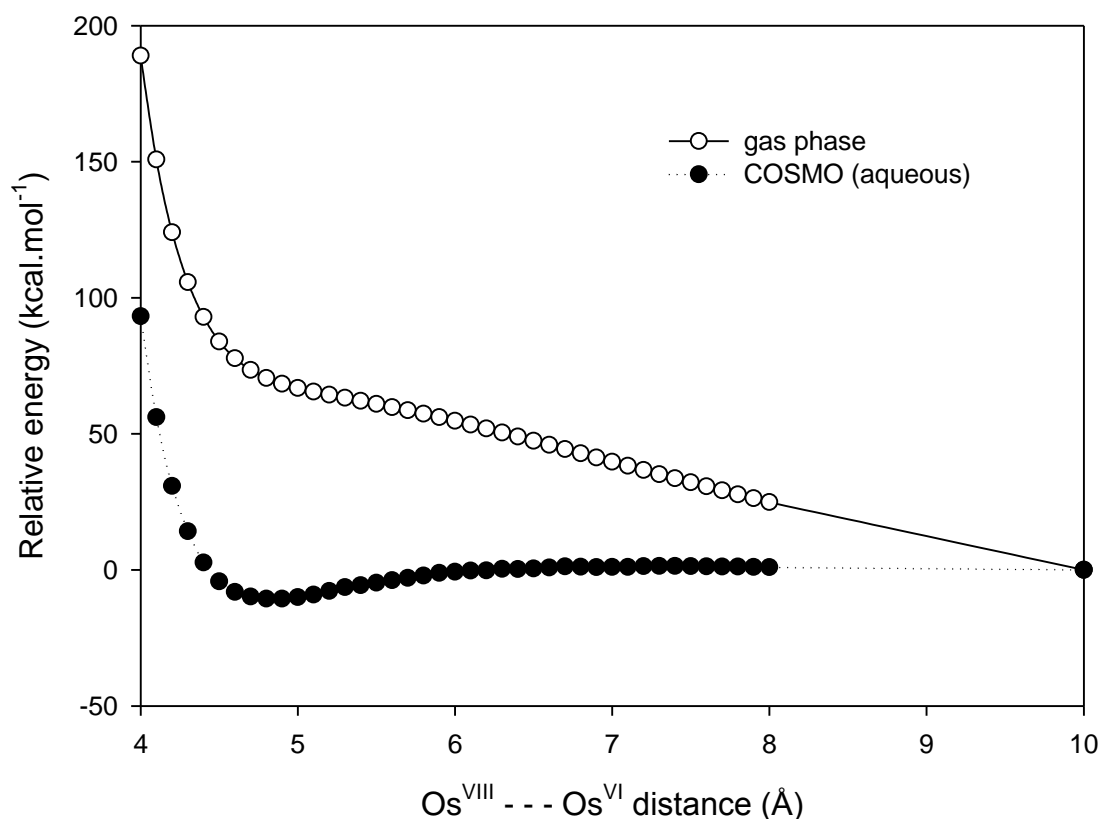


**Figure 6.5.** Relative electronic energy as a function of the distance between the osmium metal centres of *cis*-[Os<sup>VIII</sup>O<sub>4</sub>(OH)<sub>2</sub>]<sup>2-</sup> and *trans*-[Os<sup>VI</sup>O<sub>2</sub>(OH)<sub>4</sub>]<sup>2-</sup> in the gas phase (white) and in the simulated aqueous phase (black) (PBE-D functional).

In the gas phase, Figure 6.5 (white symbols), the electronic energy steadily increases as the two dianions approach one another from a Os<sup>VIII</sup> - - - Os<sup>VI</sup> distance of ten angstrom, down to approximately four and a half angstrom, followed by a sharp increase in electronic energy at even shorter distances. This sharp increase in energy clearly illustrates the relatively large Coulombic repulsion that exists between the negatively charged reactants when at close proximity to one another. It is reasonable to conclude from these computational results that comproportionation of Os<sup>VI</sup> and Os<sup>VIII</sup> does not occur in the gas phase. In contrast to the gas phase results, the monomer reactants form stable non-covalent dimers at an Os<sup>VIII</sup> - - - Os<sup>VI</sup> distance of approximately 4.80 Å (PBE-D functional) in the simulated aqueous phase, Figure 6.5 (black symbols). The local energy minimum on the PES is due to the solvation (hydration) energy contribution of the non-covalent dimer (-670.68 kcal.mol<sup>-1</sup>), which is larger than the combined hydration energies of the *cis*-[Os<sup>VIII</sup>O<sub>4</sub>(OH)<sub>2</sub>]<sup>2-</sup> (-219.68 kcal.mol<sup>-1</sup>) and *trans*-[Os<sup>VI</sup>O<sub>2</sub>(OH)<sub>4</sub>]<sup>2-</sup> (-222.36 kcal.mol<sup>-1</sup>) species (-442.04 kcal.mol<sup>-1</sup>), *i.e.* the solvation energy is 228.64 kcal.mol<sup>-1</sup> lower for the non-covalent dimer than for the sum of the monomers. The total bonding energy is therefore more favourable, resulting in a local energy minimum on

the PES. The intermolecular hydrogen bonding interactions (*vide infra*) between the monomers will also lower the total bonding energy but is not enough to overcome the large Coulombic repulsion or else a non-covalent dimer would have been found in the gas phase. Moreover, the electric polarisation field of the (aqueous) solvent for the equilibrium geometry of  $[\text{Os}^{\text{VIII}}=\text{O}\cdots\text{HO}-\text{Os}^{\text{VI}}]^{4-}$ , shown in Figure 6.6 at the 0.03 au electron density isosurface, ‘stretches’ over the entire non-covalent dimer and not simply over the two monomers separately. To our knowledge, there are two reports where a similar feature has been observed. Grimme and Djukic<sup>9</sup> utilised COSMO when they investigated cation-cation interactions between rhodium complexes (PBE-D3 functional) and report that dispersion drives the formation of a stable dimer in solution to overcome the Coulombic repulsion. Likewise, Groenewald<sup>10</sup> reported that stable  $\text{I}_3^- \cdots \text{I}_3^-$  dimers do not form in the absence of an adequate, favourable solvation energy contribution, concluding that a dielectric constant value of approximately 10 or more is necessary to obtain an equilibrium geometry.

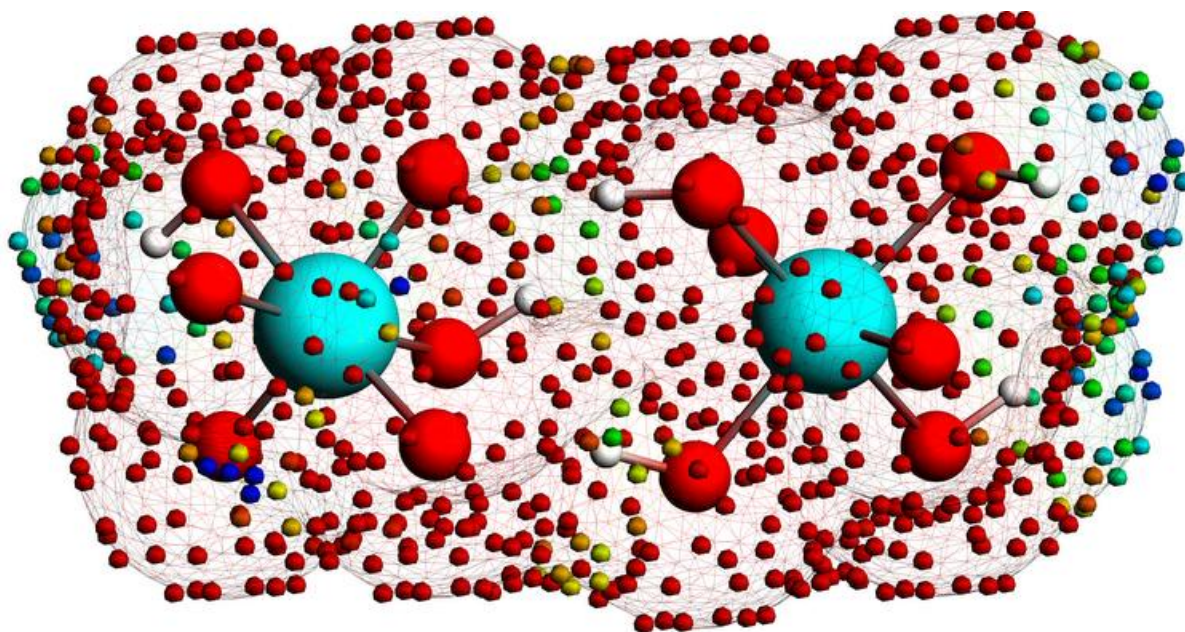


**Figure 6.6.** Electric polarisation field of the simulated aqueous phase (COSMO) surrounding the equilibrium geometry of  $[\text{Os}^{\text{VIII}}=\text{O}\cdots\text{HO}-\text{Os}^{\text{VI}}]^{4-}$  (PBE-D3 functional) corresponding to a density isosurface value of 0.03 au. Negatively and positively charged regions are indicated by blue and red colouring, respectively.

In order to further investigate the extent to which the solvation energy (COSMO) overcomes the Coulombic repulsion component between the  $[\text{Os}^{\text{VI}}-\text{OH}]^{2-}$  and  $[\text{Os}^{\text{VIII}}=\text{O}]^{2-}$  or  $[\text{Os}^{\text{VIII}}=\text{O}]^-$  anions, a series of geometry optimisation calculations of the non-covalent dimers were done in various solvents and hence differing in dielectric constant, Figures 6.7 and 6.8. Non-covalent dimer formation is favourable even at a relatively low dielectric constant value of



4.8 (chloroform) and regardless of whether dispersion corrections are included. Moreover, EDA calculations<sup>11,12</sup> of the equilibrium geometries were subsequently done in order to quantify specifically how the relative interaction energies between fragments Q and P (Q = *cis*-[Os<sup>VIII</sup>O<sub>4</sub>(OH)<sub>2</sub>]<sup>2-</sup> or [Os<sup>VIII</sup>O<sub>4</sub>(OH)]<sup>-</sup>, P = *trans*-[Os<sup>VI</sup>O<sub>2</sub>(OH)<sub>4</sub>]<sup>2-</sup>) changes as a function of the dielectric constant, Tables A.6 & A.7. For higher dielectric constant values, the solvation energy term is more negative in magnitude (contributing towards favourable interaction energy between the anions). The intermolecular oxygen to hydrogen bonding distances decrease slightly at higher dielectric constant values. The trends obtained confirm that solvation energy drives the formation of a stable dimer to overcome the Coulombic repulsion. Dispersion further contributes towards the stabilities (*vide infra*) of the non-covalent dimers but is not the primary contributing factor in promoting favourable interaction energy between the anions. To further illustrate this point, we plotted the three following trends separately as a function of the dielectric constant:  $\Delta E_{int}$ ,  $\Delta E_{solv}$  and  $\Delta E_{int} - \Delta E_{solv}$ , Figures 6.7 and 6.8. In the absence of the solvation energy term, corresponding to the interaction energy minus solvation energy alone, *i.e.*  $\Delta E_{Pauli} + \Delta E_{elstat} + \Delta E_{orb} + \Delta E_{disp}$ , yields a positive value for all dielectric constant values. Therefore, the sum of these contributions is not sufficient to facilitate aggregation.

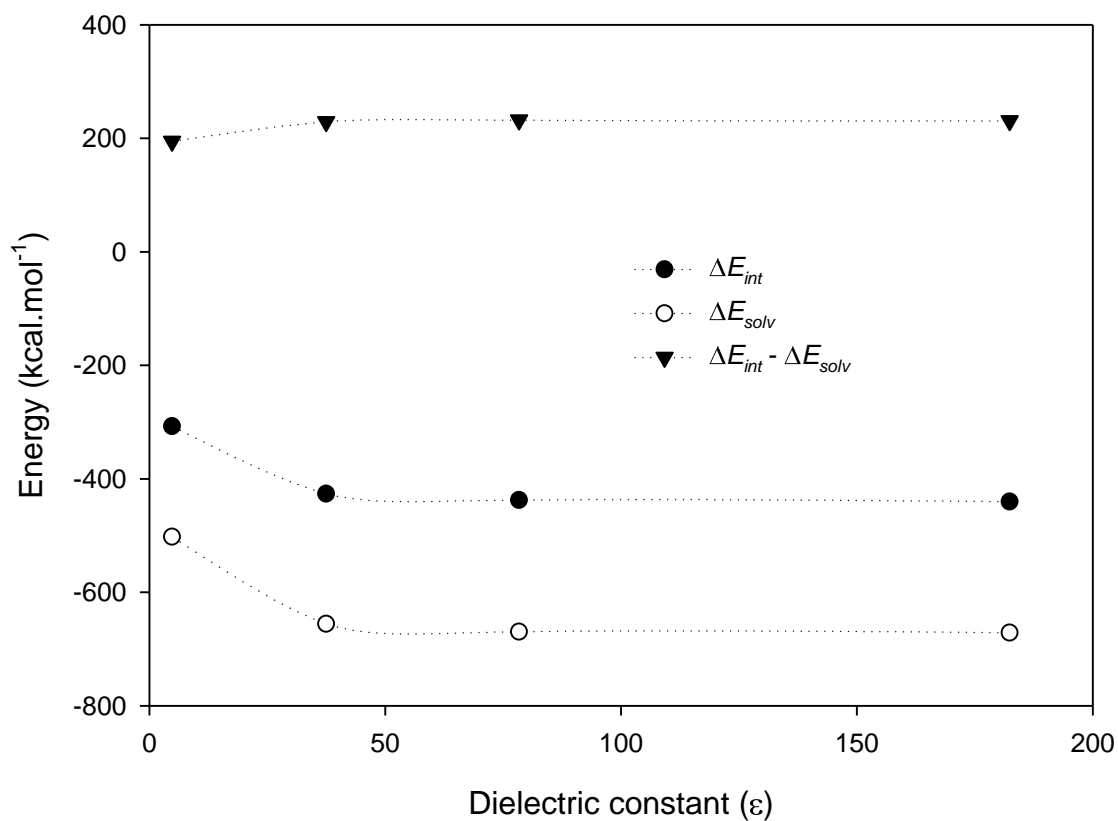


**Figure 6.7.** Interaction and solvation energies for  $[\text{Os}^{\text{VIII}}=\text{O}\cdots\text{HO-Os}^{\text{VI}}]^{4+}$  in various solvents: chloroform, acetonitrile, water and *n*-methyl-formamide with the PBE-D3 functional.

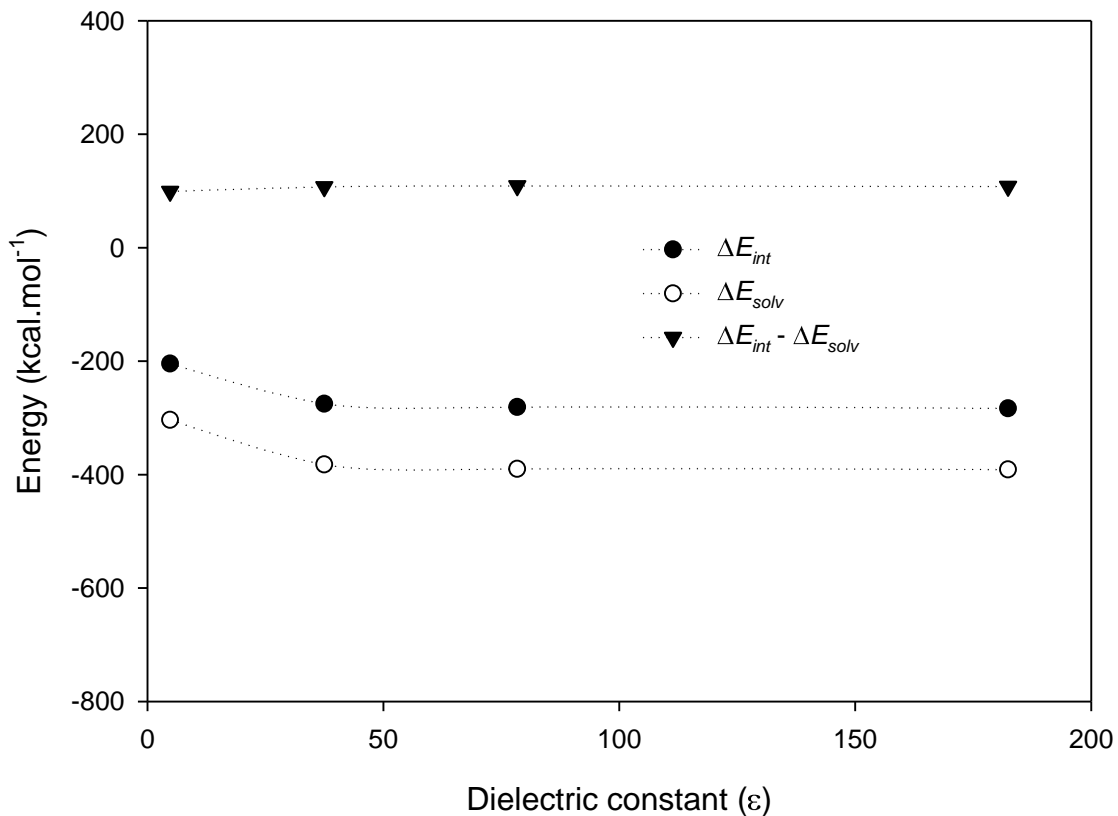


**Figure 6.8.** Interaction and solvation energies for  $[\text{Os}^{\text{VIII}}=\text{O}\cdots\text{HO-Os}^{\text{VI}}]^{3-}$  in various solvents: chloroform, acetonitrile, water and *n*-methyl-formamide with the PBE-D3 functional.

Investigation of the extent of possible aggregation in the dielectric constant range between 0 and 4.8 will not contribute to the theme of this study and was therefore not done.

The equilibrium geometries of the non-covalent dimers (in the simulated aqueous phase) are notably influenced by the inclusion of dispersion corrections. In the absence of dispersion corrections, *i.e.* PBE, the intermolecular oxygen to hydrogen distances, corresponding to hydrogen bonding interactions (*vide infra*), are approximately 0.08 Å longer whilst PBE-D yields the shortest distances, Table 6.1.

**Table 6.1. Intermolecular hydrogen bonding distances of  $[\text{Os}^{\text{VIII}}=\text{O}\cdots\text{HO}-\text{Os}^{\text{VI}}]^{4-}$  and  $[\text{Os}^{\text{VIII}}=\text{O}\cdots\text{HO}-\text{Os}^{\text{VI}}]^{3-}$  in the simulated aqueous phase (Å).**

Functional	$[\text{Os}^{\text{VIII}}=\text{O}\cdots\text{HO}-\text{Os}^{\text{VI}}]^{4-}$			$[\text{Os}^{\text{VIII}}=\text{O}\cdots\text{HO}-\text{Os}^{\text{VI}}]^{3-}$		
	O(16)-H(19)	O(14)-H(8)	O(2)-H(20)	O(16)-H(17)	O(14)-H(8)	O(2)-H(18)
PBE	1.808	1.831	2.261	1.827	2.128	1.983
PBE-D	1.724	1.762	2.148	1.750	2.045	1.878
PBE-D3	1.751	1.783	2.169	1.828	2.121	1.967
PBE-D3(BJ)	1.763	1.805	2.179	1.798	2.088	1.937
PBE-dDsC	1.722	1.767	2.164	1.792	2.094	1.940

The inclusion of dispersion corrections brings the monomers closer to one another and we anticipate that this will influence the interaction energies of the non-covalent dimers, electron densities at the BCPs and the intermolecular hydrogen bonding interactions. To characterise the possible intermolecular bonding interactions between the monomers, we performed a topological analysis of the electron density according to the quantum theory of atoms in molecules (QTAIM)<sup>13,14</sup> with and without the inclusion of dispersion corrections. The molecular graphs of  $[\text{Os}^{\text{VIII}}=\text{O}\cdots\text{HO}-\text{Os}^{\text{VI}}]^{4-}$  and  $[\text{Os}^{\text{VIII}}=\text{O}\cdots\text{HO}-\text{Os}^{\text{VI}}]^{3-}$ , Figures 6.3 {PBE-D3(BJ)} and 6.9 (PBE), (a) and (b), respectively, display the various critical points and atomic interaction lines that were obtained from QTAIM analysis using these two functionals.

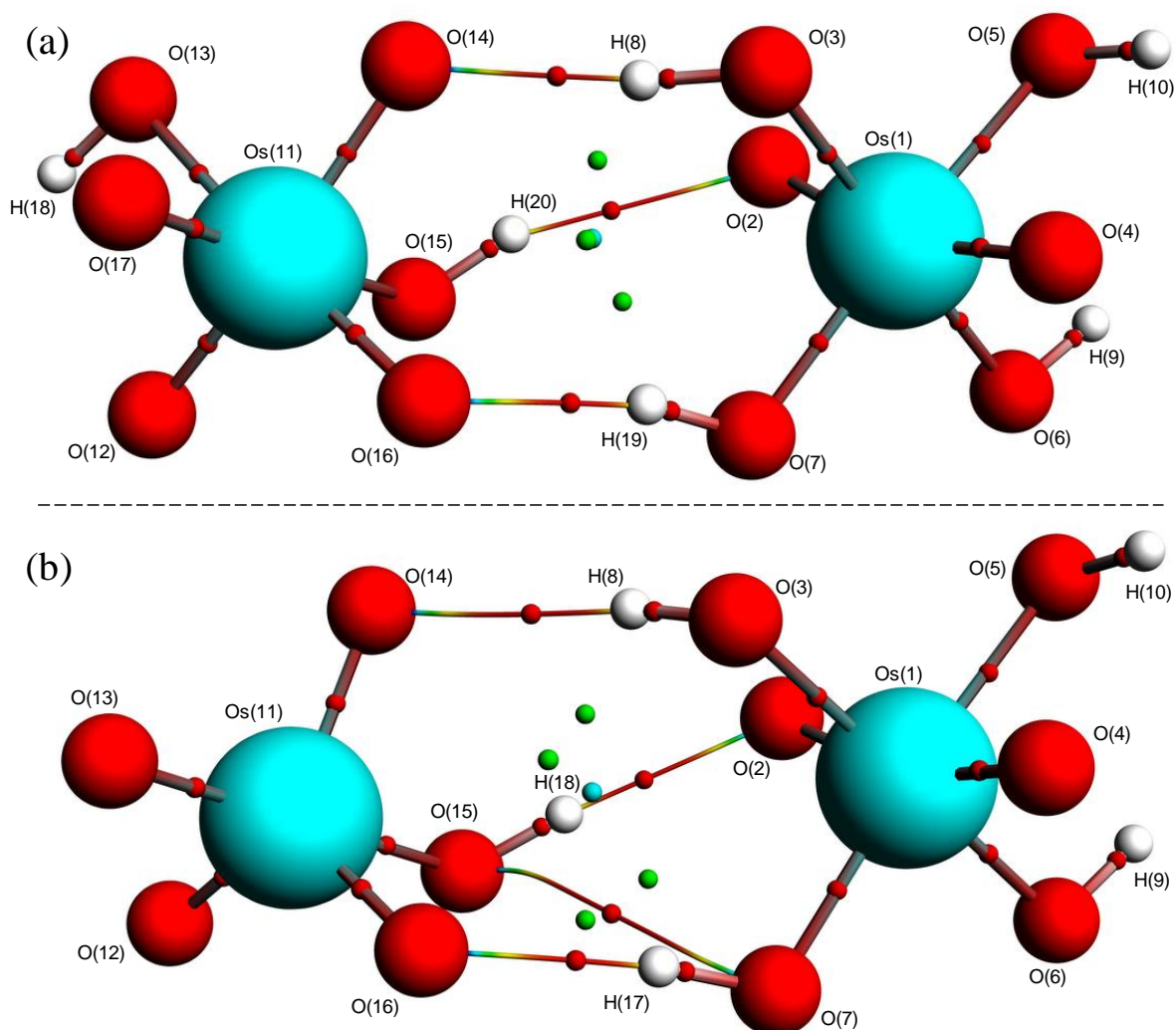


**Figure 6.9.** Molecular graphs of the quadruply-charged  $[\text{Os}^{\text{VIII}}=\text{O}\cdots\text{HO}-\text{Os}^{\text{VI}}]^4-$  (a) and triply-charged  $[\text{Os}^{\text{VIII}}=\text{O}\cdots\text{HO}-\text{Os}^{\text{VI}}]^3-$  (b) non-covalent dimers in the simulated aqueous phase (PBE functional) showing three atomic interaction lines corresponding to intermolecular hydrogen bonds between the monomers. The small red, green and blue spheres represent (3,-1), (3,+1) and (3,+3) critical points, respectively.

The calculated BCP electron density topology indices of the intermolecular atomic interaction lines (AILs) of  $[\text{Os}^{\text{VIII}}=\text{O}\cdots\text{HO}-\text{Os}^{\text{VI}}]^4-$  are listed in Table 6.2. The Laplacian at all the intermolecular BCPs, regardless of whether dispersion corrections are included, are small positive values, at approximately 0.04 (PBE) and 0.05 {PBE-D3(BJ)} for O(2)-H(20) and approximately 0.09 (PBE) and 0.10 {PBE-D3(BJ)} for H(8)-O(14) and O(16)-H(19). Moreover, the  $G_b/\rho_b$  ratio is always less than unity, ranging between approximately 0.73 and 0.77 while the  $E_b^e$  values are close to zero, from -0.004 to 0.001. Collectively, the QTAIM indices confirm that the two octahedral  $\text{Os}^{\text{VI}}$  and  $\text{Os}^{\text{VIII}}$  reactants aggregate to form non-covalent dimers *via* van der Waals, hydrogen bonding interactions. QTAIM analyses indicate the presence of three intermolecular hydrogen bonding interactions in  $[\text{Os}^{\text{VIII}}=\text{O}\cdots\text{HO}-\text{Os}^{\text{VI}}]^4-$ .

Furthermore, analysis with PBE-D3(BJ) indicates the presence of a fourth intermolecular AIL between O(7) and O(15) which is absent for the analysis done with PBE (*i.e.* without dispersion). This feature is likely because the monomers are approximately 0.08 Å closer to one another when dispersion corrections are included. As anticipated,  $\rho_b$  is greatest at the BCP between O(16) and H(19), which corresponds with the shortest interatomic distance of the three intermolecular hydrogen bonding interactions.

**Table 6.2. QTAIM indices computed at the BCPs at intermolecular AILs of quadruply-charged  $[\text{Os}^{\text{VIII}}=\text{O}\cdots\text{HO}-\text{Os}^{\text{VI}}]^{4+}$  in the simulated aqueous phase. All values are expressed in atomic units.**

Functional	Atoms	$\lambda_1$	$\lambda_2$	$\lambda_3$	$\rho_b$	$\nabla^2\rho_b$	$G_b$	$G_b/\rho_b$	$V_b$	$E_b^c$
PBE	H(8)-O(14)	-0.0500	-0.0492	0.1905	0.0340	0.0913	0.0259	0.7607	-0.0289	-0.0030
	O(2)-H(20)	-0.0134	-0.0128	0.0684	0.0127	0.0422	0.0092	0.7260	-0.0079	0.0013
	O(16)-H(19)	-0.0564	-0.0559	0.2032	0.0367	0.0910	0.0270	0.7342	-0.0311	-0.0042
PBE-D3(BJ)	H(8)-O(14)	-0.0542	-0.0535	0.2036	0.0362	0.0960	0.0277	0.7650	-0.0313	-0.0037
	O(2)-H(20)	-0.0172	-0.0162	0.0827	0.0153	0.0492	0.0113	0.7360	-0.0102	0.0010
	O(16)-H(19)	-0.0652	-0.0645	0.2270	0.0409	0.0973	0.0300	0.7340	-0.0357	-0.0057
	O(7)-O(15)	-0.0053	-0.0021	0.0399	0.0083	0.0326	0.0065	0.7824	-0.0048	0.0017

The QTAIM values obtained at intermolecular hydrogen bonding BCPs in  $[\text{Os}^{\text{VIII}}=\text{O}\cdots\text{HO}-\text{Os}^{\text{VI}}]^{3-}$ , Table 6.3, are similar in magnitude to those in  $[\text{Os}^{\text{VIII}}=\text{O}\cdots\text{HO}-\text{Os}^{\text{VI}}]^{4+}$ . The Laplacian at all the intermolecular hydrogen bonding interactions' BCPs are small positive values, at approximately 0.07 for O(2)-H(18), approximately 0.06 for H(8)-O(14) and approximately 0.09 for O(16)-H(17). The  $G_b/\rho_b$  ratio is always less than unity, ranging between approximately 0.72 and 0.76 while the  $E_b^c$  values are approximately equal to zero, from -0.04 to 0.002. The intermolecular bonding interactions can be classified as van der Waals, hydrogen bonding. In contrast to  $[\text{Os}^{\text{VIII}}=\text{O}\cdots\text{HO}-\text{Os}^{\text{VI}}]^{4+}$ ,  $[\text{Os}^{\text{VIII}}=\text{O}\cdots\text{HO}-\text{Os}^{\text{VI}}]^{3-}$  has an AIL between two oxo ligands of the monomers, O(7) and O(15), for both PBE and PBE-D3(BJ) functionals. It is evident from Table 6.1 that dispersion corrections have a much smaller influence on how far apart the monomers are from one another compared to when just PBE, *i.e.* with dispersion corrections, is used. Lastly,  $\rho_b$  is greatest at the BCP between O(16) and H(19), which corresponds with the shortest interatomic distance of the three intermolecular hydrogen bonding interactions.

**Table 6.3. QTAIM indices computed at the BCPs at intermolecular AILs of triply-charged  $[\text{Os}^{\text{VIII}}=\text{O}\cdots\text{HO}-\text{Os}^{\text{VI}}]^{3-}$  in the simulated aqueous phase. All values are expressed in atomic units.**

Functional	Atoms	$\lambda_1$	$\lambda_2$	$\lambda_3$	$\rho_b$	$\nabla^2\rho_b$	$G_b$	$G_b/\rho_b$	$V_b$	$E_b^e$
PBE	H8 - O14	-0.0203	-0.0194	0.0952	0.0173	0.0555	0.0130	0.7536	-0.0122	0.0008
	O2 - H18	-0.0308	-0.0298	0.1291	0.0237	0.0685	0.0176	0.7452	-0.0181	-0.0005
	O16 - H17	-0.0530	-0.0523	0.1918	0.0346	0.0866	0.0251	0.7245	-0.0286	-0.0035
	O7 - O15	-0.0042	-0.0009	0.0328	0.0072	0.0277	0.0055	0.7638	-0.0040	0.0015
PBE-D3(BJ)	H8 - O14	-0.0229	-0.0218	0.1044	0.0190	0.0597	0.0144	0.7587	-0.0138	0.0006
	O2 - H18	-0.0355	-0.0343	0.1446	0.0263	0.0748	0.0198	0.7511	-0.0208	-0.0011
	O16 - H17	-0.0583	-0.0574	0.2065	0.0372	0.0908	0.0270	0.7262	-0.0313	-0.0043
	O7 - O15	-0.0046	-0.0011	0.0355	0.0076	0.0298	0.0059	0.7749	-0.0043	0.0016

The ET part of EPT is induced by an electrostatic perturbation between electron donor and acceptor  $d\pi$  orbitals.<sup>2</sup> In order to potentially identify this feature visually, we used the extended transition state (ETS) method combined with natural orbitals for the chemical valence (NOCV) theory, for the quadruply-charged and triply-charged non-covalent dimers.<sup>15</sup> With ETS-NOCV analysis individual contributions to the total bonding energy are calculated for each specific orbital interaction between fragments Q and P (Q =  $[\text{Os}^{\text{VIII}}=\text{O}]^{2-}$  or  $[\text{Os}^{\text{VIII}}=\text{O}]^-$ , P =  $[\text{Os}^{\text{VI}}-\text{OH}]^{2-}$ ). ETS-NOCV has been used to yield the contributions from the different natural orbitals (constructed from the fragment orbitals) to the total orbital contribution. The natural orbitals with the largest contribution to the non-covalent dimers in the simulated aqueous phase are shown in Figure 6.10.

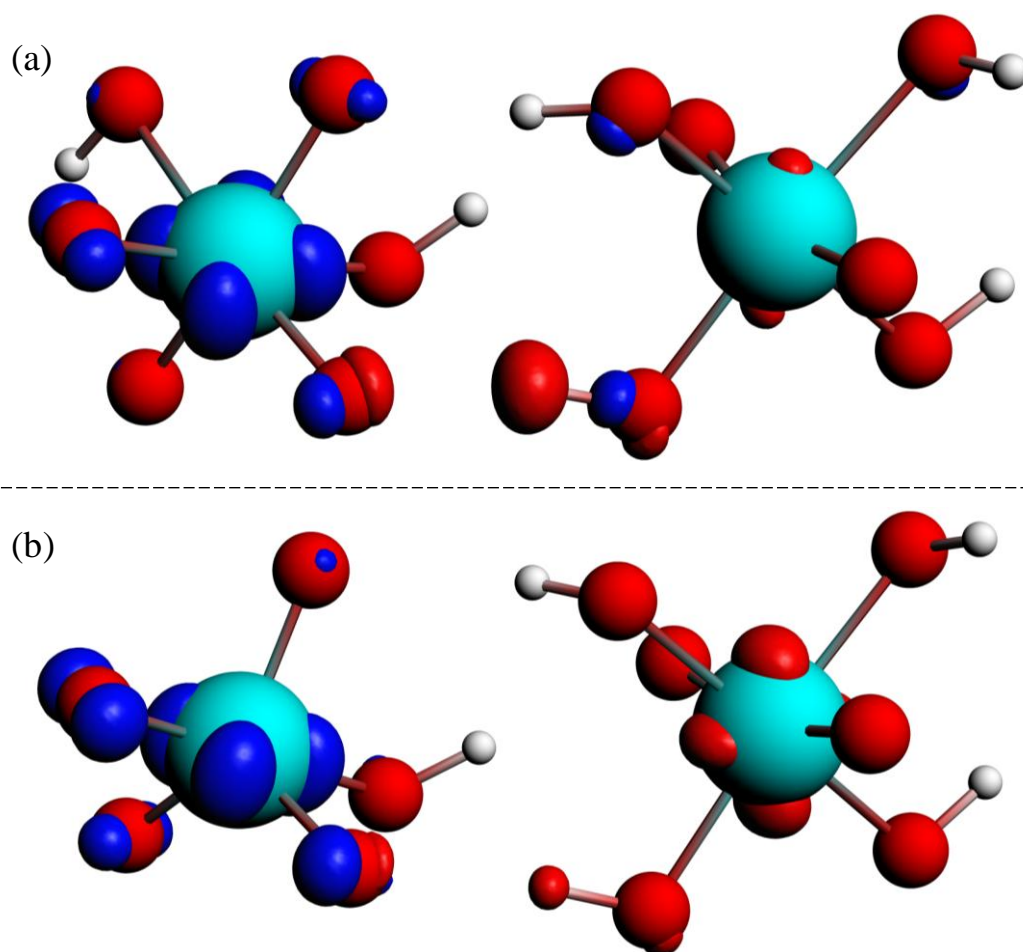


**Figure 6.10.** Highest energy deformation density channels in the quadruply-charged (a) and triply-charged (b) non-covalent dimers indicating local electron density depletion (red colouring) at the  $d\pi$ -orbitals of  $[\text{Os}^{\text{VI}}=\text{O}]^{2-}$  and local electron density accumulation (blue colouring) at the  $d\pi$ -orbitals of  $[\text{Os}^{\text{VIII}}-\text{OH}]^{2-}$  (a) and  $[\text{Os}^{\text{VIII}}-\text{OH}]^{-}$  (b). (PBE-D3 functional).

The highest deformation density channel, as calculated for both non-covalent dimers, is between the  $d\pi$ -orbitals of the donor and acceptor fragments and contributes approximately 53% ( $-8.04 \text{ kcal.mol}^{-1}$ ) in  $[\text{Os}^{\text{VIII}}=\text{O}\cdots\text{HO}-\text{Os}^{\text{VI}}]^{4-}$  and 80% ( $-13.14 \text{ kcal.mol}^{-1}$ ) in  $[\text{Os}^{\text{VIII}}=\text{O}\cdots\text{HO}-\text{Os}^{\text{VI}}]^{3-}$  (PBE-D3 functional), respectively, to the total orbital contribution. EDA calculations of the non-covalent dimers yield that the electrostatic contributions are large positive values, most probably due to the relatively large Coulombic repulsion that exists between the negatively charged reactants when at close proximity to one another. It is more than double the magnitude in the case of the quadruply-charged non-covalent dimer (the sum of two dianions) compared to the triply-charged non-covalent dimer (the sum of an anion and a dianion). When the quadruply-charged or triply-charged non-covalent dimers were submitted for geometry optimisation calculations in the gas phase, the two monomers moved progressively further and further apart from one another after each successive SCF

iteration and eventually did not converge as stable non-covalent dimers. The energies calculated from EDA provide a possible explanation for that result, *i.e.* the greatest contribution to the total bonding energies of the non-covalent dimers are those of the solvation (hydration) energies. The interaction energy minus solvation energy alone, *i.e.*  $\Delta E_{Pauli} + \Delta E_{elstat} + \Delta E_{orb} + \Delta E_{disp}$ , is positive, and therefore the sum of these contributions is not sufficient to facilitate aggregation. Noteworthy is the  $\Delta E_{solv}$  for the  $[\text{Os}^{\text{VIII}}=\text{O}\cdots\text{HO}-\text{Os}^{\text{VI}}]^{4-}$  non-covalent dimer, which is almost twice that of the  $[\text{Os}^{\text{VIII}}=\text{O}\cdots\text{HO}-\text{Os}^{\text{VI}}]^{3-}$  non-covalent dimer; this is the main reason why  $\Delta E_{int}$  for the  $[\text{Os}^{\text{VIII}}=\text{O}\cdots\text{HO}-\text{Os}^{\text{VI}}]^{4-}$  non-covalent dimer is approximately  $160 \text{ kcal.mol}^{-1}$  more favourable in comparison with the  $[\text{Os}^{\text{VIII}}=\text{O}\cdots\text{HO}-\text{Os}^{\text{VI}}]^{3-}$  non-covalent dimer. Moreover, when dispersion is included the monomers are closer to one another, leading to a higher charge density, as the van der Waals volume decreases. This, in turn, results in higher solvation energies of the non-covalent dimers, more so for the  $[\text{Os}^{\text{VIII}}=\text{O}\cdots\text{HO}-\text{Os}^{\text{VI}}]^{4-}$  non-covalent dimer than for the  $[\text{Os}^{\text{VIII}}=\text{O}\cdots\text{HO}-\text{Os}^{\text{VI}}]^{3-}$  non-covalent dimer, which is also reflected by the intermolecular hydrogen bonding distances, Table 6.1.

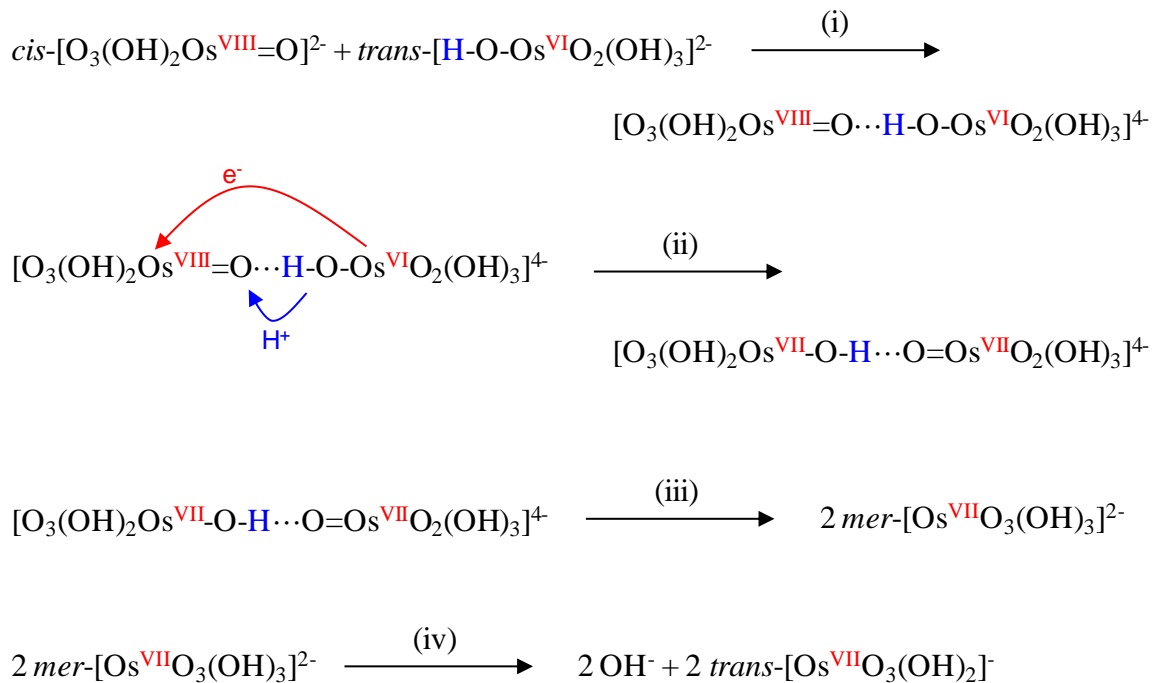
**Table 6.4.** Energy decomposition analysis (EDA,  $\text{kcal.mol}^{-1}$ ) of the intermolecular interactions in the non-covalent dimers in the simulated aqueous phase. All energies are with respect to the isolated fragments.

Non-covalent dimer	Functional	$\Delta E_{int}$	$\Delta E_{Pauli}$	$\Delta E_{elstat}$	$\Delta E_{orb}$	$\Delta E_{disp}$	$\Delta E_{solv}$	$\Delta E_{prep}$	$-D_e$
$[\text{Os}^{\text{VIII}}=\text{O}\cdots\text{HO}-\text{Os}^{\text{VI}}]^{4-}$	PBE	-433.10	45.69	199.17	-11.43	0.00	-666.53	7.41	-425.69
	PBE-D	-440.61	62.82	192.04	-17.54	-7.42	-670.51	7.68	-432.93
	PBE-D3	-437.39	55.97	195.16	-15.11	-3.97	-669.44	8.02	-429.37
	PBE-D3(BJ)	-435.67	53.43	197.66	-14.36	-3.59	-668.81	7.22	-428.45
	PBE-dDsC	-435.59	59.89	193.64	-16.67	-2.36	-670.09	8.02	-427.57
$[\text{Os}^{\text{VIII}}=\text{O}\cdots\text{HO}-\text{Os}^{\text{VI}}]^{3-}$	PBE	-277.06	41.04	87.75	-16.17	0.00	-389.68	3.85	-273.21
	PBE-D	-284.78	52.60	82.83	-20.53	-7.74	-391.94	3.07	-281.71
	PBE-D3	-281.06	41.67	87.77	-16.36	-4.17	-389.97	3.50	-277.56
	PBE-D3(BJ)	-280.68	45.49	85.76	-18.01	-3.75	-390.17	3.95	-276.73
	PBE-dDsC	-279.44	46.08	85.31	-18.23	-2.31	-390.29	3.60	-275.84

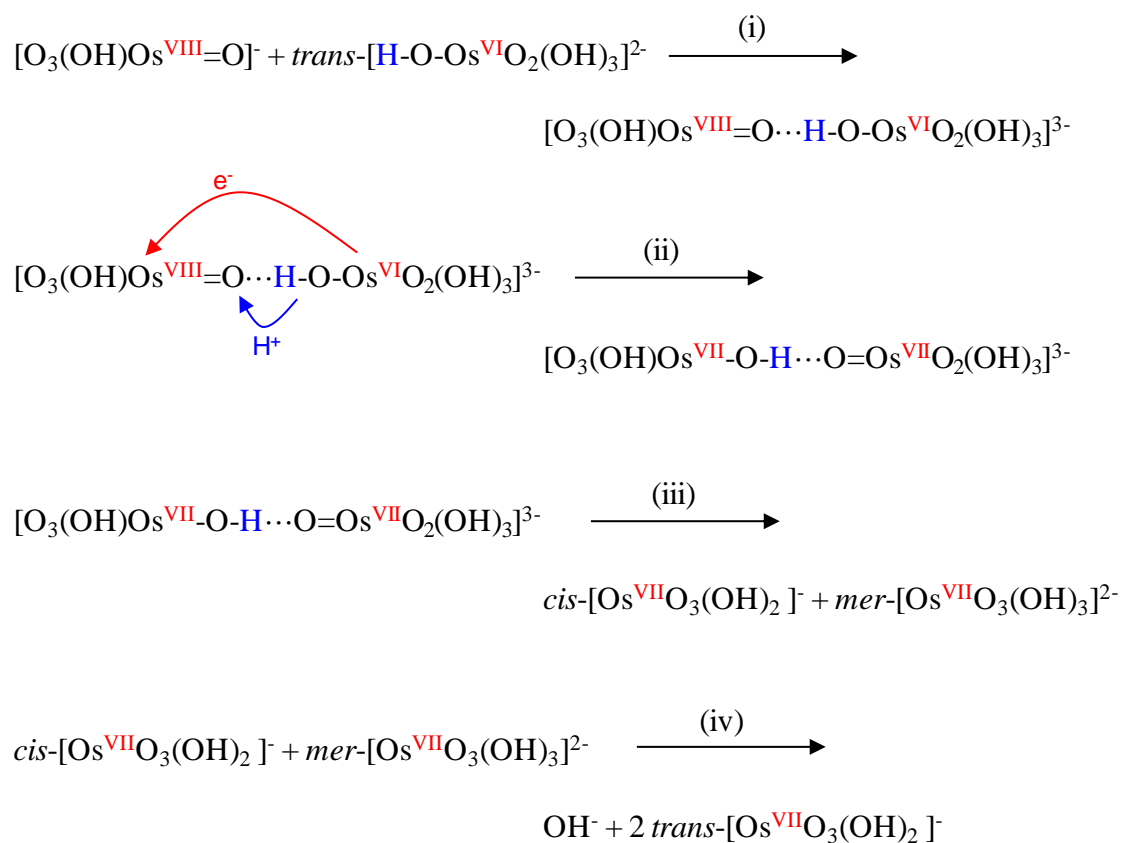
The dispersion energy contribution to the total interaction energy is relatively small compared to  $\Delta E_{solv}$  and  $\Delta E_{orb}$ . The PBE-D functional yields almost twice the  $\Delta E_{disp}$  compared to the other functional's  $\Delta E_{disp}$  as a result of the intermolecular hydrogen bonding distances being the shortest, Table 6.1, and is most probably an overestimation. Furthermore, the  $\Delta E_{orb}$  increases by approximately 46% for the  $[\text{Os}^{\text{VIII}}=\text{O}\cdots\text{HO}-\text{Os}^{\text{VI}}]^{4-}$  compared to only 13% for the  $[\text{Os}^{\text{VIII}}=\text{O}\cdots\text{HO}-\text{Os}^{\text{VI}}]^{3-}$  which is again reflected by the intermolecular hydrogen bonding distances, Table 6.1.



We propose that the first step of the comproportionation reaction consists of the formation of the  $[\text{Os}^{\text{VIII}}=\text{O}\cdots\text{HO}-\text{Os}^{\text{VI}}]^{4-}$  non-covalent dimer, Scheme 6.2 (i), or the formation of the  $[\text{Os}^{\text{VIII}}=\text{O}\cdots\text{HO}-\text{Os}^{\text{VI}}]^{3-}$  non-covalent dimer, Scheme 6.3 (i).



**Scheme 6.2.** Proposed multi-step comproportionation reaction mechanism of  $\text{trans-}[\text{Os}^{\text{VI}}\text{O}_2(\text{OH})_4]^{2-}$  and  $\text{cis-}[\text{Os}^{\text{VIII}}\text{O}_4(\text{OH})_2]^{2-}$  via EPT ('six-coordinate' pathway).



**Scheme 6.3.** Proposed multi-step comproportionation reaction mechanism of  $\text{trans-}[\text{Os}^{\text{VI}}\text{O}_2(\text{OH})_4]^{2-}$  and  $[\text{Os}^{\text{VIII}}\text{O}_4(\text{OH})]^-$  via EPT ('five-coordinate' pathway).

### Basis set superposition error (BSSE) considerations w.r.t. the non-covalent dimers

In order to provide evidence that the DFT-calculated equilibrium geometries of the non-covalent dimer are not spurious data points, *i.e.* artefacts, due to artificial stabilisation of basis function overlap between the  $\text{Os}^{\text{VIII}}$  and  $\text{Os}^{\text{VI}}$  monomers, also known as basis set superposition errors (BSSEs), a modified method to calculate counterpoise corrected energies, based on the method proposed by Boys and Bernardi,<sup>16</sup> was done. If stable non-covalent dimers were obtained in the gas phase, the BSSEs calculated for them could have been used as estimated values for those calculated in the simulated aqueous phase. Since aggregation does not take place in the gas phase (Figure 6.5), estimated BSSE values were determined by performing single-point energy calculations, using the equilibrium geometries that were obtained in the simulated aqueous phase, in the absence of any solvent (gas phase). In essence, it has to be shown that aggregation of the  $\text{Os}^{\text{VIII}}$  and  $\text{Os}^{\text{VI}}$  reactant species are not only due to BSSEs but because there is sufficient interaction energy between the monomers to promote non-covalent dimer formation. BSSE values using this methodology are listed in Table 6.5.

**Table 6.5. Estimated BSSEs of the  $[\text{Os}^{\text{VIII}}=\text{O}\cdots\text{HO}-\text{Os}^{\text{VI}}]^4+$  and  $[\text{Os}^{\text{VIII}}=\text{O}\cdots\text{HO}-\text{Os}^{\text{VI}}]^3-$  non-covalent dimers in kcal.mol<sup>-1</sup>.**

Functional	$[\text{Os}^{\text{VIII}}=\text{O}\cdots\text{HO}-\text{Os}^{\text{VI}}]^4+$			$[\text{Os}^{\text{VIII}}=\text{O}\cdots\text{HO}-\text{Os}^{\text{VI}}]^3-$		
	$E_{\text{BSSE}}(\text{Os}^{\text{VIII}})$	$E_{\text{BSSE}}(\text{Os}^{\text{VI}})$	$E_{\text{BSSE}}(\text{tot})$	$E_{\text{BSSE}}(\text{Os}^{\text{VIII}})$	$E_{\text{BSSE}}(\text{Os}^{\text{VI}})$	$E_{\text{BSSE}}(\text{tot})$
PBE	0.59	1.00	1.59	0.17	3.73	3.90
PBE-D	0.68	5.28	5.96	0.18	3.46	3.64
PBE-D3	0.61	5.63	6.24	0.12	3.68	3.80
PBE-D3(BJ)	0.61	5.73	6.34	0.18	3.86	4.04
PBE-dDsC	0.59	5.77	6.36	0.17	3.74	3.91

The calculated BSSE values are significantly smaller than the DFT-calculated interaction energies, Table 6.4, and illustrates that the non-covalent dimers are not BSSE artefacts. It is likely that the ‘true’ BSSE values are smaller than those determined using this method where solvent was not present, as the solvent perturbs the electron density. Moreover, an example<sup>17</sup> found in the ADF manual of the BSSE in the formation of  $\text{Cr}(\text{CO})_6$  from CO and  $\text{Cr}(\text{CO})_5$ , illustrates that BSSE effects diminish with larger basis sets, *e.g.* the total BSSE drops from 4.4 kcal.mol<sup>-1</sup> with basis DZ to 1.3 kcal.mol<sup>-1</sup> with basis TZP. Considering that we used relatively large basis sets, *i.e.* QZ4P for Os and ET-pVQZ for O and H, our BSSE should be small.

### The second step of the $\text{Os}^{\text{VI}}$ & $\text{Os}^{\text{VIII}}$ comproportionation reaction

With the initial, non-covalent dimers identified, we proceeded to investigate whether the subsequent reaction step may involve EPT, HAT, or a stepwise ET-PT or PT-ET pathway. According to the definition of EPT mechanism, two important conditions must be met:

- (i) the ‘PT distance’ between donor and acceptor  $\sigma(\text{O}-\text{H})$  orbitals must be minimised in order to maximise the vibrational wave function overlap since PT is fundamentally limited to short distances:<sup>2</sup>
- (ii) ET occurs from a metal-based  $d\pi$  orbital at the donor to a  $d\pi$  orbital at the acceptor:<sup>2</sup>

The formation of the non-covalent dimers, Figures 6.3 and 6.9, minimises the ‘PT distance’ between the donor  $\sigma(\text{O}-\text{H})$  orbital and the acceptor O-based lone pair orbital of the monomers and meets the criteria above, (i), as stated by Meyer *et al.*<sup>2</sup> In the case of  $[\text{Os}^{\text{VIII}}=\text{O}\cdots\text{HO}-\text{Os}^{\text{VI}}]^4+$ , two of the three hydrogens that have intermolecular hydrogen bonding interactions, H(8) & H(19), are of the electron donor monomer,  $[\text{Os}^{\text{VI}}-\text{OH}]^{2-}$ , while the other, H(20), which has the weakest intermolecular hydrogen bonding interaction of the three, Table 6.2, is

of the electron acceptor monomer,  $[\text{Os}^{\text{VIII}}=\text{O}]^{2-}$ . If PT does occur in the subsequent elementary step(s), to an oxygen with which it is intermolecularly hydrogen-bonded to in the non-covalent dimer, then there are, as a consequence, two protons that could possibly transfer from  $[\text{Os}^{\text{VI}}-\text{OH}]^{2-}$  to  $[\text{Os}^{\text{VIII}}=\text{O}]^{2-}$ . If H(8) is to transfer to O(14), the stereochemistry of the accepting monomer, still present in the non-covalent dimer, will become *fac*. In contrast to such a result, if H(19) is to transfer to O(16) the stereochemistry of both monomers, still present in the non-covalent dimer, will become *mer*.<sup>16</sup> In the  $[\text{Os}^{\text{VIII}}=\text{O}\cdots\text{HO}-\text{Os}^{\text{VI}}]^{3-}$  non-covalent dimer, transfer of either H(8) or H(17) will result in the acceptor monomer, still present in the non-covalent dimer, to form a *cis* stereoisomer. There are no non-covalent dimers found on the multidimensional PES that could possibly facilitate direct monomer formation of a *trans* stereoisomer,<sup>17</sup> *i.e.* it is not, geometrically, possible for oxo ligand O(13) and hydroxido ligand O(15)-H(18) to form intermolecular hydrogen bonding interactions with  $[\text{Os}^{\text{VI}}-\text{OH}]^{2-}$  due to the way in which the monomers are orientated towards one other, Figures 6.3 and 6.9.

Having given consideration to possible PT events and the stereochemistry as a consequence thereof, we now turn to ET contributions. The interaction between the  $d\pi$ -orbitals is by far the dominant component to the orbital stabilisation for both non-covalent dimers, Figure 6.10, which suggests<sup>18</sup> that the non-covalent dimers will react in a next step *via* concerted EPT or ET. If, for instance, the local depletion of electron density on *trans*- $[\text{Os}^{\text{VI}}-\text{OH}]^{2-}$  was predominantly at the  $\sigma(\text{O}-\text{H})$  orbital of the transferring proton with local electron density accumulation at  $d\pi$ -orbitals on the  $[\text{Os}^{\text{VIII}}=\text{O}]^{2-}$  or  $[\text{Os}^{\text{VIII}}=\text{O}]$  fragment, then one may have anticipated a subsequent HAT. Similarly, if there had not been any local depletion of electron

<sup>16</sup> The *mer*- $[\text{Os}^{\text{VII}}\text{O}_3(\text{OH})_3]^{2-}$  stereoisomer is considerably thermodynamically favoured to *fac*- $[\text{Os}^{\text{VII}}\text{O}_3(\text{OH})_3]^{2-}$  at 298.15 K (in the simulated aqueous phase), Table 5.2. Therefore, if EPT does occur in the subsequent reaction to form a non-covalent dimer that consists of two octahedral  $\text{Os}^{\text{VII}}$  species, a quadruply-charged species comprising two *mer* monomers will most likely be thermodynamically favoured to one comprising one *mer* and one *fac* monomer.

<sup>17</sup> The *trans*- $[\text{Os}^{\text{VII}}\text{O}_3(\text{OH})_2]^-$  stereoisomer is considerably thermodynamically favoured to *cis*- $[\text{Os}^{\text{VII}}\text{O}_3(\text{OH})_2]^-$  at 298.15 K (in the simulated aqueous phase), Table 5.2. Due to the geometry of the triply-charged non-covalent dimer, Figures 6.3 and 6.9, the thermodynamically more stable five-coordinate  $\text{Os}^{\text{VII}}$  species cannot form directly if EPT does occur in the subsequent reaction.

<sup>18</sup> The highest energy deformation density channel, ETS-NOCV, does not necessarily provide data to distinguish between or prove whether the subsequent reaction involves concerted or stepwise PCET, *e.g.* non-covalent dimer in Figure 7.17.

density at the  $d\pi$ -orbitals of the *trans*-[Os<sup>VI</sup>-OH]<sup>2-</sup> donor fragment, a subsequent initial PT (followed in a later event by ET) may have been anticipated. The ETS-NOCV results provide an indication of electrostatic perturbation between electron donor and acceptor  $d\pi$ -orbitals. The formation of the non-covalent dimers therefore promotes both vibrational coupling (the ‘PT distance’ is minimised) as well as  $d\pi$ - $d\pi$  electronic coupling between the monomer reactants in both [Os<sup>VIII</sup>=O...HO-Os<sup>VI</sup>]<sup>4-</sup> and [Os<sup>VIII</sup>=O...HO-Os<sup>VI</sup>]<sup>3-</sup>. Moreover, when [Os<sup>VI</sup>-OH]<sup>2-</sup> aggregates with [Os<sup>VIII</sup>=O]<sup>2-</sup>, Figure 6.10, depletion of electron density at the  $d\pi$ -orbitals of [Os<sup>VI</sup>-OH]<sup>2-</sup> is less compared to when it is aggregated with [Os<sup>VIII</sup>=O]<sup>2-</sup>.

When taking into consideration the intermolecular hydrogen bonding distances, Table 6.1, the QTAIM analyses of the intermolecular hydrogen bonding BCP indices, Tables 6.2 & 6.3, the stereochemistry of possible products and the ETS-NOCV analyses, Figure 6.10, based on the equilibrium geometries of [Os<sup>VIII</sup>=O...HO-Os<sup>VI</sup>]<sup>4-</sup> and [Os<sup>VIII</sup>=O...HO-Os<sup>VI</sup>]<sup>3-</sup>, there are three points, in summary, that are conceivable w.r.t. the subsequent reaction, *i.e.* after non-covalent dimer formation:

- (i) EPT seems more likely than initial PT (*via* stepwise PT-ET),
- (ii) H(19) likely transfers to O(16) in [Os<sup>VIII</sup>=O...HO-Os<sup>VI</sup>]<sup>4-</sup> to form two *mer* stereoisomers, and
- (iii) H(17) likely transfers to O(16) in [Os<sup>VIII</sup>=O...HO-Os<sup>VI</sup>]<sup>3-</sup> to form one *cis* and one *mer* stereoisomer.

### **Investigation of concerted electron-proton transfer (EPT) as a likely next step of the comproportionation reaction**

We proceeded to investigate the feasibility of EPT by performing a set of computational, linear transit, relaxed scan calculations in which the transferring proton, H(19) of [Os<sup>VIII</sup>=O...HO-Os<sup>VI</sup>]<sup>4-</sup> and H(17) of [Os<sup>VIII</sup>=O...HO-Os<sup>VI</sup>]<sup>3-</sup>, was systematically moved from its  $\sigma$ (O-H) orbital towards the O-based lone pair orbital at the acceptor oxygen, O(16) of [Os<sup>VIII</sup>=O...HO-Os<sup>VI</sup>]<sup>4-</sup> and O(16) of [Os<sup>VIII</sup>=O...HO-Os<sup>VI</sup>]<sup>3-</sup>, respectively. The change in electronic energy along these reaction coordinates are crucial w.r.t. distinguishing between initial PT (*via* stepwise PT-ET) and concerted electron-proton transfer, Scheme 6.1, when taking the following into consideration:

If the electronic energy reaches a maximum during the linear transit and a transition state is subsequently identified, an energy profile similar to that given by Figure 6.11 (a) should be obtained. The result would imply that the ‘product’ is also stable in the singlet spin state. If this is the case, the obtained transition state could imply that PT does not occur simultaneously with ET, essentially proving that EPT does not occur.

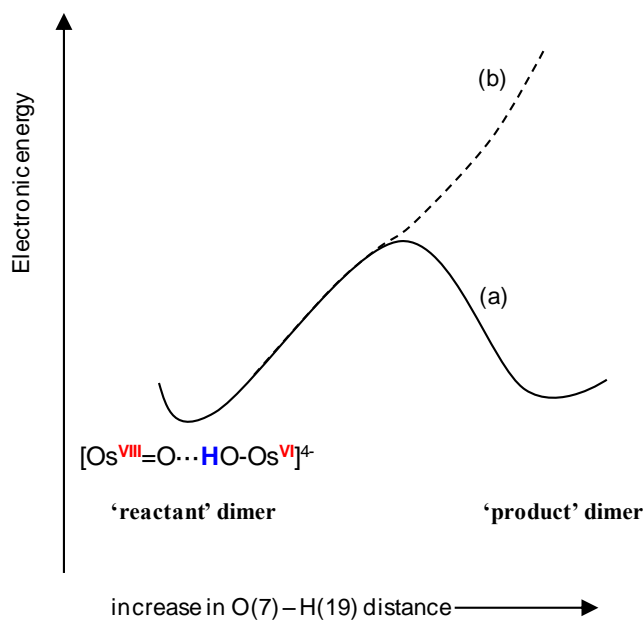


**Figure 6.11.** Envisaged qualitative electronic energy profiles for initial PT (a) and EPT (b) from linear transit, relaxed scan calculations of singlet spin state  $[\text{Os}^{\text{VIII}}=\text{O}\cdots\text{HO}-\text{Os}^{\text{VI}}]^{4-}$ .

However, as the transferring hydrogen ‘migrated’ from the ( $\text{Os}^{\text{VI}}$ ) donor towards the ( $\text{Os}^{\text{VIII}}$ ) acceptor, the total electronic energy continuously increased such that no energy maxima are observed, similar to that given by Figure 6.11 (b). This result was obtained for both the quadruply-charged and triply-charged non-covalent dimer and for all functionals used in this study. We conclude from these preliminary computational results that initial PT (*via* stepwise PT-ET) does not occur after initial non-covalent dimer formation. These results prompted us to perform geometry optimisation calculations of the ‘product’ species, *i.e.* where the hydrogen is now transferred to the acceptor oxygen, in the singlet spin state to confirm that initial PT does not take place. The conceivable ‘products’ did not converge as local energy minima on the PES. Instead, in the course of these calculations, the hydrogen ‘migrates’ all the way back to the ( $\text{Os}^{\text{VI}}$ ) donor monomer after each successive SCF iteration and converges once again as the non-covalent dimer  $[\text{Os}^{\text{VII}}-\text{OH}\cdots\text{O}=\text{Os}^{\text{VII}}]^{4-}$  or  $[\text{Os}^{\text{VII}}-\text{OH}\cdots\text{O}=\text{Os}^{\text{VII}}]^{3-}$ . This result suggests that the ‘product’ species for this reaction step could be stable in a different spin state. As the final products of the  $\text{Os}^{\text{VI}}$  &  $\text{Os}^{\text{VIII}}$  comproportionation reaction have one

unpaired electron each, *i.e.*  $\text{Os}^{\text{VII}}$  species, the same conceivable ‘product’ species (as above) was submitted for a geometry optimisation calculation, but now in the triplet (one unpaired electron per monomer yielding two unpaired electrons in total) spin state. The geometries converged relatively easily as distinct non-covalent  $\text{Os}^{\text{VII}}$  dimers and their molecular graphs are shown in Figure 6.12. The non-covalent dimers that are stable in the triplet spin state consist of two  $\text{Os}^{\text{VII}}$  monomers and are simply the initial non-covalent dimers of the reverse reaction, *i.e.* of disproportionation. Subsequent vibrational frequencies analyses confirm that the species are local minima on the PES as no negative frequencies were obtained. These non-covalent dimers consist of two *mer*  $\text{Os}^{\text{VII}}$  monomers in  $[\text{Os}^{\text{VII}}\text{-OH}\cdots\text{O}=\text{Os}^{\text{VII}}]^{4-}$  and one *cis*  $\text{Os}^{\text{VII}}$  monomer and one *mer*  $\text{Os}^{\text{VII}}$  monomer in  $[\text{Os}^{\text{VII}}\text{-OH}\cdots\text{O}=\text{Os}^{\text{VII}}]^{3-}$ .

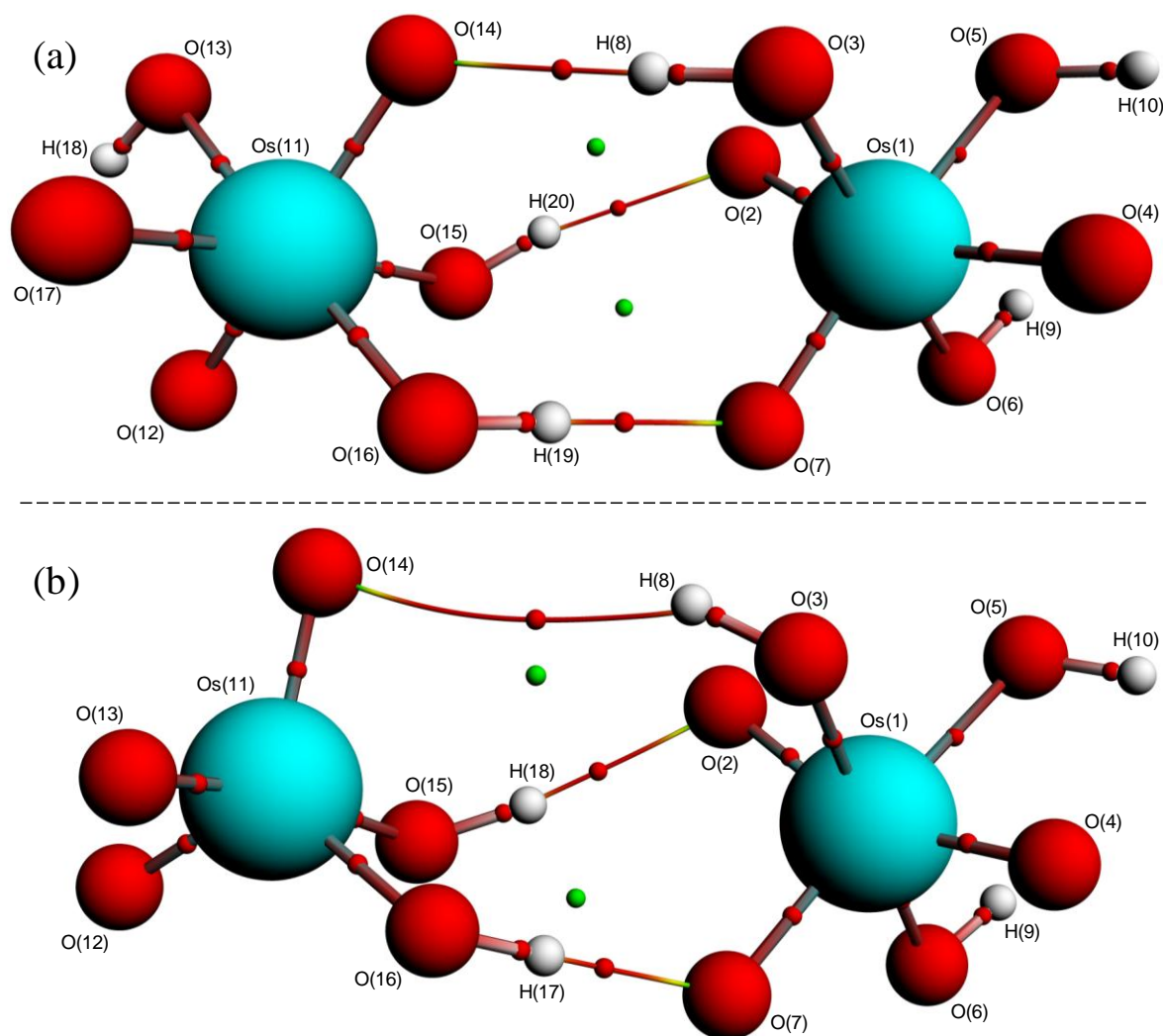


**Figure 6.12.** Molecular graphs of the quadruply-charged  $[\text{Os}^{\text{VII}}\text{-OH}\cdots\text{O}=\text{Os}^{\text{VII}}]^{4-}$  (a) and triply-charged  $[\text{Os}^{\text{VII}}\text{-OH}\cdots\text{O}=\text{Os}^{\text{VII}}]^{3-}$  (b) non-covalent dimers in the simulated aqueous phase {PBE-D3(BJ) functional} showing three atomic interaction lines corresponding to intermolecular hydrogen bonds between the monomers. The small red, green and blue spheres represent (3,-1), (3,+1) and (3,+3) critical points, respectively.

Moreover, geometry optimisation calculations of the non-covalent dimers shown in Figure 6.3 in the triplet spin state also do not converge to form local energy minima on the PES; the transferring hydrogen ‘migrates’ to the ( $\text{Os}^{\text{VIII}}$ ) ‘acceptor’ monomer after each successive SCF iteration and converges as a non-covalent dimer shown in Figure 6.12. Based on the results obtained from these linear transit calculations, we conclude that neither PT nor ET sequential pathway steps occur directly after the formation of the initial non-covalent dimers shown in Figures 6.3 and 6.9.

The equilibrium geometries of the non-covalent  $\text{Os}^{\text{VII}}$  dimers (in the simulated aqueous phase) are also influenced by the inclusion of dispersion corrections.<sup>19</sup> In the absence of dispersion corrections, *i.e.* PBE, the intermolecular oxygen to hydrogen distances, corresponding to hydrogen bonding interactions (*vide infra*), are approximately 0.05 Å longer whilst PBE-D again yields the shortest distances, Table 6.6. Furthermore, the intermolecular O(14)-H(8) distance in  $[\text{Os}^{\text{VII}}\text{-OH}\cdots\text{O}=\text{Os}^{\text{VII}}]^{4-}$  is slightly longer compared to that in  $[\text{Os}^{\text{VIII}}=\text{O}\cdots\text{HO}-\text{Os}^{\text{VI}}]^{4-}$  while O(2)-H(20) is slightly shorter. In the  $[\text{Os}^{\text{VII}}\text{-OH}\cdots\text{O}=\text{Os}^{\text{VII}}]^{3-}$  non-covalent dimer, the intermolecular O(14)-H(8) distance is significantly longer in comparison to that in  $[\text{Os}^{\text{VIII}}=\text{O}\cdots\text{HO}-\text{Os}^{\text{VI}}]^{3-}$ , except for PBE-D, while O(2)-H(18) is slightly shorter.

**Table 6.6. Intermolecular hydrogen bonding distances of the quadruply-charged  $[\text{Os}^{\text{VII}}\text{-OH}\cdots\text{O}=\text{Os}^{\text{VII}}]^{4-}$  and triply-charged  $[\text{Os}^{\text{VII}}\text{-OH}\cdots\text{O}=\text{Os}^{\text{VII}}]^{3-}$  non-covalent dimers in the simulated aqueous phase (Å).**

Functional	$[\text{Os}^{\text{VII}}\text{-OH}\cdots\text{O}=\text{Os}^{\text{VII}}]^{4-}$			$[\text{Os}^{\text{VII}}\text{-OH}\cdots\text{O}=\text{Os}^{\text{VII}}]^{3-}$		
	O(7)-H(19)	O(14)-H(8)	O(2)-H(20)	O(7)-H(17)	O(14)-H(8)	O(2)-H(18)
PBE	1.767	1.878	2.025	1.635	4.495	1.976
PBE-D	1.706	1.832	1.929	1.560	2.414	1.834
PBE-D3	1.746	1.859	2.009	1.574	3.000	1.844
PBE-D3(BJ)	1.734	1.843	1.987	1.621	3.937	1.854
PBE-dDsC	1.735	1.843	1.985	1.612	3.993	1.838

EDA of  $[\text{Os}^{\text{VII}}\text{-OH}\cdots\text{O}=\text{Os}^{\text{VII}}]^{4-}$  and  $[\text{Os}^{\text{VII}}\text{-OH}\cdots\text{O}=\text{Os}^{\text{VII}}]^{3-}$  reveal that the various energetic components involved in stabilising the non-covalent dimers are similar in magnitude compared to  $[\text{Os}^{\text{VIII}}=\text{O}\cdots\text{HO}-\text{Os}^{\text{VI}}]^{4-}$  and  $[\text{Os}^{\text{VIII}}=\text{O}\cdots\text{HO}-\text{Os}^{\text{VI}}]^{3-}$ , Table A.8. Furthermore,  $\text{Os}^{\text{VII}}$  non-covalent dimer formation does not take place in the gas phase, as solvation (hydration) energies are necessary in order to yield favourable (negative) interaction energies between the  $\text{Os}^{\text{VII}}$  monomers.

<sup>19</sup> BSSEs for the  $\text{Os}^{\text{VII}}$  non-covalent dimers, Figure 6.12, are expected to be similar to those for the  $[\text{Os}^{\text{VIII}}=\text{O}\cdots\text{HO}-\text{Os}^{\text{VI}}]^{4-}$  and  $[\text{Os}^{\text{VIII}}=\text{O}\cdots\text{HO}-\text{Os}^{\text{VI}}]^{3-}$  non-covalent dimers, Table 6.5.



The Os<sup>VIII</sup>-Os<sup>VI</sup> and Os<sup>VII</sup> non-covalent dimers are the species present, prior to and after the rate-determining EPT step on either side of the ‘five-coordinate’ and ‘six-coordinate’ reaction pathways (*vide infra*). With equilibrium geometries corresponding to the non-covalent dimer ‘reactant’ and ‘products’, for the EPT reactions confirmed, equations 6.6 & 6.7, we proceeded to the next step of our mechanistic investigation, which was to identify and calculate the ‘activation energies’ for the two pathways. Since the overall spin state changes from a singlet to a triplet for both reactions 6.6 and 6.7, we searched for the respective minimum energy crossing points (MECP). The internal geometric parameter that was kept the same for the independent PESs was the distance between O(7) and H(19) for the quadruply-charged dimer and in the triply-charged dimer, it was the distance between O(7) and H(17). The calculated PESs obtained following the geometry optimisation calculations (partial convergence) are shown in Figures 6.13 and 6.14.<sup>20</sup>

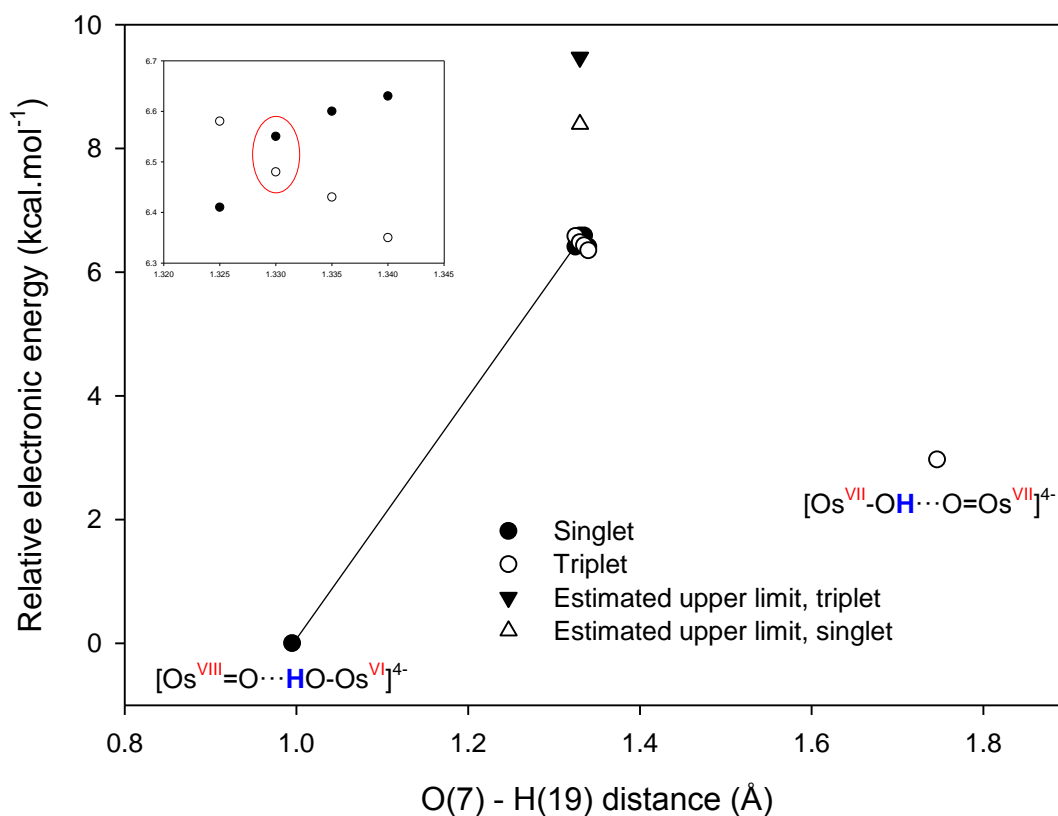


**Figure 6.13.** Energies of the partially optimised singlet and triplet states of the quadruply-charged dimer for EPT (PBE-D3). The PESs intersect, yielding a MECP, at an O(7) – H(19) distance of approximately 1.35 Å. Inset: Minimum energy crossing point (MECP).

<sup>20</sup> The choice of internal geometry parameter is obvious in this case because of the relative linearity of the O-H-O angle ( $\sim 180^\circ$  for all functionals used in this study) between the monomers. An increase in distance between the donor oxygen, O(7), and the transferring hydrogen, H(19) or H(17) facilitates product structure formation.

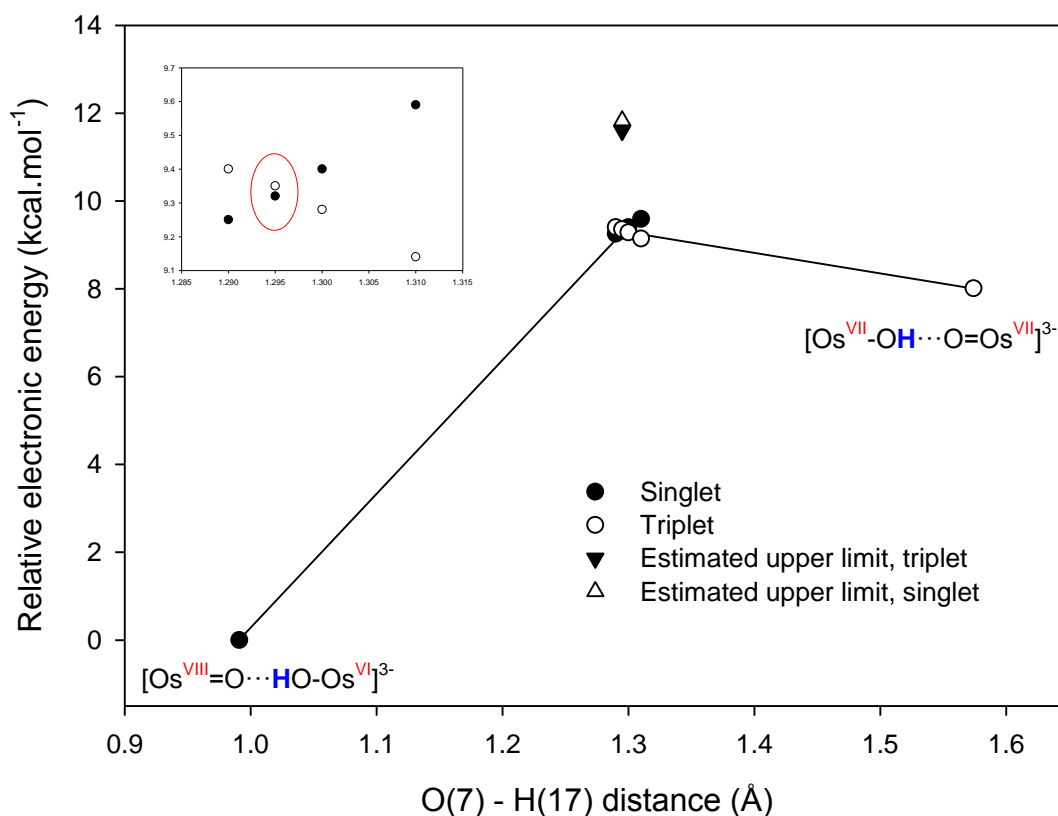
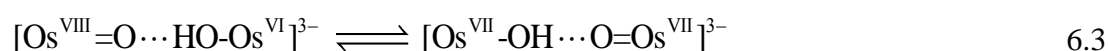
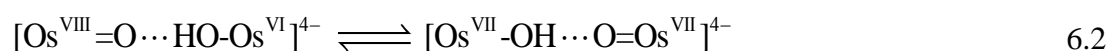


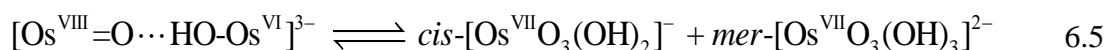
**Figure 6.14.** Energies of the partially optimised singlet and triplet states of the triply-charged dimer for EPT (PBE-D3). The PESs intersect, yielding a MECP, at an O(7) – H(17) distance of approximately 1.30 Å. Inset: Minimum energy crossing point (MECP).

Frequencies analyses of the MECPs for both the singlet and triplet spin states yield one negative frequency, which corresponds to the oscillating stretching mode of the transferring hydrogen between the oxygen of the donor monomer and the oxygen of the acceptor monomer.

Equations 6.2 and 6.3 depict the second reaction step of the ‘six-coordinate’ and ‘five-coordinate’ pathway, respectively, for the Os<sup>VI</sup> & Os<sup>VIII</sup> comproportionation reaction, Schemes 6.2 (ii) and 6.3 (ii).



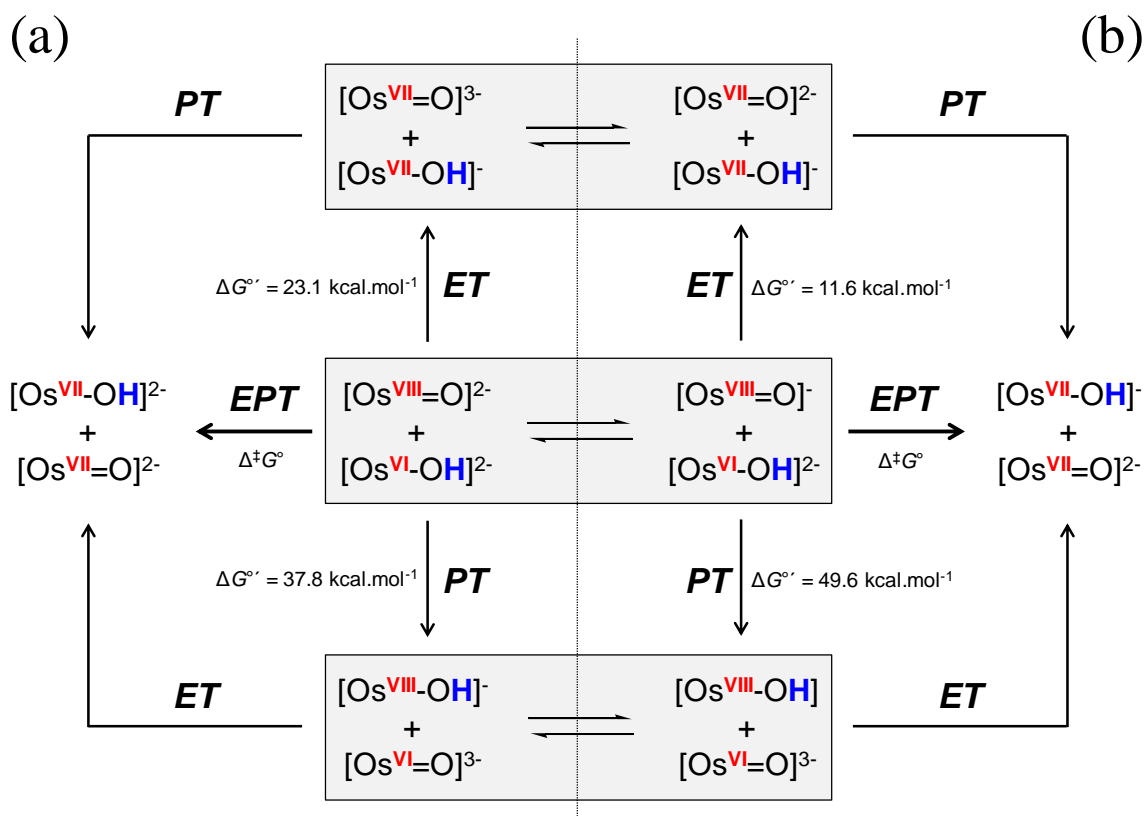
The subsequent, third reaction step (iii) of the stepwise comproportionation reaction is the separation of the Os<sup>VII</sup> monomers that are present in the Os<sup>VII</sup> non-covalent dimers, equations 6.4 and 6.5.



The *mer* and *cis*  $\text{Os}^{\text{VII}}$  monomers then interconvert to the *trans* stereoisomer, Schemes 6.2 (iv) and 6.3 (iv), as discussed in Chapter 5.

### Investigation of sequential electron-proton transfer *via* EP-PT or PT-ET

According to our stopped-flow UV-Vis spectroscopy KIE experiment, Section 4.2.2.3, the rate-determining step of the  $\text{Os}^{\text{VI}}$  &  $\text{Os}^{\text{VIII}}$  comproportionation reaction coincides with a PT event. Despite the fact that our linear transit calculations indicate that neither PT only nor ET only can occur directly after initial non-covalent dimer formation, Figures 6.13 and 6.14, we proceeded to investigate the relative thermodynamic stabilities of monomer species that may form *via* sequential pathways, ET-PT and PT-ET. The  $\Delta G^\circ_{\text{rxn}}$  values calculated for ET or PT (PBE-D3 functional) are minimum free energies of activation,  $\Delta G^\circ$ , for the initial ET or PT steps, Scheme 6.4. The obtained standard reaction thermodynamic parameters, for calculations done in the simulated aqueous phase for all five functionals used in this study, are listed in Tables 6.7 and 6.8. Gas phase calculations were not done due to the significant influence that solvation energy has on oxo/hydroxido osmium reaction energies, *e.g.* Tables 3.4, 3.7 and 5.7.



**Scheme 6.4.**  $Os^{VI}$  &  $Os^{VIII}$  comproportionation, ‘six-coordinate’ (a) and ‘five-coordinate’ (b), reaction PCET pathways by means of initial electron transfer (*via* stepwise ET-PT) initial proton transfer (*via* stepwise PT-ET) and concerted electron-proton transfer (EPT).  $\Delta G^{\circ}_{\text{rxn}}$  values for ET or PT pathways are included for comparison (PBE-D3 functional).

**Table 6.7.** Standard reaction thermodynamic parameters for sequential ET and PT monomer species (‘six-coordinate’ reaction pathway) in the simulated aqueous phase (298.15 K).

Pathway	Functional	$\Delta H^{\circ}$	$\Delta S^{\circ}$	$\Delta G^{\circ}$
ET	PBE	23.00	-0.36	23.11
	PBE-D	23.43	0.75	23.21
	PBE-D3	23.00	-0.19	23.06
	PBE-D3(BJ)	22.88	-0.14	22.92
	PBE-dDsC	23.18	-0.06	23.20
PT	PBE	33.27	-2.80	34.10
	PBE-D	33.87	-1.75	34.39
	PBE-D3	36.84	-3.23	37.80
	PBE-D3(BJ)	33.23	-3.80	34.36
	PBE-dDsC	33.53	-3.57	34.59
<b>Experimental<sup>a</sup></b>		<b><math>10.3 \pm 0.5</math></b>	<b><math>-2.6 \pm 1.6</math></b>	<b><math>11.1 \pm 0.9</math></b>

<sup>a</sup> Observed activation energies at 298.15 K obtained from stopped-flow UV-Vis kinetics experiments, Chapter 4.

**Table 6.8. Standard reaction thermodynamic parameters for sequential ET and PT monomer species ('five-coordinate' reaction pathway) in the simulated aqueous phase (298.15 K).**

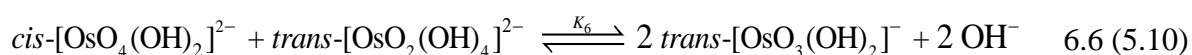
Pathway	Functional	$\Delta H^\circ$	$\Delta S^\circ$	$\Delta G^\circ$
ET	PBE	21.14	34.73	10.78
	PBE-D	22.70	35.63	12.08
	PBE-D3	22.08	35.00	11.64
	PBE-D3(BJ)	21.93	36.28	11.11
	PBE-dDsC	22.29	36.69	11.35
PT	PBE	53.68	29.96	44.75
	PBE-D	55.83	30.88	46.63
	PBE-D3	58.31	29.40	49.55
	PBE-D3(BJ)	55.80	28.97	47.17
	PBE-dDsC	56.05	33.52	46.06
<b>Experimental<sup>a</sup></b>		<b><u>10.3 ± 0.5</u></b>	<b><u>-2.6 ± 1.6</u></b>	<b><u>11.1 ± 0.9</u></b>

<sup>a</sup> Observed activation energies at 298.15 K obtained from stopped-flow UV-Vis kinetics experiments, Chapter 4.

Initial PT yields  $\Delta G^\circ$  values for the 'five-coordinate' and 'six-coordinate' pathways that are significantly larger than the experimentally obtained, observed Gibbs activation energy,  $\Delta^\ddagger G^\circ_{(obs)}$ , of the Os<sup>VI</sup> & Os<sup>VIII</sup> comproportionation reaction,  $11.1 \pm 0.9$  kcal.mol<sup>-1</sup>, effectively ruling such pathways out as major contributors. Similarly,  $\Delta G^\circ$  corresponding to ET for the 'six-coordinate' pathway is approximately 12 kcal.mol<sup>-1</sup> larger than  $\Delta^\ddagger G^\circ_{(obs)}$ , indicating that this pathway too, is not a major contributor to the comproportionation reaction mechanism. Furthermore,  $\Delta G^\circ$  corresponding to ET for the 'five-coordinate' pathway is approximately 11 kcal.mol<sup>-1</sup>, *i.e.* approximately equal to  $\Delta^\ddagger G^\circ_{(obs)}$ . However, for ET to occur there must be an overall change in electronic spin, from a singlet to a triplet spin state, such that an MECP is required to actually quantify the 'true' activation energy for such a transfer. An MECP is approximately 7 – 10 kcal.mol<sup>-1</sup> higher in Gibbs energy in relation to initial non-covalent dimer formation, Figures 6.15 and 6.16. Moreover, experimental evidence illustrates that the rate-determining step of the comproportionation reaction involves a PT event, ruling this pathway out as a major contributor. The observed standard reaction enthalpy and entropy compare poorly with the DFT-calculated values for initial ET for the 'five-coordinate' pathway. Lastly, without the formation of non-covalent dimers (*vide infra*) a negative activation enthalpy for the Os<sup>VII</sup> & Os<sup>VII</sup> disproportionation reaction,  $\Delta^\ddagger H^\circ_{dis}$ , cannot be accounted for, which effectively rules the 'five-coordinate' ET-PT pathway out. Collectively, DFT calculations leads us to the conclusion that 'five-coordinate' and 'six-coordinate' EPT pathways are more probable than any one of the four identified sequential pathways, *i.e.* ET-PT and PT-ET.

### 6.2.2 Combining all the data for the EPT pathways

The goal in this section is to try and discriminate between the ‘five-coordinate’ and ‘six-coordinate’ reaction mechanism pathways, account for the negative activation enthalpy for the Os<sup>VII</sup> & Os<sup>VII</sup> disproportionation reaction,  $\Delta^\ddagger H_{dis}^\circ$ , compare DFT-calculated and experimental activation energies and lastly, use the proposed reaction pathway(s) to recover the reaction model and rate laws used in Chapter 4. In Chapter 5 we concluded that the most probable Os<sup>VI</sup> & Os<sup>VIII</sup> comproportionation reaction, from a thermodynamic perspective, is where *cis*-[Os<sup>VIII</sup>O<sub>4</sub>(OH)<sub>2</sub>]<sup>2-</sup> and *trans*-[Os<sup>VI</sup>O<sub>2</sub>(OH)<sub>4</sub>]<sup>2-</sup> are considered the (starting) reactants and two *trans*-[Os<sup>VII</sup>O<sub>3</sub>(OH)<sub>2</sub>]<sup>-</sup> and two hydroxide species are considered the (final) products, equation 6.6.



Having defined the starting reactants and final products, relative Gibbs free energy, enthalpy and entropy reaction profile diagrams for the ‘five-coordinate’ and ‘six-coordinate’ pathways can be constructed, Figures 6.15 and 6.16, respectively, (PBE-D3 functional’s energies are illustrated as an example and the experimentally obtained activation energies and standard reaction energies are overlaid with dashed lines for comparison).

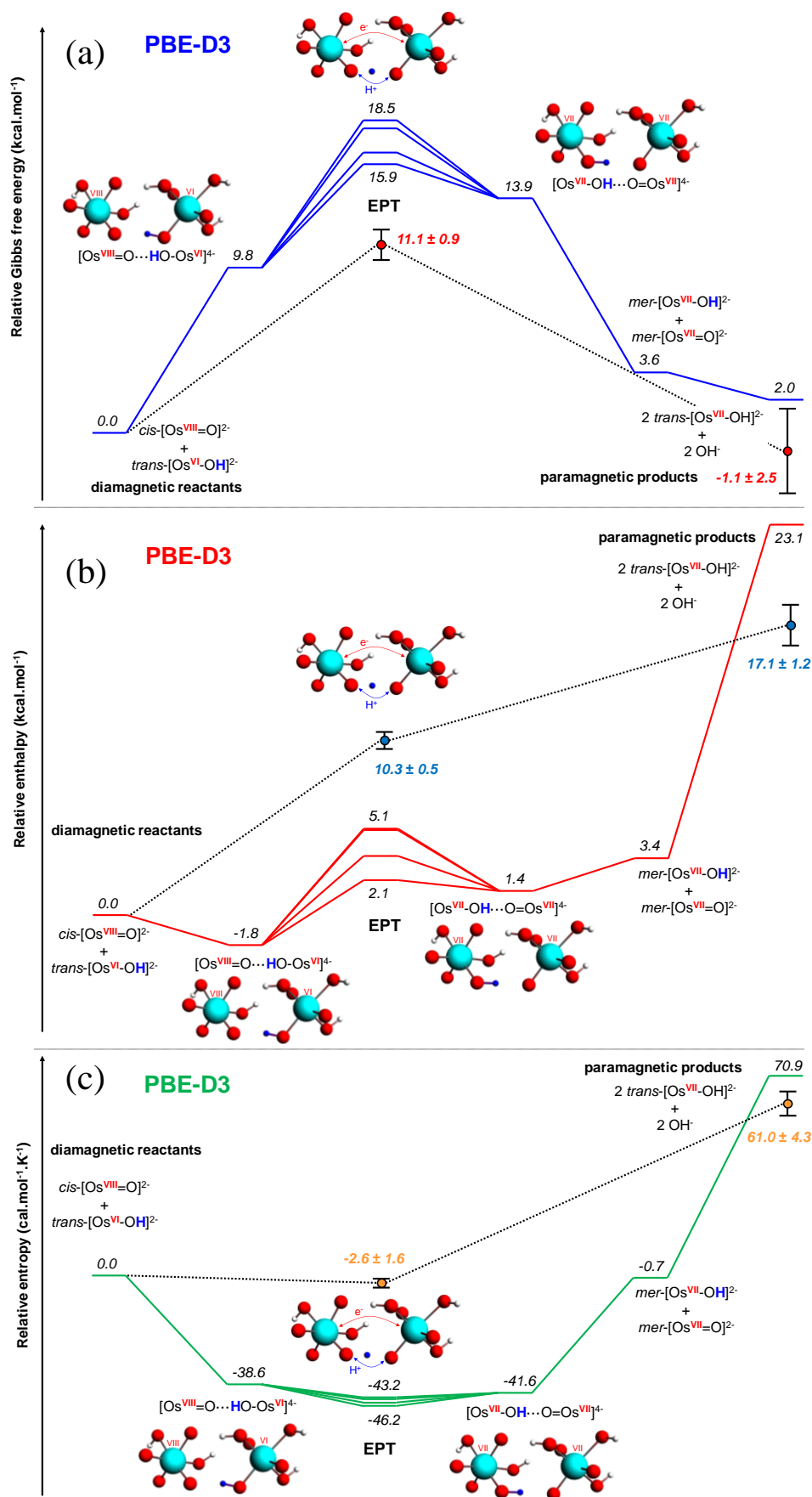


**Figure 6.15.** Reaction profile diagrams for the 'six-coordinate' comproportionation of *trans*-[Os<sup>VI</sup>O<sub>2</sub>(OH)<sub>4</sub>]<sup>2-</sup> and *cis*-[Os<sup>VIII</sup>O<sub>4</sub>(OH)<sub>2</sub>]<sup>2-</sup> with the molecular graphs of the non-covalent dimers and of the activated complex at the MECP (singlet). (PBE-D3)

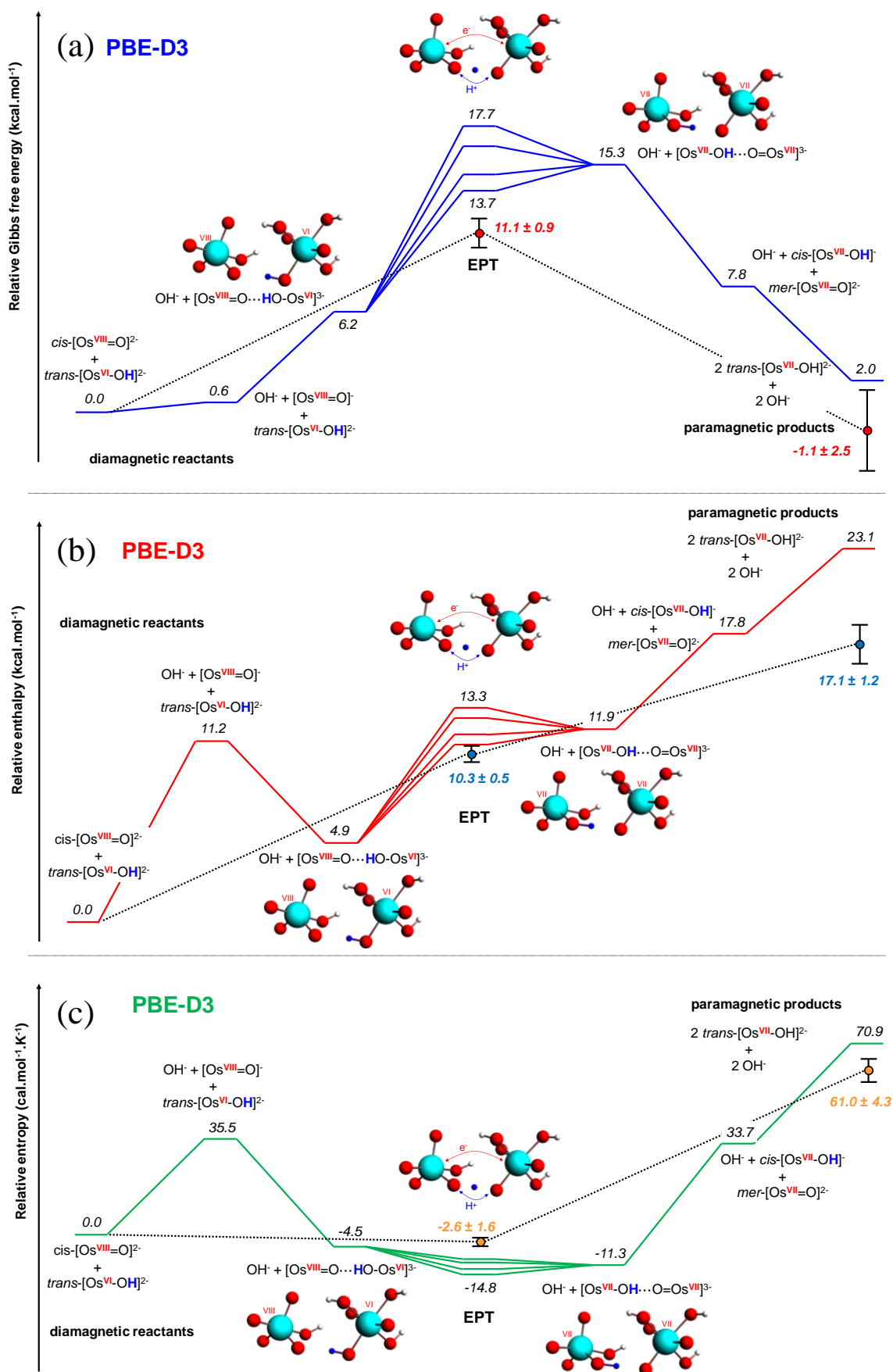


**Figure 6.16.** Reaction profile diagrams for the ‘five-coordinate’ comproportionation of  $trans\text{-}[\text{Os}^{\text{VI}}\text{O}_2(\text{OH})_4]^{2-}$  and  $cis\text{-}[\text{Os}^{\text{VIII}}\text{O}_4(\text{OH})_2]^{2-}$  with the molecular graphs of the non-covalent dimers and of the activated complex at the MECP (singlet). (PBE-D3)



As the Os<sup>VI</sup> & Os<sup>VIII</sup> comproportionation reaction is electronically spin-forbidden, we assume that spin-orbit coupling is large enough (osmium is a third row transition metal) to enable a ‘hop’ from the singlet state PES to the triplet state PES, Figures 6.13 and 6.14. Therefore, the *lower energy limit* to the MECP is used as an estimate of the activation energy required for the reaction to occur, while the relative energy differences between the *lower energy limit* and *upper energy limit* to the MECP provides a measure of how different geometries of the singlet and triplet spin state at the MECP are. It is evident from Figures 6.15 and 6.16 that the geometries are relatively similar due to the small differences in energy between the *lower energy limit* and *upper energy limit*.

It was found that for both the ‘six-coordinate’ and ‘five-coordinate’ pathways that  $\Delta^\ddagger H^\circ_{dis}$  is negative, a trend obtained for all functionals used in this study, Tables 6.10 and 6.11. The relative enthalpy reaction profile diagrams now provide a reason for how the negative activation enthalpy originated; the extensive intermolecular hydrogen bonding of the Os<sup>VII</sup> non-covalent dimer lowers the electronic energy w.r.t. the final products. The negative  $\Delta^\ddagger H^\circ_{dis}$  obtained with DFT and experiment, coupled with the result that the DFT-calculated, proposed EPT mechanism has a rate-determining step that involves the transfer of a proton, as was found experimentally, is excellent confirmation that the proposed reaction mechanisms are close to what occurs experimentally.

**Table 6.10. Standard reaction thermodynamic parameters for EPT monomer species (‘six-coordinate’ reaction pathway) in the simulated aqueous phase (298.15 K).**

Functional	Os <sup>VIII</sup> & Os <sup>VI</sup> Comproportionation			Os <sup>VII</sup> & Os <sup>VII</sup> Disproportionation		
	$\Delta^\ddagger H^\circ_{com}$ (kcal.mol <sup>-1</sup> )	$\Delta^\ddagger S^\circ_{com}$ (cal.mol <sup>-1</sup> .K <sup>-1</sup> )	$\Delta^\ddagger G^\circ_{com}$ (kcal.mol <sup>-1</sup> )	$\Delta^\ddagger H^\circ_{dis}$ (kcal.mol <sup>-1</sup> )	$\Delta^\ddagger S^\circ_{dis}$ (cal.mol <sup>-1</sup> .K <sup>-1</sup> )	$\Delta^\ddagger G^\circ_{dis}$ (kcal.mol <sup>-1</sup> )
PBE	6.79	-44.36	20.02	-14.34	-115.42	20.08
PBE-D	-0.96	-45.78	12.69	-25.27	-116.78	9.55
PBE-D3	2.78	-45.03	16.21	-20.31	-115.91	14.25
PBE-D3(BJ)	2.80	-46.99	16.81	-20.20	-119.88	15.54
PBE-dDsC	3.32	-47.09	17.36	-20.25	-120.18	15.58
<b>Experimental<sup>a</sup></b>	<b>10.3 ± 0.5</b>	<b>-2.6 ± 1.6</b>	<b>11.1 ± 0.9</b>	<b>-6.7 ± 1.0</b>	<b>-63.6 ± 3.4</b>	<b>12.2 ± 2.0</b>

<sup>a</sup> Observed activation energies at 298.15 K obtained from stopped-flow UV-Vis kinetics experiments, Chapter 4.

A comparison between the DFT-calculated and experimental  $\Delta^\ddagger G^\circ$  and  $\Delta^\ddagger H^\circ$  values for the ‘six-coordinate’ pathway compare fairly well, Table 6.10, while  $\Delta^\ddagger S^\circ$  values do not compare well at all. In contrast to the ‘six-coordinate’ pathway’s activation energies, the ‘five-

coordinate' pathway's activation energies compare well for both the comproportionation and disproportionation reactions, Table 6.11.

**Table 6.11. Standard reaction thermodynamic parameters for EPT monomer species ('five-coordinate' reaction pathway) in the simulated aqueous phase (298.15 K).**

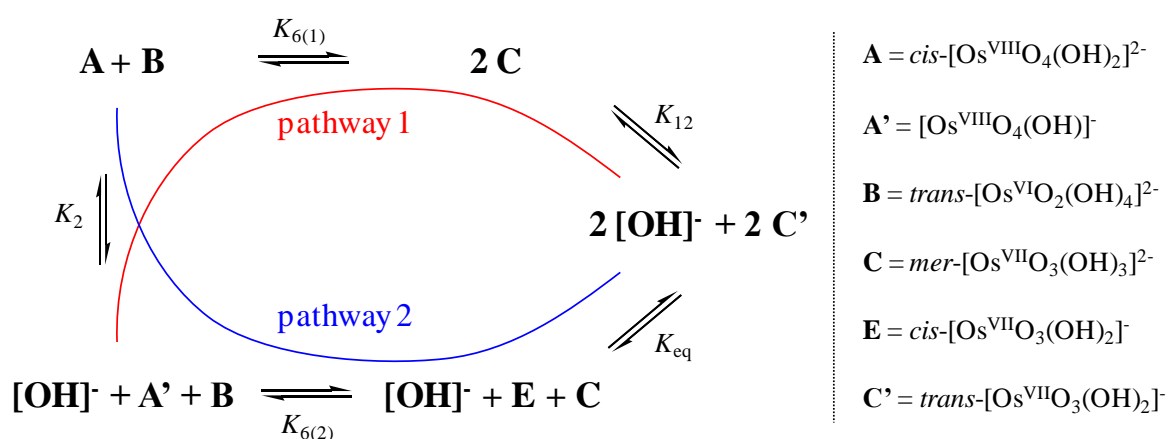
Functional	Os <sup>VIII</sup> & Os <sup>VI</sup> Comproportionation			Os <sup>VII</sup> & Os <sup>VII</sup> Disproportionation		
	$\Delta^\ddagger H^\circ_{com}$ (kcal.mol <sup>-1</sup> )	$\Delta^\ddagger S^\circ_{com}$ (cal.mol <sup>-1</sup> .K <sup>-1</sup> )	$\Delta^\ddagger G^\circ_{com}$ (kcal.mol <sup>-1</sup> )	$\Delta^\ddagger H^\circ_{dis}$ (kcal.mol <sup>-1</sup> )	$\Delta^\ddagger S^\circ_{dis}$ (cal.mol <sup>-1</sup> .K <sup>-1</sup> )	$\Delta^\ddagger G^\circ_{dis}$ (kcal.mol <sup>-1</sup> )
PBE	13.74	-7.34	15.93	-7.38	-78.40	15.99
PBE-D	8.21	-11.26	11.56	-16.10	-82.27	8.42
PBE-D3	11.29	-9.78	14.21	-11.80	-80.67	12.25
PBE-D3(BJ)	11.18	-10.92	14.43	-11.83	-83.80	13.16
PBE-dDsC	12.11	-10.57	15.27	-11.45	-83.66	13.49
<b>Experimental<sup>a</sup></b>	<b>10.3 ± 0.5</b>	<b>-2.6 ± 1.6</b>	<b>11.1 ± 0.9</b>	<b>-6.7 ± 1.0</b>	<b>-63.6 ± 3.4</b>	<b>12.2 ± 2.0</b>

<sup>a</sup> Observed activation energies at 298.15 K obtained from stopped-flow UV-Vis kinetics experiments, Chapter 4.

It is evident from the Gibbs free energy reaction profile diagram, Figure 6.16, that the MECP, and therefore the Gibbs activation energy, for the 'five-coordinate' pathway (approximately 14.2 kcal.mol<sup>-1</sup>) is approximately 2.0 kcal.mol<sup>-1</sup> lower in energy than for the 'six-coordinate' pathway (approximately 16.2 kcal.mol<sup>-1</sup>). Moreover, 14.2 kcal.mol<sup>-1</sup> is closer in absolute magnitude to the experimentally obtained, observed Gibbs activation energy value of 11.1 ± 0.9 kcal.mol<sup>-1</sup>. This feature is seen for all five functionals used in this study when comparing the data in Tables 6.10 and 6.11. When comparing the activation enthalpies of comproportionation (forward) pertaining to the 'five-coordinate' pathway to the 'six-coordinate' pathway, Figures 6.15 and 6.16, it is evident that the experimentally obtained, observed enthalpy value of 10.3 ± 0.5 kcal.mol<sup>-1</sup> is closer in absolute magnitude to the MECP of the 'five-coordinate' pathway. Another key feature of the 'five-coordinate' pathway's enthalpy reaction scheme is the better comparison of the activation energy of the disproportionation reaction which, according to our stopped-flow kinetics experiments { $\Delta^\ddagger H^\circ_{(obs)}$ }, is negative, -6.7 ± 1.0 kcal.mol<sup>-1</sup>. Similarly, from the entropy reaction profile diagrams, Figures 6.15 and 6.16, it is evident that the activation entropy corresponding to the 'five-coordinate' pathway is closer in absolute magnitude to the observed activation entropy value of -2.6 ± 1.6 kcal.mol<sup>-1</sup>, a feature observed for all five functionals used in this study, Tables 6.10 and 6.11.

This suggests that the 'five-coordinate' pathway is the energetically favoured mechanism, which is related to pathway 2 in Chapter 5, Scheme 5.3. The only difference to pathway 2 in

Scheme 5.3 and our updated proposed ‘five-coordinate’ pathway is that the *cis*-[Os<sup>VII</sup>O<sub>3</sub>(OH)<sub>2</sub>]<sup>-</sup> species must now also be taken into account in order to recover the rate laws from Chapter 4, Scheme 6.5. Even though the concentration of the *cis*-[Os<sup>VII</sup>O<sub>3</sub>(OH)<sub>2</sub>]<sup>-</sup> species is approximately 1200 times lower than that of the *mer*-[Os<sup>VII</sup>O<sub>3</sub>(OH)<sub>3</sub>]<sup>2-</sup> species, the good agreement of the activation energies with the ‘five-coordinate’ pathway favours this route in our opinion. Now we show that the DFT-calculated mechanism can be consolidated with the reaction model and rate laws used in Chapter 4.



**Scheme 6.5.** Two reaction pathways of Os<sup>VI</sup> & Os<sup>VIII</sup> and Os<sup>VII</sup> & Os<sup>VII</sup> comproportionation/disproportionation.

Pathway 2 now consists of four simultaneous equilibria, equations 6.7 – 6.10, where [Os<sup>VIII</sup>O<sub>4</sub>(OH)]<sup>-</sup> species reacts with *trans*-[Os<sup>VI</sup>O<sub>2</sub>(OH)<sub>4</sub>]<sup>2-</sup>.



The complete set of rate laws for the new pathway 2, equations 6.11 – 6.16, are therefore:

$$\frac{d[\text{A}']}{dt} = -k_2[\text{A}'][\text{OH}^-] + k_{-2}[\text{A}] - k_{6(2)}[\text{A}'][\text{B}] + k_{-6(2)}[\text{E}][\text{C}] \quad 6.11$$

$$\frac{d[\text{A}]}{dt} = +k_2[\text{A}'][\text{OH}^-] - k_{-2}[\text{A}] \quad 6.12$$

$$\frac{d[B]}{dt} = -k_{6(2)}[A'][B] + k_{-6(2)}[E][C] \quad 6.13$$

$$\frac{d[E]}{dt} = +k_{6(2)}[A'][B] - k_{-6(2)}[E][C] - k_8[E] + k_8[C'] \quad 6.14$$

$$\frac{d[C]}{dt} = +k_{6(2)}[A][B] - k_{-6(2)}[E][C] + k_{12}[\text{OH}^-][C'] - k_{-12}[C] \quad 6.15$$

$$\frac{d[C']}{dt} = +k_8[E] - k_8[C'] - k_{12}[\text{OH}^-][C'] + k_{-12}[C] \quad 6.16$$

We again assume that coordination sphere expansion/contraction reactions and isomerisation reactions are at equilibrium w.r.t. the time frame in which the comproportionation reaction occurs and, following the same rationale as discussed in Chapter 5, results in the following set of ordinary differential equations, as given by 6.17 – 6.20.

$$\frac{d[A']}{dt} = -k_{6(2)}[A'][B] + k_{-6(2)}[E][C] \quad 6.17$$

$$\frac{d[B]}{dt} = -k_{6(2)}[A'][B] + k_{-6(2)}[E][C] \quad 6.18$$

$$\frac{d[E]}{dt} = +k_{6(2)}[A][B] - k_{-6(2)}[E][C] \quad 6.19$$

$$\frac{d[C]}{dt} = +k_{6(2)}[A][B] - k_{-6(2)}[E][C] \quad 6.20$$

We now need to substitute for [A'] and [B] as done in Chapter 5, equations 6.21 – 6.24, while new expressions for [E] and [C] are required, equations 6.25 – 6.29.

$$K_2 = \left( \frac{[A]}{[A'][\text{OH}^-]} \right) \quad 6.21$$

where

$$[\text{Os}^{\text{VIII}}]_{\text{T}} = [A] + [A'] \quad 6.22$$

$$[A'] = \left( \frac{1}{K_2[\text{OH}^-] + 1} \right) [\text{Os}^{\text{VIII}}]_{\text{T}} \quad 6.23$$

Furthermore,

$$[\text{Os}^{\text{VI}}]_{\text{T}} = [\text{B}] \quad 6.24$$

Similarly:

$$K_{12} = \left( \frac{[\text{C}]}{[\text{C}'][\text{OH}^-]} \right) \quad 6.25$$

and

$$K_8 = \left( \frac{[\text{C}']}{[\text{E}]} \right) \quad 6.26$$

where

$$[\text{Os}^{\text{VII}}]_{\text{T}} = [\text{C}] + [\text{C}'] + [\text{E}] \quad 6.27$$

$$[\text{C}] = \left( \frac{1}{1 + \frac{1}{K_{12}[\text{OH}^-]} \left( 1 + \frac{1}{K_8} \right)} \right) [\text{Os}^{\text{VII}}]_{\text{T}} \quad 6.28$$

$$[\text{E}] = \left( \frac{1}{K_8 (K_{12}[\text{OH}^-] + 1) + 1} \right) [\text{Os}^{\text{VII}}]_{\text{T}} \quad 6.29$$

Substituting for [A'], [B], [E] and [C] into the ordinary differential equations 6.17 – 6.20 gives the rate laws in terms of  $[\text{Os}^{\text{VIII}}]_{\text{T}}$ ,  $[\text{Os}^{\text{VI}}]_{\text{T}}$  and  $[\text{Os}^{\text{VII}}]_{\text{T}}$ , equations 6.30 – 6.33:

$$\frac{d[\text{A}']}{dt} = -k_{6(2)} \left( \frac{1}{K_2[\text{OH}^-] + 1} \right) [\text{Os}^{\text{VIII}}]_{\text{T}} [\text{Os}^{\text{VI}}]_{\text{T}} + k_{-6(2)} \left( \frac{1}{K_8 (K_{12}[\text{OH}^-] + 1) + 1} \right) \left( \frac{1}{1 + \frac{1}{K_{12}[\text{OH}^-]} \left( 1 + \frac{1}{K_8} \right)} \right) [\text{Os}^{\text{VII}}]_{\text{T}}^2 \quad 6.30$$

$$\frac{d[\text{B}]}{dt} = -k_{6(2)} \left( \frac{1}{K_2[\text{OH}^-] + 1} \right) [\text{Os}^{\text{VIII}}]_{\text{T}} [\text{Os}^{\text{VI}}]_{\text{T}} + k_{-6(2)} \left( \frac{1}{K_8 (K_{12}[\text{OH}^-] + 1) + 1} \right) \left( \frac{1}{1 + \frac{1}{K_{12}[\text{OH}^-]} \left( 1 + \frac{1}{K_8} \right)} \right) [\text{Os}^{\text{VII}}]_{\text{T}}^2 \quad 6.31$$

$$\frac{d[E]}{dt} = +k_{6(2)} \left( \frac{1}{K_2 [\text{OH}^-] + 1} \right) [\text{Os}^{\text{VIII}}]_{\text{T}} [\text{Os}^{\text{VI}}]_{\text{T}} - k_{-6(2)} \left( \frac{1}{K_8 (K_{12} [\text{OH}^-] + 1) + 1} \right) \left( \frac{1}{1 + \frac{1}{K_{12} [\text{OH}^-]} \left( 1 + \frac{1}{K_8} \right)} \right) [\text{Os}^{\text{VII}}]_{\text{T}}^2 \quad 6.32$$

$$\frac{d[C]}{dt} = +k_{6(2)} \left( \frac{1}{K_2 [\text{OH}^-] + 1} \right) [\text{Os}^{\text{VIII}}]_{\text{T}} [\text{Os}^{\text{VI}}]_{\text{T}} - k_{-6(2)} \left( \frac{1}{K_8 (K_{12} [\text{OH}^-] + 1) + 1} \right) \left( \frac{1}{1 + \frac{1}{K_{12} [\text{OH}^-]} \left( 1 + \frac{1}{K_8} \right)} \right) [\text{Os}^{\text{VII}}]_{\text{T}}^2 \quad 6.33$$

At equilibrium  $d[A^{\prime}]/dt$ , equation 6.30, is equal to zero. Rearrangement of equation 6.30 yields equation 6.34. In a similar manner as shown in Chapter 5, *i.e.* equations 5.36 – 5.38, equations 6.35 and 6.36 are derived from equation 6.43.

$$\frac{k_{6(2)} \left( \frac{1}{K_2 [\text{OH}^-] + 1} \right)}{k_{-6(2)} \left( \frac{1}{K_8 (K_{12} [\text{OH}^-] + 1) + 1} \right) \left( \frac{1}{1 + \frac{1}{K_{12} [\text{OH}^-]} \left( 1 + \frac{1}{K_8} \right)} \right)} = \frac{[\text{Os}^{\text{VII}}]_{\text{T}}^2}{[\text{Os}^{\text{VIII}}]_{\text{T}} [\text{Os}^{\text{VI}}]_{\text{T}}} = K_{6(\text{obs})} \quad 6.34$$

$$K_{6(\text{obs})} = \frac{k_{6(\text{obs})}}{k_{-6(\text{obs})}} = \frac{k_{6(2)} \left( \frac{1}{K_2 [\text{OH}^-] + 1} \right)}{k_{-6(2)} \left( \frac{1}{K_8 (K_{12} [\text{OH}^-] + 1) + 1} \right) \left( \frac{1}{1 + \frac{1}{K_{12} [\text{OH}^-]} \left( 1 + \frac{1}{K_8} \right)} \right)} \quad 6.35$$

$$\frac{k_{6(2)}}{k_{-6(2)}} = K_{6(\text{true})} = \left[ \frac{\left( \frac{1}{K_8 (K_{12} [\text{OH}^-] + 1) + 1} \right) \left( \frac{1}{1 + \frac{1}{K_{12} [\text{OH}^-]} \left( 1 + \frac{1}{K_8} \right)} \right)}{\left( \frac{1}{K_2 [\text{OH}^-] + 1} \right)} \right] \frac{k_{6(\text{obs})}}{k_{-6(\text{obs})}} \quad 6.36$$

It is now again necessary to evaluate the term in the square brackets in equation 6.36 to determine by what magnitude  $K_{6(\text{true})}$  will differ from  $K_{6(\text{obs})}$  at 298.15 K. The experimental equilibrium constant  $K_2$  is equal to approximately 0.58,<sup>21,22</sup> Table 3.7, whilst the DFT-

calculated  $K_{12}$  and  $K_8$  equilibrium constant with the PBE functionals (with and without dispersion corrections) are listed in Table 6.12.

**Table 6.12. DFT-calculated standard reaction Gibbs free energy and corresponding equilibrium constant,  $K_{12}$ , of reaction 5.7 at 298.15 K in the simulated aqueous phase.**

Functional	$K_{12}$	$K_8$
PBE	0.05	$2.44 \times 10^{-4}$
PBE-D	0.96	$1.91 \times 10^{-4}$
PBE-D3	0.26	$2.15 \times 10^{-4}$
PBE-D3(BJ)	0.09	$1.97 \times 10^{-4}$
PBE-dDsC	0.13	$1.94 \times 10^{-4}$

For example, when substituting  $K_2$  with 0.58,  $K_{12}$  and  $K_8$  with the DFT-calculated PBE functional values of 0.05 and  $2.44 \times 10^{-4}$ , respectively, and  $[\text{OH}^-]$  with 2.0 into the square brackets term of equation 6.45 gives a correction factor of approximately  $5.15 \times 10^{-5}$ . The values for the term in square brackets, *i.e.* the correction factors, for the five functionals, together with the corresponding  $K_{6(\text{true})}$  and  $\Delta G^\circ_{rxn}$  (true) values for the new pathway 2 are listed in Table 6.13.

**Table 6.13. Correction factors for  $K_{6(\text{obs})}$  and approximate  $K_{6(\text{true})}$  and  $\Delta G^\circ_{rxn}$  (true) values for the comproportionation reaction at 298.15 K (new pathway 2).**

Functional	correction factor	$K_{6(\text{true})}$	$\Delta G^\circ_{rxn}$ (true) (kcal.mol <sup>-1</sup> )
PBE	$5.15 \times 10^{-5}$	$3.30 \times 10^{-4}$	4.75
PBE-D	$7.90 \times 10^{-4}$	$5.06 \times 10^{-3}$	3.13
PBE-D3	$2.36 \times 10^{-4}$	$1.51 \times 10^{-3}$	3.85
PBE-D3(BJ)	$8.02 \times 10^{-5}$	$5.13 \times 10^{-4}$	4.49
PBE-dDsC	$1.10 \times 10^{-4}$	$7.04 \times 10^{-4}$	4.30

Making these corrections to  $K_{6(\text{obs})}$  results in a range of  $\Delta G^\circ_{rxn}$  (true) values for the comproportionation reaction of approximately 3.13 (PBE-D) to 4.75 kcal.mol<sup>-1</sup> (PBE). The correction factors for the new pathway 2, Table 6.13, are relatively small values which translates to a considerable ‘decrease’ in the equilibrium constant for the Os<sup>VI</sup> & Os<sup>VIII</sup> comproportionation reaction. However, considering the complexity of the system, the obtained  $\Delta G^\circ_{rxn}$  (true) values are, in our opinion, still a good approximation of the experimental  $\Delta G^\circ_{rxn(\text{obs})}$ ,  $-1.1 \pm 2.5$  kcal.mol<sup>-1</sup>, Table 4.7.

It is important to take note of the following: We have used DFT-calculated equilibrium constants,  $K_8$  and  $K_{12}$ , to obtain an ‘experimental’  $\Delta G^\circ_{rxn}$  (true) value to compare with a DFT-calculated  $\Delta G^\circ_{rxn}$ . This defeats the purpose, in a sense, to compare experimentally obtained data with theory (DFT). However, the motivation for our ‘correction’ of  $\Delta G^\circ_{rxn(obs)}$  is to show that the  $\text{Os}^{\text{VI}}$  &  $\text{Os}^{\text{VIII}}$  comproportionation reaction mechanism obtained with DFT, Figure 6.16, can be consolidated with the reaction model and rate laws used in Chapter 4 and that the difference between the observed and ‘true’ values are relatively small.

### 6.3 Conclusions

Since a solution of  $\text{Os}^{\text{VIII}}$  in a 2.0 M NaOH aqueous matrix at 298.15 K contains two abundant  $\text{Os}^{\text{VIII}}$  oxo/hydroxido species (both species have  $d^0$  electron configuration), two competing reaction pathways were investigated; one where  $cis\text{-}[\text{Os}^{\text{VIII}}\text{O}_4(\text{OH})_2]^{2-}$  reacts with  $trans\text{-}[\text{Os}^{\text{VI}}\text{O}_2(\text{OH})_4]^{2-}$ , the other where  $[\text{Os}^{\text{VIII}}\text{O}_4(\text{OH})]^-$  reacts with  $trans\text{-}[\text{Os}^{\text{VI}}\text{O}_2(\text{OH})_4]^{2-}$ . Both reaction pathways were found to consist of (i) the formation of a (singlet state) non-covalent dimer,  $[\text{Os}^{\text{VIII}}=\text{O}\cdots\text{HO}-\text{Os}^{\text{VI}}]^{4-}$  or  $[\text{Os}^{\text{VIII}}=\text{O}\cdots\text{HO}-\text{Os}^{\text{VI}}]^{3-}$ , (ii) ‘spin-forbidden’, concerted electron-proton transfer (EPT) from the  $\text{Os}^{\text{VIII}}$  monomer to the  $trans\text{-}[\text{Os}^{\text{VI}}\text{O}_2(\text{OH})_4]^{2-}$  monomer to form a second (triplet state) non-covalent dimer,  $[\text{Os}^{\text{VII}}-\text{OH}\cdots\text{O}=\text{Os}^{\text{VI}}]^{4-}$  or  $[\text{Os}^{\text{VII}}-\text{OH}\cdots\text{O}=\text{Os}^{\text{VI}}]^{3-}$ , (iii) separation of the  $\text{Os}^{\text{VII}}$  monomers and ultimately (iv) interconversion of the separated species to form a combination of the  $trans\text{-}[\text{Os}^{\text{VII}}\text{O}_3(\text{OH})_2]^-$  and  $mer\text{-}[\text{Os}^{\text{VII}}\text{O}_3(\text{OH})_3]^{2-}$  stereoisomers. EPT from the  $\text{Os}^{\text{VIII}}$  monomer to the  $\text{Os}^{\text{VI}}$  monomer was found to be, in both cases, the rate-determining step of the comproportionation reaction for each pathway, and corroborated the experimental evidence (KIE), Section 4.2.2.3, that the rate-determining step involves the transfer of a proton.

Furthermore, a series of linear transit calculations provided compelling evidence that neither PT nor ET sequential pathway steps occur directly after the formation of the initial non-covalent dimers, *i.e.* for comproportionation or disproportionation. Moreover, sequential pathways, *i.e.* ET-PT and PT-ET, were found to be energetically unfavourable in comparison with EPT and the comparison with the experimental activation reaction enthalpy and entropy values was poor.

A direct comparison between the two DFT-calculated, EPT reaction pathways yields that the activation energy for the ‘five-coordinate’ pathway, *i.e.* where  $[\text{Os}^{\text{VIII}}\text{O}_4(\text{OH})]^-$  reacts with  $trans\text{-}[\text{Os}^{\text{VI}}\text{O}_2(\text{OH})_4]^{2-}$ , to be approximately  $2.0 \text{ kcal}\cdot\text{mol}^{-1}$  (for five different functionals) lower in magnitude than for the ‘six-coordinate’ pathway, *i.e.* where  $cis\text{-}[\text{Os}^{\text{VIII}}\text{O}_4(\text{OH})_2]^{2-}$



reacts with  $trans\text{-}[\text{Os}^{\text{VI}}\text{O}_2(\text{OH})_4]^{2-}$ . For the ‘six-coordinate’ pathway,  $\Delta^\ddagger H^\circ$ ,  $\Delta^\ddagger S^\circ$  and  $\Delta^\ddagger G^\circ$  (PBE-D3 functional) for the forward (comproportionation) reaction are equal to 2.8 kcal.mol<sup>-1</sup>, -45.0 cal.mol<sup>-1</sup>.K<sup>-1</sup> and 16.2 kcal.mol<sup>-1</sup>, respectively, and for the reverse (disproportionation) reaction are equal to -20.3 kcal.mol<sup>-1</sup>, -115.9 cal.mol<sup>-1</sup>.K<sup>-1</sup> and 14.3 kcal.mol<sup>-1</sup>, respectively. By contrast, for the ‘five-coordinate’ pathway,  $\Delta^\ddagger H^\circ$ ,  $\Delta^\ddagger S^\circ$  and  $\Delta^\ddagger G^\circ$  (PBE-D3 functional) for the forward (comproportionation) reaction are equal to 11.3 kcal.mol<sup>-1</sup>, -9.8 cal.mol<sup>-1</sup>.K<sup>-1</sup> and 14.2 kcal.mol<sup>-1</sup>, respectively, and for the reverse (disproportionation) reaction are equal to -11.8 kcal.mol<sup>-1</sup>, -80.7 cal.mol<sup>-1</sup>.K<sup>-1</sup> and 12.3 kcal.mol<sup>-1</sup>, respectively. While both pathways yield negative activation enthalpy values for the  $\text{Os}^{\text{VII}}$  &  $\text{Os}^{\text{VII}}$  disproportionation reaction, the agreement with experimental data for all six activation energy parameters is better for the ‘five-coordinate’ pathway. The overall enthalpy change of the MECP relative to the ‘final’ products is negative, due to the extensive intermolecular hydrogen bonding interactions of the MECP (which are absent for the ‘final’ products) which lowers the electronic energy, w.r.t. the ‘final’ products on the potential energy surface. The results of the DFT calculations lead us to conclude that ‘five-coordinate’ and ‘six-coordinate’ EPT pathways are more probable than any one of the four identified sequential pathways.

If the concentrations of all the reactant species are chosen as the standard state, the ‘five-coordinate’ pathway will be the dominant mechanism, specifically due its comparatively lower Gibbs activation energy. However, the concentration of the  $cis\text{-}[\text{Os}^{\text{VII}}\text{O}_3(\text{OH})_2]^-$  species, which features in the ‘five-coordinate’ pathway only, is considerably lower (by approximately 1200 times) than the concentration of the  $mer\text{-}[\text{Os}^{\text{VII}}\text{O}_3(\text{OH})_3]^{2-}$  species (both the  $mer\text{-}[\text{Os}^{\text{VII}}\text{O}_3(\text{OH})_3]^{2-}$  and  $trans\text{-}[\text{Os}^{\text{VII}}\text{O}_3(\text{OH})_2]^-$  species feature in both pathways). Although the ‘five-coordinate’ pathway was found to have a lower activation energy barrier, the low concentration of the  $cis\text{-}[\text{Os}^{\text{VII}}\text{O}_3(\text{OH})_2]^-$  species could be significant enough such that the ‘six-coordinate’ pathway dominates comproportionation. However, the good agreement of DFT-calculated activation energy parameters for the ‘five-coordinate’ pathway in comparison with our Eyring plot analyses values (above), indicates that the relatively low concentration of the  $cis\text{-}[\text{Os}^{\text{VII}}\text{O}_3(\text{OH})_2]^-$  species in comparison with the  $mer\text{-}[\text{Os}^{\text{VII}}\text{O}_3(\text{OH})_3]^{2-}$  species is probably not low enough such that the ‘six-coordinate’ pathway dominates comproportionation. Therefore, the ‘five-coordinate’ EPT pathway most probably dominates  $\text{Os}^{\text{VI}}$  &  $\text{Os}^{\text{VIII}}$  comproportionation and  $\text{Os}^{\text{VII}}$  &  $\text{Os}^{\text{VII}}$  disproportionation in a 2.0 M NaOH aqueous matrix.

Initially, the experimental kinetic and equilibrium analysis of the  $\text{Os}^{\text{VI}}$  &  $\text{Os}^{\text{VIII}}$  comproportionation reaction did not take into account which particular  $\text{Os}^{\text{VIII}}$  species reacts with  $\text{trans-}[\text{Os}^{\text{VI}}\text{O}_2(\text{OH})_4]^{2-}$  and neither was the “identity” or stereochemistry of the  $\text{Os}^{\text{VII}}$  product species, *i.e.* five-coordinate or six-coordinate, taken into account. However, when we took into consideration the  $\text{Os}^{\text{VIII}}$  species that actually participates ‘directly’ in the comproportionation reaction, pathway 2 in Chapter 6, we illustrated how the original reaction model, equation 8.5, and corresponding rate laws, is recovered. After correcting for the observed rate constants and observed thermodynamic parameters from stopped-flow UV-Vis spectroscopy kinetics experiments, we saw that the ‘true’ thermodynamic parameters are close in magnitude with the observed thermodynamic parameters. The assumptions that  $\text{Os}^{\text{VIII}}$  and  $\text{Os}^{\text{VII}}$  coordination sphere expansion/contraction reactions are at equilibrium while the  $\text{Os}^{\text{VI}}$  &  $\text{Os}^{\text{VIII}}$  comproportionation reaction progresses, was further validated by a set of numerical experiments where the osmium species’ conc. vs. time profiles of the comproportionation reaction were monitored while systematically decreasing the rate constants,  $k_2$  &  $k_{-2}$ , of the  $\text{Os}^{\text{VIII}}$  coordination sphere expansion/contraction reaction; only when the  $\text{Os}^{\text{VIII}}$  coordination sphere expansion/contraction reaction rate constants were decreased by approximately 10 000 times in magnitude, are visible difference noticed for the osmium species’ conc. vs. time profiles of the comproportionation reaction.

---

**References**

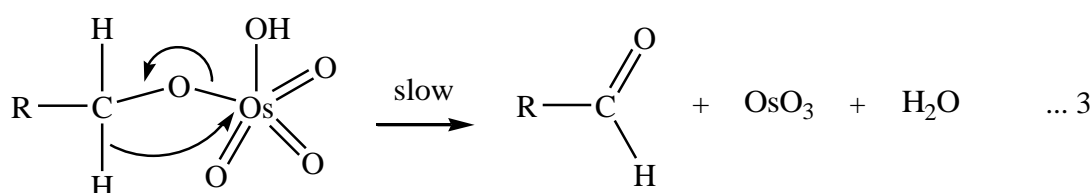
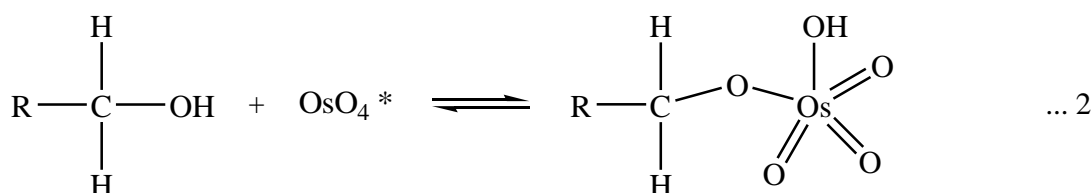
1. T. E. Geswindt, W. J. Gerber, H. E. Rohwer and K. R. Koch, *Dalton Trans.*, 2011, **40**, 8581.
2. D. R. Weinberg, C. J. Gagliardi, J. F. Hull, C. F. Murphy, C. A. Kent, B. C. Westlake, A. Paul, D. H. Ess, D. G. McCafferty and T. J. Meyer, *Chem. Rev.*, 2012, **112**, 4016.
3. X. Han, R. Lee, T. Chen, J. Luo. Y. Lu and K. –W. Huang, *Sci. Rep.*, 2013, **3**, 2557.
4. T. Shimomura, K. J. Tölle, J. Smid and M. Szwarc, *J. Am. Chem. Soc.*, 1967, **89**, 796.
5. M. T. H. Liu and R. Bonneau, *J. Am. Chem. Soc.*, 1992, **114**, 3604.
6. A. A. Boyd and R. Lesclaux, *Int. J. Chem. Kinetics*, 1997, **29**, 323.
7. L. P. Olson, K. T. Kuwata, M. D. Bartberger and K. N. Houk, *J. Am. Chem. Soc.*, 2002, **124**, 9469.
8. L. Feria, C. Gonzalez and M. Castro, *Int. J. Quantum Chem.*, 2004, **99**, 605.
9. S. Grimme and J-P. Djukic, *Inorg. Chem.*, 2011, **50**, 2619.
10. F.G. Groenewald, C. Esterhuysen and J. L. M. Dillen, *Theor. Chem. Acc.*, 2012, **131**, 1281.
11. T. Ziegler and A. Rauk, *Inorg. Chem.*, 1979, **18**, 1558.
12. T. Ziegler and A. Rauk, *Inorg. Chem.*, 1979, **18**, 1755.
13. J. I. Rodríguez, R. F. W. Bader, P. W. Ayers, C. Michel, A. W. Götz and C. Bo, *Chem. Phys. Lett.*, 2009, **472**, 149.
14. J. I. Rodríguez, *J. Comput. Chem.*, 2013, **34**, 681.
15. M. Mitoraj, A. Michalak and T. Ziegler, *J. Chem. Theory Comput.*, 2009, **5**, 962.
16. S. F. Boys and F. Bernardi, *Mol. Phys.*, 1970, **19(4)**, 553.
17. A. Rosa, A. W. Ehlers, E. J. Baerends, J. G. Snijders and G. te Velde, *J. Phys. Chem.*, 1996, **100(14)**, 5690.

# CHAPTER 7

## A Kinetic UV-Vis Spectroscopic and DFT Mechanistic Study of the Redox Reaction of $[\text{Os}^{\text{VIII}}\text{O}_4(\text{OH})_n]^{n-}$ ( $n = 1, 2$ ) and Methanol in a Basic Aqueous Matrix

### 7.1 Introduction

There are several reported kinetic studies pertaining to the reduction of  $\text{Os}^{\text{VIII}}\text{O}_4$  with molecular hydrogen, alcohols, diols and  $\alpha$ -hydroxy acids in basic aqueous matrices.<sup>1-13</sup> VeeraSomaiah *et al.*<sup>4</sup> proposed that the reaction mechanism when  $\text{Os}^{\text{VIII}}$  oxidises primary alcohols consists of a hydride ion abstraction step, as shown by reaction Scheme 7.1.

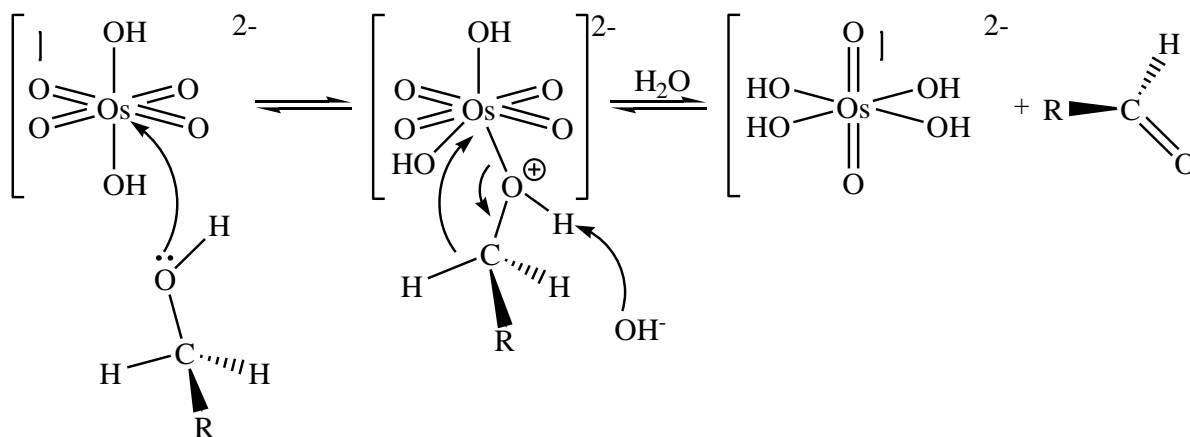


\* $[\text{OsO}_4(\text{OH})_2]^{2-}$  written as  $\text{OsO}_4$  as per original authors

**Scheme 7.1.** Proposed reaction scheme by VeeraSomaiah *et al.*<sup>4</sup> for the oxidation of primary alcohols by an  $\text{Os}^{\text{VIII}}$  species in a basic aqueous matrix.

According to our DFT speciation results in Chapters 3 and 5, it is now evident that there are several noticeable problems with the reaction mechanism proposed by VeeraSomaiah *et al.*<sup>4</sup>, Scheme 7.1. In addition to the erroneous suggested  $\text{Os}^{\text{VIII}}$  species, *i.e.* the  $\text{OsO}_4(\text{OH})\text{H}_2\text{O}$  complex, the authors do not, similarly to most of the other prior studies,<sup>2,3,5-13</sup> account for the

formation of Os<sup>VII</sup> species<sup>21</sup> (which we have confirmed does occur) during the reduction of Os<sup>VIII</sup> species<sup>22</sup> with aliphatic alcohols. Furthermore, VeeraSomaiah *et al.*<sup>4</sup> proposed that the oxygen of the alcohol's hydroxyl group coordinates directly with the osmium metal centre, to form a seven-coordinate, covalently bonded dimer species, followed by a slow and questionable rearrangement step in which OsO<sub>3</sub> and an aldehyde are formed. The confusing reaction scheme by VeeraSomaiah *et al.*<sup>4</sup> is similar to that proposed by Geswindt<sup>14</sup> several years later, Scheme 7.2.



**Scheme 7.2.** Proposed reaction scheme by Geswindt<sup>14</sup> for the oxidation of primary alcohols by an Os<sup>VIII</sup> species in a basic aqueous matrix.

Geswindt<sup>14</sup> proposed that the oxygen of the alcohol's hydroxyl group coordinates to *trans*-[Os<sup>VIII</sup>O<sub>4</sub>(OH)<sub>2</sub>]<sup>2-</sup>, a species which is present in negligible amounts in a 2.0 M NaOH matrix at 298.15 K (Chapter 3), to form a “*large, low-charge*”, seven-coordinate intermediate dimer species. Since high oxidation state osmium complexes are normally associated with strong  $\sigma$ - and  $\pi$ - donor ligands,<sup>15</sup> the author<sup>14</sup> concluded that “*initial association of the alcohol through the oxygen atom is far more favourable than through a hydrogen atom.*” Furthermore, the second step of the proposed reaction, Scheme 7.2, considered as the rate-limiting step, involves “*hydride ion transfer to the osmium metal centre, in which the hydride attached to the  $\alpha$ -carbon is transferred to the osmium with the resultant formation of a C – O double bond and the reduction of osmium(VIII) to osmium(VI). There is a rapid rearrangement of the hydrogen atom to an oxygen atom in the second step of the depicted reaction mechanism,*

<sup>21</sup> Os<sup>VII</sup> refers to a combination of the *trans*-[Os<sup>VII</sup>O<sub>3</sub>(OH)<sub>2</sub>]<sup>-</sup> and *mer*-[Os<sup>VII</sup>O<sub>3</sub>(OH)<sub>3</sub>]<sup>2-</sup> complex anions that are simultaneously present in a 2.0 M NaOH aqueous matrix, Chapter 5.

<sup>22</sup> Os<sup>VIII</sup> refers to a combination of the [Os<sup>VIII</sup>O<sub>4</sub>(OH)]<sup>-</sup> and *cis*-[Os<sup>VIII</sup>O<sub>4</sub>(OH)<sub>2</sub>]<sup>2-</sup> complex anions that are simultaneously present in a 2.0 M NaOH aqueous matrix,

*and then further interaction with water in the final step, resulting in the formation of the osmium(VI) product.”*

We do not agree with the proposed reaction schemes by VeeraSomaiah *et al.*<sup>4</sup> or Geswindt<sup>14</sup> due to the glaring inconsistencies with our own results in Chapters 3 – 6. Furthermore, neither of the two mentioned reports provide any further evidence, *e.g. via* computational chemistry methods, to substantiate their proposals and both evidently do not have detailed knowledge w.r.t. which high oxidation state osmium species are actually present in basic aqueous media. Nonetheless, the rate constants of the reversible, parallel  $\text{Os}^{\text{VI}}$  &  $\text{Os}^{\text{VIII}}$  comproportionation reaction, which produces the  $\text{Os}^{\text{VII}}$  species, have been determined accurately (Chapter 4) and the thermodynamics and mechanism have subsequently been investigated with DFT (Chapters 5 and 6). These results, together with our detailed knowledge of which high oxidation state osmium species are actually present in basic aqueous media, provides us with the necessary information required to investigate the mechanism of the reduction of  $\text{Os}^{\text{VIII}}$  with methanol in a 2.0 M NaOH aqueous matrix.

In this study we aim to incorporate our findings from Chapters 3 – 6 to elucidate the reaction mechanism of  $\text{Os}^{\text{VIII}}$  reduction with methanol in a 2.0 M NaOH aqueous matrix.

## 7.2 Results and discussion

### 7.2.1 UV-Vis kinetic investigation of $\text{Os}^{\text{VIII}}$ reduction with methanol

In order to calculate thermodynamic activation energy parameters ( $\Delta^\ddagger H^\circ$ ,  $\Delta^\ddagger S^\circ$  and  $\Delta^\ddagger G^\circ$ ) from reaction rate constants, variable temperature (Sections 7.2.1.1 and 7.2.1.3) and variable reagent concentration (Section 7.2.1.2) kinetics experiments of the reduction of  $\text{Os}^{\text{VIII}}$  oxo/hydroxido species with methanol were performed. In all the kinetic experiments, the UV-Vis absorbance signal of the reactions was monitored at 370 nm.<sup>23</sup> In order to probe the reaction mechanism, the reducing agent utilised in Section 7.2.1.1,  $\text{CH}_3\text{OH}$ , was replaced with  $\text{CD}_3\text{OD}$  in Sections 7.2.1.2 and 7.2.1.3. Since one of the three  $\alpha$ -carbon-hydrogen bonds of methanol must break in order to produce formaldehyde, a primary kinetic isotope effect (KIE) value,  $k_{\text{H}}/k_{\text{D}}$ , is expected, *i.e.* the reaction rate should decrease for the redox reaction of  $\text{Os}^{\text{VIII}}$  oxo/hydroxido species with methanol.

---

<sup>23</sup> The molar extinction coefficients of the  $\text{Os}^{\text{VI}}$ ,  $\text{Os}^{\text{VIII}}$  and  $\text{Os}^{\text{VII}}$  oxo/hydroxido species in a 2.0 M NaOH matrix have been reported at 370 nm, Chapter 4.<sup>1,2,13</sup>

Prior to each kinetic reaction, a reaction “blank” was obtained, where the Os<sup>VIII</sup> spectrum in a 2.0 M NaOH aqueous matrix was recorded in the absence of methanol. This was required in order to obtain the initial UV-Vis spectrum at time equals zero. No more than 25 seconds elapsed from initiating the reaction to the first spectral recording being made.

### 7.2.1.1 Variable temperature, constant [Os<sup>VIII</sup>] and [CH<sub>3</sub>OH]

Gerber *et al.*<sup>1</sup> investigated the kinetics of the reduction of Os<sup>VIII</sup> species as a function of methanol (CH<sub>3</sub>OH) concentration in a 2.0 M NaOH matrix at 298.15 K. They report that the reaction is first order w.r.t. both the total Os<sup>VIII</sup> and methanol (CH<sub>3</sub>OH) concentrations, with a calculated rate constant (expressed as  $k_{13}$  in this study) for the redox reaction, equation 7.1, of  $0.29 \pm 0.02 \text{ M}^{-1} \cdot \text{s}^{-1}$ .



To further investigate the reduction reaction of Os<sup>VIII</sup> with methanol (CH<sub>3</sub>OH), a variable temperature kinetic experiment was performed. The total Os<sup>VIII</sup> and methanol (CH<sub>3</sub>OH) concentrations were kept constant, at approximately 0.3 mM and 5 mM, respectively, in a 2.0 M NaOH aqueous matrix and the kinetic measurement acquisition runs were performed at five different temperatures between 285.7 and 302.3 K. The trends depicting absorbance vs. time, shown as symbols in Figure 7.1, are the obtained kinetic traces at each temperature.

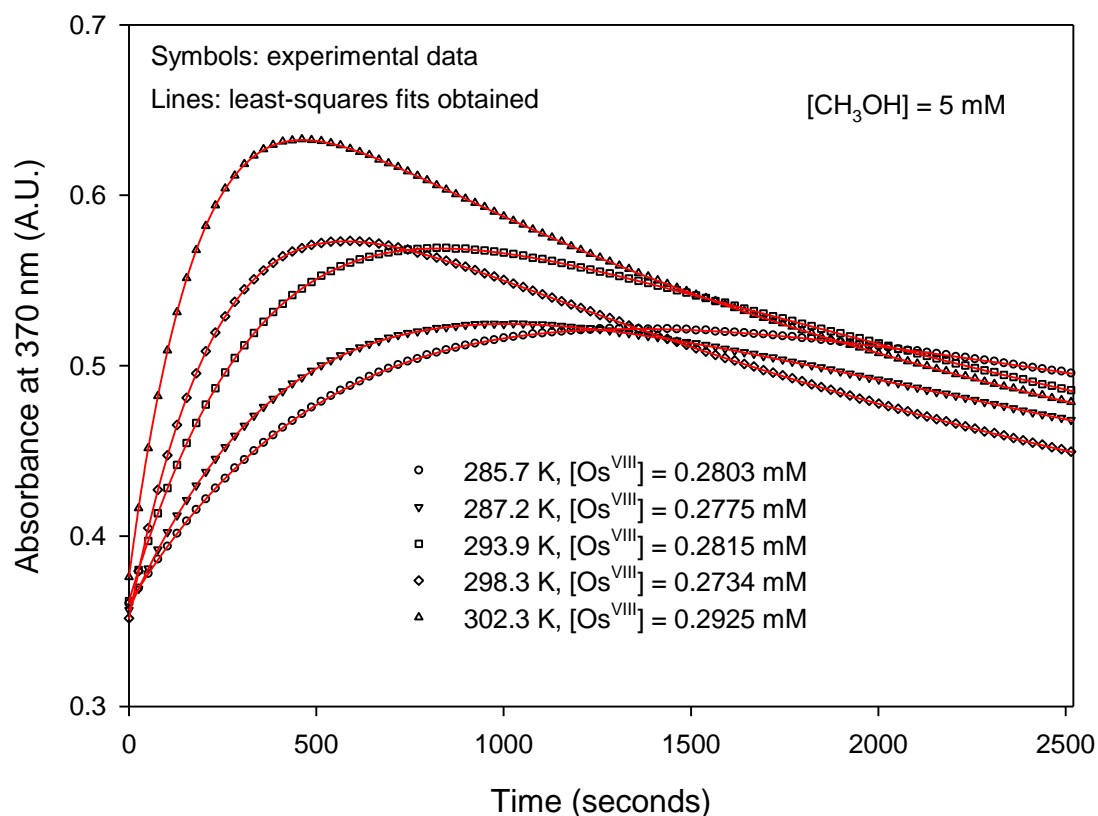


**Figure 7.1.** Kinetic traces depicting the change in absorbance during the simultaneous reduction of Os<sup>VIII</sup> with methanol (CH<sub>3</sub>OH) and the Os<sup>VI</sup> & Os<sup>VIII</sup> comproportionation reactions at various temperatures. The temperature and Os<sup>VIII</sup> concentration at which each of the acquisitions was recorded are shown.

Before the reactants are mixed, the only osmium species present are Os<sup>VIII</sup> oxo/hydroxido species.<sup>24</sup> When the reaction is initiated, the absorbance first increases with time, Figure 7.1, until a maximum is reached, after which the absorbance steadily decreases until, for all practical purposes, all the osmium species are converted to Os<sup>VI</sup>,<sup>25</sup> if the system is allowed to reach equilibrium. Moreover, at higher temperatures, the absorbance maximum is reached in less time and the absorbance value at the maximum is larger. Taking into account that the

<sup>24</sup> The absorbance values of the first data points are the same (taking into account minor variations in starting Os<sup>VIII</sup> concentration) at the different temperatures, Figure 7.1, indicating that the Os<sup>VIII</sup> species distribution is largely independent of temperature or that the molar extinction coefficients of the [Os<sup>VIII</sup>O<sub>4</sub>(OH)]<sup>-</sup> and *cis*-[Os<sup>VIII</sup>O<sub>4</sub>(OH)]<sup>2-</sup> species are close in magnitude. This observation is consistent with the recorded UV-Vis spectra of Os<sup>VIII</sup> in a 2.0 M NaOH aqueous matrix at various temperatures, Figure 4.7, and the consistent calculated molar extinction coefficients values for the Os<sup>VIII</sup> species at different temperatures, Tables 4.3, 4.6 and 4.9.

<sup>25</sup> The use of excess methanol (CH<sub>3</sub>OH) in the experiments is expected to ultimately convert all the osmium species to the *trans*-[Os<sup>VI</sup>O<sub>2</sub>(OH)<sub>4</sub>]<sup>2-</sup> species, as reported by Gerber *et al.*<sup>1</sup>, who reported that the only osmium species that remains in solution at equilibrium under such conditions are the *trans*-[Os<sup>VI</sup>O<sub>2</sub>(OH)<sub>4</sub>]<sup>2-</sup> species, *i.e.* the concentrations of Os<sup>VIII</sup> or Os<sup>VII</sup> (*vide infra*) species at equilibrium are negligible.



only species in these solutions that absorb light at 370 nm are the osmium species, several deductions regarding what reactions are occurring can be made:

Firstly, when  $\text{Os}^{\text{VIII}}$  reacts with methanol ( $\text{CH}_3\text{OH}$ ), reaction 7.1, to produce  $\text{Os}^{\text{VI}}$  and formaldehyde, it could be expected that, from the time that the reaction is initiated up until equilibrium is reached, the absorbance will only decrease in magnitude, since the molar extinction coefficient of  $\text{Os}^{\text{VI}}$  is considerably smaller than that of  $\text{Os}^{\text{VIII}}$  at 370 nm (Tables 4.3, 4.6 and 4.9). However, the absorbance first increases and then decreases. This trend can be understood when taking into account that when  $\text{Os}^{\text{VI}}$  is initially produced, equation 7.1, it will react with  $\text{Os}^{\text{VIII}}$  via a comproportionation reaction (Chapters 4 – 6), equation 7.2 (4.14), to form  $\text{Os}^{\text{VII}}$ , which has a larger molar extinction coefficient than both  $\text{Os}^{\text{VI}}$  and  $\text{Os}^{\text{VIII}}$  at 370 nm (Tables 4.3, 4.6 and 4.9). Furthermore, the mole ratio of  $\text{Os}^{\text{VIII}}$  and  $\text{Os}^{\text{VI}}$  is 1:1 when the absorbance maxima is reached.<sup>1</sup> Therefore, apart from investigating the reduction of  $\text{Os}^{\text{VIII}}$  with methanol, we are in effect performing an indirect kinetic mole ratio experiment akin to that done in Chapter 4. Moreover, since the  $\text{Os}^{\text{VI}}$  &  $\text{Os}^{\text{VIII}}$  comproportionation reaction is endothermic (Chapters 4 – 6), more  $\text{Os}^{\text{VII}}$  is produced at higher temperatures which is reflected by the increase of the absorbance value at the maximum.

It should also be noted that the rate of the  $\text{Os}^{\text{VI}}$  &  $\text{Os}^{\text{VIII}}$  comproportionation reaction is several thousand times faster than the rate of  $\text{Os}^{\text{VIII}}$  reduction with methanol ( $\text{CH}_3\text{OH}$ ),<sup>1</sup> which implies that the  $\text{Os}^{\text{VI}}$  &  $\text{Os}^{\text{VIII}}$  comproportionation reaction is essentially at equilibrium as reaction 7.1 progresses (*vide infra*). Furthermore, as discussed in Chapters 3 and 5 (Sections 3.2.2 and 5.2.4), the coordination sphere expansion/contraction reactions of  $\text{Os}^{\text{VIII}}$  and  $\text{Os}^{\text{VII}}$  species, respectively, are again, for all practical purposes, essentially at equilibrium whilst reaction 7.2 (and therefore also reaction 7.1) progresses.

In effect, we are dealing with three ‘classes’ of chemical reactions namely (i)  $\text{Os}^{\text{VIII}}$  reduction with methanol, (ii)  $\text{Os}^{\text{VI}}$  &  $\text{Os}^{\text{VIII}}$  comproportionation/ $\text{Os}^{\text{VII}}$  &  $\text{Os}^{\text{VII}}$  disproportionation and (iii) coordination sphere expansion/contraction of  $\text{Os}^{\text{VIII}}$  and  $\text{Os}^{\text{VII}}$  species, that progress at significantly different time scales.

Lastly, to account for why the absorbance maximum occurs in less time at higher temperatures is straightforward: the rate of reaction 7.1 increases, which in turn results in the faster production of  $\text{Os}^{\text{VI}}$ . This results in a shorter time at which the mole ratio of  $\text{Os}^{\text{VIII}}$  and  $\text{Os}^{\text{VI}}$  will be 1:1, the time at which the maximum amount of  $\text{Os}^{\text{VII}}$  is present in solution. Taking the above into account, while assuming that the coordination sphere

expansion/contraction reactions of Os<sup>VIII</sup> and Os<sup>VII</sup> species are at equilibrium, the simplest reaction model is given by reactions 7.1 & 7.2 (4.14), with the corresponding rate laws given by equations 7.3 – 7.7.



$$\frac{d[\text{Os}^{\text{VIII}}]}{dt} = -k_{13}[\text{Os}^{\text{VIII}}][\text{CH}_3\text{OH}] - k_{6(\text{obs})}[\text{Os}^{\text{VIII}}][\text{Os}^{\text{VI}}] + k_{-6(\text{obs})}[\text{Os}^{\text{VII}}]^2 \quad 7.3$$

$$\frac{d[\text{CH}_3\text{OH}]}{dt} = -k_{13}[\text{Os}^{\text{VIII}}][\text{CH}_3\text{OH}] \quad 7.4$$

$$\frac{d[\text{Os}^{\text{VI}}]}{dt} = k_{13}[\text{Os}^{\text{VIII}}][\text{CH}_3\text{OH}] - k_{6(\text{obs})}[\text{Os}^{\text{VIII}}][\text{Os}^{\text{VI}}] + k_{-6(\text{obs})}[\text{Os}^{\text{VII}}]^2 \quad 7.5$$

$$\frac{d[\text{CH}_2\text{O}]}{dt} = k_{13}[\text{Os}^{\text{VIII}}][\text{CH}_3\text{OH}] \quad 7.6$$

$$\frac{d[\text{Os}^{\text{VII}}]}{dt} = 2k_{6(\text{obs})}[\text{Os}^{\text{VIII}}][\text{Os}^{\text{VI}}] - 2k_{-6(\text{obs})}[\text{Os}^{\text{VII}}][\text{Os}^{\text{VII}}] \quad 7.7 \text{ (4.16)}$$

As was done in Chapter 4, we used a simplified reaction model where many ‘constant’ parameters, such as the hydroxide concentration and the equilibrium constants of the five-coordinate and six-coordinate Os<sup>VIII</sup> and Os<sup>VII</sup> species, are contained within the observed rate constants,  $k_{6(\text{obs})}$  and  $k_{-6(\text{obs})}$ . We can use the simplified reaction model since  $k_{6(\text{obs})}$  and  $k_{-6(\text{obs})}$  are close in magnitude to the ‘true’ rate constants,  $k_6$  and  $k_{-6}$ , Chapters 5 and 6. Using the software Program Dynafit,<sup>16</sup> the rate laws given above were simulated and the non-linear least squares fits obtained were excellent, Figure 7.1. It should be noted that the initial ‘trial’ rate constant values of reaction 7.2 (4.14),  $k_{6(\text{obs})}$  &  $k_{-6(\text{obs})}$ , were obtained *via* extrapolation, using the Os<sup>VI</sup> & Os<sup>VIII</sup> comproportionation and Os<sup>VII</sup> & Os<sup>VII</sup> disproportionation Eyring plots, Figure 4.8 (a) and (b), respectively. The newly optimised  $k_{6(\text{obs})}$  and  $k_{-6(\text{obs})}$  varied by less than 1% from those obtained from the “stopped-flow” experiment’s Eyring plots, Figure 7.3 (a) and (b). The calculated rate constants for reactions 7.1 and 7.2 ( $k_{13(\text{H})}$ ,  $k_{6(\text{obs})}$  and  $k_{-6(\text{obs})}$ ) are listed in Table 7.1.

**Table 7.1. Calculated rate constants of reactions 7.1 & 7.2 and the corresponding equilibrium constants of reaction 7.2 at various temperatures (exp. 7.2.1.1).**

Temperature (K)	$k_{13(H)}$ ( $M^{-1}.s^{-1}$ )	$k_{6(obs)}$ ( $M^{-1}.s^{-1}$ )	$k_{-6(obs)}$ ( $M^{-1}.s^{-1}$ )	$K_{6(obs)}$ = ( $k_{6(obs)}/k_{-6(obs)}$ )
285.7	$(1.012 \pm 0.013) \times 10^{-1}$	$(2.075 \pm 0.036) \times 10^4$	$(1.072 \pm 0.018) \times 10^4$	$1.94 \pm 0.07$
287.2	$(1.425 \pm 0.003) \times 10^{-1}$	$(2.317 \pm 0.017) \times 10^4$	$(1.026 \pm 0.008) \times 10^4$	$2.26 \pm 0.02$
293.9	$(2.082 \pm 0.002) \times 10^{-1}$	$(3.609 \pm 0.028) \times 10^4$	$(7.844 \pm 0.033) \times 10^3$	$4.60 \pm 0.02$
298.3	$(3.305 \pm 0.017) \times 10^{-1}$	$(4.795 \pm 0.021) \times 10^4$	$(6.694 \pm 0.020) \times 10^3$	$7.16 \pm 0.04$
302.3	$(4.533 \pm 0.036) \times 10^{-1}$	$(6.220 \pm 0.041) \times 10^4$	$(5.660 \pm 0.093) \times 10^3$	$10.99 \pm 0.15$
298.1 <sup>1</sup>	$(2.9 \pm 0.2) \times 10^{-1}$	-	-	-

At higher temperatures, the rate constant for the Os<sup>VIII</sup> reduction with methanol (CH<sub>3</sub>OH),  $k_{13(H)}$ , and for the Os<sup>VI</sup> & Os<sup>VIII</sup> comproportionation,  $k_{6(obs)}$ , reactions increase while the rate constant for the Os<sup>VII</sup> & Os<sup>VII</sup> disproportionation reaction,  $k_{-6(obs)}$ , decreases, which is consistent with the trends obtained from the stopped-flow UV-Vis spectroscopy experiments presented in Chapter 4 (Table 4.4). Moreover, the rate constant for reaction 7.1,  $k_{13(H)}$ , at 298.15 K is, *via* interpolation, approximately  $3.2 \times 10^{-1}$  and agrees excellently with the reported value of  $(2.9 \pm 0.2) \times 10^{-1}$  by Gerber *et al.*<sup>1</sup>

The Eyring plot for reaction 7.1 is linear, Figure 7.2. Furthermore, all five data points are within the 95% confidence interval while the calculated errors<sup>17</sup> of  $\Delta^\ddagger H^\circ$ ,  $\Delta^\ddagger S^\circ$  and  $\Delta^\ddagger G^\circ$  are relatively small, Table 7.2.

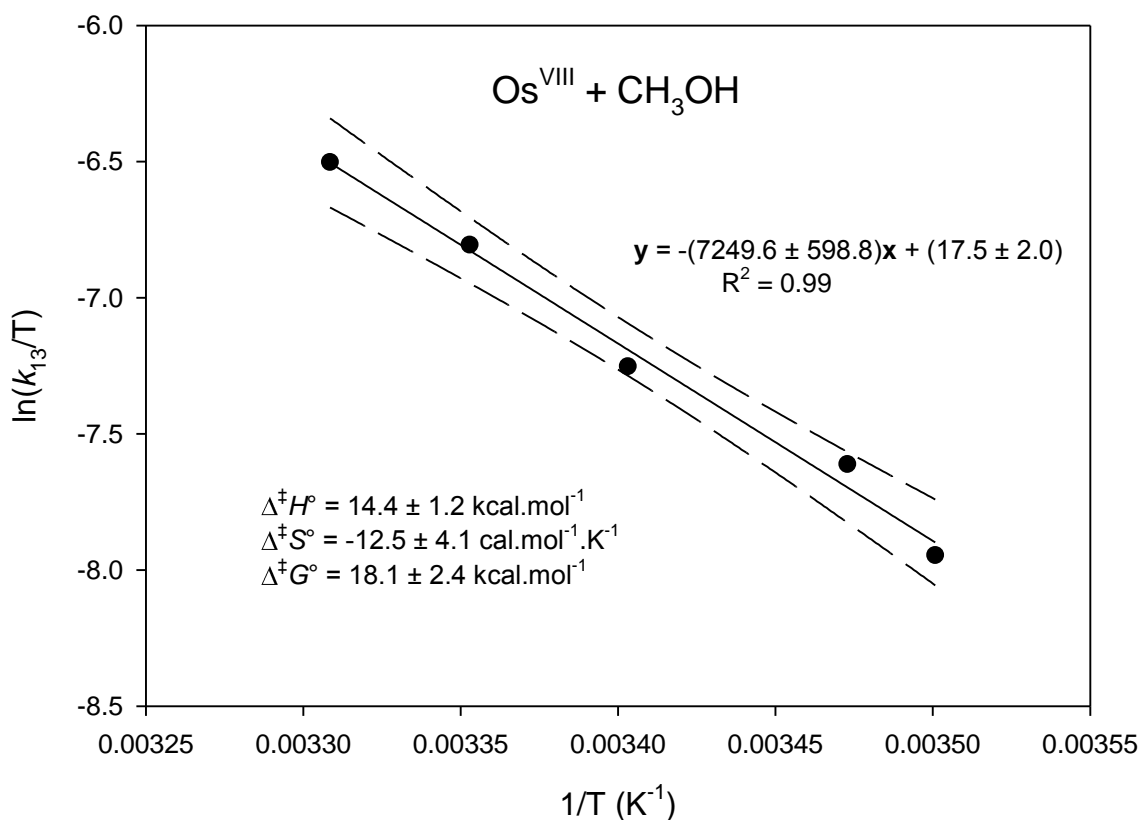


**Figure 7.2.** Eyring plot with 95% confidence intervals for the reduction of  $\text{Os}^{\text{VIII}}$  species with methanol ( $\text{CH}_3\text{OH}$ ).

**Table 7.2.** Activation energies for the reduction of  $\text{Os}^{\text{VIII}}$  species with methanol ( $\text{CH}_3\text{OH}$ ).

$\Delta^{\ddagger}H^{\circ}$ (kcal.mol <sup>-1</sup> )	$\Delta^{\ddagger}S^{\circ}$ (cal.mol <sup>-1</sup> .K <sup>-1</sup> )	$\Delta^{\ddagger}G^{\circ}_{298.15 \text{ K}}$ (kcal.mol <sup>-1</sup> )
14.4 ± 1.2	-12.5 ± 4.1	18.1 ± 2.4

The Eyring plots for both the  $\text{Os}^{\text{VI}}$  &  $\text{Os}^{\text{VIII}}$  comproportionation and  $\text{Os}^{\text{VII}}$  &  $\text{Os}^{\text{VII}}$  disproportionation reactions are linear, Figure 7.3 (a) and (b). Furthermore, all five data points are within the 95% confidence interval while the calculated errors<sup>17</sup> of  $\Delta^{\ddagger}H^{\circ}_{(\text{obs})}$ ,  $\Delta^{\ddagger}S^{\circ}_{(\text{obs})}$  and  $\Delta^{\ddagger}G^{\circ}_{(\text{obs})}$  are relatively small, Table 7.3. The obtained activation energies of the  $\text{Os}^{\text{VI}}$  &  $\text{Os}^{\text{VIII}}$  comproportionation and  $\text{Os}^{\text{VII}}$  &  $\text{Os}^{\text{VII}}$  disproportionation reactions are in excellent agreement with the directly obtained, *i.e.* with stopped-flow UV-Vis spectroscopy, values in Chapter 4, Table 4.5.

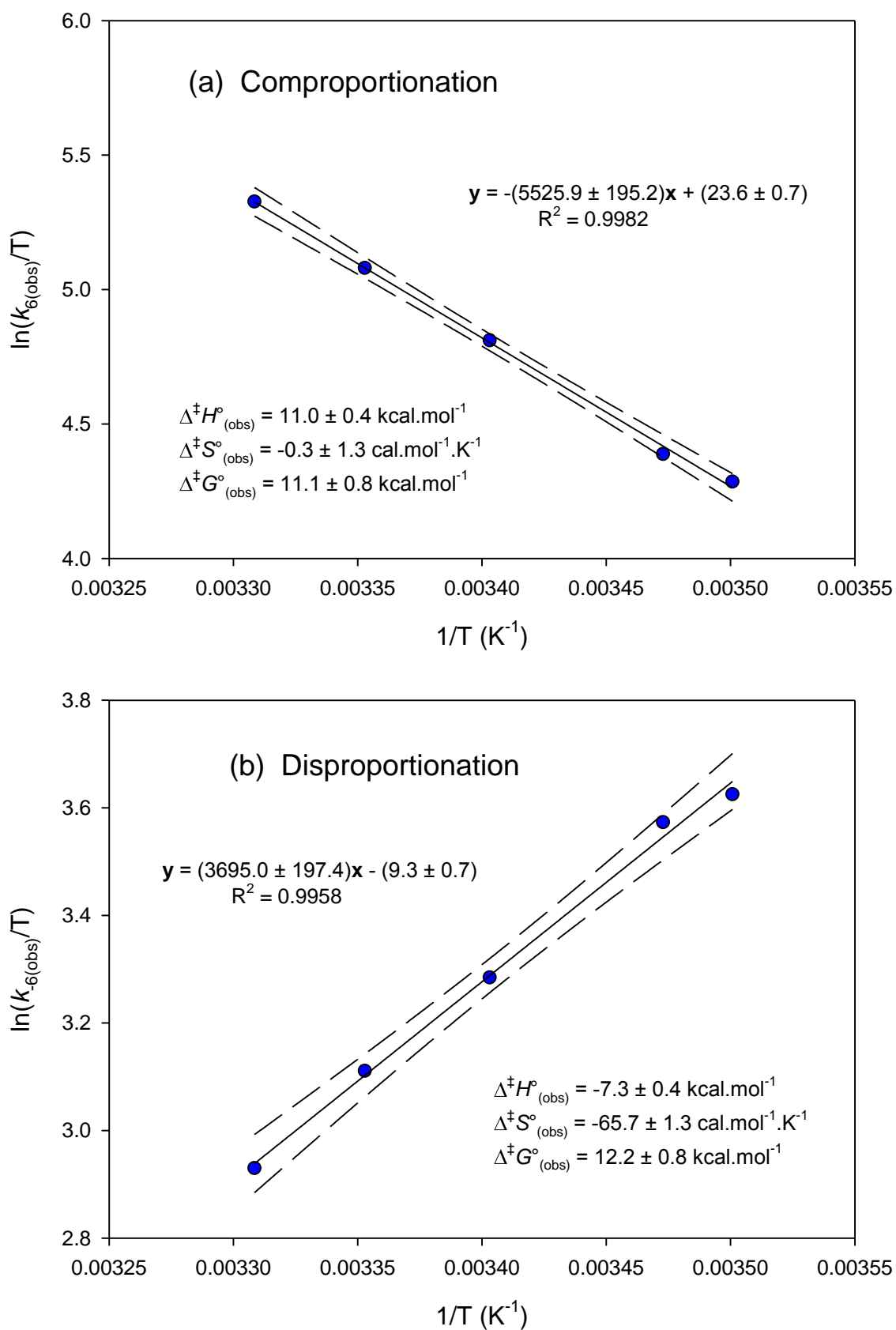


**Figure 7.3.** Eyring plots with 95% confidence intervals for the (a) Os<sup>VI</sup> & Os<sup>VIII</sup> comproportionation and (b) Os<sup>VII</sup> & Os<sup>VII</sup> disproportionation reactions (exp. 7.2.1.1).

**Table 7.3. Activation energies of the Os<sup>VI</sup> & Os<sup>VIII</sup> comproportionation and Os<sup>VII</sup> & Os<sup>VII</sup> disproportionation reactions (exp. 7.2.1.1).**

Reaction	$\Delta^\ddagger H^\circ_{(\text{obs})}$ (kcal.mol <sup>-1</sup> )	$\Delta^\ddagger S^\circ_{(\text{obs})}$ (cal.mol <sup>-1</sup> .K <sup>-1</sup> )	$\Delta^\ddagger G^\circ_{(\text{obs})}$ (kcal.mol <sup>-1</sup> )
comproportionation	11.0 ± 0.4	-0.3 ± 1.3	11.1 ± 0.8
disproportionation	-7.3 ± 0.4	-65.7 ± 1.3	12.2 ± 0.8

Calculated extinction coefficients from the non-linear least squares fits for the Os<sup>VIII</sup> and Os<sup>VI</sup> species agree well with previously reported experimental values, Table 7.4.<sup>1,2,13</sup> The good agreement of extinction coefficients with that reported in the literature as well as the linearity of the Eyring plots validates the assumptions made for the derivation of the reaction model, equations 7.1 & 7.2.

**Table 7.4. Comparison of the calculated and literature high oxidation state osmium species' molar extinction coefficients at 370 nm obtained from the variable temperature kinetics experiment (exp. 7.2.1.1).**

osmium species	Calculated (L.mol <sup>-1</sup> .cm <sup>-1</sup> )	Literature <sup>1,2,13</sup> (L.mol <sup>-1</sup> .cm <sup>-1</sup> )	
([Os <sup>VIII</sup> O <sub>4</sub> (OH)] <sup>-</sup> + <i>cis</i> -[Os <sup>VIII</sup> O <sub>4</sub> (OH) <sub>2</sub> ] <sup>2-</sup> )	1285.1 ± 2.6	1159.7 ± 7.1	1165.6 <sup>a</sup>
<i>trans</i> -[Os <sup>VI</sup> O <sub>2</sub> (OH) <sub>4</sub> ] <sup>2-</sup>	247.7 ± 2.1	210.6 ± 6.4	231.2 <sup>a</sup>
( <i>trans</i> -[Os <sup>VII</sup> O <sub>3</sub> (OH) <sub>2</sub> ] <sup>-</sup> + <i>mer</i> -[Os <sup>VII</sup> O <sub>3</sub> (OH) <sub>3</sub> ] <sup>2-</sup> )	2553.3 ± 9.7	~ 2900	-

<sup>a</sup> Values extrapolated from reported UV-Vis absorbance spectra.<sup>2,13</sup>

Combining the Eyring plots for reaction 7.2 yielded a linear van't Hoff plot, Figure 7.4, and all five data points are within the 95% confidence interval.

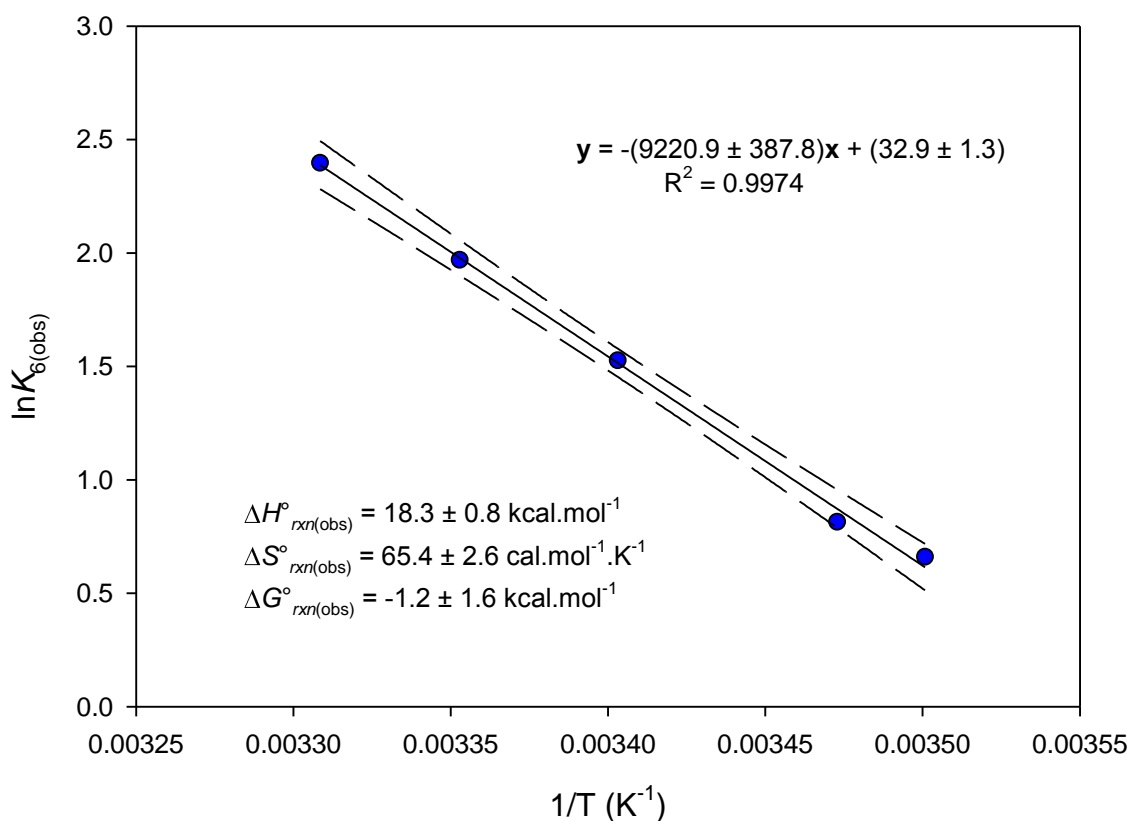


**Figure 7.4.** van't Hoff plot with 95% confidence interval for the comproportionation reaction (exp. 7.2.1.1).

The standard reaction enthalpy,  $\Delta H^\circ_{\text{rxn}(\text{obs})}$ , and entropy,  $\Delta S^\circ_{\text{rxn}(\text{obs})}$ , are both positive, at  $18.3 \pm 0.8 \text{ kcal.mol}^{-1}$  and  $65.4 \pm 2.6 \text{ cal.mol}^{-1}.\text{K}^{-1}$ , respectively, while the standard reaction Gibbs free energy,  $\Delta G^\circ_{\text{rxn}(\text{obs})}$  at 298.15 K is slightly negative, at  $-1.2 \pm 1.6 \text{ kcal.mol}^{-1}$ , Table 7.5. The excellent agreement with the values obtained from the stopped-flow UV-Vis spectroscopy experiments (Chapter 4), *i.e.* from different experimental techniques, provides even further validation regarding the accuracy of the calculated rate constants as well as the reaction model, equations 7.1 & 7.2, used as the basis to simulate the kinetic traces.

**Table 7.5.** Standard reaction energies of the  $\text{Os}^{\text{VI}}$  &  $\text{Os}^{\text{VIII}}$  comproportionation reaction (exp. 7.2.1.1).

$\Delta H^\circ_{\text{rxn}(\text{obs})}$ ( $\text{kcal.mol}^{-1}$ )	$\Delta S^\circ_{\text{rxn}(\text{obs})}$ ( $\text{cal.mol}^{-1}.\text{K}^{-1}$ )	$\Delta G^\circ_{\text{rxn}(\text{obs})}$ ( $\text{kcal.mol}^{-1}$ )
$18.3 \pm 0.8$	$65.4 \pm 2.6$	$-1.2 \pm 1.6$

### 7.2.1.2 Variable $[\text{CD}_3\text{OD}]$ , constant $[\text{Os}^{\text{VIII}}]$ and temperature

In Chapter 4 we reported that the reaction rate constants of the  $\text{Os}^{\text{VI}}$  &  $\text{Os}^{\text{VIII}}$  comproportionation and  $\text{Os}^{\text{VII}}$  &  $\text{Os}^{\text{VII}}$  disproportionation (at 294.5 K),  $k_{6(\text{obs})}$  and  $k_{-6(\text{obs})}$ , respectively, decrease by the same magnitude when the solvent composition is altered from only water, *i.e.* non-deuterated (control), to  $\text{D}_2\text{O}:\text{H}_2\text{O}$  in a 1:1 ratio by volume, while the

equilibrium constant remains the same, Table 4.8. The rate-determining step of these chemical reactions, concerted electron-proton transfer (EPT),<sup>18</sup> falls in a class of chemical reactions called proton-coupled electron transfer (PCET). We suspect that the reduction of Os<sup>VIII</sup> with methanol may also fall under this category. From a mechanistic point of view, we are interested to find out if hydrogen atom transfer (HAT) occurs directly from methanol to Os<sup>VIII</sup> and to determine which HAT, *i.e.* an O-H or an  $\alpha$ -C-H, is the rate-determining step of the redox reaction. Interestingly, Os<sup>VIII</sup> is not reduced by *tert*-butanol (Chapter 4) which indicates that an available  $\alpha$ -C-H is required for the redox reaction. For these reasons, we decided to replace CH<sub>3</sub>OH with CD<sub>3</sub>OD.

When CD<sub>3</sub>OD is added to a sample containing Os<sup>VIII</sup> oxo/hydroxido species in a 2.0 M NaOH aqueous matrix, the relatively labile deuterium of the hydroxyl functional group exchanges rapidly with hydrogen atoms from the aqueous solution. Conversely, the three deuteriums of the methyl functional group are not labile and therefore do not exchange with hydrogen atoms from the aqueous solution prior to reactions 7.1 and 7.2 occur. Consequently, the alcohol species that are then actually reduced by Os<sup>VIII</sup> species is not CD<sub>3</sub>OD, but rather CD<sub>3</sub>OH. If the rate-determining step of reaction 7.1 involves O-H transfer, we expect only small changes to the redox reaction rate. Conversely, if it involves the  $\alpha$ -C-H transfer ( $\alpha$ -C-D in this experiment), we expect that a relatively large change in the redox reaction rate will occur. Moreover, the concentration of deuterium from CD<sub>3</sub>OD used in the experiments are low enough such that the reaction rates of the Os<sup>VI</sup> & Os<sup>VIII</sup> comproportionation and Os<sup>VII</sup> & Os<sup>VII</sup> disproportionation (EPT) reactions (*vide infra*) will be unaffected, *i.e.* we expect that  $k_{6(\text{obs})}$  and  $k_{-6(\text{obs})}$  will not decrease under the conditions used to perform the experiments.

The concentration of Os<sup>VIII</sup> was kept constant at approximately 0.3 mM, while the concentration of excess methanol (CD<sub>3</sub>OD) was varied. Furthermore, the experiments were performed in a 2.0 M NaOH aqueous matrix at 298.6 K. Kinetic measurement acquisition runs were performed at six different concentrations of methanol, ranging between 15 and 40 mM. The trends depicting absorbance vs. time are shown as symbols in Figure 7.5.



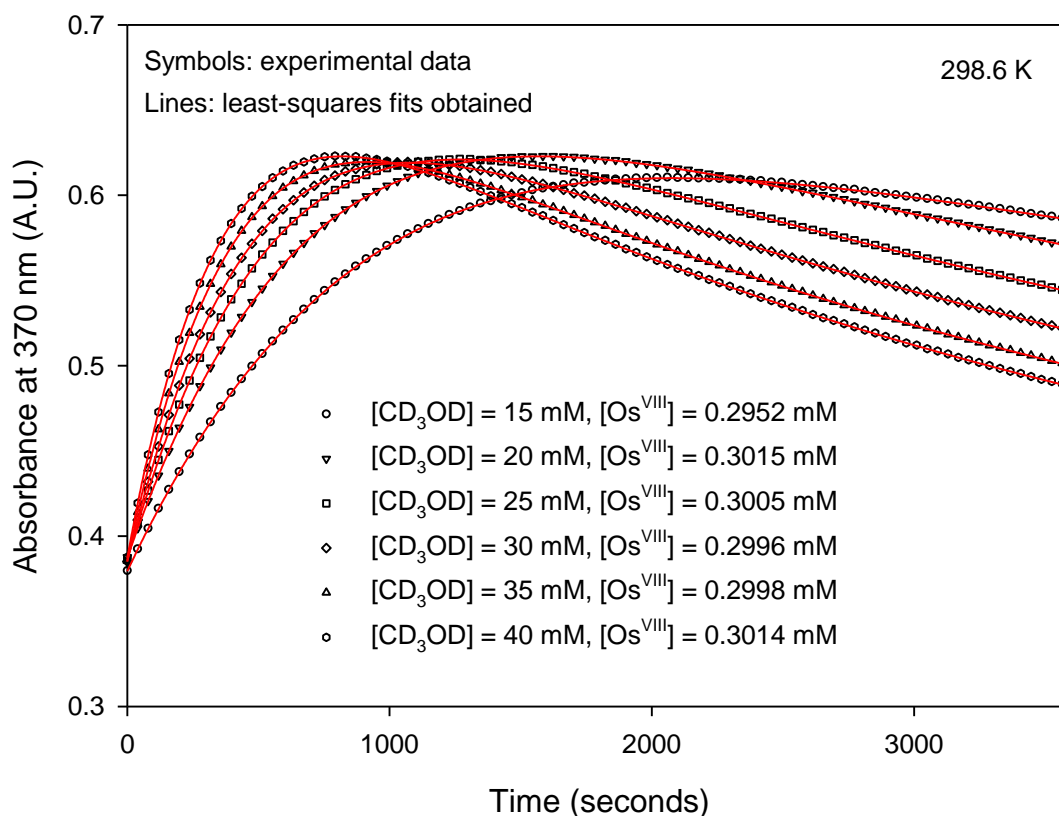


**Figure 7.5.** Kinetic traces depicting the change in absorbance during the simultaneous reduction of Os<sup>VIII</sup> with methanol (CD<sub>3</sub>OD) and the Os<sup>VI</sup> & Os<sup>VIII</sup> comproportionation reactions at various methanol (CD<sub>3</sub>OD) concentrations, at 298.6 K. The concentrations of the reactants at which each of the acquisitions were recorded are shown.

For samples containing higher methanol (CD<sub>3</sub>OD) concentration at the start, the initial increase in absorbance is steeper and the time required to reach the initial absorbance maximum is less, Figure 7.5. Furthermore, the absorbance values at the maxima of the six different kinetic traces are all approximately 0.62 au, indicating that the maximum concentration of Os<sup>VII</sup> species formed, *i.e.* when the mole ratio of Os<sup>VI</sup> and Os<sup>VIII</sup> is 1:1, from the different samples are approximately equivalent.

Using Program Dynafit,<sup>16</sup> the rate laws, equations 7.3 – 7.7, were simulated and the obtained non-linear least squares fits are excellent Figure 7.5. The calculated rate constants are listed in Table 7.6.

**Table 7.6. Calculated rate constants of reactions 7.1 & 7.2 and the corresponding equilibrium constants of reaction 7.2 at 298.6 K (exp. 7.2.1.2).**

[CD <sub>3</sub> OD] (mM)	$k_{13(D)}$ (M <sup>-1</sup> .s <sup>-1</sup> )	$k_{6(obs)}$ (M <sup>-1</sup> .s <sup>-1</sup> )	$k_{-6(obs)}$ (M <sup>-1</sup> .s <sup>-1</sup> )	$K_{6(obs)}$ = ( $k_{6(obs)}/k_{-6(obs)}$ )
15	$(3.040 \pm 0.038) \times 10^{-2}$	$(4.967 \pm 0.031) \times 10^4$	$(6.596 \pm 0.030) \times 10^3$	$7.53 \pm 0.08$
20	$(3.014 \pm 0.005) \times 10^{-2}$	$(4.924 \pm 0.001) \times 10^4$	$(6.591 \pm 0.014) \times 10^3$	$7.47 \pm 0.02$
25	$(2.985 \pm 0.006) \times 10^{-2}$	$(4.924 \pm 0.001) \times 10^4$	$(6.597 \pm 0.008) \times 10^3$	$7.46 \pm 0.01$
30	$(2.934 \pm 0.040) \times 10^{-2}$	$(4.942 \pm 0.015) \times 10^4$	$(6.638 \pm 0.073) \times 10^3$	$7.45 \pm 0.07$
35	$(2.952 \pm 0.047) \times 10^{-2}$	$(4.815 \pm 0.013) \times 10^4$	$(6.615 \pm 0.012) \times 10^3$	$7.28 \pm 0.03$
40	$(2.884 \pm 0.001) \times 10^{-2}$	$(4.922 \pm 0.005) \times 10^4$	$(6.769 \pm 0.056) \times 10^3$	$7.27 \pm 0.06$

Calculated rate constants of reaction 7.1,  $k_{13(D)}$ , remain the same irrespective of the methanol (CD<sub>3</sub>OD) concentration, confirming that reaction 7.1 is first order w.r.t. methanol (CD<sub>3</sub>OD) concentration, Table 7.6. Furthermore, the rate constants of the Os<sup>VI</sup> & Os<sup>VIII</sup> comproportionation and Os<sup>VII</sup> & Os<sup>VII</sup> disproportionation reactions,  $k_{6(obs)}$  and  $k_{-6(obs)}$ , and therefore also their equilibrium constants, also remain the same, irrespective of the starting methanol (CD<sub>3</sub>OD) concentration, confirming that the concentration of deuterium in the solution is negligible. The good non-linear least squares fits obtained and the good agreement of calculated molar extinction coefficients, Table 7.7, with that obtained in Chapter 4 as well as with the literature<sup>1,2,13</sup> provides validation of the proposed reaction model, equations 7.1 & 7.2.

**Table 7.7. Comparison of the calculated and literature high oxidation state osmium species' molar extinction coefficients at 370 nm obtained from the variable methanol (CD<sub>3</sub>OD) concentration kinetics experiment.**

osmium species	Calculated (L.mol <sup>-1</sup> .cm <sup>-1</sup> )	Literature <sup>1,2,13</sup> (L.mol <sup>-1</sup> .cm <sup>-1</sup> )	
([Os <sup>VIII</sup> O <sub>4</sub> (OH)] <sup>-</sup> + <i>cis</i> -[Os <sup>VIII</sup> O <sub>4</sub> (OH) <sub>2</sub> ] <sup>2-</sup> )	$1285.1 \pm 3.4$	$1159.7 \pm 7.1$	1165.6
<i>trans</i> -[Os <sup>VI</sup> O <sub>2</sub> (OH) <sub>4</sub> ] <sup>2-</sup>	$250.7 \pm 2.4$	$210.6 \pm 6.4$	231.2
( <i>trans</i> -[Os <sup>VII</sup> O <sub>3</sub> (OH) <sub>2</sub> ] <sup>-</sup> + <i>mer</i> -[Os <sup>VII</sup> O <sub>3</sub> (OH) <sub>3</sub> ] <sup>2-</sup> )	$2500.6 \pm 13.4$	~ 2900	-

Since the calculated rate constant of reaction 7.1,  $k_{13(D)}$  is considerably smaller in magnitude compared to when CH<sub>3</sub>OH is used as the reducing agent,  $k_{13(H)}$  in Section 7.2.1.1, which is interpolated to be approximately  $3.316 \times 10^{-1} \text{ M}^{-1} \cdot \text{s}^{-1}$  at 298.6 K (*vide supra*), it is clear that the rate-determining step of reaction 7.1, involves the cleavage of an  $\alpha$ -carbon-deuterium bond of CD<sub>3</sub>OH. At 298.6 K,  $k_{13(D)}$  is equal to approximately  $2.968 \times 10^{-2} \text{ M}^{-1} \cdot \text{s}^{-1}$ , which therefore yields a relatively large KIE value of approximately 11.17. Moreover, this result

also explains why *tert*-butanol, which does not contain a hydrogen at the  $\alpha$ -carbon position, is not oxidised by  $\text{Os}^{\text{VIII}}$  oxo/hydroxido species in the Evans method experiment, Chapter 4.

### 7.2.1.3 Variable temperature, constant $[\text{Os}^{\text{VIII}}]$ and $[\text{CD}_3\text{OD}]$

The concentrations of  $\text{Os}^{\text{VIII}}$  and excess methanol ( $\text{CD}_3\text{OD}$ ) were kept constant, at approximately 0.3 mM and 30 mM, respectively, in a 2.0 M NaOH aqueous matrix. Kinetic measurement acquisition runs were performed at five different temperatures ranging between 283.2 and 301.8 K. The trends depicting absorbance vs. time, shown as symbols in Figure 7.6, are the obtained kinetic traces at each temperature.

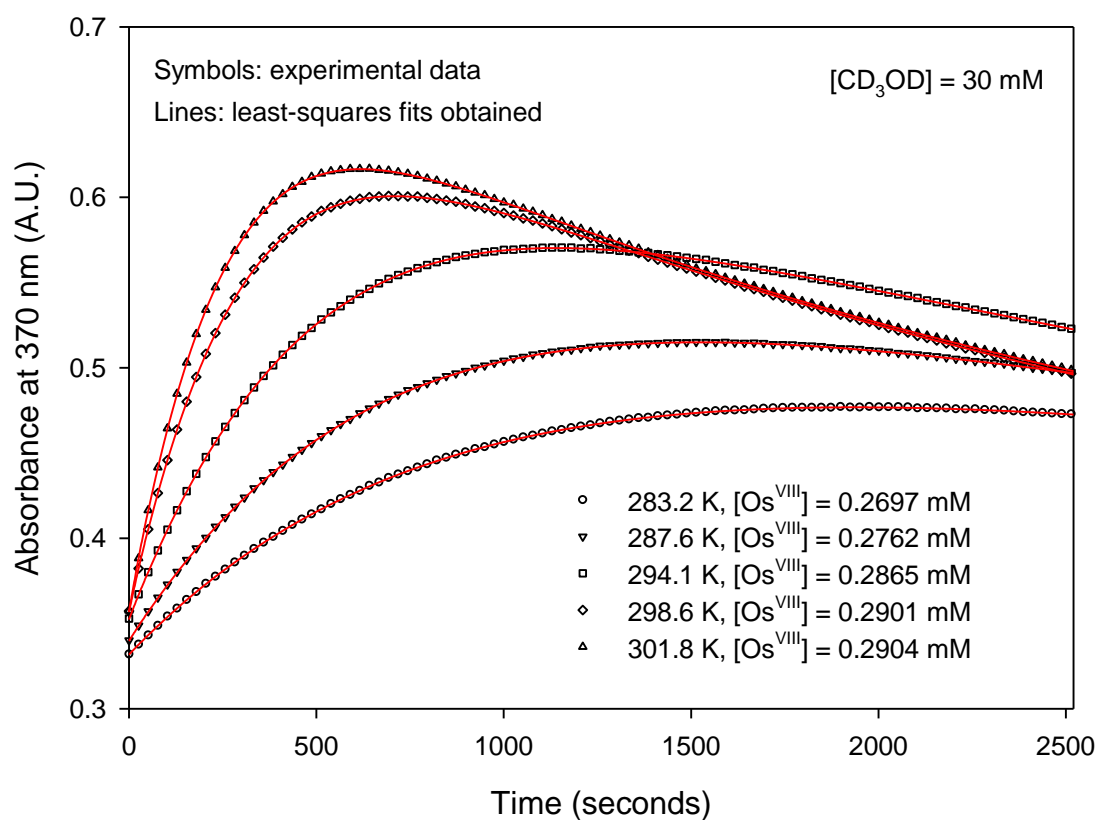


**Figure 7.6.** Kinetic traces depicting the change in absorbance during the simultaneous reduction  $\text{Os}^{\text{VIII}}$  with methanol ( $\text{CD}_3\text{OD}$ ) and the  $\text{Os}^{\text{VI}}$  &  $\text{Os}^{\text{VIII}}$  comproportionation reactions at various temperatures. The temperature and  $\text{Os}^{\text{VIII}}$  concentration at which each of the acquisitions was recorded are shown.

Similarly to the experiments presented in Sections 7.2.1.1 and 7.2.1.2, the  $\text{Os}^{\text{VIII}}$  concentrations from the five samples were not exactly the same, making it difficult to compare the differences between the kinetic traces in Figure 7.6. However, it can be seen that the time required to reach the absorbance maximum is less at higher temperatures.

Using the software Program Dynafit,<sup>16</sup> the rate laws given by equations 7.3 – 7.7 were simulated and the non-linear least squares fits obtained were excellent, Figure 7.6. The calculated rate constants are listed in Table 7.8.

**Table 7.8. Calculated rate constants of reactions 7.1 & 7.2 and the corresponding equilibrium constants of reaction 7.2 at various temperatures (exp. 7.2.1.3).**

Temperature (K)	$k_{13(D)}$ ( $M^{-1}.s^{-1}$ )	$k_{6(obs)}$ ( $M^{-1}.s^{-1}$ )	$k_{-6(obs)}$ ( $M^{-1}.s^{-1}$ )	$K_{6(obs)}$ = $k_{6(obs)}/k_{-6(obs)}$
283.2	$(7.093 \pm 0.004) \times 10^{-3}$	$(1.770 \pm 0.005) \times 10^4$	$(1.183 \pm 0.002) \times 10^4$	$1.497 \pm 0.004$
287.6	$(1.037 \pm 0.003) \times 10^{-2}$	$(2.364 \pm 0.005) \times 10^4$	$(1.002 \pm 0.001) \times 10^4$	$2.359 \pm 0.005$
294.1	$(1.645 \pm 0.001) \times 10^{-2}$	$(3.636 \pm 0.052) \times 10^4$	$(7.808 \pm 0.020) \times 10^3$	$4.656 \pm 0.060$
298.6	$(2.934 \pm 0.040) \times 10^{-2}$	$(4.942 \pm 0.015) \times 10^4$	$(6.638 \pm 0.073) \times 10^3$	$7.445 \pm 0.067$
301.8	$(3.624 \pm 0.013) \times 10^{-2}$	$(6.101 \pm 0.010) \times 10^4$	$(5.864 \pm 0.013) \times 10^3$	$10.403 \pm 0.039$

At higher temperatures, the rate constant for the Os<sup>VIII</sup> reduction with methanol (CD<sub>3</sub>OD),  $k_{13(D)}$ , and for the Os<sup>VI</sup> & Os<sup>VIII</sup> comproportionation,  $k_{6(obs)}$ , reactions increase while the rate constant for the Os<sup>VII</sup> & Os<sup>VII</sup> disproportionation,  $k_{-6(obs)}$ , reaction decreases.

A linear trend was obtained for the Eyring plot for reaction 7.1, Figure 7.7. Furthermore, all five data points are within the 95% confidence interval while the calculated errors<sup>17</sup> of  $\Delta^\ddagger H^\circ$ ,  $\Delta^\ddagger S^\circ$  and  $\Delta^\ddagger G^\circ$  are relatively small, Table 7.9.

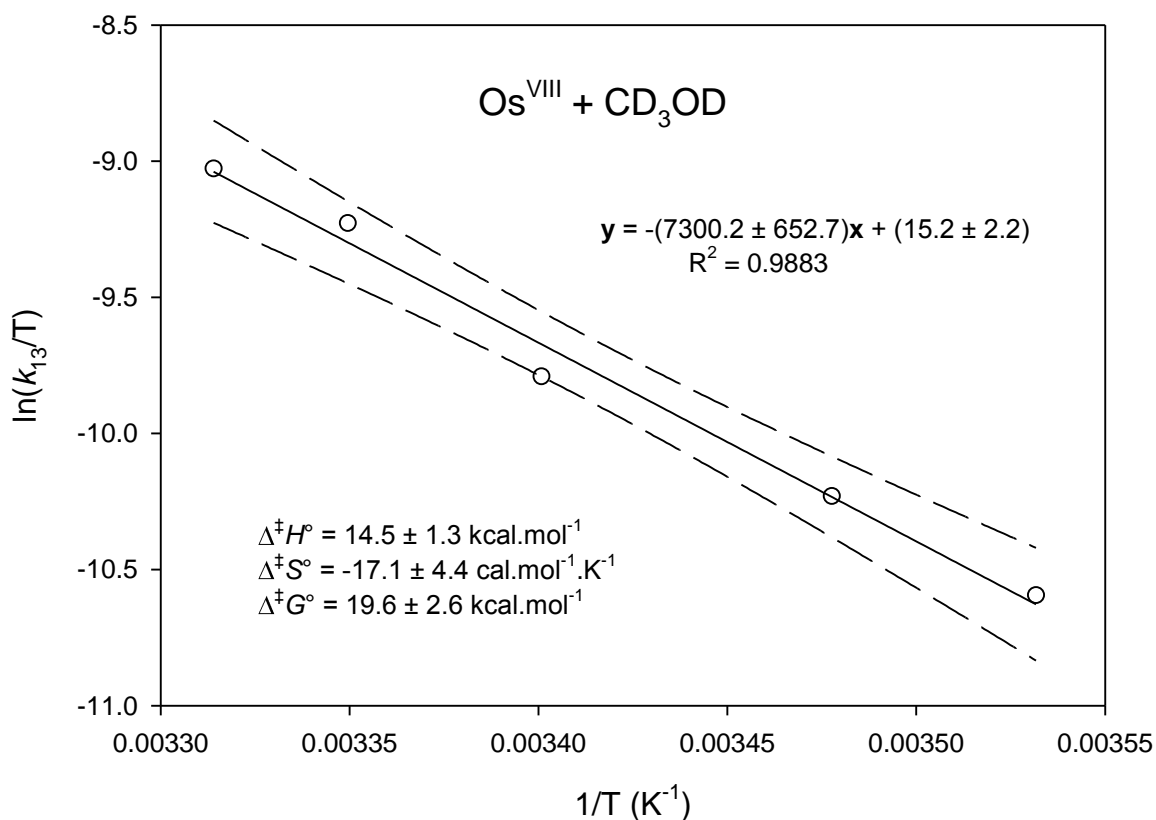


**Figure 7.7.** Eyring plot with 95% confidence intervals for the reduction of Os<sup>VIII</sup> species with methanol (CD<sub>3</sub>OD).

**Table 7.9.** Activation energies for the reduction of Os<sup>VIII</sup> species with methanol (CD<sub>3</sub>OD).

$\Delta^{\ddagger}H^{\circ}$ (kcal.mol <sup>-1</sup> )	$\Delta^{\ddagger}S^{\circ}$ (cal.mol <sup>-1</sup> .K <sup>-1</sup> )	$\Delta^{\ddagger}G^{\circ}_{298.15 \text{ K}}$ (kcal.mol <sup>-1</sup> )
14.5 ± 1.3	-17.1 ± 4.4	19.6 ± 2.6

Linear trends were obtained for the Eyring plots for the comproportionation and disproportionation reactions, Figure 7.8 (a) and (b). Furthermore, all five data points are within the 95% confidence interval while the calculated errors<sup>17</sup> of  $\Delta^{\ddagger}H^{\circ}_{(\text{obs})}$ ,  $\Delta^{\ddagger}S^{\circ}_{(\text{obs})}$  and  $\Delta^{\ddagger}G^{\circ}_{(\text{obs})}$  are relatively small, Table 7.10.

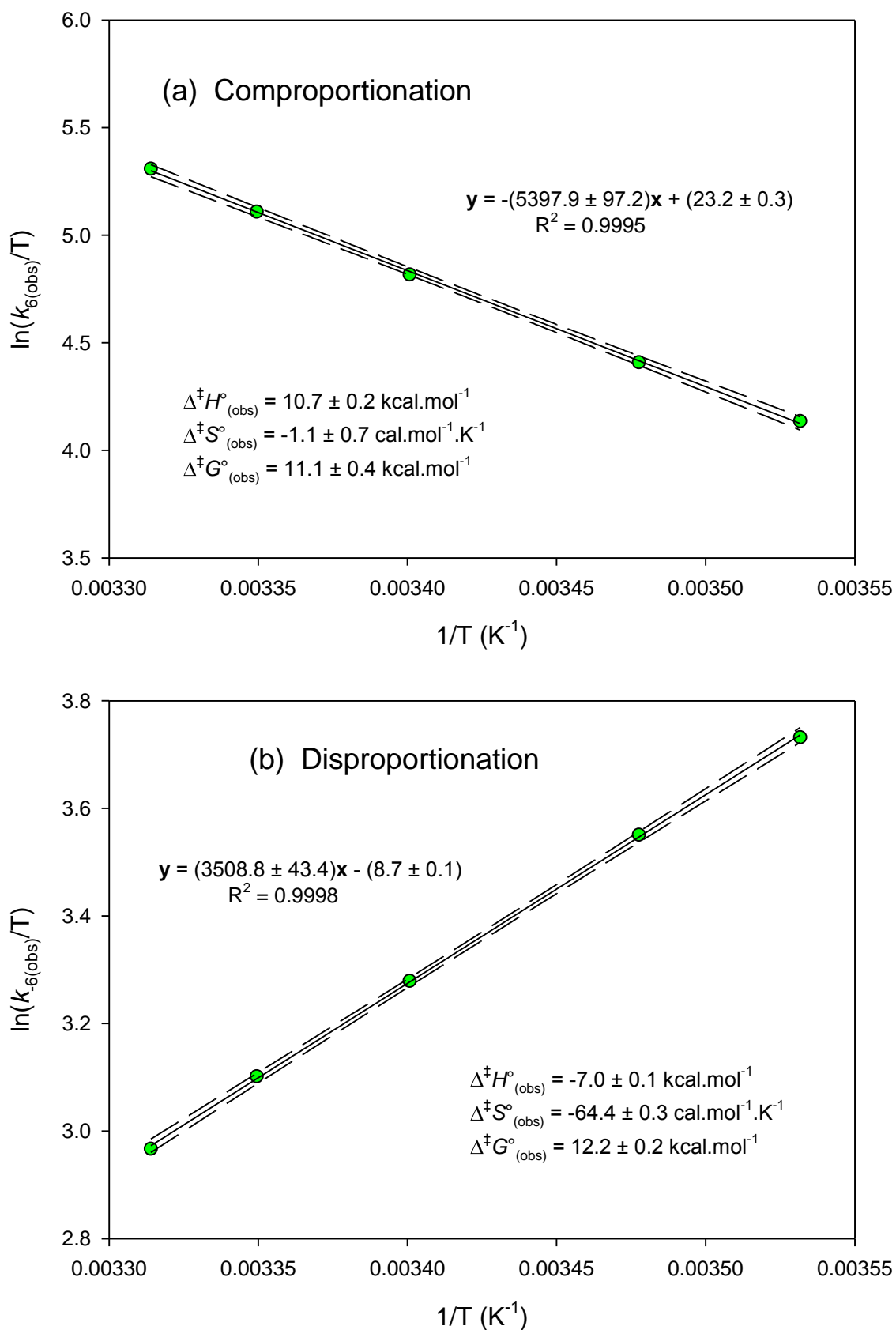


**Figure 7.8.** Eyring plots with 95% confidence intervals for the (a)  $\text{Os}^{\text{VI}}$  &  $\text{Os}^{\text{VIII}}$  comproportionation and (b)  $\text{Os}^{\text{VII}}$  &  $\text{Os}^{\text{VII}}$  disproportionation reactions (exp. 7.2.1.3).

**Table 7.10. Activation energies of the Os<sup>VI</sup> & Os<sup>VIII</sup> comproportionation and Os<sup>VII</sup> & Os<sup>VII</sup> disproportionation reactions (exp. 7.2.1.3).**

Reaction	$\Delta^\ddagger H^\circ_{\text{(obs)}} \text{ (kcal.mol}^{-1}\text{)}$	$\Delta^\ddagger S^\circ_{\text{(obs)}} \text{ (cal.mol}^{-1}\text{.K}^{-1}\text{)}$	$\Delta^\ddagger G^\circ_{\text{(obs)}} \text{ (kcal.mol}^{-1}\text{)}$
comproportionation	$10.7 \pm 0.2$	$-1.1 \pm 0.7$	$11.1 \pm 0.4$
disproportionation	$-7.0 \pm 0.1$	$-64.4 \pm 0.3$	$12.2 \pm 0.2$

Extinction coefficients calculated from the non-linear least squares fits for the Os<sup>VIII</sup> and Os<sup>VI</sup> species agree well with previously reported experimental values, Table 7.11.<sup>1,2,13</sup>

**Table 7.11. Comparison of the calculated and literature high oxidation state osmium species' molar extinction coefficients at 370 nm obtained from the variable temperature kinetics experiment (exp. 7.2.1.3).**

osmium species	Calculated (L.mol <sup>-1</sup> .cm <sup>-1</sup> )	Literature <sup>1,2,13</sup> (L.mol <sup>-1</sup> .cm <sup>-1</sup> )	
([Os <sup>VIII</sup> O <sub>4</sub> (OH)] <sup>-</sup> + <i>cis</i> -[Os <sup>VIII</sup> O <sub>4</sub> (OH) <sub>2</sub> ] <sup>2-</sup> )	$1230.7 \pm 0.2$	$1159.7 \pm 7.1$	1165.6
<i>trans</i> -[Os <sup>VI</sup> O <sub>2</sub> (OH) <sub>4</sub> ] <sup>2-</sup>	$239.3 \pm 0.3$	$210.6 \pm 6.4$	231.2
( <i>trans</i> -[Os <sup>VII</sup> O <sub>3</sub> (OH) <sub>2</sub> ] <sup>-</sup> + <i>mer</i> -[Os <sup>VII</sup> O <sub>3</sub> (OH) <sub>3</sub> ] <sup>2-</sup> )	$2525.2 \pm 15.6$	~ 2900	-

Combining the Eyring plots yielded a linear van't Hoff plot, Figure 7.9, and all five data points are within the 95% confidence interval.

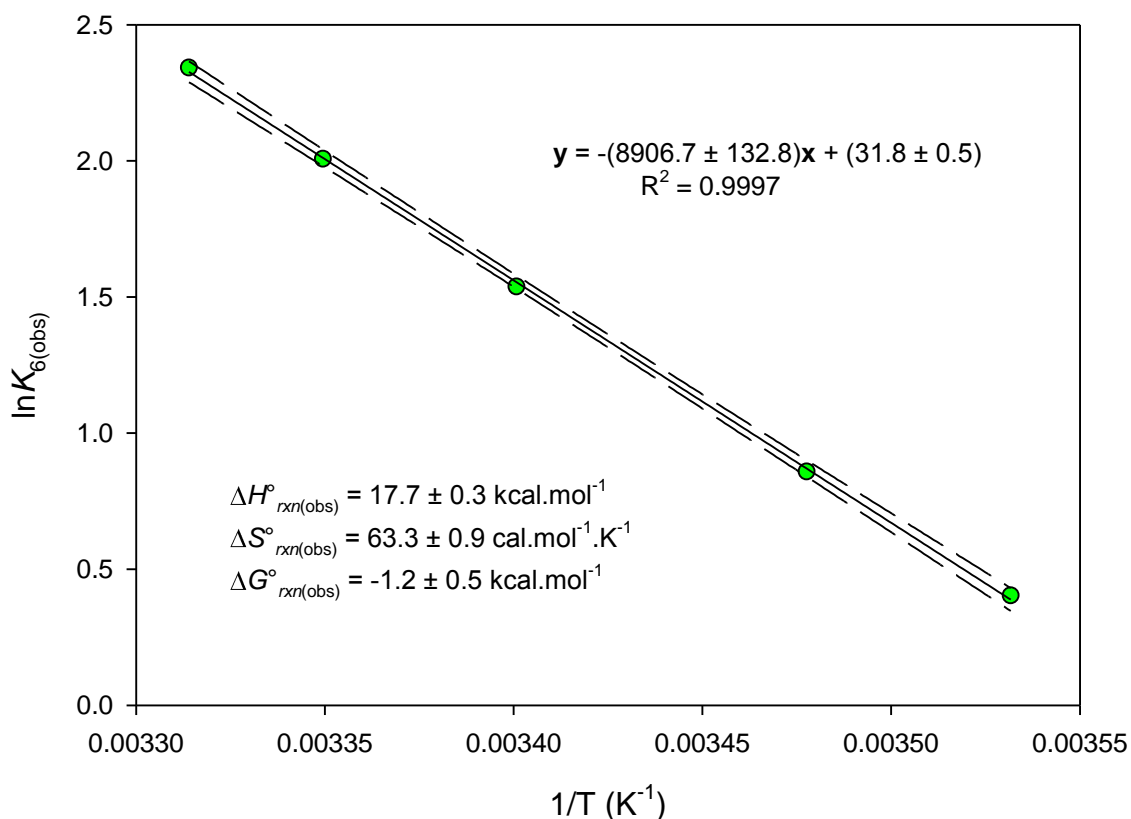


**Figure 7.9.** van't Hoff plot with 95% confidence interval for the comproportionation reaction (exp. 7.2.1.3).

The standard reaction enthalpy,  $\Delta H^\circ_{\text{rxn}(\text{obs})}$ , and entropy,  $\Delta S^\circ_{\text{rxn}(\text{obs})}$  are both positive, at  $17.7 \pm 0.3 \text{ kcal.mol}^{-1}$  and  $63.3 \pm 0.9 \text{ cal.mol}^{-1}.\text{K}^{-1}$ , respectively, while the standard reaction Gibbs free energy,  $\Delta G^\circ_{\text{rxn}(\text{obs})}$ , at 298.15 K is slightly negative, at  $-1.2 \pm 0.5 \text{ kcal.mol}^{-1}$ , Table 7.12.

**Table 7.12.** Standard reaction energies of the  $\text{Os}^{\text{VI}}$  &  $\text{Os}^{\text{VIII}}$  comproportionation reaction (exp. 7.2.1.3).

$\Delta H^\circ_{\text{rxn}(\text{obs})}$ (kcal.mol <sup>-1</sup> )	$\Delta S^\circ_{\text{rxn}(\text{obs})}$ (cal.mol <sup>-1</sup> .K <sup>-1</sup> )	$\Delta G^\circ_{\text{rxn}(\text{obs})}$ (kcal.mol <sup>-1</sup> )
$17.7 \pm 0.3$	$63.3 \pm 0.9$	$-1.2 \pm 0.5$

The  $\text{Os}^{\text{VI}}$  &  $\text{Os}^{\text{VIII}}$  comproportionation and  $\text{Os}^{\text{VII}}$  &  $\text{Os}^{\text{VII}}$  disproportionation stopped-flow data (Chapter 4) and the  $\text{Os}^{\text{VIII}}$  reduction with methanol ( $\text{CH}_3\text{OH}$ , Section 7.2.1.1, or  $\text{CD}_3\text{OD}$ , Section 7.2.1.3) data are plotted altogether in 'new', composite Eyring plots, Figure 7.10 (a) and (b).



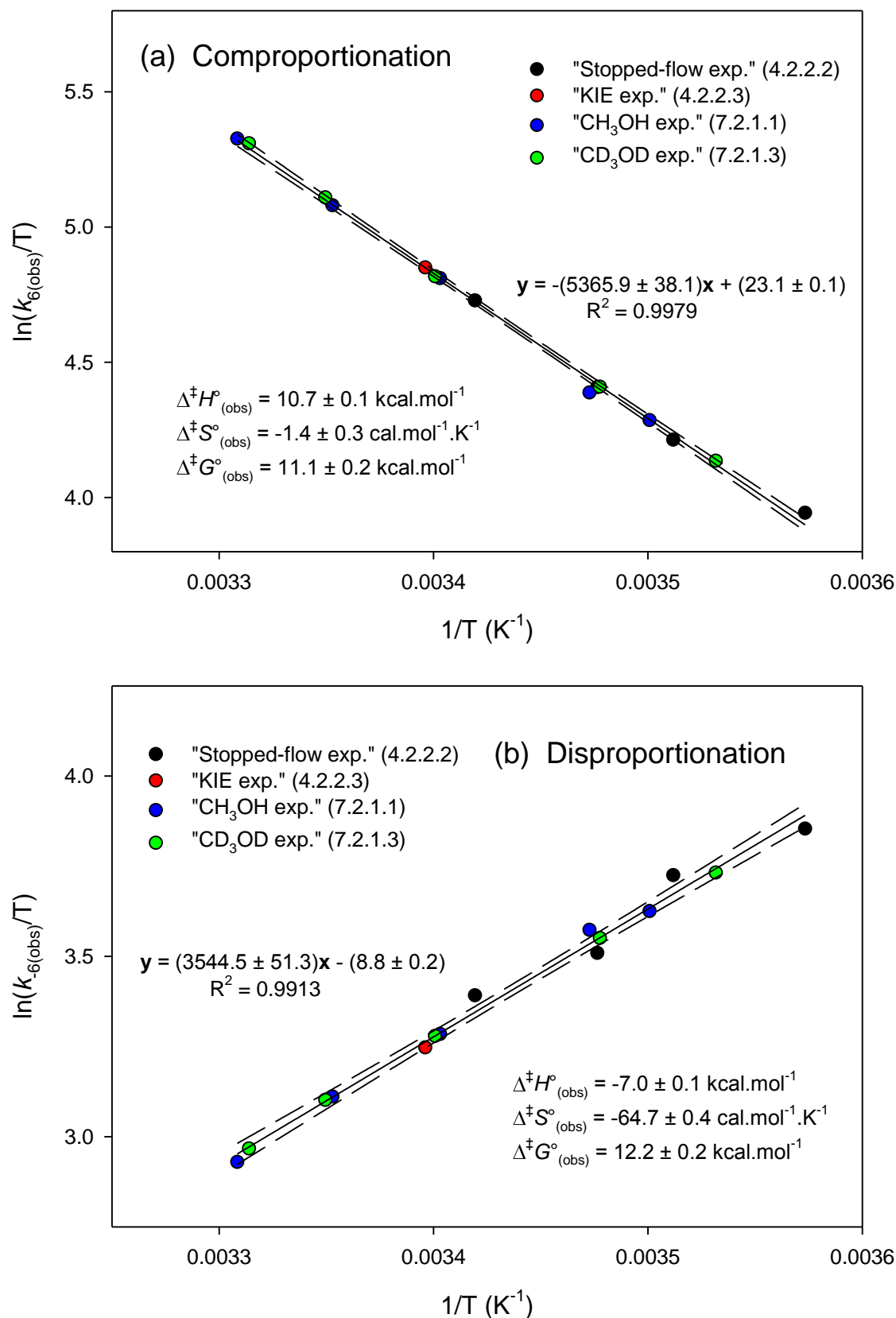


**Figure 7.10.** Composite Eyring plots, from four different experimental procedures, with 95% confidence intervals for the (a) Os<sup>VI</sup> & Os<sup>VIII</sup> comproportionation and (b) Os<sup>VII</sup> & Os<sup>VII</sup> disproportionation reactions.

The linearity of the composite Eyring plots indicates that the UV-Vis data obtained in the various experiments are accurate, precise and reliable and that the reaction model used to simulate the kinetic traces is valid. The composite Eyring plots now yield thermodynamic activation energies with significantly smaller experimental error values, Table 7.13.

**Table 7.13. Activation energies of the Os<sup>VI</sup> & Os<sup>VIII</sup> comproportionation and Os<sup>VII</sup> & Os<sup>VII</sup> disproportionation reactions (composite).**

Reaction	$\Delta^\ddagger H^\circ_{(obs)}$ (kcal.mol <sup>-1</sup> )	$\Delta^\ddagger S^\circ_{(obs)}$ (cal.mol <sup>-1</sup> .K <sup>-1</sup> )	$\Delta^\ddagger G^\circ_{(obs)}$ (kcal.mol <sup>-1</sup> )
comproportionation	10.7 ± 0.1	-1.4 ± 0.3	11.1 ± 0.2
disproportionation	-7.0 ± 0.1	-64.7 ± 0.4	12.2 ± 0.2

The corresponding composite van't Hoff plot from the various experiments is shown in Figure 7.11.

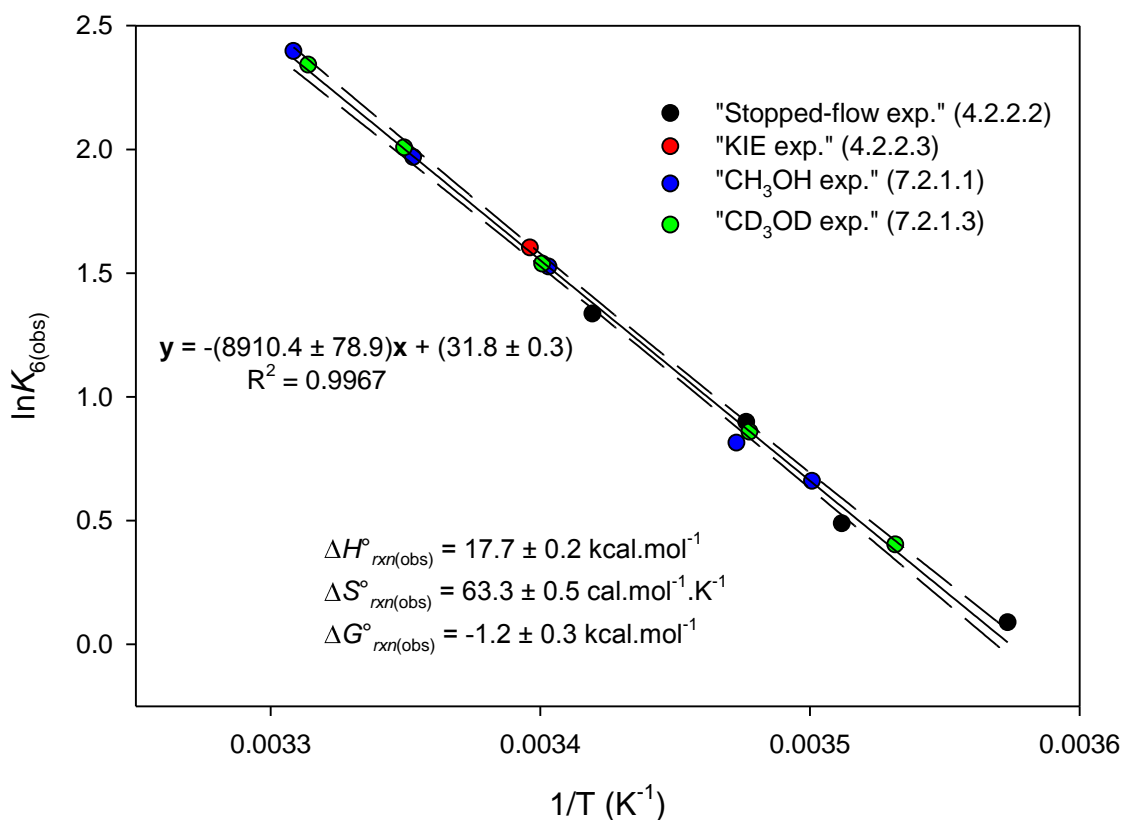


**Figure 7.11.** Composite van't Hoff plot, from four different experimental procedures, with 95% confidence interval for the Os<sup>VI</sup> & Os<sup>VIII</sup> comproportionation reaction.

Similar to the composite Eyring plots, the fifteen data points used to construct the composite van't Hoff plot are linear and the thermodynamic reaction energies now have significantly smaller experimental error values, Table 7.14.

**Table 7.14. Standard reaction energies of the Os<sup>VI</sup> & Os<sup>VIII</sup> comproportionation reaction (composite).**

$\Delta H^\circ_{rxn(obs)}$ (kcal.mol <sup>-1</sup> )	$\Delta S^\circ_{rxn(obs)}$ (cal.mol <sup>-1</sup> .K <sup>-1</sup> )	$\Delta G^\circ_{rxn(obs)}$ (kcal.mol <sup>-1</sup> )
17.7 ± 0.2	63.3 ± 0.5	-1.2 ± 0.3

The Eyring plots obtained for the reduction of Os<sup>VIII</sup> oxo/hydroxido species with CH<sub>3</sub>OH, Figure 7.2, and with CD<sub>3</sub>OH, Figure 7.7, have, to within experimental error, the same gradient, at  $-(7249.6 \pm 598.8)$  and  $-(7300.2 \pm 652.7)$ , respectively, and are therefore parallel to one another. By contrast, the plots have significantly different intercept values, at  $(17.5 \pm 2.0)$  and  $(15.2 \pm 2.2)$ , respectively, Figure 7.12. This is further reflected by the similar values of  $\Delta^\ddagger H^\circ$  for these reactions, at  $(14.4 \pm 1.2)$  and  $(14.5 \pm 1.3)$  kcal.mol<sup>-1</sup>, respectively, while  $\Delta^\ddagger S^\circ$  differ, at  $-(12.5 \pm 4.1)$  and  $-(17.1 \pm 4.4)$  cal.mol<sup>-1</sup>.K<sup>-1</sup>, respectively. From the parallel Eyring plots, the following can be derived:

- (i) the KIE does not change as a function of temperature and
- (ii) precise experimental work and resultant non-linear least squares kinetic analyses were performed.

To explain (ii) above, one can consider the following argument: The  $\Delta H^\circ_{rxn}$  for reaction 7.1 remains unchanged, whether CH<sub>3</sub>OH or CD<sub>3</sub>OD is utilised as the reducing agent and can be obtained by subtracting  $\Delta^\ddagger H^\circ$  for the reverse reaction from  $\Delta^\ddagger H^\circ$  for the forward reaction. In order to obtain the same  $\Delta H^\circ_{rxn}$  for both the CH<sub>3</sub>OH and CD<sub>3</sub>OD reactions, the slopes of the respective Eyring plots must be the same, or rather, two Eyring plots that are parallel to one another must be obtained.

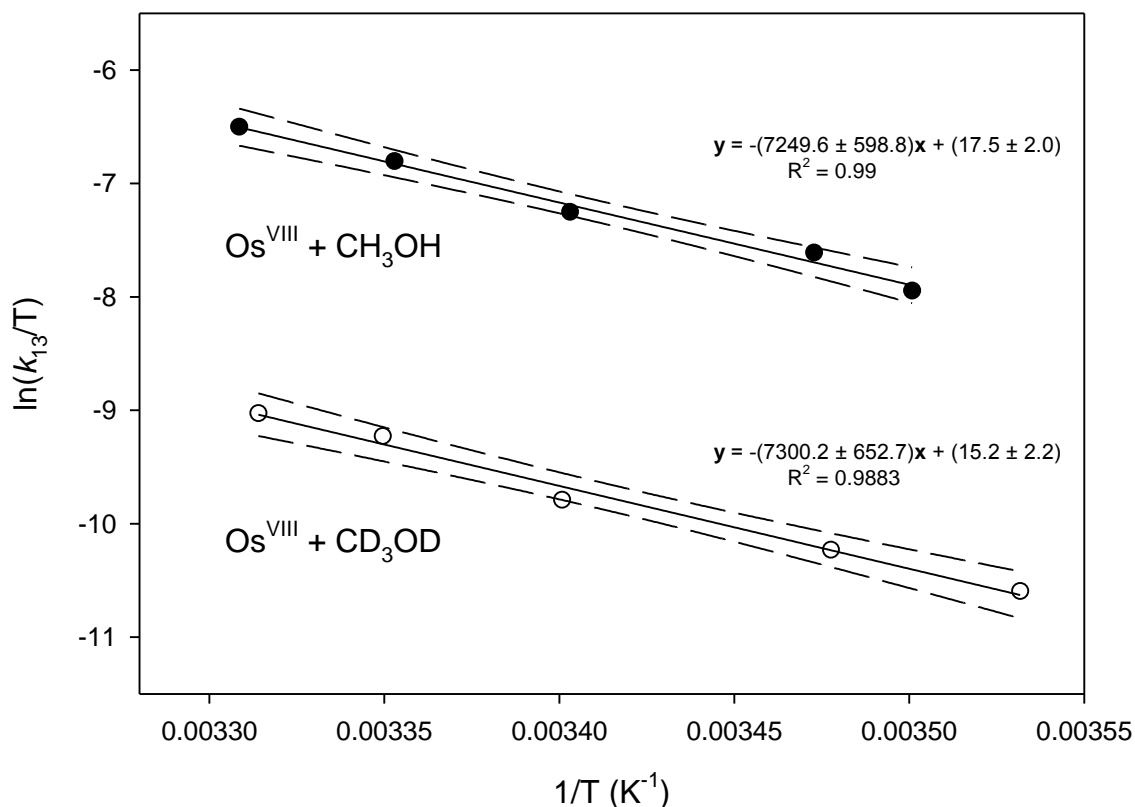


**Figure 7.12.** Eyring plots with 95% confidence intervals for the reduction of  $\text{Os}^{\text{VIII}}$  with  $\text{CH}_3\text{OH}$  (black symbols) and with  $\text{CD}_3\text{OH}$  (white symbols).

$k_{13(\text{H})}/k_{13(\text{D})}$  is approximately 11.82 and confirms that the cleavage of an  $\alpha\text{-C-H}$  bond in  $\text{CH}_3\text{OH}$  and the cleavage of an  $\alpha\text{-C-D}$  bond in  $\text{CD}_3\text{OH}$  are the rate-determining steps in the two reactions. If the Eyring plot slopes for the two experiments were not parallel to one another, it could be that either:

- (i) the mechanisms of the two reactions are different, yielding different rate-determining steps,
- (ii) the UV-Vis data is unreliable or inaccurate,
- (iii) the reaction model used to simulate the kinetic traces, equations 7.1 & 7.2, is invalid.

However, all three of these possibilities can now be ruled out with certainty, specifically due to the parallel Eyring plot slopes, Figure 7.12. Lastly, the relatively large value of  $k_{13(\text{H})}/k_{13(\text{D})}$  ( $\gg 1$ ) indicates a normal, primary isotope effect.

Furthermore, if methanol were to reduce the  $\text{Os}^{\text{VII}}$  oxo/hydroxido species (*trans*- $[\text{Os}^{\text{VII}}\text{O}_3(\text{OH})_2]^-$  or *mer*- $[\text{Os}^{\text{VII}}\text{O}_3(\text{OH})_3]^{2-}$ ), an  $\text{Os}^{\text{V}}$  ( $d^3$ ) species and formaldehyde (*e.g.* the transfer of two electrons and two protons), or an  $\text{Os}^{\text{VI}}$  species and either a high-energy intermediate methoxy radical or high-energy intermediate hydroxymethyl radical (*e.g.* the

transfer of one electron and one proton) will form. However, there is no experimental evidence to support the formation of an  $\text{Os}^{\text{V}}$  species. If an  $\text{Os}^{\text{V}}$  species were present in solution, Figures 7.1, 7.5 and 7.6, the calculated molar extinction coefficients for the  $\text{Os}^{\text{VI}}$ ,  $\text{Os}^{\text{VII}}$  and  $\text{Os}^{\text{VIII}}$  species would have compared poorly with reported values.<sup>1,2,13</sup> Moreover, the reaction model used to simulate the kinetic traces, equations 7.1 & 7.2, would have been invalidated if an  $\text{Os}^{\text{V}}$  species were present as non-linear Eyring plots would have been obtained. Methanol does not reduce  $\text{Os}^{\text{VII}}$  oxo/hydroxido species because such hypothetical reaction pathways will result in the formation of either high-energy intermediate radical species or an  $\text{Os}^{\text{V}}$  species, for which there is no evidence.

## 7.2.2 DFT investigation of $\text{Os}^{\text{VIII}}$ reduction with methanol ( $\text{CH}_3\text{OH}$ )

### 7.2.2.1 Thermodynamics of $\text{Os}^{\text{VIII}}$ reduction with methanol

Before we set out to elucidate the mechanism of the reduction of  $\text{Os}^{\text{VIII}}$  with methanol in a basic aqueous matrix, equation 7.1, we optimised the geometries of the reactants and products in order to calculate standard reaction energies  $\Delta H^\circ_{\text{rxn}}$ ,  $\Delta S^\circ_{\text{rxn}}$  and  $\Delta G^\circ_{\text{rxn}}$ . The only conformer of the  $\text{Os}^{\text{VI}}$  product is the octahedral osmate dianion, *trans*- $[\text{Os}^{\text{VI}}\text{O}_2(\text{OH})_4]^{2-}$ , which simplifies matters considerably in comparison with the  $\text{Os}^{\text{VI}}$  &  $\text{Os}^{\text{VIII}}$  comproportionation reaction where we had to consider several product species, Chapter 5. Methanol has two conformers, *i.e.* one staggered and one eclipsed, equation 7.8, while formaldehyde has only one conformation. In the simulated aqueous phase the  $\Delta G^\circ_{\text{rxn}}$  for reaction 7.8 at 298.15 K is  $-0.75 \text{ kcal.mol}^{-1}$ , which equates to an equilibrium constant of approximately 3.56, indicating that significant amounts of both methanol conformers are present at equilibrium.



The relative standard Gibbs energy of formation diagram of the reactants and products for reaction 7.1 is illustrated in Figure 7.13.

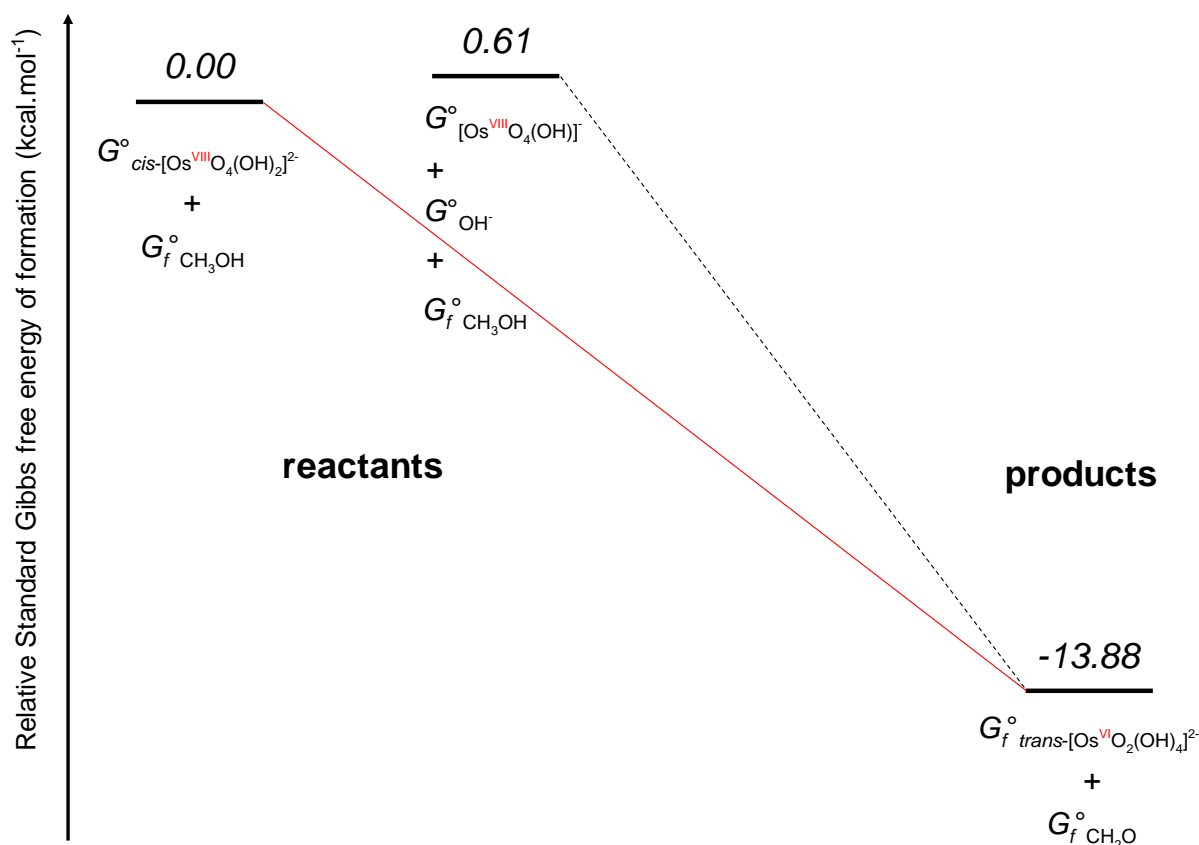


**Figure 7.13.** Relative standard Gibbs free energies of formation ( $\text{kcal.mol}^{-1}$ ) of the reactants and products of the reduction of  $\text{Os}^{\text{VIII}}$  with methanol in the simulated aqueous phase (PBE-D3 functional). Solid red line depicts the energy change between the reactant and product states of lowest Gibbs energy.

Using the same approach as in Chapter 5, which is to consider the energy differences between the reactant and product states that are lowest in Gibbs energy, yields a relatively large negative  $\Delta G_{\text{rxn}}^\circ$  of  $-13.88$   $\text{kcal.mol}^{-1}$  for reaction 7.1, which implies that only a negligible amount of  $\text{Os}^{\text{VIII}}$  species are present once equilibrium is reached, *i.e.* reaction 7.1 lies far to the right. Moreover,  $\Delta H_{\text{rxn}}^\circ$  for reaction 7.1 is also a relatively large negative value of  $-13.41$   $\text{kcal.mol}^{-1}$  while  $\Delta S_{\text{rxn}}^\circ$  is  $1.57$   $\text{cal.mol}^{-1}.\text{K}^{-1}$ . Unfortunately, there are no reliable half-cell redox potentials for the  $\text{Os}^{\text{VIII}}$  and  $\text{Os}^{\text{VI}}$  oxo/hydroxido species,  $\text{Os}^{\text{VIII}}/\text{Os}^{\text{VI}}$ , that can be used in conjunction with the  $\text{CH}_2\text{O}/\text{CH}_3\text{O}$  redox potential to compare an experimental  $\Delta G_{\text{rxn}}^\circ$  for reaction 7.1. However the large negative  $\Delta G_{\text{rxn}}^\circ$  obtained with DFT justifies our decision to simulate equation 7.1 (Sections 7.2.1.1, 7.2.1.2 and 7.2.1.3) as an irreversible reaction.

### 7.2.2.2 Preliminary mechanistic considerations of $\text{Os}^{\text{VIII}}$ reduction with methanol

Meyer *et al.*<sup>18</sup> reported that the reduction of  $\text{Ru}^{\text{IV}}(\text{bpy})_2(\text{py})(\text{O})^{2+}$  ( $[\text{Ru}^{\text{IV}}=\text{O}]^{2+}$ ) complex with benzaldehyde, Scheme 1.7, consists of HAT from the organic compound to the metal

complex. In that reaction mechanism, both the transferring electron and proton come from the same C-H bond in benzaldehyde. Electron transfer (ET) occurs to the  $d\pi$  electron acceptor orbital at  $[\text{Ru}^{\text{IV}}=\text{O}]^{2+}$ , while simultaneous proton transfer (PT) occurs to a lone pair in a proton-acceptor orbital at  $[\text{Ru}^{\text{IV}}=\text{O}]^{2+}$ . However, it is not clear from the reaction scheme reported by Meyer *et al.*<sup>18</sup> whether or not the organic and inorganic reactants first aggregate to form a preassociation complex in the way, proposed by Meyer *et al.*<sup>18</sup>, that  $[\text{Ru}^{\text{II}}-\text{OH}_2]^{2+}$  and  $[\text{Ru}^{\text{IV}}=\text{O}]^{2+}$  do in the EPT reaction mechanism shown in Scheme 1.5. Since the PT distance must be minimised in order to maximise the vibrational wave function overlap (PT is fundamentally limited to short distances), we suspect that HAT reaction mechanisms, such as that reported by Meyer *et al.*<sup>18</sup> or in the reduction of  $\text{Os}^{\text{VIII}}$  with methanol here, most probably consist of preassociation of the reactants to form non-covalent dimers.

Furthermore, the reduction of  $[\text{Ru}^{\text{IV}}=\text{O}]^{2+}$  with benzaldehyde consists of the transfer of only one electron and one proton to form  $[\text{Ru}^{\text{III}}-\text{OH}]^{2+}$  and a benzaldehyde radical, Scheme 1.7, whereas the reduction of  $\text{Os}^{\text{VIII}}$  oxo/hydroxido species with methanol presumably consists of the transfer of two electrons and two protons, equation 7.1. The oxygen-hydrogen bond, O-H, and an  $\alpha$ -carbon-hydrogen bond, C-H, of methanol must conceivably be cleaved in order to form formaldehyde, while *cis*- $[\text{Os}^{\text{VIII}}\text{O}_4(\text{OH})_2]^{2-}$  must receive two protons and two electrons in order to form *trans*- $[\text{Os}^{\text{VI}}\text{O}_2(\text{OH})_4]^{2-}$ . Moreover, if the other abundant  $\text{Os}^{\text{VIII}}$  species,  $[\text{Os}^{\text{VIII}}\text{O}_4(\text{OH})]^-$ , receives two protons and two electrons, a five-coordinate  $\text{Os}^{\text{VI}}$  product could form, *i.e.*  $[\text{Os}^{\text{VI}}\text{O}_2(\text{OH})_3]^-$ . However, crystal structure data and our DFT results, Chapter 5, provide reasonable evidence that the only  $\text{Os}^{\text{VI}}$  oxo/hydroxido species is the octahedral dianion, which suggests, at this stage, that  $[\text{Os}^{\text{VIII}}\text{O}_4(\text{OH})]^-$  does not oxidise methanol, as a high energy intermediate,  $[\text{Os}^{\text{VI}}\text{O}_2(\text{OH})_3]^-$  anion most likely has to form.

The proposed mechanisms for reaction 7.1 presented here are based on our detailed knowledge w.r.t. which oxo/hydroxido osmium species are actually present in basic aqueous media, Chapters 3 and 5, together with our experimentally obtained data, Figure 7.12, which provides good evidence that the  $\alpha$ -carbon-hydrogen bond of methanol is broken in the rate-determining step of the redox reaction. We therefore aim to find a plausible reaction mechanism where electron and proton transfer occurs directly from methanol to  $\text{Os}^{\text{VIII}}$ , *i.e.* where there are no exchanges of protons (or electrons) with the 2.0 M NaOH aqueous matrix. Furthermore, the activation energies obtained from the UV-Vis kinetics experiments can also be compared to DFT-calculated activation energies, as was done for the  $\text{Os}^{\text{VI}}$  &  $\text{Os}^{\text{VIII}}$  comproportionation reaction in Chapters 4 and 6. All calculations are done in the simulated

aqueous phase, COSMO, and the functional used is PBE-D3, in order to account for dispersion.<sup>26</sup>

### 7.2.2.3 DFT mechanistic study of *cis*-[Os<sup>VIII</sup>O<sub>4</sub>(OH)<sub>2</sub>]<sup>2-</sup> reduction with methanol

For a bimolecular chemical reaction to occur, the reactants must, at some stage, be in close proximity with one another. Therefore, in a similar way in which the thermodynamically stable, non-covalent dimers [Os<sup>VIII</sup>=O...HO-Os<sup>VI</sup>]<sup>4-</sup> and [Os<sup>VIII</sup>=O...HO-Os<sup>VI</sup>]<sup>3-</sup> were identified, Chapter 6, we first analysed the calculated electrostatic surface potentials of the equilibrium structures of [Os<sup>VIII</sup>=O]<sup>2-</sup>, Figure 6.2, and methanol (staggered), Figure 7.14. The electrostatic surface potential for methanol defined at the 0.03 au electron density isosurface indicates that the most negatively charged region is located at the hydroxyl oxygen while the positively charged regions are located at the four hydrogens. It is also noted that the electrostatic potential at the hydroxyl hydrogen is slightly more positive than the hydrogens of the  $\alpha$ -carbon, which is to be expected considering the relative electronegativities of oxygen and carbon.

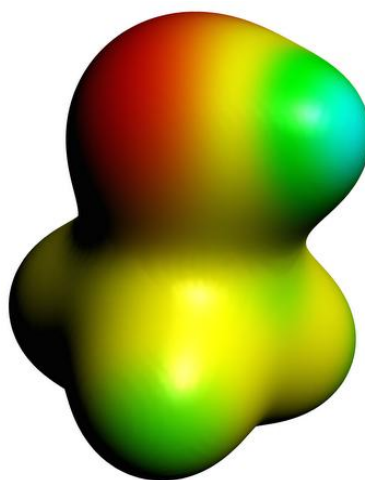


**Figure 7.14.** Electrostatic surface potential map of the optimised geometry of methanol (staggered) in the simulated aqueous phase (PBE-D3 functional) corresponding to a density isosurface value of 0.03 au. Negatively and positively charged regions are indicated by red and blue colouring, respectively.

<sup>26</sup> The agreement with experimentally determined energies with PBE-D3 has been relatively good in this study compared to most of the other functionals used, *e.g.* Tables 3.4, 3.7 and 5.7. Furthermore, PBE-D3 was preferred to the more accurate PBE-D3(BJ) functional because vibrational frequencies analyses can be done by analytical evaluation, which is considerably less computationally expensive than analyses done by numerical differentiation, an option not available for PBE-D3(BJ) with ADF.<sup>19-21</sup>



Moreover, since the stereochemistry of the Os<sup>VI</sup> product species is *trans* for reaction 7.1, Figure 5.1(a), the initial starting geometry that was submitted for geometry optimisation calculations had the hydroxyl hydrogen and an  $\alpha$ -carbon hydrogen aligned ‘towards’ the two oxo ligands positioned *trans* from the two Os<sup>VIII</sup>-OH bonds of *cis*-[Os<sup>VIII</sup>O<sub>4</sub>(OH)<sub>2</sub>]<sup>2-</sup>, Figure 3.2.

Taking the above into consideration, we subsequently performed a geometry optimisation calculation of a conceivable non-covalent dimer in the simulated aqueous phase. The information proved to be particularly useful as the adduct geometry converged relatively easily, Figures 7.15 and 7.16. Subsequent vibrational frequencies analysis confirms that the species is a local minimum on the PES as no negative frequencies were obtained. The electrostatic surface potential defined at the 0.03 au electron density isosurface of the non-covalent dimer, Figure 7.15, illustrates how the relative charge distribution of the organic and inorganic species changes when aggregated to one another in the simulated aqueous phase. Due to intermolecular hydrogen bonding interactions between the monomers (*vide infra*), negative charge slightly decreases on the interacting oxygens and correspondingly increases on the interacting hydrogens. In particular, the relatively negative charge in the region of the hydroxyl oxygen of methanol decreases considerably.

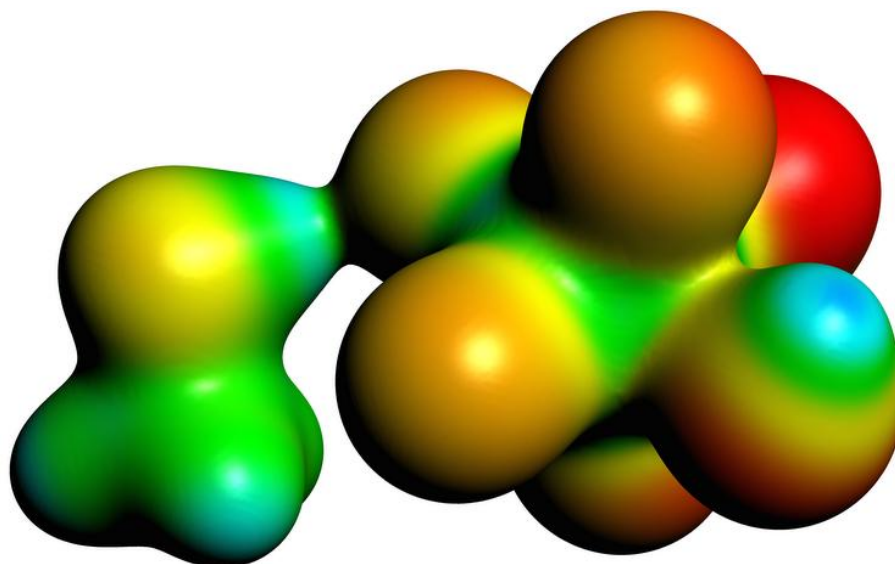


**Figure 7.15.** Electrostatic surface potential map of initial non-covalent dimer CH<sub>3</sub>OH,[*cis*-Os<sup>VIII</sup>O<sub>4</sub>(OH)<sub>2</sub>]<sup>2-</sup> in the simulated aqueous phase (PBE-D3 functional) corresponding to a density isosurface value of 0.03 au. Negatively and positively charged regions are indicated by red and blue colouring, respectively.

The molecular graph of CH<sub>3</sub>OH,[*cis*-Os<sup>VIII</sup>O<sub>4</sub>(OH)<sub>2</sub>]<sup>2-</sup>, Figure 7.16, displays the various critical points and atomic interaction lines that were obtained from AIMs analysis.<sup>22-23</sup>

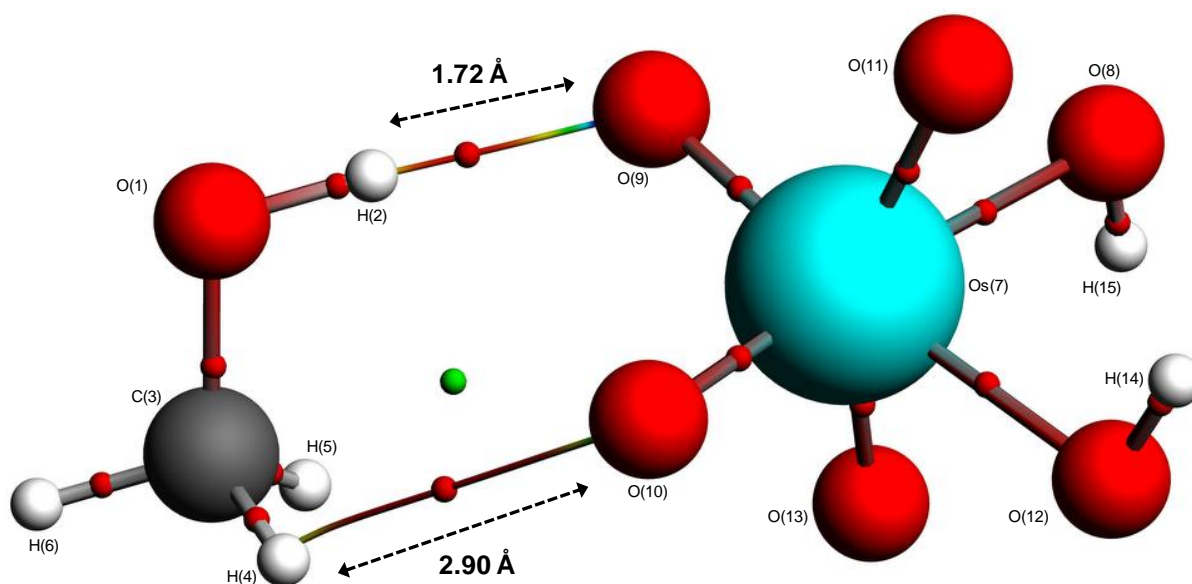


**Figure 7.16.** Molecular graph of  $\text{CH}_3\text{OH}, [\text{cis-Os}^{\text{VIII}}\text{O}_4(\text{OH})_2]^{2-}$  (PBE-D3 functional) showing two atomic interaction lines corresponding to intermolecular hydrogen bonds between the monomers. The small red and green spheres represent (3,-1) and (3,+1) critical points, respectively.

AIMs analysis indicates the presence of two intermolecular hydrogen bonding interactions between the monomers due to the presence of a bond critical point (BCP) between the relatively short  $\text{O}(1)\text{-H}(2)\cdots\text{O}(9)$  (1.72 Å) and a BCP between the relatively long  $\text{C}(3)\text{-H}(4)\cdots\text{O}(10)$  (2.90 Å). Furthermore, at the intermolecular  $\text{O-H}\cdots\text{O}$  BCP,  $\rho_b$  is 0.044 au whereas at the intermolecular  $\text{C-H}\cdots\text{O}$  BCP,  $\rho_b$  is approximately ten times smaller, at 0.005 au, indicative of a far weaker hydrogen bonding interaction.

We further analysed the bonding properties of the non-covalent dimer with the extended transition state (ETS) method combined with natural orbitals for the chemical valence (NOCV) theory, which is a combined charge and energy decomposition scheme for bond analysis.<sup>24</sup> With ETS-NOCV analysis the energy contributions to the total bonding energy are calculated for each specific orbital interaction between fragments Q and P (Q =  $\text{CH}_3\text{OH}$ , P =  $\text{cis-}[\text{Os}^{\text{VIII}}\text{O}_4(\text{OH})_2]^{2-}$ ). The natural orbital with the largest contribution to the non-covalent dimer is shown in Figure 7.17.

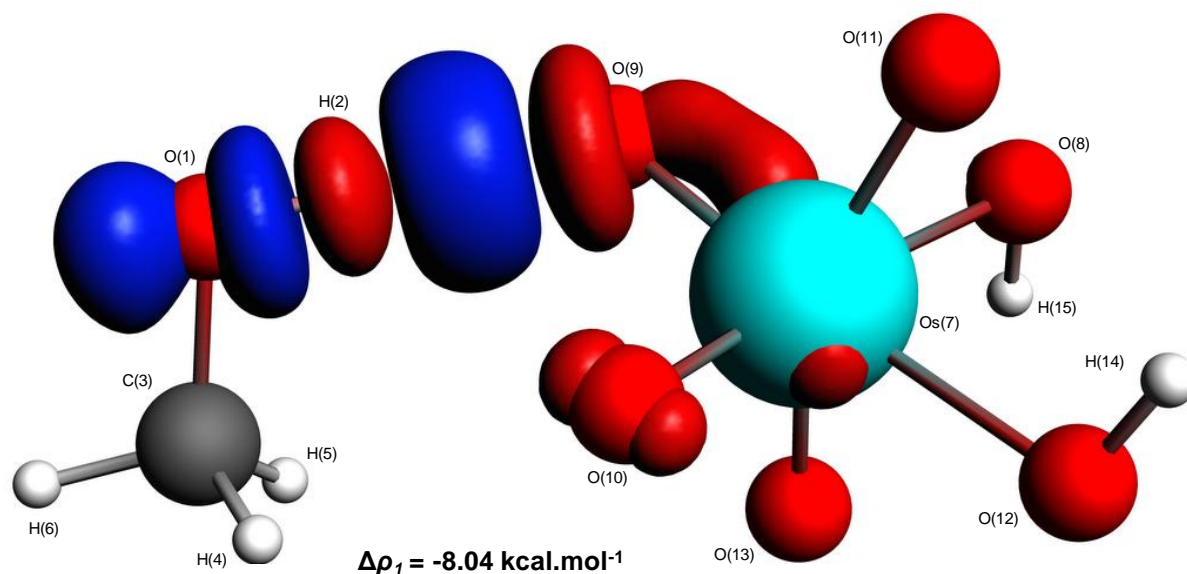


**Figure 7.17.** Natural orbitals for the Chemical Valence (NOCV) showing the largest contribution to the orbital energy between methanol and *cis*-[Os<sup>VIII</sup>O<sub>4</sub>(OH)<sub>2</sub>]<sup>2-</sup> in the simulated aqueous phase (PBE-D3 functional).

The energy of the highest deformation-density channel is more negative than the sum of all the orbital interaction energy contributions ( $\Delta E_{orb} = -7.50 \text{ kcal.mol}^{-1}$ ), Table 7.15. In Figure 7.17, it is evident that  $\Delta\rho_1$  corresponds with a considerable accumulation of electron density in the vicinity of the intermolecular BCP at O(1)-H(2)···O(9) and is the largest orbital contribution in stabilising the non-covalent dimer, while electron density depletion is mostly located at the metal-oxo  $\pi$ -bond of Os(7)-O(9).

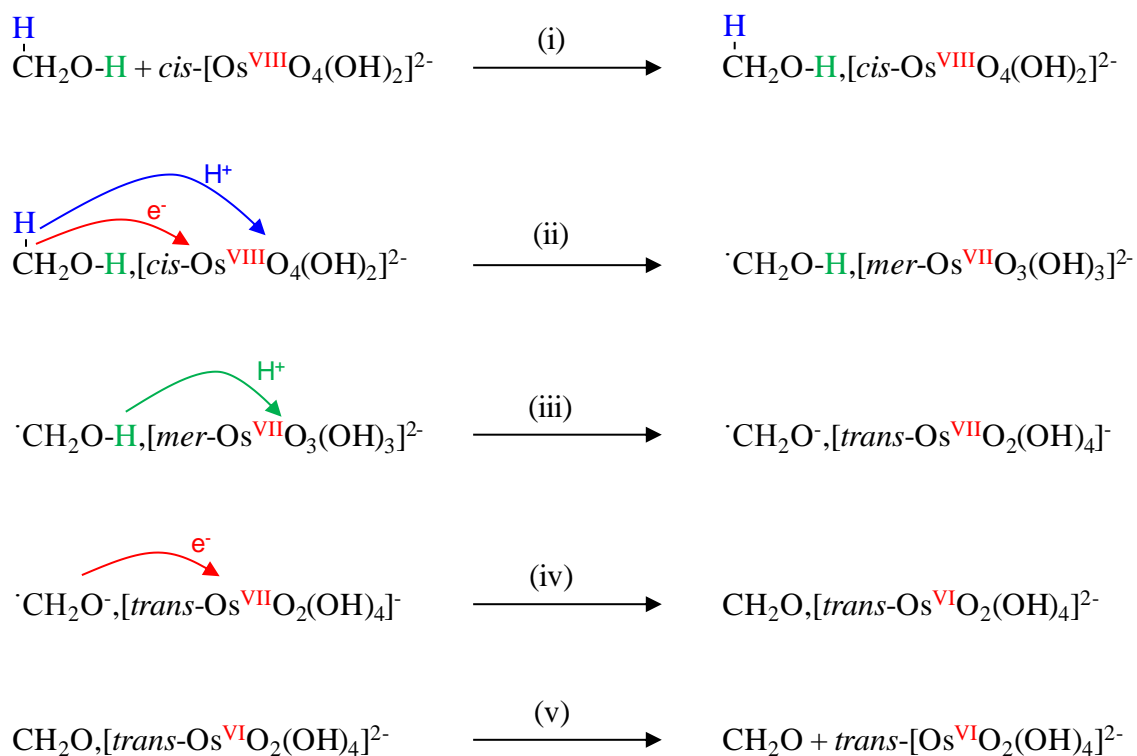
**Table 7.15.** Energy decomposition analysis (EDA)<sup>25-26</sup> in  $\text{kcal.mol}^{-1}$  of the organic and inorganic fragments of  $\text{CH}_3\text{OH}_2[\text{cis-Os}^{\text{VIII}}\text{O}_4(\text{OH})_2]^{2-}$  (PBE-D3 functional) in the simulated aqueous phase. All energies are with respect to the isolated fragments.

$\Delta E_{tot}$	$\Delta E_{int}$	$\Delta E_{Pauli}$	$\Delta E_{elstat}$	$\Delta E_{orb}$	$\Delta E_{disp}$	$\Delta E_{solv}$	$\Delta E_{prep}$	$-D_e$
-222.31	-14.68	16.00	-21.17	-7.50	-2.01	-207.63	0.59	-221.72

EDA reveals that the contribution of  $\Delta E_{disp}$ ,  $-2.01 \text{ kcal.mol}^{-1}$ , to the total interaction energy,  $\Delta E_{int}$ ,  $-14.68 \text{ kcal.mol}^{-1}$ , is relatively small in comparison with contributions from  $\Delta E_{Pauli}$ ,  $16.00 \text{ kcal.mol}^{-1}$ , or  $\Delta E_{elstat}$ ,  $-21.17 \text{ kcal.mol}^{-1}$ . Even though  $\Delta E_{disp}$  does not seem to contribute by a large factor, we suspect that the inclusion of dispersion brings the monomers closer together (in comparison to if dispersion corrections were not to have been included), decreasing  $\Delta E_{elstat}$  and  $\Delta E_{orb}$  in a similar fashion as was observed for  $[\text{Os}^{\text{VIII}}=\text{O}\cdots\text{HO-Os}^{\text{VI}}]^{4-}$  and  $[\text{Os}^{\text{VIII}}=\text{O}\cdots\text{HO-Os}^{\text{VI}}]^{3-}$ , Chapter 6. However, the largest energetic contribution to the interaction energies is that of solvation (hydration) energy,  $\Delta E_{solv}$ . In contrast to the EDA

analyses of the Os<sup>VI</sup> and Os<sup>VIII</sup> fragments in the non-covalent dimers of [Os<sup>VIII</sup>=O...HO-Os<sup>VI</sup>]<sup>4-</sup> and [Os<sup>VIII</sup>=O...HO-Os<sup>VI</sup>]<sup>3-</sup>,  $\Delta E_{elstat}$  is negative. Hydration energy is thus not necessary to facilitate the formation of CH<sub>3</sub>OH,[*cis*-Os<sup>VIII</sup>O<sub>4</sub>(OH)<sub>2</sub>]<sup>2-</sup> from the isolated monomers.

The first step (i) of the reduction of *cis*-[Os<sup>VIII</sup>O<sub>4</sub>(OH)<sub>2</sub>]<sup>2-</sup> with methanol, formation of non-covalent dimer CH<sub>3</sub>OH,[*cis*-Os<sup>VIII</sup>O<sub>4</sub>(OH)<sub>2</sub>]<sup>2-</sup>, is depicted in the complete reaction mechanism Scheme 7.3 and in the relative Gibbs energy diagram, Figure 7.18.



**Scheme 7.3.** Complete, five-step reaction mechanism for the reduction of *cis*-[Os<sup>VIII</sup>O<sub>4</sub>(OH)<sub>2</sub>]<sup>2-</sup> with methanol.

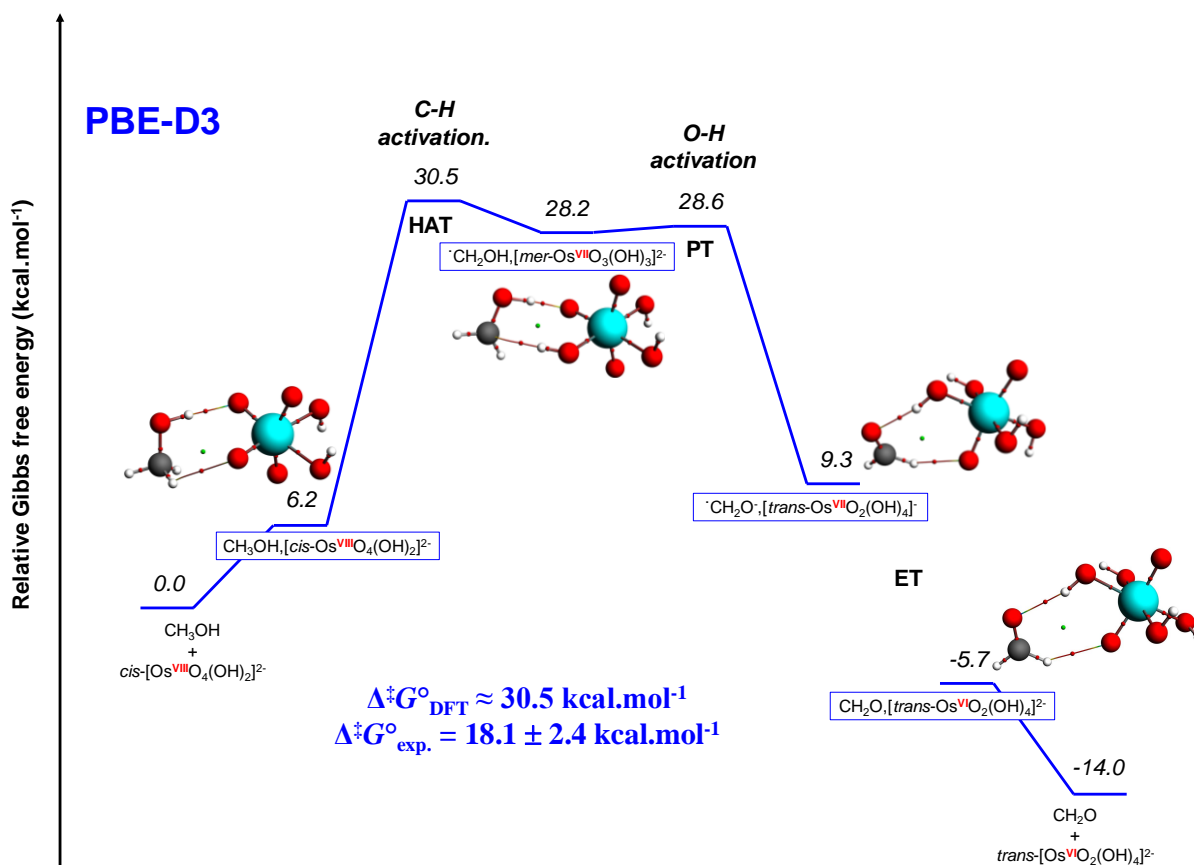
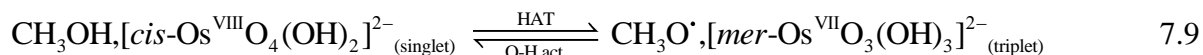


**Figure 7.18.** Gibbs free energy reaction profile diagram for the reduction of  $cis\text{-[Os}^{\text{VIII}}\text{O}_4(\text{OH})_2\text{]}^{2-}$  with methanol (PBE-D3).

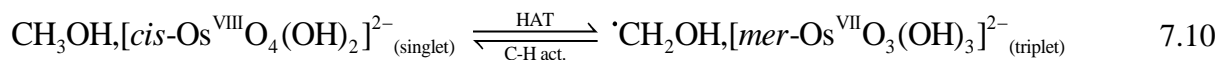
With the initial, non-covalent dimer identified, we proceeded to investigate whether the subsequent reaction step may involve HAT. Based on the equilibrium geometry of  $\text{CH}_3\text{OH}, [cis\text{-Os}^{\text{VIII}}\text{O}_4(\text{OH})_2]^{2-}$ , the possibility of initial O-H activation or C-H activation of methanol, to the  $\text{Os}^{\text{VIII}}$  monomer, may occur. However, based on the results that (i) the distance between H(2) and O(9) is 1.18 Å shorter than between H(4) and O(10), (ii) the  $\rho_b$  is approximately ten times larger in magnitude at the BCP between H(2) and O(9) compared to the BCP between H(4) and O(10) and that (iii) the main stabilising orbital contribution between the monomers is at O(1)-H(2)⋯O(9), it may be expected that the hydroxyl hydrogen is more likely to transfer to  $[\text{Os}^{\text{VIII}}=\text{O}]^{2-}$  compared to the  $\alpha$ -carbon hydrogen. In Section 7.2.1, we obtained compelling evidence to suggest that C-H activation of methanol coincides with the rate-determining step of reaction 7.1. The DFT results of the initial non-covalent dimer (above) seem to conflict with what was deduced from the KIE experiments.

In order to probe whether the hydroxyl hydrogen O-H or  $\alpha$ -carbon hydrogen of methanol first transfers to  $cis$ -[Os<sup>VIII</sup>O<sub>4</sub>(OH)<sub>2</sub>]<sup>2-</sup>, we first submitted geometry optimisation calculations of possible HAT non-covalent dimer ‘products’ corresponding to the two following scenarios:

(i) The O-H hydrogen of methanol transfers to  $cis$ -[Os<sup>VIII</sup>O<sub>4</sub>(OH)<sub>2</sub>]<sup>2-</sup>, such that a methoxy radical, CH<sub>3</sub>O<sup>·</sup>, and  $mer$ -[Os<sup>VII</sup>O<sub>3</sub>(OH)<sub>3</sub>]<sup>2-</sup> non-covalent dimer ‘product’ is formed, equation 7.9.



(ii) The  $\alpha$ -C-H hydrogen of methanol transfers to  $cis$ -[Os<sup>VIII</sup>O<sub>4</sub>(OH)<sub>2</sub>]<sup>2-</sup>, such that a hydroxymethyl radical, <sup>·</sup>CH<sub>2</sub>OH, and  $mer$ -[Os<sup>VII</sup>O<sub>3</sub>(OH)<sub>3</sub>]<sup>2-</sup> non-covalent dimer ‘product’ is formed, equation 7.10.



Geometry optimisation calculations of the conceivable non-covalent dimer ‘product’ complexes in the simulated aqueous phase converged relatively easily, Figures 7.19 and 7.20. Subsequent vibrational frequencies analyses confirm that the species are local minima on the PES as no negative frequencies were obtained. The molecular graphs of CH<sub>3</sub>O<sup>·</sup>, [mer-Os<sup>VII</sup>O<sub>3</sub>(OH)<sub>3</sub>]<sup>2-</sup>, Figure 7.19, and <sup>·</sup>CH<sub>2</sub>OH, [mer-Os<sup>VII</sup>O<sub>3</sub>(OH)<sub>3</sub>]<sup>2-</sup>, Figure 7.20, display the various critical points and atomic interaction lines that were obtained from AIMs analysis.

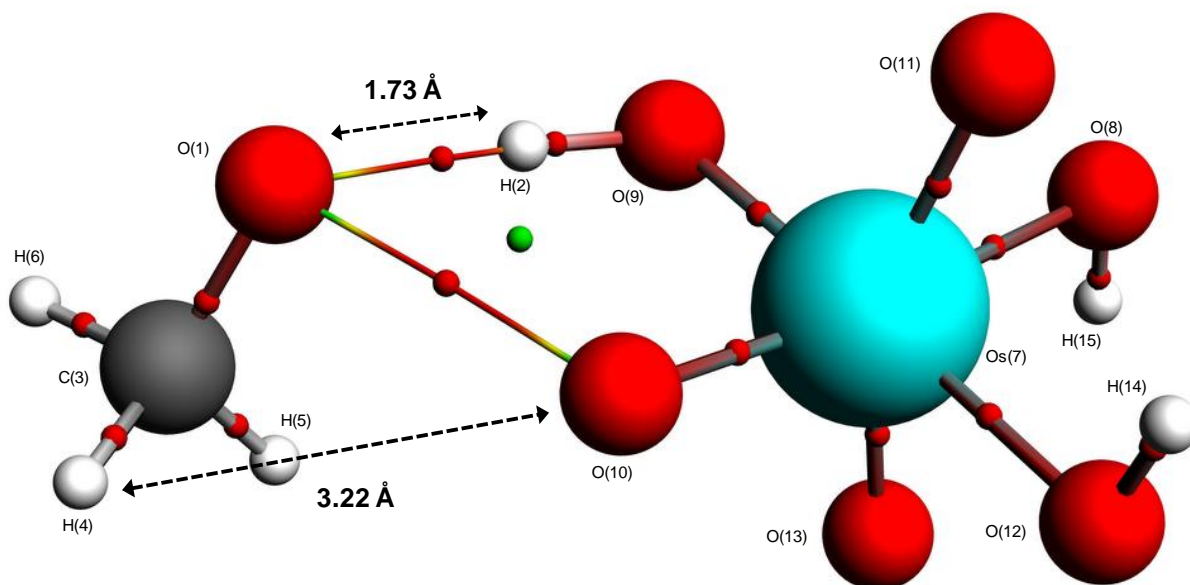


**Figure 7.19.** Molecular graph of  $\text{CH}_3\text{O}\cdot, [\text{mer-Os}^{\text{VII}}\text{O}_3(\text{OH})_3]^{2-}$  (PBE-D3 functional) showing two atomic interaction lines corresponding to intermolecular hydrogen bonds between the monomers. The small red and green spheres represent (3,-1) and (3,+1) critical points, respectively.

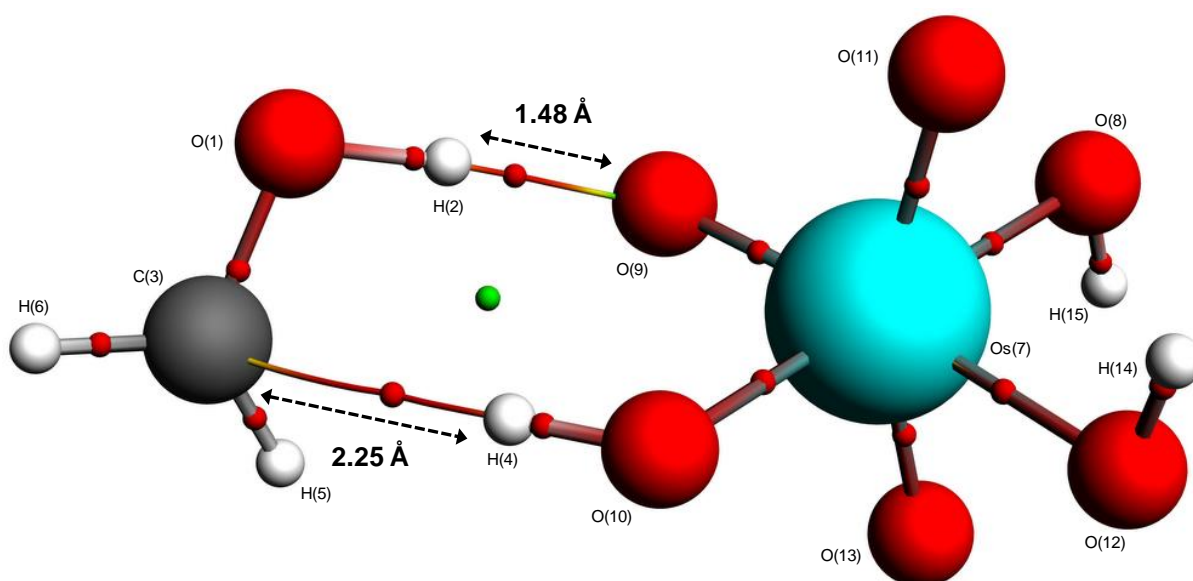


**Figure 7.20.** Molecular graph of  $\cdot\text{CH}_2\text{OH}, [\text{mer-Os}^{\text{VII}}\text{O}_3(\text{OH})_3]^{2-}$  (PBE-D3 functional) showing two atomic interaction lines corresponding to intermolecular hydrogen bonds between the monomers. The small red and green spheres represent (3,-1) and (3,+1) critical points, respectively.

There is a relatively large difference in Gibbs energy between the two non-covalent dimer ‘products’, *i.e.* the O-H activated HAT product, Figure 7.19, is 16.01 kcal.mol<sup>-1</sup> higher in Gibbs energy than the C-H activated HAT product, Figure 7.20. Furthermore, the intermolecular hydrogen bonding interaction between O(10) and H(4) is no longer present in  $\text{CH}_3\text{O}\cdot, [\text{mer-Os}^{\text{VII}}\text{O}_3(\text{OH})_3]^{2-}$  {instead there are two atomic interaction lines from O(1) to

O(10) and to H(2)}. By contrast, the  $\cdot\text{CH}_2\text{OH}, [\text{mer-Os}^{\text{VII}}\text{O}_3(\text{OH})_3]^{2-}$  non-covalent dimer has two, relatively short, intermolecular interactions, where the O(9) - H(2) distance has become shorter and the C(3) - H(4) distance is 2.25 Å.

With equilibrium geometries corresponding to the non-covalent dimer ‘reactant’ and ‘products’, for two conceivable HAT reactions confirmed, equations 7.9 & 7.10, we proceeded to the next step of our mechanistic investigation, which was to identify and calculate the ‘activation energies’ for the two reactions. Since the overall spin state changes from a singlet to a triplet for both reactions, we searched for the respective minimum energy crossing points (MECP). The internal geometric parameter that was kept the same for the independent PESs was the distance between O(9) and H(2) in scenario one and in scenario two, it was the distance between O(10) and H(4). The calculated PESs obtained following the geometry optimisation calculations (partial convergence) are shown in Figures 7.21 and 7.22.

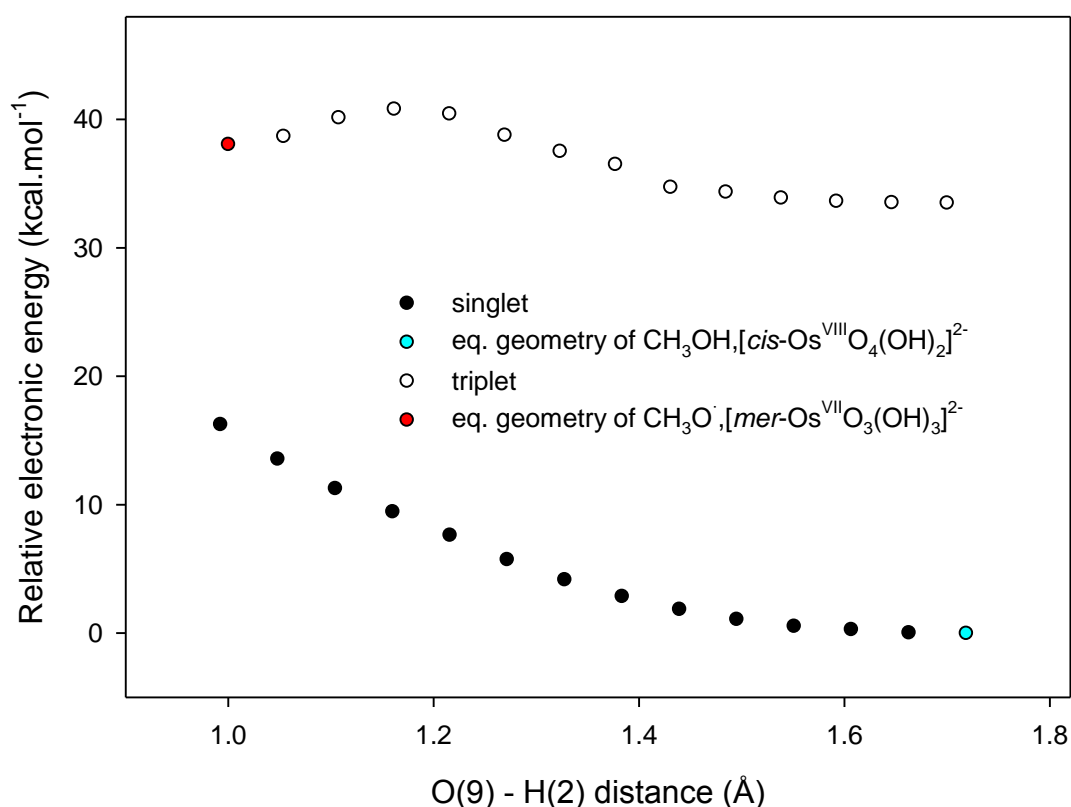


**Figure 7.21.** Energies of the partially optimised singlet and triplet states for O-H activation of methanol with  $\text{cis-}[\text{Os}^{\text{VIII}}\text{O}_4(\text{OH})_2]^{2-}$ . The hydroxyl hydrogen of methanol cannot transfer to  $\text{Os}^{\text{VIII}}$  since the PESs of the singlet (corresponding to the spin state of the ‘reactant’ non-covalent dimer) and triplet (‘product’ non-covalent dimer) spin states do not cross one another at all; no MECP is obtained.



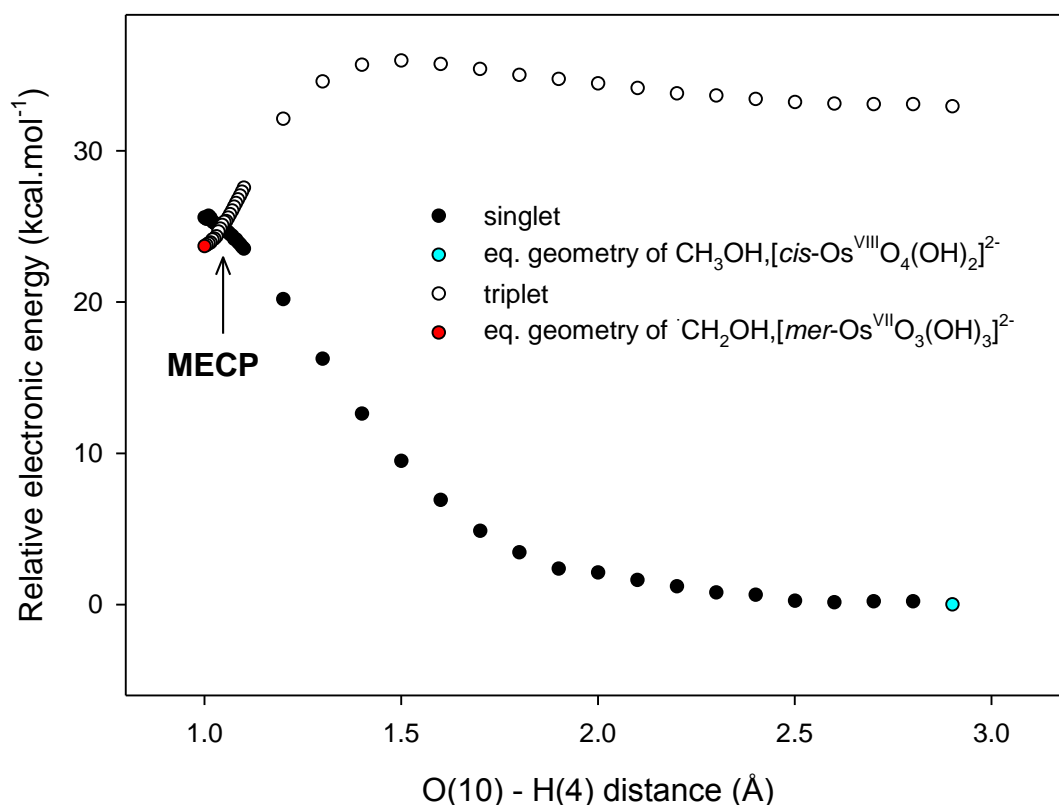
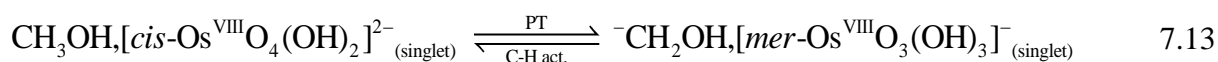
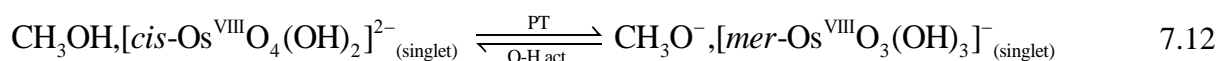


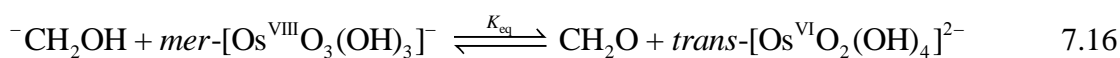
**Figure 7.22.** Energies of the partially optimised singlet and triplet states for C-H activation of methanol.

It is seen in Figure 7.21 that O-H activation does not have a PES crossover of spin states whereas C-H activation, Figure 7.22, does. From the linear transit calculations results and the result that the equilibrium geometry of  ${}^{\cdot}\text{CH}_2\text{OH}, [\text{mer-Os}^{\text{VII}}\text{O}_3(\text{OH})_3]^{2-}$  is 16.01 kcal.mol $^{-1}$  thermodynamically favoured to  $\text{CH}_3\text{O}^{\cdot}, [\text{mer-Os}^{\text{VII}}\text{O}_3(\text{OH})_3]^{2-}$ , we conclude that the second step (ii) of the reaction mechanism is where an  $\alpha$ -carbon hydrogen bond of methanol transfers to  $\text{Os}^{\text{VIII}}$  via HAT. The second reaction step is shown in Scheme 7.3 and Figure 7.18.

Furthermore, initial electron transfer, via ET-PT, or initial proton transfer, via PT-ET, non-covalent dimer ‘products’ were also submitted for geometry optimisation calculations. The formation of such species is given by the hypothetical reactions 7.11 – 7.13.



The ‘product’ non-covalent dimers represented in equations 7.11 – 7.13 did not converge as local energy minima. When initial geometries corresponding to such species, *i.e.*  $^+\text{CH}_3\text{OH}, [\text{cis-Os}^{\text{VII}}\text{O}_4(\text{OH})_2]^{3-}$  (triplet),  $\text{CH}_3\text{O}^-, [\text{mer-Os}^{\text{VIII}}\text{O}_3(\text{OH})_3]^-$  (singlet) or  $^-\text{CH}_2\text{OH}, [\text{mer-Os}^{\text{VIII}}\text{O}_3(\text{OH})_3]^-$  (singlet) were submitted for geometry optimisation calculations, the species converged as local minima corresponding to either one of the three non-covalent dimers shown in Figures 7.16, 7.19 or 7.20. We can conclude from these results that sequential PCET pathways do not occur subsequent to the formation of the non-covalent dimer shown in Figure 7.16. However, this does not prove that such anionic and cationic monomer species are not present. The Gibbs energies of these species in comparison with those of the final products, formaldehyde and *trans*- $[\text{Os}^{\text{VI}}\text{O}_2(\text{OH})_4]^{2-}$ , provides an indication w.r.t. their relative abundance in the 2.0 M NaOH aqueous solution at 298.15 K once equilibrium has been reached, equations 7.14 – 7.16.



$\Delta G^\circ_{\text{rxn}}$  for the hypothetical reactions 7.14 – 7.16 yield extremely large negative values, at -102.2, -39.3 and -75.7 kcal.mol<sup>-1</sup>, respectively, which equates to  $K_{\text{eq}}$  values of approximately  $7 \times 10^{66}$ ,  $6 \times 10^{25}$  and  $3 \times 10^{49}$ , respectively. The formation of these anionic and cationic monomer species (including a methanol cation, *cis*- $[\text{Os}^{\text{VII}}\text{O}_4(\text{OH})_2]^{3-}$ , methoxy anion, *mer*- $[\text{Os}^{\text{VIII}}\text{O}_3(\text{OH})_3]^-$  and a hydroxymethyl cation) are all highly thermodynamically unfavourable and at concentrations that are essentially non-existent at equilibrium.

We proceeded to investigate whether the hydroxymethyl radical  $^-\text{CH}_2\text{OH}$  and *mer*- $[\text{Os}^{\text{VIII}}\text{O}_3(\text{OH})_3]^-$  in the non-covalent dimer  $^-\text{CH}_2\text{OH}, [\text{mer-Os}^{\text{VIII}}\text{O}_3(\text{OH})_3]^-$  will undergo PT, ET or HAT in the subsequent elementary step of the reaction mechanism. To do this, we performed a linear transit, relaxed scan calculation where we monitored the electronic energy of the system as a function of the distance between O(9) and H(2). The electronic energy increased towards a maximum value, corresponding to an initial estimate of a true, *i.e.* not a spin-avoided crossing point, transition state at a O(9) to H(2) distance of approximately 1.33 Å, Figure 7.23.

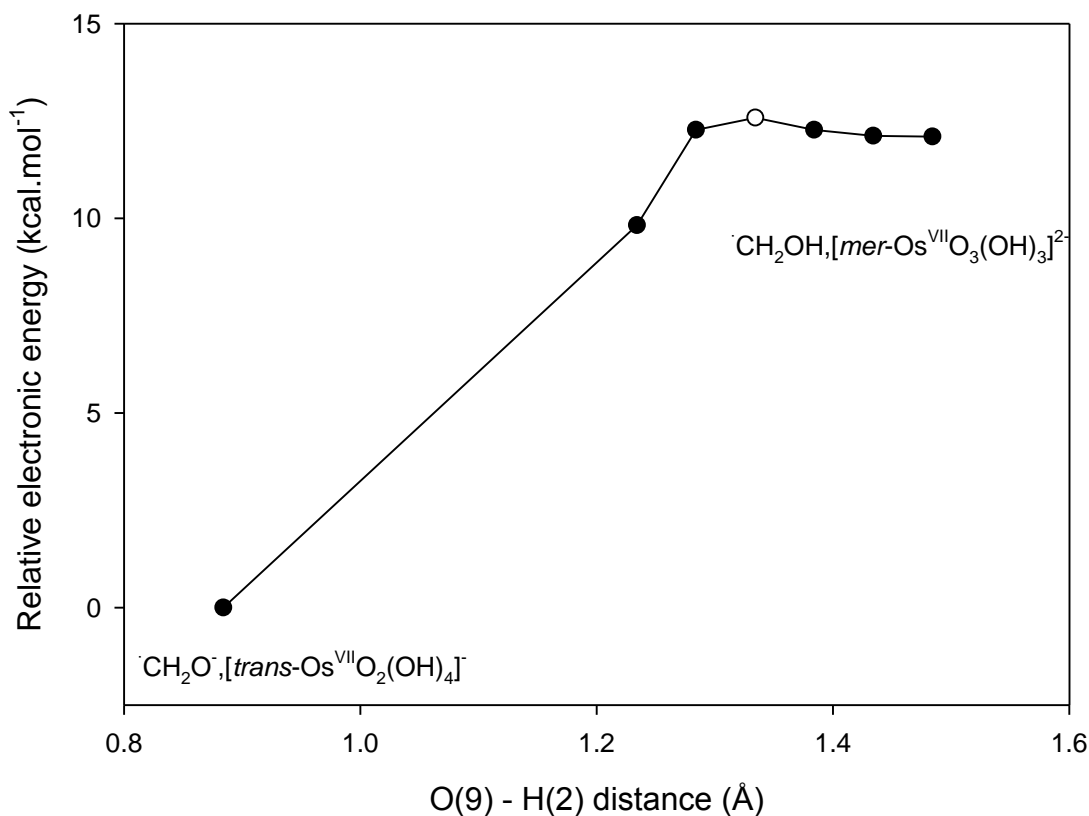


**Figure 7.23.** Relative electronic energy as a function of the O(9) - H(2) distance for  $\text{CH}_2\text{OH}, [\text{mer-Os}^{\text{VII}}\text{O}_3(\text{OH})_3]^{2-}$ .

The structure of the non-covalent dimer at the energy maximum in Figure 7.23 was submitted for a frequencies calculation. One negative frequency, corresponding to O(1)-H(2) stretching towards O(9), was obtained. The initial geometry, for which the Hessian matrix was calculated in the frequencies calculation, was submitted for a transition state search calculation and then a second vibrational frequencies analysis to confirm the presence of one imaginary frequency, Figure 7.24. The third step (iii) of the reaction mechanism, shown in Scheme 7.3 and Figure 7.18, is therefore where the O-H hydrogen of the organic fragment,  $\text{CH}_2\text{OH}$ , transfers to the inorganic fragment,  $\text{mer-}[\text{Os}^{\text{VII}}\text{O}_3(\text{OH})_3]^{2-}$ , via PT.

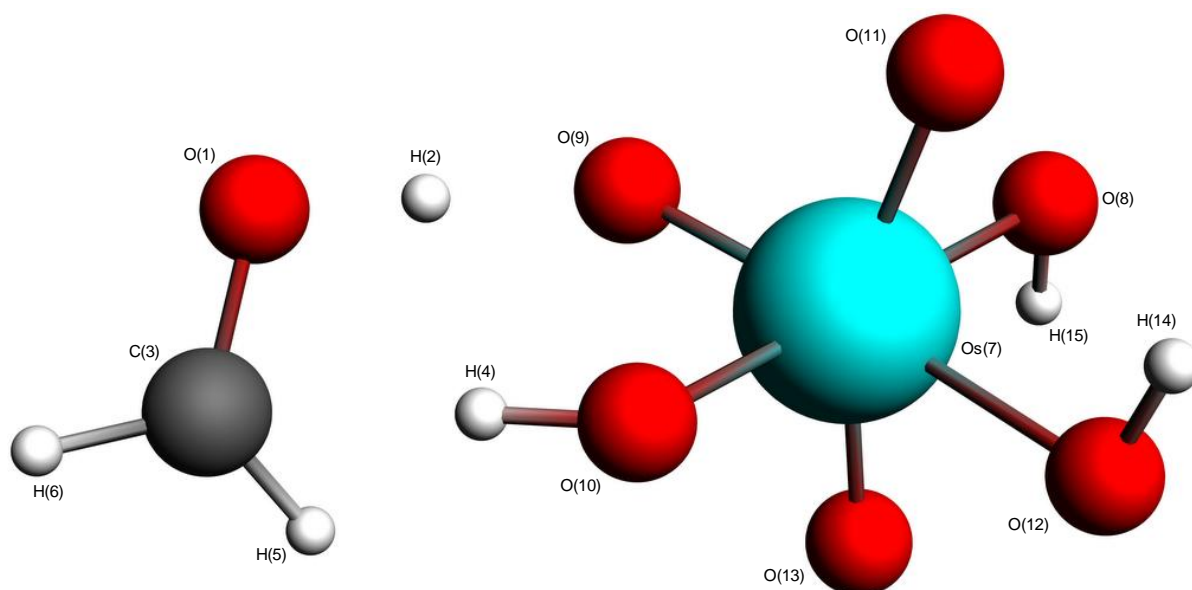


**Figure 7.24.** Transition state for PT from  $\text{CH}_2\text{OH}$  to  $\text{mer-}[\text{Os}^{\text{VII}}\text{O}_3(\text{OH})_3]^{2-}$ .

The confirmed transition state implies that the product of the PT must be stable in the triplet spin state. The geometry of the non-covalent dimer at the ‘first’ data point in Figure 7.23, *i.e.* at the O(9) – H(2) distance of 0.88 Å, was submitted for a geometry optimisation calculation in the triplet spin state and eventually converged as a local minimum at a O(9) – H(2) distance of 0.98 Å, Figure 7.25.

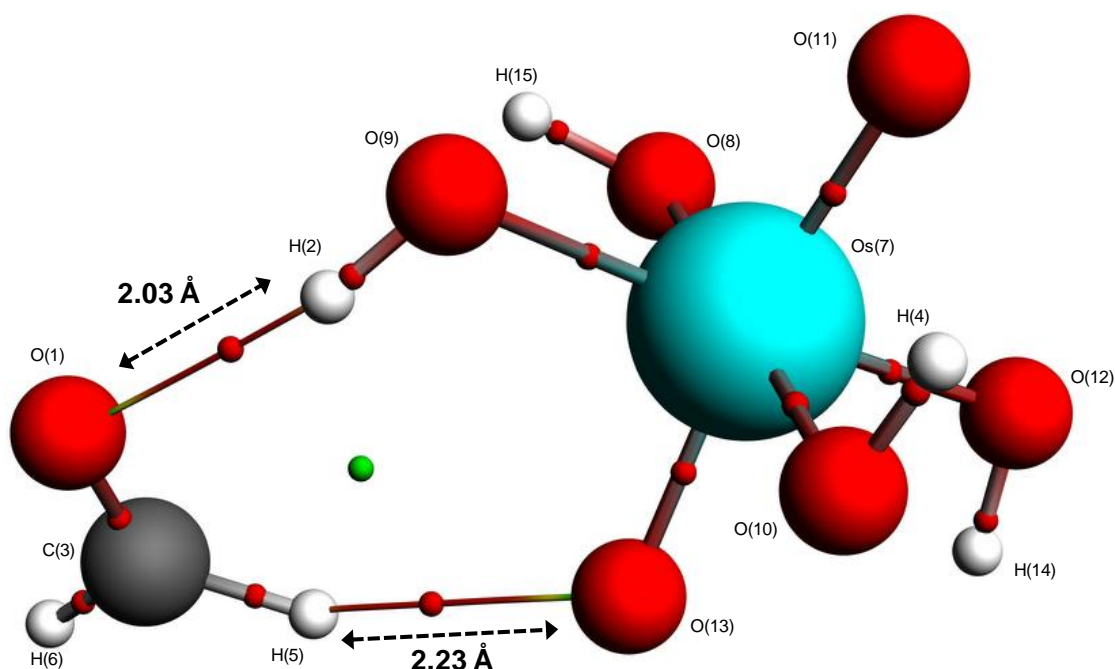


**Figure 7.25.** Molecular graph of  $\text{CH}_2\text{O}\cdots[\text{trans-Os}^{\text{VII}}\text{O}_2(\text{OH})_4]$  (PBE-D3 functional) showing two atomic interaction lines corresponding to intermolecular hydrogen bonds between the monomers. The small red and green spheres represent (3,-1) and (3,+1) critical points, respectively.

Subsequent vibrational frequencies analysis confirms that the triplet spin state species, Figure 7.25, is a local minimum as no negative frequencies were obtained. Moreover, the equilibrium geometry in Figure 7.25 provides further confirmation that the third step (iii) of the reaction mechanism is PT, Scheme 7.3.

The only remaining transfer required to yield the final products of reaction 7.1, step (iv) in Scheme 7.3, is of an electron from the organic monomer,  $\text{CH}_2\text{O}$ , to the inorganic monomer,  $\text{trans-}[\text{Os}^{\text{VII}}\text{O}_2(\text{OH})_4]^-$ . The structure shown in Figure 7.25 (triplet) was therefore submitted for a geometry optimisation calculation in the singlet spin state, which would be representative of the last non-covalent dimer species to form before formaldehyde and  $\text{trans-}[\text{Os}^{\text{VI}}\text{O}_2(\text{OH})_4]^{2-}$  would separate from one another, *i.e.* the final step (v) of the reaction mechanism. The geometry converged relatively easily, Figure 7.26. In comparison with  $\text{CH}_2\text{O}\cdots[\text{trans-Os}^{\text{VII}}\text{O}_2(\text{OH})_4]^-$ , the intermolecular hydrogen bonding distances, *i.e.* between O(1) and H(2) and between O(13) and H(5), are longer, while only small geometric changes are otherwise observed. Subsequent vibrational frequencies analysis confirms that the species is a local minimum as no negative frequencies were obtained.

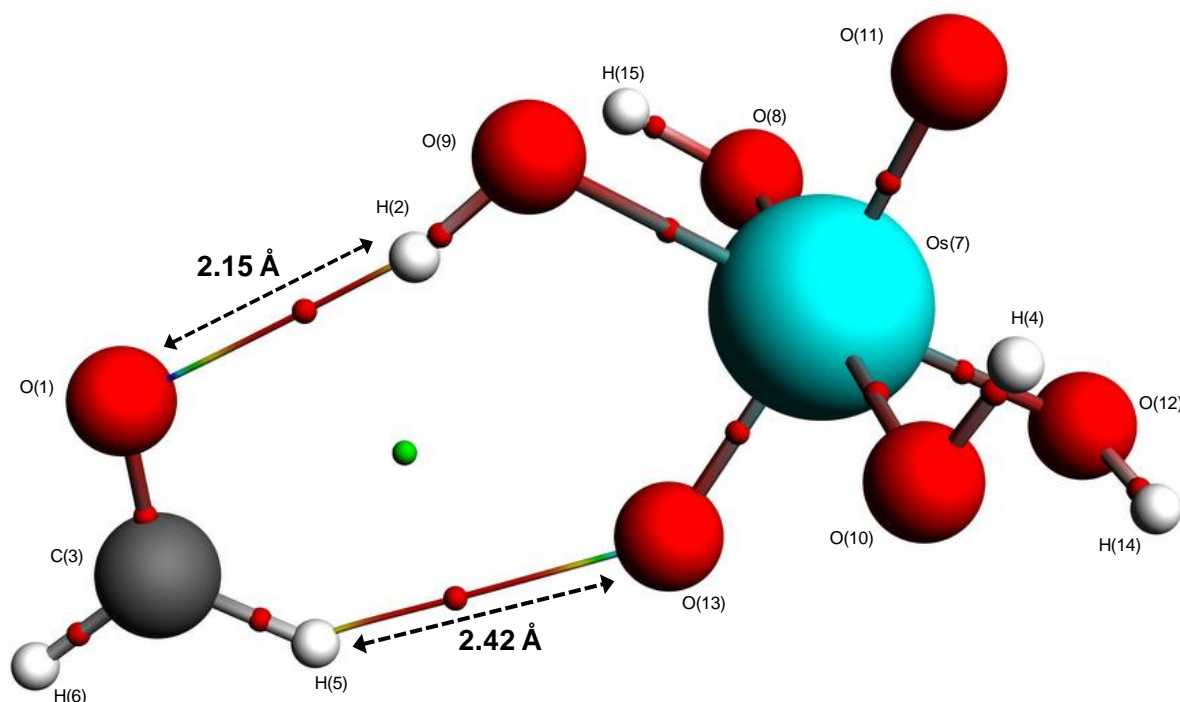


**Figure 7.26.** Molecular graph of  $\text{CH}_2\text{O}\cdots[\text{trans-Os}^{\text{VI}}\text{O}_2(\text{OH})_4]^{2-}$  (PBE-D3 functional) showing two atomic interaction lines corresponding to intermolecular hydrogen bonds between the monomers. The small red and green spheres represent (3,-1) and (3,+1) critical points, respectively.

The complete, five-step reaction mechanism for the reduction of  $cis-[Os^{VIII}O_4(OH)_2]^{2-}$  with methanol shown in Scheme 7.3 and Figure 7.18 consists of (i) non-covalent dimer formation of the reactants, (ii) HAT of an  $\alpha$ -C-H bond of  $CH_3OH$  to  $cis-[Os^{VIII}O_4(OH)_2]^{2-}$ , (iii) PT of the O-H hydrogen of  $\cdot CH_2OH$  to  $mer-[Os^{VII}O_3(OH)_3]^{2-}$ , (iv) ET from  $\cdot CH_2O^-$  to  $trans-[Os^{VII}O_4(OH)_2]^-$ , and (v) separation of the products. The organic and inorganic monomers involved in the reaction mechanism do not separate from one another in between steps (ii) to (iv), but stay bound to one another *via* intermolecular hydrogen bonding interactions in order to firstly, decrease the PT/ET transfer distance between them, and secondly, to avoid the formation of highly energetically unfavourable cationic, anionic or radical monomer species.

In order to establish the validity of the found reaction mechanism of  $cis-[Os^{VIII}O_4(OH)_2]^{2-}$  reduction with methanol, we can compare our experimental, Table 7.2, and DFT-calculated activation energies. The agreement of the energies is neither particularly good but not drastically poor, Table 7.16.

**Table 7.16. Activation energies for a reaction pathway of the reduction of  $cis-[Os^{VIII}O_4(OH)_2]^{2-}$  with methanol ( $CH_3OH$ ).**

Procedure	$\Delta^\ddagger H^\circ$ (kcal.mol <sup>-1</sup> )	$\Delta^\ddagger S^\circ$ (cal.mol <sup>-1</sup> .K <sup>-1</sup> )	$\Delta^\ddagger G^\circ_{298.15\text{ K}}$ (kcal.mol <sup>-1</sup> )
UV-Vis kinetics	14.4 ± 1.2	-12.5 ± 4.1	18.1 ± 2.4
DFT (PBE-D3)	19.1	-38.1	30.5

The activation enthalpy with PBE-D3 is overestimated by approximately 4.7 kcal.mol<sup>-1</sup> and the activation entropy is underestimated, by approximately 25.6 cal.mol<sup>-1</sup>.K<sup>-1</sup>, which suggests that the dominant mechanism for reaction 7.1 does not occur according to that which we have found here. In particular, the experimentally obtained activation entropy, at -12.5 cal.mol<sup>-1</sup>.K<sup>-1</sup>, may indicate that the dominant mechanism for reaction 7.1 does not consist of the formation of the  $CH_3OH, [cis-Os^{VIII}O_4(OH)_2]^{2-}$  non-covalent dimer, *i.e.* the local minimum on the PES shown in Figure 7.16, or that the dominant mechanism for reaction 7.1 may be where the five-coordinate  $Os^{VIII}$  complex,  $[Os^{VIII}O_4(OH)]^-$ , reacts with methanol.

#### 7.2.2.4 DFT mechanistic study of $[Os^{VIII}O_4(OH)]^-$ reduction with methanol

We have already done preliminary DFT calculations of conceivable non-covalent dimers, Figures 7.27 & 7.28, and a covalently bonded dimer, Figure 7.29, (PBE-D3 functional in the simulated aqueous phase) for reaction pathways that may involve  $[Os^{VIII}O_4(OH)]^-$  as the

oxidising agent. We suspect that a complete investigation of the reaction mechanism where  $[\text{Os}^{\text{VIII}}\text{O}_4(\text{OH})]^-$  is reduced by methanol may be very time consuming and computationally expensive due to the vast number of possibilities that subsequent pathways may entail. The two dissimilar non-covalent dimers, Figures 7.27 & 7.28, and one covalently bonded dimer, Figure 7.29, have been confirmed as local energy minima on the PES, as subsequent vibrational frequencies analyses yielded no negative frequencies.

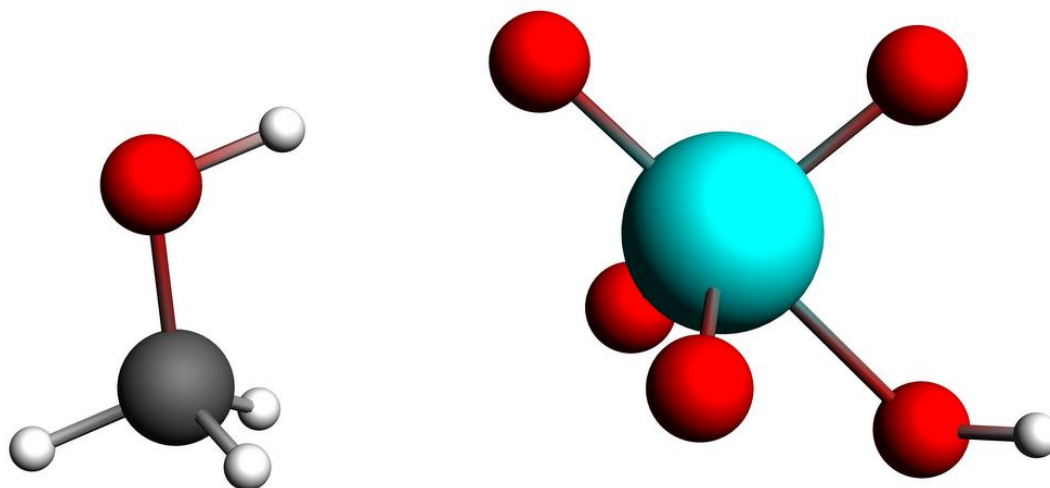


**Figure 7.27.** Molecular graph of non-covalent dimer,  $\text{CH}_3\text{OH}, [\text{Os}^{\text{VIII}}\text{O}_4(\text{OH})]^-$  (PBE-D3 functional). The O-H hydrogen of methanol is in close proximity to the oxo ligand of  $[\text{Os}^{\text{VIII}}\text{O}_4(\text{OH})]^-$  positioned *trans* to the hydroxido ligand.

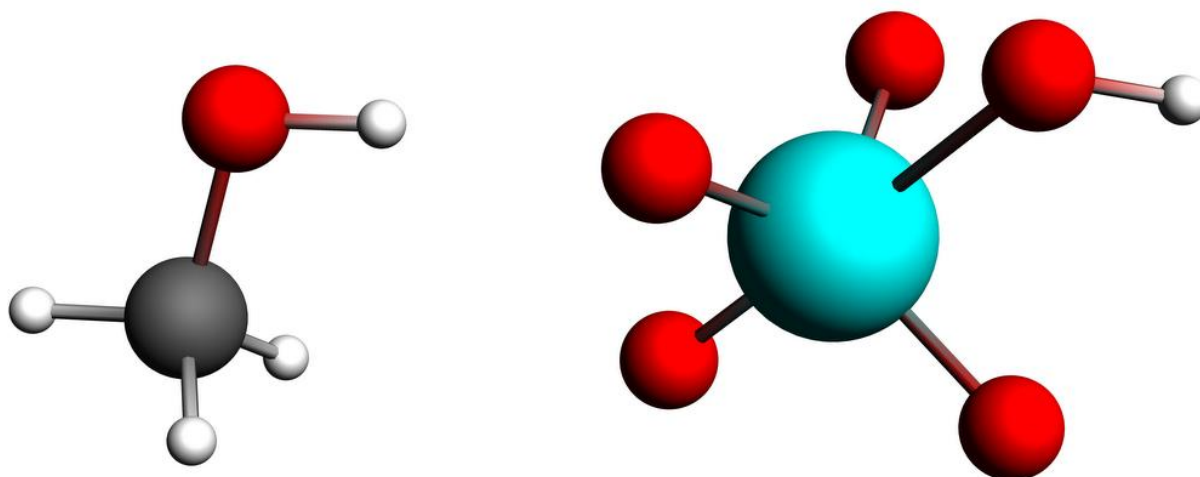


**Figure 7.28.** Molecular graph of non-covalent dimer,  $\text{CH}_3\text{OH}, [\text{Os}^{\text{VIII}}\text{O}_4(\text{OH})]^-$  (PBE-D3 functional). The O-H hydrogen of methanol is in close proximity to an oxo ligand of  $[\text{Os}^{\text{VIII}}\text{O}_4(\text{OH})]^-$  positioned *cis* to the hydroxido ligand.

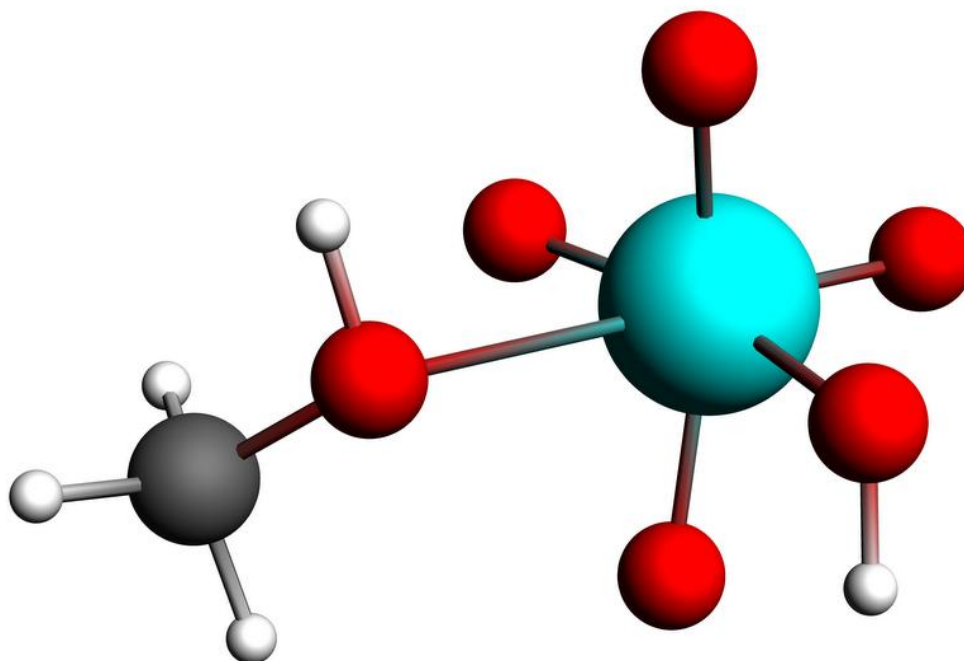


**Figure 7.29.** Molecular graph of covalently bonded dimer,  $\text{CH}_3\text{OH}, [\text{Os}^{\text{VIII}}\text{O}_4(\text{OH})]^-$  (PBE-D3 functional). The O-H oxygen of methanol forms a covalent bond with the osmium metal centre of  $[\text{Os}^{\text{VIII}}\text{O}_4(\text{OH})]^-$ .

It is evident from the three equilibrium geometries in Figures 7.27 – 7.29, corresponding to initial dimer (non-covalent and covalently bonded) formation between methanol and  $[\text{Os}^{\text{VIII}}\text{O}_4(\text{OH})]^-$ , that numerous subsequent PCET reaction pathways are possible. To elucidate the reaction mechanism for  $\text{Os}^{\text{VIII}}$  reduction with methanol using DFT is relatively complex and is left as future work.

### 7.3 Conclusions

The rate constant of  $\text{Os}^{\text{VIII}}$  reduction with methanol ( $\text{CH}_3\text{OH}$ ),  $k_{13(\text{H})}$ , in a 2.0 M NaOH aqueous matrix at various temperatures has been determined using UV-Vis spectroscopy kinetics analyses and at 298.15 K, agrees excellently,  $3.2 \times 10^{-1} \text{ M}^{-1} \cdot \text{s}^{-1}$ , with the Gerber *et al.*<sup>1</sup> reported literature value,  $2.9 \times 10^{-1} \text{ M}^{-1} \cdot \text{s}^{-1}$ . The reaction model used to simulate the obtained kinetic data was validated by the linearity of the Eyring plots for reaction 7.1 and Eyring and van't Hoff plots for reaction 7.2, the good agreement of calculated molar extinction coefficients of osmium species with those reported in the literature<sup>1,2,13</sup> and the good agreement of the standard reaction Gibbs free energy ( $\Delta G^\circ_{\text{rxn}(\text{obs})} = -1.2 \pm 0.3 \text{ kcal} \cdot \text{mol}^{-1}$ ) for the reversible comproportionation reaction with that reported by Gerber *et al.*<sup>1</sup>. Furthermore, the irreversible redox reaction of  $\text{Os}^{\text{VIII}}$  and methanol ( $\text{CH}_3\text{OH}$  or  $\text{CD}_3\text{OD}$ ) is first order w.r.t.  $\text{Os}^{\text{VIII}}$  and methanol concentrations, corroborating the literature.<sup>1-13</sup>



According to our Eyring plot analysis, the activation enthalpy, entropy and Gibbs free energies of Os<sup>VIII</sup> reduction with methanol (CH<sub>3</sub>OH) are  $14.4 \pm 1.2 \text{ kcal.mol}^{-1}$ ,  $-12.5 \pm 4.1 \text{ cal.mol}^{-1}.\text{K}^{-1}$  and  $18.1 \pm 2.4 \text{ kcal.mol}^{-1}$ . Replacing CH<sub>3</sub>OH with CD<sub>3</sub>OH as the reducing agent in the kinetics experiments decreases the rate constant,  $k_{13}$ , by approximately an order of magnitude in the investigated temperature range and the Eyring plot has the same gradient as the one where CH<sub>3</sub>OH was utilised as the reducing agent. The activation enthalpy, entropy and Gibbs free energies of Os<sup>VIII</sup> reduction with methanol (CD<sub>3</sub>OH) are  $14.5 \pm 1.3 \text{ kcal.mol}^{-1}$ ,  $-17.1 \pm 4.4 \text{ cal.mol}^{-1}.\text{K}^{-1}$  and  $19.6 \pm 2.6 \text{ kcal.mol}^{-1}$ , confirming that the cleavage of an  $\alpha$ -C-H bond in CH<sub>3</sub>OH and the cleavage of an  $\alpha$ -C-D bond in CD<sub>3</sub>OH are the rate-determining steps for reaction 7.1. The cleavage of the relatively more labile O-H bond of CH<sub>3</sub>OH or CD<sub>3</sub>OH is not the rate-determining step of reaction 7.1. Moreover, the parallel Eyring plots also indicates that the UV-Vis data is reliable and accurate, and that the reaction model used to simulate the kinetic traces, equations 7.1 & 7.2, is valid. The relatively large KIE value,  $k_{13(\text{H})}/k_{13(\text{D})}$ , of approximately 11.82 (298.15 K) is indicative of a normal, primary isotope effect. Composite Eyring plots for reaction 7.2 further validate the stopped-flow UV-Vis spectroscopy kinetics analyses presented in Chapter 4.

It was found that Os<sup>VII</sup> oxo/hydroxido species (*trans*-[Os<sup>VII</sup>O<sub>3</sub>(OH)<sub>2</sub>]<sup>-</sup> or *mer*-[Os<sup>VII</sup>O<sub>3</sub>(OH)<sub>3</sub>]<sup>2-</sup>), do not react with methanol since a one- or two-electron transfer would result in thermodynamically unfavoured species. We therefore envisage that Os<sup>VII</sup> oxo/hydroxido species would not be catalytically active in cases where the reducing agent transfers two electrons. However, in cases where the reducing agent transfers only one electron, *e.g.* benzaldehyde {with [Ru<sup>IV</sup>(bpy)<sub>2</sub>(py)(O)]<sup>2+</sup> in Figure 1.7}<sup>18</sup>, we expect that an Os<sup>VII</sup> species may be catalytically active.

DFT calculations of the reactants and products of the Os<sup>VIII</sup> reduction with methanol, with the PBE-D3 functional in the simulated aqueous phase, yields a relatively large negative  $\Delta G^{\circ}_{rxn}$  of  $-13.88 \text{ kcal.mol}^{-1}$ , *i.e.* reaction 7.1 lies far to the right, justifying our decision to simulate the reaction (Sections 7.2.1.1, 7.2.1.2 and 7.2.1.3) as irreversible. Moreover,  $\Delta H^{\circ}_{rxn}$  is also a relatively large negative value of  $-13.41 \text{ kcal.mol}^{-1}$  while  $\Delta S^{\circ}_{rxn}$  is  $1.57 \text{ cal.mol}^{-1}.\text{K}^{-1}$ .

A mechanistic study of *cis*-[Os<sup>VIII</sup>O<sub>4</sub>(OH)<sub>2</sub>]<sup>2-</sup> reduction with methanol agrees qualitatively with our experimentally determined result that the rate-determining step of the reaction involves the cleavage of an  $\alpha$ -C-H bond in CH<sub>3</sub>OH. Initial O-H HAT from methanol to Os<sup>VIII</sup> cannot occur following the formation of the non-covalent dimer found, Figure 7.16, due to

the absence of a transition state or MECF to connect the PESs of the ‘reactant’ non-covalent dimer with the ‘product’ non-covalent dimer states. By contrast, a MECF was found for an initial C-H HAT from methanol to *cis*-[Os<sup>VIII</sup>O<sub>4</sub>(OH)<sub>2</sub>]<sup>2-</sup>, in which case, the overall spin state changes from a singlet to a triplet. The subsequent reactions are PT of the O-H hydrogen of  $\cdot\text{CH}_2\text{OH}$  to *mer*-[Os<sup>VII</sup>O<sub>3</sub>(OH)<sub>3</sub>]<sup>2-</sup>, followed by ET from  $\cdot\text{CH}_2\text{O}^\cdot$  to *trans*-[Os<sup>VII</sup>O<sub>4</sub>(OH)<sub>2</sub>]<sup>-</sup> to form a non-covalent dimer consisting of the final products, CH<sub>2</sub>O, [i*trans*-Os<sup>VI</sup>O<sub>2</sub>(OH)<sub>4</sub>]<sup>2-</sup>. The final step of the reaction is separation of the monomers in the non-covalent dimer, yielding the final products, formaldehyde and *trans*-[Os<sup>VI</sup>O<sub>4</sub>(OH)<sub>2</sub>]<sup>2-</sup>. The DFT-calculated activation enthalpy,  $\Delta^\ddagger H^\circ$ , compares well with the experimentally determined value, differing by less than 5.0 kcal.mol<sup>-1</sup>. However, the DFT-calculated activation Gibbs energy,  $\Delta^\ddagger G^\circ$ , differs by approximately 12 kcal.mol<sup>-1</sup> to the experimental results due to the DFT-calculated activation entropy,  $\Delta^\ddagger S^\circ$ , being three times more negative than that obtained from Eyring plot analysis, Figure 7.2. Overall, the agreement between DFT and experimental thermodynamic activation parameters are not good but also not drastically poor. Possible reasons for the discrepancies could be that:

- (i) a lower energy pathway which consists of an initial non-covalent dimer with only one intermolecular hydrogen bonding interaction, is thermodynamically favoured to that found in our investigation,
- (ii) the MECF used as an approximation of the transition state for obtaining DFT-calculated activation energies (Section 1.7.2) is slightly overestimated in this case, or
- (iii) the dominant pathway may involve the other abundant Os<sup>VIII</sup> species, *i.e.* the five-coordinate [Os<sup>VIII</sup>O<sub>4</sub>(OH)]<sup>-</sup> complex, reacting with methanol.

Based on the preliminary equilibrium geometries of the non-covalent and covalently bonded dimers of CH<sub>3</sub>OH, [Os<sup>VIII</sup>O<sub>4</sub>(OH)]<sup>-</sup> that have been found, we suspect that to eventually identify the most probable reaction pathway may be extremely computationally expensive. There are far too many possible (and reasonable) reaction pathways to all be investigated thoroughly in a limited amount of time or computational power. Even though the pathway found and presented here took into consideration very specific information w.r.t. our detailed knowledge of which high oxidation state osmium species are actually present in basic aqueous media, the exact stereochemistry of the osmium reactants, intermediates and products, as well as the initial estimate of the what the thermodynamically most stable non-covalent dimer may be (geometry optimisation of the initial geometry with as many

intermolecular hydrogen bonding interactions as possible) it is clear that even more information is required.

---

**References**

1. T. E. Geswindt, W. J. Gerber, H. E. Rohwer and K. R. Koch, *Dalton Trans.*, 2011, **40**, 8581.
2. A. Dehestani, W. H. Lam, D. A. Hrovat, E. R. Davidson, W. T. Borden and J. M. Mayer, *J. Am. Chem. Soc.*, 2005, **127**, 3423.
3. P. VeeraSomaiah, K. B. Reddy, B. Sethuram and T. Navaneeth Rao, *J. Indian Chem. Soc.*, 1988, **27A**, 876.
4. P. VeeraSomaiah, K. B. Reddy, B. Sethuram and T. Navaneeth Rao, *J. Indian Chem. Soc.*, 1989, **66**, 755.
5. H. S. Singh, S. P. Singh, S. M. Singh, R. K. Singh and A. K. Sisodia, *J. Phys. Chem.*, 1975, **79(18)**, 1920.
6. N. P. Singh, V. N. Singh, H. S. Singh and M. P. Singh, *Aust. J. Chem.*, 1970, **23**, 921.
7. V. N. Singh, H. S. Singh and B. B. L. Saxena, *J. Am. Chem. Soc.*, 1969, **91(10)**, 2643.
8. H. S. Singh, *Oxidation of Organic Compounds with Osmium Tetroxide, in Organic synthesis by oxidation with metal compounds*, ed. W. J. Mijs and C. R. H. de Jonge, Plenum Press, New York, 1986.
9. N. P. Singh, V.N. Singh and M. P. Singh, *Aust. J. Chem.*, 1968, **21**, 2913.
10. B. Singh, A. K. Singh, M. B. Singh and A. P. Singh, *Tetrahedron*, 1986, **42**, 715.
11. K. K. S. Gupta and B. A. Begum, *Transition Met. Chem.*, 1998, **23**, 295.
12. K. K. S. Gupta and B. A. Begum, *Int. J. Chem. Kinet.*, 1999, **31(7)**, 477.
13. W. P. Griffith and M. Suriaatmaja, *Can. J. Chem.*, 2001, **79**, 598–606.
14. T. E. Geswindt, MSc Thesis, 2009, NMMU, South Africa.
15. W. P. Griffith, *Comprehensive Coordination Chemistry. The synthesis, reactions, properties and applications of coordination compounds. Vol. 4*. Ed. G. Wilkinson. Pergamon Press, Oxford, 1987.
16. P. Kuzmic, *Anal. Biochem.*, 1996, **237**, 260.

17. J. N. Miller, *Analyst*, 1991, **116**, 3.
18. D. R. Weinberg, C. J. Gagliardi, J. F. Hull, C. F. Murphy, C. A. Kent, B. C. Westlake, A. Paul, D. H. Ess, D. G. McCafferty and T. J. Meyer, *Chem. Rev.*, 2012, **112**, 4016.
19. G. te Velde, F. M. Bickelhaupt, S. J. A. van Gisbergen, C. Fonseca Guerra, E. J. Baerends, J. G. Snijders and T. Ziegler, *J. Comput. Chem.*, 2001, **22**, 931.
20. C. Fonseca Guerra, J. G. Snijders, G. te Velde and E. J. Baerends, *Theor. Chem. Acc.*, 1998, **99**, 391.
21. E. J. Baerends, J. Autschbach, D. Bashford, A. Bérces, F. M. Bickelhaupt, C. Bo, P. M. Boerrigter, L. Cavallo, D. P. Chong, L. Deng, R. M. Dickson, D. E. Ellis, M. van Faassen, L. Fan, T. H. Fischer, C. Fonseca Guerra, A. Ghysels, A. Giammona, S. J. A. van Gisbergen, A. W. Götz, J. A. Groeneveld, O. V. Gritsenko, M. Grüning, F. E. Harris, P. van den Hoek, C. R. Jacob, H. Jacobsen, L. Jensen, G. van Kessel, F. Kootstra, M. V. Krykunov, E. van Lenthe, D. A. McCormack, A. Michalak, M. Mitoraj, J. Neugebauer, V. P. Nicu, L. Noodleman, V. P. Osinga, S. Patchkovskii, P. H. T. Philipsen, D. Post, C. C. Pye, W. Ravenek, J. I. Rodríguez, P. Ros, P. R. T. Schipper, G. Schreckenbach, M. Seth, J. G. Snijders, M. Solà, M. Swart, D. Swerhone, G. te Velde, P. Vernooijs, L. Versluis, L. Visscher, O. Visser, F. Wang, T. A. Wesolowski, E. M. van Wezenbeek, G. Wiesenekker, S. K. Wolff, T. K. Woo, A. L. Yakovlev, and T. Ziegler, ADF2012.02, SCM, Theoretical Chemistry, Vrije Universiteit, Amsterdam, The Netherlands, <http://www.scm.com>.
22. J. I. Rodríguez, R. F. W. Bader, P. W. Ayers, C. Michel, A. W. Götz and C. Bo, *Chem. Phys. Lett.*, 2009, **472**, 149.
23. J. I. Rodríguez, *J. Comput. Chem.*, 2013, **34**, 681.
24. M. Mitoraj, A. Michalak and T. Ziegler, *J. Chem. Theory Comput.*, 2009, **5**, 962.
25. T. Ziegler and A. Rauk, *Inorg. Chem.*, 1979, **18**, 1558.
26. T. Ziegler and A. Rauk, *Inorg. Chem.*, 1979, **18**, 1755.

# CHAPTER 8

---

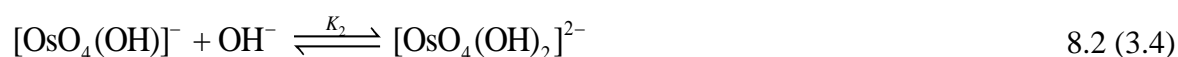
## Conclusions

In this Chapter we will review the three themes outlined in Chapter 1 and discuss the most important results that were obtained with regards to each one, in conjunction with the conclusions that can now be made from the results.

(i) Detailed thermodynamic speciation studies of Os<sup>VIII</sup> (Chapter 3), Os<sup>VI</sup> and Os<sup>VII</sup> (Chapter 5) oxo/hydroxido species in basic aqueous media with density functional theory (DFT).

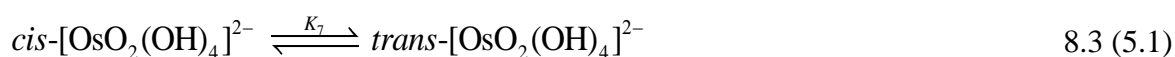
We realised, at the outset of this project, that the speciation of Os<sup>VIII</sup>, Os<sup>VI</sup> and Os<sup>VII</sup> complexes in aqueous basic solutions are important to understand catalytic redox reactions that utilise these complexes,<sup>1-5</sup> *i.e.* which of these oxo/hydroxido species actually participate in reported catalytic reactions. We subsequently demonstrated that DFT computational methodologies, mainly with GGA functionals, provided evidence that the Os<sup>VIII</sup> species present in basic aqueous solutions are Os<sup>VIII</sup>O<sub>4</sub>, [Os<sup>VIII</sup>O<sub>4</sub>(OH)]<sup>-</sup> and two *cis*-[Os<sup>VIII</sup>O<sub>4</sub>(OH)<sub>2</sub>]<sup>2-</sup> complexes and that water-bonded Os<sup>VIII</sup> species most likely do not exist. These results are in contrast to what Galbács *et al.*<sup>6</sup> and Griffith<sup>7</sup> had proposed earlier: Galbács *et al.*<sup>6</sup> proposed that the three abundant Os<sup>VIII</sup> species in solution are all six-coordinate complexes, Os<sup>VIII</sup>O<sub>2</sub>(OH)<sub>4</sub>, [Os<sup>VIII</sup>O<sub>3</sub>(OH)<sub>3</sub>]<sup>-</sup> and [Os<sup>VIII</sup>O<sub>4</sub>(OH)<sub>2</sub>]<sup>2-</sup>, while Griffith<sup>7</sup> proposed that a six-coordinate species containing a water ligand, [Os<sup>VIII</sup>O<sub>4</sub>(OH)(H<sub>2</sub>O)]<sup>-</sup> is also present in solution.

The DFT-calculated  $\Delta G^{\circ}_{rxn}$  in the simulated aqueous phase (COSMO) for the coordination sphere expansion reactions, equations 8.1 & 8.2, are -2.42 kcal.mol<sup>-1</sup> and -0.61 kcal.mol<sup>-1</sup> (PBE-D3 functional), respectively, and agree to within 1 kcal.mol<sup>-1</sup> with reported values, at -2.69 and 0.33 kcal.mol<sup>-1</sup>, respectively.<sup>6,8,9</sup> The good agreement between DFT and reported, experimentally obtained  $\Delta G^{\circ}_{rxn}$  values validated the DFT methodology used.



The thermodynamic driving force for reaction 8.1 is the bonding energy of the Os<sup>VIII</sup>-OH metal-hydroxido ligand present in [Os<sup>VIII</sup>O<sub>4</sub>(OH)]<sup>-</sup> and for reaction 8.2 it is the larger hydration energy of the doubly-charged *cis*-[Os<sup>VIII</sup>O<sub>4</sub>(OH)<sub>2</sub>]<sup>2-</sup> species in comparison with that of the two, singly-charged reactants, *i.e.* [Os<sup>VIII</sup>O<sub>4</sub>(OH)]<sup>-</sup> and a hydroxide anion. The latter result highlighted the importance that solvation (hydration) energies have in describing the relative thermodynamic stabilities of Os<sup>VIII</sup> monomer species. Further evidence for the importance of hydration energies were the DFT-calculated thermodynamic parameters obtained in the gas phase, which in contrast to calculations done in a simulated aqueous phase (COSMO), compared rather poorly with available experimental data. Both reactions 8.1 & 8.2 were found to have relatively low transition state energy,  $\Delta^\ddagger G^\circ$ , barriers. Moreover, QTAIM and EDA analyses of the Os<sup>VIII</sup> monomer species indicated that Os=O bonding interactions are ionic (closed-shell) whereas the Os-OH bonding interactions are polar covalent (dative). NCI analysis of both the [Os<sup>VIII</sup>O<sub>4</sub>(OH)]<sup>-</sup> and *cis*-[Os<sup>VIII</sup>O<sub>4</sub>(OH)<sub>2</sub>]<sup>2-</sup> species indicated the presence of weak, intramolecular hydrogen bonding interactions between neighbouring oxo and hydroxido ligands.

From DFT-calculated data, the most abundant Os<sup>VI</sup> species is the octahedral *trans*-[Os<sup>VI</sup>O<sub>2</sub>(OH)<sub>4</sub>]<sup>2-</sup> stereoisomer. The global minimum energy conformation of the *trans* stereoisomer is approximately thirty times more abundant than any other *trans* conformer, and approximately 10 kcal.mol<sup>-1</sup> (PBE functional) thermodynamically more stable than that of the *cis* stereoisomer, equation 8.3.



Moreover, DFT-calculated metal-ligand bond lengths of the global minimum *trans* stereoisomer species' equilibrium geometry correlates well with reported values obtained from X-ray crystal structure data.<sup>10,11</sup>

The most abundant Os<sup>VII</sup> species in aqueous solutions, according to our DFT speciation calculations, are a combination of the *trans*-[Os<sup>VII</sup>O<sub>3</sub>(OH)<sub>2</sub>]<sup>-</sup> and *mer*-[Os<sup>VII</sup>O<sub>3</sub>(OH)<sub>3</sub>]<sup>2-</sup> stereoisomers. We suspect that these two Os<sup>VII</sup> complexes are, similarly to the two Os<sup>VIII</sup> complexes, related to one another by way of a coordination sphere expansion/contraction reaction with a hydroxide anion, equation 8.4.



The thermodynamic driving force of reaction 8.4 is the larger hydration energy of the doubly-charged, octahedral *mer*-[Os<sup>VII</sup>O<sub>3</sub>(OH)<sub>3</sub>]<sup>2-</sup> species in comparison with that of the two, singly-charged reactants. This result, combined with the analysis of reaction 8.2 (above), highlights again the importance of the inclusion of solvation (hydration) energies. Lastly, QTAIM and EDA analyses of the Os<sup>VII</sup> (and Os<sup>VI</sup>) monomer species indicated that Os=O bonding interactions are ionic (closed-shell) whereas the Os-OH bonding interactions are polar covalent (dative).

The obtained thermodynamic speciation data of Os<sup>VIII</sup>, Os<sup>VI</sup> and Os<sup>VII</sup> oxo/hydroxido monomer species with DFT were successful in providing clarity w.r.t. which osmium species are most abundant in basic aqueous media, in addition to providing an understanding of what the actual catalytically active osmium species in solution are likely to be in reported studies.<sup>1-5</sup> Furthermore, these studies provided a platform for subsequent investigations pertaining to the proposed Os<sup>VI</sup> & Os<sup>VIII</sup> comproportionation reaction in basic aqueous media, which brings us to the second main theme that was outlined for this PhD project:

(ii) Investigation of the proposed Os<sup>VI</sup> & Os<sup>VIII</sup> comproportionation reaction in basic aqueous media, using <sup>1</sup>H NMR and stopped-flow UV-Vis spectroscopy kinetics methods to prove that the reaction does indeed occur (Chapters 4 and 5), and DFT studies to subsequently ascertain the reaction mechanism (Chapter 6).

An Evans method,<sup>12-15</sup> <sup>1</sup>H NMR spectroscopy experiment confirmed that the reaction of diamagnetic Os<sup>VIII</sup> oxo/hydroxido and *trans*-[Os<sup>VI</sup>O<sub>2</sub>(OH)<sub>4</sub>]<sup>2-</sup> species, in an 2.0 M NaOH aqueous matrix at 298.15 K, does in fact occur and that the product species that are formed are paramagnetic, thereby corroborating the postulate by Gerber *et al.*<sup>16</sup> Moreover, the stoichiometric ratio of the Os<sup>VI</sup> and Os<sup>VIII</sup> reactants in the comproportionation reaction was found to be 1:1, equation 8.5.



The calculated effective magnetic moment,  $\mu_{\text{eff}}$ , of the product species determined from the <sup>1</sup>H NMR data (at 298.15 K), initially took into consideration that the only Os<sup>VII</sup> species that form are octahedral *mer*-[Os<sup>VII</sup>O<sub>3</sub>(OH)<sub>3</sub>]<sup>2-</sup> species, which yielded an estimated value for the number of unpaired electrons, per monomer product, as approximately 1.10. When the Evans method data was later re-evaluated taking into consideration the five-coordinate, *trans*



stereoisomer, the calculated effective magnetic moment,  $\mu_{eff}$ , and hence the calculated number of unpaired electrons of the products species did not change qualitatively, *i.e.* approximately 1.15 electrons per product monomer was obtained.

The spectroscopic data provided evidence to prove that Mayer *et al.*<sup>8</sup> were mistaken when concluding that paramagnetic Os<sup>VII</sup> species are not present in basic aqueous matrices:

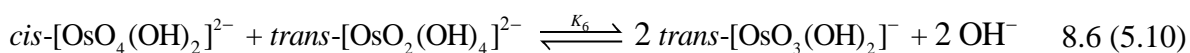
“ $[\text{Os}^{\text{VII}}\text{O}_3(\text{OH})_3]^{2-}$ ” is not observed in alkaline mixtures of  $\text{Os}^{\text{VIII}}\text{O}_4(\text{OH})_n^{n-}$  and  $\text{Os}^{\text{VI}}\text{O}_2(\text{OH})_4^{2-}$ .

We recommend that Mayer *et al.*<sup>8</sup> and all other reported studies<sup>17-27</sup> that had previously failed to detect paramagnetic Os<sup>VII</sup> species (which forms due to an Os<sup>VI</sup> & Os<sup>VIII</sup> comproportionation reaction) during the reduction of Os<sup>VIII</sup> to Os<sup>VI</sup>, reinterpret their experimental data in light of the newly acquired information.

The Os<sup>VI</sup> & Os<sup>VIII</sup> comproportionation reaction model that was fitted to the stopped-flow UV-Vis spectroscopy kinetic data is given by equation 8.5. From the non-linear least squares fits obtained, observed rate constants and osmium species' molar extinction coefficients were obtained. The forward (comproportionation) reaction was found to be first order w.r.t. Os<sup>VI</sup> and Os<sup>VIII</sup> concentrations while the reverse (disproportionation) reaction was found to be second order w.r.t. Os<sup>VII</sup> concentration. The good non-linear least squares fits with the experimental data,<sup>8,16,27</sup> the linearity of the obtained Eyring plots and the good agreement of extinction coefficients with that reported in the literature validated the reaction model, equation 8.5. Activation energies for both comproportionation ( $\Delta^\ddagger H^\circ_{(obs)} = 10.3 \pm 0.5 \text{ kcal.mol}^{-1}$ ,  $\Delta^\ddagger S^\circ_{(obs)} = -2.6 \pm 1.6 \text{ cal.mol}^{-1}.\text{K}^{-1}$ ,  $\Delta^\ddagger G^\circ_{(obs)} = 11.1 \pm 0.9 \text{ kcal.mol}^{-1}$ ) and disproportionation ( $\Delta^\ddagger H^\circ_{(obs)} = -6.7 \pm 1.0 \text{ kcal.mol}^{-1}$ ,  $\Delta^\ddagger S^\circ_{(obs)} = -63.6 \pm 3.4 \text{ cal.mol}^{-1}.\text{K}^{-1}$ ,  $\Delta^\ddagger G^\circ_{(obs)} = 12.2 \pm 2.0 \text{ kcal.mol}^{-1}$ ) reactions at 298.15 K were subsequently determined using the Eyring plot data, *i.e.* slopes and intercepts. In contrast to what was expected, we found a negative enthalpy of activation for the Os<sup>VII</sup> & Os<sup>VII</sup> disproportionation reaction.

According to our van't Hoff plot analysis, the observed  $\Delta H^\circ_{rxn(obs)}$ ,  $\Delta S^\circ_{rxn(obs)}$  and  $\Delta G^\circ_{rxn(obs)}$  values of the Os<sup>VI</sup> & Os<sup>VIII</sup> comproportionation reaction at 298.15 K are  $17.1 \pm 1.2 \text{ kcal.mol}^{-1}$ ,  $61.0 \pm 4.3 \text{ cal.mol}^{-1}.\text{K}^{-1}$  and  $-1.1 \pm 2.5 \text{ kcal.mol}^{-1}$ , respectively. These energies compared well with DFT-calculated energies (in the simulated aqueous phase only) when taking into consideration the energy differences between the reactant and product species that are lowest in Gibbs energy to describe the reaction, *i.e.* *cis*- $[\text{Os}^{\text{VIII}}\text{O}_4(\text{OH})_2]^{2-}$  and *trans*- $[\text{Os}^{\text{VI}}\text{O}_2(\text{OH})_4]^{2-}$

as the ('starting') reactants and two *trans*-[Os<sup>VII</sup>O<sub>3</sub>(OH)<sub>2</sub>]<sup>-</sup> and two hydroxide anions as the ('final') products, equation 8.6. For example, PBE yielded values for  $\Delta H^\circ_{rxn}$ ,  $\Delta S^\circ_{rxn}$  and  $\Delta G^\circ_{rxn}$  of 21.13 kcal.mol<sup>-1</sup>, 71.06 cal.mol<sup>-1</sup>.K<sup>-1</sup> and -0.06 kcal.mol<sup>-1</sup>, respectively. Apart from LDA, all other functionals consistently yielded that reaction 8.6 is the thermodynamically favoured Os<sup>VI</sup> & Os<sup>VIII</sup> comproportionation reaction in the simulated aqueous phase and with similar standard reaction energies, as those for PBE (above), were obtained.

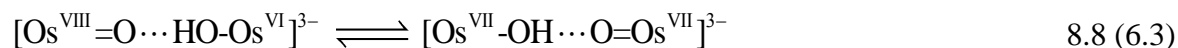
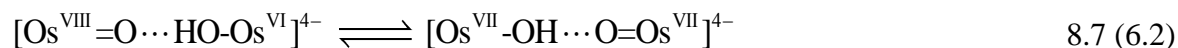


Moreover, the  $\Delta G^\circ_{rxn(obs)}$  value obtained in our study is in excellent agreement with the Gerber *et al.*<sup>16</sup> reported  $\Delta G^\circ_{rxn}$  at 298.15 K, at approximately -1.3 kcal.mol<sup>-1</sup>.

In order to probe the mechanism of reaction 8.6, we performed a stopped-flow UV-Vis spectroscopy kinetics experiment in a 2.0 M NaOH aqueous solution with a solvent composition, by volume, of D<sub>2</sub>O:H<sub>2</sub>O in a 1:1 ratio, at 294.5 K. The reaction that contained the partially deuterated solutions reached equilibrium in a longer period of time compared to the non-deuterated (control), *i.e.* essentially 'protonated', solutions. The kinetic isotope effect (KIE) for the forward and reverse reactions is approximately 1.1 and provided evidence that the rate-determining step of the Os<sup>VI</sup> & Os<sup>VIII</sup> comproportionation reaction coincides with a proton transfer (PT) event and that PT from Os<sup>VI</sup> to Os<sup>VIII</sup> and from Os<sup>VII</sup> to Os<sup>VII</sup> most probably does occur.

The mechanism of the Os<sup>VI</sup> & Os<sup>VIII</sup> comproportionation reaction was subsequently investigated with DFT. Since a solution of Os<sup>VIII</sup> in a 2.0 M NaOH aqueous matrix at 298.15 K contains two abundant Os<sup>VIII</sup> oxo/hydroxido species (both species have *d*<sup>0</sup> electron configuration), equation 8.2, two competing reaction pathways were investigated; one where *cis*-[Os<sup>VIII</sup>O<sub>4</sub>(OH)<sub>2</sub>]<sup>2-</sup> reacts with *trans*-[Os<sup>VI</sup>O<sub>2</sub>(OH)<sub>4</sub>]<sup>2-</sup>, the other where [Os<sup>VIII</sup>O<sub>4</sub>(OH)]<sup>-</sup> reacts with *trans*-[Os<sup>VI</sup>O<sub>2</sub>(OH)<sub>4</sub>]<sup>2-</sup>. Both reaction pathways were found to consist of (i) the formation of a (singlet state) non-covalent dimer, [Os<sup>VIII</sup>=O...HO-Os<sup>VI</sup>]<sup>4-</sup> or [Os<sup>VIII</sup>=O...HO-Os<sup>VI</sup>]<sup>3-</sup>, (ii) 'spin-forbidden', concerted electron-proton transfer (EPT)<sup>28</sup> from the Os<sup>VIII</sup> monomer to the *trans*-[Os<sup>VI</sup>O<sub>2</sub>(OH)<sub>4</sub>]<sup>2-</sup> monomer to form a second (triplet state) non-covalent dimer, [Os<sup>VII</sup>-OH...O=Os<sup>VII</sup>]<sup>4-</sup> or [Os<sup>VII</sup>-OH...O=Os<sup>VII</sup>]<sup>3-</sup>, (iii) separation of the Os<sup>VII</sup> monomers and ultimately (iv) interconversion of the separated species to form a combination of the *trans*-[Os<sup>VII</sup>O<sub>3</sub>(OH)<sub>2</sub>]<sup>-</sup> and *mer*-[Os<sup>VII</sup>O<sub>3</sub>(OH)<sub>3</sub>]<sup>2-</sup> stereoisomers. EPT<sup>28</sup> from the Os<sup>VIII</sup> monomer to the Os<sup>VI</sup> monomer was found to be, in both cases, the rate-determining step of

the comproportionation reaction for each pathway, and corroborated the experimental evidence (KIE) that the rate-determining step involves the transfer of a proton, equations 8.7 and 8.8.



Furthermore, a series of linear transit calculations provided compelling evidence that neither PT nor electron transfer (ET) sequential pathway steps occur directly after the formation of the initial non-covalent dimers, *i.e.* for comproportionation or disproportionation. Moreover, sequential proton-coupled electron transfer (PCET)<sup>28</sup> pathways, *i.e.* ET-PT and PT-ET, were found to be energetically unfavourable in comparison with EPT<sup>28</sup> and the comparison with the experimental activation reaction enthalpy and entropy values was poor.

A direct comparison between the two DFT-calculated, EPT<sup>28</sup> reaction pathways yields that the activation energy for the ‘five-coordinate’ pathway, *i.e.* where  $[\text{Os}^{\text{VIII}}\text{O}_4(\text{OH})]^-$  reacts with *trans*- $[\text{Os}^{\text{VI}}\text{O}_2(\text{OH})_4]^{2-}$ , to be approximately 2.0 kcal.mol<sup>-1</sup> (for five different functionals) lower in magnitude than for the ‘six-coordinate’ pathway, *i.e.* where *cis*- $[\text{Os}^{\text{VIII}}\text{O}_4(\text{OH})_2]^{2-}$  reacts with *trans*- $[\text{Os}^{\text{VI}}\text{O}_2(\text{OH})_4]^{2-}$ . For the ‘six-coordinate’ pathway,  $\Delta^\ddagger H^\circ$ ,  $\Delta^\ddagger S^\circ$  and  $\Delta^\ddagger G^\circ$  (PBE-D3 functional) for the forward (comproportionation) reaction are equal to 2.8 kcal.mol<sup>-1</sup>, -45.0 cal.mol<sup>-1</sup>.K<sup>-1</sup> and 16.2 kcal.mol<sup>-1</sup>, respectively, and for the reverse (disproportionation) reaction are equal to -20.3 kcal.mol<sup>-1</sup>, -115.9 cal.mol<sup>-1</sup>.K<sup>-1</sup> and 14.3 kcal.mol<sup>-1</sup>, respectively. By contrast, for the ‘five-coordinate’ pathway,  $\Delta^\ddagger H^\circ$ ,  $\Delta^\ddagger S^\circ$  and  $\Delta^\ddagger G^\circ$  (PBE-D3 functional) for the forward (comproportionation) reaction are equal to 11.3 kcal.mol<sup>-1</sup>, -9.8 cal.mol<sup>-1</sup>.K<sup>-1</sup> and 14.2 kcal.mol<sup>-1</sup>, respectively, and for the reverse (disproportionation) reaction are equal to -11.8 kcal.mol<sup>-1</sup>, -80.7 cal.mol<sup>-1</sup>.K<sup>-1</sup> and 12.3 kcal.mol<sup>-1</sup>, respectively. While both pathways yield negative activation enthalpy values for the Os<sup>VII</sup> & Os<sup>VII</sup> disproportionation reaction, the agreement with experimental data for all six activation energy parameters is better for the ‘five-coordinate’ pathway. The overall enthalpy change of the MECF relative to the ‘final’ products is negative, due to the extensive intermolecular hydrogen bonding interactions of the MECF (which are absent for the ‘final’ products) which lowers the electronic energy, w.r.t. the ‘final’ products on the potential energy surface. The results of the DFT calculations lead us to conclude that ‘five-coordinate’

and ‘six-coordinate’ EPT<sup>28</sup> pathways are more probable than any one of the four identified sequential pathways.

If the concentrations of all the reactant species are chosen as the standard state, the ‘five-coordinate’ pathway will be the dominant mechanism, specifically due its comparatively lower Gibbs activation energy. However, the concentration of the *cis*-[Os<sup>VII</sup>O<sub>3</sub>(OH)<sub>2</sub>]<sup>-</sup> species, which features in the ‘five-coordinate’ pathway only, is considerably lower (by approximately 1200 times) than the concentration of the *mer*-[Os<sup>VII</sup>O<sub>3</sub>(OH)<sub>3</sub>]<sup>2-</sup> species (both the *mer*-[Os<sup>VII</sup>O<sub>3</sub>(OH)<sub>3</sub>]<sup>2-</sup> and *trans*-[Os<sup>VII</sup>O<sub>3</sub>(OH)<sub>2</sub>]<sup>-</sup> species feature in both pathways). Although the ‘five-coordinate’ pathway was found to have a lower activation energy barrier, the low concentration of the *cis*-[Os<sup>VII</sup>O<sub>3</sub>(OH)<sub>2</sub>]<sup>-</sup> species could be significant enough such that the ‘six-coordinate’ pathway dominates comproportionation. However, the good agreement of DFT-calculated activation energy parameters for the ‘five-coordinate’ pathway in comparison with our Eyring plot analyses values (above), indicates that the relatively low concentration of the *cis*-[Os<sup>VII</sup>O<sub>3</sub>(OH)<sub>2</sub>]<sup>-</sup> species in comparison with the *mer*-[Os<sup>VII</sup>O<sub>3</sub>(OH)<sub>3</sub>]<sup>2-</sup> species is probably not low enough such that the ‘six-coordinate’ pathway dominates comproportionation. Therefore, the ‘five-coordinate’ EPT<sup>28</sup> pathway most probably dominates Os<sup>VI</sup> & Os<sup>VIII</sup> comproportionation and Os<sup>VII</sup> & Os<sup>VII</sup> disproportionation in a 2.0 M NaOH aqueous matrix.

Initially, the experimental kinetic and equilibrium analysis of the Os<sup>VI</sup> & Os<sup>VIII</sup> comproportionation reaction did not take into account which particular Os<sup>VIII</sup> species reacts with *trans*-[Os<sup>VI</sup>O<sub>2</sub>(OH)<sub>4</sub>]<sup>2-</sup> and neither was the “identity” or stereochemistry of the Os<sup>VII</sup> product species, *i.e.* five-coordinate or six-coordinate, taken into account. However, when we took into consideration the Os<sup>VIII</sup> species that actually participates ‘directly’ in the comproportionation reaction, pathway 2 in Chapter 6, we illustrated how the original reaction model, equation 8.5, and corresponding rate laws, is recovered. After correcting for the observed rate constants and observed thermodynamic parameters from stopped-flow UV-Vis spectroscopy kinetics experiments, we saw that the ‘true’ thermodynamic parameters are close in magnitude with the observed thermodynamic parameters. The assumptions that Os<sup>VIII</sup> and Os<sup>VII</sup> coordination sphere expansion/contraction reactions are at equilibrium while the Os<sup>VI</sup> & Os<sup>VIII</sup> comproportionation reaction progresses, was further validated by a set of numerical experiments where the osmium species’ conc. vs. time profiles of the comproportionation reaction were monitored while systematically decreasing the rate constants,  $k_2$  &  $k_{-2}$ , of the Os<sup>VIII</sup> coordination sphere expansion/contraction reaction; only

when the Os<sup>VIII</sup> coordination sphere expansion/contraction reaction rate constants were decreased by approximately 10 000 times in magnitude, are visible difference noticed for the osmium species' conc. vs. time profiles of the comproportionation reaction.

The Os<sup>VIII</sup>, Os<sup>VI</sup> and Os<sup>VII</sup> speciation data, in conjunction with the results obtained for the Os<sup>VI</sup> & Os<sup>VIII</sup> comproportionation reaction in basic aqueous solutions brings us to the third main theme for this PhD project, *i.e.* the study of the reduction of Os<sup>VIII</sup> with methanol:

(iii) Spectroscopic and DFT speciation study of the kinetics, thermodynamics and reaction mechanism pertaining to the reduction of Os<sup>VIII</sup> oxo/hydroxido species with methanol in basic aqueous media (Chapter 7).

The information gathered for the Os<sup>VIII</sup>, Os<sup>VI</sup> and Os<sup>VII</sup> speciation and Os<sup>VI</sup> & Os<sup>VIII</sup> comproportionation reaction then allowed for the investigation of Os<sup>VIII</sup> reduction with methanol, equation 8.9.



The reaction model that was fitted to the UV-Vis spectroscopy kinetic data of the Os<sup>VIII</sup> reduction with methanol and Os<sup>VI</sup> & Os<sup>VIII</sup> comproportionation reactions is given by equations 8.5 and 8.9. The non-linear least squares fits calculations yielded observed rate constants for reactions 8.5 and 8.9 and osmium species' molar extinction coefficients. The comproportionation (forward) reaction was confirmed to be first order w.r.t. Os<sup>VI</sup> and Os<sup>VIII</sup> concentrations while the disproportionation (reverse) reaction was confirmed to be second order w.r.t. Os<sup>VII</sup> concentration. The good non-linear least squares fits obtained, linearity of the obtained Eyring plots and the good agreement of extinction coefficients with that reported in the literature<sup>8,16,27</sup> validated the reaction model, equations 8.5 and 8.9. The rate constant of Os<sup>VIII</sup> reduction with methanol (CH<sub>3</sub>OH),  $k_{13(\text{H})}$ , at 298.15 K, was found to be  $3.2 \times 10^{-1} \text{ M}^{-1} \cdot \text{s}^{-1}$ , and is in excellent agreement with the Gerber *et al.*<sup>16</sup> reported literature value of  $2.9 \times 10^{-1} \text{ M}^{-1} \cdot \text{s}^{-1}$ . Good agreement of the standard reaction Gibbs free energy ( $\Delta G^\circ_{rxn(\text{obs})} = -1.2 \pm 0.3 \text{ kcal} \cdot \text{mol}^{-1}$ ) for the reversible comproportionation reaction, equation 8.5, with that reported by Gerber *et al.*<sup>16</sup> and the stopped-flow UV-Vis spectroscopy kinetics experiments was obtained. Furthermore, the reduction of Os<sup>VIII</sup> with methanol (CH<sub>3</sub>OH or CD<sub>3</sub>OD) was found to be first order w.r.t. Os<sup>VIII</sup> and methanol concentrations, thereby corroborating the literature.<sup>8,16-27</sup>

According to our Eyring plot analysis, the activation enthalpy, entropy and Gibbs free energies of reaction 8.9 at 298.15 K when CH<sub>3</sub>OH is utilised as the reducing agent are  $14.4 \pm 1.2$  kcal.mol<sup>-1</sup>,  $-12.5 \pm 4.1$  cal.mol<sup>-1</sup>.K<sup>-1</sup> and  $18.1 \pm 2.4$  kcal.mol<sup>-1</sup>, respectively. When CH<sub>3</sub>OH is replaced by CD<sub>3</sub>OH as the reducing agent, the rate constant,  $k_{13}$ , decreases by approximately an order of magnitude in the investigated temperature range. Moreover, parallel Eyring plots were obtained for the two experiments (above) which indicated that the UV-Vis data was reliable and accurate, and that the reaction model used to simulate the kinetic traces, equations 8.5 & 8.9, is valid. The activation enthalpy, entropy and Gibbs free energies of reaction 8.9 where CD<sub>3</sub>OH was utilised are  $14.5 \pm 1.3$  kcal.mol<sup>-1</sup>,  $-17.1 \pm 4.4$  cal.mol<sup>-1</sup>.K<sup>-1</sup> and  $19.6 \pm 2.6$  kcal.mol<sup>-1</sup>, which confirmed that the cleavage of an  $\alpha$ -C-H bond in CH<sub>3</sub>OH and the cleavage of an  $\alpha$ -C-D bond in CD<sub>3</sub>OH are the rate-determining step for reaction 8.9. The cleavage of the relatively more labile O-H bond of CH<sub>3</sub>OH or CD<sub>3</sub>OH was thereby confirmed to not be the rate-determining step of reaction 8.9. The difference in Gibbs activation energy for the oxidation of CH<sub>3</sub>OH and CD<sub>3</sub>OH is only 1.5 kcal.mol<sup>-1</sup>, resulting in a reaction rate decrease of approximately 11 times. This result puts into perspective the preference of the ‘five-coordinate’ reaction pathway compared to the ‘six-coordinate’ reaction pathway for the Os<sup>VI</sup> & Os<sup>VIII</sup> comproportionation reaction, equation 8.5, where the difference in Gibbs activation energies is approximately 2.0 kcal.mol<sup>-1</sup>. The relatively large KIE value,  $k_{13(H)}/k_{13(D)}$ , of approximately 11.82 (298.15 K) is indicative of a normal, primary isotope effect. Composite Eyring plots for reaction 8.5 were constructed from four different experiments which yielded linear trends for both the comproportionation and disproportionation reactions. The linearity obtained further validated the stopped-flow UV-Vis spectroscopy kinetics analyses presented in Chapter 4.

DFT studies pertaining to reaction 8.9 were done in the simulated aqueous phase with the PBE-D3 functional. A relatively large negative  $\Delta G^\circ_{rxn}$  of -13.88 kcal.mol<sup>-1</sup> was obtained for reaction 8.9, *i.e.* equilibrium lies far to the right, which provided justification for our decision to simulate the reaction in the UV-Vis spectroscopy kinetics experiments as irreversible. Moreover, the DFT-calculated  $\Delta H^\circ_{rxn}$  and  $\Delta S^\circ_{rxn}$  is -13.41 kcal.mol<sup>-1</sup> and 1.57 cal.mol<sup>-1</sup>.K<sup>-1</sup>, respectively.

A reaction mechanism where ET and PT occurs directly from methanol to *cis*-[Os<sup>VIII</sup>O<sub>4</sub>(OH)<sub>2</sub>]<sup>2-</sup> was investigated in which there are no exchanges of protons (or electrons) with the 2.0 M NaOH aqueous matrix. The complete, five-step reaction mechanism for the

reduction of  $cis\text{-}[\text{Os}^{\text{VIII}}\text{O}_4(\text{OH})_2]^{2-}$  with methanol consists of (i) non-covalent dimer formation of the reactants, (ii) hydrogen atom transfer (HAT)<sup>28</sup> of an  $\alpha\text{-C-H}$  bond of  $\text{CH}_3\text{OH}$  to  $cis\text{-}[\text{Os}^{\text{VIII}}\text{O}_4(\text{OH})_2]^{2-}$ , (iii) PT of the O-H hydrogen of  $\text{CH}_2\text{OH}$  to  $mer\text{-}[\text{Os}^{\text{VII}}\text{O}_3(\text{OH})_3]^{2-}$ , (iv) ET from  $\text{CH}_2\text{O}^-$  to  $trans\text{-}[\text{Os}^{\text{VII}}\text{O}_4(\text{OH})_2]^-$ , and (v) separation of the products. The organic and inorganic monomers involved in the reaction mechanism do not separate from one another in between steps (ii) to (iv), but stay bound to one another *via* intermolecular hydrogen bonding interactions in order to firstly, decrease the PT/ET transfer distance between them, and secondly, to avoid the formation of highly energetically unfavourable cationic, anionic or radical monomer species. It was also found that initial O-H HAT<sup>28</sup> from methanol to  $\text{Os}^{\text{VIII}}$  in the non-covalent dimer,  $\text{CH}_3\text{OH}, [cis\text{-}\text{Os}^{\text{VIII}}\text{O}_4(\text{OH})_2]^{2-}$ , is implausible due to the absence of a transition state or MECF to ‘connect’ the PESs of the ‘reactant’ non-covalent dimer (singlet) with the ‘product’ non-covalent dimer (triplet) states. By contrast, a MECF was found for an initial C-H HAT<sup>28</sup> from methanol to  $cis\text{-}[\text{Os}^{\text{VIII}}\text{O}_4(\text{OH})_2]^{2-}$  in the non-covalent dimer in which the overall spin state changes from a singlet to a triplet. The mechanistic study agreed with our experimentally determined result that the rate-determining step of the reaction involves the cleavage of an  $\alpha\text{-C-H}$  bond in  $\text{CH}_3\text{OH}$ . The DFT-calculated activation enthalpy,  $\Delta^\ddagger H^\circ$ , compared relatively well with the experimentally determined value, differing by less than  $5.0 \text{ kcal.mol}^{-1}$ . However, the DFT-calculated activation Gibbs energy,  $\Delta^\ddagger G^\circ$ , differed by approximately  $12 \text{ kcal.mol}^{-1}$  to the experimental results, due to the DFT-calculated  $\Delta^\ddagger S^\circ$  being three times more negative than that obtained from Eyring plot analysis. Overall, the agreement between DFT and experimental thermodynamic activation parameters was not good but also not drastically poor. We identified a few possible reasons for the discrepancies:

- (i) a lower energy pathway which consists of an initial non-covalent dimer with only one intermolecular hydrogen bonding interaction, could be thermodynamically favoured to that found in our investigation,
- (ii) the MECF used as an approximation of the transition state for obtaining DFT-calculated activation energies (Section 1.7.2) is slightly overestimated in this case, or
- (iii) the dominant reaction pathway may involve the other abundant  $\text{Os}^{\text{VIII}}$  species, *i.e.* the five-coordinate  $[\text{Os}^{\text{VIII}}\text{O}_4(\text{OH})]^-$  complex, reacting with methanol.

Based on the preliminary equilibrium geometries of the non-covalent and covalently bonded dimers of  $\text{CH}_3\text{OH}, [\text{Os}^{\text{VIII}}\text{O}_4(\text{OH})]^-$  that were found, we suspect that to eventually identify the most probable reaction pathway may be extremely computationally expensive.

Lastly, if methanol were to reduce the Os<sup>VII</sup> oxo/hydroxido species (*trans*-[Os<sup>VII</sup>O<sub>3</sub>(OH)<sub>2</sub>]<sup>-</sup> or *mer*-[Os<sup>VII</sup>O<sub>3</sub>(OH)<sub>3</sub>]<sup>2-</sup>), an Os<sup>V</sup> (*d*<sup>3</sup>) species and formaldehyde (*e.g.* the transfer of two electrons and two protons), or an Os<sup>VI</sup> species and either a high-energy intermediate methoxy radical or high-energy intermediate hydroxymethyl radical (*e.g.* the transfer of one electron and one proton) will form. However, there is no experimental evidence to support the formation of an Os<sup>V</sup> species. If an Os<sup>V</sup> species were present in solution, Figures 7.1, 7.5 and 7.6, the calculated molar extinction coefficients for the Os<sup>VI</sup>, Os<sup>VII</sup> and Os<sup>VIII</sup> species would have compared poorly with reported values.<sup>8,16,27</sup> Moreover, the reaction model used to simulate the kinetic traces, equations 7.1 & 7.2, would have been invalidated if an Os<sup>V</sup> species were present as non-linear Eyring plots would have been obtained. Methanol does not reduce Os<sup>VII</sup> oxo/hydroxido species because such hypothetical reaction pathways will result in the formation of either high-energy intermediate radical species or an Os<sup>V</sup> species, for which there is no evidence. We therefore envisage that Os<sup>VII</sup> oxo/hydroxido species would not be catalytically active in cases where the reducing agent transfers two electrons. However, in cases where the reducing agent transfers only one electron, *e.g.* benzaldehyde {with [Ru<sup>IV</sup>(bpy)<sub>2</sub>(py)(O)]<sup>2+</sup>}<sup>28</sup>, we expect that an Os<sup>VII</sup> species may be catalytically active.



**References**

1. A. H. Éll, A. Closson, H. Adolfsson and J.-E. Bäckvall, *Adv. Synth. Catal.*, 2003, **345**, 1012.
2. S. M. Desai, N. N. Halligudi and S. T. Nandibewoor, *Int. J. Chem. Kinet.*, 1999, **31**, 583.
3. N. P. Shetti, R. R. Hosamani and S. T. Nandibewoor, *Research Letters in Inorganic Chemistry*, 2008, 216058.
4. K. Byadagi, M. Meti, S. Nandibewoor and S. Chimatadar, *Ind. Eng. Chem. Res.*, 2013, **52**, 9011.
5. M. P. Singh, H. S. Singh, M. C. Gangwar, P. Thakur and A. K. Singh, *P. Indian Acad. Sci. A.*, 1975, 41.
6. Z. M. Galbács, A. Zsednai and L. J. Csányi, *Transition Met. Chem.*, 1983, **8**, 328.
7. W. P. Griffith, *The Chemistry of the Rarer Platinum Metals (Os, Ru, Ir & Rh)*, Chapter 3, Interscience, 1967.
8. A. Dehestani, W. H. Lam, D. A. Hrovat, E. R. Davidson, W. T. Borden and J. M. Mayer, *J. Am. Chem. Soc.*, 2005, **127**, 3423.
9. B. J. McFadzean, PhD Dissertation, 2008, NMMU, South Africa.
10. R. K. Murmann and C. L. Barnes, *Z. Krist. - New Cryst. St.*, 2002, **217**, 303.
11. L. O. Avtomyan, V. G. Andrianov and M. A. Porai-Kohits, *Zh. Strukt. Khim.*, 1962, **3**, 685.
12. D. F. Evans, *J. Chem. Soc.*, 1959, 2003.
13. J. Löligler and R. Scheffold, *J. Chem. Educ.*, 1972, **49**, 646.
14. T. H. Crawford and J. Swanson, *J. Chem. Educ.*, 1971, **48**, 382.
15. D. F. Evans and T. A. James, *J. Chem. Soc. Dalton Trans.*, 1979, 723.
16. T. E. Geswindt, W. J. Gerber, H. E. Rohwer and K. R. Koch, *Dalton Trans.*, 2011, **40**, 8581.

17. P. VeeraSomaiah, K. B. Reddy, B. Sethuram and T. Navaneeth Rao, *J. Indian Chem. Soc.*, 1988, **27A**, 876.
18. P. VeeraSomaiah, K. B. Reddy, B. Sethuram and T. Navaneeth Rao, *J. Indian Chem. Soc.*, 1989, **66**, 755.
19. H. S. Singh, S. P. Singh, S. M. Singh, R. K. Singh and A. K. Sisodia, *J. Phys. Chem.*, 1975, **79(18)**, 1920.
20. N. P. Singh, V. N. Singh, H. S. Singh and M. P. Singh, *Aust. J. Chem.*, 1970, **23**, 921.
21. V. N. Singh, H. S. Singh and B. B. L. Saxena, *J. Am. Chem. Soc.*, 1969, **91(10)**, 2643.
22. H. S. Singh, *Oxidation of Organic Compounds with Osmium Tetroxide*, in *Organic synthesis by oxidation with metal compounds*, ed. W. J. Mijs and C. R. H. de Jonge, Plenum Press, New York, 1986.
23. N. P. Singh, V.N. Singh and M. P. Singh, *Aust. J. Chem.*, 1968, **21**, 2913.
24. B. Singh, A. K. Singh, M. B. Singh and A. P. Singh, *Tetrahedron*, 1986, **42**, 715.
25. K. K. S. Gupta and B. A. Begum, *Transition Met. Chem.*, 1998, **23**, 295.
26. K. K. S. Gupta and B. A. Begum, *Int. J. Chem. Kinet.*, 1999, **31(7)**, 477.
27. W. P. Griffith and M. Suriaatmaja, *Can. J. Chem.*, 2001, **79**, 598–606.
28. D. R. Weinberg, C. J. Gagliardi, J. F. Hull, C. F. Murphy, C. A. Kent, B. C. Westlake, A. Paul, D. H. Ess, D. G. McCafferty and T. J. Meyer, *Chem. Rev.*, 2012, **112**, 4016.

# APPENDIX

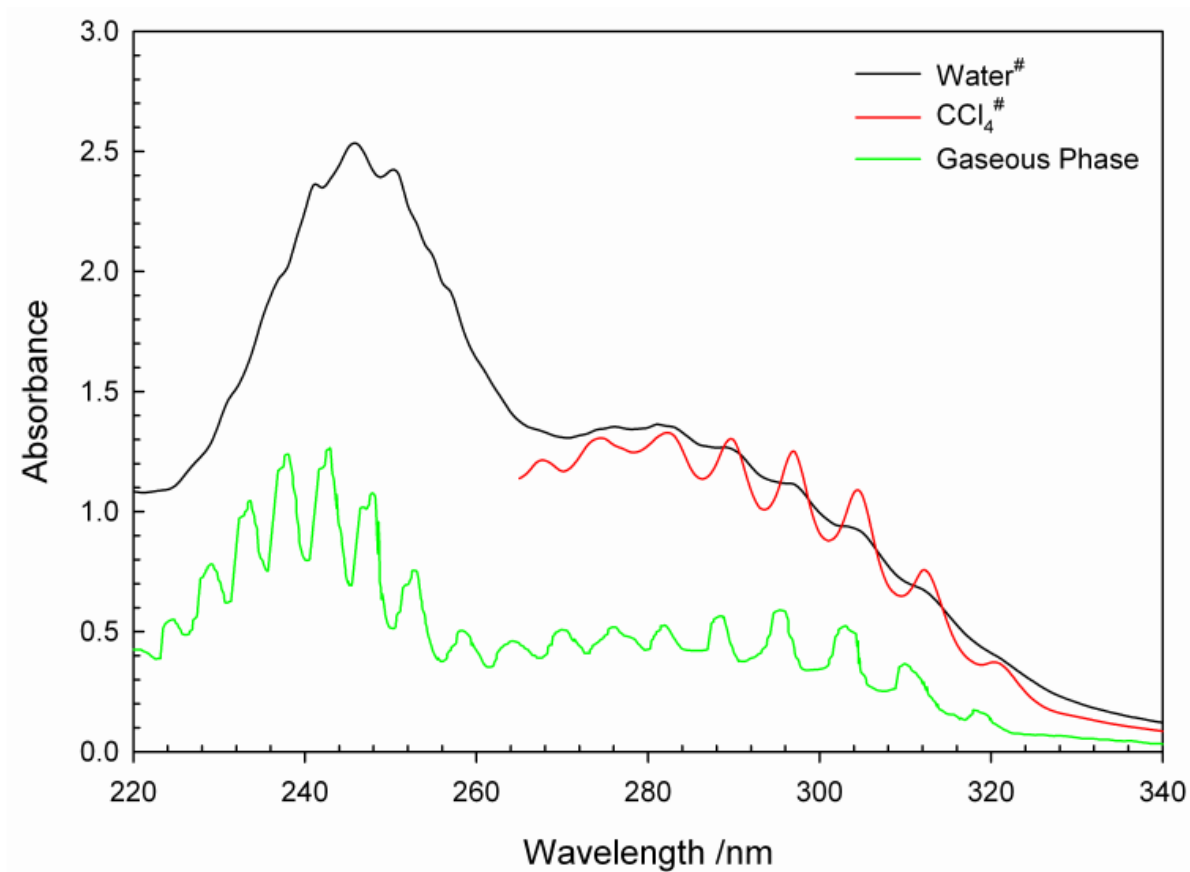


**Figure A.1.** The UV-Vis spectra of  $\text{Os}^{\text{VIII}}\text{O}_4$  in water, carbon tetrachloride ( $\text{CCl}_4$ ) and the gas phase. Reprinted with permission.

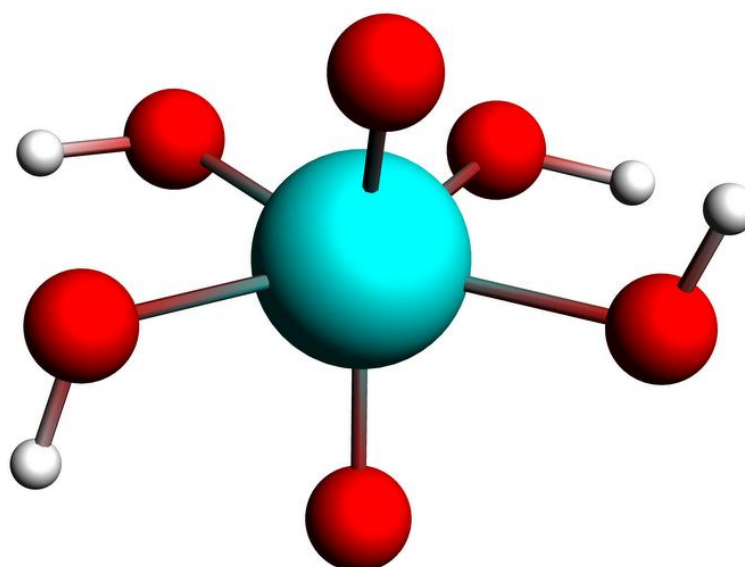


**Figure A.2.** Molecular graph for the equilibrium geometry of  $\text{Os}^{\text{VIII}}\text{O}_2(\text{OH})_4$  in the simulated aqueous phase (COSMO). (PBE functional)

**Table A.1. QTAIM indices computed at the BCPs {PBE-D3(BJ) functional} in the simulated aqueous phase (COSMO). All values are expressed in atomic units.**

Species	BCP #	Atoms	$\lambda_1$	$\lambda_2$	$\lambda_3$	$\rho_b$	$\nabla^2\rho_b$	$G_b$	$G_b/\rho_b$	$V_b$	$E_b^e$
Os <sup>VIII</sup> O <sub>4</sub>	1	Os1 - O2	-0.4491	-0.4491	1.8614	0.2692	0.9631	0.3971	1.4752	-0.5816	-0.1845
	2	Os1 - O3	-0.4491	-0.4491	1.8614	0.2692	0.9631	0.3971	1.4752	-0.5816	-0.1845
	3	Os1 - O4	-0.4491	-0.4491	1.8614	0.2692	0.9631	0.3971	1.4752	-0.5816	-0.1845
	4	Os1 - O5	-0.4491	-0.4491	1.8614	0.2692	0.9631	0.3971	1.4752	-0.5816	-0.1845
[Os <sup>VIII</sup> O <sub>4</sub> (OH)] <sup>-</sup>	1	Os1 - O2	-0.3581	-0.3375	1.5650	0.2227	0.8693	0.3224	1.4476	-0.4473	-0.1249
	2	Os1 - O3	-0.4214	-0.4191	1.7195	0.2535	0.8790	0.3577	1.4112	-0.5203	-0.1626
	3	Os1 - O4	-0.3671	-0.3504	1.6142	0.2286	0.8967	0.3343	1.4629	-0.4655	-0.1312
	4	Os1 - O6	-0.2098	-0.1921	0.8067	0.1366	0.4048	0.1454	1.0640	-0.1965	-0.0511
	5	Os1 - O5	-0.4211	-0.4189	1.7178	0.2533	0.8779	0.3573	1.4102	-0.5197	-0.1625
	6	O6 - H7	-1.8300	-1.8020	1.2741	0.3631	-2.3578	0.0843	0.2323	-0.7582	-0.6738
<i>cis</i> <sub>1</sub> - [Os <sup>VIII</sup> O <sub>4</sub> (OH) <sub>2</sub> ] <sup>2-</sup>	1	Os1 - O2	-0.1352	-0.1243	0.5826	0.1006	0.3231	0.1061	1.0542	-0.1356	-0.0295
	2	Os1 - O3	-0.3695	-0.3666	1.6558	0.2330	0.9197	0.3427	1.4711	-0.4782	-0.1354
	3	Os1 - O4	-0.3702	-0.3670	1.6599	0.2333	0.9227	0.3438	1.4735	-0.4795	-0.1358
	4	Os1 - O5	-0.3503	-0.3357	1.5342	0.2188	0.8482	0.3126	1.4288	-0.4325	-0.1199
	5	Os1 - O6	-0.1364	-0.1252	0.5869	0.1013	0.3253	0.1069	1.0560	-0.1367	-0.0298
	6	Os1 - O7	-0.3641	-0.3481	1.6023	0.2259	0.8901	0.3290	1.4564	-0.4562	-0.1273
	7	O6 - H8	-1.7935	-1.7686	1.3011	0.3684	-2.2611	0.0945	0.2566	-0.7543	-0.6598
	8	O2 - H9	-1.7916	-1.7665	1.3009	0.3684	-2.2572	0.0947	0.2570	-0.7537	-0.6590
<i>cis</i> <sub>2</sub> - [Os <sup>VIII</sup> O <sub>4</sub> (OH) <sub>2</sub> ] <sup>2-</sup>	1	Os1 - O2	-0.1337	-0.1229	0.5752	0.0998	0.3187	0.1047	1.0492	-0.1338	-0.0291
	2	Os1 - O3	-0.3701	-0.3671	1.6580	0.2332	0.9209	0.3432	1.4717	-0.4789	-0.1357
	3	Os1 - O4	-0.3709	-0.3677	1.6615	0.2336	0.9229	0.3441	1.4732	-0.4802	-0.1361
	4	Os1 - O5	-0.3576	-0.3421	1.5693	0.2225	0.8697	0.3210	1.4430	-0.4447	-0.1237
	5	Os1 - O6	-0.1363	-0.1250	0.5858	0.1011	0.3245	0.1067	1.0550	-0.1364	-0.0297
	6	Os1 - O7	-0.3573	-0.3418	1.5684	0.2223	0.8692	0.3208	1.4427	-0.4443	-0.1236
	7	O6 - H8	-1.7929	-1.7683	1.3004	0.3684	-2.2609	0.0944	0.2563	-0.7540	-0.6596
	8	O2 - H9	-1.7918	-1.7669	1.3009	0.3685	-2.2578	0.0946	0.2569	-0.7537	-0.6591

**Table A.2. QTAIM indices computed at the BCPs (PBE functional) in the gas phase. All values are expressed in atomic units.**

Species	BCP #	Atoms	$\lambda_1$	$\lambda_2$	$\lambda_3$	$\rho_b$	$\nabla^2\rho_b$	$G_b$	$G_b/\rho_b$	$V_b$	$E_b^e$
Os <sup>VIII</sup> O <sub>4</sub>	1	Os1 - O2	-0.4501	-0.4501	1.8644	0.2701	0.9641	0.3989	1.4769	-0.5849	-0.1860
	2	Os1 - O3	-0.4501	-0.4501	1.8644	0.2701	0.9641	0.3989	1.4769	-0.5849	-0.1860
	3	Os1 - O4	-0.4501	-0.4501	1.8644	0.2701	0.9641	0.3989	1.4769	-0.5849	-0.1860
	4	Os1 - O5	-0.4501	-0.4501	1.8644	0.2701	0.9641	0.3989	1.4769	-0.5849	-0.1860
[Os <sup>VIII</sup> O <sub>4</sub> (OH)] <sup>+</sup>	1	Os1 - O2	-0.3496	-0.3280	1.5249	0.2185	0.8473	0.3133	1.4335	-0.4337	-0.1204
	2	Os1 - O3	-0.4148	-0.4125	1.6969	0.2508	0.8696	0.3524	1.4050	-0.5115	-0.1591
	3	Os1 - O4	-0.3752	-0.3583	1.6451	0.2327	0.9116	0.3423	1.4709	-0.4783	-0.1361
	4	Os1 - O6	-0.2021	-0.1855	0.7768	0.1334	0.3892	0.1401	1.0505	-0.1894	-0.0493
	5	Os1 - O5	-0.4159	-0.4141	1.7001	0.2514	0.8701	0.3531	1.4048	-0.5130	-0.1598
	6	O6 - H7	-1.8126	-1.7846	1.2886	0.3634	-2.3086	0.0883	0.2429	-0.7537	-0.6654
<i>cis</i> <sub>1</sub> - [Os <sup>VIII</sup> O <sub>4</sub> (OH) <sub>2</sub> ] <sup>2-</sup>	1	Os1 - O2	-0.1238	-0.1130	0.5286	0.0946	0.2919	0.0964	1.0198	-0.1235	-0.0271
	2	Os1 - O3	-0.3592	-0.3559	1.6144	0.2285	0.8994	0.3333	1.4588	-0.4635	-0.1302
	3	Os1 - O4	-0.3590	-0.3558	1.6142	0.2284	0.8994	0.3333	1.4589	-0.4634	-0.1301
	4	Os1 - O5	-0.3269	-0.3134	1.4370	0.2079	0.7967	0.2903	1.3962	-0.3987	-0.1085
	5	Os1 - O6	-0.1227	-0.1121	0.5241	0.0940	0.2893	0.0956	1.0169	-0.1224	-0.0268
	6	Os1 - O7	-0.3724	-0.3558	1.6407	0.2302	0.9126	0.3385	1.4705	-0.4707	-0.1321
	7	O6 - H8	-1.7716	-1.7478	1.3104	0.3682	-2.2090	0.0980	0.2662	-0.7483	-0.6503
	8	O2 - H9	-1.7729	-1.7492	1.3104	0.3682	-2.2117	0.0979	0.2660	-0.7488	-0.6509
<i>cis</i> <sub>2</sub> - [Os <sup>VIII</sup> O <sub>4</sub> (OH) <sub>2</sub> ] <sup>2-</sup>	1	Os1 - O2	-0.1216	-0.1114	0.5163	0.0934	0.2832	0.0939	1.0061	-0.1205	-0.0266
	2	Os1 - O3	-0.3611	-0.3571	1.6190	0.2292	0.9008	0.3343	1.4588	-0.4652	-0.1309
	3	Os1 - O4	-0.3614	-0.3574	1.6195	0.2293	0.9007	0.3344	1.4585	-0.4654	-0.1310
	4	Os1 - O5	-0.3500	-0.3344	1.5439	0.2193	0.8594	0.3154	1.4382	-0.4356	-0.1202
	5	Os1 - O6	-0.1223	-0.1120	0.5191	0.0937	0.2848	0.0944	1.0080	-0.1212	-0.0267
	6	Os1 - O7	-0.3498	-0.3341	1.5428	0.2192	0.8589	0.3152	1.4379	-0.4352	-0.1200
	7	O6 - H8	-1.7786	-1.7550	1.3091	0.3685	-2.2245	0.0972	0.2638	-0.7506	-0.6533
	8	O2 - H9	-1.7779	-1.7544	1.3091	0.3684	-2.2232	0.0972	0.2639	-0.7502	-0.6530

**Table A.3. QTAIM indices computed at the BCPs {PBE-D3(BJ) functional} in the simulated aqueous phase (COSMO). All values are expressed in atomic units.**

Species	BCP #	Atoms	$\lambda_1$	$\lambda_2$	$\lambda_3$	$\rho_b$	$\nabla^2\rho_b$	$G_b$	$G_b/\rho_b$	$V_b$	$E_b^e$
Os <sup>VIII</sup> O <sub>4</sub>	1	Os1 - O2	-0.4470	-0.4470	1.8523	0.2688	0.9584	0.3960	1.4730	-0.5801	-0.1842
	2	Os1 - O3	-0.4470	-0.4470	1.8523	0.2688	0.9584	0.3960	1.4730	-0.5801	-0.1842
	3	Os1 - O4	-0.4470	-0.4470	1.8523	0.2688	0.9584	0.3960	1.4730	-0.5801	-0.1842
	4	Os1 - O5	-0.4470	-0.4470	1.8523	0.2688	0.9584	0.3960	1.4730	-0.5801	-0.1842
[Os <sup>VIII</sup> O <sub>4</sub> (OH)] <sup>+</sup>	1	Os1 - O2	-0.3497	-0.3280	1.5243	0.2185	0.8467	0.3131	1.4330	-0.4335	-0.1204
	2	Os1 - O3	-0.4157	-0.4134	1.6999	0.2512	0.8708	0.3531	1.4058	-0.5127	-0.1596
	3	Os1 - O4	-0.3756	-0.3587	1.6459	0.2328	0.9117	0.3424	1.4708	-0.4787	-0.1362
	4	Os1 - O6	-0.2033	-0.1865	0.7811	0.1339	0.3913	0.1409	1.0521	-0.1906	-0.0497
	5	Os1 - O5	-0.4155	-0.4134	1.6982	0.2511	0.8693	0.3526	1.4044	-0.5122	-0.1595
	6	O6 - H7	-1.8104	-1.7824	1.2878	0.3631	-2.3050	0.0882	0.2429	-0.7527	-0.6645
<i>cis</i> <sub>1</sub> - [Os <sup>VIII</sup> O <sub>4</sub> (OH) <sub>2</sub> ] <sup>2-</sup>	1	Os1 - O2	-0.1235	-0.1129	0.5276	0.0945	0.2913	0.0963	1.0191	-0.1233	-0.0270
	2	Os1 - O3	-0.3595	-0.3564	1.6173	0.2287	0.9015	0.3340	1.4604	-0.4644	-0.1304
	3	Os1 - O4	-0.3602	-0.3570	1.6204	0.2290	0.9032	0.3347	1.4617	-0.4655	-0.1307
	4	Os1 - O5	-0.3263	-0.3128	1.4351	0.2076	0.7959	0.2898	1.3959	-0.3980	-0.1082
	5	Os1 - O6	-0.1260	-0.1150	0.5381	0.0958	0.2971	0.0982	1.0254	-0.1259	-0.0276
	6	Os1 - O7	-0.3720	-0.3555	1.6402	0.2301	0.9127	0.3384	1.4708	-0.4704	-0.1320
	7	O6 - H8	-1.7758	-1.7523	1.3109	0.3684	-2.2172	0.0979	0.2658	-0.7501	-0.6522
	8	O2 - H9	-1.7723	-1.7486	1.3109	0.3683	-2.2100	0.0981	0.2664	-0.7488	-0.6506
<i>cis</i> <sub>2</sub> - [Os <sup>VIII</sup> O <sub>4</sub> (OH) <sub>2</sub> ] <sup>2-</sup>	1	Os1 - O2	-0.1216	-0.1114	0.5162	0.0934	0.2833	0.0940	1.0063	-0.1206	-0.0266
	2	Os1 - O3	-0.3617	-0.3578	1.6229	0.2295	0.9035	0.3352	1.4609	-0.4664	-0.1312
	3	Os1 - O4	-0.3623	-0.3583	1.6244	0.2297	0.9037	0.3356	1.4607	-0.4671	-0.1315
	4	Os1 - O5	-0.3501	-0.3345	1.5441	0.2193	0.8595	0.3154	1.4381	-0.4356	-0.1202
	5	Os1 - O6	-0.1245	-0.1139	0.5286	0.0949	0.2902	0.0962	1.0143	-0.1235	-0.0273
	6	Os1 - O7	-0.3494	-0.3337	1.5411	0.2190	0.8579	0.3148	1.4372	-0.4346	-0.1198
	7	O6 - H8	-1.7838	-1.7604	1.3104	0.3689	-2.2338	0.0973	0.2637	-0.7530	-0.6557
	8	O2 - H9	-1.7801	-1.7567	1.3102	0.3687	-2.2266	0.0974	0.2642	-0.7514	-0.6541

**Table A.4. QTAIM indices computed at the BCPs {PBE-D3(BJ) functional} in the simulated aqueous phase (COSMO). All values are expressed in atomic units.**

Species	BCP #	Atoms	$\lambda_1$	$\lambda_2$	$\lambda_3$	$\rho_b$	$\nabla^2 \rho_b$	$G_b$	$G_b/\rho_b$	$V_b$	$E_b^e$
<i>trans</i> -[Os <sup>VI</sup> -OH] <sup>2-</sup>	1	Os1 - O2	-0.1797	-0.1151	0.8217	0.1302	0.5268	0.1663	1.2772	-0.2093	-0.0430
	2	Os1 - O3	-0.3765	-0.3660	1.7665	0.2304	1.0240	0.3603	1.5641	-0.4896	-0.1292
	3	Os1 - O4	-0.1303	-0.0773	0.5373	0.0959	0.3296	0.1045	1.0896	-0.1309	-0.0264
	4	Os1 - O5	-0.1797	-0.1159	0.8212	0.1302	0.5256	0.1661	1.2752	-0.2092	-0.0431
	5	Os1 - O6	-0.3758	-0.3652	1.7632	0.2300	1.0222	0.3596	1.5631	-0.4884	-0.1289
	6	Os1 - O7	-0.1306	-0.0764	0.5381	0.0960	0.3312	0.1049	1.0917	-0.1312	-0.0264
	7	O4 - H8	-1.7909	-1.7617	1.2995	0.3686	-2.2530	0.0954	0.2588	-0.7540	-0.6586
	8	O7 - H9	-1.7903	-1.7610	1.2996	0.3685	-2.2517	0.0954	0.2589	-0.7538	-0.6583
	9	O2 - H10	-1.7587	-1.7342	1.2761	0.3607	-2.2168	0.0899	0.2493	-0.7341	-0.6441
	10	O5 - H11	-1.7566	-1.7320	1.2749	0.3602	-2.2136	0.0898	0.2493	-0.7330	-0.6432
<i>trans</i> -[Os <sup>VII</sup> -OH] <sup>-</sup>	1	Os3 - O7	-0.1842	-0.1665	0.8579	0.1354	0.5072	0.1660	1.2261	-0.2136	-0.0475
	2	O1 - Os3	-0.3976	-0.3597	1.6377	0.2383	0.8804	0.3391	1.4231	-0.4811	-0.1420
	3	Os3 - O4	-0.3680	-0.3216	1.5071	0.2265	0.8174	0.3123	1.3788	-0.4405	-0.1282
	4	Os3 - O5	-0.1846	-0.1668	0.8597	0.1356	0.5083	0.1664	1.2270	-0.2140	-0.0477
	5	Os3 - O6	-0.4418	-0.4186	1.8284	0.2565	0.9680	0.3798	1.4806	-0.5449	-0.1651
	6	H2 - O7	-1.8169	-1.7949	1.2684	0.3649	-2.3433	0.0867	0.2376	-0.7593	-0.6726
	7	O5 - H8	-1.8164	-1.7945	1.2682	0.3649	-2.3428	0.0867	0.2376	-0.7591	-0.6724
<i>cis</i> -[Os <sup>VII</sup> -OH] <sup>-</sup>	1	Os3 - O7	-0.1644	-0.1535	0.7735	0.1239	0.4555	0.1486	1.1995	-0.1899	-0.0413
	2	Os3 - O8	-0.2247	-0.2084	0.9672	0.1529	0.5342	0.1841	1.2037	-0.2446	-0.0605
	3	Os3 - O4	-0.4485	-0.4409	1.8366	0.2623	0.9473	0.3818	1.4558	-0.5549	-0.1731
	4	Os3 - O6	-0.3778	-0.3494	1.5310	0.2319	0.8038	0.3149	1.3583	-0.4499	-0.1350
	5	Os3 - O5	-0.3383	-0.3051	1.5100	0.2195	0.8666	0.3160	1.4399	-0.4356	-0.1195
	6	H2 - O7	-1.8190	-1.7977	1.2656	0.3641	-2.3511	0.0866	0.2379	-0.7611	-0.6744
	7	H1 - O8	-1.8243	-1.8017	1.2522	0.3602	-2.3739	0.0820	0.2276	-0.7575	-0.6755
<i>mer</i> -[Os <sup>VII</sup> -OH] <sup>-</sup>	1	Os1 - O2	-0.3707	-0.3552	1.6692	0.2276	0.9433	0.3410	1.4987	-0.4689	-0.1278
	2	Os1 - O3	-0.1567	-0.1151	0.6408	0.1103	0.3691	0.1205	1.0927	-0.1542	-0.0337
	3	Os1 - O4	-0.3721	-0.3547	1.6726	0.2277	0.9458	0.3417	1.5008	-0.4697	-0.1280
	4	Os1 - O5	-0.1242	-0.0950	0.5380	0.0939	0.3188	0.1020	1.0865	-0.1281	-0.0260
	5	Os1 - O6	-0.1829	-0.1653	0.8455	0.1343	0.4973	0.1630	1.2139	-0.2100	-0.0470
	6	Os1 - O7	-0.3228	-0.2800	1.4409	0.2099	0.8382	0.2993	1.4259	-0.4080	-0.1087
	7	O3 - H8	-1.8004	-1.7709	1.2956	0.3683	-2.2757	0.0933	0.2533	-0.7555	-0.6622
	8	O6 - H9	-1.7934	-1.7702	1.2720	0.3623	-2.2916	0.0882	0.2436	-0.7494	-0.6611
	9	O5 - H10	-1.7822	-1.7615	1.2995	0.3681	-2.2443	0.0952	0.2586	-0.7514	-0.6562
<i>fac</i> -[Os <sup>VII</sup> -OH] <sup>-</sup>	1	Os1 - O2	-0.1487	-0.1346	0.6618	0.1117	0.3785	0.1239	1.1094	-0.1585	-0.0346
	2	Os1 - O3	-0.1570	-0.1311	0.6451	0.1100	0.3570	0.1185	1.0770	-0.1527	-0.0343
	3	Os1 - O4	-0.3754	-0.3584	1.6369	0.2323	0.9031	0.3366	1.4492	-0.4704	-0.1338
	4	Os1 - O5	-0.1333	-0.1066	0.5871	0.1006	0.3471	0.1117	1.1111	-0.1409	-0.0292
	5	Os1 - O6	-0.3857	-0.3743	1.6949	0.2372	0.9349	0.3492	1.4721	-0.4888	-0.1396
	6	Os1 - O7	-0.3154	-0.2833	1.4410	0.2092	0.8423	0.2999	1.4336	-0.4079	-0.1080
	7	O3 - H8	-1.8155	-1.7893	1.2892	0.3653	-2.3156	0.0917	0.2509	-0.7622	-0.6706
	8	O5 - H9	-1.7859	-1.7643	1.2928	0.3665	-2.2574	0.0941	0.2567	-0.7525	-0.6584
	9	O2 - H10	-1.7912	-1.7658	1.2832	0.3646	-2.2737	0.0914	0.2507	-0.7513	-0.6598

**Table A.5. Calculated standard reaction thermodynamic energies for reaction 5.11.**

XC category	Functional	gas phase			COSMO (aqueous)		
		$\Delta H_{rxn}^{\circ}$ (kcal.mol <sup>-1</sup> )	$\Delta S_{rxn}^{\circ}$ (cal.mol <sup>-1</sup> .K <sup>-1</sup> )	$\Delta G_{rxn}^{\circ}$ (kcal.mol <sup>-1</sup> )	$\Delta H_{rxn}^{\circ}$ (kcal.mol <sup>-1</sup> )	$\Delta S_{rxn}^{\circ}$ (cal.mol <sup>-1</sup> .K <sup>-1</sup> )	$\Delta G_{rxn}^{\circ}$ (kcal.mol <sup>-1</sup> )
LDA	LDA	-31.21	38.81	-42.79	26.25	38.16	14.87
GGA	PBE	-45.92	36.68	-56.85	10.85	36.69	-0.09
	PBE-D	-44.76	35.93	-55.47	12.97	41.72	0.53
	PBE-D3	-45.13	36.59	-56.03	11.91	35.42	1.34
	PBE-D3(BJ)	-44.83	37.31	-55.96	12.36	36.98	1.33
	PBE-dDsC	-44.49	37.39	-55.63	12.68	37.12	1.61
	mPBE	-47.49	36.16	-58.27	8.95	38.97	-2.66
	BLYP	-49.83	35.33	-60.36	6.30	43.53	-6.68
	BLYP-D	-47.40	41.07	-59.64	8.71	44.64	-4.60
	BLYP-D3	-47.71	41.57	-60.10	8.09	43.84	-4.98
	PW91	-44.84	37.49	-56.02	11.70	39.25	0.00
MetaGGA	M06L	-40.51	38.93	-52.11	16.70	28.34	8.24
<b>Experimental <sup>a</sup></b>				<b>17.1 ± 1.2</b>	<b>61.0 ± 4.3</b>	<b>-1.1 ± 2.5</b>	

<sup>a</sup> Observed standard reaction energies obtained from stopped-flow UV-Vis kinetics experiments, Chapter 4.

**Table A.6. Energy decomposition analysis (EDA, kcal.mol<sup>-1</sup>) of the intermolecular interactions in [Os<sup>VIII</sup>=O...HO-Os<sup>VI</sup>]<sup>4+</sup> in various simulated solvents. All energies are with respect to the isolated Os<sup>VIII</sup> and Os<sup>VI</sup> fragments.**

Functional	Solvent (ε)	$\Delta E_{int}$	$\Delta E_{Pauli}$	$\Delta E_{elstat}$	$\Delta E_{orb.}$	$\Delta E_{disp.}$	$\Delta E_{solv.}$
PBE	chloroform (4.8)	-305.32	22.48	189.26	-12.91	-504.15	0.00
	acetonitrile (37.5)	-422.01	48.30	197.80	-14.31	-653.80	0.00
	water (78.39)	-433.10	45.69	199.17	-11.43	-666.53	0.00
	<i>n</i> -methyl-formamide (182.4)	-436.66	53.31	195.89	-15.49	-670.37	0.00
PBE-D	chloroform (4.8)	-309.46	35.57	184.99	-18.40	-507.86	-3.76
	acetonitrile (37.5)	-429.91	63.05	191.15	-19.94	-656.78	-7.39
	water (78.39)	-440.61	62.82	192.04	-17.54	-670.51	-7.42
	<i>n</i> -methyl-formamide (182.4)	-444.14	63.65	191.40	-18.68	-673.07	-7.44
PBE-D3	chloroform (4.8)	-307.40	15.97	190.37	-9.72	-501.97	-2.05
	acetonitrile (37.5)	-426.24	55.60	194.74	-17.18	-655.42	-3.98
	water (78.39)	-437.39	55.97	195.16	-15.11	-669.44	-3.97
	<i>n</i> -methyl-formamide (182.4)	-440.26	56.51	194.79	-16.40	-671.18	-3.98
PBE-D3(BJ)	chloroform (4.8)	-307.28	25.20	188.52	-14.11	-504.83	-2.06
	acetonitrile (37.5)	-425.02	56.48	195.10	-17.90	-655.12	-3.58
	water (78.39)	-435.67	53.43	197.66	-14.36	-668.81	-3.59
	<i>n</i> -methyl-formamide (182.4)	-439.61	56.79	195.37	-16.42	-671.74	-3.61
PBE-dDsC	chloroform (4.8)	-306.65	26.96	187.96	-14.80	-505.59	-1.18
	acetonitrile (37.5)	-424.34	56.84	194.78	-18.07	-655.48	-2.41
	water (78.39)	-435.59	59.89	193.64	-16.67	-670.09	-2.36
	<i>n</i> -methyl-formamide (182.4)	-438.00	55.97	196.44	-16.10	-671.91	-2.40



**Table A.7. Energy decomposition analysis (EDA, kcal.mol<sup>-1</sup>) of the intermolecular interactions in [Os<sup>VIII</sup>=O...HO-Os<sup>VI</sup>]<sup>3-</sup> in various simulated solvents. All energies are with respect to the isolated Os<sup>VIII</sup> and Os<sup>VI</sup> fragments.**

Functional	Solvent ( $\epsilon$ )	$\Delta E_{int}$	$\Delta E_{Pauli}$	$\Delta E_{elstat}$	$\Delta E_{orb.}$	$\Delta E_{disp.}$	$\Delta E_{solv.}$
PBE	chloroform (4.8)	-200.46	39.67	86.65	-23.47	-303.31	0.00
	acetonitrile (37.5)	-271.13	41.96	86.96	-17.93	-382.12	0.00
	water (78.39)	-277.06	41.04	87.75	-16.17	-389.68	0.00
	<i>n</i> -methyl-formamide (182.4)	-279.50	41.65	87.08	-16.99	-391.24	0.00
PBE-D	chloroform (4.8)	-207.78	50.54	81.52	-27.88	-304.52	-7.44
	acetonitrile (37.5)	-278.42	52.05	82.62	-22.04	-383.41	-7.64
	water (78.39)	-284.78	52.60	82.83	-20.53	-391.94	-7.74
	<i>n</i> -methyl-formamide (182.4)	-286.93	52.23	82.81	-20.95	-393.34	-7.68
PBE-D3	chloroform (4.8)	-204.43	40.31	86.67	-23.73	-303.56	-4.12
	acetonitrile (37.5)	-275.22	42.51	86.82	-18.08	-382.30	-4.17
	water (78.39)	-281.06	41.67	87.77	-16.36	-389.97	-4.17
	<i>n</i> -methyl-formamide (182.4)	-283.31	42.38	87.08	-17.41	-391.19	-4.17
PBE-D3(BJ)	chloroform (4.8)	-203.79	40.88	86.28	-23.94	-303.40	-3.61
	acetonitrile (37.5)	-274.37	43.05	86.57	-18.61	-381.69	-3.69
	water (78.39)	-280.68	45.49	85.76	-18.01	-390.17	-3.75
	<i>n</i> -methyl-formamide (182.4)	-282.73	42.60	86.99	-17.45	-391.18	-3.69
PBE-dDsC	chloroform (4.8)	-202.48	41.24	86.07	-23.97	-303.57	-2.25
	acetonitrile (37.5)	-273.17	43.44	86.33	-18.52	-382.14	-2.28
	water (78.39)	-279.44	46.08	85.31	-18.23	-390.29	-2.31
	<i>n</i> -methyl-formamide (182.4)	-281.30	42.74	86.96	-17.41	-391.32	-2.27

**Table A.8. Energy decomposition analysis (EDA, kcal.mol<sup>-1</sup>) of the intermolecular interactions in the Os<sup>VII</sup> non-covalent dimers in the simulated aqueous phase. All energies are with respect to the isolated fragments.**

Non-covalent dimer	Functional	$\Delta E_{int}$	$\Delta E_{Pauli}$	$\Delta E_{elstat}$	$\Delta E_{orb.}$	$\Delta E_{disp.}$	$\Delta E_{solv.}$	$\Delta E_{prep}$	$-D_e$
[Os <sup>VII</sup> -OH...O=Os <sup>VII</sup> ] <sup>4+</sup>	PBE	-430.68	51.39	195.79	-9.40	0.00	-668.46	16.58	-414.10
	PBE-D	-439.37	64.14	191.30	-13.71	-7.38	-673.72	16.44	-422.93
	PBE-D3	-434.91	55.08	194.57	-10.81	-3.91	-669.84	16.52	-418.39
	PBE-D3(BJ)	-434.63	57.84	193.36	-11.96	-3.57	-670.30	16.70	-417.93
	PBE-dDsC	-433.48	58.31	193.16	-12.03	-2.43	-670.49	16.35	-417.13
[Os <sup>VII</sup> -OH...O=Os <sup>VII</sup> ] <sup>3-</sup>	PBE	-280.43	32.31	78.59	-12.69	0.00	-378.64	19.14	-261.29
	PBE-D	-291.21	51.10	73.06	-22.08	-7.52	-385.77	20.72	-270.49
	PBE-D3	-286.53	45.09	75.20	-19.98	-3.89	-382.95	20.67	-265.86
	PBE-D3(BJ)	-284.82	38.33	76.35	-15.99	-3.06	-380.45	19.89	-264.93
	PBE-dDsC	-284.07	39.81	75.70	-16.80	-2.15	-380.63	19.94	-264.13